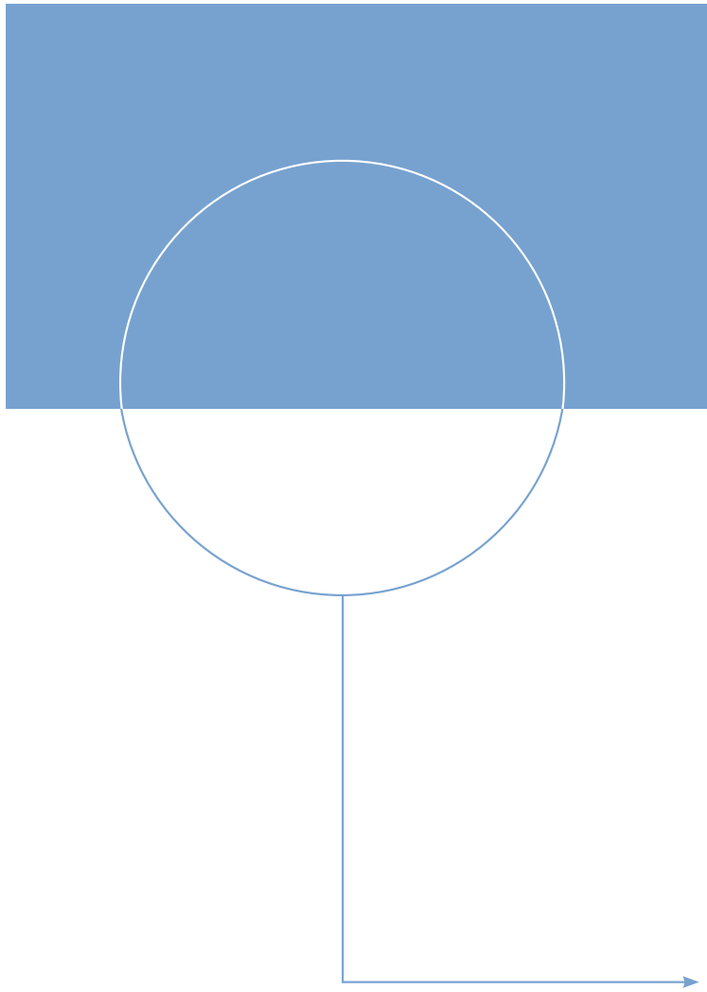

Master's thesis

2020

Anders Meihack

NTNU
Norwegian University of
Science and Technology
Faculty of Engineering
Department of Geoscience and Petroleum

Anders Meihack

Pyroxenite Pegmatites in the Reinfjord Ultramafic Complex

June 2020

NTNU
Norwegian University of
Science and Technology

NTNU
Norwegian University of
Science and Technology

NTNU
Norwegian University of
Science and Technology

Pyroxenite Pegmatites in the Reinfjord Ultramafic Complex

Anders Meihack

Master's thesis in Bedrock and Resource Geology
Submission date: June 2020
Supervisor: Rune Berg-Edland Larsen
Co-supervisor: Bjørn Eske Sørensen

Norwegian University of Science and Technology
Department of Geoscience and Petroleum

Abstract

The genesis of the pyroxenite pegmatites in the Reinfjord Ultramafic Complex (RUC) is examined. The RUC, which forms part of the Seiland Igneous Province (SIP), is a rare example of a well exposed deep crustal ultramafic conduit system, where large volumes of ultramafic, mafic, silicic and alkaline melts have intruded the mid to lower crust. The RUC and SIP are part of a Large Igneous Province (LIP) within the Central Iapetus Magmatic Province (CIMP).

In an endevour to understand the role of the pyroxenite pegmatites in the RUC, a detailed examination is conducted. This examination is assisted by comprehensive petrographical and geochemical study, with further assistance by XRD and EPMA. Large ortho- and clinopyroxene grains (>1 cm) with interstitial growth of pyroxene and olivine are combined with compacted, fine-grained, pyroxene and olivine groundmass. Characteristic poikilitic textures and demixing lamellaes are found in all pyroxenite pegmatite samples.

Few pyroxenite pegmatites in ultramafic to mafic settings have been described. In order to furthering the understanding of pyroxenite pegmatites in such settings, a comparison with the Merensky Reef has therefore been included. Clear similarities, such as large pyroxene grain size (>1 cm) and grain boundary relationships, are present. However, there are distinct differences noted, such as plagioclase content and chromium appearance. Further, there are two distinct pyroxenite pegmatites recognised in the Merensky Reef; normal pyroxenite and pegmatitic pyroxenite. This study identifies only one pyroxenite pegmatite type. Lastly, pluming (high R-factor) plays a bigger role in the Merensky Reef as opposed to fountaining (low R-factor) in the RUC.

The pyroxenite pegmatites have formed from a number of recharge events. It is proposed here that an initial injection of picritic melt was followed by a magmatic injection of pyroxenite-forming melt, possibly combined with carbonate-rich melt of lamproitic composition. This was followed by a recharge event, mixing with pre-existing melts. Ortho- and clinopyroxene would be stable and create large crystals, possibly ensued by increasing P/T conditions leading up to the next recharge event. New magmatic recharge by hotter pyroxenite-forming melt and relatively rapid crystal growth, which have later been recrystallised, is shown by triple junctions. Chromitite, followed by orthopyroxene, would have crystallised at some stage following this. Pyroxenes and olivine possibly grew simulatenously at different nucleation rates, causing the poikilitic textures, though at which stage in the sequence is uncertain. A lack of amphibole, biotite and plagioclase suggest water content was low to absent during the formation. Additionally, a lack of carbonates suggests pyroxenites were poor in volatiles. Annealing of pre-existing pyroxene, olivine and trace minerals ensued prior to the last melt injection. This was initially olivine saturated and reacted with Upper Layered Series (ULS) cumulates to form replacive dunite and completing the melt sequence.
Pyroxene classification, compared with previous recordings, suggest that the pyroxenite-forming melts was more evolved than the pre-existing melts that formed ULS and CS. Lastly, this study finds that the pyroxenite pegmatites play a minor role in the formation of the Ni-Cu-PGE reefs, compared to role played by wehrlite and dunite.

The proposed genetic model is based on the pyroxenite pegmatites from the Upper Layered Series and does not take into consideration the pyroxenite pegmatites at the gabbronorite-wehrlite boundaries.

Sammendrag

Genesen til pyroksenitt pegmatittene i Reinfjord Ultramafiske Kompleks (RUK) er undersøkt. RUK, som utgjør en del av Seiland Magmatiske Provins (SIP), er et sjeldent eksempel på utmerket eksponering av et magmatisk røranleggssystem hvor store mengder av ultramafiske til mafiske, karbonate og alkaliske smelter gjennomtrengte den midtre til nedre delen av jordskorpen. RUK og SIP utgjør en del av en stor magmatisk provins (LIP), som er en del av den sentrale Iapetus magmatiske provins (CIMP).

I et forsøk på å forstå rollen til pyroksenitt pegmatittene i RUK, vil en detaljert undersøkelse bli gjennomført. Denne undersøkelsen assisteres av omfattende petrografisk og geokjemisk studie, med ytterligere assistanse av XRD og EPMA.
Store orto- og klinopyroksen (>1 cm) med internvekst av pyroksen og olivin er kombinert med komprimert, fin-kornet, pyroksen og olivin grunnmasse. Karakteristiske poikilittiske strukturer og demikserende lamellaer finnes i alle pyroksenitt pegmatittene.

Få pyroksen pegmatitter i ultramafisk til mafisk omgivelser er beskrevet. For å fremme forståelsen av pyroksenitt pegmatitter i disse omgivelser, har derfor en sammenligning med Merensky revet blitt inkludert. Klare sammenligninger, som pyroksenstørrelse og korngrenseforhold, er tydelige. Imidlertid er det tydelig forskjell med plagioklas innhold og krom strukturer. Videre er det to distinkte pyroksenitt pegmatitter i Merensky revet; normal pyroksenitt og pegmatitisk pyroksenitt. Denne studien identifiserer kun en type pyroksenitt pegmatitt. Til slutt spiller pluming (høy R-faktor) en større rolle i Merensky revet i motsetning til fontenene (lav R-faktor) i RUK.

Pyroksenitt pegmatittene har blitt dannet fra en rekke magmatiske injeksjonsbegivenheter. Det foreslås her at en innledende injeksjon av pikritisk smelte ble etterfulgt av en magmatisk injeksjon av pyroksenitt-dannede smelte, muligens kombinert med karbonatrik smelte av lamproittisk sammensetning. Dette ble fulgt av en ny injeksjon, som blandet seg med eksisterende smelter. Orto- og klinopyroksen vil ha vært i et stabilt system til å danne store krystaller, muligens etterfulgt av økende P/T forhold frem til neste injeksjon. En ny magmatisk injeksjon med varmere pyroksenitt-dannede smelter og relativ rask krystallvekst følger, som senere er blitt omkrystallisert, vist ved trippelkryss. Kromitt, etterfulgt av ortopyroksen, vil ha krystallisert på et uvisst tidspunkt etter dette. Pyroksener og olivin vokste muligens samtidig med forskjellige kjerneinnholdshastigheter, noe som forårsaket de poikilitiske strukturene, men på hvilke stadium i sekvensen er usikkert. Mangel på amfibol, biotitt og plagioklas antyder at vanninnholdet var lavt eller fraværende under dannelsen. I tillegg antyder mangel på karbonater at pyroksenittene var fattige på volatiler. Annealing av eksisterende pyroksen, olivin og sporminerаler fulgte før den siste smelte injeksjonen. De siste smeltene ble opprinnelig mettet med olivin og reagerte med Upper Layered Series (ULS) kumulater som dannet erstattende dunitt og fullførte smeltesekvensen.
Pyroksen klassifisering, sammenliknet med tidligere studier, foreslår at den pyroksen-dannede smelten var mer utviklet enn den foregående smelten som dannet ULS og CS. Til slutt finner studien at pyroksenitt pegmatittene spiller en mindre rolle i dannelsen av Ni-Cu-PGE rev, sammenliknet med rollen fra wehrlitt og dunitt.

Den foreslåtte genetiske modellen er basert på pyroksenitt pegmatitter fra Upper Layered Series, og tar ikke hensyn til pyroksenitt pegmatittene ved gabbronoritt-wehrlitt grensene.

Acknowledegments

This thesis concludes my Master of Science in Bedrock and Resource at the Norwegian University of Technology (NTNU). It has been 2 years that have flown by and I have grown both on a personal and professional level and made life-long friendships. My insecurities as a geologist from doing a BSc has dissolved after attending NTNU and learning from experts in the field. For that I am very grateful, and I look forward to continuing growing and always seek to evolve in the professional work force, knowing I have received the best possible education.

I would like to thank my Supervisor Rune Berg-Edland Larsen for all your help and incredible knowledge. It is truly fun and exciting to learn from you and I have enjoyed every second of the classes you taught as well as field trips. Although we have two accents that people struggle to understand, we have somehow grown to be able to communicate quite nicely!

Kjetil Eriksen, thank you for all your help and assistance in both thin section preparation and SEM setup. You always made yourself available to help which is greatly appreciated. Kristian Drivenes, thank you for your in-depth knowledge with EPMA and always making yourself available to help. Additionally, your great sense of humour makes any day better in addition to the music you produce!

I would like to thank my mother-in-law to be, Julie Lawrence, for her patience in going over the grammar. When I word-vomit it can be quite a challenge to fix the sentences and make them understandable! I really appreciate your help and owe you both a lovely meal and cold pint next time I see you in Australia.

Tamsin, my fiancé, has managed to stick with me despite my mood swings and that particularly saw its awful daylight this spring when I accepted a full-time job offer in addition to completing my thesis. I tend to make life difficult for myself and fill up a calendar that is already full, so I hope you know what you are signing up for by spending your life with me. I appreciate your help, support and patience.

I would also like to thank my mother for hosting me for two months while I was flying back and forth between Stavanger and Trondheim more than I was doing food shopping. Your dinners and support for my writing is just one of many examples why you are the best possible mother a son could want. My good friend Jarle Lycke Austbø have shown great patience in helping me with the technical aspects in the thesis, a process where I tend to lose patience very quickly.

Lastly, I would like to thank Oddmund Hansen for hosting us in Reinfjord and the Reinfjord field crew for a fun and memorable field trip. The accommodation up there was 10/10 and the experience is something I will never forget. Some days can be hard, some days are just lovely, all in all just how it is supposed to be for a field geologist. We do, after all, attend the school of hard knocks.

Dedicated to my late grandfather.

May I someday be half the man you were.

Rest in peace, høvding.

Table of Contents

Abstract v
Sammendrag vi
Acknowledegments vii
List of Figures xii
List of Tables xvi
Abbreviations xviii
1 Introduction 1
1.1 Geological setting 3
1.1.1 Seiland Igneous Province (SIP) 3
1.1.2 The Reinfjord Ultramafic Complex (RUC) 6
1.1.3 P-T conditions in the RUC 14
2 Theory 16
2.1 Igneous rock classification 17
2.2 Partition coefficients and trace element compatibility 18
2.2.1 The R-factor 20
2.3 Elementary concepts of thermodynamics 22
2.4 Irvine Model 24
2.5 Magmatic processes 26
2.5.1 Partial melting and fractional crystallisation as ore-forming processes 26
2.5.2 Concept of magmatic recharge events 26
2.5.3 Fountaining and Pluming 27
2.6 Platinum Group Minerals and PGE deposits 28
2.7 Pyroxenite pegmatite 30
2.8 Geology of similar layered intrusions worldwide 30
2.8.1 Bushveld Complex (South Africa) 30
2.8.2 Norilsk and Talnak (Russia) 32
2.8.3 Jinchuan (China) 33
2.8.4 Great Dyke (Zimbabwe) 34
3 Methodology 35
3.1 Field Methods 36
3.2 Laboratory 37
3.2.1 Sample preparation 37
3.2.2 Thin sections 37
3.2.3 Whole-rock analysis 40
3.3 Analytical methods 40

3.3.1 Optical microscopy 40
3.3.2 X-Ray Diffraction (XRD) 41
3.3.3 Scanning Electron Microscope (SEM) 42
3.3.4 Electron Probe Micro Analyzer (EPMA) 43
3.4 Sources of error 43
3.5 Literature search 44
3.6 Health, safety and environment (HS&E) 44
4 Results 45
4.1 Field observations 46
4.1.1 Upper Layered Series 46
4.1.2 Central Series 48
4.2 Petrography 51
4.2.1 Silicates 51
4.2.2 Sulfides 60
4.2.3 Oxides 63
4.3 Geochemical analysis 65
4.3.1 Bulk-rock chemistry analysis 65
4.3.2 XRD analysis 72
4.4 Pyroxenite pegmatite composition 73
4.4.1 Geochemical analysis 73
4.4.2 Mineralogy and textural characteristics 73
4.4.3 Zonation patterns in pyroxene grains from EPMA analysis 77
4.4.4 Host-rock relationship 82
5 Discussion 86
5.1 Pyroxenite pegmatite genesis 87
5.1.1 Pyroxenite pegmatite in M/UM setting in the RUC – state of the art 87
5.1.2 Formation of pegmatitic textures 89
5.1.3 Formation of the pyroxenite pegmatite 96
5.1.4 Sulfide oversaturation 98
5.1.5 Comparison to drillhole RF-1 99
5.2 Parental melt composition and mantle source 100
5.2.1 Crystallisation sequence 102
5.2.2 Open system behaviour 103
5.3 Pyroxenite pegmatite role in Ni-Cu-PGE ore forming processes 103
5.4 Conceptual emplacement model for pyroxenite pegmatite 104
6 Conclusion 105
7 Recommendations 108

Bibliography 110
Appendices 1
Appendix A Thin Section Scans 2
Appendix B Whole-Rock Analysis 12
Appendix C Normative Calculations From Whole-Rock Analysis 16
Appendix D SEM Analysis Graphs and Tables 42
Appendix E EPMA Analysis Tables 57
Appendix F XRD Analysis 110
Appendix G Geochemical Comparison: Drillhole RF-1 to Pyroxenite Pegmatite 123

List of Figures

Figure 1.1: *Map of the regional geological setting of the Seiland Igneous Province (SIP) from Larsen et. al. (2018)* 4
Figure 1.2: *Geometric 3-D model of the Seiland Igneous Province (Pastore et al., 2016)* 5
Figure 1.3a – f: *Evolution of the ultramafic complexes during the formation of SIP, modelled by Larsen et al. (2018)* 7
Figure 1.4: *Geological map of the RUC created by Grant et al. (2016b) presenting the separate ultramafic intrusive stages* 8
Figure 1.5: *In-field observations of structures in the ULS* 10
Figure 1.6: *Load structure in the ULS disrupting clinopyroxene-wehrlite layering* 11
Figure 1.7: *One of the four, and the largest, putative fountain structure that was discovered in RUC* 12
Figure 1.8: *Summary of the sequence of intrusive stages* 13
Figure 1.9: *Summary of structures in the RUC by Grant et al. (2016b)* 14
Figure 1.10: *P-T loop of the RUC (Larsen at al., 2018).*. 15
Figure 2.1: *QAPF ternary diagram modified from Streckeisen (1974)* 17
Figure 2.2: *Diagram edited from Best (2003) based on data from Shannon (1976)* 19
Figure 2.3: *Nature of igneous processes giving rise to chromite and PGE-base metal sulfide deposits associated with layered mafic intrusions. Diagram from Robb (2005) modified after Naldrett (1997)* 21
Figure 2.4: *Diagram from Robb (2005), edited from Naldrett & von Grünewaldt (1989). Diagram illustrates the effects of a varying R-factor on the concentration of Ni and Pt in an immiscible sulfide fraction in equilibrium with a basaltic magma.* 21
Figure 2.5: *Diagram from Best (2003) showing end-member thermodynamic systems.* .23
Figure 2.6a – d: *A portion of the ternary system Qtz-Ol-Cr from Robb (2005)* 25
Figure 2.7: *A fractionating magma with variable density, with starting composition based on the Bushveld Complex (Robb, 2005).* 27
Figure 2.8: *Two scenarios when new magma is injected in an evolved magma chamber, where a fountain-like and plume-like feature are created. Figure modified from Robb (2005).* 28
Figure 2.9: *Map of the major PGE-deposits known globally. Map from Godel (2015).* 29
Figure 2.10: *Simplified geological map of the Bushveld Complex with Rustenburg Layered Suite stratigraphy (Godel, 2015).* 31
Figure 2.11: *Magma replenishment (Kinnaird et al., 2002).* 32
Figure 2.12: *Model showing the lateral and vertical zonality in contact-metamorphic aureoles of differentiated ultramafic to mafic intrusives in the Norilsk region (Turovtsev, 2002)* 33
Figure 3.1: *Selected sample spots from one of the largest and most prominent pyroxenite pegmatites* 37
Figure 3.2a – b: *Thin section images in PPL and XPL sample AM19-010* 39
Figure 3.3: *Re-calculated Michel-Lévy interference colour chart (Sørensen, 2013).* 41
Figure 3.4: *Schematic showing how incident X-rays are reflected at an angle of 2θ according to Bragg's Law, and diffracted (Touloukian, 1977).* 42
Figure 3.5: *XRD graph example.* 42
Figure 4.1: *Characteristic boundary relationship with pyroxenite pegmatite, wehrlite and replacive dunite.* 47
Figure 4.2: *Overview photo of one of the most prominent pyroxenite pegmatite bodies.* 47

Figure 4.3: *A) Characteristic emplacement of a smaller pyroxenite pegmatite body, S-W of the primary pyroxenite pegmatite body. B) Close-up of 4.2(a). A mafic dyke crosscuts the pegmatitic 'branching', indicating later emplacement.* 48
Figure 4.4: *Characteristic display of the dyke swarms in the northern section of the CS* 49
Figure 4.5: *Characteristic representation of CS outcrop. Magma mixing between olivine-rich and pyroxene-rich melts are abundant throughout.* 50
Figure 4.6: *Overview photo of ULS, CS and Langstrand gabbronorite, covering a large part of the RUC field area* 50
Figure 4.7: *Example of type 1 olivine, described in text, from thin section AM19-008-1.* 52
Figure 4.8: *Type 2 olivine grains with distinct triple junction formation, from thin section AM19-XX.* 52
Figure 4.9: *Example of type 3 olivine in a shear zone appearing as very fine-grained matrix. From thin section AM19-008-1.* 53
Figure 4.10: *Clinopyroxene (XPL) interference colours, from thin section AM19-006-XA* 54
Figure 4.11: *Clinopyroxene (XPL) with interstitial networks of olivine and orthopyroxene, from thin section AM19-006-XB.*.....54
Figure 4.12: *Clinopyroxene with exsolution lamellae and interstitial orthopyroxene growth (XPL), from thin section AM19-006-XB.* 55
Figure 4.13: *Characteristic twinning as seen in most samples, here from thin section AM19-006-XA.* 55
Figure 4.14: *Orthopyroxene with distinct ilmenite lamellae in PPL, from thin section AM19-008-3 (left) and another example in XPL from thin section AM19-008-4 (right).* ..56
Figure 4.15: *Examples of a typical coarse-grained orthopyroxene with a subhedral grain shape (central) and closely packed equigranular grains to the right (XPL). From thin section AM19-008-3..*.....57
Figure 4.16: *Orthopyroxene grains forming triple junction (XPL), from thin section AM19-010.*.....58
Figure 4.17: *EDS image and graph from SEM, where point 3 matches amphibole composition* 59
Figure 4.18: *Examples of chalcopyrite (Ccp) appearance* 60
Figure 4.19: *(Cbn) associated with pyrrhotite (Po). Surrounding host mineral is orthopyroxene. From sample AM19-010.* 61
Figure 4.20: *EDS image of the same grain as Figure 4.18, verifying mineralogy* 61
Figure 4.21: *Typical assemblage of the three most common sulfides, here with one grain being pyrrhotite dominated (top) and one grain being pentlandite dominated (bottom). From sample AM19-006-XB.* 62
Figure 4.22: *Common appearance of chalcocite (Cct) associated with ilmenite (Ilm) from sample AM19-XX.* 63
Figure 4.23: *Ilmenite mostly appears as lamellae in Opx in all samples, in addition to μm – scale grains mostly associated with sulfides.* 64
Figure 4.24: *IUGS ternary classification diagram for Ol-Opx-Cpx, normalised for all 24 ALS samples (Table 8.11), modified from Streckeisen (1974)*.....66
Figure 4.25: *Variation of all samples plotted against normalised primitive mantle (Sun & McDonough, 1989).* 66
Figure 4.26: *Wehrlite and pyroxenite samples combined plotted against normalised primitive mantle (Sun & McDonough, 1989)*.....67
Figure 4.27: *Follow-up to plot in Fig.4.25, with wehrlite samples singled out. Plotted against normalised primitive mantle (Sun & McDonough, 1989).* 67
Figure 4.28: *Follow-up to plot in Fig. 4.26, with pyroxenite pegmatite samples singled out. Plotted against normalised primitive mantle (Sun & McDonough, 1989).* 68

Figure 4.29: *All samples normalised to REE-Chondrite from McDonough & Sun, 1995* ...68
Figure 4.30: *REE – Chondrite normalised (McDonough & Sun, 1995) from pyroxenite and wehrlite samples* ...69
Figure 4.31: *Variation of V vs Cr for all samples* ...69
Figure 4.32: *Sr vs Cr for all samples* ...70
Figure 4.33: *Y vs V for all samples.* ...70
Figure 4.34: *V/Cr plotted against all trace elements for all samples* ...71
Figure 4.35: *Cr wt.% vs Mg/(Mg+Fe) mol% for all pyroxenite samples* ...73
Figure 4.36: *Diopside grains with characteristic interstitial growth of olivine and enstatite appearing parallel to lamellae* ...74
Figure 4.37: *Grain boundary relationship between diopside and enstatite* ...75
Figure 4.38: *Diopside grain with intergrowth of sub-rounded olivine and euhdreal enstatite (appearing fine-grained) within a deformation band/shear zone* ...75
Figure 4.39: *Diopside typically contains needles and cubes of ilmenite/rutile.* ...76
Figure 4.40: *Showing the characteristic relationship between coarse-, and fine-grained pyroxenes* ...76
Figure 4.41: *Ternary plot for pyroxene classification (Morimoto, 1988)* ...77
Figure 4.42: *Thin section AM19-006-XA chosen for EPMA analysis representing a mixed sample (pyroxenite-wehrlite).* ...78
Figure 4.43: *Thin section AM19-006-XB representing a more or less pure pyroxenite pegmatite sample.* ...79
Figure 4.44: *Profile 1 of diopside* ...79
Figure 4.45: *Profile 2 of diopside with a good indication of zonation in increase of MgO and FeO combined with a decrease of CaO and TiO_2 towards the border..* ...80
Figure 4.46: *A weak indicator of zonation towards the right-hand side of graph with MgO and FeO increase combined with CaO, Al_2O_3, Cr_2O_3 and TiO_2 decrease.* ...80
Figure 4.47: *A weak zonation pattern in enstatite with various inclusions disrupting results across the line, particularly apparent in drastic TiO_2 increase (likely rutile).* ...81
Figure 4.48: *General increasing trend across the line disrupted by sharp TiO_2 increases (variable inclusions).* ...81
Figure 4.49: *Sample AM19-006-1-1 (left) and AM19-008-1 (right) in PPL used for comparison.* ...82
Figure 4.50: *Comparison of primary oxides from ALS data for sample AM19-006-1-1 (pyroxenite pegmatite) and AM19-002-7 (wehrlite).* ...83
Figure 4.51: *Comparison of the same samples as Fig. 4.49..* ...83
Figure 4.52: *FeO vs MgO for pyroxenite and wehrlite samples, showing a clearly different trend* ...84
Figure 4.53: *MnO vs MgO for pyroxenite and wehrlite samples* ...84
Figure 4.54: *Variation of K_2O vs Zr for all pyroxenite pegmatite samples..* ...85
Figure 5.1: *Skeletal quartz in granite pegmatite (London & Kontak, 2012), which is a unique pegmatitic texture. Somewhat similar textures can be seen with ilmenite/rutile within both opx and (some) cpx in many of the pyroxenite pegmatite samples.* ...90
Figure 5.2: *Poikilitic texture development by simulatenous growth at different nucleation rates. This classic example involves pyroxene (green) and plagioclase (blue), from Vale (2020).* ...91
Figure 5.3: *Variation in lamellae appearance. From sample AM19-006-XB (left) and AM19-008-4 (right).* ...91
Figure 5.4: *Chromite layer coating large orthopyroxene grains (Cawthorn & Boerst, 2006).* ...92

Figure 5.5: *Possible T and density range scenario (circled red) for the primary pyroxenite pegmatite formation, based largely on whole-rock composition and geochemical signatures* 92
Figure 5.6: *Ternary system Qtz-Ol-Cr (Robb, 2005)*.....93
Figure 5.7: *Outlining surface-view of proposed 'plug' shape of pegmatites in the eastern corner of gabbronorite/marginal zone/wehrlite contact* 95
Figure 5.8: *Sulfide solubility variation as a function of progressive crystallisation in a mafic magma as exemplified in the Bushveld Complex (Naldrett & Von Grünewaldt, 1989).* 99
Figure 5.9: *Image from Schanche et al. (2012). Ccp (dark brown-yellow), Pn (bright yellow) and Po (cream-ish brown) from drillhole RF-1.* 100
Figure 5.10: *Comparison of pyroxene classification results from pyroxenite pegmatite samples. Plot (left) of 145 data points from EPMA analysis, whereas plot (right) is from Orvik (2019).* 102
Figure 8.1: *Scan of thin section AM19-006-XA in XPL.* 3
Figure 8.2: *Scan of thin section AM19-006-XB in XPL.* 4
Figure 8.3: *Scan of thin section AM19-006-XB in reflected light, highlighting sulfides.* 5
Figure 8.4: *Scan of thin sections AM19-006-1 (left) and AM19-008-1 (right) in PPL.* 6
Figure 8.5: *Scan of thin sections AM19-008-2 (left) and AM19-008-3 (right) in XPL.* 7
Figure 8.6: *Scan of thin sections AM19-008-4 (left) and AM19-008-5A (right) in XPL.* 8
Figure 8.7: *Scan of thin section AM19-010 in XPL.* 9
Figure 8.8: *Scan of thin section AM19-010 in reflected light, highlighting sulfides.* 10
Figure 8.9: *Scan of thin section AM19-XX in XPL.* 11
Figure 8.10: *EDS image from thin section AM19-006-XA depicting an example of host-rock to sulfide analysis.* 43
Figure 8.11: *EDS image from thin section AM19-006-XA depicting an example of host-rock to sulfide analysis.* 47
Figure 8.12: *EDS image and graph from SEM, where point 3 matches amphibole composition.* 51
Figure 8.13: *EDS image of sample AM19-010 verifying mineralogy Cbn and Po.* 53
Figure 8.14: *XRD results from sample AM19-006-1.* 111
Figure 8.15: *XRD results from sample AM19-006-XA.* 113
Figure 8.16: *XRD results from sample AM19-006-XB.* 115
Figure 8.17: *XRD results from sample AM19-008-1.* 117
Figure 8.18: *XRD results from sample AM19-010.*.....119
Figure 8.19: *XRD results from sample AM19-XX.* 121

List of Tables

Table 2.1: *Trace elements substituting for major elements, depicted in Figure 2.2*.....18
Table 4.1: *Olivine results from EPMA (Table 8.24; Table 8.30).* 53
Table 4.2: *Clinopyroxene results from EPMA (Table 8.15).* 56
Table 4.3: *Orthopyroxene results from EPMA (Table 8.22).* 58
Table 4.4: *Amphibole results from EPMA (Table 8.18).* 59
Table 4.5: *XRD results from 6 thin sections.* 72
Table 4.6: *Mineral ID table with typical characteristics for pyroxene grains for all pyroxenite pegmatite samples.*.....74
Table 5.1: *Typical concentrations that are required for an exploitable ore deposit (Robb, 2005).* 88
Table 8.1: *Major elements whole-rock analysis for all samples.* 13
Table 8.2: *Minor elements whole-rock analysis for all samples.* 14
Table 8.3: *Normalisation calculation values of samples AM19-006-1, AM19-006-2 and AM19-006-3.* 17
Table 8.4: *Normalisation calculation values samples AM19-008-2-1, AM19-008-2-2 and AM19-008-2-3.* 20
Table 8.5: *Normalisation calculation values of samples AM19-008-1, AM19-008-3 and AM19-008-4.* 23
Table 8.6: *Normalisation calculation values of samples AM19-XX, AM19-005-1A and AM19-005-1B.*.....26
Table 8.7: *Normalisation calculation values of samples AM19-XX1, AM19-002-1 and AM19-002-2.* 29
Table 8.8: *Normalisation calculation values of samples AM19-002-3, AM19-002-4 and AM19-002-5.* 32
Table 8.9: *Normalisation calculation values of samples AM19-002-6, AM19-002-7 and AM19-002-8.* 35
Table 8.10: *Normalisation calculation values of samples AM19-002-9, AM19-007-X and AM19-007-02.*.....38
Table 8.11: *Normative calculation data for rock IUGS classification identification (Figure 4.24). Yellow = pyroxenite pegmatite and ol-websterite, orange = lherzolite, blue = dunite, green = wehrlite.*.....41
Table 8.12: *EPMA data point results from XA_Diop1-15 with accompanying image (next page).*.....58
Table 8.13: *EPMA data point results from profile XA1_Diop1-10 with accompanying image (next page).* 60
Table 8.14: *EPMA data points from profile XA2_Diop1-9 with accompanying image (next page).*.....62
Table 8.15: *EPMA data points from profile XA3_Diop1-21 with accompanying image (next page).*.....64
Table 8.16: *EPMA data point results from profile XA1_Ol1-10 with accompanying images (next page).* 66
Table 8.17: *EPMA data points from profile XA2_Ol1-10 (no accompanying image).* 68
Table 8.18: *EPMA data points from profile XA1_Aeg1-30 with accompanying images (next 2 pages).*.....69
Table 8.19: *EPMA data point results from profile XA4_Diop1-20 with accompanying image (next page).* 72

Table 8.20: *EPMA data point results from profile XA5_Diop1-20 with accompanying images (next page).* 74
Table 8.21: *EPMA data point results from profile XA1_Enst1-20 with accompanying image (next page).* 76
Table 8.22: *EPMA data point results from profile XA2_Enst1-20 (no accompanying image).* 78
Table 8.23: *EPMA data point results from profile XA3_Enst1-20 with accompanying images (next page).* 79
Table 8.24: *EPMA data points from profile XA3_Ol1-20 with accompanying images (next page).* 81
Table 8.25: *EPMA data point results from profile XB_Diop1-30 with accompanying images (next 2 pages).* 83
Table 8.26: *EPMA data point results from profile XB1_Enst1-20 with accompanying images (next page).* 86
Table 8.27: *EPMA data point results from profile XB2_Enst1-20 with accompanying images (next two pages).* 88
Table 8.28: *EPMA data point results from profile XB2_Diop1-20 with accompanying images (next page).* 91
Table 8.29: *EPMA data point results from profile XB3_Enst1-4 with image (below).* 93
Table 8.30: *EPMA data points (complete table for all samples, including all calibration points).* 94
Table 8.31: *Geochemical analysis of major elements comparing drillhole RF-1 to pyroxenite pegmatite samples from this study. Highlighted in yellow is primary and notable differences of interest.* 124
Table 8.32: *Geochemical analysis of minor elements comparing drillhole RF-1 to pyroxenite pegmatite samples from this study. Highlighted in red is primary and notable differences of interest.* 125

Abbreviations

Symbol	**definition**
Al	Aluminium
Ag	Silver
ALS	Australian Laboratory Services
AMPH	Amphibole
As	Arsenic
Au	Gold
Ba	Barium
Be	Beryllium
BIBSYS	NTNU Online University Library
BSE	Back Scattered Electrons
Ca	Calcium
Chr	Chromite
CIMP	Central Iapetus Magmatic Province
Cpx	Clinopyroxene
CS	Central Series
Co	Cobalt
Cu	Copper
Cr	Chromium
Dio	Diopside
EDS	Energy Dispersive Spectrometry
Ens	Enstatite
EPMA	Electron Probe Micro Analyzer
Eu	Europium
Fa	Fayalite
Fe	Iron
Fo	Forsterite
HREE	Heavy Rare Earth Elements
IUGS	International Union of Geological Sciences
Ir	Iridium
KNC	Kanak Nappe Complex
LA-ICP-MS	Laser Ablation Inductively Coupled Plasma Mass Spectrometry
Li	Lithium
LIP	Large Igneous Province
LLD	Lower Limit of Detection
LREE	Light Rare Earth Elements
LLS	Lower Layered Series
Mg	Magnesium
MZ	Marginal Zone
Nb	Niobium
Ni	Nickel
NTNU	Norwegian University of Science and Technology
Ol	Olivine
Opx	Orthopyroxene
Os	Osmium

PGE	Platinum Group Elements
PGM	Platinum Group Minerals
PPB	Parts Per Billion
PPL	Plain-Polarized Light
PPM	Parts Per Million
Pd	Palladium
Po	Pyrrhotite
Pn	Pentlandite
Plag	Plagioclase
Pt	Platinum
QAPF	Quartz-Alkali Feldspar-Plagioclase-Felspathoid
Qtz	Quartz
Rb	Rubidium
REE	Rare Earth Elements
Rh	Rhodium
Ru	Ruthenium
RUC	Reinfjord Ultramafic Complex
S	Sulfur
SEM	Scanning Electron Microscope
SIP	Seiland Igneous Province
Sr	Strontium
Te	Tellerium
TEM	Transient Electron Microscopy
Ti	Titanium
U	Uranium
UM	Ultramafic
UPS	Upper Layered Series
WDS	Wavelength Dispersive Spectrometry
XPL	Cross-Polarized Light
XRD	X-ray Diffraction
XRF	X-ray Fluorescence
Zr	Zirconium

1

Introduction

Aim of study

The current state of knowledge surrounding the processes involved in the Seiland Igneous Province (*SIP*) and Reinfjord Ultramafic Complex (*RUC*) is constantly improving. However, there are still several aspect of the final stages of solidification that have not been documented. In order to gain a better understanding of some of these processes, this thesis will attempt to provide a better insight into the nature of the multiple recharge events in the Reinfjord Ultramafic Complex, more specifically analyse the mineralisation in the pyroxenite pegmatites, raising questions such as if the pyroxenite pegmatites have fasciliatated oversaturation with sulfide and formation of the widespread Ni-Cu-PGE reef mineralisation in the area. This thesis will attempt to characterise the pyroxenite pegmatite mineralogically in a mafic to ultramafic setting, which have not been done previously.

Further, a brief comparison of the pyroxenite pegmatites in various settings such as margins and interiors will be conducted. Fieldwork, geochemical analysis from petrography, SEM, EPMA and whole-rock analysis will be used in this study, in addition to comprehensive research on literature from the area. To solidify the research, appropriate comparisons to worldwide locations with similar geological setting have also been considered in this thesis.

Previous work

The SIP was first mapped by Pettersen (1875), which created the foundations of the more detailed mapping done later (Barth, 1927; Barth, 1954; Oosterom, 1963). The early work primarily focussed on the SIP, and more targeted focus on the RUC was not conducted until the 1970's (Bennett, 1971; Bennett 1974). With this work came the first description of the different magmatic series of the RUC, later revised and reclassified by Emblin (1985). The four magmatic bodies of the SIP were later classified by Bennett et. al. (1986), and this classification is still used today. The Norwegian Geological Society found economically viable resources of nepheline syenite in 1952 at Stjernøya, where mining operations of nephelinesyenite started in 1961 and is still being mined today.

An increasingly well-constrained understanding of the SIP and RUC formation is due to an extensive amount of research and work that has been conducted in the area in recent years. This is largely owing to a considerably sized scientifically and economically interesting Ni-Cu-PGE reef deposit. This finding lead to the Platinum-Probe Project, run by prof. Rune Berg-Edland Larsen from Norwegian University of Science and Technology (NTNU). Additionally, Nordic Mining ASA conducted a transient electromagnetic (*TEM*) investigation and a drilling program in 2012, resulting in two drill cores and a model depicting a 600 by 600 m conductive body at approximately 70-100 m in depth (Schance et. al., 2012). Drilling were later supplemented by another two scientific cores in conjuction with the Platinum-Probe Project.

The most recent paper by Berg-Edland Larsen et al. (2018) describes the magmatic nature behind the ultramafic complexes and portays the giant deep-seated magmatic conduit system of the SIP. Sørensen et. al. (2019) documents fascinating in-situ evidence of earthquakes near the mantle-crust boundary which has been initiated by CO_2 fluxing and reaction-driven strain softening in the SIP, and the reader is encouraged to investigate this paper for the most recent published research of the area.

1.1 Geological setting

1.1.1 Seiland Igneous Province (SIP)

The Norwegian Caledonian orogenic belt comprises a series of thrust sheets grouped into the basal level of the Upper Allochthon, of which thrusted eastward during the continental collision between Baltica and Laurentia. This event caused the closure of the Iapetus Ocean of Early Palaeozoic age (Pastore, 2016). During the same period there was a considerable outpouring of magmatism, forming numerous dyke swarms throughout Scandinavia, North American and West Greenland, which is associated with several Large Igneous Provinces, abbreviated to *LIP* (Larsen et al. 2018). These are collectively known as the Central Iapetus Magmatic Province (*CIMP*). Only deep crustal exposures of the CIMP are observable in the Seiland Igneous Province (*SIP*). The deep roots of LIP's are still poorly understood and studies of the few known localities, such as the SIP, are of particular importance.

The SIP is part of the Kalak Nappe Complex (*KNC*), placed within the basal levels of the Upper Allochthon (Andréasson, Svenningsen & Albrecht, 1998), of which >5000 km^2 of mafic and ultramafic intrusions from the lower crust from at least 30-40 km depth are well-exposed (Larsen et al., 2018). At least 25,000 km^3 of igneous rocks intruded the metasediments, with this volume likely being even greater due to upper crustal levels being eroded away, in addition to a presumption that the SIP has been separated from the KNC by thrust faults of Caledonian age during nappe emplacement (Grant et al., 2016a). It cannot with certainty be stated that the SIP fed a LIP system, but tens of thousands of km^3 of dense ultramafic and mafic magma certainly passed through the SIP while ascending to higher levels in the continental lithosphere (Larsen et al., 2018). Field observations and literature indicates that the gabbros were not completely crystallised upon being intruded by ultramafic melts, suggesting a relatively short time span between ultramafic and gabbro intrusion (Bennett et al., 1986). Larsen et al. (2018) presents a revised geological map of the area (Figure 1.1), where the gabbroic units marked by grey are made up of olivine-, pegmatitic-, meta-, pyroxene-, and syenogabbro, making up approximately 85% of the igneous rocks within the SIP. The ultramafic rocks are marked by green, whereas the metasediments are marked by yellow, making up the large-scale regional geological setting for the RUC.

The SIP consists of the three islands; Seiland, Stjernøya, Sørøya and the Øksfjord peninsula (Figure 1.1), The age of the SIP has long been disputed, however, recent studies from Roberts et al. (2005) suggests an age of 560-610 Ma. This is related geochemically to dyke swarms throughout Scandinavia, and further correlated to magmatic provinces in W-Greenland and NE-America (ref: CIMP). A geometric 3D-model (Figure 1.2) was created by Pastore et al. (2016) using gravimetric data, and this model was used to propose a varying thickness of 2 to 4 km in the SIP.

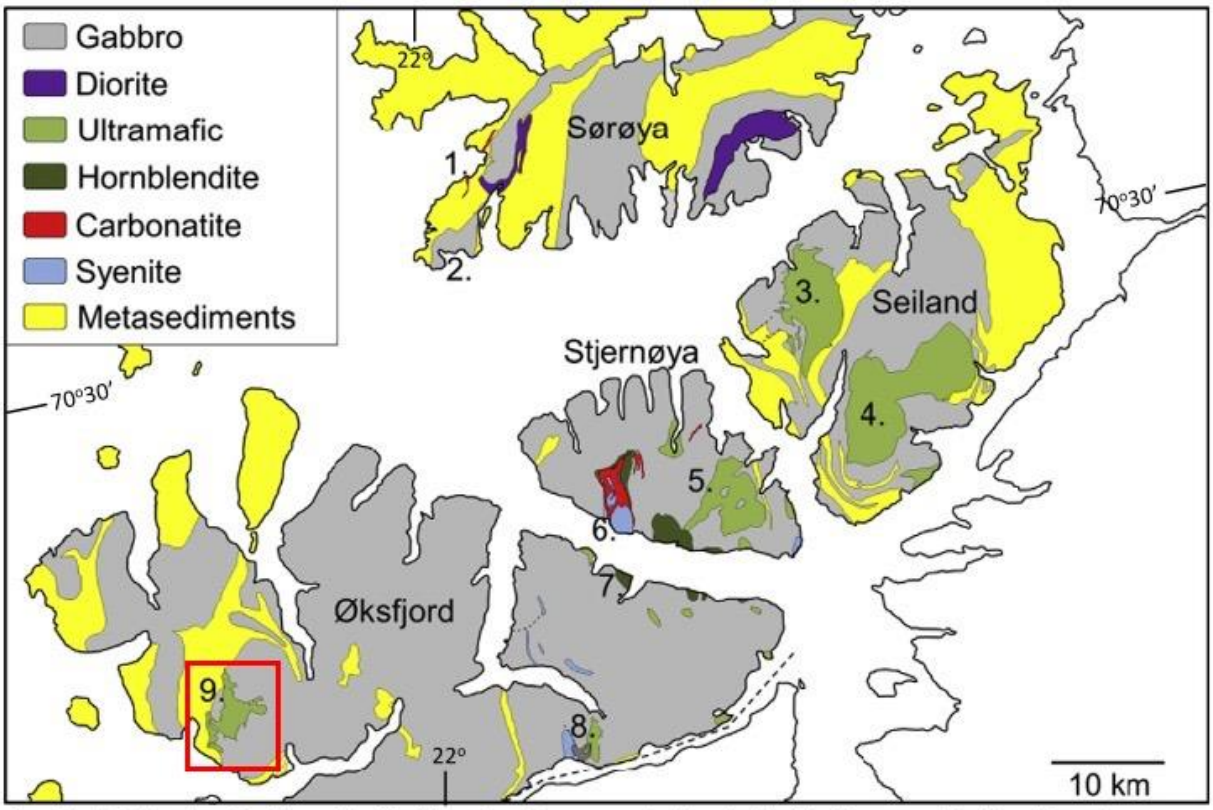

Figure 1.1: *Map of the regional geological setting of the Seiland Igneous Province (SIP), from Larsen et. al., 2018. The area of interest in this thesis, the Reinfjord Ultramafic Complex (RUC), is marked with a red box (number 9 in map).*

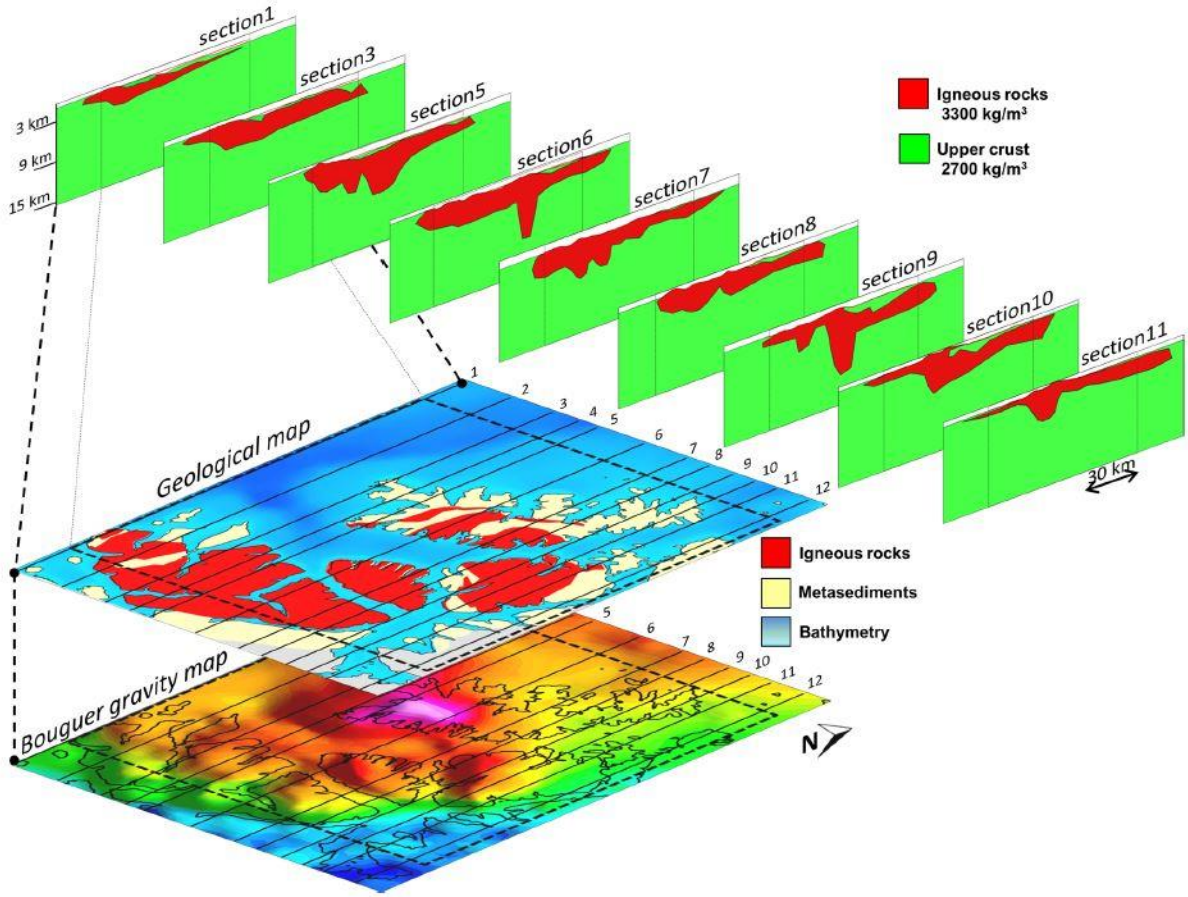

Figure 1.2: *Geometric 3-D model of the Seiland Igneous Province, created with assistance of gravimetric data, by Pastore et al. (2016). The positions of section 1 to 11 is shown on the geological map and bouguer gravity map.*

A model created by Larsen et al. (2018) summarises the evolution of the main conduit systems in the SIP (Figure 1.3a - f) and how the ultramafic complexes have been assembled. From A to F, the evolution goes as follows: (A) Picritic to komaiititic melts assimilate at approximately 1400°C shortly after gabbro emplacement, of which is still hot, leading to partial melting of Cpx *(Cpx)* and orthopyroxene *(Opx)*. (B) Repetitive recharge events and formation of the hybrid marginal zone, olivine (*Ol*) melagabbro to clinopyroxene. (C) Temperature rises and magma chamber grows, and new recharge events leads to formation of wehrlitic cumulates. (D) With further T-rise and magma chamber growth, replacive dunite and dunitic cumulates forms, as well as wehrlitic pyroxenite assimilation, in addition to economic elements Cu-Ni-PGE starting to form in a reef-structure. (E) The unconsolidated dunitic cumulates ae infiltrated by aqueous-carbonic alkaline melts, and PGE-Au (principally Au and Pd) forms by local remobilisation. (F) The final stages comprise of dyke emplacement with evolving compositions komaiititic/picritic to gabbroic and alkaline. Reinfjord Ultramafic Complex (marked with red dotted lines) shows a deeper emplacement that the other complexes of which are located closer to the roof (displaying more hybrid compositions).

1.1.2 The Reinfjord Ultramafic Complex (RUC)

The Reinfjord Ultramafic Complex (RUC) which forms a part of the Seiland Igneous Province (SIP), is a rare example of a well exposed deep crustal ultramafic conduit system (Grant et al., 2016a). Other worldwide known locations such as the Chillas complex, Sapat feeder pipes in Pakistan, Emeishan Large Igneous Province in China and Kondyor in Russia have been described (Grant et al., 2016a), which have a general trend being zoned intrusions with ultramafic cores (dunite) and mafic rims (gabbro). A comparison to similar economic deposits as those found in Reinfjord, around the globe can be found in Chapter 2.8.

The RUC itself is unique in that it allows us to examine the petrological processes that have facilitated the ascend of thousands of km^3 of mafic-ultramafic igneous melts, from depths of 30 km up 50 km (Larsen et al., 2018; Orvik, 2019). The area is signified by multiple magmatic recharge events and has economically interesting amounts of Ni, Cu, Platinum Group Elements (*PGE*) and Au from drilling executed by Nordic Mining in collaboration with NTNU in 2012 (Schanche et al., 2012), and considerable studies have provided a complex insight into the processes in and behind this deposit. To gain a better understanding of the recharge events role in facilitating sulfide oversaturation and formation of Ni-Cu-PGE mineralisation, the pyroxenite pegmatites have been investigated in this thesis.

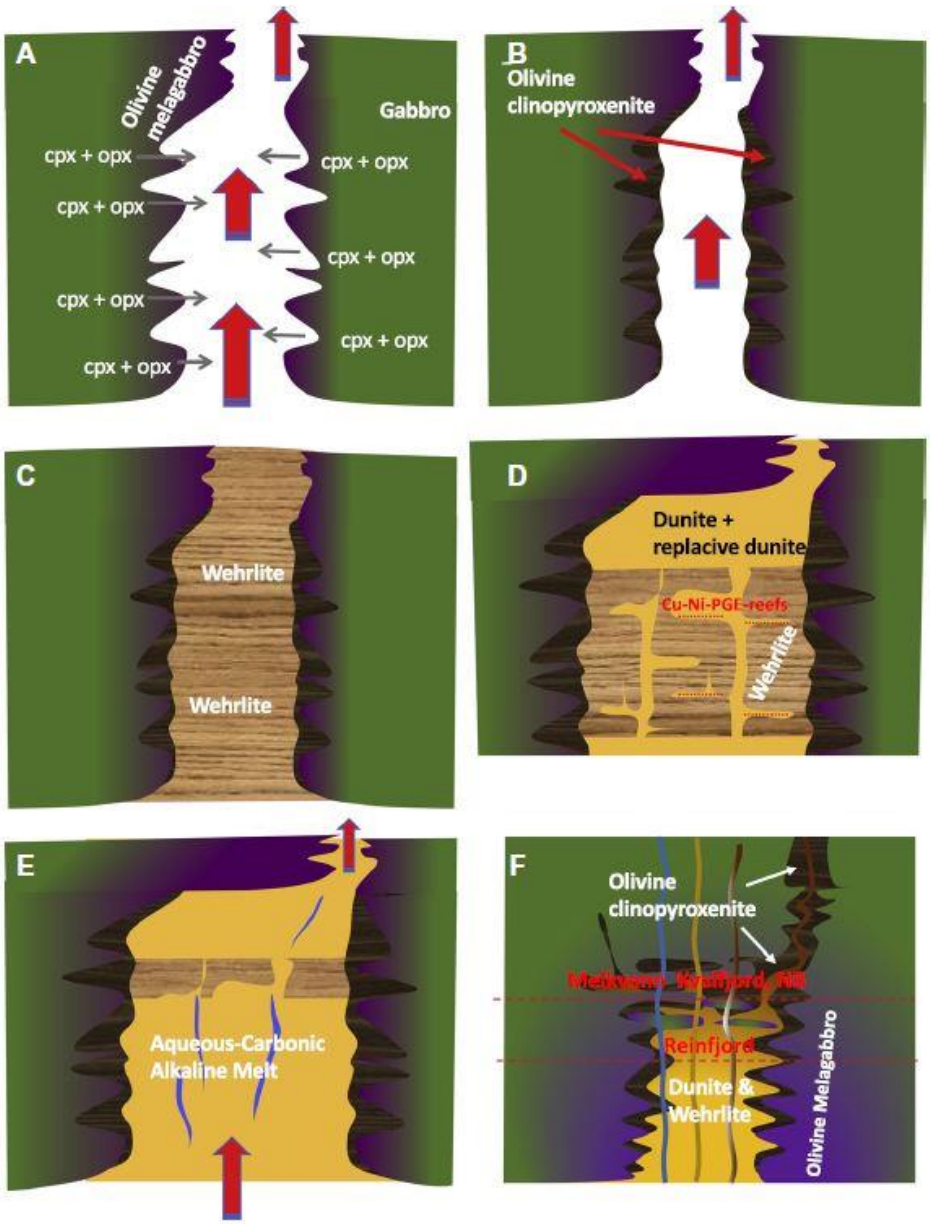

Figure 1.3a – f: *Evolution of the ultramafic complexes during the formation of SIP, modelled by Larsen et al. (2018). See in-text for detailed information.*

The RUC consist of cumulative and replacive ultramafic rocks that have intruded the Langstrand gabbro and paragneisses (Grant et al., 2016b). The RUC is divided into three separate ultramafic intrusive stages; Upper Layered Series (*ULS*), Lower Layered Series (*LLS*) and Central Series (*CS*), each of the series with clear differentiation from one another. There is one marginal zone (*MZ*) which vary in composition and features depending on which series (LLS, ULS or CS) it is bordering with, as a result of the host rocks (gneiss and gabbro). The separate stages are presented in Figure 1.4.

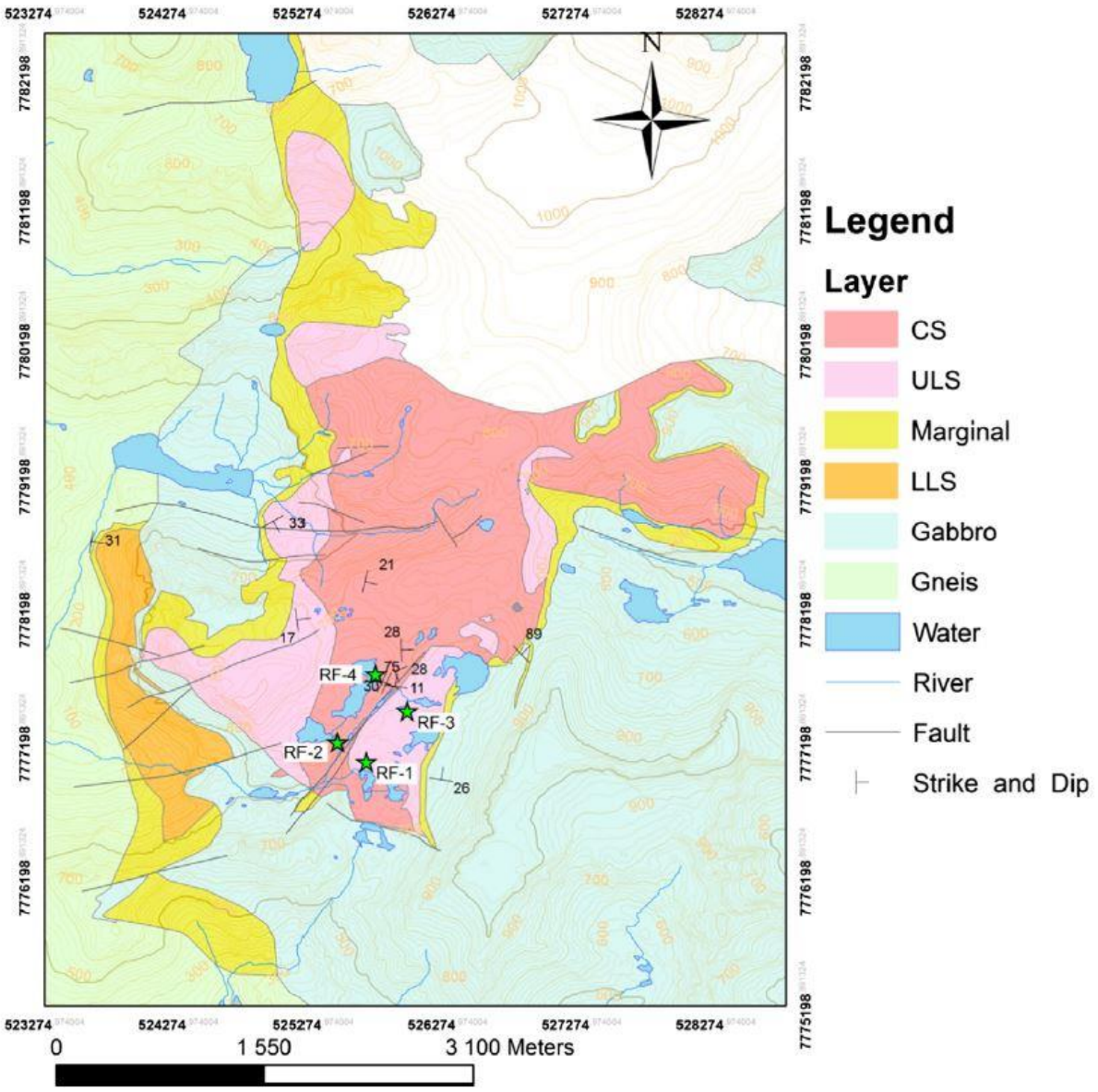

Figure 1.4: *Geological map of the RUC created by Grant et al. (2016b) presenting the separate ultramafic intrusive stages.*

Langstrand gabbronorite

The Langstrand gabbronorite is a large mafic pluton and consist of sequences of clinopyroxene-olivine-plagioclase, with accessory apatite, zirconium and biotite. The contact zone with country rocks dips steeply, whereas layering within the gabbronorite moderately dips from 10-30°, trending north-northeast. Concordant to the gabbronorite layering there are xenoliths and large rafts of the metasediments (Grant et al., 2016b).

Lower Layered Series (LLS)

The Lower Layered Series is composed of four units of cyclic olivine and pyroxene-rich cumulates, of which olivine-rich lherzolites with large oikocrystic orthopyroxene and poikilitic wehrlites make up the base of each unit (Grant et al., 2016a). The layers above are richer in clinopyroxene, essentially grading more into olivine-clinopyroxenite and wehrlite (Bennett et al., 1986).

Upper Layered Series (ULS)

An approximately 50 m thick gabbro screen spatially separates the Lower Layered Series from the Upper Layered Series, where the gabbro screen is likely part of the host gabbro-norite. The ULS is modally layered, is made up of seven cyclic units stretching approximately 250 m and consists of olivine and olivine-clinopyroxene cumulates (Emblin, 1985). The base of each unit is dominated by olivine, which in turn forms occasional dunite and poikilitic spinel wehrlites, whereas the top of each unit is made up of olivine-clinopyroxenites and wehrlites (Emblin, 1985; Bennett et al., 1986). The ULS contains some excellent exposures of cumulate forming processes and, along with the CS, is of most interest concerning the thesis objectives in this study. The ULS dips moderately to shallow at 10° - 25° toward ENE, with each layer thickness varying in centimetre to meter scale. Structures that can be observed in the ULS include slumping, load structures, synmagmatic folding (sheath, isoclinal, overturned), horizontal layering and crossbedding (Figure 1.5; Figure 1.6).

Many of the well-exposed pyroxenite pegmatites in the ULS, close to the CS border, appeared as fountain structures (section 2.5.3). To the best of the authors knowledge and research background, these particular structures have not been described in literature before (Figure 1.7). Based on this, the structures are of interest and merits further work and will form a part of the discussion in Chapter 5.

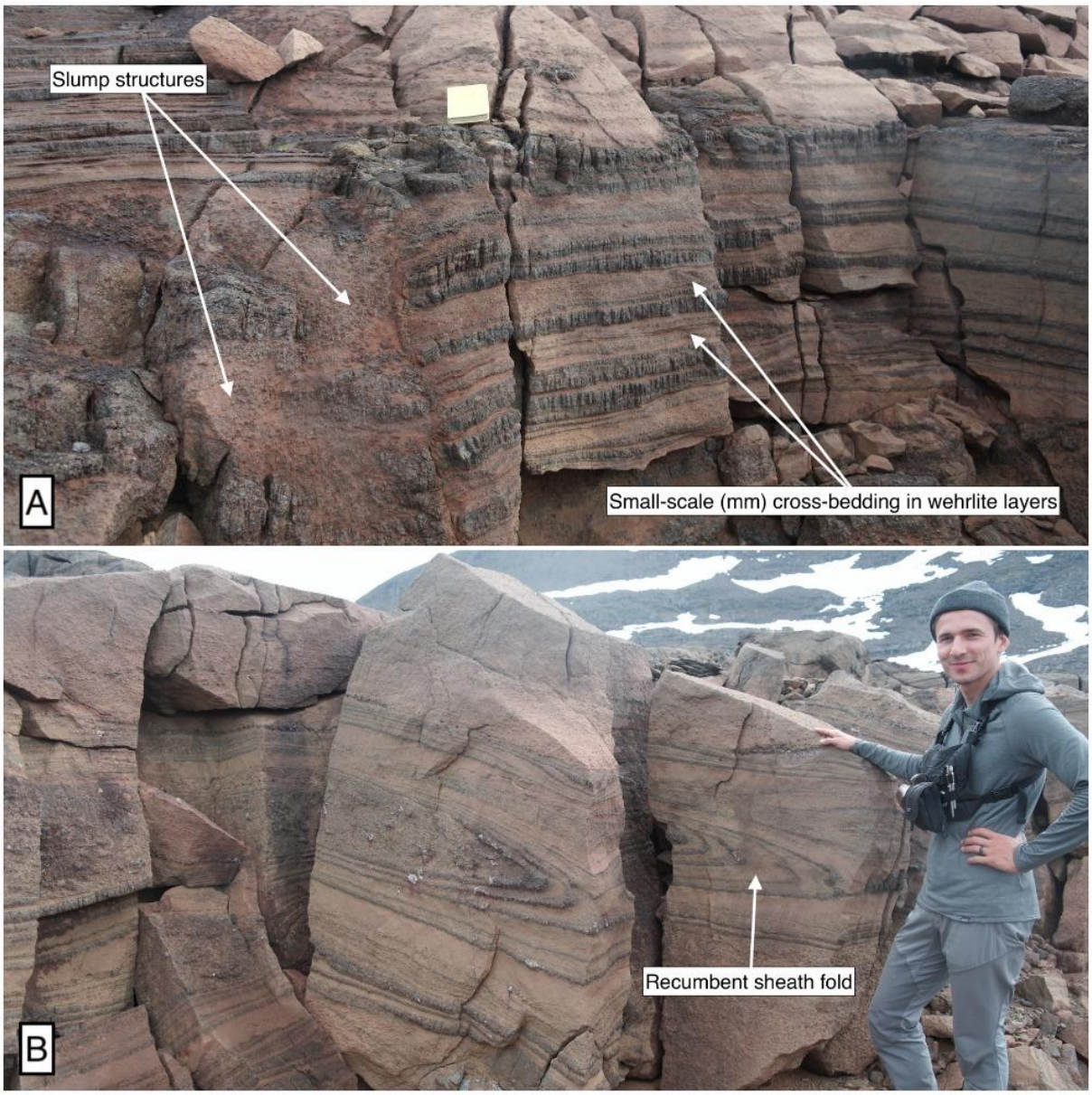

Figure 1.5: *In-field observations of structures in the ULS. A: Likely slump structures disrupting the Cpx-wehrlite horizontal layering post-deposition. B: Recumbent sheath fold (tens of meters long, extending out of picture to the left). The slumping/load structures have been documented in Grant et al. (2016b). Field book and Eric J. Ryan (Phd. Candidate at NTNU) for scale.*

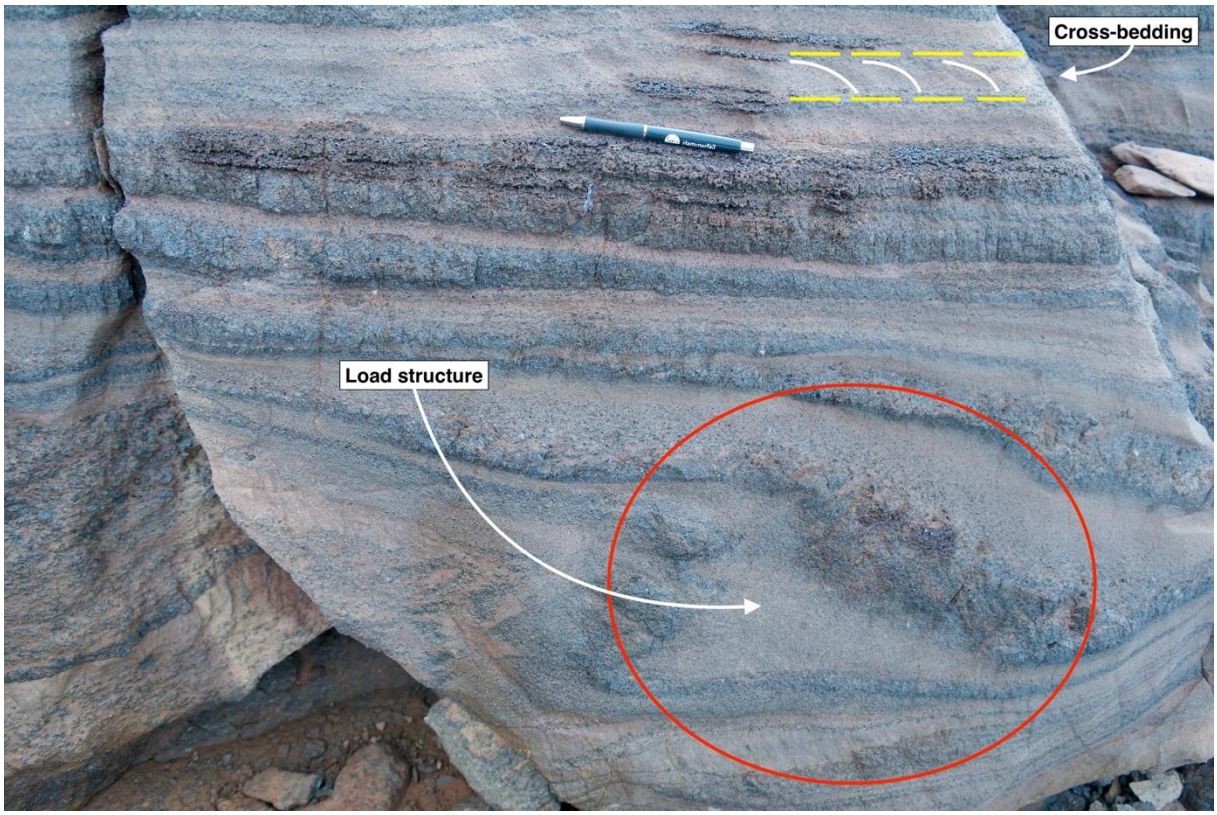

Figure 1.6: *Load structure in the ULS disrupting Cpx-wehrlite layering. Ol-Cpx-rich crossbedding and dunite-wehrlite layers observed in the upper section in a consistent horizontal manner.*

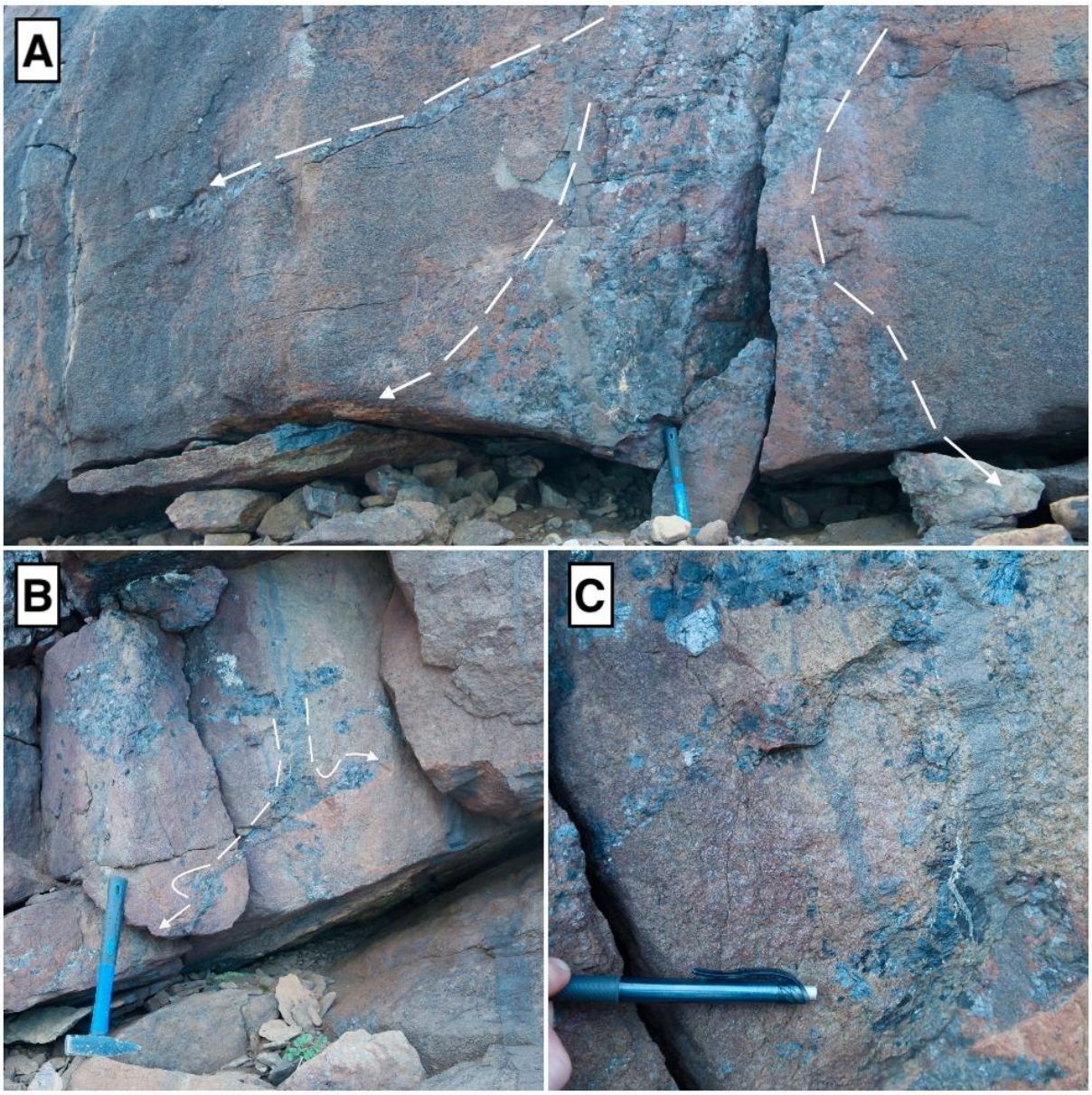

Figure 1.7: *One of the four, and the largest, putative fountain structure that was discovered in RUC. They are particularly prominent in the lower parts of the ULS.*

Central Series (CS)

The Central Series makes up c. 70% of the RUC and consists of dunite and poikilitic wehrlite. It is clear that CS formed after ULS, based on in-field observed intrusive relationships such as 1-5m wide dykes cross-cutting the ULS layering at the western contact (Grant et al., 2016b). The dykes seem to originate from CS to the NE and fade into the ULS towards SW, suggesting that the melt forming replacive dunite dykes is the same melt that form CS dunites (Orvik, 2019). Based on replacive dunite features occurring at a range of scales, Grant et al. (2016b) suggests that the ULS was not fully crystallised during the CS intrusion, which disturbed the layering in a ductile manner.

A dyke swarm varying in thickness from mm – cm also cuts the CS (Orvik, 2019). The reader is encouraged the read that dissemination for a better overview of the dyke swarms' role in the CS.

Marginal zone

The marginal zones form where the LLS, ULS and CS intrude the gabbronorite and the gneiss host lithologies. The marginal zones are made up by a range of rock types such as websterites to Ol-websterites, xenoliths of gneiss or gabbro, plagioclase (*Plag*) bearing ultramafic rocks and mafic pegmatites of coarse-grained pyroxene in a plagioclase matrix (Grant et al., 2016b). Due to the great variety in rock types, this sequence is treated as one (variable) unit, rather than several units. At the eastern contact, at the ULS/CS – gabbronorite contact, a 2-5 m apophysis containing olivine, clinopyroxene, orthopyroxene, plagioclase, spinel and amphibole (*Amph*) intrudes the gabbro and stretches for over 300 m. The marginal zones that are formed in the gabbronorite contacts all share some common characteristics: plagioclase is generally absent in CS and ULS but appears within 50 m of the gabbro contact zone in the form of plagioclase veins, poikilitic plagioclase and/or interstitial plagioclase.

The marginal zones typically consist of coarse-grained websterite to Ol-websterite, however, gabbro and ULS boundaries are highly irregular. Recrystallised and foliated leucogabbro is cut by mafic dykes close to the marginal zone, and meter-scale pods of pyroxene-rich UM rocks are common within these gabbros. This trend continues for several tens of meters, until the gabbro becomes more layered and mafic pods dykes is non-existent (Grant et al., 2016b).
The sequence from youngest to oldest in geological age are CS – UPS – LLS – Langstrand gabbronorite and is summarised in Figure 1.8.

Figure 1.8: *Summary of the sequence of intrusive stages from youngest to oldest in age.*

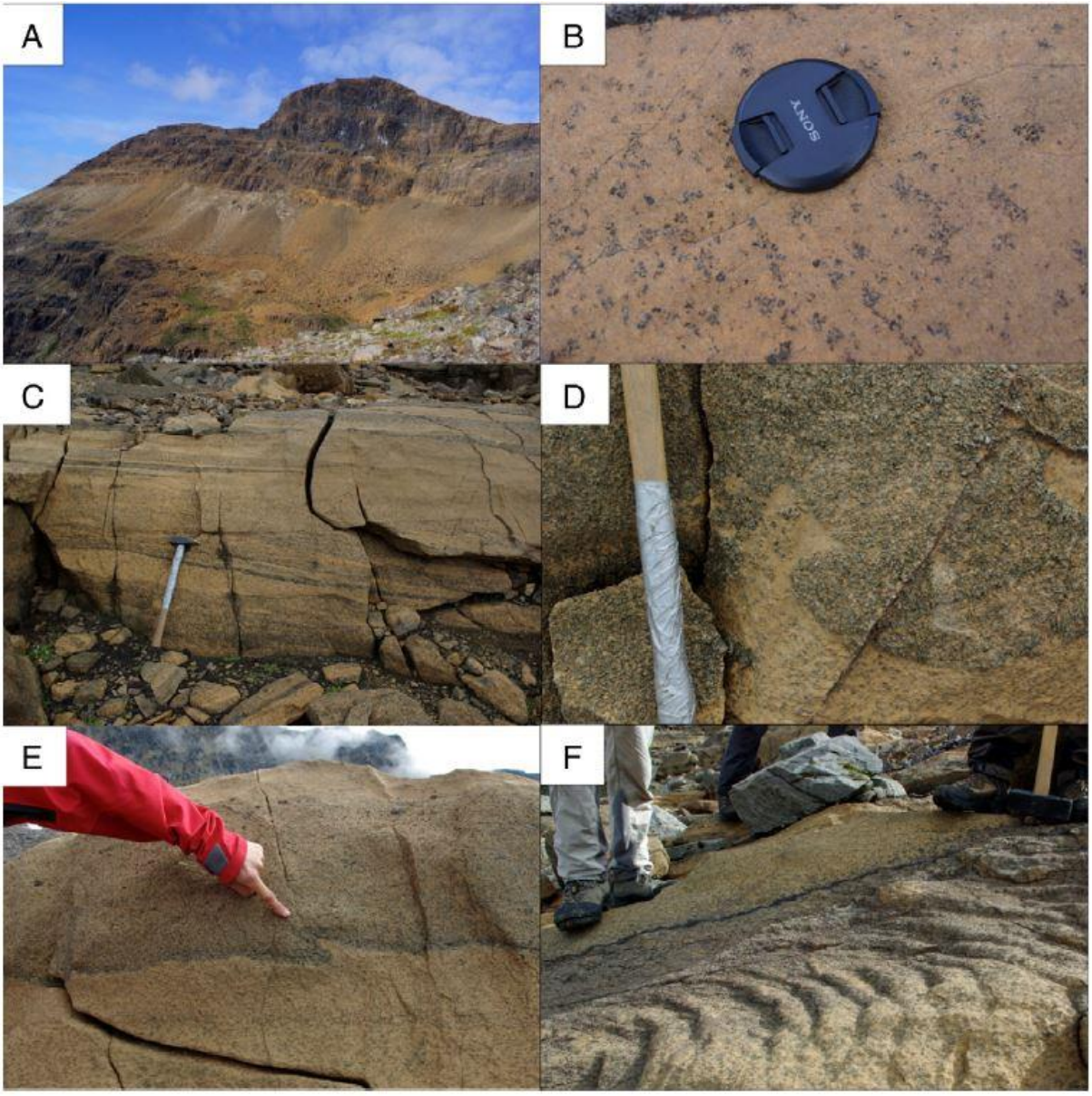

Figure 1.9: *Summary of structures in the RUC by Grant et al. (2016b). A: Cumulate forming processes where LLS is exposed (SW-facing cliff) with the marginal zone between country rock (gneiss) and LLS at the bottom of the cliff. The top of the cliff exposes the ULS. B: Dunite-wehrlite in the CS with knobs of Cpx. C: Crossbedding in the ULS. D: Load structures in the ULS. E, F: 2D and 3D views of slumping structures.*

1.1.3 P-T conditions in the RUC

A very significant part of the igneous evolution in the SIP, and particularly in the RUC, is the P-T conditions which the ultramafic magmas were emplaced. Several studies have addressed this issue (Grant et al., 2016b; Griffin et al., 2013; Bennett et al.,1986; Orvik, 2019). Figure 1.10 presents a possible evolution of the substantial pressure increase, with the emplacement of several kilometres of flood basalts at the surface, similar to the Skaergaard intrusion (Larsen, 2006). A more recent hypothesis by Larsen et al. (2018) suggests that large volumes of dense ultramafic cumulates made the continental lithosphere subside for the lithosphere to regain its isostatic mass balance. Orvik (2019) calculated a higher pressure than previously suggested for the RUC, with the dyke swarms forming at 10-14 kbar with similar T's as Figure 1.10.

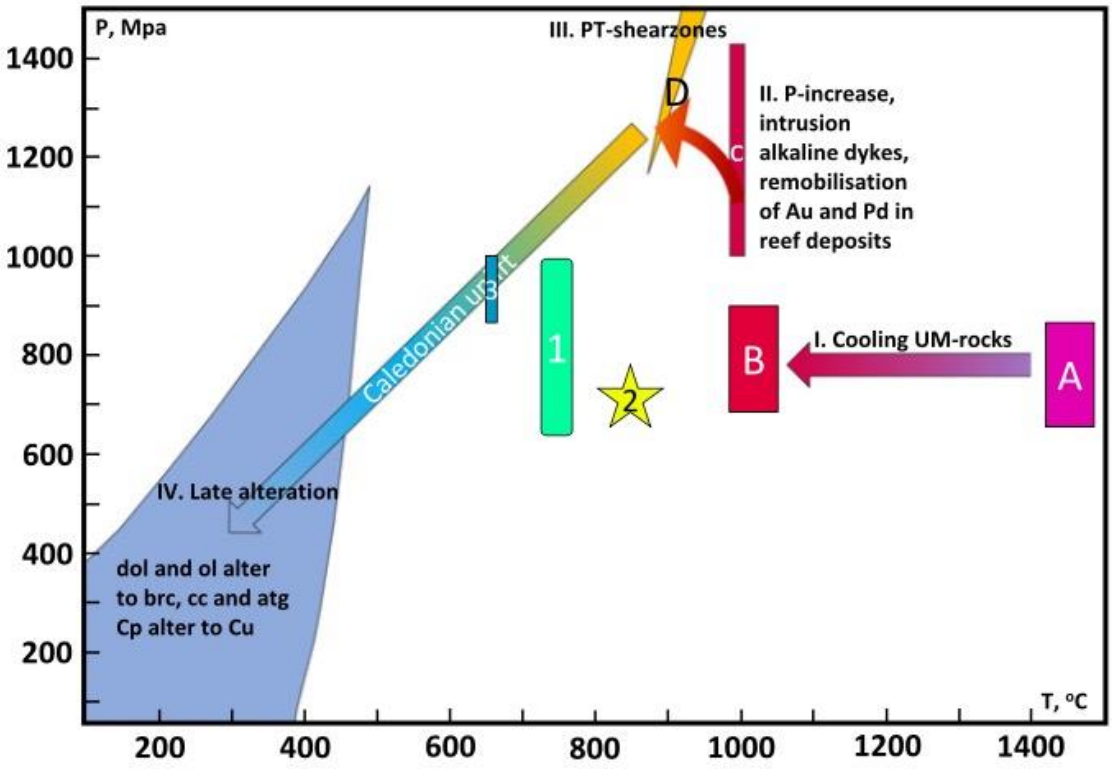

Figure 1.10: *P-T loop of the RUC (Larsen at al., 2018). 1: Pre-intrusion temperature of approximately 750℃. 2: Contact metamorphism conditions. A: Pictritic/komatiitic melts with pressure of approximately 800 Mpa and temperature 1450℃. B: Cooling temperatures of the RUC from two-pyroxene thermometry. C: Crystallisation temperatures of lamproitic dykes. D: P-T from pseudosections of the extensional shear zones. 3: Caledonian uplift P-T conditions from Hasvik gabbro. 4: Late alteration of dolomite and Ol, forming native copper.*

2

Theory

2.1 Igneous rock classification

Igneous rocks are commonly formed by partial melting of the crust or mantle. The mineral assemblage is used in assisting classification by ternary diagrams, divided into felsic and mafic rocks. *QAPF* (quartz-alkali feldspar-plagioclase-felspathoid) is the most commonly used diagram, fostered by Streckeisen (1974), and accepted by Earth Scientists globally. The diagram (Figure 2.1) is very useful in unravelling further information about temperature, pressure and chemical composition of the parental melts.

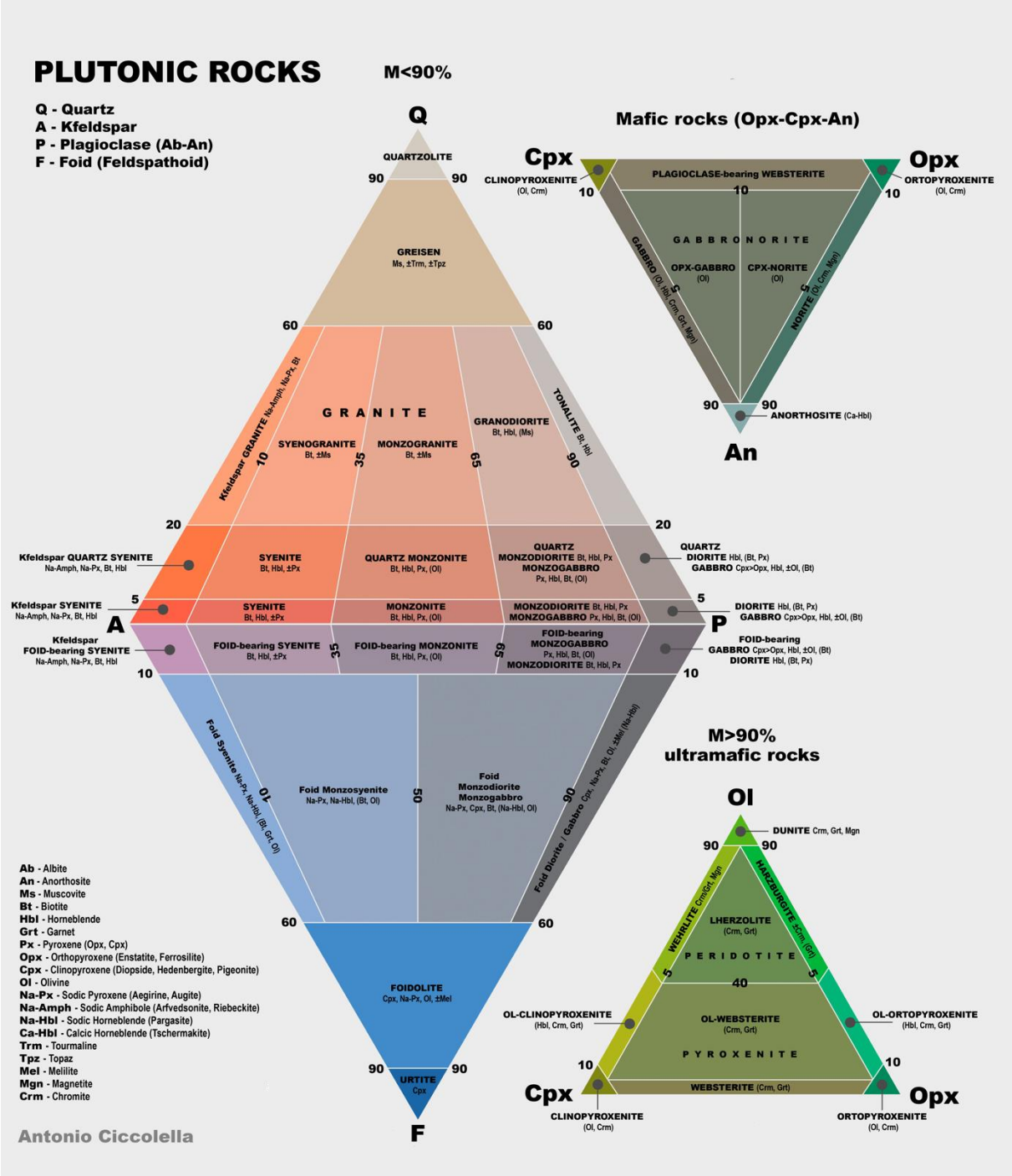

Figure 2.1: *QAPF ternary diagram modified from Streckeisen (1974). The sub-diagram Ol-Cpx-Opx (bottom right) for ultramafic rocks presents the most widespread hostrocks of RUC, namely dunite and wehrlite in addition to pyroxenite (Cpx and Opx).*

For example, a rock containing less than 10% felsic minerals requires usage of sub-diagrams, an example of this is outlined in the bottom-right corner of Figure 2.1. This diagram is applicable for the RUC, with clinopyroxene, orthopyroxene and olivine representing rocks of ultramafic origin; pyroxenite and peridotite. In the instance of RUC, large areas of exposed outcrop with ≥90% olivine, are classified as dunites, whereas exposures of ≥40% olivine, >10 - 60% clinopyroxene and minor orthopyroxene (up to 5%) are classified as wehrlites.

2.2 Partition coefficients and trace element compatibility

The generation from magma to solid rock only involves partial melting, where orthopyroxene, clinopyroxene and olivine (+ minor phases) in peridotites from the upper mantle are partially melted (Best, 2003). This melt constitutes ions of **incompatible** and **compatible** major and trace elements. The incompatible trace elements partition into the loosely structured melt, whereas compatible trace elements prefer to partition into the crystalline phase (Robb, 2005). This difference leads to the formalised concentration ratio called **partition coefficient**, *D;*

$$D\,\frac{Crystal}{Melt} = \frac{(Concentration\ in\ mineral)}{(Concentration\ in\ melt)}$$

From this partition coefficient we can gather that compatible trace elements have $D > 1$. For example, if feldspars in silicic magmas is crystallising, elements such as Ba, Eu and Sr will strongly partition into the feldspars (Best, 2003). Another example is Cr, Ni and Co being compatible if olivine and orthopyroxene in basaltic magmas are crystallising. Incompatible trace elements (i.e. Rb, Li, Nb, REE), on the other hand, have $D < 1$ and will consequently only weakly partition into major minerals in basaltic magmas. When these melts have developed towards more granitic compositions at lower T, the incompatible elements may become compatible in phases such as orthoclase, micas, apatite etc. (Best, 2003).

Table 2.1: *Trace elements substituting for major elements, depicted in Figure 2.2***.**

Trace Elements Substituting for Major Elements of Similar Ionic Size and Charge

Major Element	Substituting Trace Element(S)
Fe	Cr, Co, Ni
Mg	Cr, Co, Ni
Ca	Sr, Eu, REEs
Na	Eu
K	Rb, Ba, Sr, Eu
Si	Ge, P
Ti	V
Al	Ga

Due to different ionic charge and/or radius, incompatible trace elements will not readily substitute for major elements in crystalline phases (Figure 2.2; Table 2.1). Examples of this are Be^{2+} (small size precludes substitution for divalent ions; low charge precludes substitution for similarly sized Si^{4+} → incompatible), and U^{4+} (large charge and radius). It is, however, important to note that compatibility is dependent on mineralogy of the magma, thus a silicic magma with crystallising zircon makes U^{4+} compatible as it substitutes for Zr^{4+} (Best, 2003).

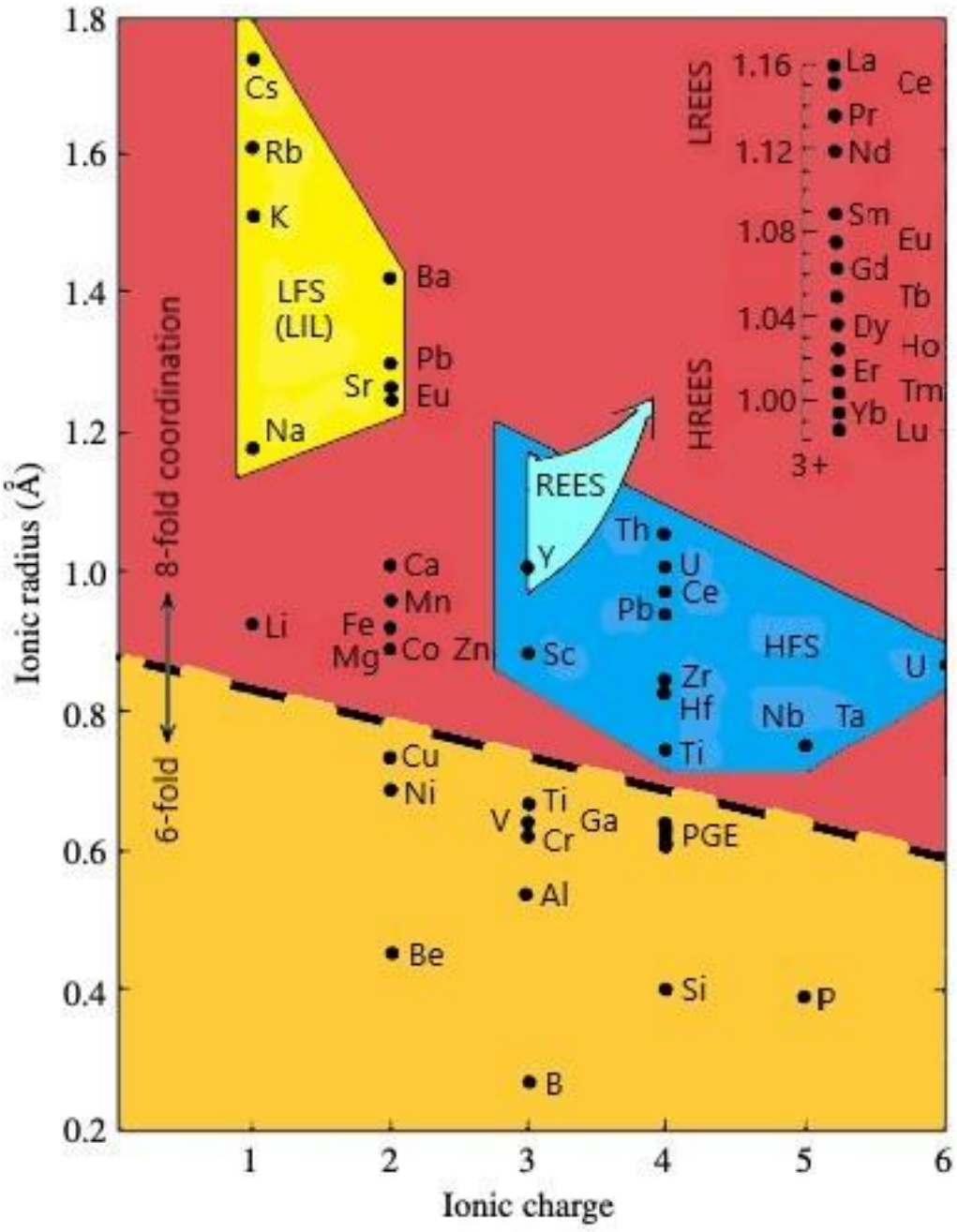

Figure 2.2: *Diagram edited from Best (2003) based on data from Shannon (1976). Radii and classification of positively charged ions of major and trace elements. Major elements include K, Na, Ca, Mn, Fe, Mg, Ti, Al and Si.*

One cannot use a single partition coefficient to decipher the behaviour of a particular trace element in all magmas as both magma and mineral composition affects the *D* value (Best, 2003). A more silicic magma generally means that the coefficient for the same element in the same mineral will increase. Additionally, a decrease in *T* is generally linked to an increasing coefficient. Silicic melts that are cooler will commonly be tightly structured, or simply more viscous due to higher SiO_2 contents, with trace elements forced into coexisting crystals (Best, 2003). The effect of *P* is theoretically small, and in the opposite direction of *T*.

2.2.1 The R-factor

The relationship of liquid mass ratio of silicate/sulfide in a magma chamber can be explained using the R-factor. It was first defined by Campbell & Naldrett (1979) and can simply be outlined; a high R-factor means that the amount of sulfide droplets in a magma has been in contact with more silicate melt. For example, an R-factor of 1000 means the droplets have been in contact with 1000 times the amount of silicate melt. A high R-factor, or concentration, of economic elements such as Cu-Ni-PGE in sulfides result in a higher ore grade, thus being beneficial, if not essential, in ore-forming processes. In such a scenario it would be ideal with the economic elements partitioning into a small number of sulfide droplets in the magma. Campbell & Naldrett (1979) defined the the R-factor with the following equation:

$$C_{sul} = \frac{C_0 D(R+1)}{(R+D)}$$

Where:
C_{sul} = trace element concentration
C_0 = original trace element concentration in host rock (D=sulfide/silicate partition coefficient).
R = R-factor

A sulfide droplet that have been in interaction with large amounts of magma and consequently scavenged strongly chalcophile elements from it, will have a high C_{sul}, thus high R-factor. Figure 2.4 shows the effects of variations in R-factor on Ni and Pt concentrations that are in an immiscible sulfide fraction in equilibrium with a basaltic magma (Robb, 2005). In this diagram, Ni partitions heavily into sulfide liquid immediately after maximum partition is reached at approximately $R=10^{4.5}$, whereas Pt starts partitioning into sulfide liquid at $R=10^3$ (maximum at $R=10^7$). Another aspect influencing R-factor is pluming (2.5.3). When new, lighter, magma replenishes a magma chamber it can create turbulence, with the magmas being well mixed and exposed towards the chamber roof. These scenarios do, in other words, create ideal environments for the formation of a PGE deposit that requires a high R-factor, along with the concepts of 'pluming' and 'fountaining' as well as the 'Irvine Model'. These concepts are described in section 2.5.3 and 2.4 and outlined in Fig. 2.3 by Robb (2005).

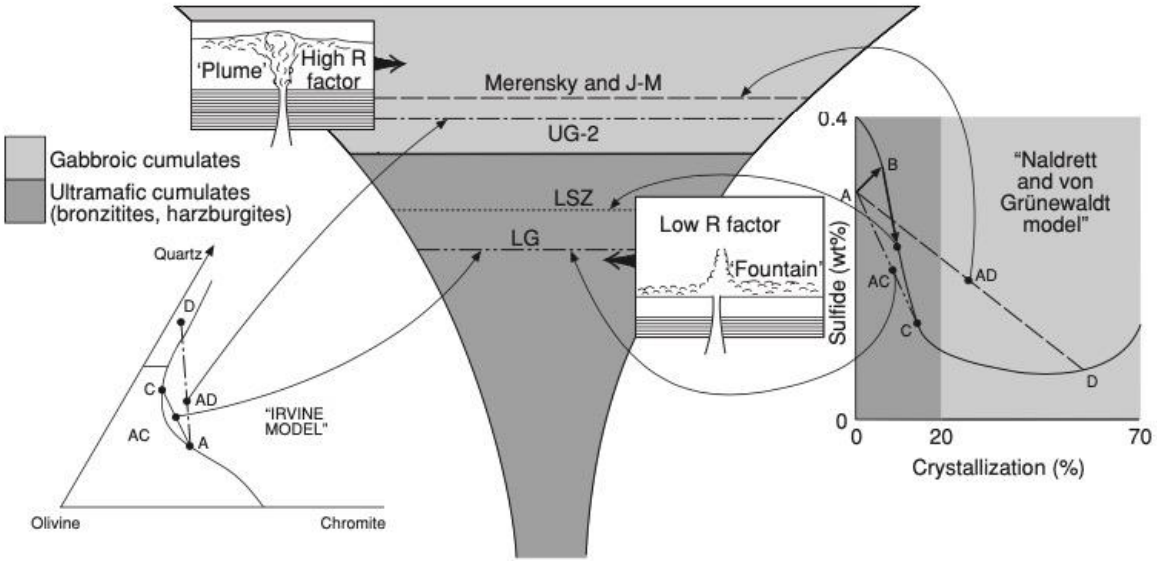

Figure 2.3: *Outlines the nature of igneous processes giving rise to chromite (Chr) and PGE-base metal sulfide deposits associated with layered mafic intrusions. Diagram from Robb (2005) modified after Naldrett (1997). LG and UG represents Chr seams of the Bushveld Complex (section 2.8.1); LSZ (Lower Sulfide Zone) represents PGE mineralisation in the Great Dyke; Merensky and J-M refers to the Merensky Reef in the Bushveld Complex and J-M reef of the Stillwater Complex, respectively, both of which contains PGE-sulfide mineralisation. Ultramafic and gabbroic cumulate difference is marked by first appearance of cumulus Plag in gabbroic cumulates.*

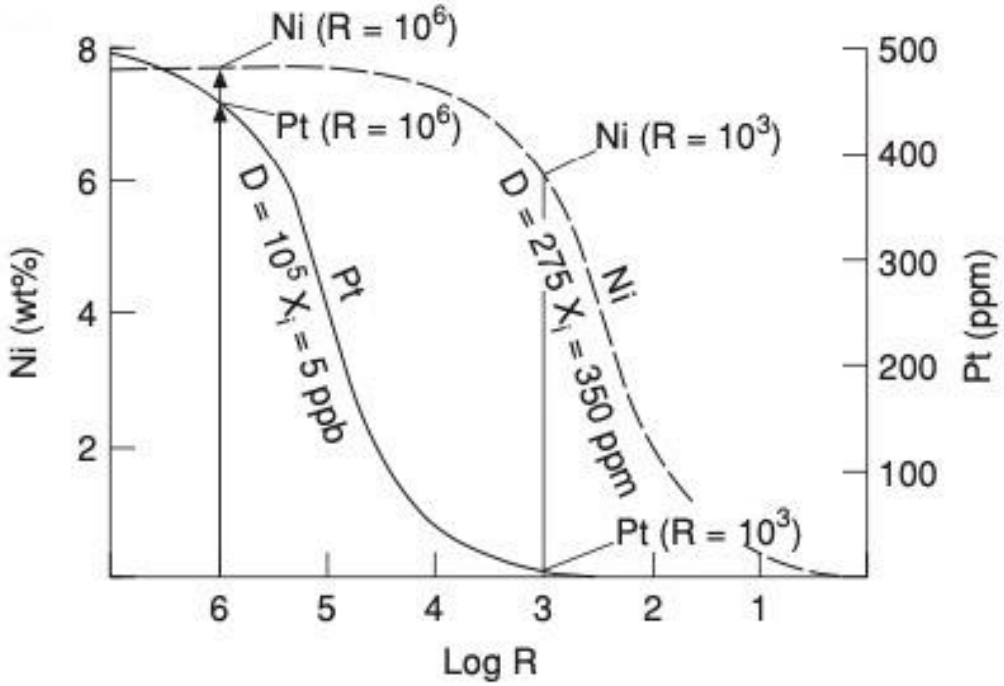

Figure 2.4: *Diagram from Robb (2005), edited from Naldrett & von Grünewaldt (1989). Diagram illustrates the effects of a varying R-factor on the concentration of Ni and Pt in an immiscible sulfide fraction in equilibrium with a basaltic magma.*

2.3 Elementary concepts of thermodynamics

To gain an understanding of Gibbs free energy, it is necessary to first obtain a general understanding of the basic end-member thermodynamic system components: isolated, closed, open and adiabatic systems. As the Earth is ever changing and cannot be theoretically defined, these systems cannot singularly be applied, however, they do play a part of the larger picture. The systems presented below are based on the definitions from Best (2003).

A **system** is the part of the universe that is being considered, and a system is distinguished by how it is interacting with the environment, outlined by the endmembers. An **isolated system** is, as the name suggest, is a system where no matter or energy can be transferred in or out of the system and no work can be done on or by the system. In geological terms, this is not applicable to Earth due to its ever-changing nature. Matter and energy can cross boundaries in an **open system** and work can be done on or by the system, and most geologic systems are open. A **closed system** is a mixture of the two above-mentioned systems, where energy (i.e. heat) can flow across the boundary but matter cannot, meaning the system will always be constant. A rapidly cooling think dike can be considered a closed system as the matter movement across boundaries are slow. An **adiabatic system** is thermally insulated, but energy can be transferred across boundaries based on work done on or by it. An example of this is a magma body or plume that cools and expands while it is ascending and decompressed, where little to no heat is conducted due to slow conduction rate. Although adiabatic systems do not exist in nature, mentioned example is the closest resemblance. A diagram of all systems is presented in Figure 2.5.

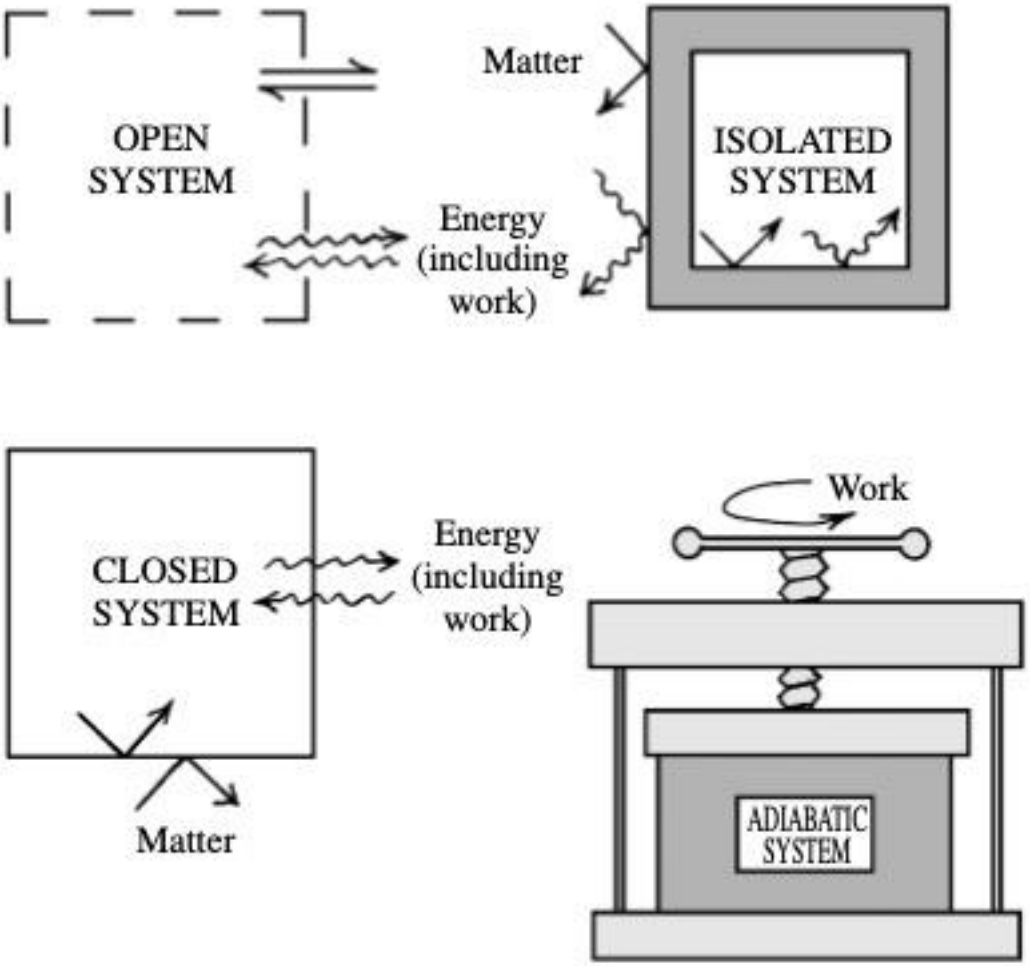

Figure 2.5: *Diagram from Best (2003) showing end-member thermodynamic systems.*

In addition to a system, any of the endmembers and constituents, there are a few more definitions that are important to understand:

Phase (ϕ) A phase is a structurally and chemically homogeneous part of a system, physically separable from other phases. A phase is bound by distinctive borders with adjacent phases. A phase may be liquid, solid or gaseous (Best, 2003).

Component (*C*) A component is any individual chemical constituent that defines a system. To make sure a list of constituents is not too long, a provision that a component of a system is added. This states that the smallest number of chemical entities is required to define the composition of every phase that exists in the system (Best, 2003). In other words, the phase constituting a system must be identified in order to decide what the components of that system are.

Variance (f) Variance is the same as 'degrees of freedom' and outlines the number of intensive variables that must be specified to fully characterise the state of equilibrium (Best, 2013)

The phase rule is an essential tool in interpreting phase diagrams, which provide inventory information on the number of phases, components and variance in a system at equilibrium (Best, 2003).

2.4 Irvine Model

The Irvine Model is a phase diagram where only olivine-chromite-silica endmembers are represented. The phase diagram specifically refers to basaltic systems (Robb, 2005). Robb (2005) presents a thorough description of the Irvine model of which is the basis in this section.

Figure 2.6 outlines the usual crystallisation pattern. In this pattern the basaltic magma usually starts with composition A (Figure 2.6b), where only olivine is on the liquidus. This will result in settling and formation of a dunitic cumulate rock. The magma will evolve towards composition B (cotectic phase boundary), if the olivine is extracted at composition A, where both the wt.% of SiO_2 and chromite is increased. At this point (B) a small portion of chromite (approximately 1%) will start to crystallise along with olivine. In this process, the magma will gradually increase along the cotectic line towards composition C. At this point, olivine and chromite can no longer be a stable liquidus assemblage due to the high SiO_2 content in the magma. At this stage, orthopyroxene will start to crystallise, forming a bronzitic cumulate rock. The magma will slowly evolve towards composition D and continued crystallisation will eventually see the appearance of plagioclase along with orthopyroxene at the liquidus. Chromite will no longer form at this stage, and only appear as an accessory phase. At this stage something extraordinary, away from the norm, needs to happen in order to create an ore-deposit. One way to do this is by introducing new and less primitive magma (compared to the original magma) into the system, essentially disturbing the crystallisation sequence. This creates a magma mixing and/or mingling scenario with composition D and E where the mixed composition lies somewhere in between those two points (Figure 2.6c). Exact location depends on the relative proportions of D and E compositions. Chromite will be stable at composition F due to the magma being within its stability field, in fact only chromite will crystallise at a short sequence of this composition. This is due to chromite being quite dense and settle efficiently, and a near monomineralic chromite layer will form. A great example of this is the Bushveld Complex (2.8.1), where a large magma chamber has developed, and chromite layers have crystallised to create remarkable ore bodies (Robb, 2005; Cawthorn, 2010).

Once the magma has evolved to composition G (chromite being extracted), olivine returns to dominate the crystallisation and only accessory contents of chromite will appear (seams in hanging wall). Figure 2.6d depicts a slightly different scenario of magma being forced into chromite field. Here, the magma becomes contaminated by silicious material (composition E), having a composition somewhere along the mixing line that joins composition E to SiO_2. Such a composition will lie transiently in the chromite field, forming a monomineralic chromite layer (between composition H and G). The examples in this section proves how major of a role contamination of a magma can play in ore-forming processes and is also valuable theory in understanding the processes that have may have played a role in mineralised pyroxenite pegmatites in the RUC.

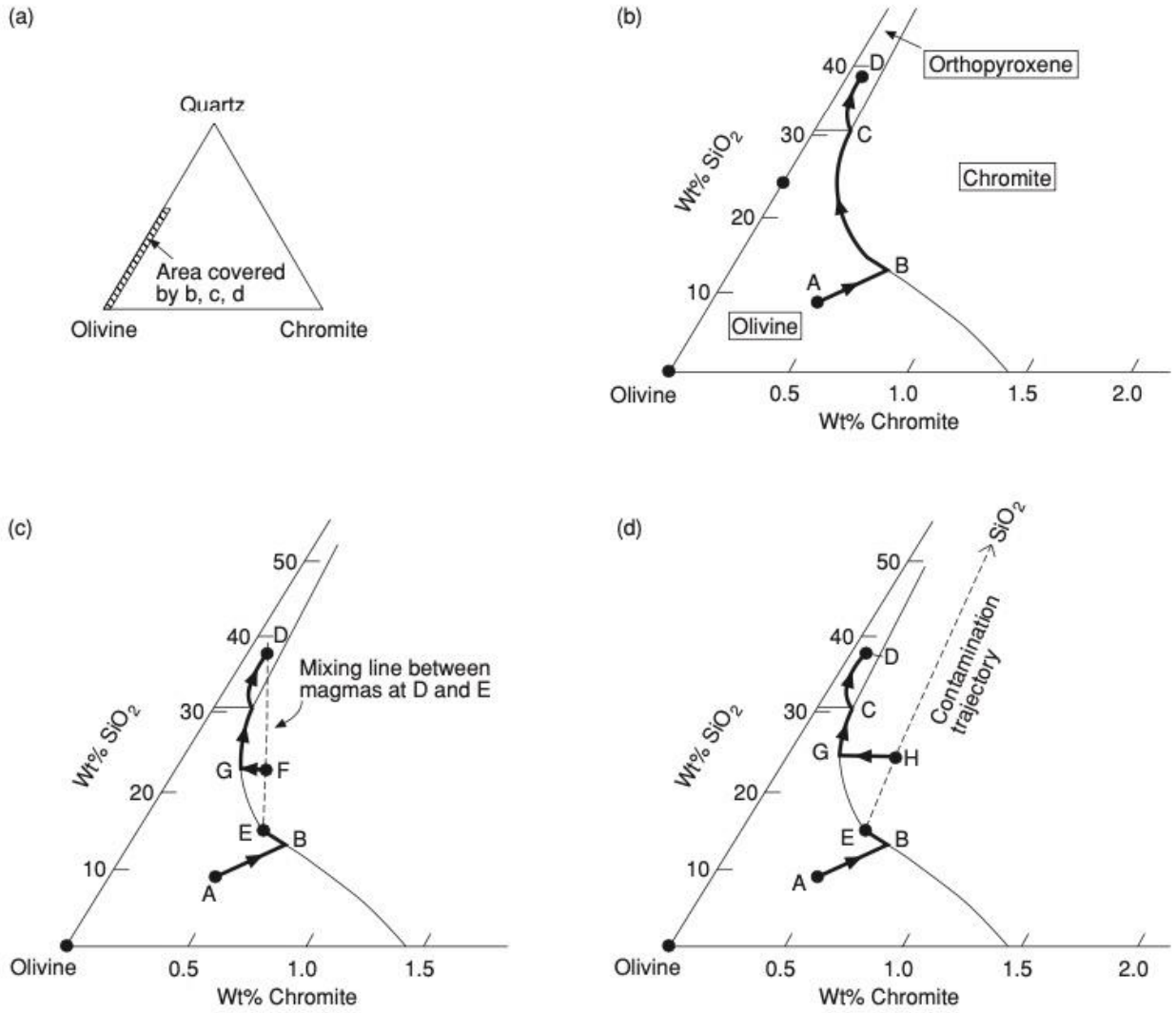

Figure 2.6a – d: *A portion of the ternary system Qtz-Ol-Cr from Robb (2005). See in-text for details.*

2.5 Magmatic processes

2.5.1 Partial melting and fractional crystallisation as ore-forming processes

Investigation of trace element behaviour during igneous processes can be very useful in understanding ore-forming processes (Robb, 2005). To appreciate an understanding of trace element behaviour, it is important to fully grasp the processes and roles of partial melting and fractional crystallisation. Trace elements partition themselves between solid residue and a melt phase during partial melting, with elements preferring the solid referred to as compatible and elements preferring melt referred to as incompatible (Robb, 2005).

2.5.2 Concept of magmatic recharge events

It is now well established that RUC has undergone multiple magmatic recharge events, most notably of picritic melts, but also of pyroxenite and alkaline melts (Larsen et al., 2018). The idea behind a recharge event is simply a new injection of magma in an already established magma chamber. These injections can be singular or multiple depending on the geological setting, and in RUC the evidence for multiple recharge events is well established. The nature of recharge events themselves are not simple, rather, they involve a complex set of variables that will control the outcome of a magma recharge.

Although it may be tempting to view crystallisation of a new batch of magma as an ordered event forming-, sub-horizontal layering, such as the Skaergaard intrusion (with gravitational crystal settling), it is more complex in most other instances (McBirney & Noyes, 1979). A cooling magmatic body with associated temperature gradients and magma density variations often result in prominent density stratification with development of liquid layers where elements are dispersed due to both temperature and chemical gradients (Huppert & Sparks, 1980; Turner, 1980; Irvine et al., 1983; McBirney, 1985). Crystal fractionation also plays a role in prolonged density variations in a magma chamber, and in Figure 2.7 it is clear that the residual magma density decreases in the early stages of olivine crystallisation due to the chemical components extracted from the olivine are denser than the initial liquid (Robb, 2005). This trend changes at around 1300°C with the introduction of orthopyroxene, and furthermore so at approximately 1175°C with a mineral such as plagioclase introduced, being less dense than the magma. In such an outlined situation (with starting composition based on the Bushveld Complex), it is possible for the final residual magma to be denser than when it started to solidify (Robb, 2005).

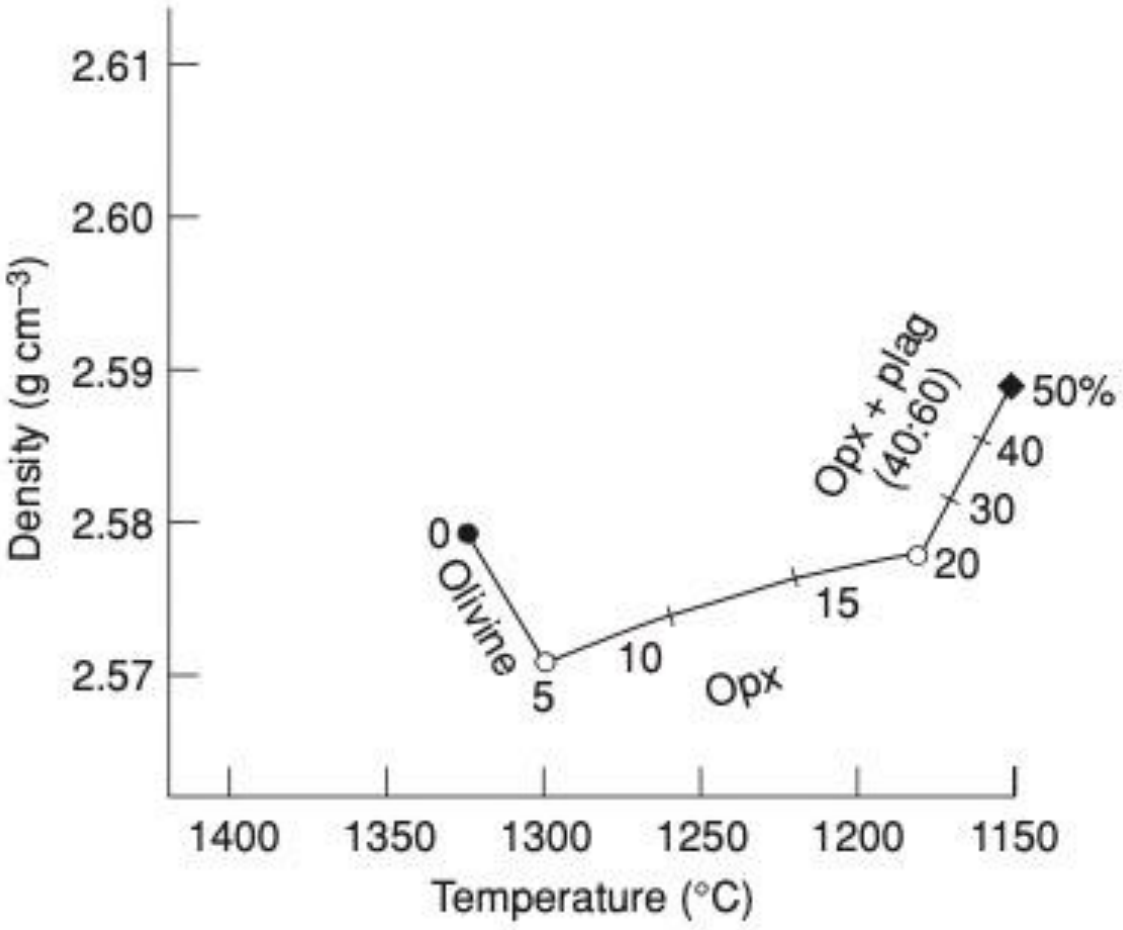

Figure 2.7: *A fractionating magma with variable density, with starting composition based on the Bushveld Complex. Figure from Robb (2005).*

2.5.3 Fountaining and Pluming

The nature of crystal settling in a magma chamber is greatly affected by density variation, particularly when an already evolved magma chamber is recharged with new magma. Two scenarios are considered in such a situation, namely 'fountaining' and 'pluming'. These two concepts are essential in understanding the key topics of this thesis, in particular fountaining and its nature in RUC. The concepts outlined below are based on the definitions set out by Robb (2005).

Fountaining

In a scenario where new magma is denser than the liquid residue in the magma chamber, often the case if new magma was injected in the early stages of crystallisation, then a fountain-like structure will shape (Figure 2.8). Mixing of the two liquids will primarily occur at the base of the ambient melt column. Fountaining has been recorded in the Bushveld Complex and is also evident in the RUC. As shown in Figure 1.7 there may very well be an excellent example of fountaining exposed in the lower parts of the ULS in the RUC.

Pluming

In an opposite scenario, where new magma is injected late in the crystallisation sequence, it is likely to have less density than the residual liquid, shaping a plume-like feature (Figure 2.8) where the new magma would ascend to its own density levels at the

roof of the chamber. A scenario where a plume has been injected and interacted with the roof of the magma chamber has been suggested to be the case for the Bushveld Complex, strongly implicated by both Chr and PGE mineralisation (Schoenberg et al., 1999; Kinnaird et al., 2002).

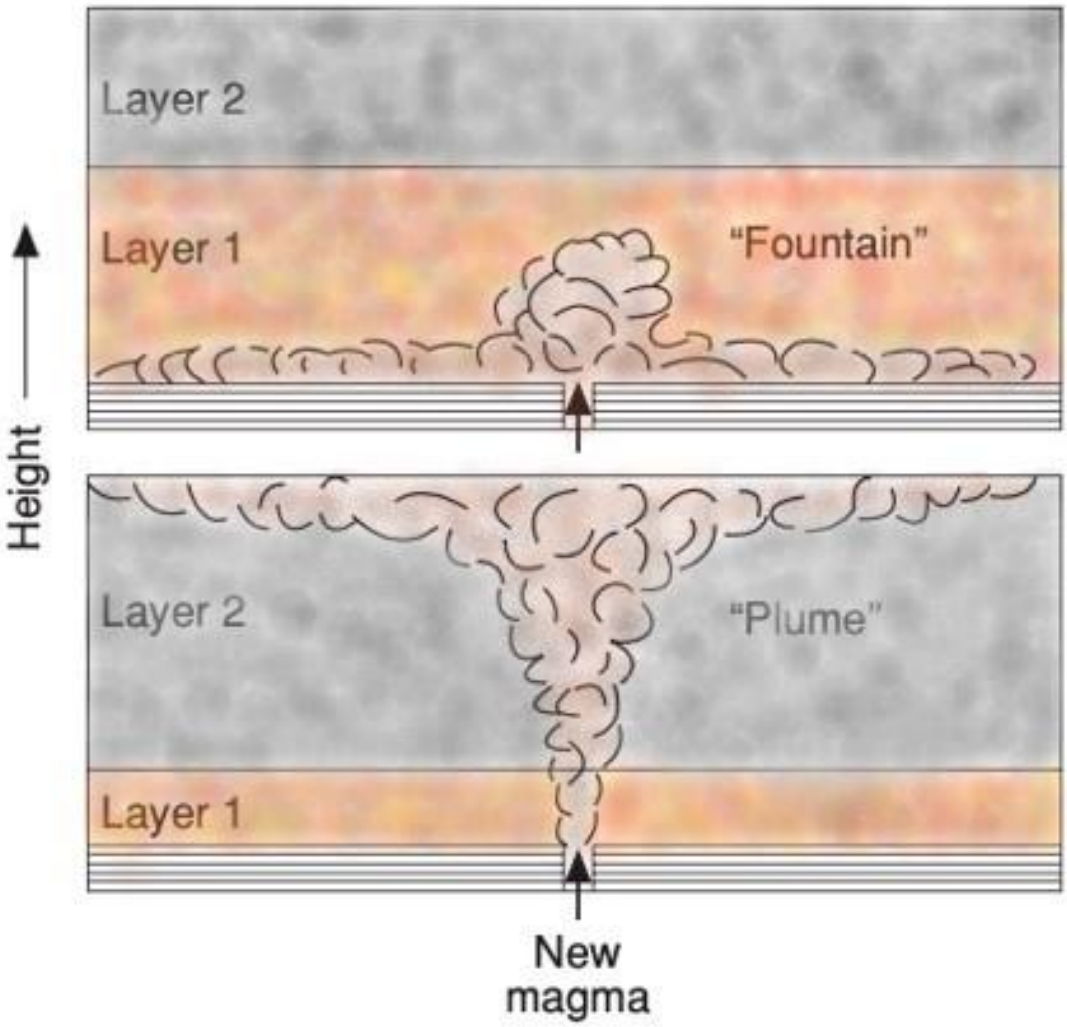

Figure 2.8: *Two scenarios when new magma is injected in an evolved magma chamber, where a fountain-like and plume-like feature are created. See in-text for details. Figure has been modified from Robb (2005).*

2.6 Platinum Group Minerals and PGE deposits

Platinum Group Minerals (*PGM*) are a varied group of elements including osmium (*Os*), iridium (*Ir*), ruthenium (*Ru*), rhodium (*Rh*), palladium (*Pd*) and platinum (*Pt*), (O'Driscoll & González-Jiménez, 2015). The PGE's belong to the transitional metals in the periodic table and can be subdivided into the light (Ru, Rh and Pd) and heavy (Os, Ir and Pt) PGE's. These elements are naturally enriched in the Earth's core due to their strong siderophile nature and are found in low abundance. Due to this nature, the major ore deposits we have (i.e. Bushveld and Norilsk) are derived from parental melts formed by partial melting in the mantle which contains intermediate concentrations of PGE. From here they can become economic ore deposits from sulfide immiscibility and being replenished in a larger magma chamber in Earth's crust (Daltry & Wilson, 1997). The most common PGM's form with sulfur (*S*), arsenic (*As*), tellurium (*Te*) or iron (*Fe*) as the

bonding elements and particularly S, As and Te are associated with ultrabasic magmatic systems, often in monosulfide solution as inclusions in chalcopyrite, pentlandite and pyrrhotite (Daltry & Wilson, 1997). The PGM's can be divided into 5 groups based on their crystallographic structure: arsenopyrite, cobalite, melonite, nickeline and pyrite group (Nicolaisen, 2016).

Most of Earth's major PGE deposits are associated with mafic and ultramafic igneous rocks (Godel, 2015). PGE-mineralised horizons usually occur as lateral and uniform layers extending for hundreds of kilometres along strike, however, the origin of these PGE-rich layers remain controversial and debatable (Godel, 2015). With advancement in technology comes improved multidisciplinary spatial resolution and detection limit datasets, which creates new models. These models consider geochemical and physical processes over a range of scales and temperatures, thus making our modern understanding of PGE deposits better yet ever challenging.

Major intrusions around the world contains excellent well-exposed PGE deposits. Famous examples can be seen in Figure 2.9 and include the Bushveld Complex (South Africa), Norilsk and Talnak (Russia) and the Skaergaard (Greenland). These deposits all share some common traits leading to a chain of events eventually forming stratabound Cu-Ni-PGE deposits, but also differ significantly with other characteristics, of which will be further presented in section 2.8.

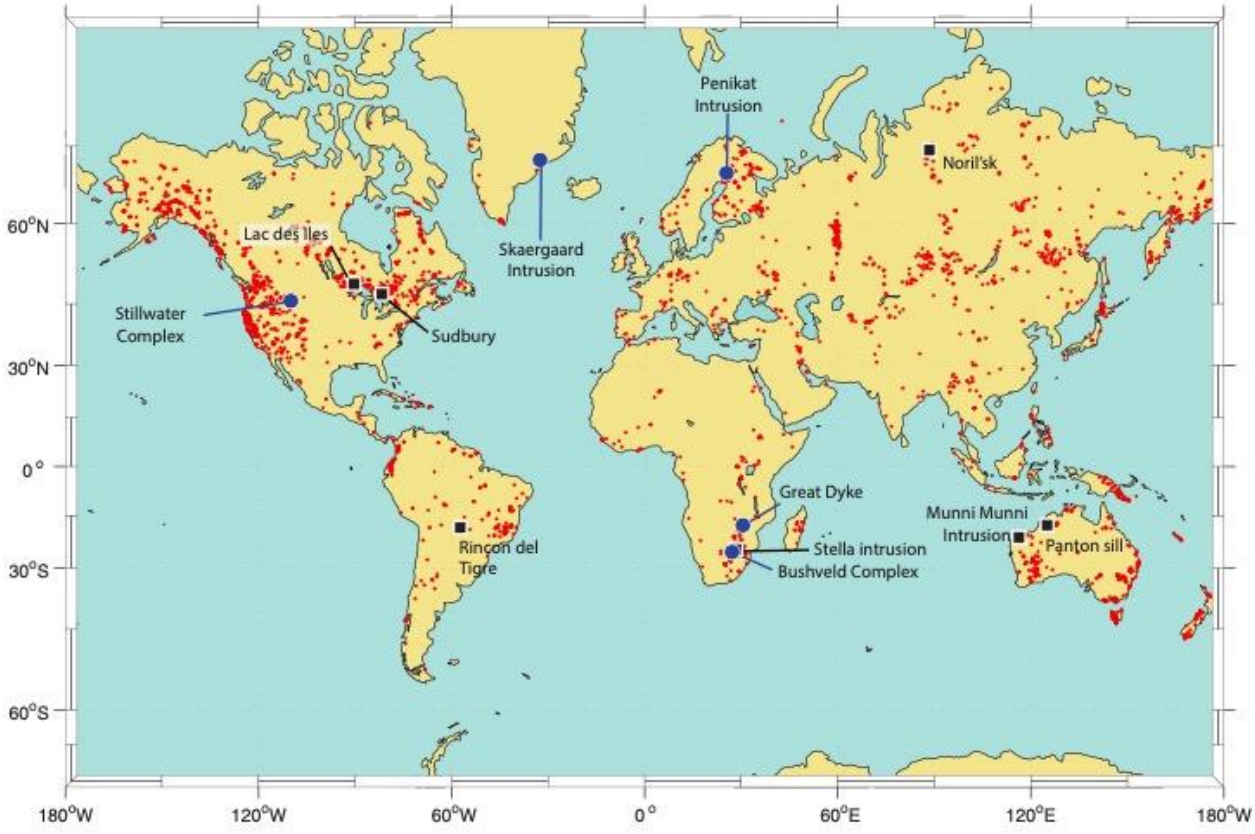

Figure 2.9: *Map of the major PGE-deposits known globally. A brief presentation of the deposits that share similar characteristic with the RUC can be found in section 2.8. Map retrieved from Godel (2015).*

2.7 Pyroxenite pegmatite

One of the main objectives in this thesis is to investigate mineralisation in the pyroxenite pegmatites in the RUC. Numerous outcrops have been sampled and described worldwide, with a range of geochemical and petrological methods used to unravel its nature. The most famous comparison to date is found in the Bushveld Complex, particularly the Merensky Reef. Here, there are well-documented studies in examining the trends and nature of the pegmatitic pyroxenites. The PGE mineralisation in the Merensky Reef is associated with pyroxenite pegmatite, with many models developed in attempts to find a common process for pegmatitic texture formation and PGE mineralisation occurrences (Cawthorn, 2006). Several models include late-stage, evolved, water-enriched magma involvement, produced by magma fractionation, however, other models propose high-temperature, primary magmatic processes (Cawthorn, 2010). Both models rely on large pyroxene grain size, as is also the case in the RUC, however, Cawthorn et al. (2002a) emphasise that PGE mineralisation is not only confined to pegmatitic pyroxenites. These studies are important tools in trying to investigate what may be a plausible scenario in the RUC.

2.8 Geology of similar layered intrusions worldwide

Though world class examples of well exposed deep crustal ultramafic intrusions considered a conduit system are rare, there are localities with similarities (Grant et al., 2016b). The extended research conducted in many of these areas, particularly the Bushveld Complex, Norilsk & Talnak and Jinchuan, can be very useful in furthering our understanding of the SIP. A common feature in these examples are zoning, ultramafic (dunitic) cores and mafic (gabbro) rims (Grant et al., 2016b). Further similarities include evidence of multiple recharge injections and reactions with pre-existing cumulates. Although there are multiple world-class examples, only the most prominent and large ones that can be related to the SIP and RUC will be mentioned. This section will be kept rather short as some of these localities, particularly the Bushveld Complex (focussing on the Merensky Reef), will be re-visited in Chapter 5.

2.8.1 Bushveld Complex (South Africa)

The Bushveld Complex located north of Johannesburg, South Africa, is host to one of the most significant reserves of PGE, producing approximately 80% Pt and 20% Pd of the total PGE mined annually (Cawthorn, 2010). There are also considerable amounts of Ni, V and U (Cawthorn, Merkle, & Viljoen., 2002a). These elements are layered in orthopyroxenite, chromitite and vanadiferous magnetite layers, ranging from mm to tens of m in thickness. It is by far the largest layered intrusion in the world, extending 450km east-west and 350km north-south (Godel, 2015). The ultramafic and mafic rocks at the Bushveld were emplaced into a stable cratonic shield around 2.06 b.y. ago, and have been exceptionally well preserved (Cawthorn, 2015). They are commonly referred to as the Rustenburg Layered Suite (South African Committee For Stratigraphy, 1980). Little deformation and metamorphism have taken place after solidification. The Rustenburg Layered Suite has been divided into five major zones based on cumulus mineral assemblage; Marginal Zone (fine-grained norite), Lower Zone (cyclic units of orthopyroxenite-harzburgite-chromitite), Critical Zone (pyroxenite, norite, anorthosite and chromitite), Main Zone (gabbronorite) and Upper Zone (anorthosite, diorite and magnetitite), all zones outlined in Figure 2.10.

Up to 1 million km^3 of magma was emplaced over 65,000 years and the intrusion is exposed as a three-lobed body up to 7km in thickness with inward dipping dunite to monzonite layers (Cawthorn, 2015). The exact compositions of the parental magmas of the Bushveld are still disputed, as is also the feeder to the intrusion's identity (Cawthorn, 2015). This is largely due to magma mixing and models of magma additions which makes interpretations challenging based on both rapidity and vertical extents of affected sequences. As the Bushveld is known as the largest mafic intrusion, it represents an endmember for magma chamber processes (Cawthorn, 2015).

Although the Bushveld Complex consist of numerous layers, only three are significant and PGE-enriched enough to be called reefs, namely the Upper Chromitite 2 (UG-2), Merensky Reef and the Platreef (Figure 2.10), and these three reefs represent the largest PGE horizons (Cawthorn 1999; Naldrett, 2011a). The Platreef is located at the base in the Northern Limb, whereas the UG-2 chromitite and Merensky Reef are located in the upper part of the Critical Zone (Cawthorn, 1999).

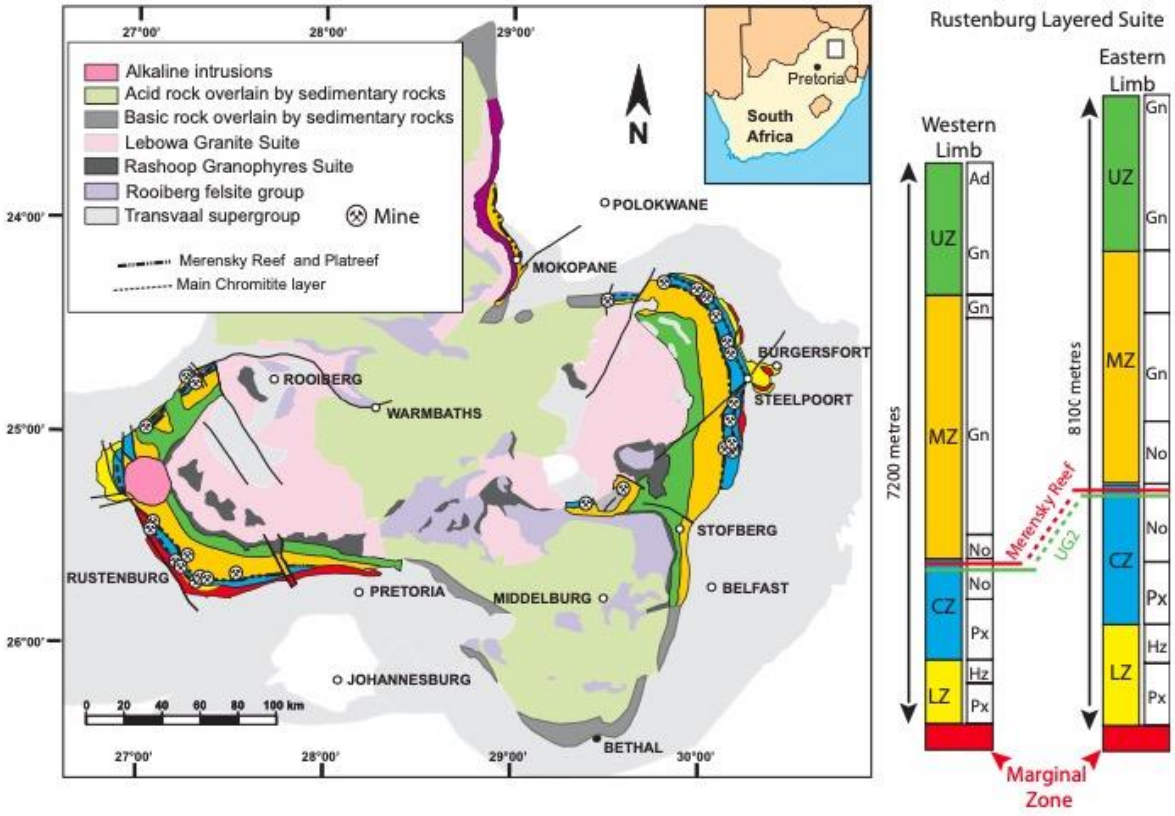

Figure 2.10: *Simplified geological map of the Bushveld Complex with Rustenburg Layered Suite stratigraphy (Godel, 2015).*

As briefly mentioned in Chapter 1, there are several excellent exposures of fountaining structures in the RUC (Figure 1.7). Fountaining is not unheard of in the Bushveld Complex, though, to the best of the authors knowledge, it has not been described in journal articles to date. Kinnaird et al. (2002) describe the nature of magma replenishment (Figure 2.11), and this, along with literature on parental magma in the Bushveld Complex, will be further assessed in aiding the discussion in Chapter 5.

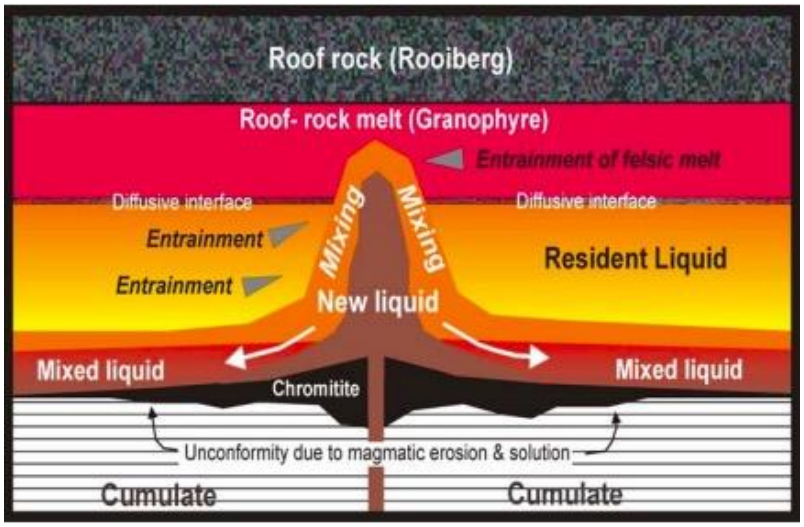

Figure 2.11: *Magma replenishment causing fountaining in the chamber that partially melts rocks in chamber roof, causing contamination and magma mixing, leading to formation of chromitite (Kinnaird et al., 2002).*

2.8.2 Norilsk and Talnak (Russia)

One of the largest Cu-Ni-Pd deposits of its kind can be found in the Norilsk-Talnak region in Russia. The most recent interpretation by Naldrett (2013) places the deposit of Upper Permian to Lower Triassic in age and is believed to be a feeding system to the Siberian Trap flood basalts. Starostin & Sorokhtin (2011) suggests that the ore elements (except Fe) are derived from the crust rather than the mantle. This deposit differs from the Bushveld and the Skaergaard Intrusion in that it is believed to have been replenished multiple times with magma in several different magma chambers, with various levels of magma mixing enrichment (Naldrett, 1997).

Prior to the discovery of the Norilsk deposit, all large and well-known Cu-Ni and PGE deposits in the world were associated with enormous ultramafic to mafic intrusions of Proterozoic Age (Starostin & Sorokhtin, 2011). With the discovery of the new type of ore deposit in the Talnak deposit, the understanding of magmatic sulfide ore formation was strongly improved.

Starostin & Sorokhtin (2011) suggest that the regenerated sulfide ores of the Norilsk type could have formed from 4 conditions:

(1) The presence of a large aulacogen initiated in the Early Proterozoic, filled with terrigenous, gypsiferous and coaliferous hydrocarbon-saturated sediments. The aulacogen is associated with magmatic sulfide Cu-Ni mineralisation. Basalts above these ore bodies are often marked by high magnesium content and carbonates being present as Iceland spar crystals. This factor is favourable for the discovery of a large ore body of such type.
(2) Hundreds of millions of years old fault zones containing confinement of perspective areas to troughs, either cross cutting thick continental plates or occurring at its own boundaries.
(3) Island-arc systems and tectono-magmatic activation zones or mobile orogenic belts.
(4) Global periods of boundaries which is characterised by active processes of breakup of continents and large-scale trap magmatism.

With similar geochemical characteristics of intrusive rocks and lavas in the Nadezhda Formation, in addition to similarities in depletion of nonferrous and noble metals, a genetic concept was developed and widely accepted for the Norilsk deposit (Starostin & Sorokhtin, 2011). This concept suggests an open magmatic system involving common tholeiitic melts during ascending and eruption with the sulfide ores forming as a result of interaction between the magmas and country rock (Lightfoot et al., 1993; Naldrett, 2003). This concept also played a pivotal role in developing genetic models for other famous Ni-Cu deposits such as the Jinchuan (described in section 2.8.3), Kalatongke (China) and Voisey's Bay (Canada). Figure 2.12 outlines the lateral and vertical zonality in contact-metamorphic aureoles of differentiated ultramafic to mafic intrusives in the Norilsk region.

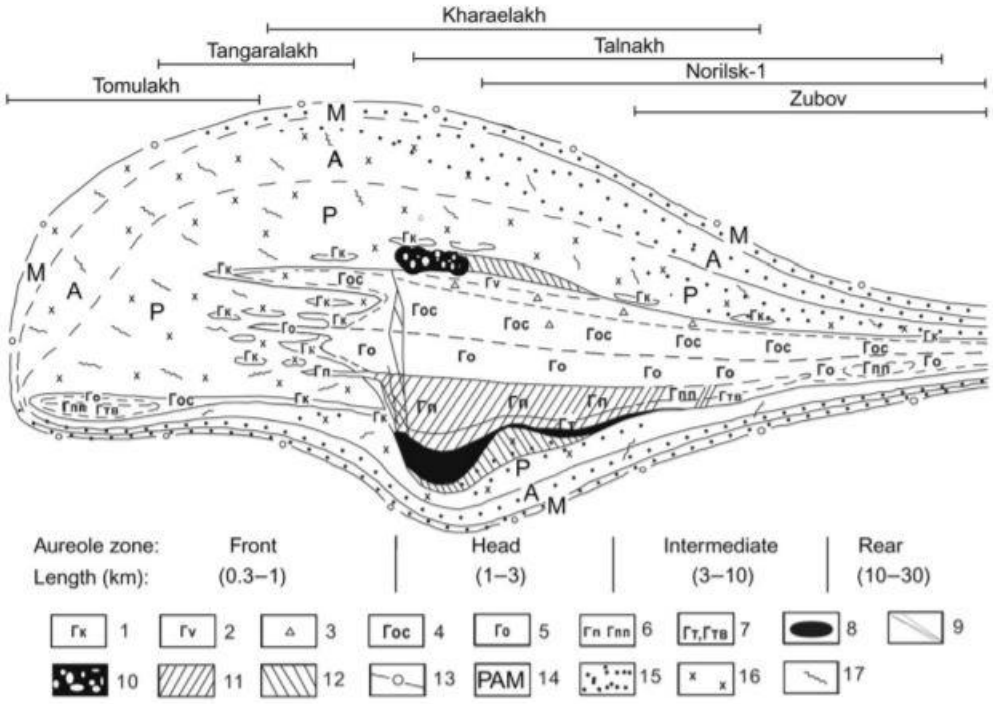

Figure 2.12: *Model showing the lateral and vertical zonality in contact-metamorphic aureoles of differentiated ultramafic to mafic intrusives in the Norilsk region (Turovtsev, 2002). 1-7 marks intrusive rocks, whereas 8-12 marks the sulfide ores. 13: outer contour of aureole; 14: metamorphic facies of hornfelses and marbles (P: pyroxene-hornfels; A: amphibole-hornfels; M: muscovite); 15: metamorphic rocks; 16: metasomatic rocks; 17: hydrothermal rocks.*

2.8.3 Jinchuan (China)

The Jinchuan intrusion is a Ni-Cu-PGE rich deposit that occurs as a 6000x300x1100 meter NW oriented lens, with occurrence of three PGE mineralisation groups (Yang, Ishihara & Zhao, 2005). Group I was formed at magmatic temperatures (with PGM's associated with chalcopyrite, pyrrhotite and pentlandite), Group II at hydrothermally altered zones of the intrusion and Group III in sheared dunite and lherzolite (Yang, Ishihara & Zhao, 2005). The most common PGM in all groups is sperrylite. The general consensus is that the Jinchuan deposit occurred as a result of primary magmatic crystallisation which was followed by hydrothermal remobilisation, transport and finally PGE deposition (Yang, Ishihara & Zhao, 2005). The deposit is to date considered the third world largest economic Ni-Cu deposit (Naldrett, 2004).

2.8.4 Great Dyke (Zimbabwe)

The Great Dyke is the second largest single resource of PGE on the Earth and is a linear mafic-ultramafic intrusion that formed at 2575.4 ± 0.7 Ma (Cawthorn, 2010; Oberthür et al. 2002). The highly elongated shape makes it different to other PGE deposit hosts such as the Bushveld and Stillwater Complexes (Oberthür et al., 2002). The Great Dyke was emplaced by a series of initially isolated magma chambers that eventually became linked at the latter stages of the intrusion (Cawthorn, 2010). The Great Dyke is subdivided into a lower Ultramafic Sequence and upper Mafic Sequence, with interplay between crystallisation and magma emplacement giving rise to cyclic units within the Ultramafic Sequence (Wilson, 1982). These units consists in the top of dunite or harzburgite overlain by pyroxenite and the lower part of chromitite intercalated within dunite (Wilson, 1982). The uppermost part of the Ultramafic Sequence is associated with the PGE mineralisation (Oberthür, 2002).

3

Methodology

3.1 Field Methods

Fieldwork was conducted in August 2019 over a period of two weeks. The weather conditions were highly variable and at times challenging, making some of the fieldwork difficult. Each day was made the most out of with an attitude of 'more sampling is better than less'. Due to the remote locality of the RUC, all field participants were transported by means of helicopter to a plateau, where camp was set up for the duration of the fieldwork. The objectives were quite broad initially but narrowed down after becoming familiar with the regional geology. One of the primary objectives was to investigate if recharge events marked by pyroxenite pegmatites, the characteristics of the pyroxenite pegmatites and its role in facilitating sulfide oversaturation and formation of Cu-Ni-PGE mineralisation. This was combined with field mapping and continuous sampling from day one until completion. Figure 3.1 shows the sampling from one of the largest and most prominent pyroxenite pegmatites.

Field descriptions were documented in *Rite in the Rain Universal Field Book*, and later transferred digitally on an *Apple Macbook Air*. Some field descriptions were recorded digitally in-field, using an *Apple iPad (4th Gen.)* with *Midland Valley's* software *Field Move*. These descriptions were documented in accordance with mapping out a contact zone between the Langstrand gabbronorite and wehrlite/dunite variation, in trying to gain an overview of pegmatites in the area and potential similarity to other pegmatites in the field area. These were observational studies and mapping only and will not be presented further in this thesis. To gain precise GPS coordinates of each locality with descriptions, a *Garmin GPSMAP 64s* with a horizontal and vertical precision of 5 meters was used. Most samples were either knocked out with a sledgehammer or chiselled out with an *Estwing No.3.* The purpose of the task was to get a representative collection of the pyroxenite pegmatites and recharge zones; thus, sampling was concentrated within pegmatites, boundary pegmatite-host rock, host rock (wehrlite and/or replacive dunite), and any other surrounding structures of interest. Each sample was approximately 'fist-sized' or smaller to gain as much of a variable geochemical content as possible, and to create as representative samples as possible.

Figure 3.1: *Selected sample spots from one of the largest and most prominent pyroxenite pegmatites.*

3.2 Laboratory

3.2.1 Sample preparation

All samples collected in field were investigated at Norwegian University of Science of Technology (*NTNU*) for further analysis preparation. Due to the large number of samples, only the most representative samples for the objectives of the thesis were chosen for further analysis. These were first cut in the thin section preparation laboratory at NTNU. The cut slices (approximately 1 cm thick) prepared for thin sections, of which 24 samples were chosen and 12 eventually made into thin sections (due to both capacity in the laboratory and an appropriate number of representative thin sections for the thesis). The remainders of the samples after cutting were sent to *Australian Laboratory Services* (ALS) in Sweden for whole-rock geochemical analysis. After petrographical analysis on the thin sections, they were carbon-coated and analysed using SEM and EPMA. All these methods will be further described in detail in the following sections.

3.2.2 Thin sections

Twelve samples containing the most prominent features related to the thesis objective were chosen for diamond blade rock slicing. Each sample was sliced to 1 cm thickness at NTNU, under the supervision of Kjetil Eriksen. Tungsten carbide jaws were used to avoid Fe-contamination, and ironized parts of the samples were avoided due to both brittleness during cutting and creating possible false geochemical results from thin surface layers. Between each sample the blades were washed, and any rock remains removed to avoid cross-contamination. Representative areas of each sample were marked (28x44 mm) and made into polished thin sections, and later used for SEM and

EPMA analysis. The remains from each of the samples were put into a 50g bag for further whole rock analysis conducted at ALS in Sweden. Each thin section was later scanned in plane polarised light (*PPL*), cross-polarised light (*XPL*) and reflected light using *EPSON v600* photo scanner with polarizing film (Figure 3.2). These photos were used both for reference and close observation due to its excellent resolution during petrology work. Structures and points of interest were photographed with *Nikon Eclipse E600* microscope connected to a *Spot Insight CMOS* camera.

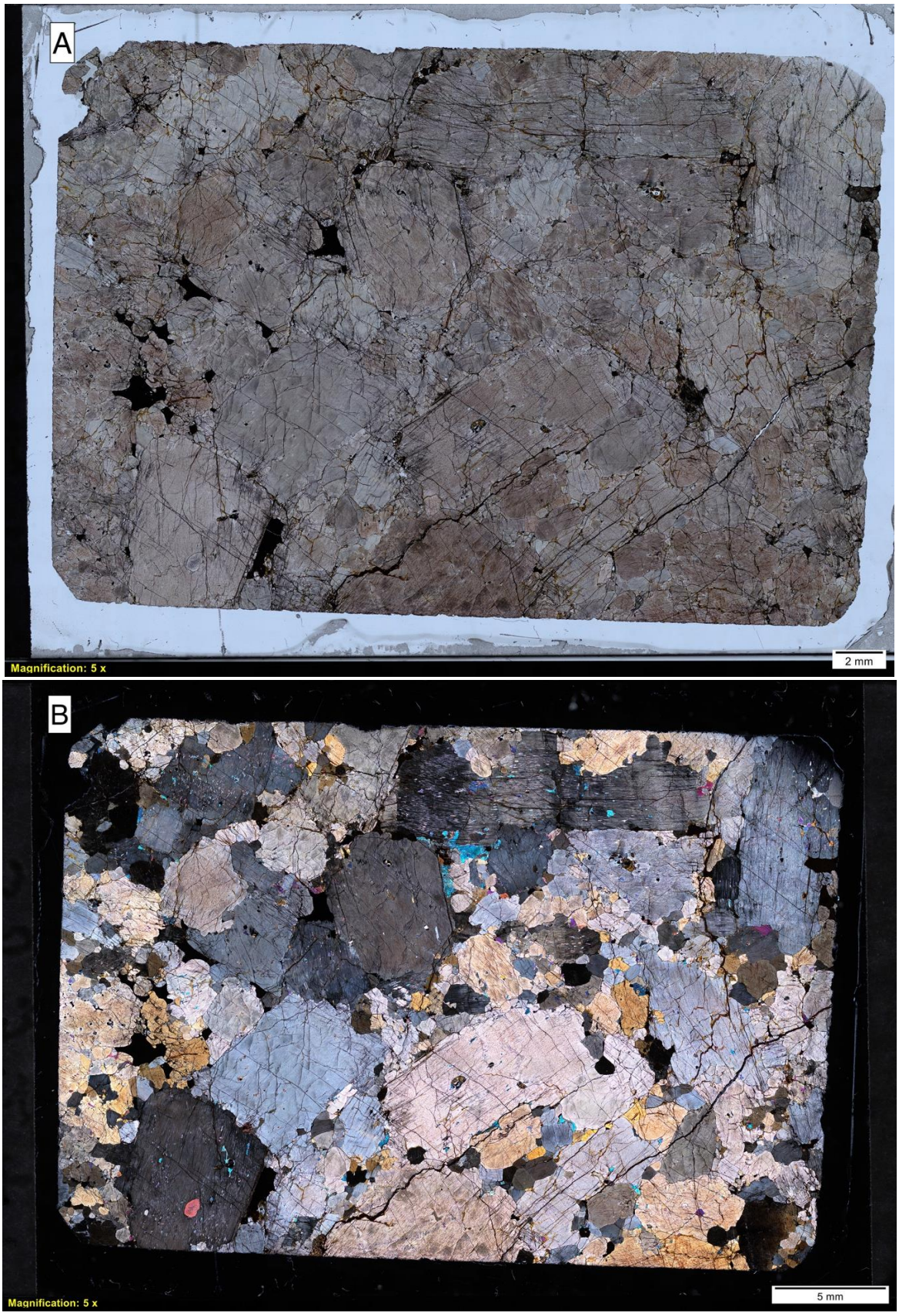

Figure 3.2a – b: *Thin section images in PPL (top) and XPL (bottom) of sample AM19-010.*

3.2.3 Whole-rock analysis

A total of 24 rocks samples were sent off to ALS to conduct major- and trace element chemical analysis in Pitea, Sweden. This was done due to both their expertise in the field, time pressure, and lack of resources available at NTNU. The samples chosen match 12 of those of which thin sections were made, with additional 12 with no supporting thin section, and each sample sent off was carefully chosen considering brittleness and removal of any weathering of which would disturb the results. The samples were prepared simultaneously with the thin sections in the *Rock Mechanics Laboratory at the Department of Geoscience and Petroleum* at NTNU. Diamond bladed cutting machines were used in this process.

3.3 Analytical methods

3.3.1 Optical microscopy

Two separate microscopes were used to observe general petrological structures and textures in thin sections prepared at NTNU. A total of 12 thin sections have been investigated. At NTNU, an *Olympus-BX51* microscope was used. The microscope was fitted with *Olympus UIS2 Mplan* objectives and *Jenoptik ProgRes-Speed XT5 core* camera. Images of particularly interesting sections were captured using *ProgRes CapturePro* software. Appropriate software magnification and scale calibration was completed by using the calibration sample delivered with the camera. At *Stratum Reservoir* in Sandnes, Norway, a *Zeiss AX10* has been used.

An essential tool in petrology is the optical microscope of which can be used to determine mineralogy, approximate bulk-rock mineralogy, textures and ore-forming processes. The latter is naturally essential in this thesis, along with the investigation of both translucent and opaque minerals and their textures.

In optical microscopy, there are two views primarily used: **plane-polarized light (PPL)** and **cross-polarised light (XPL).** Additionally, reflected light is used to observe opaque minerals. In PPL the light is oriented in one direction and filtered, and when the light is passing through it scatters in all directions, depending on the optical properties of the mineral (i.e. Figure 3.2a). Sørensen (2013) revised the *Michel-Lévy interference colour chart*, showing white light being dominant followed by opaque minerals blocking light (Figure 3.3). Certain minerals have different colours when observed at different angles in PPL, of which is referred to as pleochroism. In XPL, a second polarizing filter (analyser) oriented perpendicular to the first filter, is added, hence the colour scheme of each mineral changes (Figure 3.2b). In XPL view wavelengths are only transmitted in a certain direction after passing through a mineral, referred to **interference colours**. These colours are divided accordingly in the Michel-Lévy interference colour chart, which can be used to identify XPL colours for all anisotropic minerals. Another consideration in petrography work is **relief**, which can also be used as an optical identification reference, seen as minerals appearing to protrude from the background as a result of mineral refraction index. Lastly, **reflected light microscopy** is useful for identification of opaque minerals. Here, each mineral is identified by the amount of light reflected, colour and neighbouring grain relationships. In the investigated thin sections minerals such as chalcopyrite, pyrrhotite, pentlandite, spinel and pyrite appeared in highest abundance.

All abovementioned criteria are essential in petrography and a natural part of the workflow in identifying and understand the evolution of the sample. Each sample that

was found most relevant for the objectives was mapped out using optical microscopes. Based on this a better understanding of the pegmatitic pyroxenite ore-forming processes was gained, along with the relationship with the host-rock and the petrographic evolution.

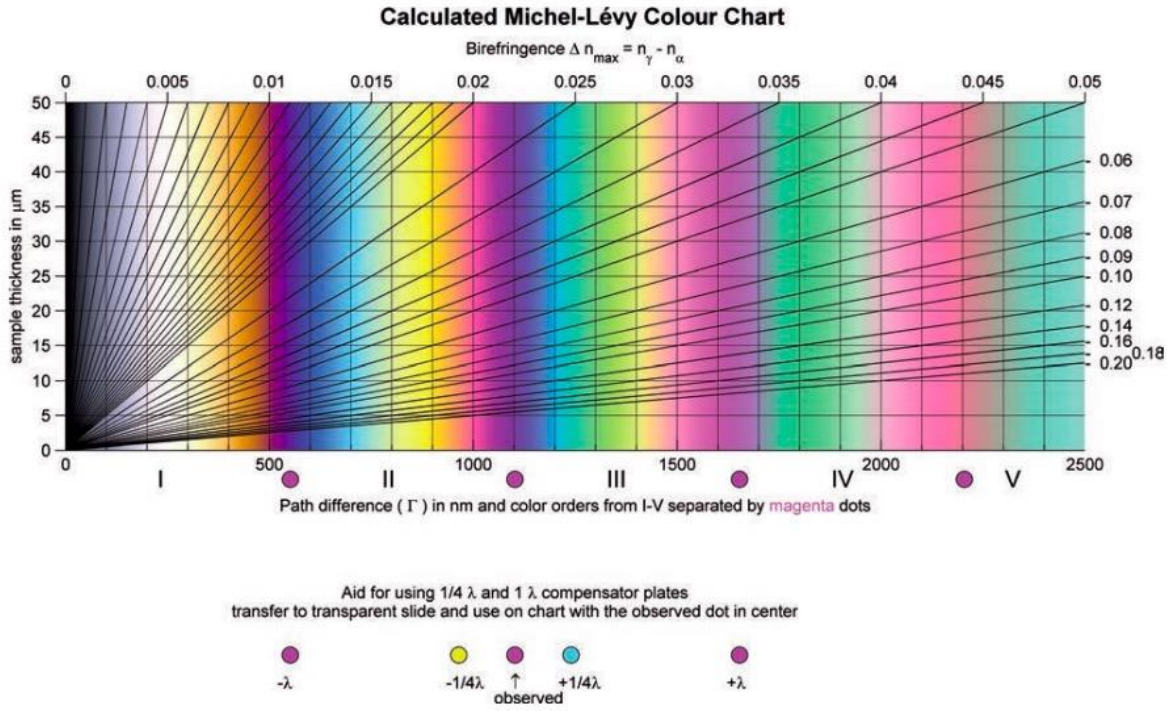

Figure 3.3: *Re-calculated Michel-Lévy interference colour chart (Sørensen, 2013).*

3.3.2 X-Ray Diffraction (XRD)

X-ray diffraction is a very useful tool for gaining a rapid identification of unknown crystalline phases (minerals) in a sample. In its simplest terms, the XRD consists of three elements: sample holder, the X-ray tube and X-ray detector. A filament is heated to generate X-rays and these produce electrons of which are accelerated towards a target by applying voltage. These essentially lead to a bombardment of X-rays on the target. Eventually, the electrons will be sufficiently energized and dislodge from the inner shell of the target material, producing distinctive X-ray spectra. These spectra consist of specific wavelengths (Kα and Kβ) of which are characteristic of the target material (Cu, Ni, Co, Fe, Mo, Cr, Ag), theorised in Figure 3.4. Cu is the most common target material for single-crystal diffraction, having radiation (CuKα) = 1.5418 Å, with the X-rays being collimated and directed onto sample. A collimated light beam or other electromagnetic radiation has parallel beams and will, therefore, spread minimally when propagating. Over the course of an analysis, the detector and sample are rotated, reflecting off different X-ray intensities of which is recorded. When the geometry of the X-rays satisfies Bragg's Equation, constructive interference occurs and a peak in intensity occurs. An example of how an interpreted analysis may look like can be seen in Figure 3.5. XRD is an excellent analysis method to use for a quick quantification of whole-rock analysis.

Six samples of particular interest were chosen for XRD analysis to quantify whole-rock mineralogy. The analysis was conducted at Stratum Reservoirs office in Sandnes, Norway, using *MDI Jade 9* software.

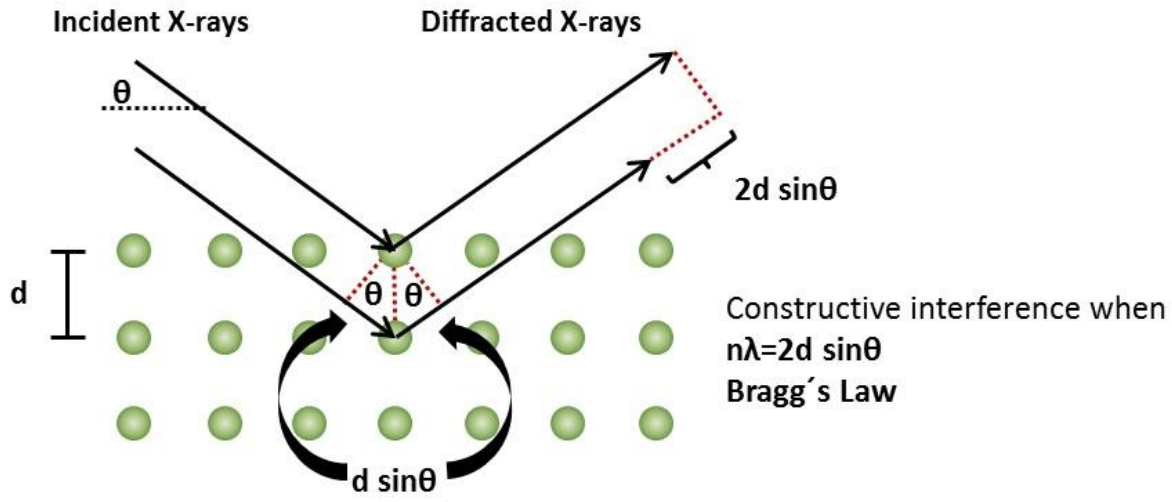

Figure 3.4: *Schematic showing how incident X-rays are reflected at an angle of 2θ according to Bragg's Law, and diffracted (Touloukian, 1977). Data collected of typical powder patterns is at 2θ from approximately 5-70°.*

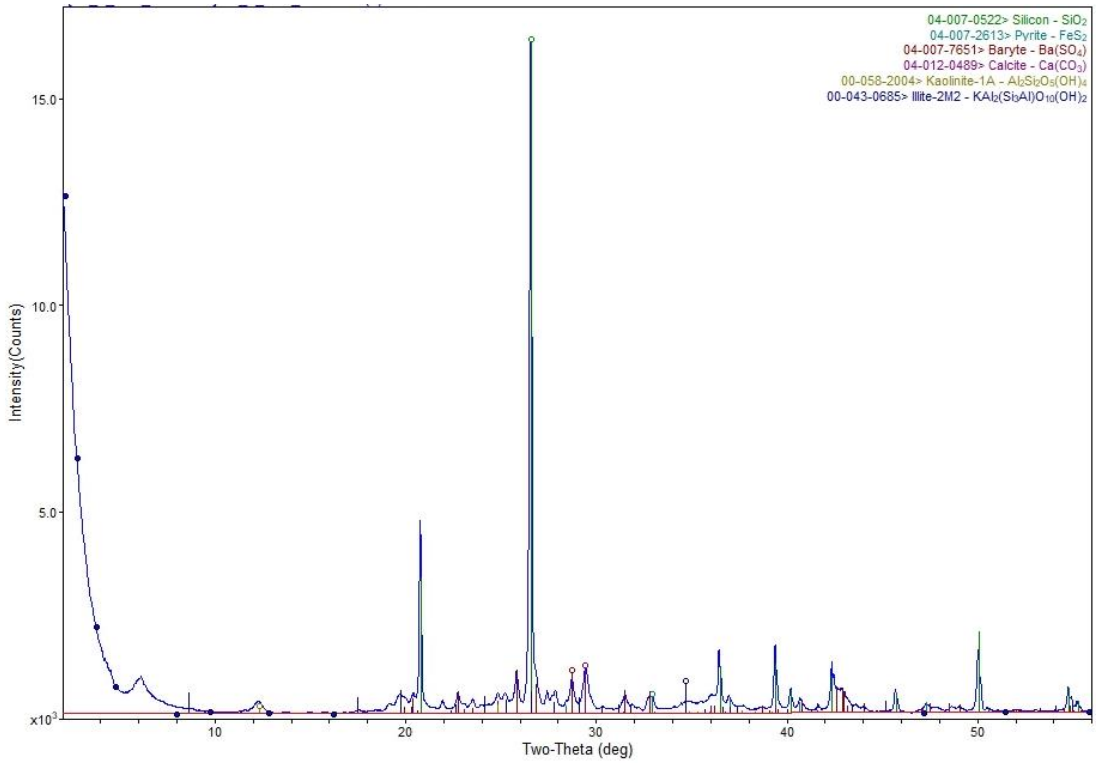

Figure 3.5: *Results are commonly presented in an x-y plot with peak positions at 2θ and intensity (X-ray counts). Shown here is an example from one of the analysis conducted during this research.*

3.3.3 Scanning Electron Microscope (SEM)

To gain valuable information on automated mineralogy, the thin sections were carbon coated using *Cressington Carbon Coater 208* and analysed by using back-scattered electrons (*BSE*). The SEM analysis was completed at NTNU's new laboratory facilities using a *Hitachi SU6600*. Contrast differences are produced in each mineral phase by the elastically scattering of primary electrons by a function of the mean atomic number. This creates bright or dark shaded faces depending on the atomic number,

bright indicating high atomic number and vice versa. The step size was set to 15 μm with a 5% overlap. The acceleration voltage was set to 15 kV, with a working distance of 15 mm. The aperture was set to 120μm with a 60x zoom (on polaroid), and the Energy Dispersive Spectrometry (*EDS*) analysis per pixel was 0.004 seconds analysis time, with a minimum of 1000 counts to classify minerals.

3.3.4 Electron Probe Micro Analyzer (EPMA)

JEOL JXA-8530F Electron Probe Micro Analyzer (*EPMA*) was used to analyse major- and minor mineral chemistry at the Electron Microscopy Laboratory at NTNU in Trondheim. The instrument is fundamentally the same as SEM, only differing in being capable of chemical analysis with higher accuracy. With EPMA one can acquire accurate quantitative elemental analysis by using wavelength-dispersive spectrometry (*WDS*) at a precision down to 1-2 μm. WDS has lower elemental detection limits, higher peak to background ratio and higher spectral resolution, providing high accuracy (Cameca, 2017). The standard selection for minerals and measuring settings were set under supervision of Post Doc. Kristian Drivenes. Measuring settings were set to 15 keV, 20 nA and beam width 2 μm. All elements were, unless otherwise stated, measured with the time on the background (T_B) of 10 seconds and time on the peak (T_P) set to 5 seconds. Reed (2005) equation to calculate lower limit of detection (*LLD*) was used, and is as follows:

$$LLD = \frac{3\sqrt{R_B x T_B}\ x\ C_{std}}{R_{nP}\ x\ T_P}$$

Where:
R_B = Rate of background intensity (cps)
C_{std} = Concentration in standard (wt.% or ppm)
R_{nP} = Rate of net peak intensity (cps)

The primary focus with EPMA was set on clinopyroxene and orthopyroxene grains in sample AM19-006-XA and AM19-006-XB. Additionally, olivine, plagioclase and amphibole (*Amph)* grains were chosen for analysis. These particular thin section samples were chosen due to a great variety and amount of the grains. Over 500 points were chosen for close analysis. This high number, limited to two samples only, was due to time limitation due to the outbreak of COVID-19 forcing laboratory closure.

3.4 Sources of error

There are numerous sources of errors in sampling, preparation, analysis and interpretation of results. Samples may be mislabelled during field work and preparation of thin sections and whole-rock analysis. Additionally, samples may be contaminated unless accurate precautions and laboratory standards are followed during sample preparation. In preparing samples for thin sections it is also important to remove any weathered surfaces as these may yield unrepresentative results. Results from i.e. SEM

and EPMA may be misinterpreted, as is also the case with microscopy work. Set standards are followed to avoid any such errors in all sections from field work to results and interpretation.

3.5 Literature search

All literature referred to in this thesis have been accessed from BIBSYS (*NTNU Online University Library*). Supervisor Rune Berg-Edland Larsen also shared many useful books and journal articles. Special access was also given to certain journal articles by Chris Kirkland from *Curtin University of Technology*.

3.6 Health, safety and environment (HS&E)

As the Reinfjord area can be very unpredictable with both weather conditions and loose scree, proper health and safety precautions were taken throughout the entire field work. A plan for the day with GPS locality was shared amongst field participants and most of the work was conducted in pairs. Breaks were taken when particularly hazardous weather such as lightning took place.

All training and certifications had to be completed at NTNU before any laboratory work could be conducted with certified personnel. Access to laboratories were only given once training was successfully completed.

4

Results

4.1 Field observations

Prior to focussing on the objectives of this thesis, a few days were spent becoming familiarised with a larger section of the area, namely the ULS, CS, LLS, MZ and Langstrand gabbronorite. A section with wehrlite - gabbronorite and contact zone was mapped with particular focus on pegmatitic pyroxenites. This will be briefly discussed at the end of section 5.1.2, where an overview of the pyroxenite pegmatites in the RUC is presented. Additionally, systematic sediment sampling of scree cones was conducted in a section NE of the field area, in search of potential mineralisation in the ULS/CS rocks appearing in the cliff above the scree. In collaboration with supervisor it was decided that this part of the project was partially irrelevant for the objectives of this thesis, and samples are stored for recommended future research. Consequently, only ULS and CS in the S-parts of RUC will be presented here. This sub-chapter only comprises own in-field observations.

4.1.1 Upper Layered Series

The ULS primarily consists of a series of ultramafic rocks in a non-consistent order. The rocks were identified as wehrlite, replacive dunite and olivine-rich clinopyroxenite (with varying mineralogy, presented in section 4.2). The wehrlite appeared with varying pyroxene contents throughout the field area. The ULS appeared on the eastern and western side of the CS.

Most time was spent in the ULS and borderline CS, investigating pyroxenite pegmatites, where width of the pegmatites towered from 70 cm to 100 cm with overall mineral sizes ranging from <1 mm to at most 11 cm. The pegmatites were similarly shaped in the area with one primary pyroxene-rich body branching out on either side. In-field investigation of mineralogy indicated a pyroxene dominant mass (likely diopside (*Dio*) and enstatite (*Ens*)) with some sulphides (chalcopyrite, pentlandite and pyrrhotite) and possibly a few grains of rare plagioclase. The pyroxene grains mostly appear euhedral with a varying grain size averaging from 1 cm to as large as 11 cm. Some pegmatites appeared similar to the slumping structures seen further north in the field area, at approximately the same stratigraphic level.

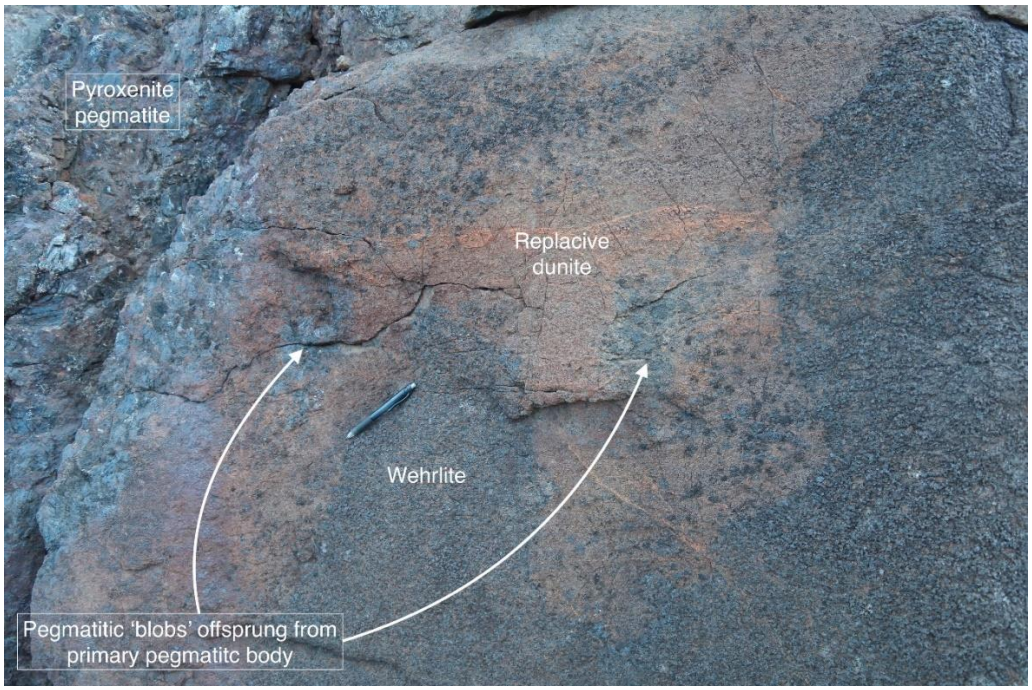

Figure 4.1: *Showing characteristic boundary relationship with pyroxenite pegmatite, wehrlite and replacive dunite.*

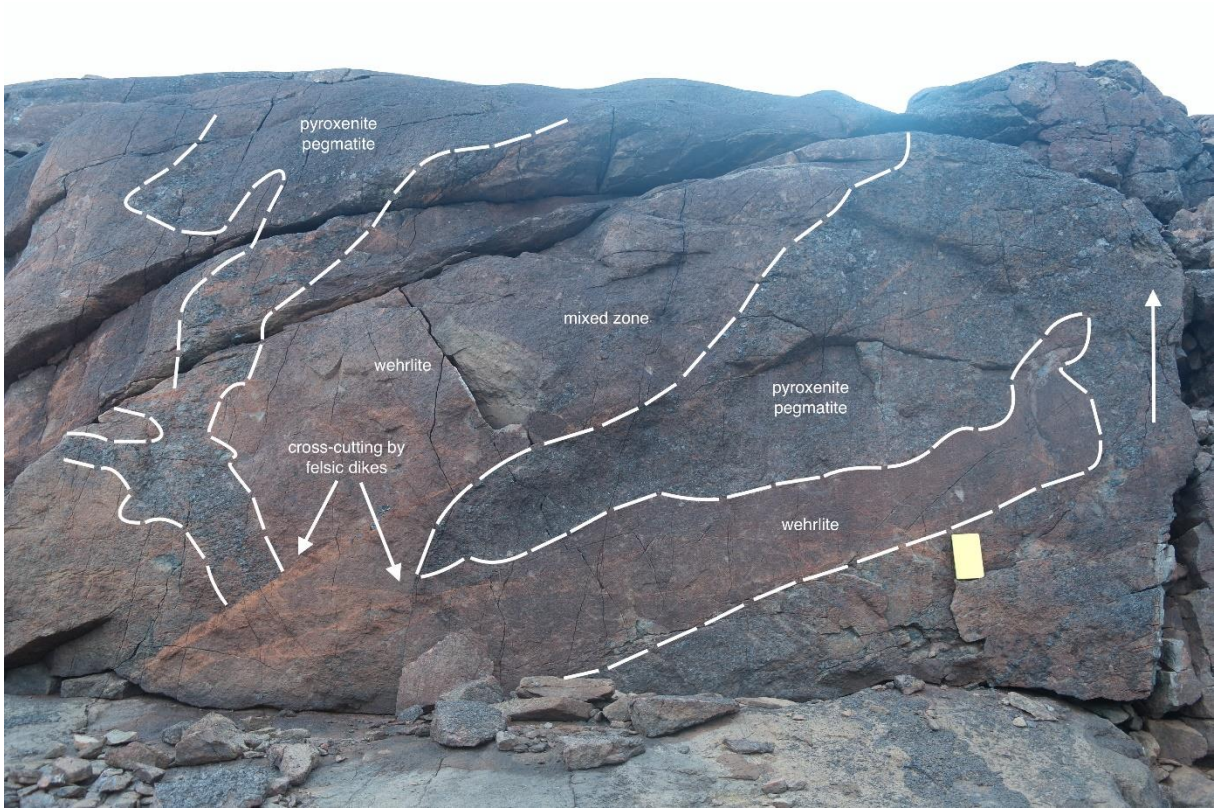

Figure 4.2: *Overview photo of one of the most prominent pyroxenite pegmatite bodies. Cross-cutting relationships between host rock (wehrlite), felsic dikes (ranging in thickness) and pegmatite bodies can also be seen. Mixed (or 'mush') zone is a combination of wehrlite and pyroxenite pegmatite. White arrow indicates stratigraphic way up to clarify the fountaining/slumping structures. Field book for scale.*

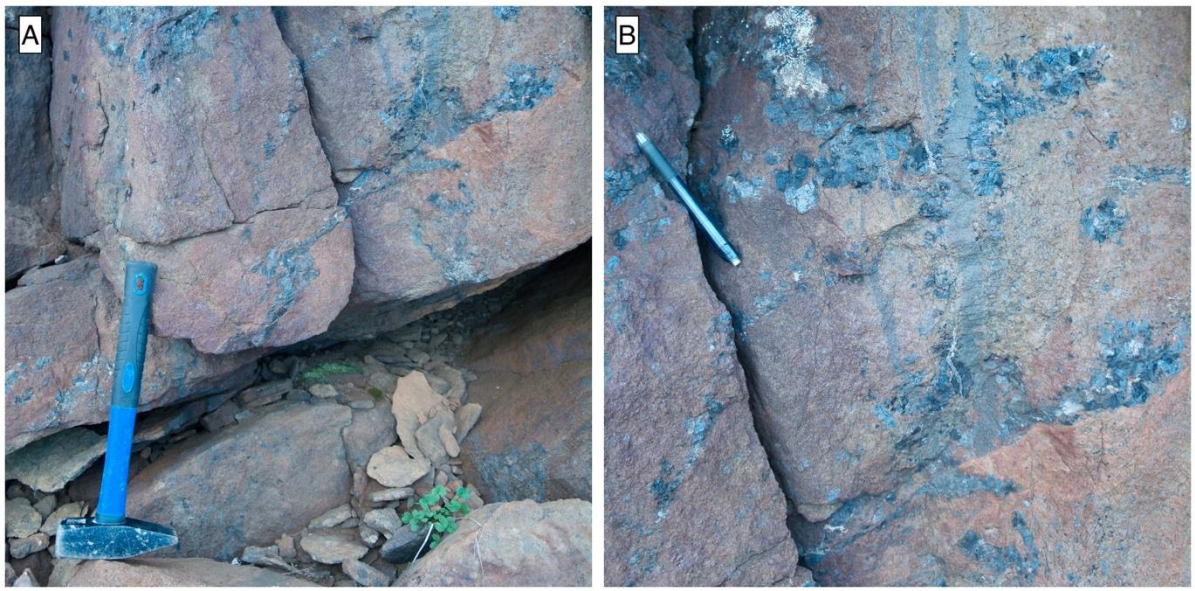

Figure 4.3: *A) Characteristic emplacement of a smaller pyroxenite pegmatite body, S-W of the primary pyroxenite pegmatite body (Figure 4.2). These bodies often appeared in a fountain-like structure, branching out on both sides and eventually 'thinning' out. B) Close-up of 4.2(a). A mafic dyke crosscuts the pegmatitic 'branching', indicating later emplacement.*

4.1.2 Central Series

The CS differed from the ULS by having dunitic compositions with >90% olivine. This series makes up most of the RUC. CS consist primarily of dunite with wehrlitic segments with outstanding dyke swarms particularly prominent in the northern section (Figure 4.4). It is clear that the dykes present different generations by the various compositions, however, how many is uncertain from field observations.

Figure 4.4: *Characteristic display of the dyke swarms in the northern section of the CS.*

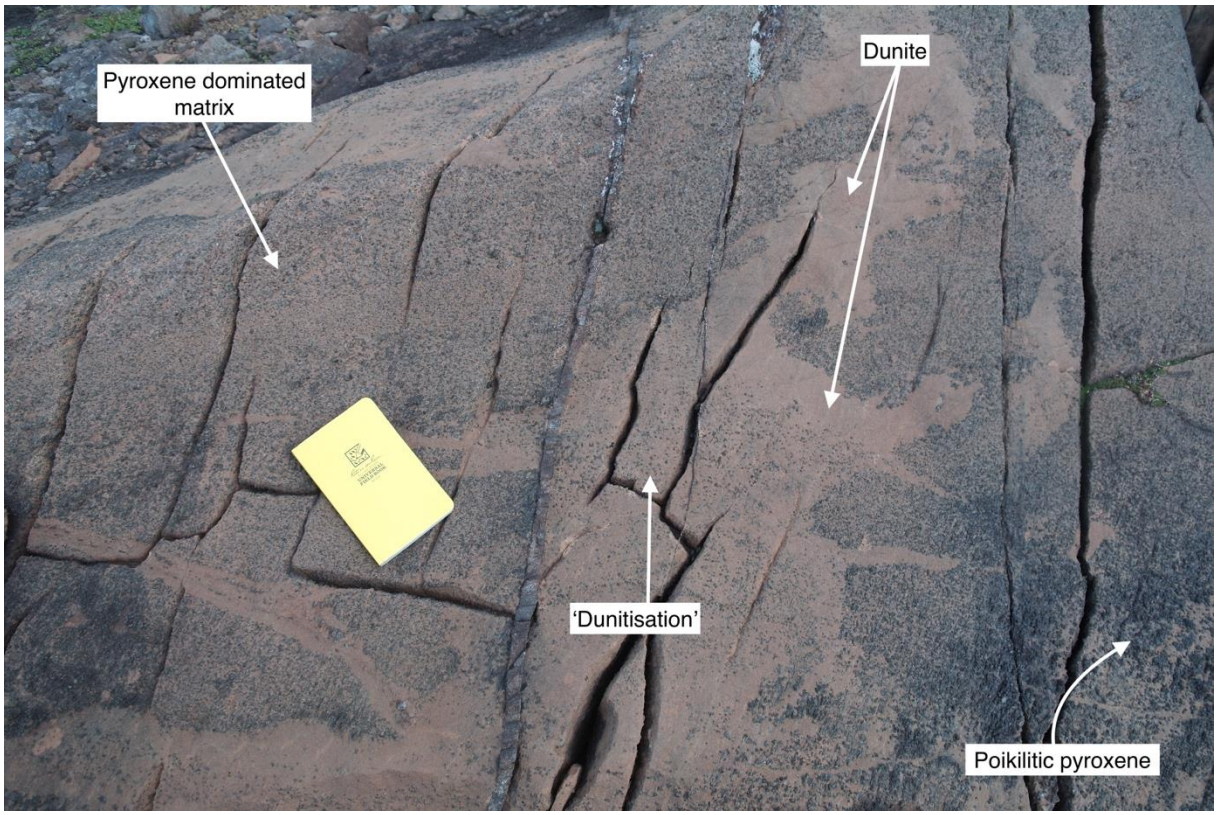

Figure 4.5: *Characteristic representation of CS outcrop. Magma mixing between Ol-rich and pyroxene-rich melts are abundant throughout. Please note: the term 'dunitisation' is not yet an official term and is only included as a reference-point from in-field observations. Essentially, the terms 'replacive dunite' and 'dunitisation' is the same.*

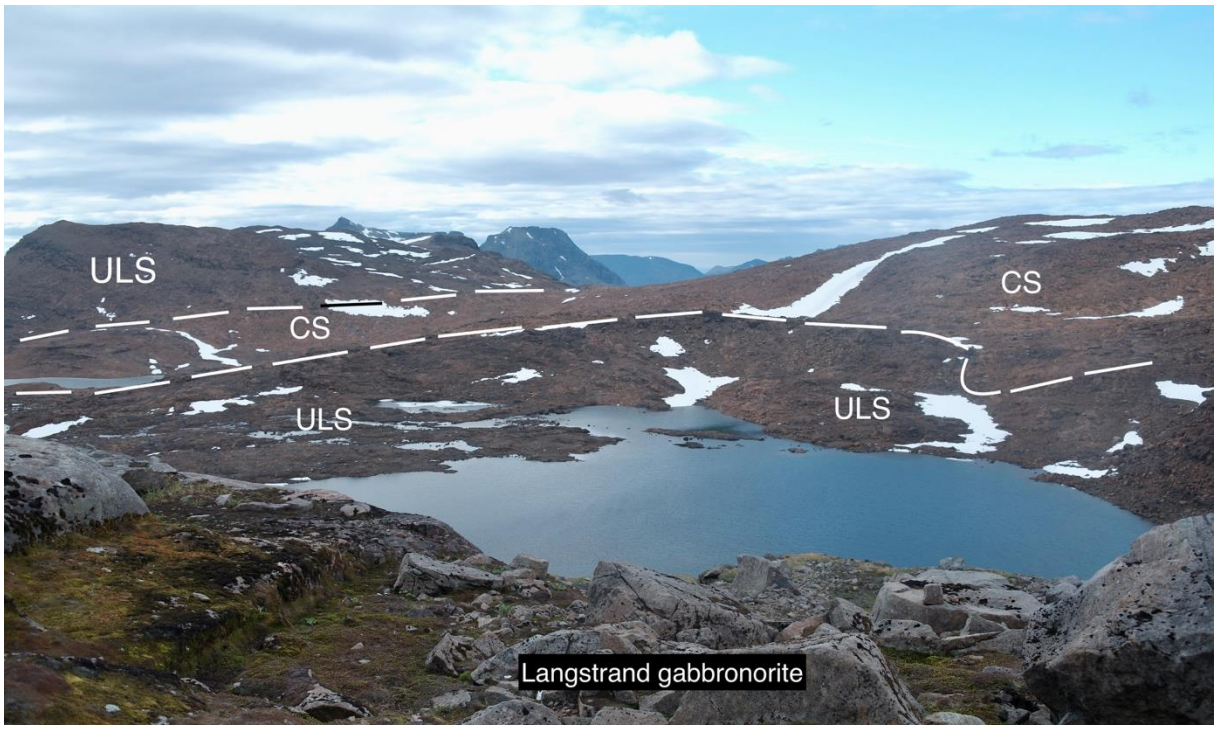

Figure 4.6: *Overview photo of ULS, CS and Langstrand gabbronorite, covering a large part of the RUC field area. The primary work in this thesis is from the mid-far left in the photo.*

4.2 Petrography

A combination of the methods described in Chapter 3 was used to identify mineralogy, assess textural and mineralogical relationships and identify mineral abundance from all field samples and subsequent thin section and geochemical data. The following section will present results from microscopy, SEM, EPMA and geochemical work on the 24 chosen samples, with particular focus on eight thin sections best representing the study area.

4.2.1 Silicates

Olivine - $(Mg, Fe)_2SiO_4$

Olivine belongs to the nesosilicate group and orthorhombic crystal system and consists of the two end-members forsterite (Mg end-member) and fayalite (Fe end-member), abbreviated *Fo* and *Fa*, respectively. It is optically observed colourless in PPL with no pleochroism and with very high interference colours, high relief and irregular fractures in XPL, of which is often filled with altered minerals. Olivine is present in all thin section samples, with lesser abundance in the pyroxenite pegmatite samples with large grain size (i.e. sample AM19-008-3 in Figure 8.5). It is also the dominant silicate in the RUC (dunite and wehrlite being host rocks).

Up to three generations have previously been described (Grant et al., 2016b). Very broadly speaking these three generations are differentiated by grain size, the first type with the largest grain size (up to 1-2 cm) and the third type with the smallest grain size (< 30 μm), in addition to textural differences. The reader is encouraged to investigate the paper by Grant et al. (2016b) for further information. All three generations appear to be present in most of the thin sections and can be seen particularly well in thin sections AM19-006-XA and AM19-008-1. The first generation is subhedral to euhedral, contains irregular fractures and, quite often, contains deformation bands. The second generation is finer grained, euhedral in grain shape, often forming distinct triple junctions, and deformation bands being less common. The third generation is evermore fine-grained (<50 μm), closely packed and subhedral to euhedral in grain shape, appearing mylonitic. It is often associated with shear zones and a characteristic example of this can be seen in Figure 4.9.

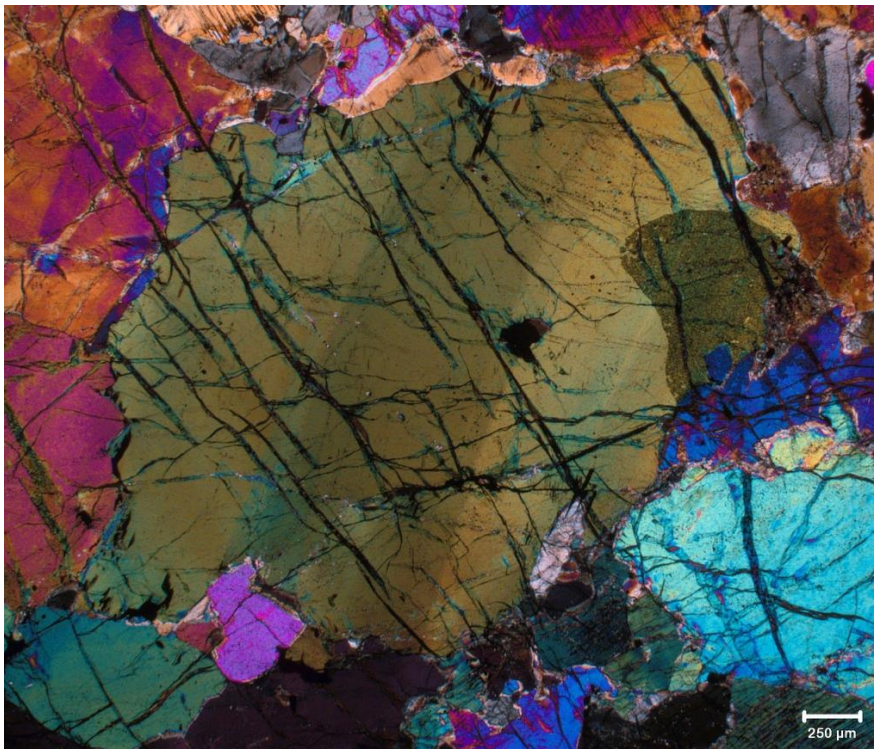

Figure 4.7: *Example of type 1 Ol, described in text, from thin section AM19-008-1.*

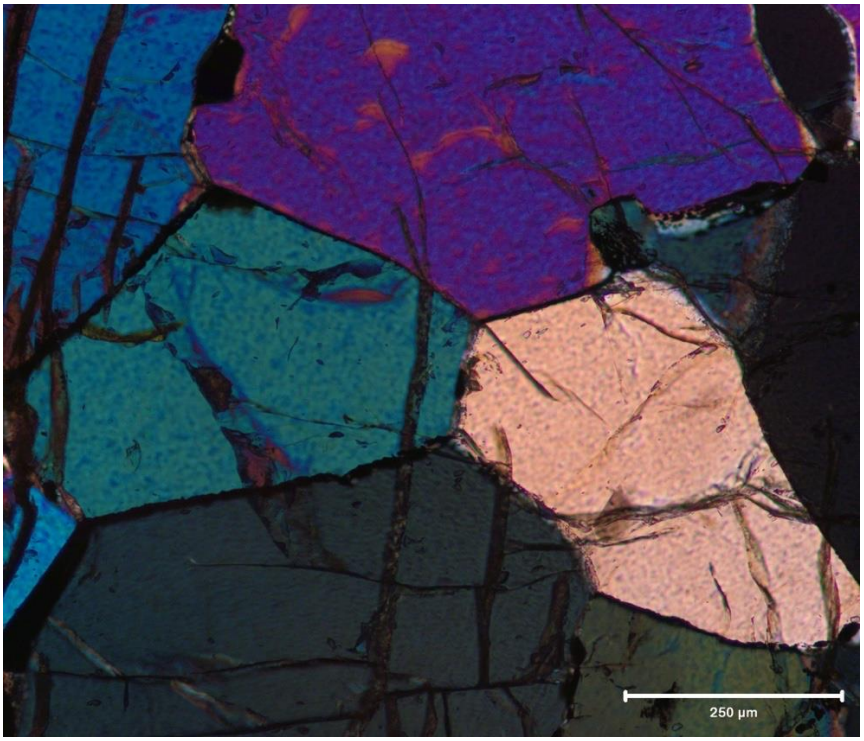

Figure 4.8: *Type 2 Ol grains with distinct triple junction formation, from thin section AM19-XX.*

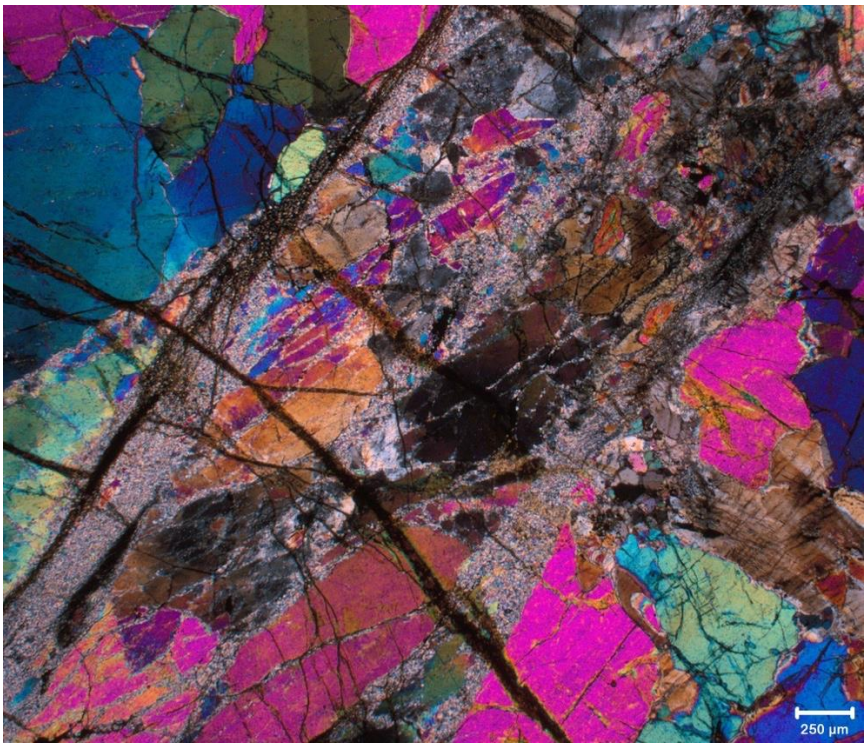

Figure 4.9: *Example of type 3 Ol in a shear zone appearing as very fine-grained matrix. From thin section AM19-008-1.*

Table 4.1: *Ol results from EPMA (Table 8.24; Table 8.30).*

	MgO	SiO_2	FeO
Wt.% oxide	41.36	39.01	20.26

Clinopyroxene (diopside) – $CaMgSi_2O_6$

Clinopyroxene belongs to the inosilicate group and the monoclinic crystal system. It is colourless in PPL with green-brown-grey weak pleochroism. In XPL it is identified by second order interference colours (Figure 3.3), high relief and irregular/conchoidal fractures. Based on literature, analytical results, petrography and being a common clinopyroxene-member, it is classified as diopside.

In the pegmatitic pyroxenite samples, clinopyroxene is more or less equigranular and occurs as interstitial networks and exsolution lamellae, often within orthopyroxene grains. Singular grains are subhedral to euhedral, with one good cleavage on {110}. In the dunitic and wehrlitic samples the appearance changes slightly, being surrounded by olivine, and smaller in grain size. Most of the clinopyroxene grains display characteristic simple and lamellar twinning (Figure 4.10; Figure 4.12).

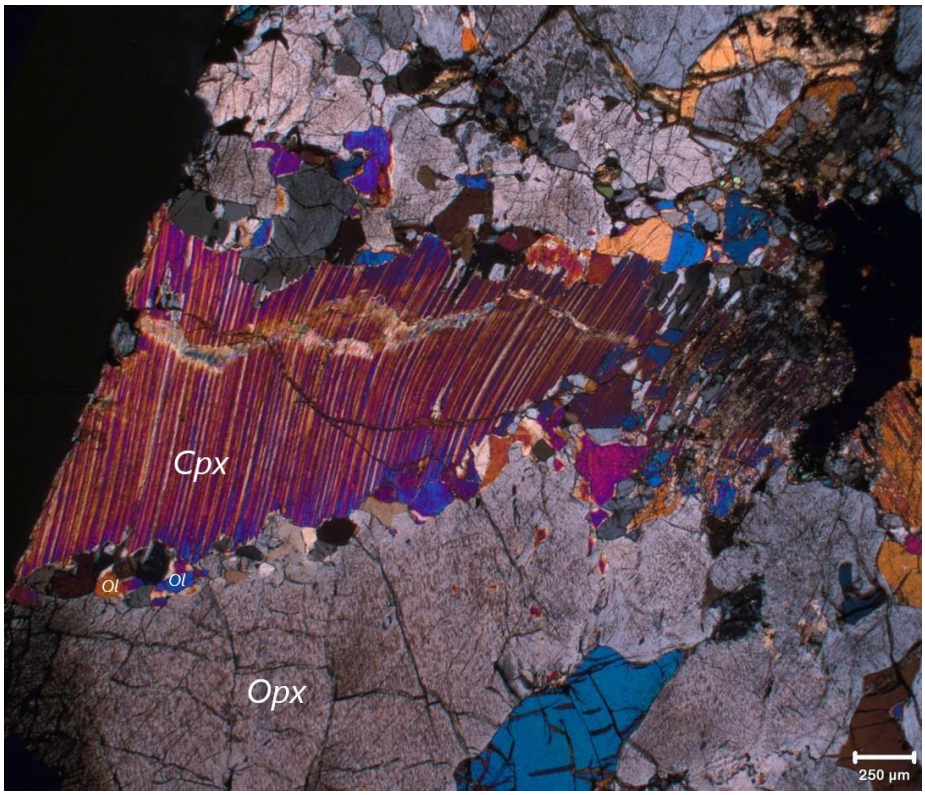

Figure 4.10: *Cpx (XPL) interference colours, from thin section AM19-006-XA. Note the fine-grained pyroxenes and Ol bordering the Cpx grain, followed by larger grains of Opx with interstitial Cpx growth.*

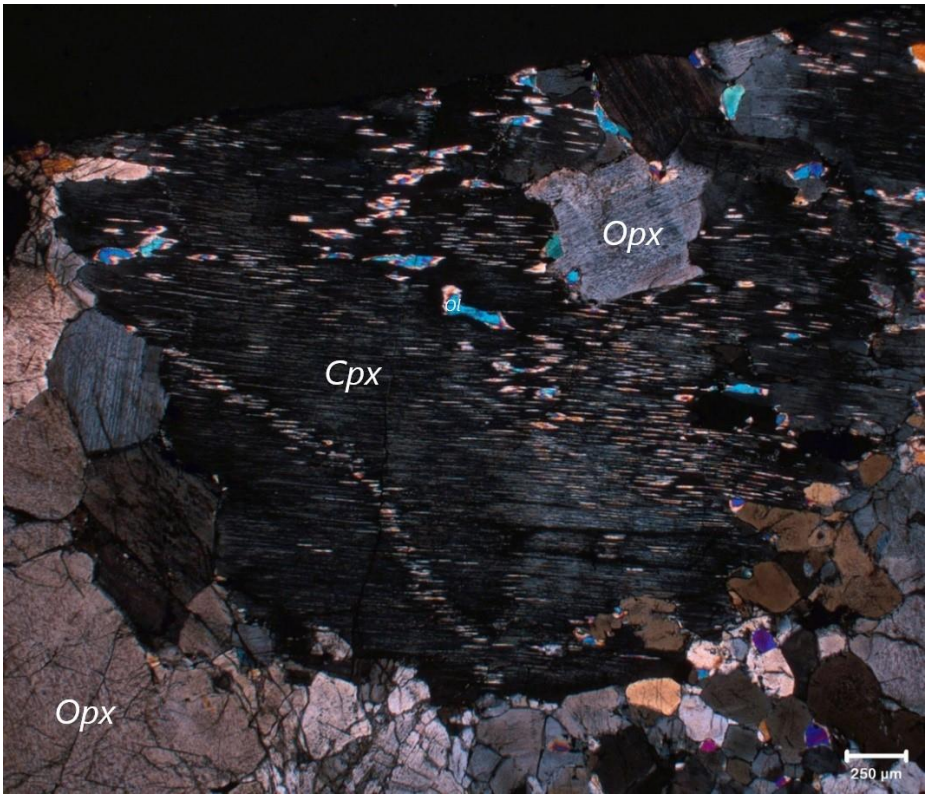

Figure 4.11: *Cpx (XPL) with interstitial networks of Ol and Opx, from thin section AM19-006-XB.*

Figure 4.12: *Cpx with exsolution lamellae and interstitial Opx growth (XPL), from thin section AM19-006-XB.*

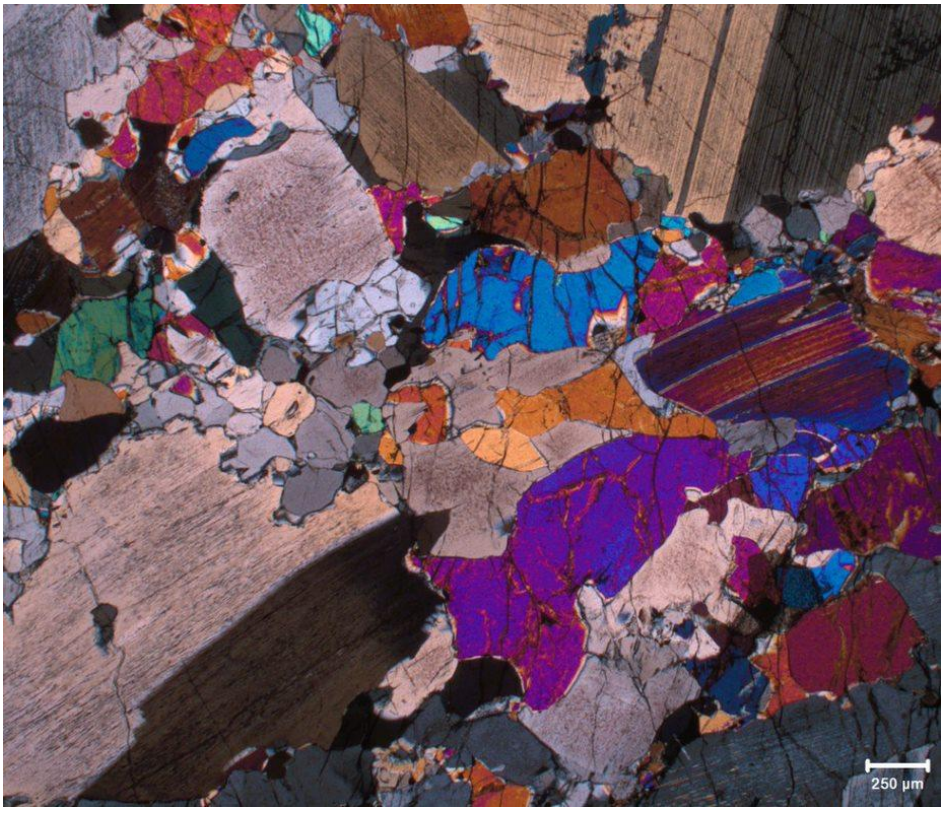

Figure 4.13: *Characteristic twinning as seen in most samples, here from thin section AM19-006-XA.*

Table 4.2: *Cpx results from EPMA (Table 8.15).*

	MgO	Al_2O_3	CaO	FeO	SiO_2
Wt.%	14.65	4.76	22.41	4.85	48.67

Orthopyroxene (enstatite) – $Mg_2Si_2O_6$

Orthopyroxene belongs to the orthorhombic crystal system and is as beige to light brown colour in PPL. In XPL it is characterised by low interference colours, moderate relief, extinction parallel to cleavages in addition to distinct ilmenite exsolutions (Figure 4.14). It can be differentiated from clinopyroxene by different extinction angles and lower interference colours, usually first order yellow (Figure 3.3).

Orthopyroxene is the primary phase in the pegmatitic pyroxenite samples, appearing subhedral to anhedral with an overall grain size of 1 cm - > 5 cm. It also appears in pegmatitic interior as intergranular subhedral to euhedral grains. In the dunitic and wehrlitic samples the grain size is generally smaller, though with a near identical grain shape, of which assists in unravelling melt evolution, discussed further in Chapter 5. In samples with equigranular size it is often seen with triple junction (Figure 4.16).

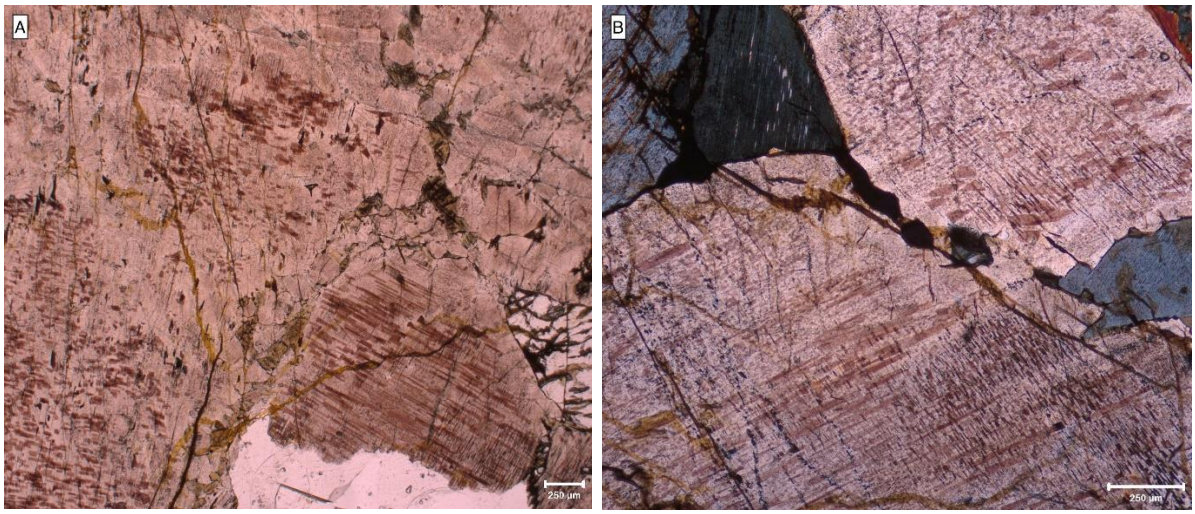

Figure 4.14: *Orthopyroxene with distinct ilmenite lamellae in PPL, from thin section AM19-008-3 (A) and another example in XPL from thin section AM19-008-4 (B).*

Figure 4.15: *Examples of characteristic coarse-grained Opx with subhedral grain shape (central) and closely packed equigranular grains to the right (XPL). From thin section AM19-008-3. This fine to coarse grain boundary relationship is prominent in most of the pyroxenite pegmatite samples.*

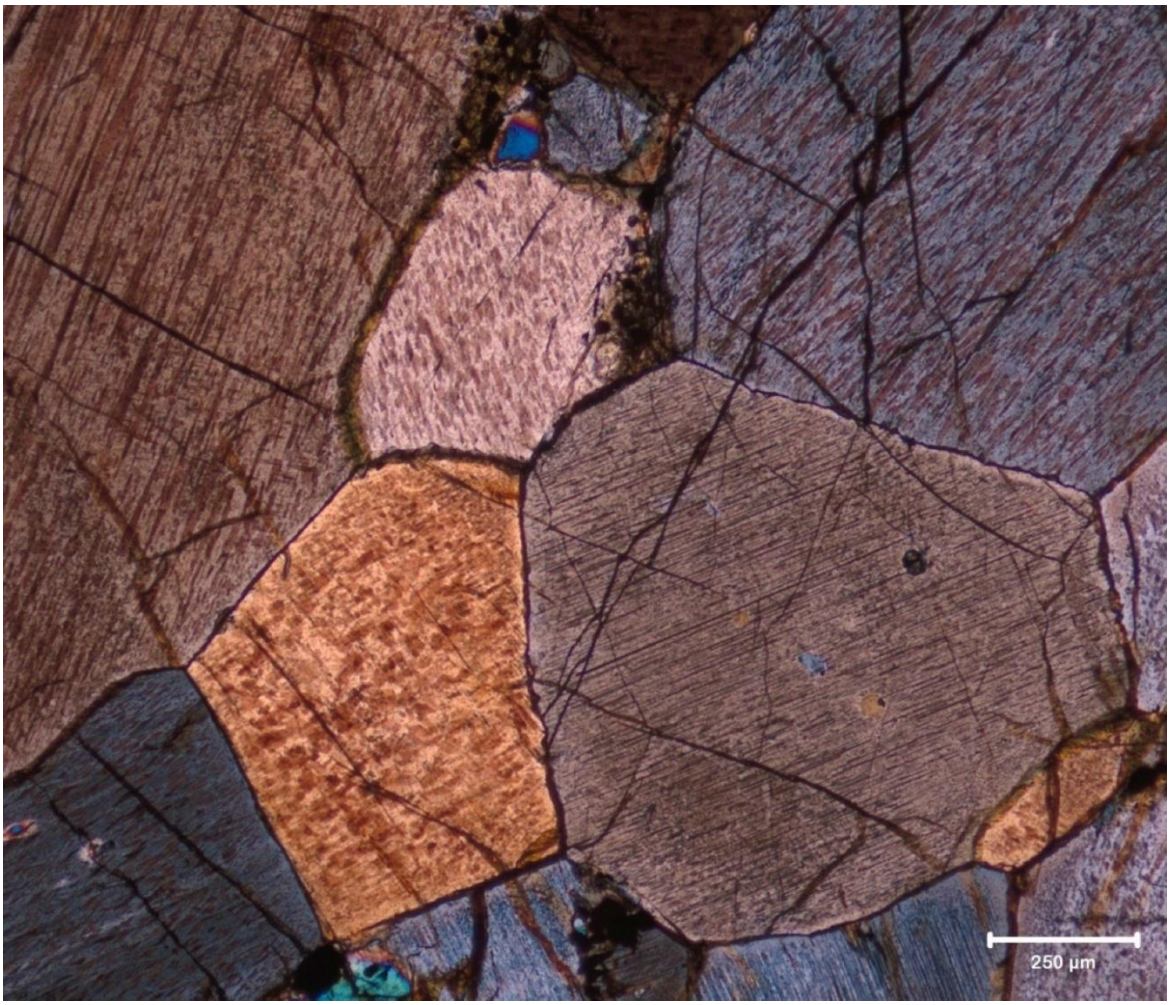

Figure 4.16: *Opx grains forming triple junction (XPL), from thin section AM19-010.*

Table 4.3: *Opx results from EPMA (Table 8.22).*

	MgO	Al_2O_3	FeO	SiO_2
Wt.% oxide	29.87	1.97	12.68	54.17

Amphibole (magnesiohastingsite) – ($NaCa_2(Mg_4,Fe^{2+})Si_6Al_{22}(OH)_2$)

Amphibole belongs to the inosilicate group and is identified in XPL by strong pleochroism and inclined extinction. It is hard to distinguish from clinopyroxene due to similar birefringence and inclined extinction, in addition to being considerably less abundant and with a smaller grain size. Magnesiohastingsite was found from XRD analysis in most samples, but only in trace amounts (<0.1%). Amphibole (not defined by sub-group) was also found by SEM and EPMA analysis (Figure 4.17). It was challenging to confidently identify amphibole by microscopy due to small, very fine-grained amounts present. Thus, less time was spent looking for potential amphibole grains due to not being decidedly important to thesis objectives in addition to showing its presence from other geochemical data.

Table 4.4: *Amphibole results from EPMA (Table 8.18).*

	Na_2O	MgO	Al_2O_3	CaO	FeO	TiO_2	SiO_2
Wt.% oxide	1.83	16.44	7.75	18.45	5.75	1.52	46.85

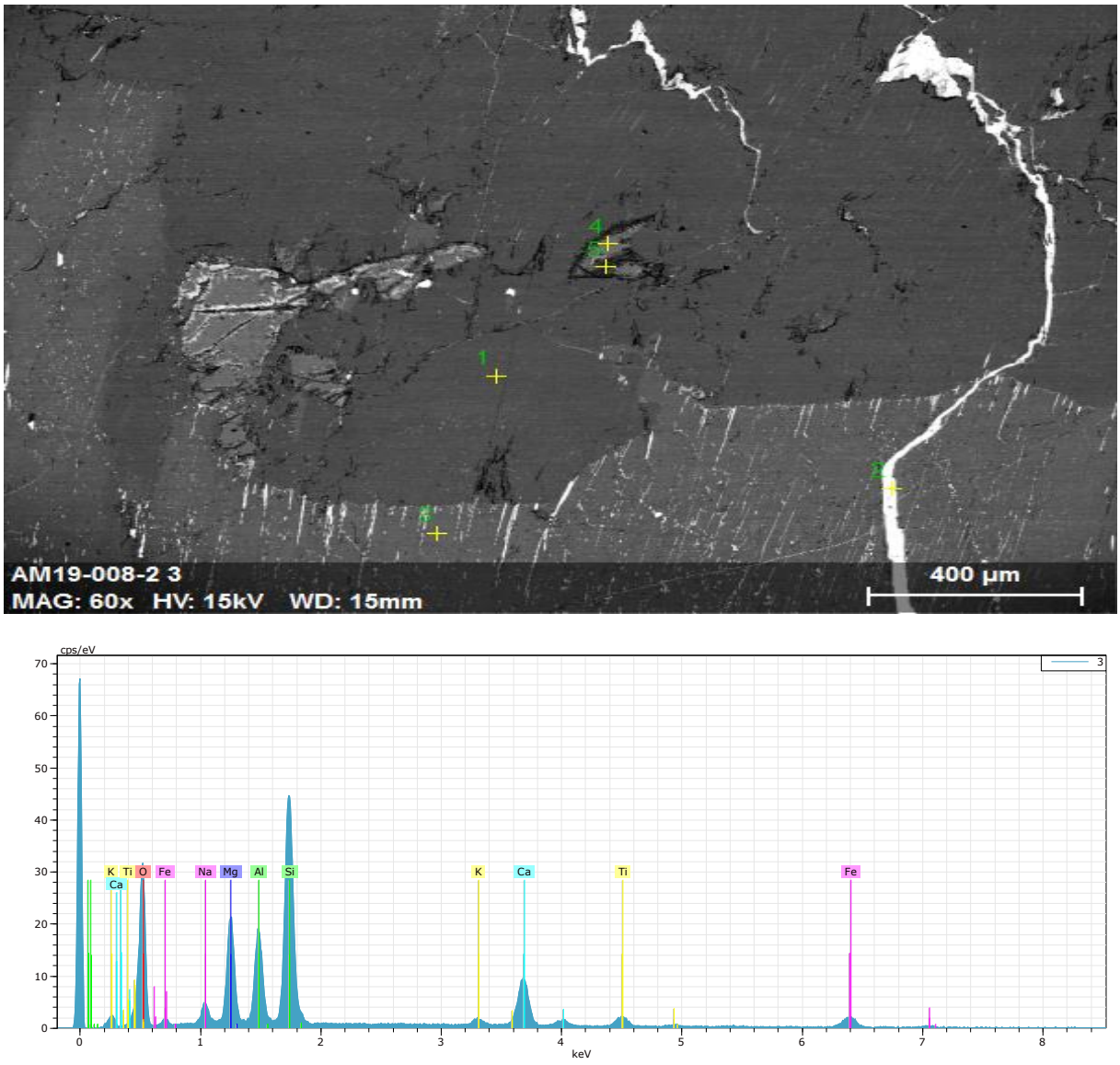

Figure 4.17: *EDS image and graph from SEM, where point 3 matches amphibole composition. Graphs with similar results and same identification can be found in Figure 8.12; Figure 8.12a.*

4.2.2 Sulfides

Sulfides can provide useful information for the pyroxenite pegmatite characterisations, thus taking time to identify sulfide phases and assessing all petrological and textural features is important. The (opaque) sulfides are identified in optical microscopy by using reflected light and can be verified by SEM, XRD and EPMA results.

Chalcopyrite – $CuFeS_2$

Chalcopyrite belongs to the tetragonal crystal system and is a common copper sulfide often associated with pentlandite, pyrrhotite and pyrite (Figure 4.18). It is recognised with its bright 'brass' yellow reflectance with no cleavage. Common impurities are Ag, Au and Ti ("Mindat", 2020).

Chalcopyrite is often found associated with pyrrhotite and pentlandite, usually along the grain boundaries in connection with either orthopyroxene, clinopyroxene or olivine, in addition to bordering oxides such as ilmenite. It is seen some places as inclusions, usually surrounded by pyrrhotite. Chalcopyrite usually appears with a smaller grain size than pyrrhotite and pentlandite of which tend to dominate the space. Grain boundaries are generally irregular to straight.

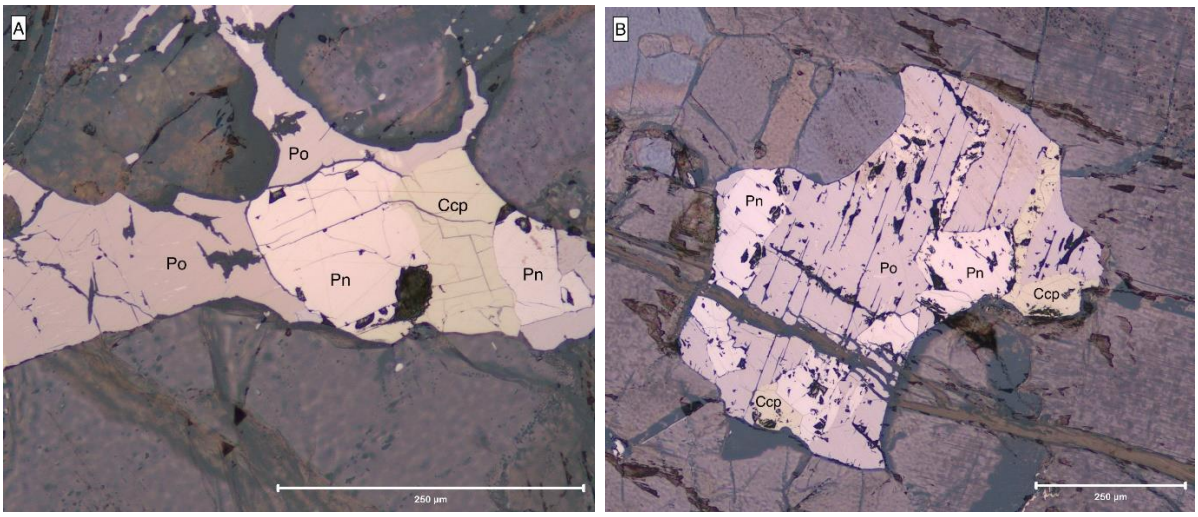

Figure 4.18: *Examples of chalcopyrite (Ccp) appearance. Both examples have a grain boundary association with pyrrhotite (Po) and pentlandite (Pn) in addition to Opx, which is the general trend in all pyroxenite pegmatite samples. Picture (A) is from sample AM19-008-1 and picture (B) is from sample AM19-006-XA. A characteristic geochemical relationship between sulfides and host-rock can be found in Figure 8.10.*

Cubanite – $CuFe_2S_3$

Cubanite is optically very similar to chalcopyrite, making it challenging to differentiate the two. Cubanite appears slightly pale creamy-yellow and seems to be associated with orthopyroxene and pyrrhotite (Figure 4.19; Figure 4.20). Identifying cubanite is with grades of uncertainty as it has not been verified by other analytical methods.

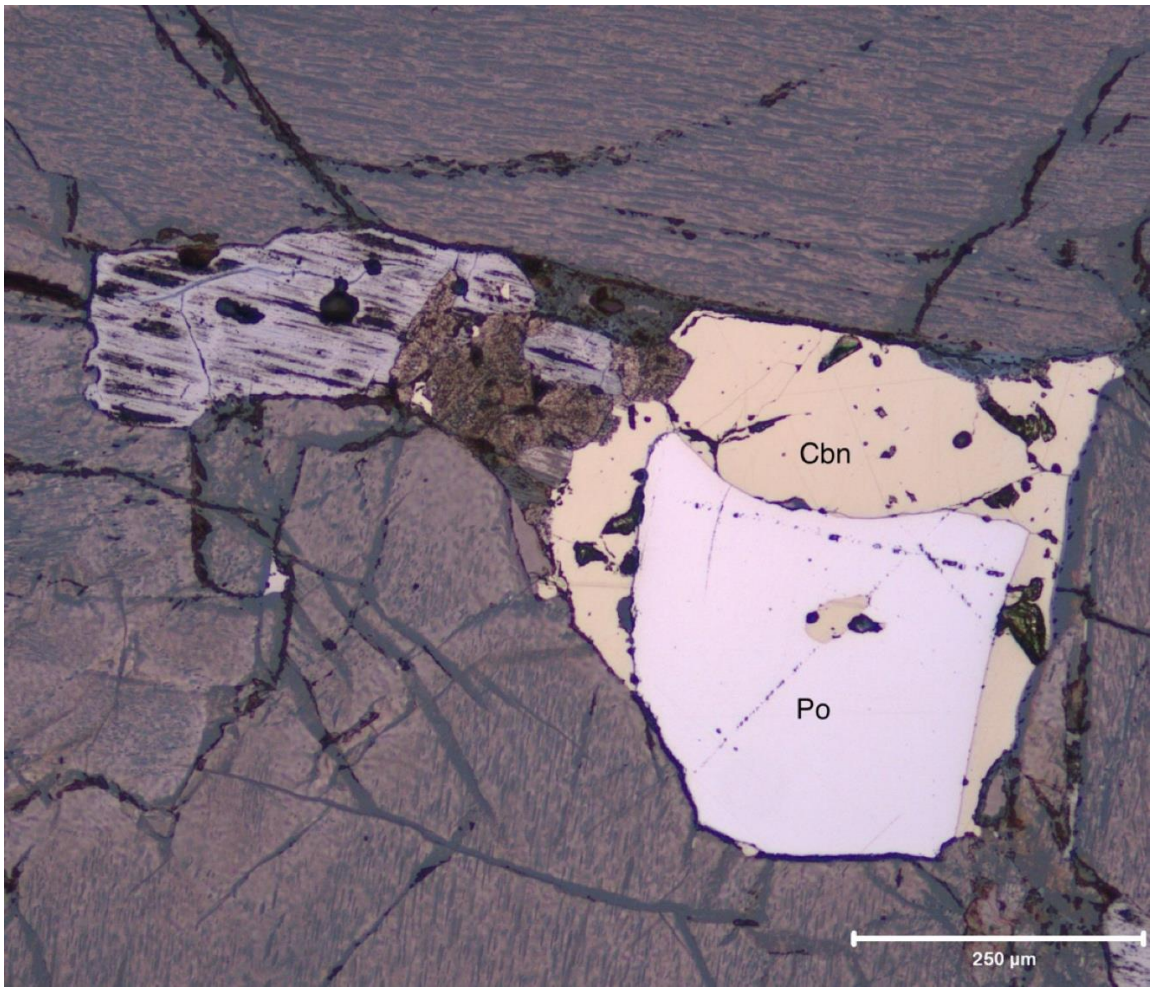

Figure 4.19: *(Cbn) associated with pyrrhotite (Po). Surrounding host mineral is Opx. From sample AM19-010.*

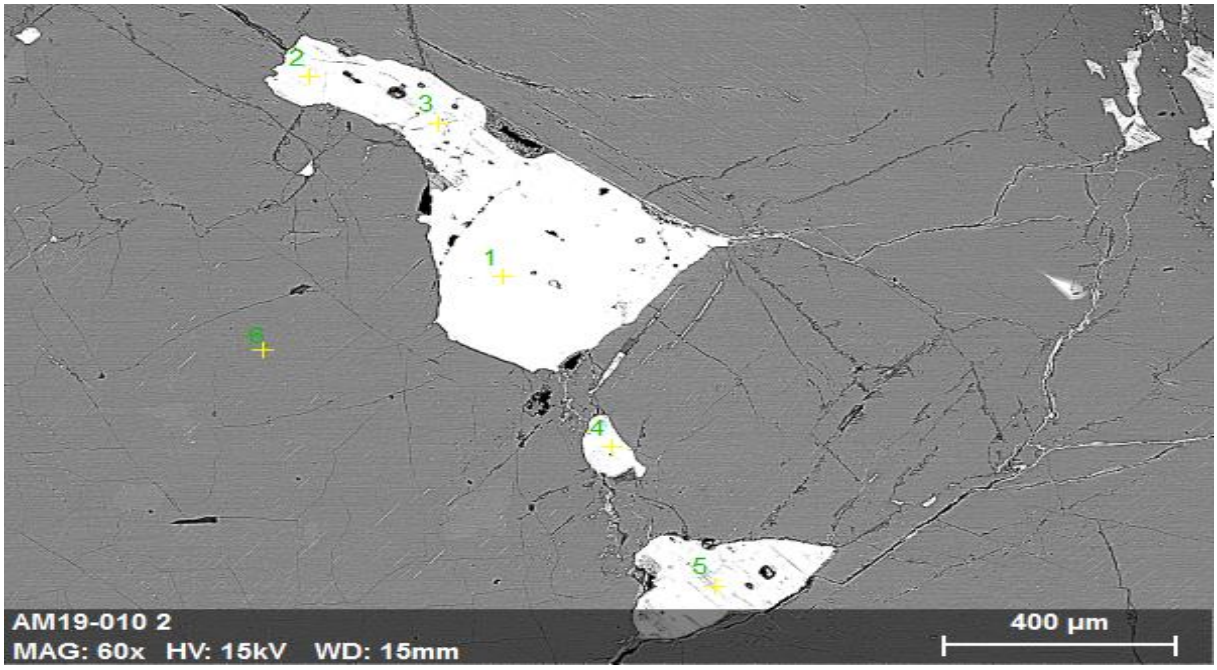

Figure 4.20: *EDS image of the same grain as Figure 4.18, verifying mineralogy (Figure 8.13; Figure 8.13c).*

Pyrrhotite – $Fe_{1-x}S$

Pyrrhotite belongs to the monoclinic crystal system and is one of the most common sulfides found in the samples presented in this thesis. Pyrrhotite appears creamy to pale brown with a lower reflectance than pentlandite. Common impurities are Ni, Co and Cu ("Mindat", 2020). It is the most dominant sulfide in most samples and appear with irregular grain boundaries with inclusions of Pn and Ccp (Figure 4.21).

Pentlandite – $(Fe, Ni)_9S_8$

Pentlandite belongs to the isometric crystal system and is one of the most common and important nickel-iron ores, commonly associated with pyrrhotite. It can be challenging to differentiate the two, however, pentlandite has a brighter reflection than pyrrhotite and is paler, being creamy-white, in colour (Figure 4.21). Common impurities are Co, Ag and Cu ("Mindat", 2020).

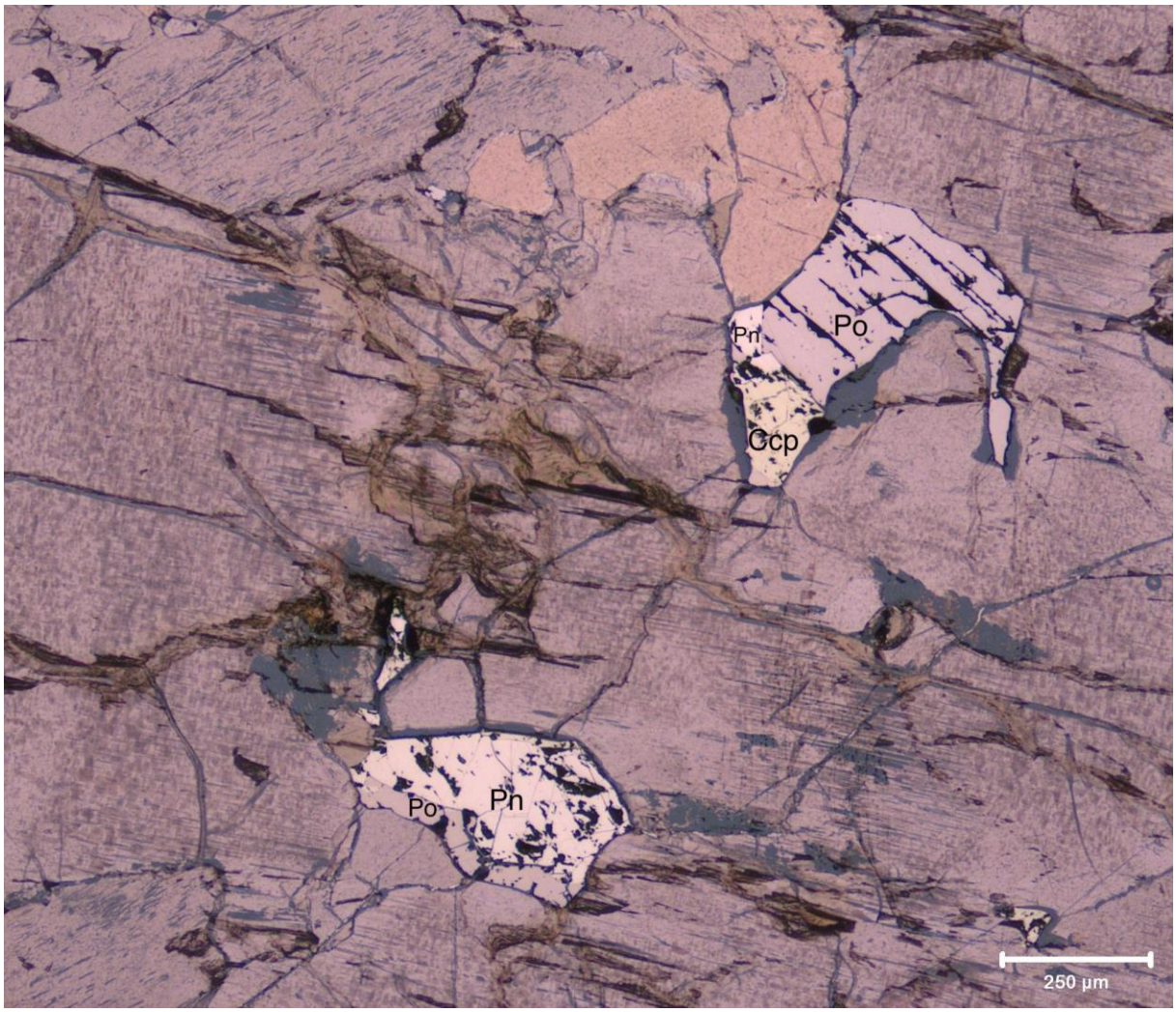

Figure 4.21: *Typical assemblage of the three most common sulfides, here with one grain being pyrrhotite dominated (top) and one grain being pentlandite dominated (bottom). From sample AM19-006-XB.*

Chalcocite – Cu_2S

Chalcocite belongs to the monoclinic crystal system and is a Cu-rich sulfide identified by blue-grey colour visible in reflected light (Figure 4.22). It was particularly common in AM19-XX, appearing in greater abundance than Ccp, Po and Pn. It is mostly associated with ilmenite. Common impurities in chalcocite is Fe ("Mindat", 2020).

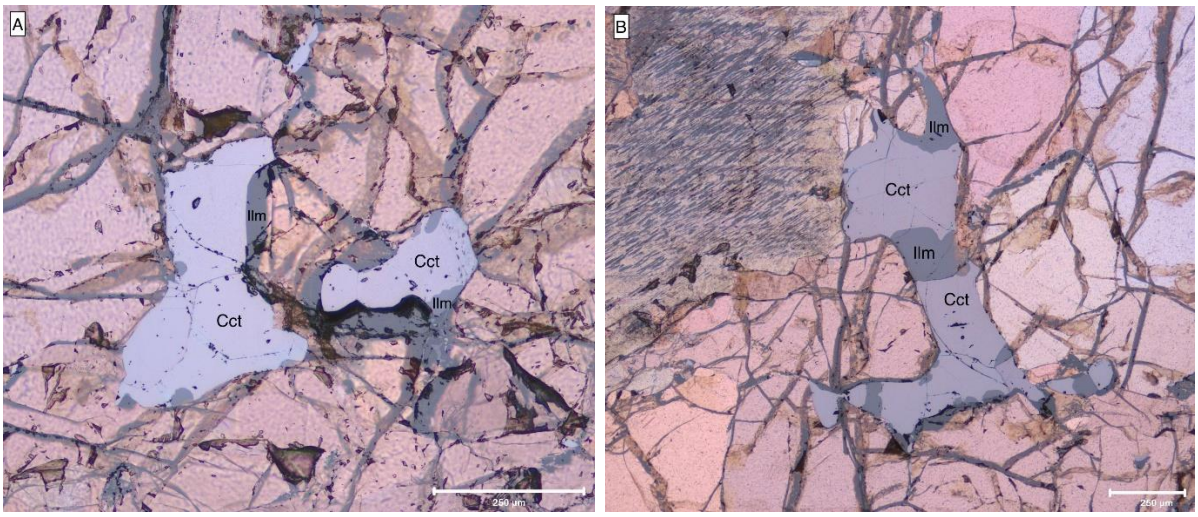

Figure 4.22: *Common appearance of chalcocite (Cct) associated with ilmenite (Ilm) from sample AM19-XX.*

4.2.3 Oxides

Ilmenite – $Fe^{2+}TiO_3$

Ilmenite belongs to the trigonal crystal system and is identified by very low reflectance and anisotropy. It is particularly apparent in large grain sizes in sample AM19-XX, appearing with Cct (Figure 4.22). It is also very common as exsolution lamellae in orthopyroxene (Figure 4.23), a texture that is clearly seen in all settings under the microscope (i.e. Figure 4.14 in PPL and Figure 4.16 in XPL).

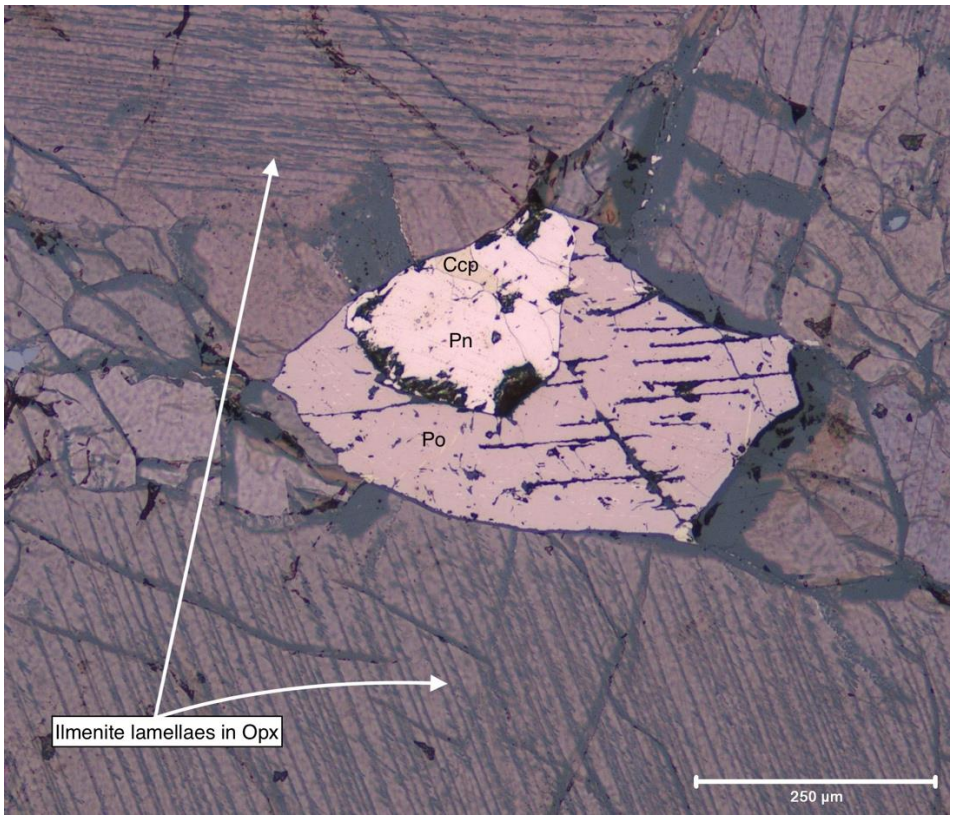

Figure 4.23: *Ilmenite mostly appears as lamellae in Opx in all samples, in addition to μm – scale grains mostly associated with sulfides.*

4.3 Geochemical analysis

Average whole rock geochemistry was obtained from ALS and is presented in Appendix B (Table 8.1; Table 8.2). This section will present these analyses combined with a variation in diagrams where selected major- and minor elements have been plotted. All relevant samples have been included in this section, which is used for correlation in investigating the pyroxenite pegmatites and host rocks relationship in chapter 5. Section 4.4 involves a presentation of *only* pyroxenite pegmatite samples. Elements which may yield 'false' readings or disturb plot results in being overquantified have been removed. These elements are Cs, Nb, Sn, Ta, Tb, Th, Tm, U and W. Additionally, Fe_2O_3 has been recalculated to FeO to obtain the correct balance in comparing to i.e. MgO and MnO. Recalculation method and all other calculations (i.e. normalising) can be found in Appendix C.

4.3.1 Bulk-rock chemistry analysis

Major and trace elements in all samples

Wehrlite, dunite and pyroxenite was identified based on element composition from ALS data that was normalised and plotted in International Union of Geological Sciences (*IUGS*) classification diagram (Figure 4.24). Further identification was conducted with a combination of petrography, SEM, XRD and EPMA. The following is a presentation based on ALS bulk-rock geochemistry results.

Wehrlite

Samples matching wehrlitic composition contain between 40-50 wt.% SiO_2, between 15-20 wt.% Fe_2O_3, between 20-40 wt.% MgO and <5 wt.% CaO. Notable trace element compositions are from Cr, Sr and V. Cr content is generally high, with a low of 960 ppm to a high of 2260 ppm. Sr averages at 9 ppm with an anomaly of a considerably higher amount (53.1 ppm) in one sample. V has a similar trend, averaging at 46 ppm, with two anomalies of 10 ppm and 135 ppm.

Lherzolite

There are a handful of samples matching lherzolitic composition, verified by IUGS plotting (Figure 4.24). These samples have not been included in the graphs and plots for the remainder of this chapter due to not appearing in considerable amounts. These samples average at 38 wt.% SiO_2, 34 wt.% MgO and 14 wt.% FeO. Cr content is low compared to wehrlitic and pyroxenitic samples, averaging at 978 ppm.

Dunite

There are, as predicted, not many samples matching dunitic composition, with most sampling conducted in wehrlitic-pyroxenitic rich areas (Figure 3.1). One sample matching this composition has 38.5 wt.% SiO_2, 40,5 wt.% MgO and 14.2 wt.% FeO. Naturally there is less Cr content (820ppm) than the wehrlitic and pyroxenitic samples. Zirconium (*Zr*) content (24 ppm) is considerably higher than most other wehrlitic samples (averaging at 6 ppm).

Pyroxenite *(including Ol-websterite and not differentiating Opx and Cpx)*

Pyroxenite samples average at 48.9 wt.% SiO_2, 24,6 wt.% MgO, 14.8 wt.% Fe_2O_3 and 6.1 wt.% CaO. As with the abovementioned, Cr, Sr and V are present in notable amount, in addition to Ba and Ga. Cr range from 1710 – 2290 ppm and average higher than wehrlite and dunite. Sr ranges from a low of 11.2 ppm to a high of 55.8 ppm. V ranges from 119 – 247 ppm. Ba and Ga range from 3.6 – 15.7ppm and 6.8 – 8.4ppm, respectively. The pyroxenite pegmatite samples are presented in more detail in section 4.4.

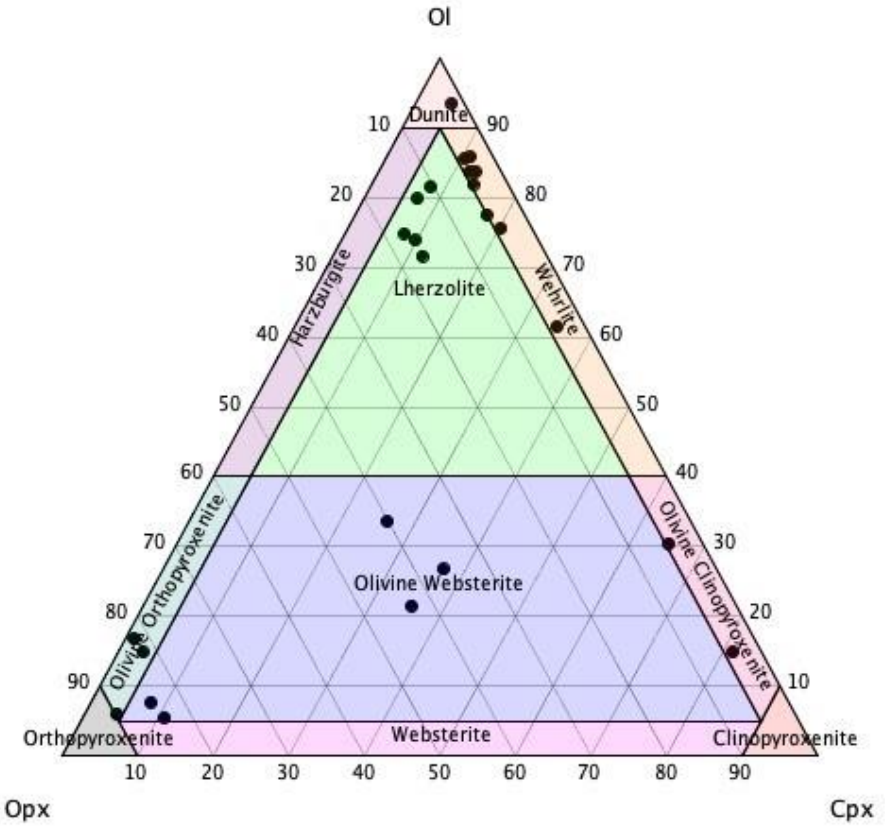

Figure 4.24: *IUGS ternary classification diagram for Ol-Opx-Cpx, normalised for all 24 ALS samples (Table 8.11), modified from Streckeisen (1974). Ol-websterite bear resemblance to some of the MZ lithology, whereas lherzolite can indicate a typical wehrlite-dunite mix ('mixed' zone), typically seen in LLS.*

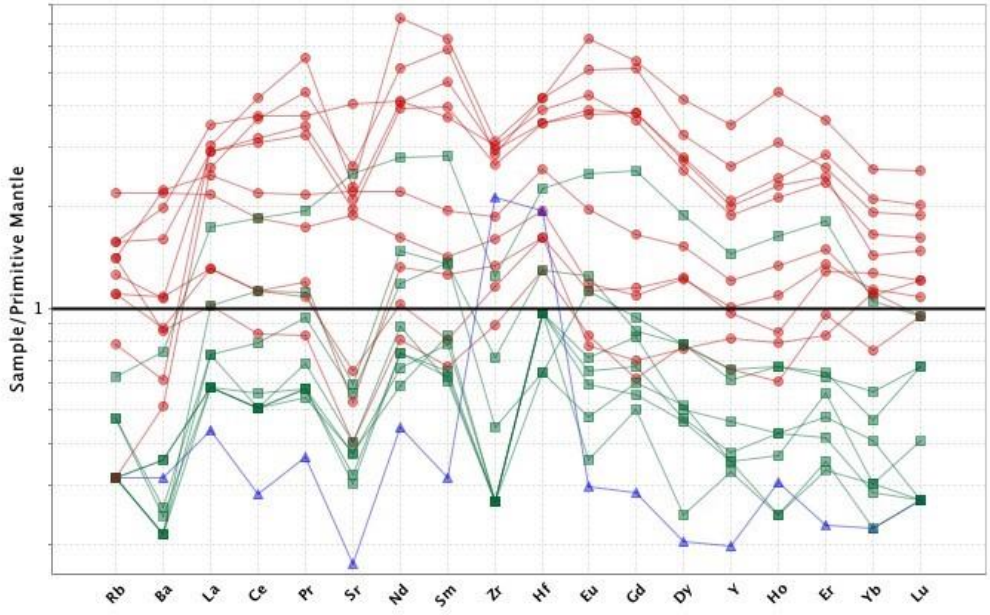

Figure 4.25: *Variation of all samples plotted against normalised primitive mantle (Sun & McDonough, 1989). Symbol designation for samples is as follows: pyroxenite (red), wehrlite (green) and dunite (blue) and is used in all graphs and plots hereafter. From this graph it is apparent with the difference in pyroxenite and wehrlite trace element enrichment.*

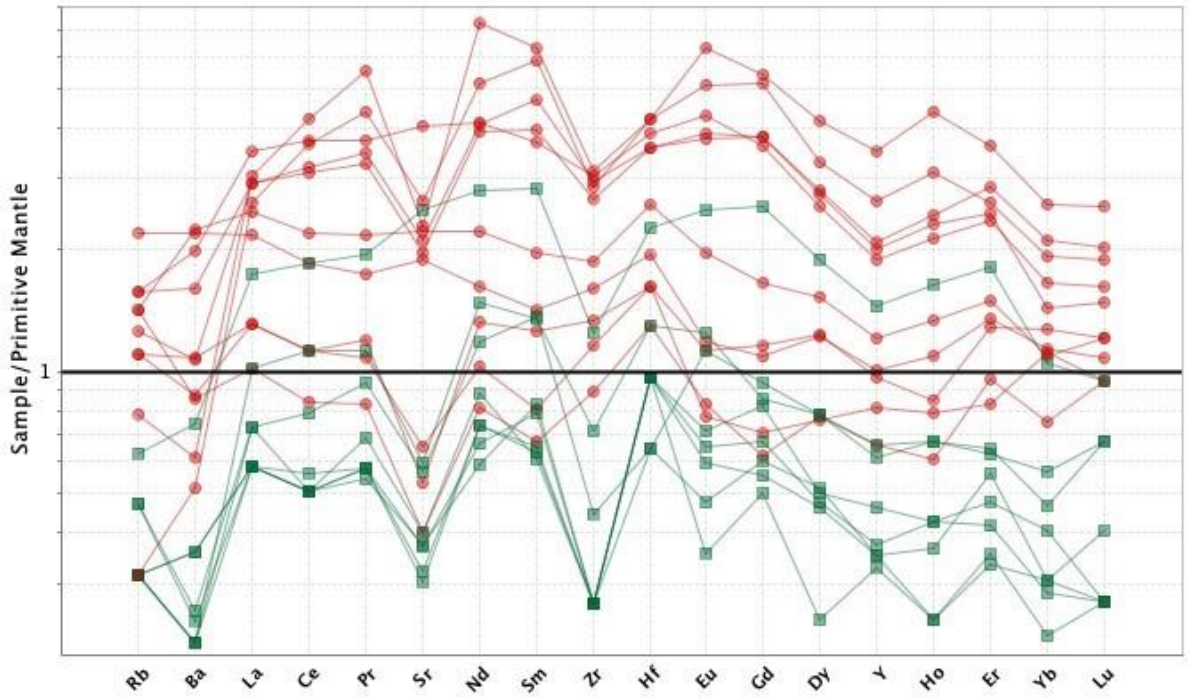

Figure 4.26: *Wehrlite and pyroxenite samples combined plotted against normalised primitive mantle (Sun & McDonough, 1989). In doing this one can see the relationship and correlation with the pyroxenite being enriched in mostly all elements at a consistent trend, whereas wehrlitic samples show a depletion at a slightly more inconsistent rate. The variable content seen in wehrlite samples here is likely due to variable Ol content.*

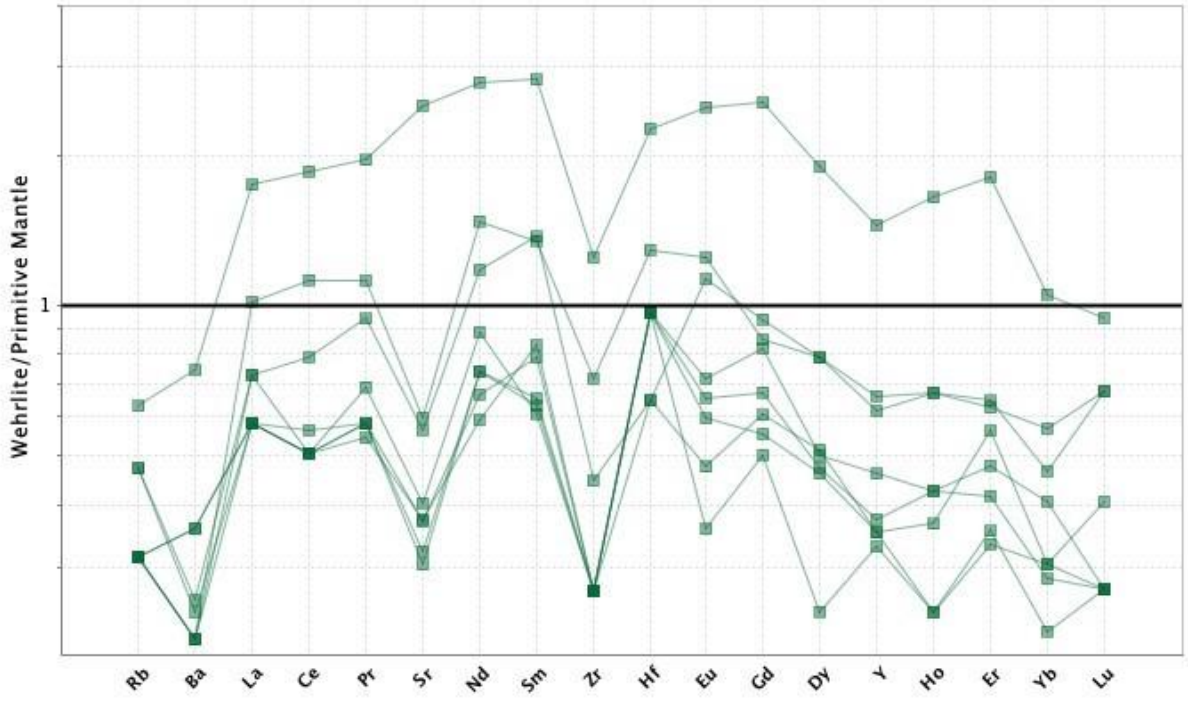

Figure 4.27: *Follow-up to plot in Fig.4.25, with wehrlite samples singled out. Plotted against normalised primitive mantle (Sun & McDonough, 1989).*

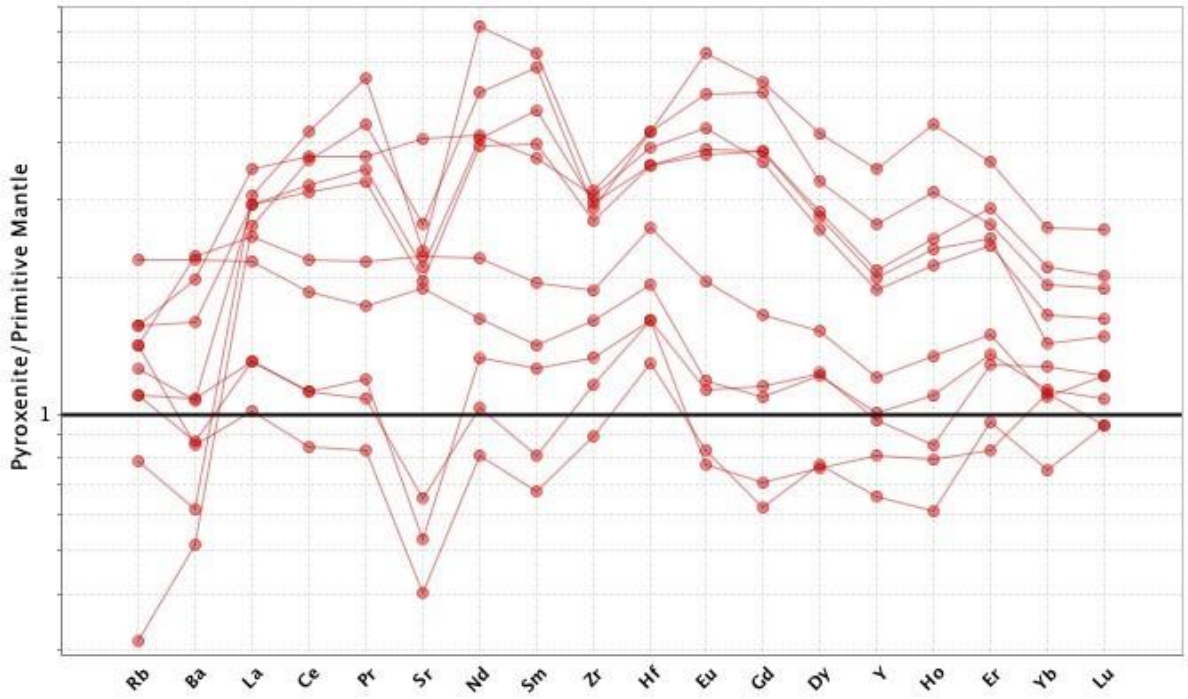

Figure 4.28: *Follow-up to plot in Fig. 4.26, with pyroxenite pegmatite samples singled out. Plotted against normalised primitive mantle (Sun & McDonough, 1989).*

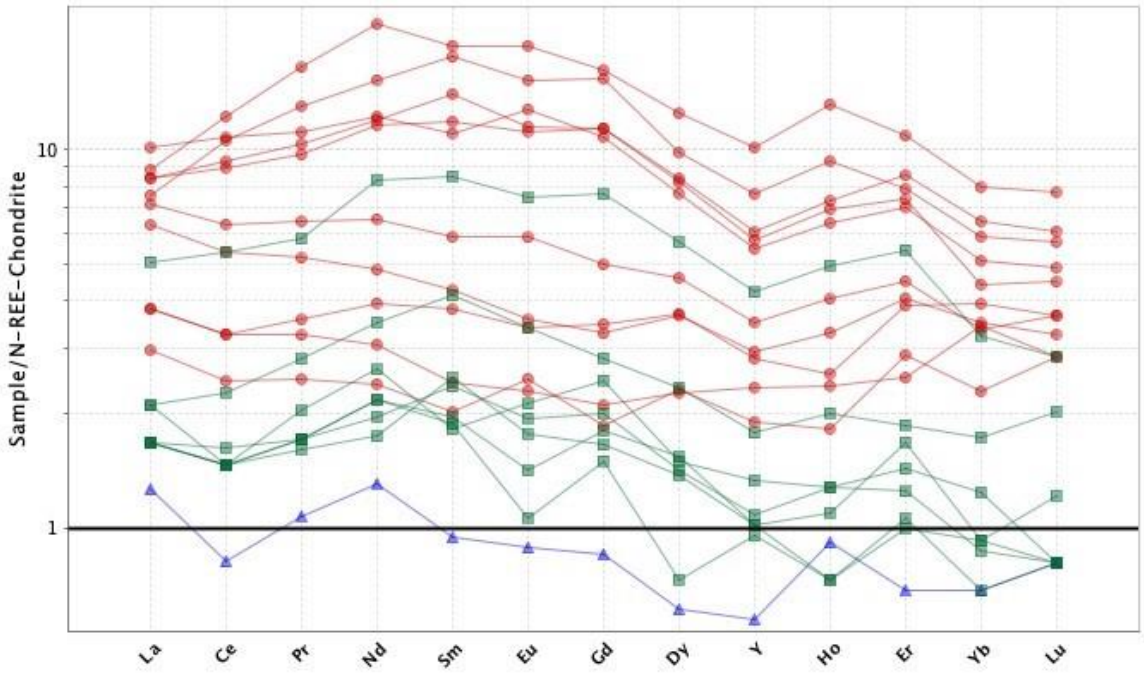

Figure 4.29: *All samples normalised to REE-Chondrite from McDonough & Sun, 1995. A trend can be seen here with pyroxenite pegmatite samples differentiating from wehrlitic and dunitic samples. There is a slightly depleted signature in all samples from Gd to Lu (HREE). This depletion is likely due to higher Ol content in samples. This also makes sense with dunite constituting >90% Ol, thus plotting consistently at the bottom of the graph. Essentially, decreasing Ol content is seen by samples plotting higher in the graph, matching IUGS classification of rock types for this area.*

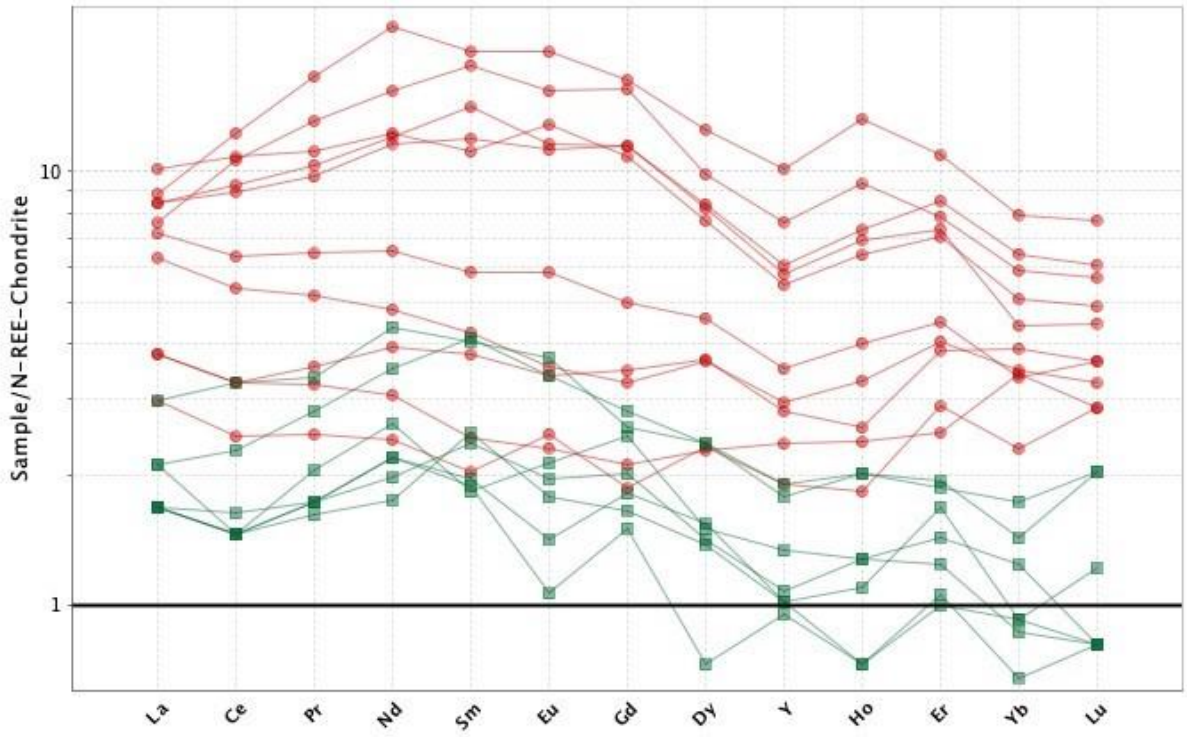

Figure 4.30: *REE – Chondrite normalised (McDonough & Sun, 1995) from pyroxenite and wehrlite samples. All samples show a slightly higher abundance in LREE with a slight decrease towards HREE. A few samples show negative anomalies in Dy, Ho, Yb and Lu, this may be due to variable Ol and Cpx content.*

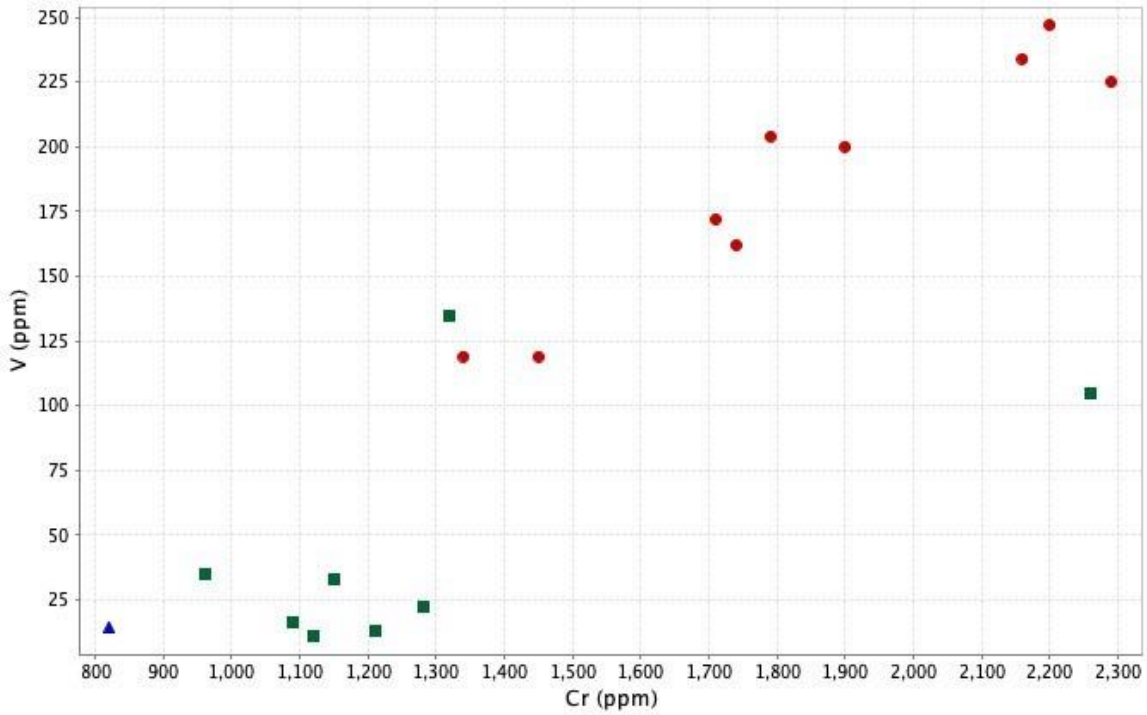

Figure 4.31: *Variation of V vs Cr for all samples. Wehrlite is scattered whereas dunite is poorly represented with only one sample. However, this is useful in observing where dunite plots as opposed to wehrlite and pyroxenite. Pyroxenite show a positive, near linear, trend. Sample AM19-XX (values of 301 ppm V and 4560 pm Cr) was removed from graph to better display overall trend, as this samples contained twice as much Cr as the average.*

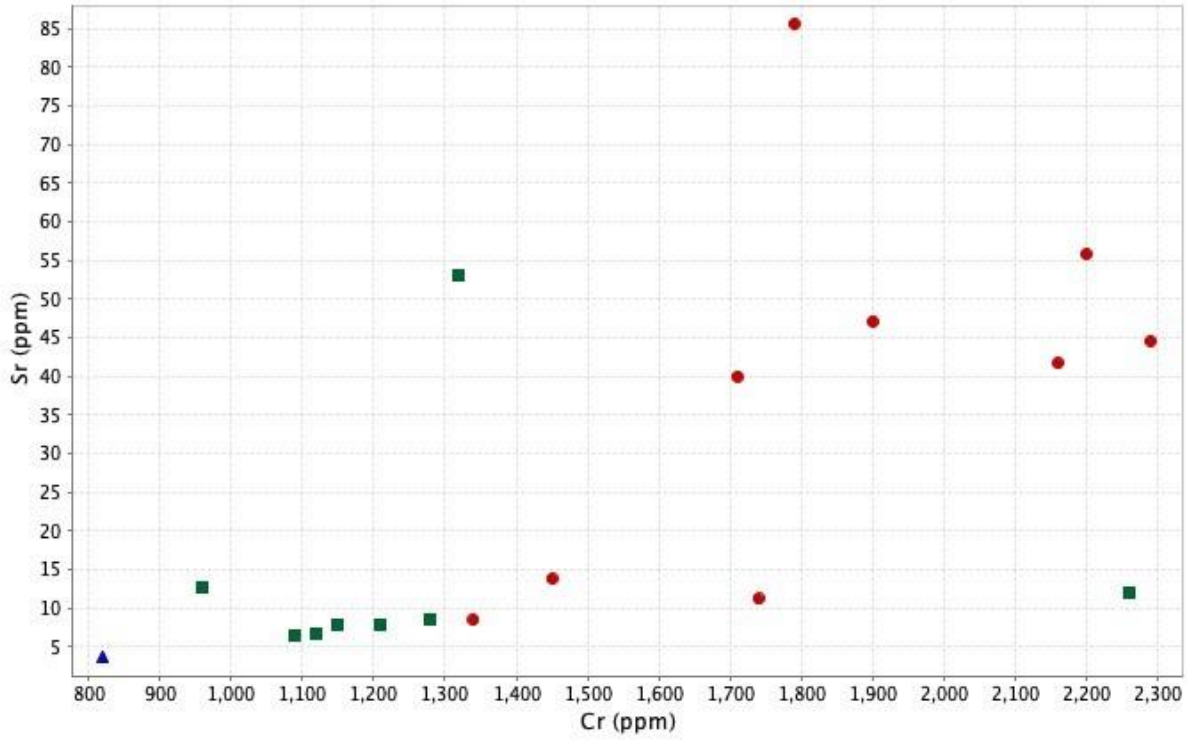

Figure 4.32: *Sr vs Cr for all samples. Wehrlite and pyroxenite samples are more scattered, where pyroxenite shows a very slight positive linear trend. As with Figure 4.31, sample AM19-XX was removed from this plot (48.4ppm Sr and 4560ppm Cr) to display a more representative overall trend.*

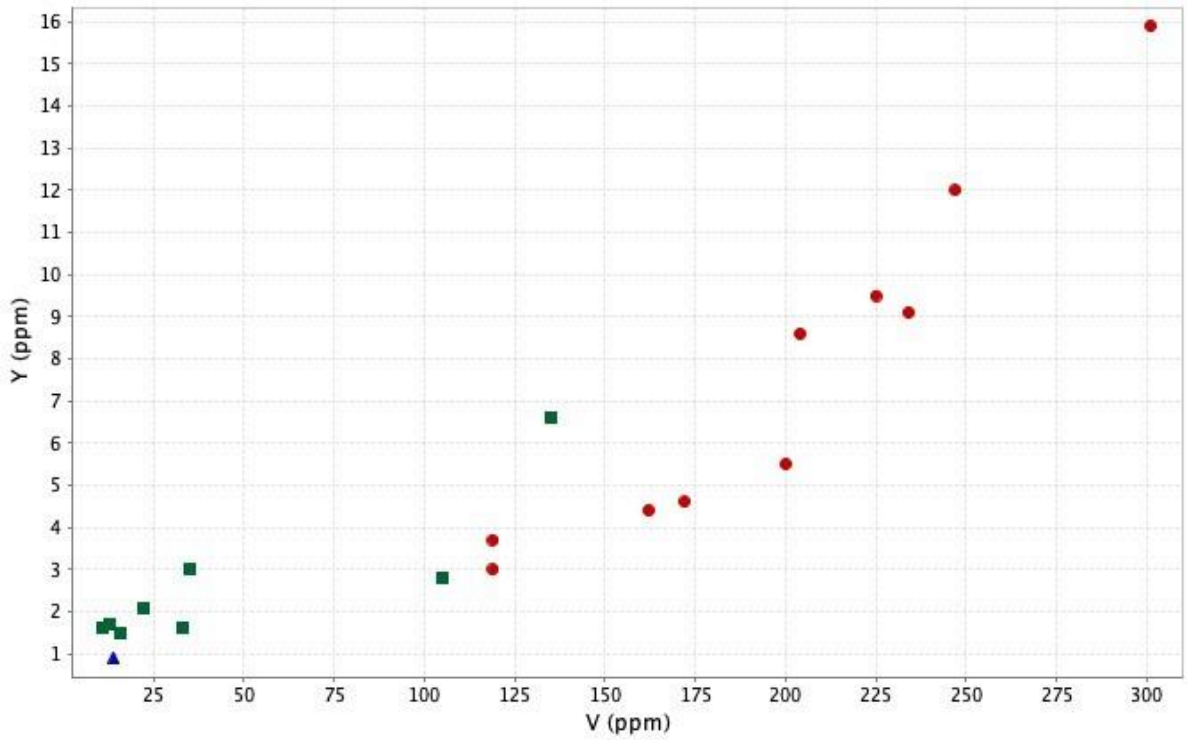

Figure 4.33: *Y vs V for all samples. A clear positive linear trend can be seen for pyroxenite, with an ambiguously similar trend for wehrlite.*

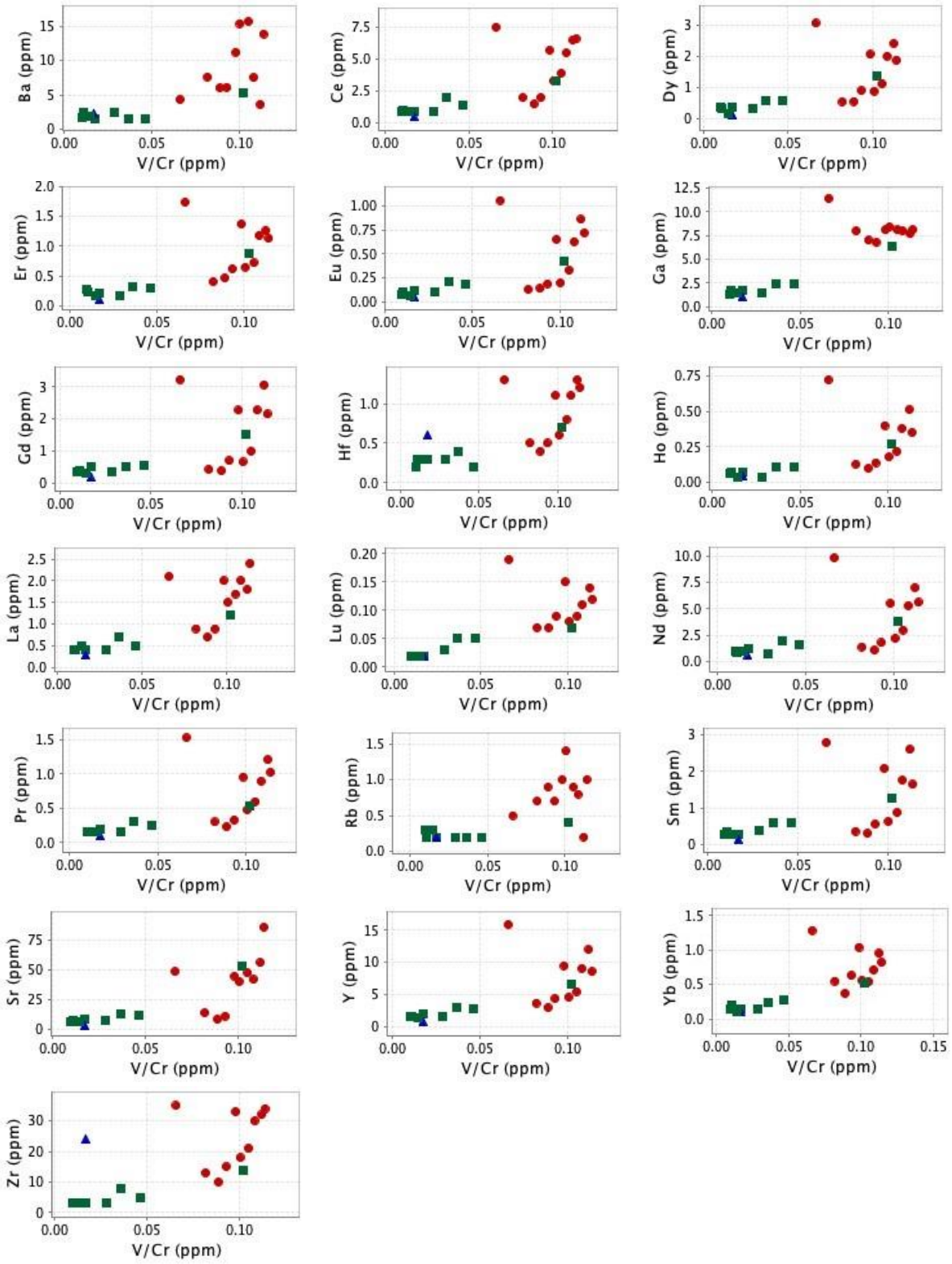

Figure 4.34: *V/Cr plotted against all trace elements for all samples. These plots indicates a typical fractional crystallisation sequence and enrichment in incompatible elements trend for the RUC. Most pyroxenite samples show a linear trend, indicative of magmatic evolvement (discussed in Chapter 5).*

4.3.2 XRD analysis

Analysis by X-Ray Diffraction was useful to verify and quantify mineralogy. All XRD results can be found in Appendix F and is summarised below in Table 4.5. Six samples were chosen based on petrological studies. The samples were chosen to represent host rock, mixed host rock/pyroxenite pegmatite and pure pyroxenite pegmatite.

Table 4.5: *XRD results (in %) showing the mineralogical variation from the chosen samples. 'Exotic' minerals such as ferroedenite, edenite and magnesiohastingsite belongs to the Amphibole Supergroup (Hawthorne & Oberti, 2006), whereas ferrosilite, being Fe-dominant, (part of enstatite-ferrosilite series) belongs to the Opx Subgroup (Tarantino et al., 2002). Trace amounts of dioptase may be due to low-T oxidation of metallic Cu. This may also be the case for azurite, which is a secondary Cu mineral frequently found in oxidised zones of Cu-bearing ore deposits.*

Sample	Edenite	Ferroedenite	Pentlandite	Chalcopyrite	Chalcocite	Ferrosilite	Magnesiohastingsite	Pyrrhotite	Dioptase	Azurite	Aragonite	Forsterite	Enstatite	Diopside	Ilmenite
AM19-006-1	1.5	1.0	1.2	0.9	1.6	1.7						18.4	73.7		
AM19-006-XA				1.6		0.8	0.8	3.3	1.3			60.9	3.7	27.6	
AM19-006-XB					0.6	2.0	0.3	1.9	0.6			20.6	60.7	13.2	
AM19-008-1							0.4	2.6	1.6			84.9	2.3	8.1	
AM19-010							1.0						94.9	3.7	0.5
AM19-XX			0.7	0.5			2.9			7.7	0.9	14.0	17.4	56.0	

Based on the XRD results one can identify with a higher sense of security, in combination with the other geochemical analysis, which mineral is in abundance in each sample. Sample AM19-010 and sample AM19-006-1 show a high percentage of enstatite (>70%), with small amounts of diopside and forsterite and traces of magnesiohastingsite. This can also clearly be seen from the thin sections in addition to the ALS data. Apparent here also is the mineralogical difference between AM19-006-XA and AM19-006-XB, being rich in forsterite (wehrlite) and enstatite (pyroxenite pegmatite), respectively. AM19-006-XA contains smaller amounts of enstatite, diopside, chalcopyrite and pyrrhotite, whereas AM19-006-XB is opposite, with smaller amounts of forsterite and traces of chalcocite, ferrosilite and pyrrhotite. Both samples contain accessory minerals which may be useful in understanding various factors controlling the magmatic evolvement. The forsterite-enstatite overall relationship is of utmost significance and importance in understanding the genetic relationship between the rocks and pyroxenite pegmatite itself. Both of these samples were chosen for EPMA analysis, with a focus on mapping out profiles of zonations. Essentially, these two samples, combined with the other thin sections of similar mineralogy, are very useful in investigating grain relationships, possible zonation, textural differences and attempting to correlate the relationship between pyroxenite pegmatite and host rock.

4.4 Pyroxenite pegmatite composition

The pyroxenite overall composition, including textural and geochemical analysis in addition to zonation patterns and relationship with host rock will be presented in this section. Useful information in attempting to unravel the pyroxenite pegmatite genesis presented in Chapter 5 can be obtained from this.

4.4.1 Geochemical analysis

Based on results in section 4.3, useful information can be drawn out to single out other analyses for pyroxenite pegmatite samples in addition to see any correlation between specific elements. Other important parameters, such as Cr over Mg/(Mg/Fe) relationship, which can be useful in understanding some aspects of the parental melt, will be presented here

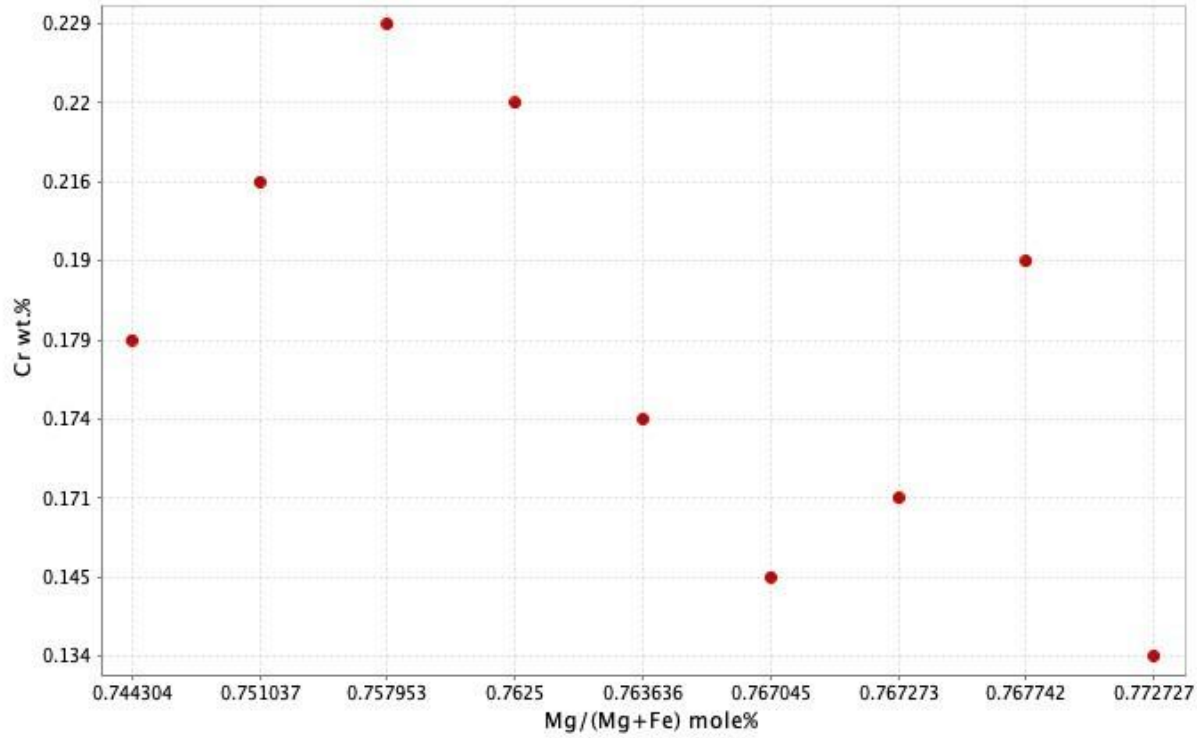

Figure 4.35: *Cr wt.% vs Mg/(Mg+Fe) mole% for all pyroxenite samples. This shows variability across samples, half being Cr enriched and half being Cr depleted. High Cr, in combination with high Mg, may be indicative of a primitive melt, the latter being well documented (Grant et al., 2016b) for the primitive (Mg-rich) melts forming ULS and CS.*

4.4.2 Mineralogy and textural characteristics

The pyroxenite pegmatite samples largely consists of coarse-grained enstatite and diopside. Grain shape is mostly euhedral to subhedral. The smaller enstatite and diopside grains appear subrounded to euhedral. Coarse-grained diopside grains appear with demixing lamellae in addition to interstitial enstatite and subordinate poikilitic olivine (mostly forsterite) grains, usually appearing as fine-grained matrix. The finer-grained equigranular diopside and enstatite grains do not have the same amount of interstitial networks nor poikilitic textures. There are examples of both enstatite and diopside grains with deformation bands, though this is seen far more in diopside grains. Accessory minerals observed from petrological study shows very fine-grained (<1 mm) chromite and possibly magnetite. Additionally, mostly all enstatite grains appear with interstitial

ordered ilmenite/rutile needles. All three types of olivine (described in section 4.2.1) appear in all pyroxenite pegmatite samples both interstitially, next to pyroxene grains and as dominant matrix constituent.

Sulfides (chalcopyrite, pyrrhotite and pentlandite) are mostly found in surrounding matrix, and not within pyroxene grains. Additionally, it does not appear in great abundance, rather, it is relatively scarce in pure pyroxenite pegmatite samples. There is one exception; sample AM19-010 which contains sizable (up to 2 mm) sulfides appearing in surrounding matrix. Sulfides are found in greater abundance in mixed (pyroxenite – wehrlite) samples (Figure 4.43; Figure 8.3). The sulfides are mostly combined with all three types (Ccp, Po, Pn) within one grain with straight to slightly irregular grain boundaries between one another. Surrounding sulfides are often oxides such as ilmenite/rutile and in some instances, inclusions of magnetite in chalcopyrite.

Table 4.6: *Mineral ID table with typical characteristics for pyroxene grains from all pyroxenite pegmatite samples.*

Clinopyroxene: diopside	**Orthopyroxene: enstatite**
■ Coarse-grained euhedral mineral with interstitial enstatite and olivine grains. ■ Often appears with demixing lamellae. ■ Characteristic with interstitial rutile/ilmenite.	■ Coarse-grained euhedral mineral with far less interstitial growth of diopside and/or olivine grains. ■ Fine-grained enstatite often appears with triple junction. ■ Dominate most pyroxenite pegmatite samples. ■ Appears with some interstitial rutile/ilmenite growth.

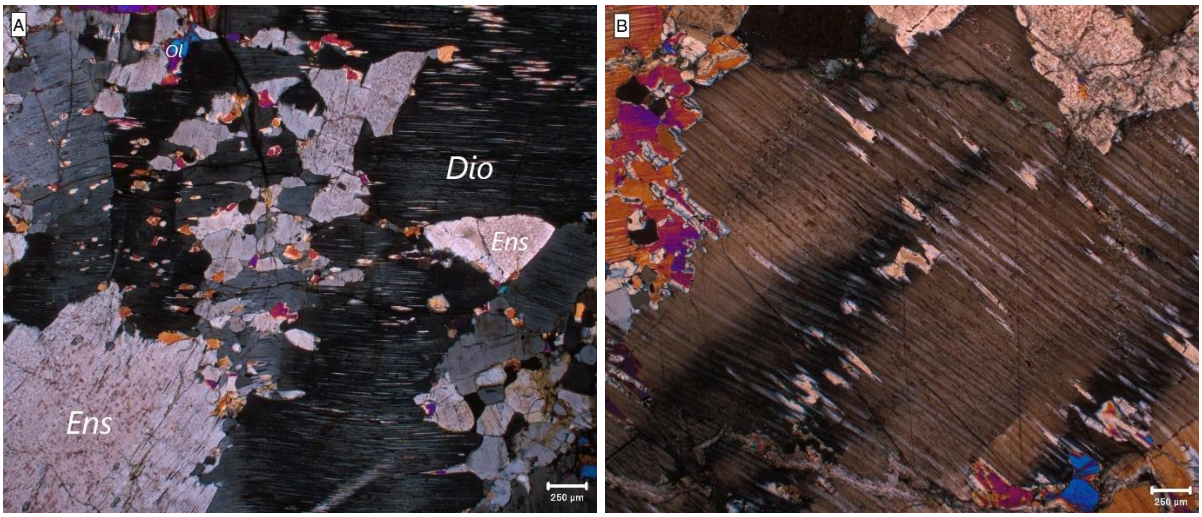

Figure 4.36: *Dio grains with characteristic interstitial growth of Ol and Ens appearing parallel to lamellae. From sample AM19-008-4 (A) and AM19-006-XB (B). Cubic-needle shaped ilmenite/rutile can again be seen within diopside grains (bottom left corner) in (A). (B) not labelled to display textures clearly.*

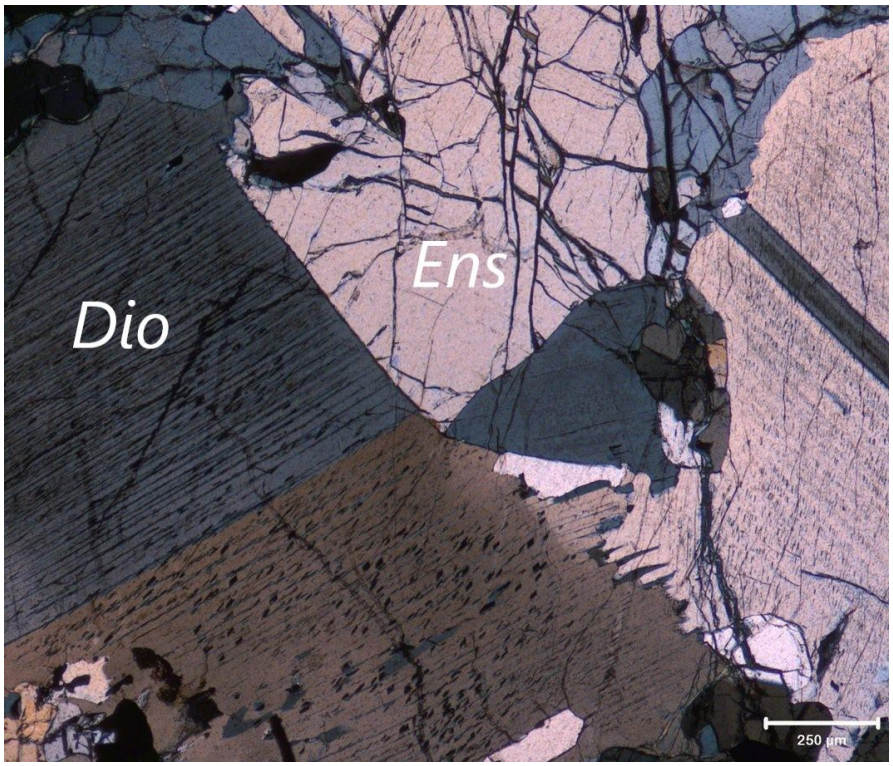

Figure 4.37: *Grain boundary relationship between Dio and Ens. Boundaries often appear very straight to slightly irregular, with some instances of diffuse boundaries possibly indicating syn-magmatic intergrowth.*

Figure 4.38: *Dio grain with intergrowth of sub-rounded Ol and euhdreal enstatite (appearing fine-grained) within a deformation band/shear zone. The fine-grained Ens grains appear with triple junction growth and neighbouring sulfide grains (appearing black in XPL). Within Dio grain one can also see the ilmenite/rutile needles.*

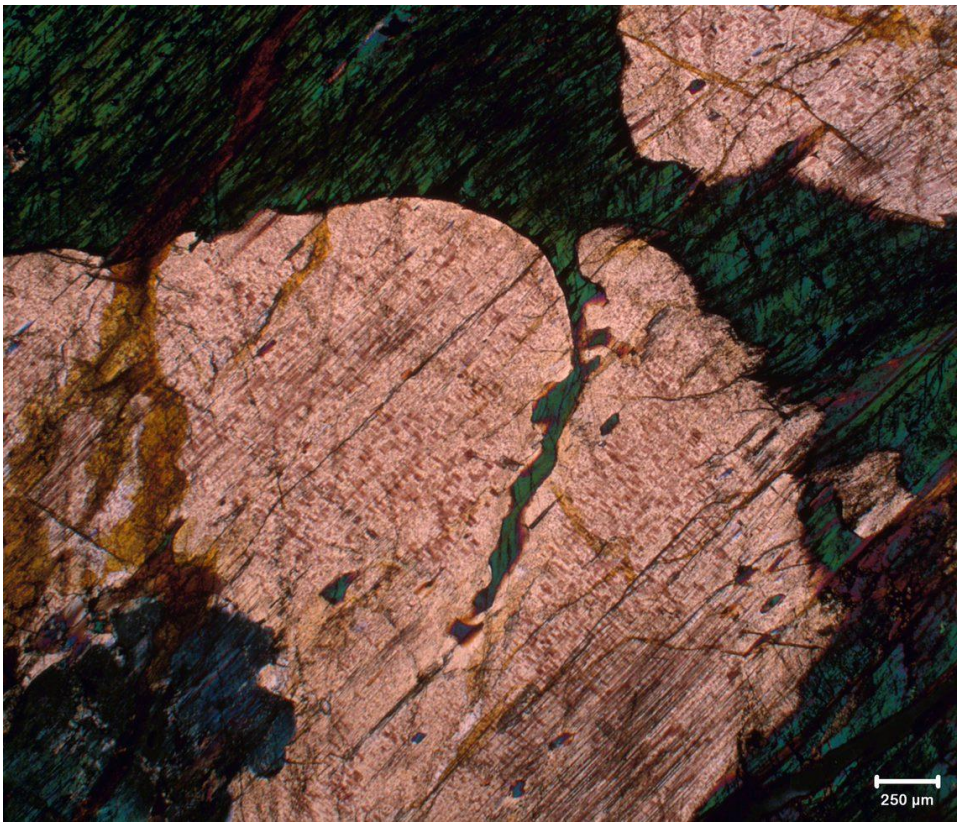

Figure 4.39: *Diopside typically contains needles and cubes of ilmenite/rutile as is also the case with many enstatite grains.*

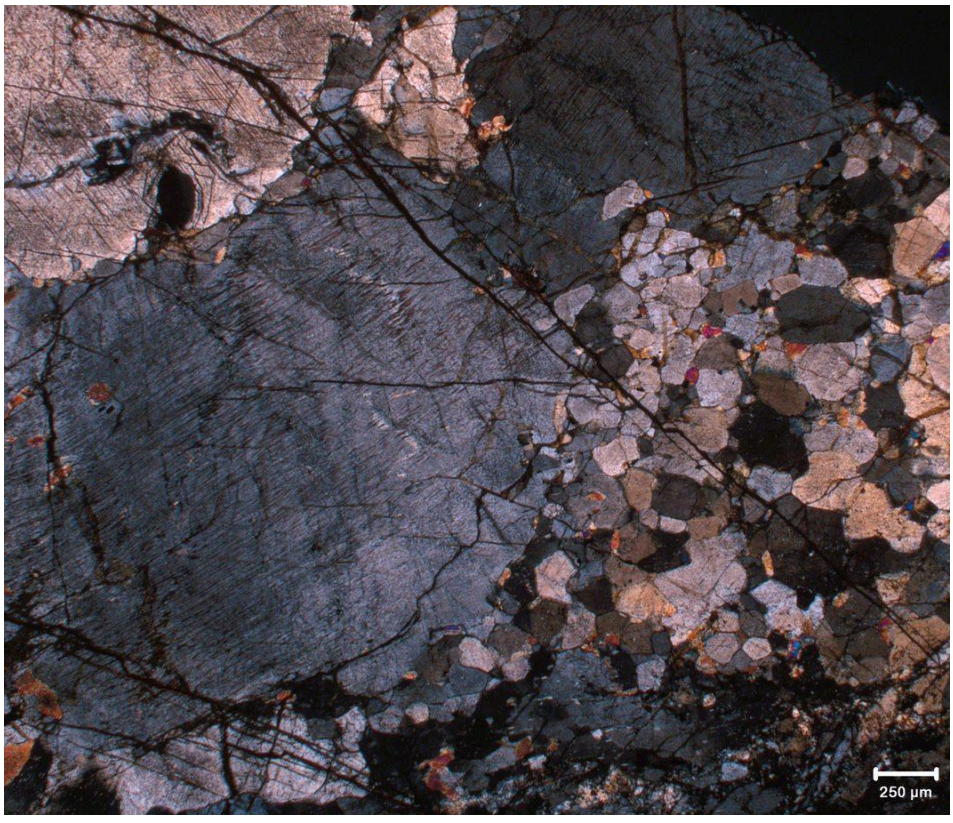

Figure 4.40: *Showing the characteristic relationship between coarse-, and fine-grained pyroxenes. Please note the same image have been used in Figure 4.15.*

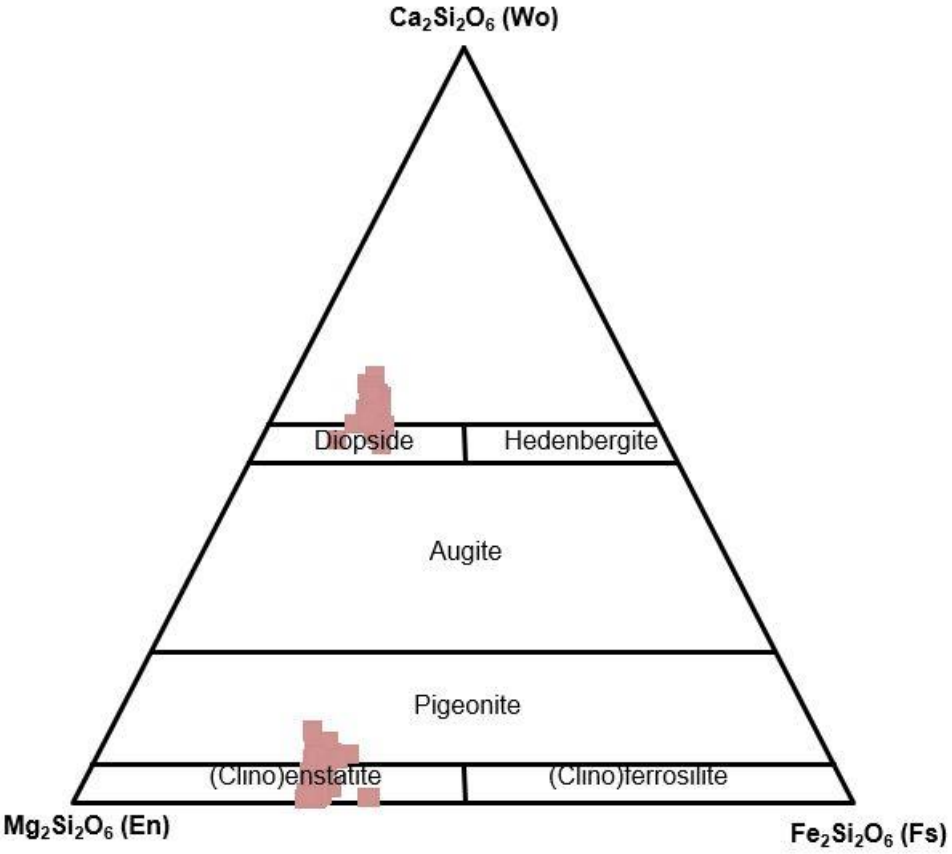

Figure 4.41: *Ternary plot for pyroxene classification (Morimoto, 1988). 145 normalised data points from EPMA analysis (Table 8.30) have been plotted, appearing as brown clusters. From these results one can compare to previous pyroxene classification diagrams from RUC (i.e. Orvik, 2019). This will be discussed further in section 5.2.*

4.4.3 Zonation patterns in pyroxene grains from EPMA analysis

Upon investigating the pyroxenite pegmatite samples, evidence for possible zonation patterns appeared in pyroxene grains. Based on this, EPMA analysis was chosen as the preferred method for verification. Additionally, EPMA provides useful element information to verify whether, for instance, a singular grain is orthopyroxene or clinopyroxene. The possible zonation patterns were investigated by applying several datapoints across a line in a grain. In doing so, the elements, given in oxides, can be investigated and profiles can be made. Any element increases or decrease, across the line, can give clues to genesis of the grain and provide useful information in unravelling the chain of events.

To gain a best possible picture of the pyroxenite pegmatite and host rock lithology, sample AM19-006-XA and AM19-006-XB (Figure 4.42; Figure 4.43) was chosen for analysis. These samples had intriguing grain size and shape variety, representative mineralogy, mixing lamellae and essentially what appeared, from petrology investigations, to be possible zonation patterns. EPMA data tables and profiles from spot images can be found in Appendix E.

To make accurate profiles, as many data points as possible is desired, though with a limit. A limit of 30 data points was used here to maintain higher accuracy, and between each round of up to 30 data points, calibration was executed on known minerals (relating

to minerals in own samples) and their position (garnet, olivine, diopside and albite). In attempting to avoid disruptive results in data or simply avoiding overquantified oxides (essentially dominating plots so certain data points do not show up), certain measures were taken;

1. SiO_2 was not included due to be overquantified and making it hard to see other oxides of interest.
2. Two plots were made for each profile, one containing CaO, FeO, MgO and Al_2O_3 and one containing TiO_2, Cr_2O_3 and NiO.

Profiles have been sorted according to mineral type and appear in such order. Some samples showed disruptive results (likely due to inclusions within measured grains) and have not been included.

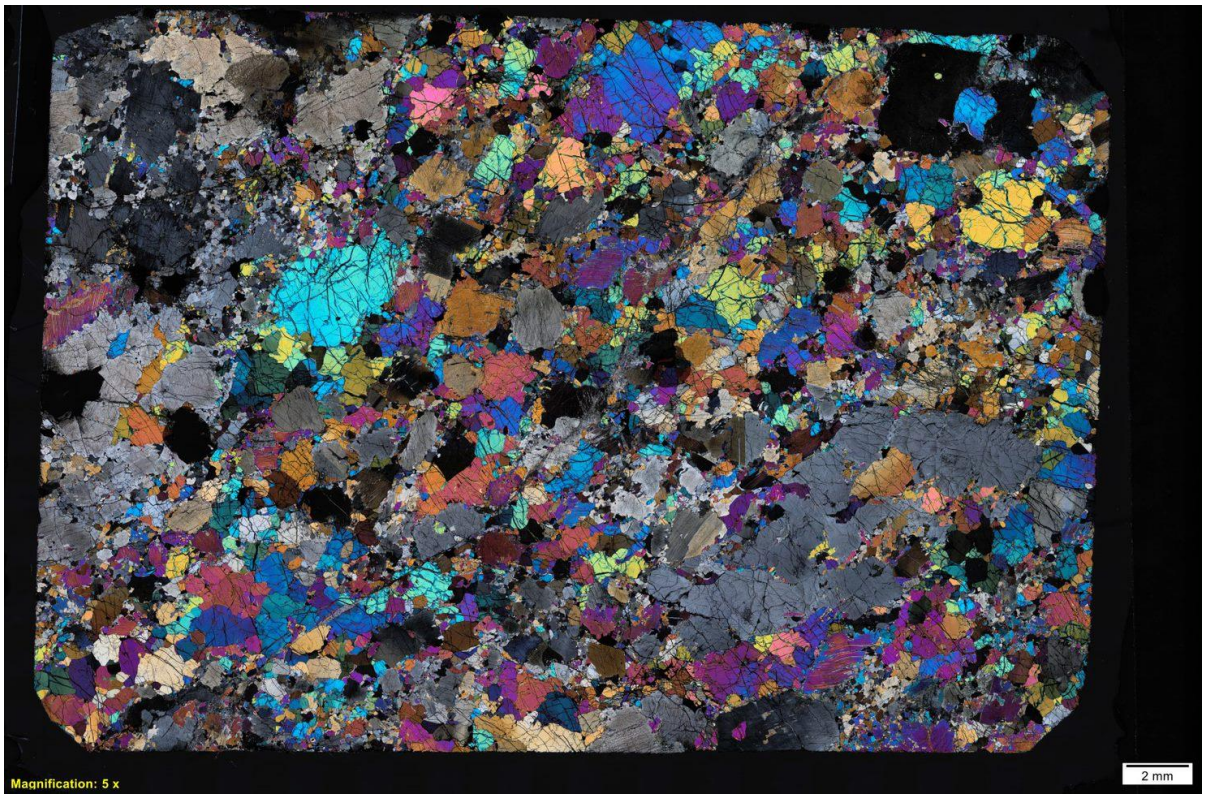

Figure 4.42: *Thin section AM19-006-XA chosen for EPMA analysis representing a mixed sample (pyroxenite-wehrlite).*

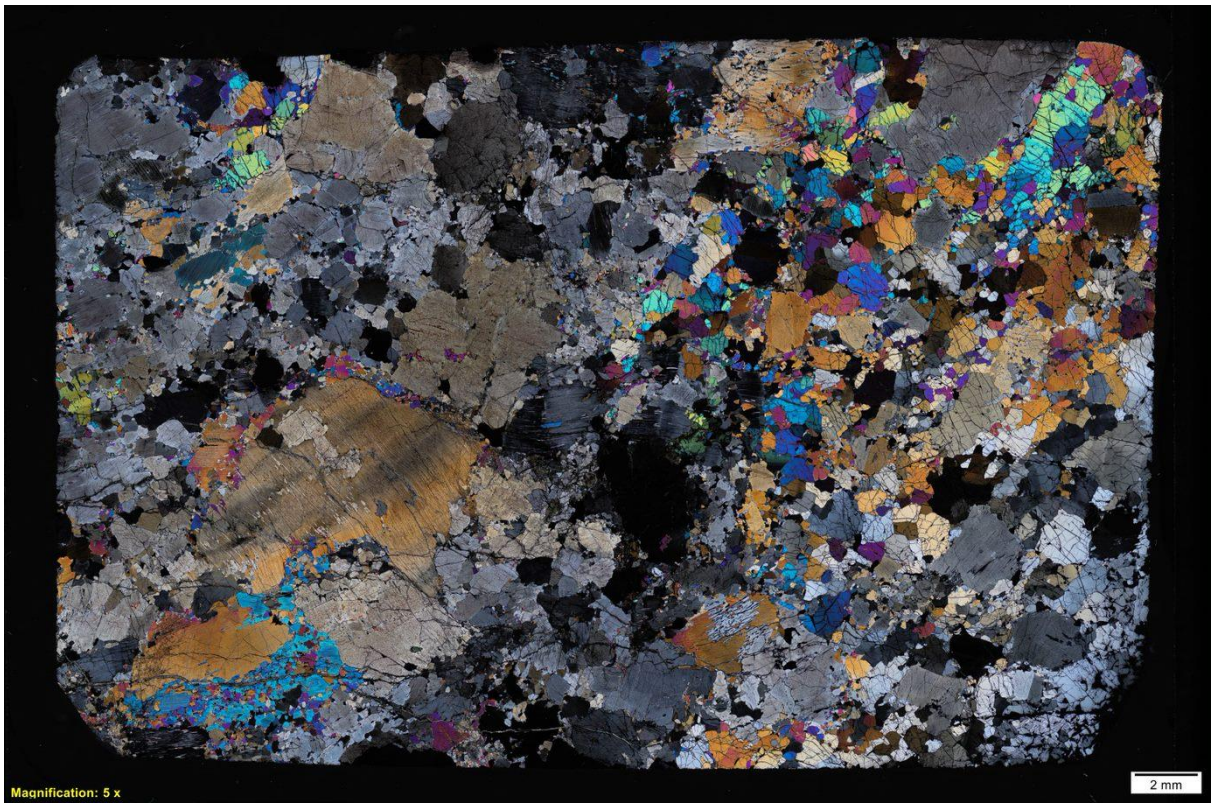

Figure 4.43: *Thin section AM19-006-XB representing a more or less pure pyroxenite pegmatite sample.*

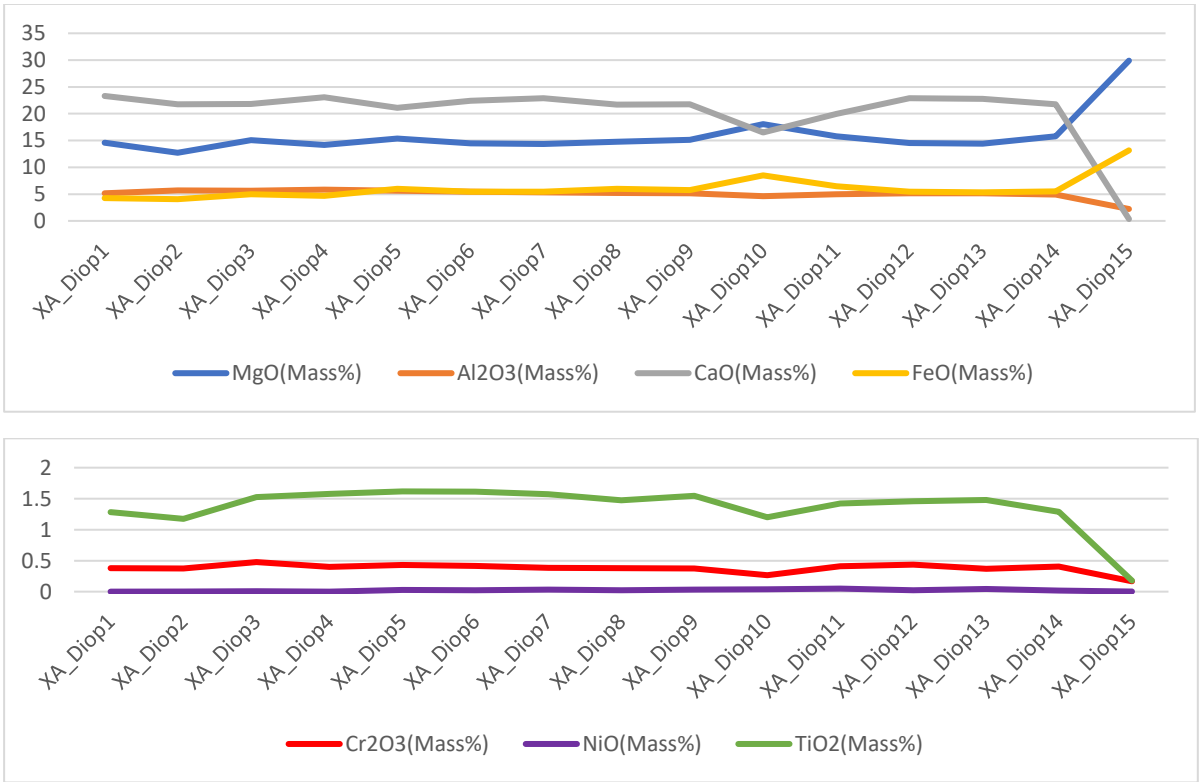

Figure 4.44: *Profile 1 of diopside. Slight element changes towards right-hand side border. XA_Diop10 is possibly an inclusion disrupting the trend.*

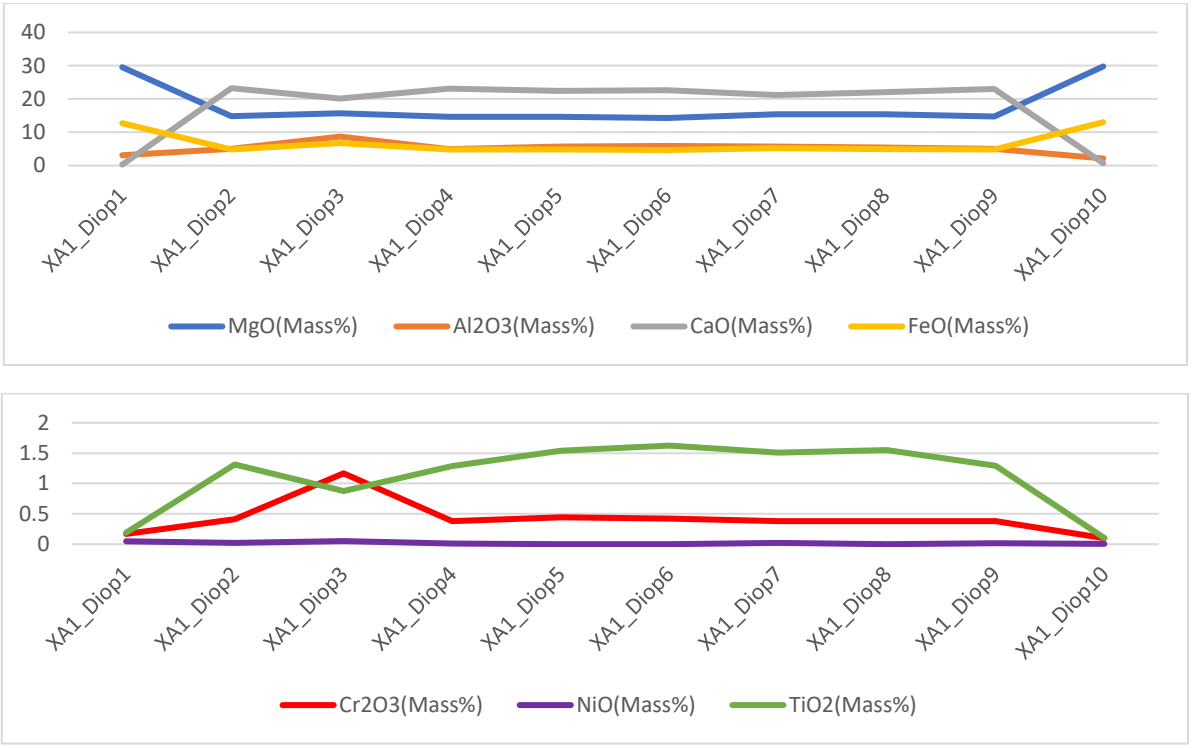

Figure 4.45: *Profile 2 of diopside with a good indication of zonation in increase of MgO and FeO combined with a decrease of CaO and TiO_2 towards the border. An enrichment in TiO_2 from grain border to border may also indicate zonation.*

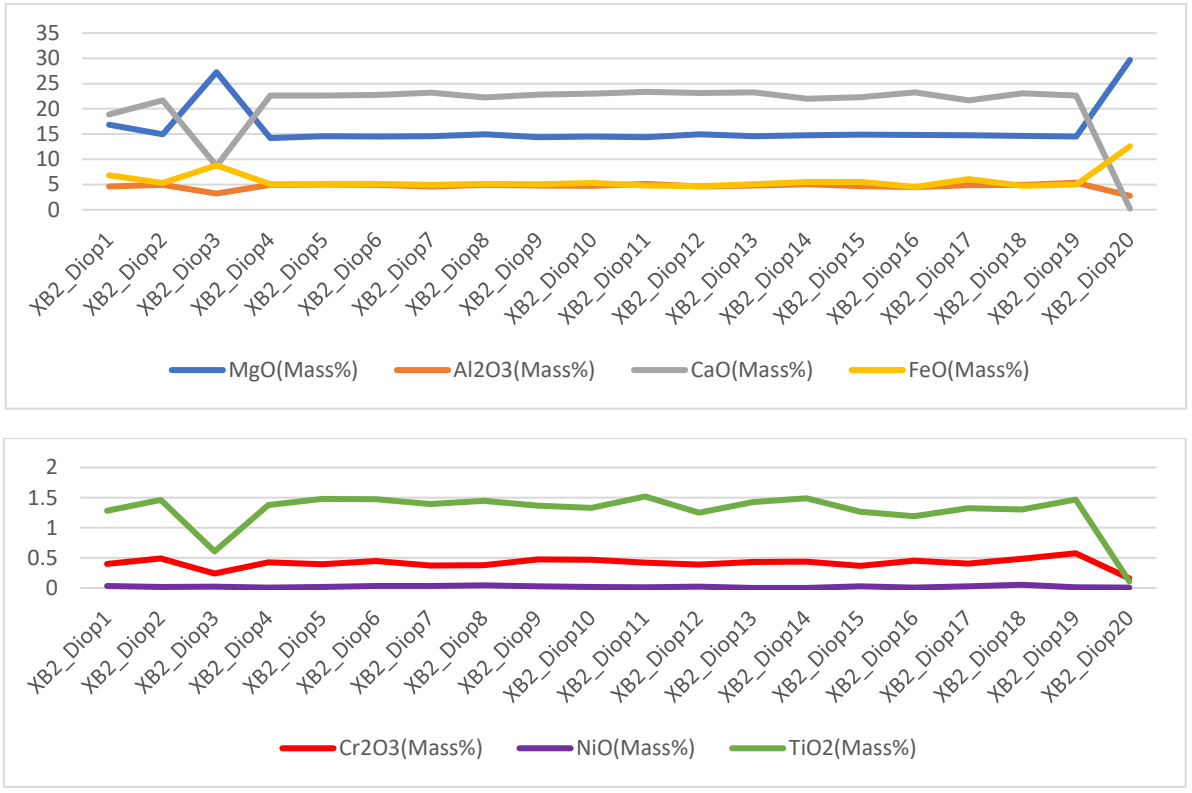

Figure 4.46: *A weak indicator of zonation towards the right-hand side of graph with MgO and FeO increase combined with CaO, Al_2O_3, Cr_2O_3 and TiO_2 decrease.*

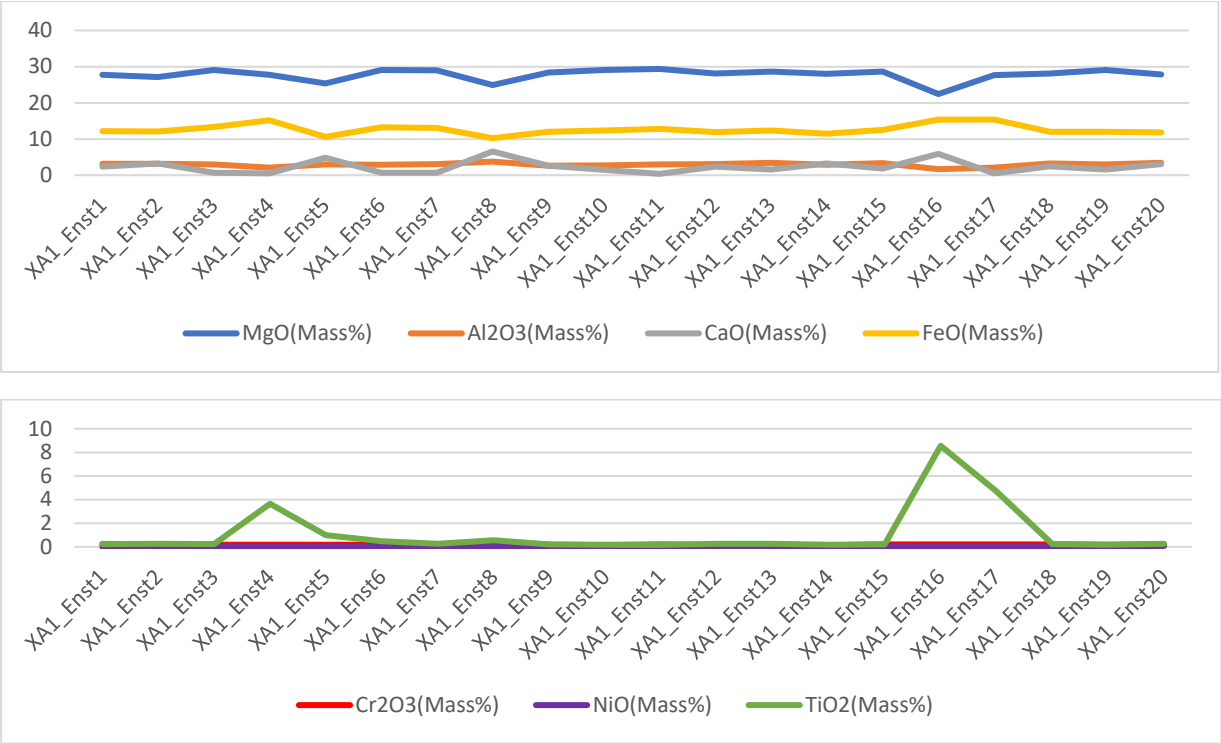

Figure 4.47: *A weak zonation pattern in enstatite with various inclusions disrupting results across the line, particularly apparent in drastic TiO_2 increase (likely rutile).*

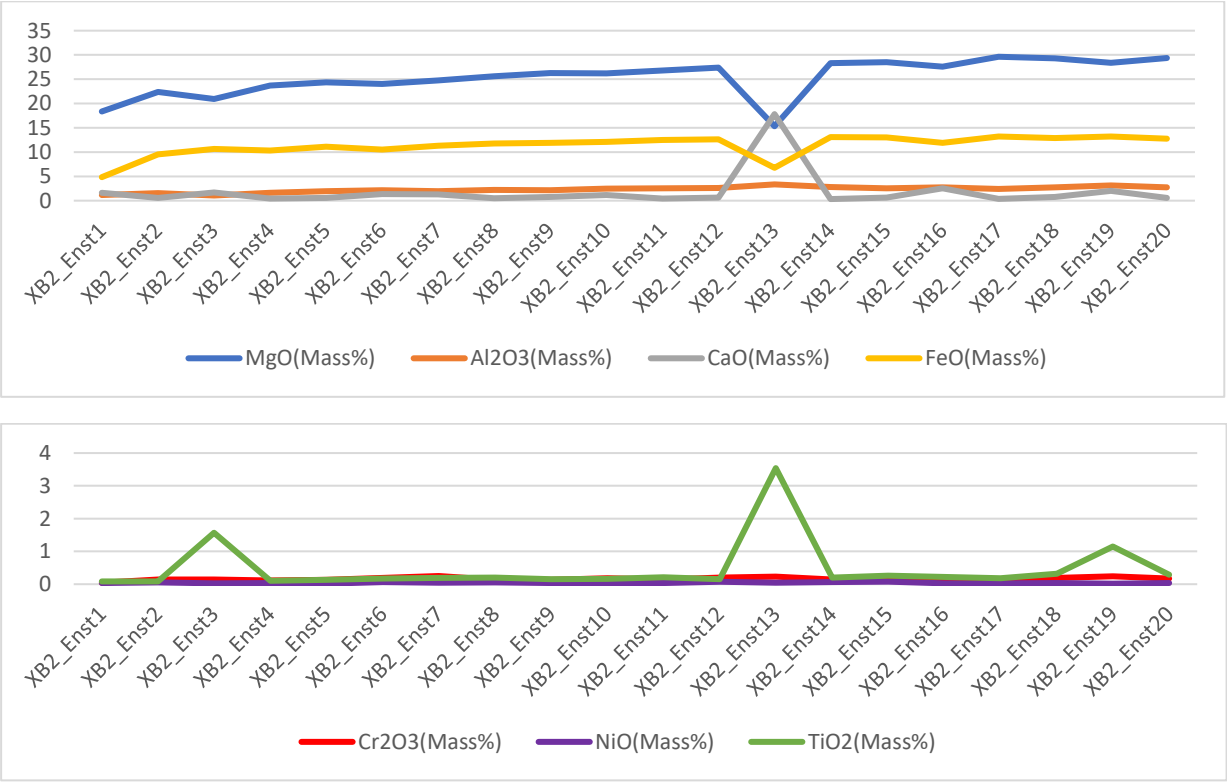

Figure 4.48: *General increasing trend across the line disrupted by sharp TiO_2 increases (variable inclusions). Possibly zonation from left-hand side of upper graph, seen with slow increase across the line, though with a great deal of uncertainty.*

4.4.4 Host-rock relationship

The pyroxenite pegmatite and wehrlitic/dunitic relationship was obtained from sampling the borderline in-field. This can be challenging as the boundaries often appear with a wide mixed zone, so no clear borderline can be obtained from thin sections. However, in-field descriptions along with comparing the pyroxenitic and wehrlitic samples can give a good indication of the relationship, and more importantly the inclusions in the pyroxenite pegmatites that matches wehrlitic and dunitic compositions (i.e. various olivine types, shapes and sizes). Additionally, wehrlite and dunite compositions from ULS and CS are well documented (Nicolaisen, 2016; Grant et al., 2016b, Larsen et al., 2018; Orvik, 2019) and may be used for comparison. Samples AM19-XX1, AM19-006-1 and AM19-008-1 was quite useful for this work, showing wehrlitic (with varied and comparable pyroxene) composition, pyroxenite pegmatite composition and wehrlitic composition, respectively.

Most of the pyroxenite pegmatite samples appear with type 1 olivine grains in similar (if not identical) shape as those found in wehrlite samples. Additionally, type 3 olivine grains can be seen in most of the shear zones/deformation zones and as matrix in the pyroxenite pegmatite samples. Triple junction can be seen for many of the olivine in both wehrlite and pyroxenite pegmatite, as is also the case for most of the enstatite grains. Comparable is also coarse-grained olivine and enstatite being surrounded by compacted fine-grained constituents of similar mineralogy. Most of the demixing lamellae and deformation textures seen in most of the pyroxenite pegmatite samples does not seem to be as prominent in many of the grains in wehrlite samples.

Figure 4.49: *Sample AM19-006-1-1 (left) and AM19-008-1 (right) in PPL used for comparison.*

It can also be useful to compare whole-rock geochemistry from ALS data to see if there are any similar trends apparent (Figure 4.49; Figure 4.50). Two samples, AM19-006-1-1 and AM19-008-1, are suitable candidates for pyroxenite pegmatite and wehrlite

and have thus been plotted. Trace elements are in far greater abundance in pyroxenite pegmatite samples.

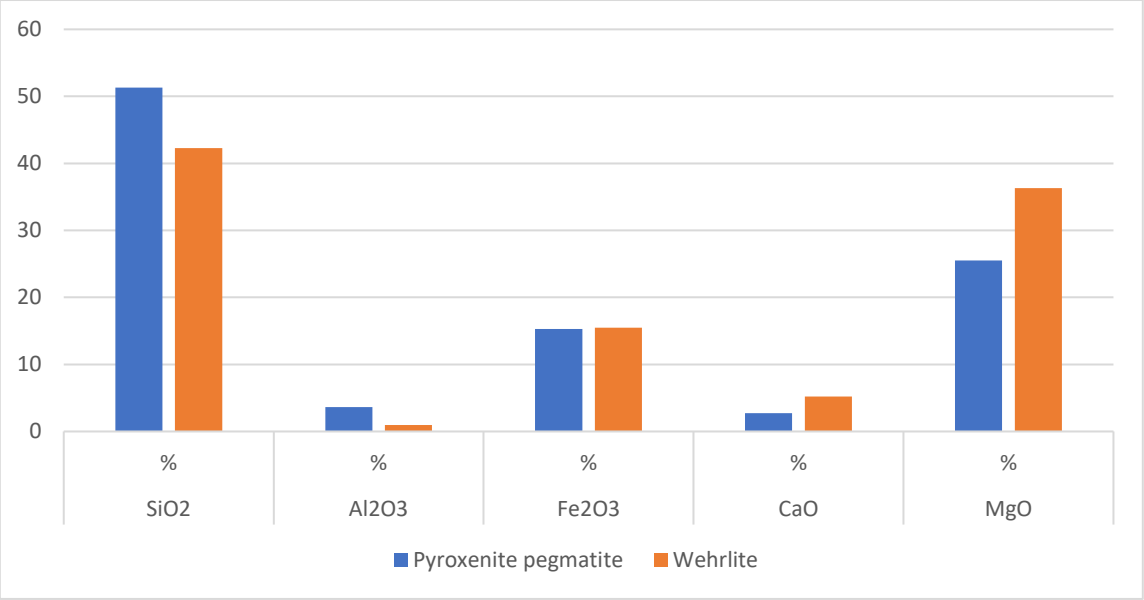

Figure 4.50: *Comparison of primary oxides from ALS data for sample AM19-006-1-1 (pyroxenite pegmatite) and AM19-002-7 (wehrlite).*

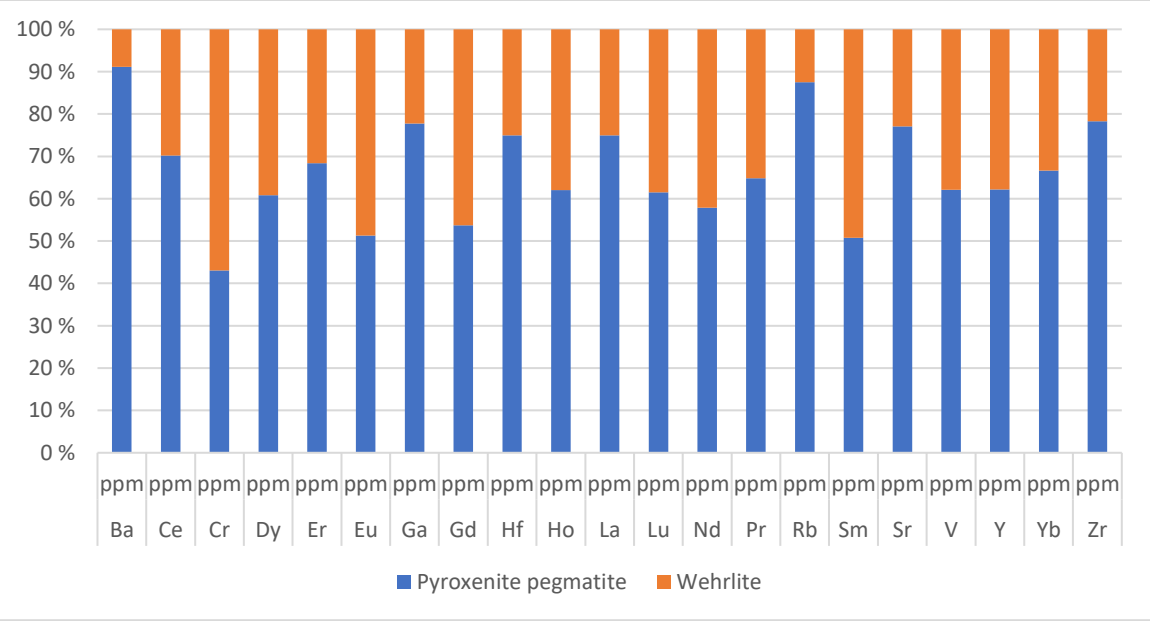

Figure 4.51: *Comparison of the same samples as Figure 4.50. Shows how each trace element (ppm) value contributes to the total amount when samples are stacked against one another.*

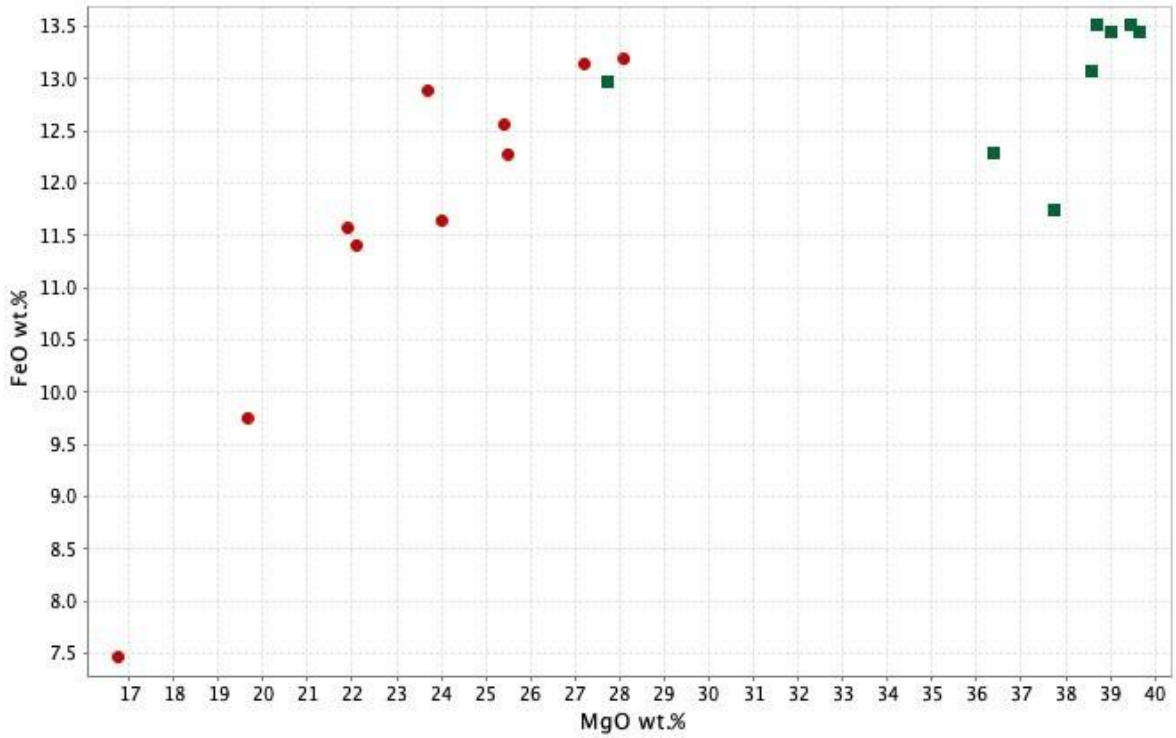

Figure 4.52: *FeO vs MgO for pyroxenite and wehrlite samples, showing a clearly different trend. Where pyroxenite plot at a near positive linear trend, wehrlite is more clustered. This can assist in understanding substitutional relationships (Chapter 5).*

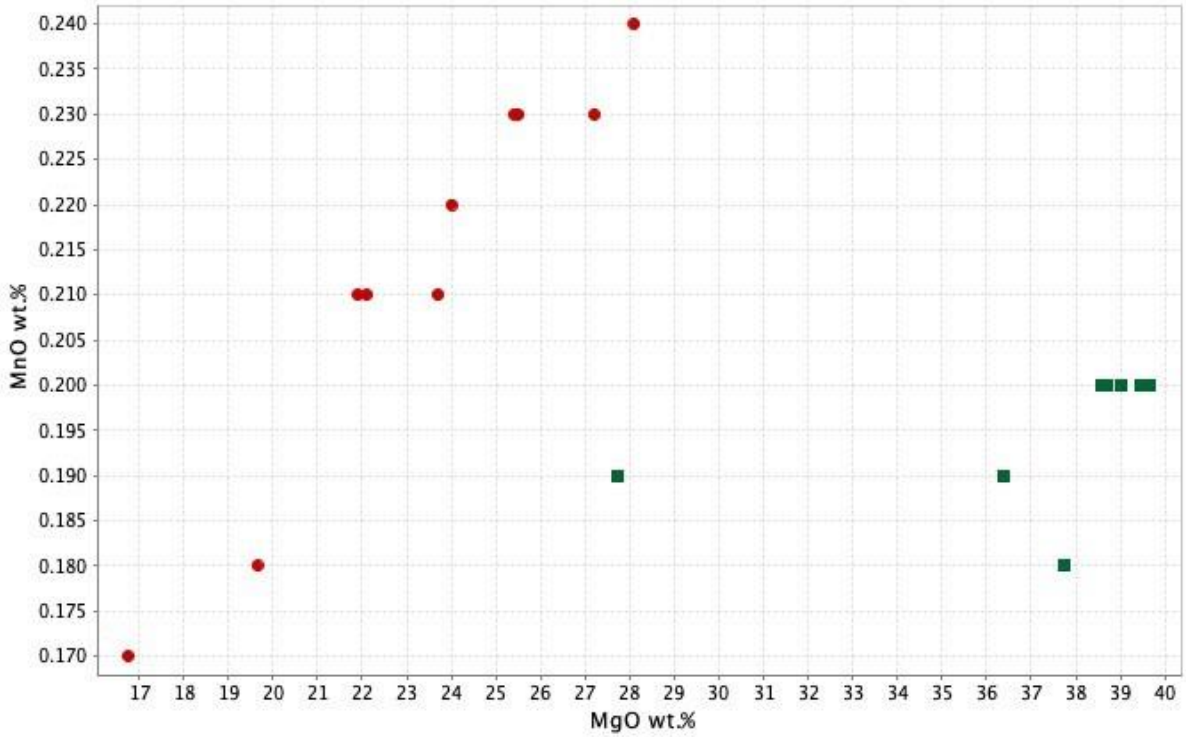

Figure 4.53: *MnO vs MgO for pyroxenite and wehrlite samples. A positive linear trend can be seen with pyroxenite samples, whereas little trend is shown with the wehrlite samples.*

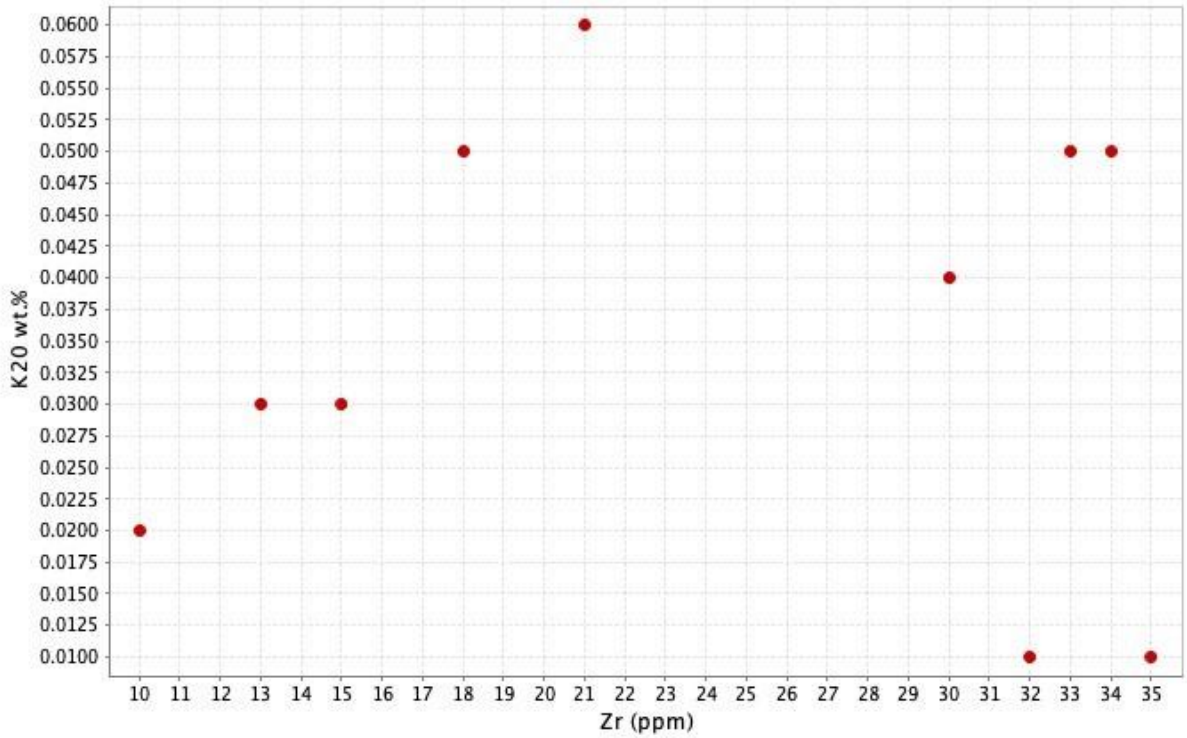

Figure 4.54: *Variation of K_2O vs Zr for all pyroxenite pegmatite samples. Samples plot highly variable. It can be inferred that the pyroxenite pegmatite generally have low abundances of these incompatible trace elements, though it would be highly interesting to see more pyroxenite pegmatite samples plotted to gain a broader portrait to compare this with the pyroxenite pegmatite and normal pegmatite and its inferred magma composition in the Merensky Reef (Cawthorn & Boerst, 2006).*

Based on the results in this chapter, one can start to create an image of the pyroxenite pegmatite genesis and nature of emplacement and possibly dig deeper in attempting to find clues on parental melt composition and mantle source. Useful geological setting comparisons, such as the Bushveld Complex, are important pieces in this geological puzzle. Though there are many limitations with the data (and lack thereof) it will be attempted to investigate the pyroxenite pegmatite in an ultramafic-mafic setting – the state of the art of the RUC.

5

Discussion

5.1 Pyroxenite pegmatite genesis

In order to understand the genesis of the pyroxenite pegmatites in the RUC, it is necessary to make appropriate comparisons to similar geological settings elsewhere in the world aided by own observations from field work and post-field analysis. In doing so, one can attempt to construct an understanding of its nature and ultimately create a genetic concept. The generic processes behind the origin of pegmatites are well understood, however, this knowledge is more or less restricted to pegmatite bodies of granitic compositions. Pegmatites in mafic to ultramafic settings, such as in the RUC, remain complex and somewhat contentious, and so begin the discussion of the pyroxenite pegmatites genesis in the Reinfjord Ultramafic Complex.

5.1.1 Pyroxenite pegmatite in M/UM setting in the RUC – state of the art

In creating a portrayal of the pyroxenite pegmatite in the mafic to ultramafic setting in RUC, it is useful to consider what we already know, and are yet to discover, about them – the current state of the art. Grant et al. (2016b) describes the RUC as an open magmatic system that was affected by several cycles of magmatic recharge events. Initial melts were of mafic composition, forming layered gabbro-norites, followed by ultramafic melts forming layered pyroxene-dominated cumulates (Grant et al., 2016b). The accompanying marginal zones are clear indicators of partial melting of initially formed gabbro-norite and ultramafic melt contamination (Grant et al., 2016b). The last melts were initially olivine saturated and reacted with ULS cumulates to form replacive dunite – completing the melt sequence.

The Merensky Reef in the Bushveld Complex is the closest resemblance to this unusual type of open system with continuous magmatic recharge. Both systems are products of high R-factor and, with the recharge events, meticulously mixed the pre-existing melts. As such, it is appropriate to draw comparisons to the Merensky Reef in attempting to further the understanding of the pyroxenite pegmatites in the RUC.

The Merensky Reef is remarkable in that the layers, stretching over 100 km, contains consistent PGE grades. The compositional layering in the RUC may not stretch over 100 km but the similarity in layering is remarkable. There is a perceived view that the pyroxenite pegmatites in the Merensky Reef are associated with PGE mineralisation, with models suggesting involvement of late-stage, evolved, water-enriched magma, produced by fractionation of the magma (Lauder, 1970; Vermaak, 1976; von Gruenewaldt, 1979; Ballhaus & Stumpfl, 1985; Boudreau et al., 1986; Mathez et al., 1997). There are several direct comparisons with this model for what is, seemingly, the scenario for the RUC. Still, this model also poses some challenges:

1. There is certainly exploitable PGE mineralisation associated with the pyroxenite pegmatites observed and described in this thesis. With values averaging 9 ppb Pt and 7 ppb Pd (Table 8.1), it is above the typically exploitable grade (Table 5.1) described by Robb (2005). However, it does not come anywhere nearly as close as the values found in the RUC reef deposits of dunitic and wehrlitic composition, where values range 69 – 419 ppb Pt and 116 – 730 ppb Pd, described, amongst others, by Larsen et al. (2018) and Nicolaisen (2016). Therefore, this value may be a part of the parental melts and not the ore-deposit. As such, PGE mineralisation may be considered associated with pyroxenite pegmatite, but not uniquely so as PGE appear far more enriched in the host rock (wehrlite), as is also well-documented (i.e. Nicolaisen, 2016). Further, PGE mineralisation

may not be present in other pyroxenite pegmatites in the area, as for instance within the gabbronorite-wehrlite-marginal contact zones.

Ultimately, Cawthorn & Boerst (2006) finds that the pyroxenite pegmatite in the Merensky Reef is, in fact, not directly associated with PGE mineralisation over the entire layering sequence, as it appears with highly sporadic PGE values throughout. In other words, the PGE mineralisation in the Merensky Reef does not seem to have been directly affected by the pyroxenite pegmatite. This may also be the case in the RUC where PGE values seem to vary in the pyroxenite pegmatite, possibly in a sporadic manner like Merensky. This is supported by the fact that borehole RF-1 was found with far more significant PGE values within the pyroxenite pegmatite sequences than recorded in any of the samples from this thesis, discussed further in section 5.1.5.

2. Evidence for a water-enriched magma is scarce in the studied pyroxenite pegmatites. No fluid inclusions were found in any of the samples in this study, however, at the very high ambient pressures, a free fluid phase is unlikely anyway. Additionally, typical constituents in a hydrous magma, such as amphibole and biotite, are only found in negligible amounts in the pyroxenite pegmatites. In fact, biotite has not been observed at all.

3. The pyroxenite pegmatites in RUC are emplaced in a slightly different fashion, seemingly sporadically within the central portions of CS and with a certain degree of systematic emplacement at the gabbronorite-marginal zone-wehrlite contact zones. Additionally, it appears with different geometry in the latter example, appearing in a 'plug/pipe'-like manner, differing to these of the Merensky Reef. To which degree, if any, this affects the overall genetic evolution is uncertain.

4. The pyroxenite pegmatites in the Merensky Reef contain a considerable amount of cumulus and intercumulus plagiolcase as opposed to the ones described here. As such, there are geochemical differences to consider in the pegmatitic genesis.

Table 5.1: *Typical concentrations that are required for an exploitable ore deposit (Robb, 2005).*

	Average crustal abundance	Typical exploitable grade	Approximate concentration factor
Al	8.2%	30%	×4
Fe	5.6%	50%	×9
Cu	55 ppm	1%	×180
Ni	75 ppm	1%	×130
Zn	70 ppm	5%	×700
Sn	2 ppm	0.5%	×2500
Au	4 ppb	5 g t^{-1}	×1250
Pt	5 ppb	5 g t^{-1}	×1000

Note: 1 ppm is the same as 1 g t^{-1}.

5.1.2 Formation of pegmatitic textures

Most analyses of pyroxenite pegmatite in the RUC have been of isolated samples, and so it cannot be confirmed that such analysis is wholly representative for the entirety of pyroxenite pegmatites in the RUC. Here, I report a detailed description of the most prominent pyroxenite pegmatites in addition to a general overview from all observed pyroxenite pegmatites elsewhere in the RUC. The mineralogical and textural properties in the pyroxenite pegmatites, presented in Chapter 4, provide crucial constraints on the genesis of these rocks.

Grain size, shape and textural relationships

It is well established that pegmatites are coarse-grained for specific reasons (Evans, 1993; Robb, 2005):

1. Volatile-related depression of magmatic solidus (water and 'fluxing agents' (Li, B, P, F) increase water solubility in melt).

2. Rapid diffusion of elements to sites of crystallisation (due to high water content).

3. Undercooling of magma below solidus temperature causing nucleation suppression → large crystals instead of new crystals.

It is certainly true that the pyroxenes in the pegmatites in the RUC are very large in grain size, at largest 11 cm. However, it cannot resolutely be said that all three points above apply as the reason behind this. Understanding what else the cause may be is decidedly challenging, but one can make some assumptions based on pegmatitic textures along with geochemical data. Extreme pyroxene growth requires silicon, which is present in considerable amounts by SiO_2 46-52 wt.% in all samples (Appendix B). It is suggested that the large ortho- and clinopyroxene grains formed by annealing of many small, euhedral, primary grains, seen typically as surrounding mass in all samples. There is a consistent coarse-fine grained relationship between the pyroxenes. All the fine-grained pyroxenes appear with triple junctions, indicative of recrystallisation from equigranular mosaics with 120˚ interfacial angles. The general trend of the fine-grained pyroxenes is that they do *not* contain interstitial diopside and/or enstatite and/or olivine. This is opposed to the coarse-grained pyroxenes which is mostly found with this intergrowth of diopside and/or enstatite and/or olivine ± trace minerals. Additionally, most samples appear with a very fine-grained matrix generally consisting of an equal parts olivine/pyroxene mixture. In all, one has three distinct grain size differences in the pegmatites.

Orthopyroxene is the dominating pyroxene mineral in all pegmatite samples. Orthopyroxene grains contain inclusions of diopside and olivine (mostly fayalite), from which may have grown from superheated liquid and primary orthopyroxene (enstatite) grains. This superheated liquid would have come from one of the recharge events. Clinopyroxene grains often appear with intergrowth of skeletal/needle-like ilmenite and/or rutile. This can resemble the typical intergrowth of skeletal quartz and feldspar, found only in granitic pegmatites. Such textures are due to undercooled melts, that is, rapid crystallisation of quartz (compared to silica diffusion rate), such that quartz crystals are "unfinished" or skeletal (Evans, 1993). The skeletal/needle-like ilmenite and rutile often appear with a sense of 'flow direction', however, the striking resemblance to skeletal quartz and feldspar growth may be used in supporting evidenced for rapid

crystallisation of ilmenite and rutile within clino- and orthopyroxene (Figure 5.1). However, another route to make this texture is by subsolidus exsolution of ilmenite and rutile during cooling of the pyroxenes, which may be more plausible for the scenario in the RUC.

Most olivine grains appear sub-rounded to sub-angular and does not vary as distinctively in size as seen with the pyroxene grains. They appear as very fine-grained dominant groundmass, bordering to coarse-grained pyroxenes (often seen as triple junction with pyroxenes) or as poikilitic textures within pyroxenes – essentially olivine comes in all shapes and forms in relation to the pyroxenes. Olivine can be seen with distinct growth shapes, sharp borders to pyroxenes, but also intermixing across borders with pyroxenes. The variation in grain size and textures indicates a chaotic magmatic system with several stages of crystal growth affected by variable P/T conditions.

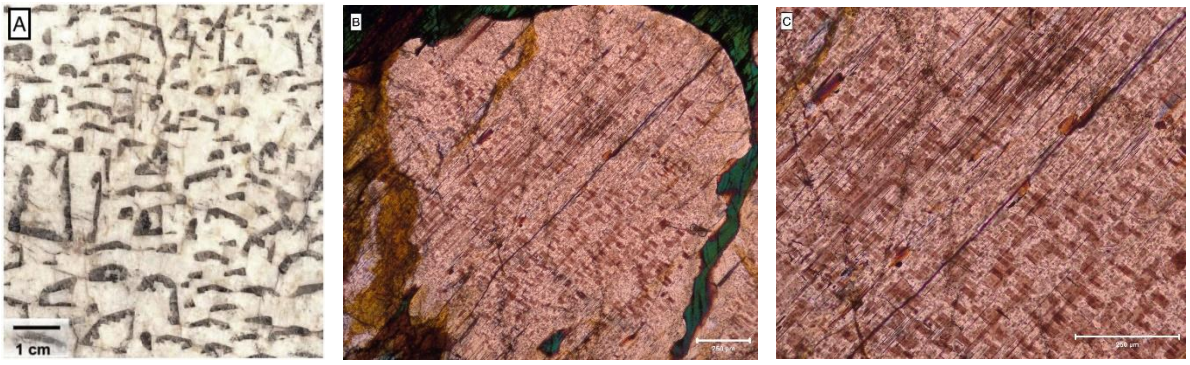

Figure 5.1: *(A): skeletal quartz in granite pegmatite (London & Kontak, 2012), which is a unique pegmatitic texture. Somewhat similar textures can be seen with ilmenite/rutile within both Cpx and (some) Opx in many of the pyroxenite pegmatite samples (B and C).*

Poikilitic textures

The poikilitic texture is characteristic in a range of different grains in, for instance, the CS and ULS (Nicolaisen, 2016; Larsen et al., 2018; Orvik, 2018). This texture is also seen in abundance in all pyroxenite pegmatite samples (i.e. Figure 4.36; Figure 4.38). Poikilitic textures are useful in unravelling order of crystallisation (Figure 5.2). Usually a mineral enclosed in another grain must have crystallised first, however, this is not always the case. This texture could also be a result of different nucleation and growth rates where crystals (i.e. pyroxene) nucleate and grow large (low nucleation rate), whereas other minerals (i.e. olivine) have a higher nucleation rate (meaning smaller grain growth and consequently size) and essentially becomes entrapped within the pyroxene grain (McBirney & Noyes, 1979). Most poikilitic textures show randomly oriented crystals, and this is also the case for the pyroxenite pegmatite samples. No particular trend in grain orientation is found within the samples. It is therefore difficult to correlate a precise crystallisation sequence, adding the fact of variable grain size with the overall poikilitic textures. Based on EPMA results, where several profiles crossed grains with inclusions of other mineral(s), there are usually sharp increase/decrease in elements (depending on mineral), indicating sharp contacts thus separate growth stages. However, whether they grew simultaneously or at different times, cannot be concluded from this.

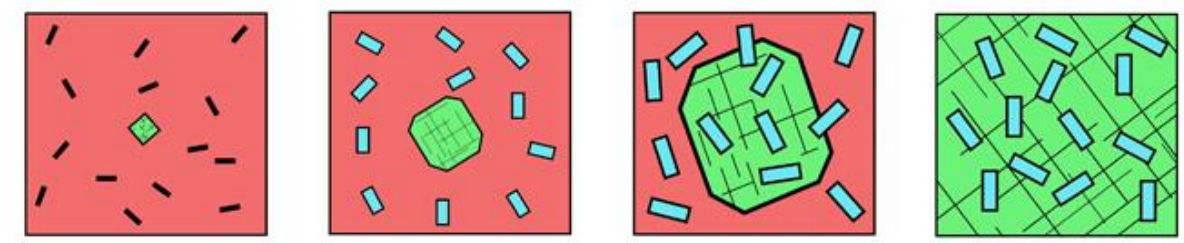

Figure 5.2: *Poikilitic texture development by simulatenous growth at different nucleation rates. This classic example involves pyroxene (green) and Plag (blue), from Vale (2020).*

Pyroxene lamellae, nucleation rates and growth

A distinct feature in many of the coarse-grained pyroxenes are the demixing lamellae. This texture is seen less distinctively in the finer-grained pyroxenes. Exsolution lamellae in igneous pyroxenes are quite common as they only occur in minerals where the composition varies between two or more pure endmembers (Deer, Howie & Zussman, 2013). The result of this texture is due to exsolution of an isolated pyroxene phase from a host grain due to sub-solidus re-equilibration, occurring through solid state of the mineral, during slow cooling (Deer, Howie & Zussman, 2013). The lamellae increase in size during this slow cooling process, as the host crystal (and lamellae) changes as an effect of T. Lamellae width will essentially depend on cooling rate and original crystal composition (Deer, Howie & Zussman, 2013). Some grains show exsolutions in only one half of the grain (Figure 4.13), whereas other grains show exsolution as perpendicular, repetitive units (Figure 5.3). Usually, exsolution lamellae appear planar and are crystallographically controlled in orientation. The miscibility of Ca-poor orthopyroxene and Ca-rich clinopyroxene reduces with decreasing T, where each may exsolve the other (Deer, Howie & Zussman, 2013). Two sets of lamellae may also develop, one within 20˚ of (001) and the other within 20˚(100), and this can also be seen, with no particular preference, in most samples.

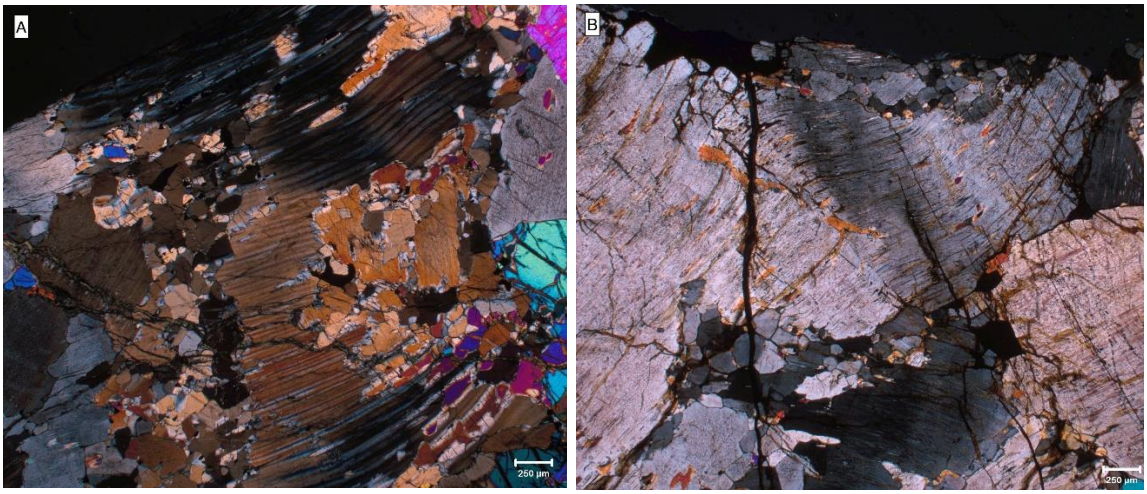

Figure 5.3: *Variation in lamellae appearance. From sample AM19-006-XB (A) and AM19-008-4 (B).*

Chromite content in the pegmatites and what it tells us

There is a need to discuss the Cr content in the pegmatites as they average with higher concentrations in the pegmatites compared to wehrlite (Table 8.2). Firstly, chromite appears with no resemblance as to what Cawthorn & Boerst (2006) describe in their pyroxenite pegmatite, namely a thin chromite layer running through the middle of a number of large orthopyroxene grains (Figure 5.4). Rather, chromite grains appear amongst surrounding groundmass, bordering both ortho- and clinopyroxene grains. In the pyroxenite pegmatite described by Cawthorn & Boerst (2006) it is suggested that these are post-cumulus textural growths (hence not part of the igneous primocryst assemblage). In the RUC, chromite appears with increasing abundance from wehrlite to pyroxenite pegmatite, and being texturally different to Merensky pegmatite, perhaps they were introduced with a wehrlite forming melt and re-introduced with recharge event(s) by hotter pyroxenite pegmatite-forming melts or perhaps they are associated with the PGE formation. This claim builds on the Irvine Model.

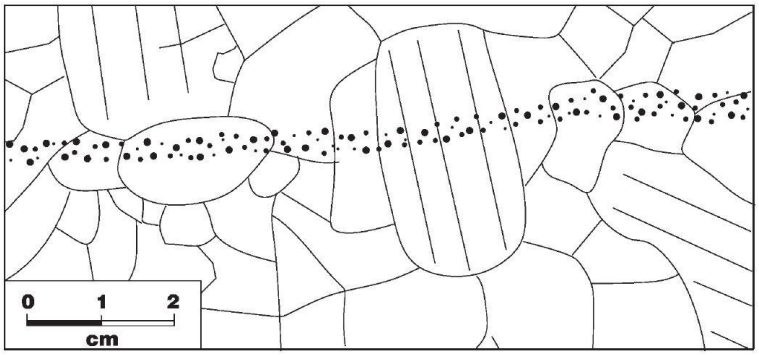

Figure 5.4: *Chr layer coating large Opx grains (Cawthorn & Boerst, 2006).*

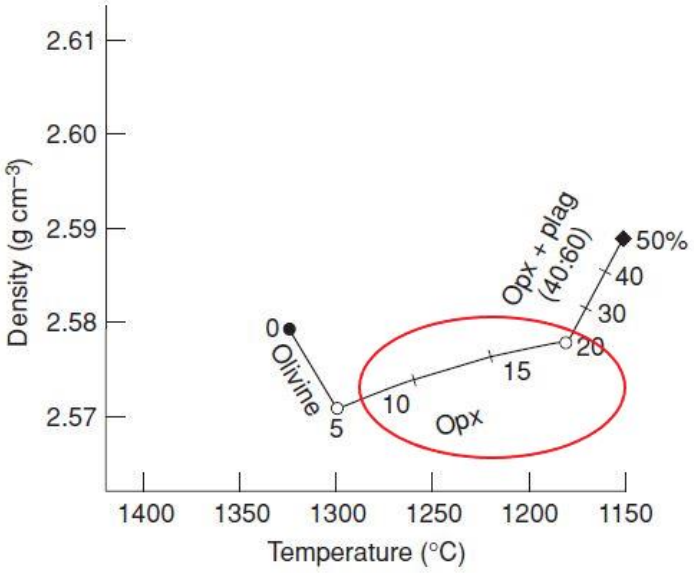

Figure 5.5: *Possible T and density range scenario (circled red) for the primary pyroxenite pegmatite formation, based largely on whole-rock composition and geochemical signatures. With a significant lack of Plag in the pegmatite samples, melt temperatures must have been from approximately 1200 ℃ and up. A stronger case for this would be to obtain thermobarometry calculations, this has not been conducted in this research.*

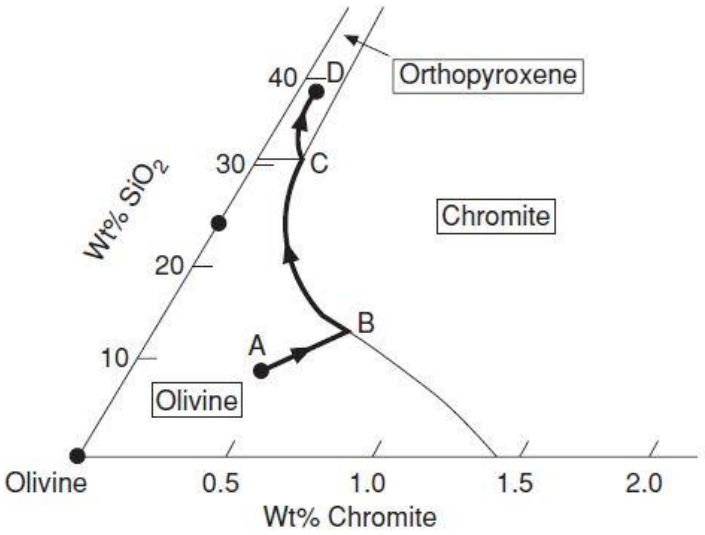

Figure 5.6: *Chr would start to crystallise at point B (together with Ol), with magma evolving cotectically towards point C. At this point SiO_2 content in magma is at a level where Ol and Chr can no longer be the stable liquidus assemblage, and Opx crystallise. As described in text, based on the amount of Chr in the pyroxenite pegmatite, perhaps Chr has come in several stages (recharge events). That is, first along with Ol (when wehrlite was emplaced) and later between point B and D, where a larger amount of Chr formed, along with Opx. Based on the lack of Plag in the samples it is suggested that crystallisation stopped sometime before reaching temperature and density requirements leading to Plag crystallisation.*

The Irvine model very neatly explains typical characteristics of chromitite layers, however, as always with nature, it does not necessarily mean it is as straight forward as such. Several other mechanisms might be in play, pertaining to the accumulation of monomineralic layers, two of the most likely (experimentally confirmed) being oxygen fugacity changes and total pressure of crystallising magma (Robb, 2005).

The following theories behind pegmatites being coarse-grained was introduced at the start of this section:

1. Volatile-related depression of magmatic solidus (water and 'fluxing agents' (Li, B, P, F) increase water solubility in melt).

2. Rapid diffusion of elements to sites of crystallisation (due to high water content).

3. Undercooling of magma below solidus temperature causing nucleation suppression, leading to the growth of larger crystals instead of new crystals.

The discussion thus far has supporting evidence for point three in considering the scenario in the RUC. To a certain extent one can support a rapid diffusion to sites of crystallisation claim. However, how significant the water content has played a role for this specific pegmatite, in ultramafic setting, is uncertain.

Zonation

Zonation is a common feature in pegmatites. However, no well-developed zoning has been observed from petrological studies nor from specific zonation investigation by EPMA. With close inspection of the samples chosen for EPMA analysis, one can find vague examples of zonation, typically seen with an increase of MgO and FeO coupled with decrease of CaO along borders. However, of more interest, is what happens within the core of a grain. A typical example is a grain being enriched in Mg in its core, meaning the melt was more primitive than the Fe-rich margins. Most samples, having interstitial olivine and/or clinopyroxene growth, are disturbed in the analysis of zonation (shown by drastic positive and negative peaks). Based on this it can be concluded that the vast majority of pyroxene grains are not zoned whatsoever. With this lack of zonation evidence, it cannot be said that zonation is an imperative part of the pegmatitic genesis, in any such way. This is also comparable to what Cawthorn & Boerst (2006) describes in the genesis of the pyroxenite pegmatite in the Merensky Reef. As such, perhaps little, if any, zonation is one of the distinct signatures of pyroxenite pegmatites in mafic to ultramafic settings?

Tentatively suggested crystallisation sequence

To initialise a suggestive crystallisation sequence, based on descriptions and interpretations thus far, a proposed genetic evolution is as follows:

1. Initial wehrlite-, and dunite-forming melts (ULS and CS), based on high MgO → olivine content.
2. Very fine-grained groundmass of various pyroxenite-olivine plus trace elements emplacement, possibly syn-magmatic as a part of initial wehrlite emplacement. Either 2nd or 3rd stage melt injection based on Grant et al. (2016b).
3. Recharge event(s) consisting largely of coarse-grained pyroxene enters the system, mixing with olivine and pre-existing pyroxenes, causing interstitial growth. Likely simultaneous or very close to simultaneous growth based on poikilitic and lamellae textures.
4. Re-crystallisation of fine-grained pyroxene, likely from another recharge event.
5. Possibly a late injection of Mg-rich picritic melt, mixing olivine and pyroxene grains.

Pyroxenite pegmatite elsewhere in RUC

Although a few very prominent pyroxenite pegmatites was studied in detail, a day was spent covering a larger area to observe any trend in emplacement. A trend was certainly found at the wehrlite – gabbronorite contacts, where the pegmatites appeared in a consistent (aerial view) 'finger' shape (Figure 5.7). That is, appearing as intrusions in gabbronorite and cut off by wehrlite, very simplistically explained as looking like fingers in-field. Within the gabbronorite, the pegmatites may appear as spherical 'plug' like shapes. This is only based on field observations and requires far more detailed study to be confirmed. This was only briefly seen in-field, by the fact that the pegmatites appeared to have penetrated gabbronorite with a blub-like surface shape. Additionally, nearly all contacts are vertical in the surrounding area, such that the pegmatites, containing minerals of high specific gravity, may also be shaped as vertical 'plugs' or 'pipes'. In combination with other models from RUC (Larsen et al., 2018) and geometry

observed in-field (with field sketches) it is perhaps possible that the pegmatites generally form 'plugs' in the eastern corner.

These pyroxenite pegmatites differ in that they are likely a result of two melts of different composition mixing (a basaltic melt formed the gabbronorite, perhaps a more picritic melt entered the system, forming pyroxenite pegmatite, and these two melts mixed). These types of pegmatites seem to only appear along this border in a S-SW direction. Perhaps they represent a different generation of pyroxenite pegmatites, based on the open conduit system in RUC. Considering the two different pegmatites identified in the Merensky Reef, it is certainly not unlikely to have several generations of pegmatites also in the RUC. However, this is merely speculation for now. Far more detailed research is required to solidify or falsify any such claims. A start would be to investigate relative chronology in addition to describing these pegmatites in detail. Additionally, it would be interesting to see if these pyroxenite pegmatites have any relation to the pyroxenite pegmatites in the ULS and CS.

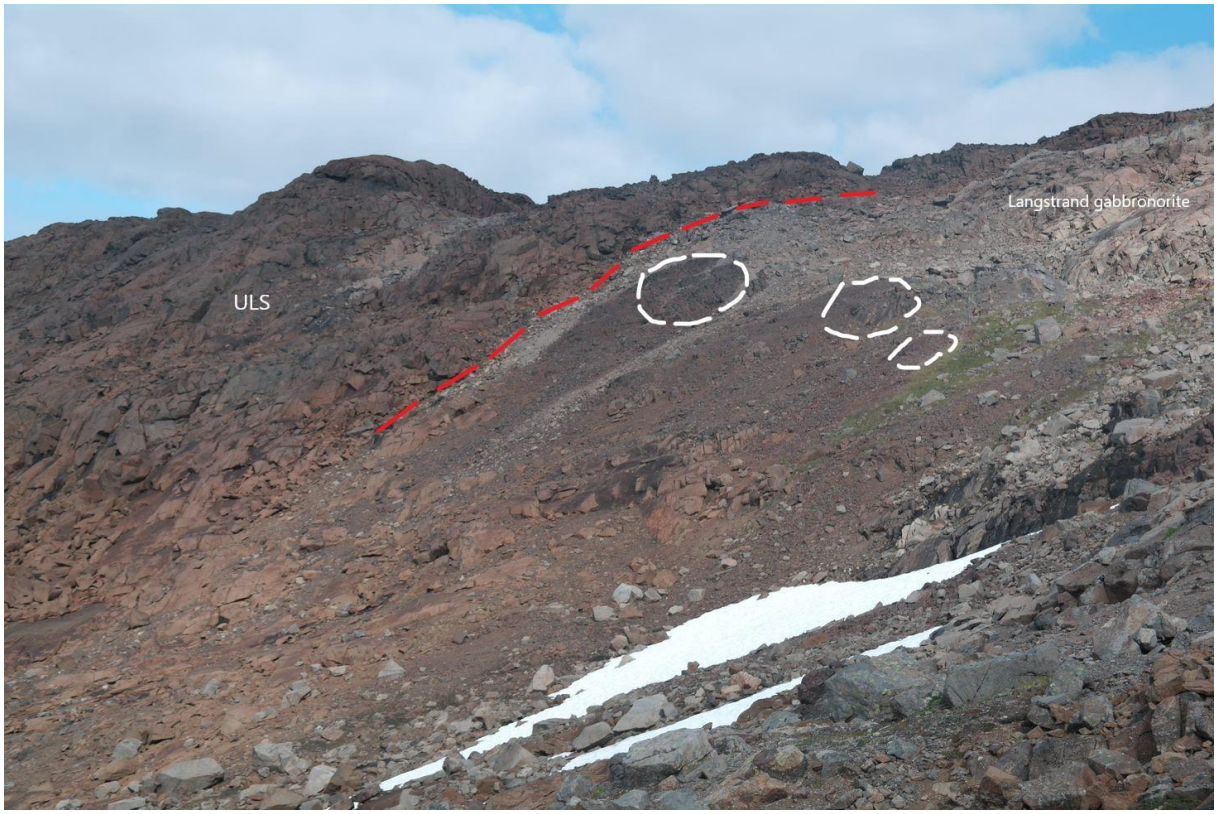

Figure 5.7: *Outlining surface-view of proposed 'plug' shape of pegmatites in the eastern corner of gabbronorite/marginal zone/wehrlite contact. Important to note is that this possible shape may not be the case in the study area, where the pegmatites appear as fountain structures and cannot be seen in any systematic order. Of interest is the gabbroic shoulder S-SE of field area, where pegmatites appeared somewhat similar to how they appear in this photo. Any suggested systematic order described here, with pegmatite in relation to gabbronorite, need careful follow-up and is possibly a research in itself as it covers a sizeable area in RUC. Although not seen clearly on a large scale here, the pegmatite appearance in-field was more or less consistent from this position along the contact, following a S-SE direction (where 1-day mapping was executed). The sporadic appearance of pegmatites along marginal zone-gabbronorite contact was seen as described above on a large-scale, whereas flaming structures could be seen on a smaller scale.*

Field observation of the variable pyroxenite pegmatite appearances may be used in attempting to understand how it behaves in-field in relation to surrounding cumulates. With the high specific gravity of pyroxenes, the pyroxenite-forming melt composition is 'heavy' compared to the previously emplaced 'mush' of gabbro-norite forming melt. As such, it is useful to discuss the formation of pyroxenite pegmatites.

5.1.3 Formation of the pyroxenite pegmatite

Grant et al. (2016b) states that there is a clear sequential story to tell from the Reinfjord intrusion, with a history from increasingly olivine-rich cumulates with time from gabbro to olivine-clinopyroxenites (the Lowered Layered Series) to wehrlites to dunites. A classic perception for (any compositional) pegmatite is that they enter a system very late, if not last, during crystallisation and emplacement. With this in mind, it is necessary to put a certain constraint on what makes sense in Reinfjord and attempt to explain the following questions;

- When did the pyroxenite pegmatites form considering the sequence proposed by Grant et al. (2016b)?
- Did all pegmatites form more or less simultaneously, or over a long period of time, considering varying grain sizes and shapes?
- Were there periods of hiatus, as described in the Merensky Reef by Cawthorn & Boerst (2006)?
- Which mechanisms played a pivotal part in the formation?
- What role did REE and volatiles play, considering the importance in classic granitic pegmatite formation?

It is nearly impossible to answer these questions confidently, however, a prudish approach may be suggested in order to explain the genesis of the pyroxenite pegmatites in RUC.

The pegmatitic textures, nor the pegmatite formation, in the RUC have not been described in detail previously and as such, the author has to lean heavily on own observations and attempt to find similarities/differences with the textures described by Cawthorn & Boerst (2006) as this is one of very few pyroxenite pegmatites displaying similar characteristics. Additionally, Nicolaisen (2016) describes PGE in relation with pyroxenite pegmatite, although only two samples were analysed. Accordingly, models are scarce, and it may therefore be more useful to implement models from Merensky, combined with what is known about RUC, in discussing the hypothesis for the formation of pyroxenite pegmatites in RUC. Additionally, previously described parental melt compositions (Grant et al., 2016b; Larsen et al., 2018), will be used in trying to understand the many processes involved in forming the pyroxenite pegmatites. There is not, at the time of writing, any universally accepted model for the formation of ultramafic pegmatites.

Intraplutonic quenching

The large crystal sizes of the pegmatites are not consistent with intraplutonic quenching. The mechanisms for the highly variable pegmatitic textures, and grain sizes, could not have been produced by rapid cooling. In a scenario of intraplutonic quenching, rocks with high proportions of trapped liquid would have been produced (Cawthorn & Boerst, 2006), and this is not supportive of the scenario in RUC where no trapped liquid seems to be present.

Syn-magmatic processes

The textural maturity may be a result of a range of processes which are collectively known as 'crystal ageing' (Hunter, 1996; Boorman et al., 2004), close to a crystal-liquid interface. During the course of several recharge events and crystal growth, there may have been a hiatus with no more crystal accumulation (where a number of processes may have caused a crystal growth suspension), possibly explaining the varying grain size in the pyroxenes. This scenario, however, is better envisioned by several magma recharges of different P/T conditions and time lapses, leading to distinctively different crystal growth opportunities. There may have been several instances of annealing of many small orthopyroxene grains, growing into a single, large grain. Hence, syn-magmatic processes are believed to have played a part in the genesis.

Continuous recharge events and fountaining

There is no doubt that significant volumes of magma have been in place to produce a pressurised magma chamber to release large volumes of magma vertically (i.e. in shape of proposed pegmatite plugs/pipes). How many recharge events have occurred is speculative, in fact almost impossible, to establish and it cannot be said how prolonged these events were. However, based on the similarity in pegmatitic textures (variable grain size and contacts) and geochemistry, it can be loosely proposed that a few (perhaps up 3-5, if not more) recharge events have taken place, each event altering the pegmatite to the way we see it today. There would also have been significant differences in time lapses with each recharge event in considering highly variable grain sizes.

In producing the fountain structures that are seen in the RUC (Figure 4.3), the new magma must have had a density greater that the liquid residue in the chamber (Robb, 2005), mixing new and evolved liquids to a limited layer along the base of the chamber, in a low R-factor scenario. This is plausible considering the physical and chemical nature of pyroxenes, with its high specific gravity and addition to lower sulfide content that the Merensky Reef. The scenario for the Merensky Reef, however, is more that of pluming, with high R-factor. Whether a pegmatitic and wehrlite forming melt entered simultaneously or not requires more evidence (and calculations), however, based on the olivine content, it can be thought that at one point there was a mixed melt, and later the melts have formed pure pyroxenite, and possibly concluded with a olivine enriched (wehrlite-forming) melt.

Based on these models, keeping the geological setting of RUC in mind, this leads to an updated scenario from the proposed crystallisation sequence presented in section 5.1.2 for RUC:

1. Initial injection of picritic melt.
2. New magmatic injection with pyroxenite-forming melt, mixing with pre-existing melt.
3. Recharge event with a hotter pyroxenite-forming melt, still with considerable SiO_2 content, with relatively rapid crystal growth, later recrystallised (shown with triple junction).
4. Additional recharge event, richer in chromite and orthopyroxene, with large orthopyroxene grains consisting of interstitial olivine and clinopyroxene growth. Each new recharge event is considered to have variable density and temperature conditions, producing crystal fractionation.

5. One or more recharge events with pure pyroxene grains, still considerably large in grain size.
6. Possibly a new Mg-rich picritic melt injection intermixing with pre-existing pyroxenite-forming melts.

5.1.4 Sulfide oversaturation

One of the objectives in this thesis was to investigate whether the pyroxenite pegmatites have facilitated oversaturation with sulfides. There have been many recordings of sulfides from field observations, commonly 1-2 mm in size, associated with the pegmatites. This can also clearly be seen in thin sections (i.e. Figure 8.8), where sulfides usually surround coarse-grained pyroxenes (mostly orthopyroxene), with up to 5% of whole-rock composition at most. It has been suggested that the recharging magma has entered the system under significant pressure and in such scenario the mafic magma will show exponentially decreasing ability to dissolve sulfur (Mavrogenes & O'Neill, 1999). However, the magma entering the system here comes from even higher pressure (Orvik, 2019), making this scenario unlikely.

With a recharge magma rich in both SiO_2 and S, the S will likely reach oversaturation and form S droplets, whereas the mixed magma may be pushed into the Chr crystallisation field (Irvine, 1965). With this, S will crystallise from the magma, and form the various sulfides we see in the pegmatites.

With a drastic pressure release with ascending melt, sulfide solubility will increase (Naldrett, 2004) and to reach strong sulfide oversaturation two options may apply (Figure 5.8):

1. Total sulfur amount increases through assimilation of S-rich lithologies or recharge by S-rich melt (the latter possibly being the instance with pyroxenite-forming melt).
2. Partial magma crystallisation with residual magma becoming S-oversaturated.

It is suggested that an immiscible sulfide liquid precipitated together with the pyroxenite forming recharge event(s) and percolated in pyroxene crystal mush. Some silicate liquid would have been displaced, producing high concentrations of incompatible elements. Which event that directly leads to sulfide oversaturation is uncertain. In furthering the understanding of the sulfides' role in the pegmatites it would be useful with $\delta^{34}S$ measurements, suggested for future research.

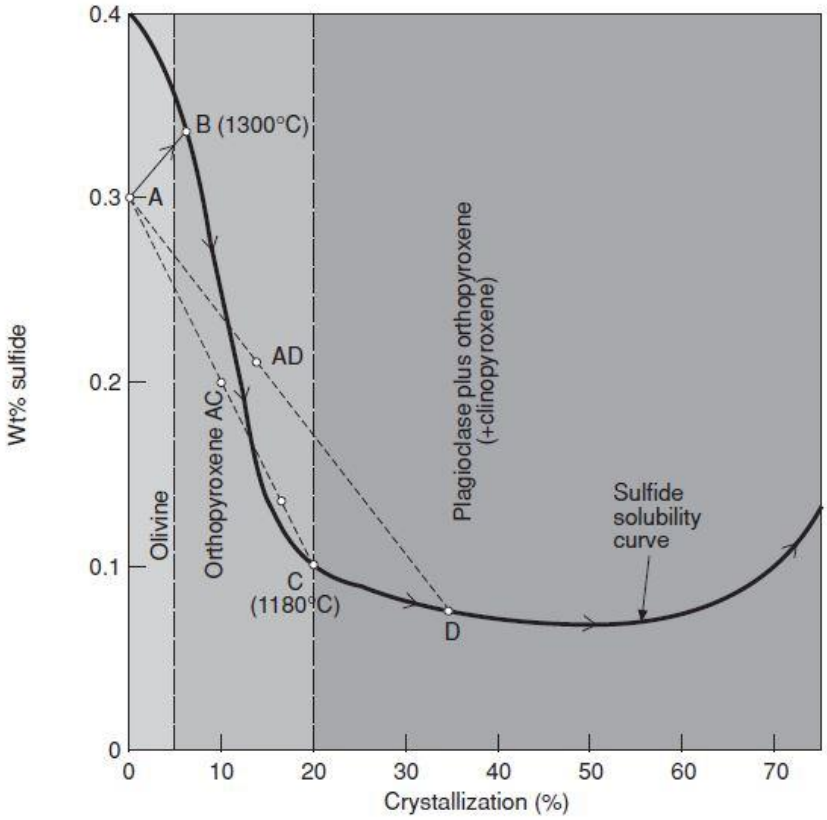

Figure 5.8: *Sulfide solubility variation as a function of progressive crystallisation in a mafic magma as exemplified in the Bushveld Complex (Naldrett & Von Grünewaldt, 1989).*

5.1.5 Comparison to drillhole RF-1

In furthering the understanding of what may lead to sulfide oversaturation, it is useful to investigate core logs from previous drilling campaigns conducted in the RUC. Additionally, this investigation is useful for a general comparison of pyroxenite pegmatite at surface and below ground. By investigating Drillhole 1 to 4, it becomes clear that Drillhole RF-1 convey limited, yet valuable, information of depth (m) sequences 107.75 – 109.50 and 110.20 – 110.65, identified as pyroxenite pegmatite interlayered between Fe-rich dunite layers. A notable difference is the PGE (Au, Pd and Pt) content, being far more enriched in RF-1 than all samples from this study (Table 8.31). Additionally, trace elements such as Ba, Ce, Ga, La, Nb, Sr and V differ markedly, being far more enriched in the samples from this study compared to RF-1. This difference is remarkable in that:

- The drill sequences of pyroxenite pegmatite composition is 0.5 m – 2 m, of such a size that it is comparable to the size of the pyroxenite pegmatite exposed some places in ULS, CS, as well as the pyroxenite pegmatite 'plugs' observed in relation to the gabbronorite. Essentially, most of the pyroxenite pegmatite bodies observed at the surface are roughly in this size range*. And;*
- RF-1 is interlayered with Fe-dunite, not necessarily always the case with the pyroxenite pegmatites in this study, however RF-1 is in close proximity stratigraphically to the majority of the samples in this study and, as such, have surrounding rock of both wehrlitic and dunitic compositions.

The question is why RF-1 is far more enriched in Au, Pt and Pd? Perhaps the 2 m zone in RF-1 have been coincidentally PGE-enriched from another ultramafic melt not associated with pegmatite formation, or perhaps affected by a post-dunite-forming melt enriched with PGE. Similarity can also be seen from thin section images, where sulfides appear with similar grain relationships to the samples in this study (Figure 5.9), that is, any one single sulfide grain typically consisting of the combination Ccp, Pn and Po. It can merely be proposed that there is a rather impetuous relationship between the PGE mineralisation and the pyroxenite pegmatites, perhaps in a similar manner to that described by Cawthorn & Boerst (2006) and Robb (2005), where periodic magma injections of a less differentiated magma interrupts crystallisation, often in a sporadical sense. However, this comparison is naturally very ambiguous and inadequate and as such the author chooses not to delve deeper into understanding this difference as it may very well be a completely random factor at play here. Several more sequences of similar nature would have to be provided to show that any potential trend, nevertheless, the data here is a starting point for investigating this further in the future.

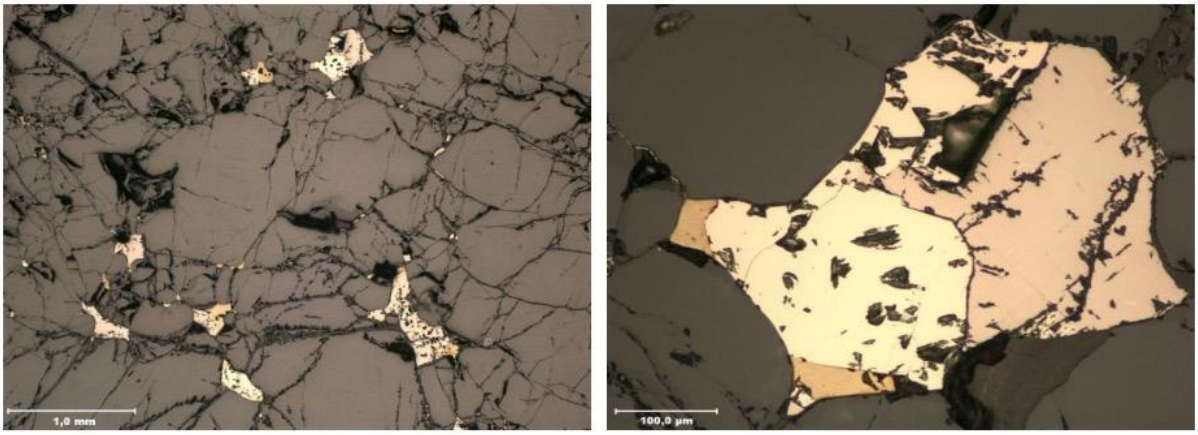

Figure 5.9: *Image from Schanche et al. (2012). Ccp (dark brown-yellow), Pn (bright yellow) and Po (cream-ish brown) from drillhole RF-1, very similar sulfide-relationships can be seen in Figure 4.17; Figure 4.20 and Figure 4.22.*

5.2 Parental melt composition and mantle source

Ultramafic parental melt composition and origin is heavily debated and controversial at this time. Few models proposed for the RUC are plausible with supporting evidence based on results from this thesis. The rocks in the RUC do not represent the parental melt composition, with cumulates likely to have formed from a combination of fractional crystallisation, melt-rock reactions and melts contaminated by partial melting mantle with residual garnet and Cpx (Grant et al., 2016b). Consequently, a qualitatively, rather than quantitatively, assessment of processes involved in the pyroxenite pegmatite formation, will be discussed.

Griffin et al. (2013) proposed a model, based on Nordre Brumandsfjord setting (Fig. 1.1), where it is suggested that the parental melts were derived from an extremely hot mantle plume with temperatures up to 1650˚C from the core-mantle boundary. These melts are suggested to contain as much as 40 wt.% MgO (Griffin et al., 2013). Under such heat the host gabbro experienced complete melting during formation of 'hybrid rock' with composition varying from pyroxenitic to dunitic. There is also field evidence for such 'hybrid rocks' in RUC and, essentially, gabbro assimilation may very well be an important magmatic process in RUC. Another idea originally presented by Bennett et al.

(1986) and later elaborated by Larsen et al. (2018) suggests a picritic to komatiitic parental melt composition with high volatile contents, temperatures of 1400 – 1450˚C and 16-25 wt.% MgO, 642 ppm Ni and 1596 ppm Cr. Both the MgO content and Cr are very comparable to the pyroxenite pegmatite samples.

In furthering the pyroxenite pegmatite characterisation it is important to have a certain idea about the possible roles played by volatile-rich minerals, in building on ideas of how the melt behaviour has been. Small amounts of carbonates such as amphibole and biotite are useful indicators. No biotite has been recorded in any of the pegmatites here, as such there is only small amounts of amphibole to work with. With the presence of amphibole in relation to the fine-grained pyroxenes it is believed that when melt enters a system under high pressure, it enters with an abundance of volatile-rich components. This is primarily based on descriptions made by Grant et al. (2016b) and Larsen et al. (2018). However, the author argues that perhaps there was not an abundance of volatile-rich components entering the system with the pyroxenites, also suggesting a different melt composition. Rather, it is suggested that these pyroxenites were poor in volatiles based on lack of carbonates in all samples. Additionally, Nicolaisen (2016) recorded a lack of interstitial carbonates in his pyroxenite pegmatites, comparing them to dunites where they appear frequently.

In classifying the pyroxenes (Figure 4.41), supporting evidence of conceptual parental melt composition compared to previous recordings can be developed. Figure 5.10 shows a comparison with Orvik (2019), displaying a clear difference in that pyroxenes here are more evolved. This imply that:

1. Melts that formed the pyroxenes was more evolved than melts from pyroxenes plotted by Orvik (2019), meaning there was a higher SiO_2 and Fe content, combined with less Mg content.

   or;

2. Pyroxenite-forming melts mixed with interstitial melts in ULS/CS which was very evolved.

Essentially, this suggest that the pyroxenite-forming melts was more evolved than the pre-existing melts that formed ULS and CS.

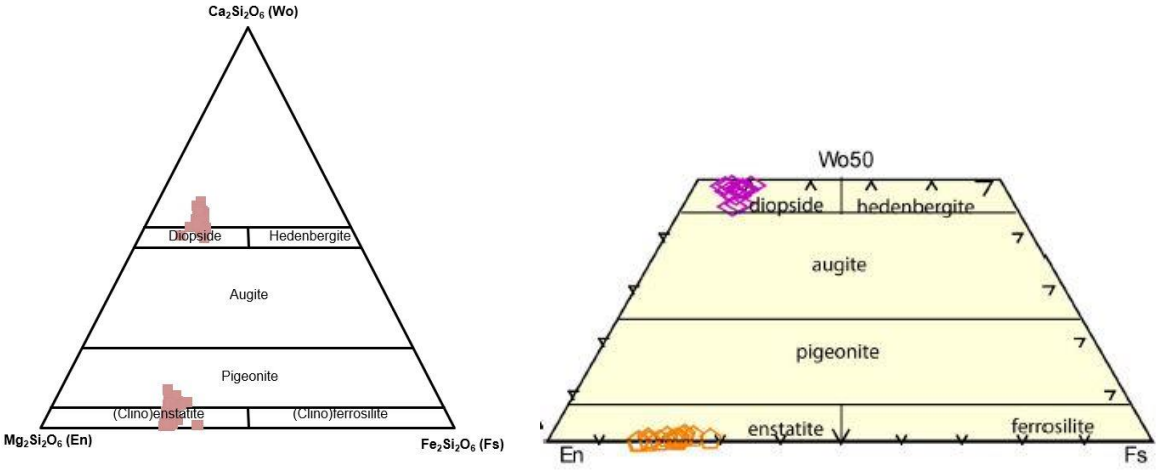

Figure 5.10: *Comparison of pyroxene classification results from pyroxenite pegmatite samples. Plot (left) of 145 data points from EPMA analysis, whereas plot (right) is from Orvik (2019).*

5.2.1 Crystallisation sequence

With lacking plagioclase and amphibole content in the pyroxenite pegmatite, it poses a different view on the sequence of crystallisation from that described by Grant et al. (2016b). One the other hand, as described previously, there are small amounts of amphibole present, evident from XRD and EPMA as well as very fine-grained amphiboles observed by petrography. Hence, the overall trend in the ULS may be used in support when considering the sequence of crystallisation. The dominating cumulates in ULS are olivine (dunite), interstitial clinopyroxene (wehrlite) and the combination of the two (olivine-clinopyroxenite), essentially becoming more olivine enriched and showing lesser degrees of fractional crystallisation. This is consistent with the crystallisation sequence outlined by Presnall et al. (1978), recited by Grant et al. (2016b), in that olivine crystallise followed by olivine + clinopyroxene, concluded by cotectic precipitation of olivine + clinopyroxene. Notably, plagioclase is absent from the crystallisation sequence, only occurring in marginal zones, and it is further stated that field and petrographic evidence shows clinopyroxene crystallising prior to plagioclase (Grant et al., 2016b). This is indeed consistent with evidence in this thesis. The trend in geochemical data (Figure 4.30) is very similar to that of Grant et al. (2016b) Figure 6. This data indicates a primitive mantle, likely with variable olivine and clinopyroxene content.

Investigating the V/Cr ratio is useful in understanding fractionation processes and magma evolvement. Figure 4.31 shows a near linear trend for all pyroxenite pegmatite samples. Following the Irvine model (1967) it goes that chromite will crystallise along with olivine, followed by pyroxenes, and as such this graph shows a typical crystallisation sequence for RUC. This is also evident in Figure 4.34, where nearly all plots show a linear trend, indicative of magmatic evolvement.

Pyroxenite pegmatites are proven here, as well as by Nicolaisen (2016) and Schanche et al. (2012), to host PGE's. Though not in great abundance (likely due to absence of carbonates), compared to i.e. drillhole RF-1, the amount is still considerable in exploitable terms. An interesting observation, first pointed out by Nicolaisen (2016), is the orthopyroxene difference in dunite and pegmatites. This was also investigated here, though with only one dunite sample, it cannot scientifically solidify the comparison with Nicolaisen (2016). Here, it is recorded far more Al_2O_3 in the pyroxenites (2.62 – 4.54 wt.%, averaging 3.8 wt.%), more or less matching that of Nicolaisen (2016), whereas

the dunite contains 0.32 wt.% Al_2O_3. The contact between both coarse-, and fine-grained orthopyroxenes and what can be described as olivine-rich (dunitic/wehrlitic/lherzolitic) zones seen in some samples (i.e. Figure 8.1; Figure 8.2; Figure 8.6) may be described as quenched zones. This suggests a hotter pegmatite pyroxenite-forming melt that entered later, coming in contact with a cooler dunite-forming melt. Based on this, it is suggested that the pyroxenite pegmatite entered the system in several pulses, *at different stages*, both before and after dunite-forming and wehrlite-forming melts. Essentially, it is suggested that the pyroxenite pegmatite-forming melt entered the system pre-, and post-dunite-, and wehrlite-forming melt emplacements. There is also evidence for mixing with wehrlite-forming melts, that is syn-magmatic, activity. However, the pyroxenite-forming melt is argued to have been more evolved than melts forming ULS and CS based on Fe (higher) and Mg (lower) content in all samples and pyroxene classification.

In combining all scenarios and descriptions above, it is suggested that superheated magma leads to one of many recharge events. This, combined with release in pressure in the magma chamber, caused pyroxene crystal mush to become supersaturated. With a stasis in crystallisation, crystal ageing occurred at the interface, and produced the pegmatitic textures. Some diffusion would also have occurred.

5.2.2 Open system behaviour

The Reinfjord Ultramafic Complex cumulates evolved from mafic plagioclase-clinopyroxene-olivine to clinopyroxene-dominated to olivine-dominated through time, from contact to centre (Larsen et al., 2018). Such a sequence is a good indicator evolved in a refractory sense, becoming increasingly MgO-enriched, hence termed 'regressive fractionation sequence' (Larsen et al., 2018). This sequence, described by (Grant et al., 2016b), developed as a result of repetitive recharge events with gradually more primitive magma, in an open magma chamber system. This state of affairs is also evident and supportive with the high MgO and Cr content in nearly all samples in this study.

5.3 Pyroxenite pegmatite role in Ni-Cu-PGE ore forming processes

The last topic to discuss is whether the pyroxenite pegmatite forming melts played an important role in the formation of the widespread Ni-Cu-PGE reef mineralisation in RUC. There is no prominent evidence in this study to propose a significant role from the pyroxenite pegmatites in Ni-Cu ore forming processes. However, the pyroxenite pegmatites in the RUC are sporadically emplaced where large PGE reefs are present, suggesting a rather unpremeditated relationship. With notable amounts of Pt and Pd present in nearly all samples, there is likely a genetic link present between PGE and pyroxenite pegmatite. The pegmatitic texture and orthopyroxene-sulfide relationship may indicate a mixed sulfur/silicate-rich melt (from recharge) that may lead to enrichment of PGE-rich horizons. Based on this and Larsen et al. (2018) model (Figure 1.3), it is suggested that the pyroxenite pegmatite played an inconsistent role in PGE formation. Essentially, it is proposed that the pyroxenite pegmatite played a part in some of the PGE formation but was not the primary source of this. Rather, it is suggested that the dunitic and wehrlite-forming melts are the primary sources of this enrichment, likely along with enrichment in Ni and Cu. This is also supported by the proposed genesis where sulfide deposits in the Reinfjord conduit system involves liquid immiscibility of a sulfide liquid at or shortly after dunite forming melt emplacement (Larsen et al., 2018). The irregularity in sulfide enrichment (as also described with particular PGE's in relation

to pyroxenite pegmatite in section 5.1.5) implies several episodes of remobilisation in an open system, exposed to multiple recharge events (Larsen et al., 2018). All this makes it clear that Cu-Ni and PGE are not directly related, and it is suggested that pyroxenite pegmatite only played an irregular and minor part in PGE formation.

5.4 Conceptual emplacement model for pyroxenite pegmatite

Based on all descriptions and interpretations involved in forming the pyroxenite pegmatite we see today; a final conceptual emplacement model is proposed:

1. Initial picritic magma forming ULS and CS (high olivine content and small amounts of clinopyroxene), commences initial crystallising.
2. This event is combined or shortly followed by an injection with magma of different composition (pyroxenite-forming melts) entering the system (based on absence of carbonates, and far less amphibole and PGE content compared to wehrlite).
3. Initial pyroxenite-forming melt is possibly combined with carbonate-rich melt of lamproitic composition (rich in alkali and CO_2, based on findings by Larsen et al., 2018). These initial melts likely do not mix with pre-existing melts based.
4. Recharge of pyroxenite-forming melt, mixing with pre-existing (wehrlite-forming) melt and effectively affecting the system. Clinopyroxene and orthopyroxene are stable and create large crystals. Possibly ensued by increasing P/T conditions leading up to next event.
5. New recharge event with a hotter pyroxenite-forming melt, still with considerable SiO_2 content, with relatively rapid crystal growth (later recrystallised, shown with triple junction). Chromite, followed by orthopyroxene, crystallise. At this stage there may also be large orthopyroxene grains with interstitial olivine and clinopyroxene growth. Each new recharge event is considered to have variable density and temperature conditions, producing crystal fractionation.
6. Recrystallisation (annealing) of pre-existing pyroxene and olivine + trace elements.
7. The last melts were initially olivine saturated and reacted with ULS cumulates to form replacive dunite – completing the melt sequence.

It must be noted that there may not be as many recharge pulses as outlined above. This is merely a proposal based on the variable textures observed in the samples that must be a result of variable P/T conditions and effectively caused by different mechanisms – likely from different magmatic recharge events. There may also have been more magmatic recharge events. It is nearly impossible to accurately estimate how many recharge events have taken place, but one can make educated conjectures based on evidence presented here.

6

Conclusion

This contribution provides a detailed description of the pyroxenite pegmatites in the Reinfjord Ultramafic Complex. Comparison with similar intrusions worldwide, in particular the Merensky Reef, conclude that the pyroxenite pegmatite in the RUC share similarities, but also remarkable differences. Where plagioclase content plays a small role in the genesis of pyroxenite pegmatite in the Merensky Reef, it plays no role in the RUC. Additionally, chromitite textures are markedly different, appearing as seams across pyroxenite grains in the Merensky Reef, while appearing as surrounding or interstitial growth in relation to pyroxene grains in the RUC. Lastly, two pegmatites are identified in the Merensky Reef, whereas only one is identified in the RUC from this contribution.

Several magmatic recharge events have been at play in creating the pyroxenite pegmatite textures we see today. The characteristic poikilitic textures seen in pyroxenes are comparable to the textures described previously in wehrlites from the CS.

It is argued that there was not an abundance of volatile-rich components entering the system with the pyroxenites. Rather, it is suggested that these pyroxenites were poor in volatiles based on lack of carbonates in all samples. Additionally, a lack of amphibole, biotite and plagioclase suggest water content was low to absent during the formation.

It is suggested that an immiscible sulfide liquid precipitated together with the pyroxenite forming recharge event(s) and percolated in pyroxene crystal mush. Some silicate liquid would have been displaced, producing high concentrations of incompatible elements. Which event that directly leads to sulfide oversaturation is uncertain and requires further research.

Pyroxenes classification, compared with previous models, may suggest that the pyroxenite-forming melts was more evolved than the pre-existing melts that formed ULS and CS.

It is proposed that the pyroxenite pegmatite played a part in some of the PGE formation but was not the primary source of this. Rather, it is suggested that the dunitic and wehrlitic melts are the primary sources of this enrichment, likely along with enrichment in Ni and Cu. It is suggested that Cu-Ni and PGE are not directly related, and that pyroxenite pegmatite only played an irregular and minor part in PGE formation.

This contribution proposes that the following chain of events in the RUC led to the formation of the pyroxenite pegmatites we see today:

1. Initial picritic magma forming ULS and CS (high olivine content and small amounts of clinopyroxene), commences initial crystallising.
2. This event is combined or shortly followed by an injection with magma of different composition (pyroxenite-forming melts) entering the system.
3. Initial pyroxenite-forming melt is possibly combined with carbonate-rich melt of lamproitic composition (rich in alkali and CO_2). These initial melts likely do not mix with pre-existing melts based.
4. Recharge of pyroxenite-forming melt, mixing with pre-existing (wehrlite-forming) melt and thus affecting the system. Clinopyroxene and orthopyroxene are stable and create large crystals. Possibly ensued by increasing P/T conditions.
5. New recharge event with a hotter pyroxenite-forming melt, still with considerable SiO_2 content, with relatively rapid crystal growth (later recrystallised, shown with triple junction). Chromite, followed by orthopyroxene, crystallise. At this stage there may also be large orthopyroxene grains with interstitial olivine and

clinopyroxene growth. Each new recharge event is considered to have variable density and temperature conditions, producing crystal fractionation.

6. Recrystallisation (annealing) of pre-existing pyroxene and olivine + trace elements.
7. The last melts were initially olivine saturated and reacted with ULS cumulates to form replacive dunite – completing the melt sequence.

A brief part of the thesis compares pyroxenite pegmatites in various setting such as margins and interiors. These pyroxenite pegmatites differ in that they are likely a result of two melts of different composition mixing (a basaltic melt formed the gabbronorite, perhaps a more picritic melt entered the system, forming pyroxenite pegmatite, and these two melts mixed). These types of pegmatites seem to only appear along this border in a S-SW direction. Perhaps they represent a different generation of pyroxenite pegmatites, based on the open conduit system in RUC. Considering the two different pegmatites identified in the Merensky Reef, it is certainly not unlikely to have several generations of pegmatites also in the RUC. However, this is merely speculation for now. Far more detailed research is required to solidify or falsify this suggestion.

7

Recommendations

During this research it became obvious that there is a lot more work to be done in the RUC in relation to the pyroxenite pegmatite genesis. The author argue that this thesis only skims the surface of the pyroxenite pegmatite formation and role in Ni-Cu-PGE formation in the RUC. Another field season would be of utmost usefulness to build on observations in- and post-field work. As such, the following recommendations, in no particular order, are made for future research:

1. Map out the pyroxenite pegmatites gabbro-wehrlite boundary. Compare to ULS and CS pegmatites and correlate. Systematic sampling of pyroxenite pegmatite to create genetic models of geometry and emplacement. This thesis provides a map from (created only over 1 day) and some inconsistent sampling. This should be expanded upon for more accurate results and broader overview of pyroxenite pegmatite relationship to host rock.
2. Map out the pegmatite from this thesis along with more in the immediate surrounding environment. Inspection for possible grain size variation is important as it may suggest two types of pegmatites, as in the Merensky Reef. This would require detailed in-field observations and descriptions, along with consistent sampling.
3. Continuation of sediment scree sampling conducted north-east of field area – search for mineralisation. This area also needs to be mapped thoroughly as this has never been done. No pegmatitic pyroxenite found in area at the time spent there, however this needs much more investigation, as there may very well be a relationship to the pegmatites observed in the field area.
4. Post-field analysis by EPMA to investigate possible zonation in deeper detail. If zonation is observed, then it will have impacts on the proposed evolution of the pyroxenite pegmatite.
5. Sole focus on sulfides within the pyroxenite pegmatite. Investigate more on evidence for oversaturation, textural properties and overall content from a larger number of pyroxenite pegmatites. This may be combined with a sole focus on plagioclase content (drawing resemblance to the Merensky Reef), in addition to any possible carbonate content.
6. P-T conditions must be configured. Additionally, thermobarometry from amphiboles (LA-ICP-MS) and any possible fluid inclusion, may provide a complete research in itself.
7. Borehole drilling of the pyroxenite pegmatites to provide a clear overview in depth, in combination with drillhole comparisons.

Bibliography

Andréasson, P., Svenningsen, O.M., & Albrecht, L. (1998). Dawn of Phanerozoic orogeny in the North Atlantic tract; evidence from the Seve-Kalak superterrane, Scandinavian caledonites. *GFF, 120*(2), 159-172. doi: 10.1080/11035899801202159

Barth, T. F. W. (1927). Die pegmatitgange der kaledonischen Intrusiv-Gesteine im Seilandgebiet. Skr. utg. av Det Norske Vidensk. *Akad., Oslo. IM-N. Kl*(8).

Barth, T. F. W. (1952). Layered Gabbro Series at Seiland. Norges Geologiske Undersøkelse*, Årbok 184,* 191 – 200.

Bennett, M. C. (1971). The Reinfjord Ultramafic Complex. Norges Geologiske Undersøkelse. *The Caledonian Geology of Northern Norway, 269,* 165 – 171.

Bennett, M. C. (1974). The emplacement of a high temperature peridotite in the Seiland province of the Norwegian Caledonides. *Journal of the Geological Society, 130,* 205 – 228.

Bennett, M.C., Emblin, S.R., Robins, B., & Yeo, W.J.A. (1986). High-temperature ultrmafic complexes in the North Norwegian Caledonides: I – regional setting and field relationships. *Norges Geologiske Undersøkelse Bulletin 405,* 1 – 41.

Best, M. (2003). *Igneous and metamorphic petrology*. 2nd ed. Malden, MA: Blackwell Publishers.

Campbell, I., & Naldrett, A. (1979). The influence of silicate: sulfide ratios on the geochemistry of magmatic sulfides. *Economic geology, 74*(6), 1503-1506.

Cawthorn, R.G. (1999). The platinum and palladium resources of the Bushveld Complex. *South African Journal of Science 95*(11/12):481

Cawthorn, R.G., Merkle, R.K.W., & Viljoen, M.J. (2002a). Platinum-group element deposits in the Bushveld Complex, South Africa. In the Geology, Geochemistry Mineralogy and Mineral Beneficiation of Platinum-Group Elements (L.J. Cabri, editor) *Canadian Institute of Mining, Metallurgy and Petroleum*, *Special Volume: 54:* 389-429.

Cawthorn, R. (2006). Origin of the Pegmatitic Pyroxenite in the Merensky Unit, Bushveld Complex, South Africa. *Journal of Petrology, 47*(8), 1509-1530. doi: 10.1093/petrology/egl017

Cawthorn, R.G., & Ashwal, L.D. (2009). Origin of the anorthosite and magnetite layers in the Bushveld Complex, constrained by the major element compositions of plagioclase*. J Petrol 50*:1607-1637.

Cawthorn, R. (2010). The Platinum Group Element Deposits of the Bushveld Complex in South Africa. *Platinum Metals Review, 54*(4), 205-215. doi: 10.1595/147106710x520222

Cawthorn, R.G. (2015). The Bushveld Complex, South Africa. In: Charlier B., Namur O., Latypov, R., Tegner, C. (eds) *Layered Intrusions*. Springer Geology. Springer, Dordrecht. doi: 10.1007/978-94-017-9652-1_12

Daltry, V., & Wilson, A. (1997). Review of platinum-group mineralogy: compositions and elemental associations of the PG-minerals and unidentified PGE-phases. *Mineralogy and Petrology, 60*(3-4), 185-229.

Deer, W., Howie, R., & Zussman, J. (2013). *Rock forming minerals.* London: Longman.

Emblin, S.R. (1985). The Reinfjord Ultramafic Complex, Seiland Province: Emplacement history and Magma Chamber Model. *(Unpublished Ph.D. thesis).* University of Bristol, U.K.

Evans, A.M. (1993). *Ore Geology and Industrial Minerals, 3rd Edition.* Wiley-Blackwell.

Godel, B. (2015). Platinum-Group Element Deposits in Layered Intrusions: Recent Advances in the Understand of the Ore Forming Processes. In: Charlier B., Namur O., Latypov, R., Tegner, C. (eds) *Layered Intrusions.* Springer Geology. Springer, Dordrecht. doi: 10.1007/978-94-017-9652-1_12

Grant T.B., Larsen, R.B., & Müller, A. (2016a). Composition and evolution of plume melts in the lower crust. Seiland Igneous Province. *Conference Proceedings, Nordic Geological Winter Meeting, Helsinki.*

Grant, T., Larsen, R., Anker-Rasch, L., Grannes, K., Iljina, M., McEnroe, S., Nikolaisen, E., Schanche, M. & Øen, E. (2016b). Anatomy of a deep crustal volcanic conduit system; The Reinfjord Ultramafic Complex, Seiland Igneous Province, Northern Norway. *Lithos*, *252-253*, pp.200-215.

Griffin, W.L., Sturt, B.A., O'neill, C.J., Kirkland, C.L., & O'reilly, S.Y. (2013). Intrusion and contamination of high temperature dunitic magma: the Nordre Bumandsfjord pluton, Seiland, Arctic Norway*. Contributions to Mineralogy and Petrology, 165*, 903-930.

Hawthorne, F., & Oberti, R. (2006). On the classification of amphiboles. *The Canadian Mineralogist, 44*(1), 1-21. doi: 10.2113/gscanmin.44.1.1

Higgins, M.D (2005). A new interpretation of the structure of the Sept Iles Intrusive Suite, Canada*. Lithos 83*:199-213.

Huppert, H. & Sparks, R. (1980). Restrictions on the compositions of mid-ocean ridge basalts: a fluid dynamical investigation. *Nature*, *286*(5768), pp.46-48.

Irvine, T.N. (1965). Chromian spinel as a petrogenetic indicator. Part 1. Theory. *Canadian Journal of Earth Sciences, 2*, 648-672.

Irvine, T., Keith, D. & Todd, S. (1983). The J-M platinum-palladium reef of the Stillwater Complex, Montana; II, Origin by double-diffusive convective magma mixing and implications for the Bushveld Complex. *Economic Geology*, *78*(7), pp.1287-1334.

Irvine, T.N., Andersen, J.C., & Brooks, C.K. (1998). Included blocks (and blocks within blocks) in the Skaergaard intrusion: geologic relations and the origins of rhythmic modally graded layers*. Geol Soc Am Bull 110*:1398-1447.

Kinnaird, J.A., Kruger, F.J., Nex, P.A.M. & Cawthorn, R.G. (2002). Chromitite Formation: a key to understanding processes of platinum enrichment. In I. McDonald, A.G. Gunn and H.M. Prichard (eds), 21st Century of Pt-Pd Deposits: Current and Future Potential*. Transactions of the Institute of Mining Metallurgy*, pp. 23-35.

Larsen, R., Grant, T., Sørensen, B., Tegner, C., McEnroe, S., Pastore, Z., Fichler, C., Nikolaisen, E., Grannes, K., Church, N., ter Maat, G. & Michels, A. (2018). Portrait of a giant deep-seated magmatic conduit system: The Seiland Igneous Province. *Lithos*, *296-299*, pp.600-622.

Lightfoot, P.C., Howkesworth, C.J., Hergt, J., Naldrett, A.J., Gorbachev, N.S., Fedorenko, V.A., & Doherty, W. (1993). Remobilisation of the continental lithosphere by a mantle plume: major-, trace-element, and Sr-, Nd-, and Pb-isotopic evidence from picritic and tholeiitic lavas of the Norilsk district, Siberian trap, Russia. *Contributions to Mineralogy and Petrology 114,* 171-188.

London, D., & Kontak, D. (2012). Granitic Pegmatites: Scientific Wonders and Economic Bonanzas. *Elements, 8*(4), 257-261. doi: 10.2113/gselements.8.4.257

Mavrogenes, J.A., & O'neill, H.S.C. (1999). The relative effects of pressure, temperature and oxygen fugacity on the solubility of sulfide in mafic magmas. *Geochemica Et Cosmochimica Acta, 63*(7-8), 1173-1180. doi: 10.1016/s00167037(98)00289-0

McBirney, A. (1985). Further Considerations of Double-Diffusive Stratification and Layering in the Skaergaard Intrusion. *Journal of Petrology*, *26*(4), pp.993-1001.

McBirney, A. & Noyes, R. (1979). Crystallization and Layering of the Skaergaard Intrusion. *Journal of Petrology*, *20*(3), pp.487-554.

McDonough, W., & Sun, S. (1995). The composition of the Earth. *Chemical Geology, 120*(3-4), 223-253. doi: 10.1016/0009-2541(94)00140-4

Mindat. (2020). Retrieved 4 February 2020, from *https://www.mindat.org/*

Morimoto, N. (1988). Nomenclature of pyroxenes. *Bulletin De Minéralogie, 111*(5), 535-550. doi: 10.3406/bulmi.1988.8099

Naldrett, A., & von Grünewaldt, G. (1989). Association of platinum-group elements with chromitite in layered intrusions and ophiolite complexes. *Economic Geology, 84*(1), 180-187. doi: 10.2113/gsecongeo.84.1.180

Naldrett, A. (1997). Key factors in the genesis of Noril'sk, Sudbury, Jinchuan, Voisey's Bay and other world-class Ni-Cu-PGE deposits: Implications for exploration. *Australia Journal of Earth Sciences, 44*(3), 283-315.

Naldrett, A. (2004). The Jinchuan deposit, China. *Magmatic Sulfide Deposits,* 373-404. doi: 10.1007/978-3-662-08444-1_7

Naldrett, A., Kinnaird, J., Wilson, A., Yudovskaya, M., & Chunnett, G. (2011a). Genesis of PGE-enriched Merensky Reef and chromitite seams of the Bushveld Complex. *Reviews in Econ Geol (17)*235-296.

Naldrett, A. (2013). *Magmatic sulfide deposits: geology, geochemistry and exploration.* Springer Science & Business Media.

Oosterom, M. G. (1963). The ultramafites and layerd gabbro sequences: In the granulite facies rocks on Stjernøy (Finnmark, Norway). *Leidse Geologische Mededelingen, 28,* 177 – 296.

Pastore, Z., Fichler, C., & McEnroe, S. (2016). The deep crustal structure of the mafic-ultramafic Seiland Igneous Province of Norway from 3D gravity modelling and geological implications. *Geophysical Journal Internation 207*(3), 1653-1666.

Pettersen, K. (1875). Short stretch of the geology of the North of Norway. *Geological Magazine, 2,* 385 – 391.

Presnall, D., Dixon, S., Dixon, J., O'Donnell, T., Brenner, N., Schrock, R., & Dycus, D. (1978). Liquidus phase relations on the join diopside-forsterite-anorthite from 1 atm to 20 kbar: Their bearing on the generation and crystallization of basaltic magma. *Contributions To Mineralogy And Petrology, 66*(2), 203-220. doi: 10.1007/bf00372159

Reed, S. J., 2005. *Electron microprobe analysis and scanning electron microscopy in geology.* Vol. 9780521848.

Robb, L. (2005). *Introduction to ore-forming processes*. 1st ed. Blackwell Science Ltd.

Roberts, R.J., Corfu, F., Torsvik, T.H., Hetherington, & C.J., Ashwal, L.D. (2010). Age of alkaline rocks in the Seiland Igneous Province, Northern Norway. *Journal of the Geological Society 167,* 71-81.

Schanche, M., Iljina, M., & Berg-Edland Larsen, R. (2012). New nickel, copper and platinum-group element discoveries in northern Norway. *Mineralproduksjon*, *(2),* 91-99. Retrieved from http://mineralproduksjon.no/wp-content/uploads/2017/03/mp2-09-fn-mona-schanche.pdf

Schoenberg, R., Kruger, F., Nägler, T., Meisel, T. & Kramers, J. (1999). PGE enrichment in chromitite layers and the Merensky Reef of the Western Bushveld Complex; a Re-Os and Rb-Sr isotope study. *Earth and Planetary Science Letters, 172*(1-2), pp. 49-64.

Shannon, R. (1976). Revised effective ionic radii and systematic studies of interatomic distances in halides and chalcogenides. *Acta Crystallographica Section A, 32*(5), 751-767. doi: 10.1107/s0567739476001551

South African Committee For Stratigraphy (1980). Stratigraphy of Southern Africa. Part 1. Lithostratigraphy of South Africa, South West/Namibia, and the Republics of the Boputhatswana, Trankei, and Venda. *In: Geological Survey of South Africa Handbook, vol. 8*, p. 690.

Starostin, V., & Sorokhtin, O. (2011). A new interpretation for the origin of the Norilsk type PGE-Cu-Ni sulfide deposits. *Geoscience Frontiers, 2*(4), 583-591. doi: 10.1016/j.gsf.2011.09.005

Streckeisen, A. (1974). Classification and nomenclature of plutonic rocks Recommendations of the IUGS subcommission on the systematics of Igneous Rocks. *Geologische Rundschau, 63*(2), 773-786. Doi: 10.1007/bf01820841

Sun, S., & McDonough, W. (1989). Chemical and isotopic systematics of oceanic basalts: implications for mantle composition and processes. *Geological Society, London, Special Publications, 42*(1), 313-345. doi: 10.1144/gsl.sp.1989.042.01.19

Sørensen, B. (2013). A revised Michel-Lévy interference colour chart based on first-principles calculations. *European Journal of Mineralogy, 25*(1), 5-10. doi: 10.1127/0935-1221/2013/0025-2252

Sørensen, B., Grant, T., Ryan, E., & Larsen, R. (2019). In situ evidence of earthquakes near the crust mantle boundary initiated by mantle CO_2 fluxing and reaction-driven strain softening. *Earth And Planetary Science Letters, 524,* 115713. doi: 10.1016/j.epsl.2019.115713

Tarantino, S., Ballaran, T., Carpenter, M., Domeneghettim M., & Tazzoli, V. (2002). Mixing properties of the enstatite-ferrosilite solid solution: II. A microscopic perspective. *European Journal Of Mineralogy, 14*(3), 537-547. doi: 10.1127/0935-1221/2002/0014-0537

Tegner, C., Cawthorn, R.G., & Kruger, F.J. (2006). Cyclicity in the main and upper zones of the Bushveld complex, South Africa: crystallisation from a zoned magma sheet. *J Petrol 47*:2257-2279.

Touloukian, Y. (1977). *Thermophysical properties of matter.* New York: IFI/Plenum.

Turner, J. (1980). A fluid-dynamical model of differentiation and layering in magma chambers. *Nature*, *285*(5762), pp.213-215.

Turovtsev, D.M. (2002). Contact Metamorphism of Norilsk Intrusions. *Nauchnyi Mir,* Moscow, p. 319.

Oberthür, T., Davis, D.W., Blenkinsop, T.G., & Hohndorf, A. (2002). Precise U-Pb mineral ages, Rb-Sr and Sm-Nd systematic for the Great Dyke, Zimbabwe-constraints on late Archean events in the Zimbabwe craton and Limpopo belt*. Precambrian Res 113*(3):293-305.

O'Driscoll, B. & González-Jiménez, J. (2015). Petrogenesis of the Platinum-Group Minerals. *Review in Mineralogy and Geochemistry, 81*(1), pp.489-578.

Orvik, A.A. (2019). *The dyke swarm in the Reinfjord Ultramafic Complex – A window into the terminal stages forming the Seiland Igneous Province.* Msc, Norwegian University of Science and Technology.

Vale, L. (2020). *Alex Strekeisen*. Retrieved 21 May 2020, from http://www.alexstrekeisen.it/english/pluto/poikilitic.php

Verma, S.P., Guevara, M., & Agrawal, S. (2006). Discriminating four tectonic settings: Five new geochemical diagrams for basic and ultrabasic volcanic rocks based on Log-ratio transformation of major-element data. *Journal Of Earth System Science, 115*(5), 485-528. doi: 10.1007/bf02702907

Wilson, A.H. (1982). The Geology of the Great Dyke, Zimbabwe: The Ultramafic Rocks*. J Petrol 23*(2):240-292.

Yang. X., Ishihara, S., & Zhao, D. (2005). Genesis of the Jinchuan PGE deposit, China: evidence from fluid inclusions, mineralogy and geochemistry of precious elements. *Mineralogy And Petrology, 86*(1-2), 109-128. doi: 10.1007/s00710-005-0094-4.

(Page intentionally left blank).

Appendices

Appendix A Thin Section Scans

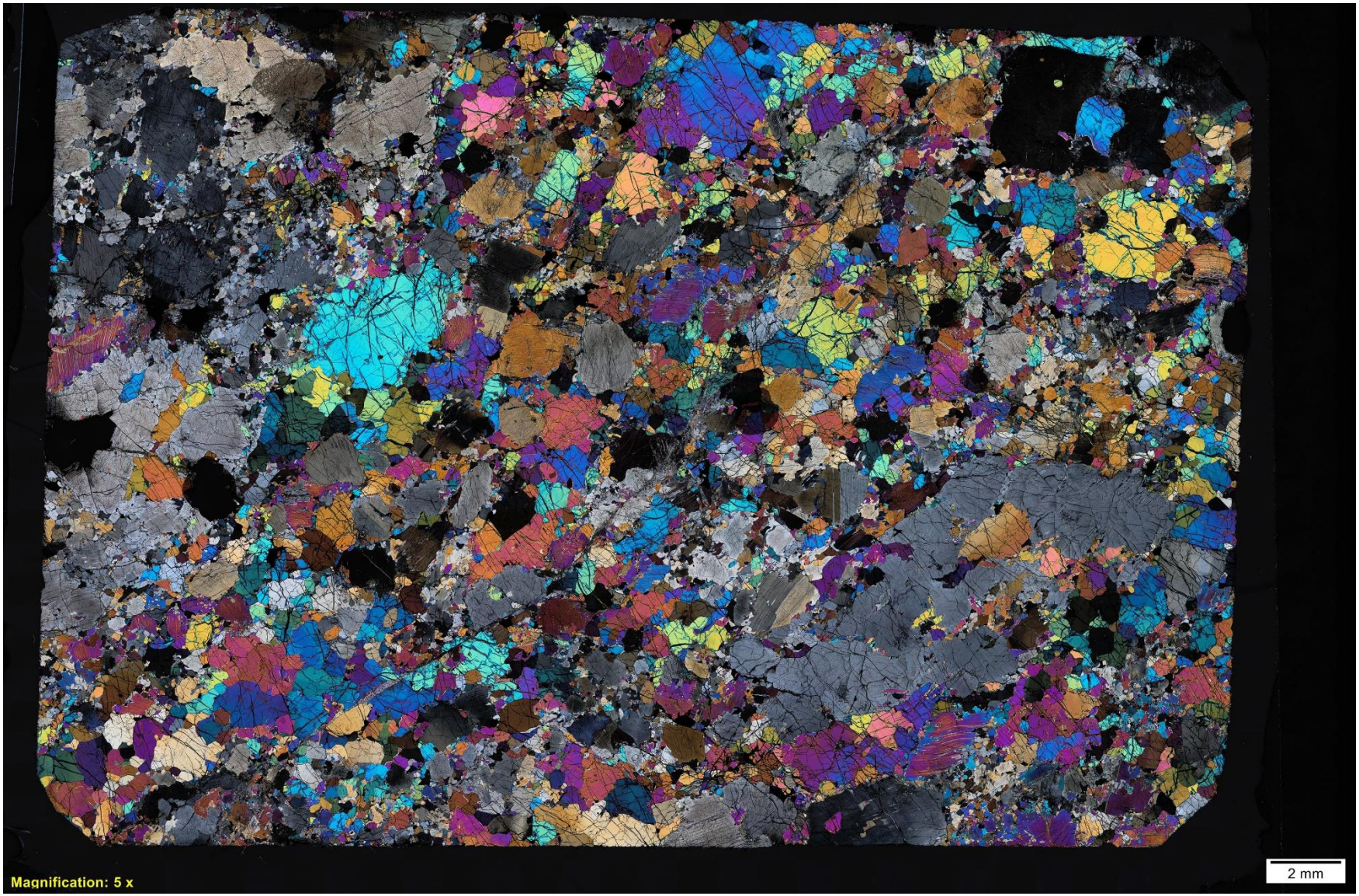

Figure 8.1: *Scan of thin section AM19-006-XA in XPL.*

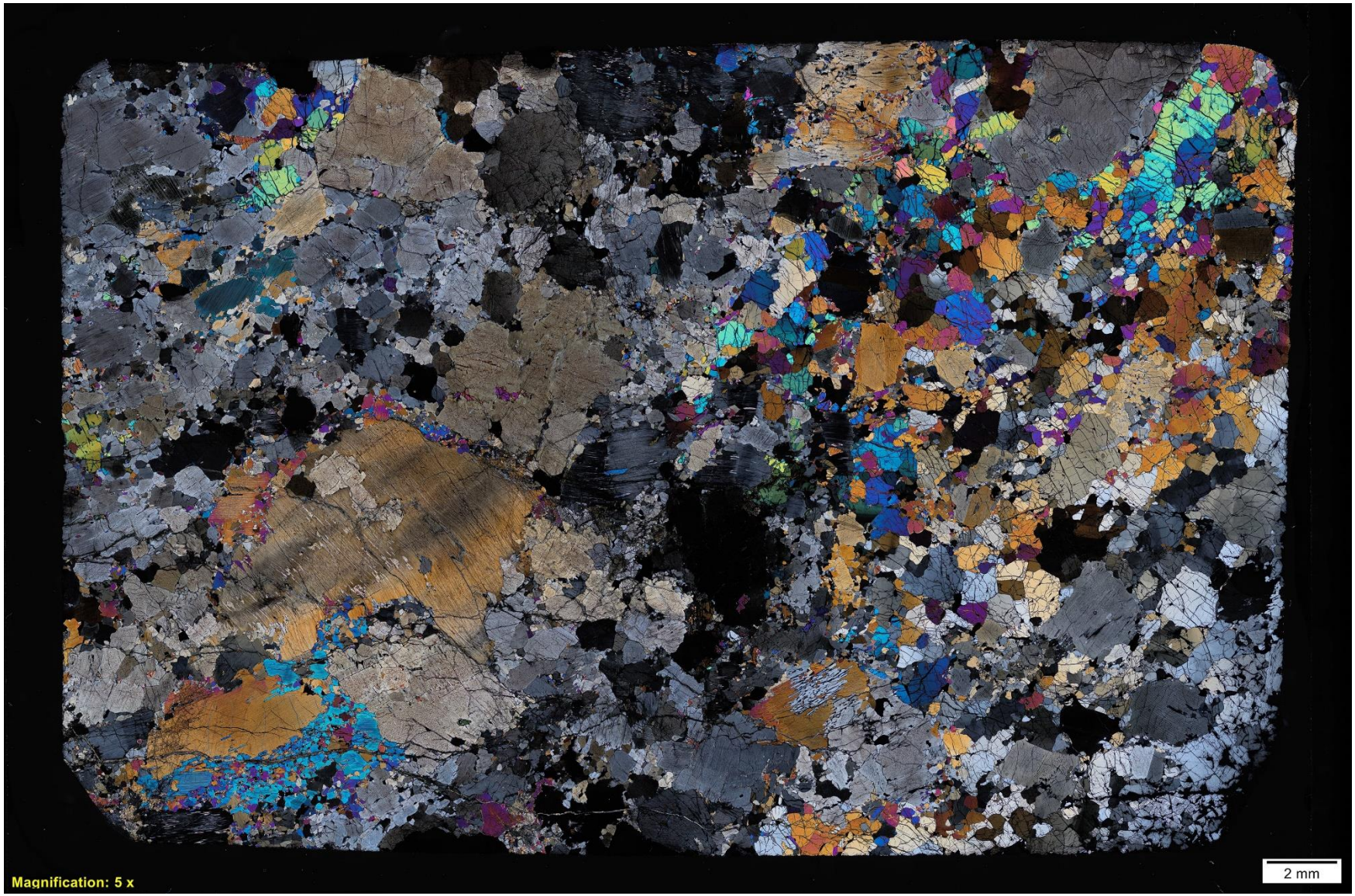

Figure 8.2: *Scan of thin section AM19-006-XB in XPL.*

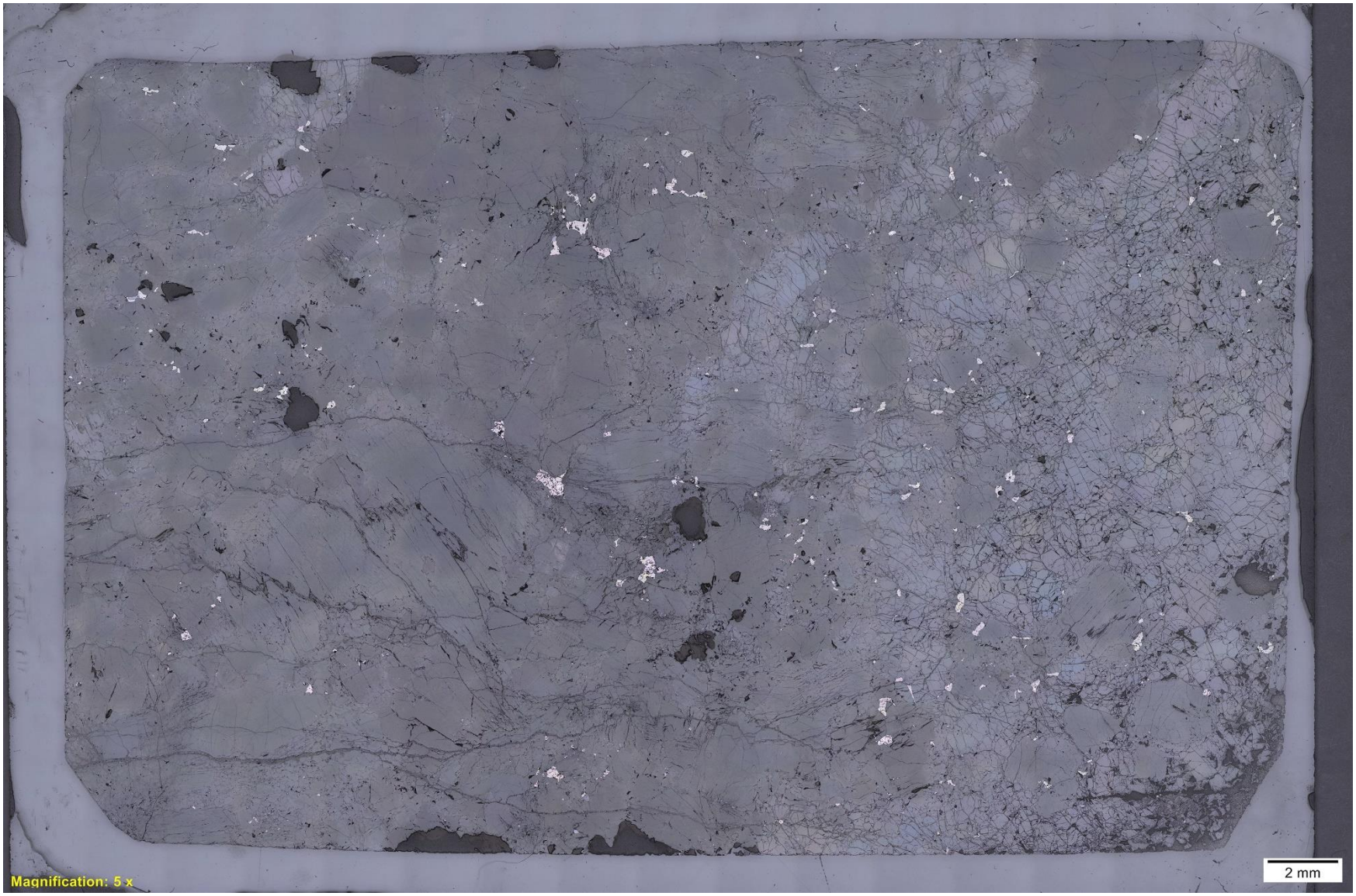

Figure 8.3: *Scan of thin section AM19-006-XB in reflected light, highlighting sulfides.*

Figure 8.4: *Scan of thin sections AM19-006-1 (left) and AM19-008-1 (right) in PPL.*

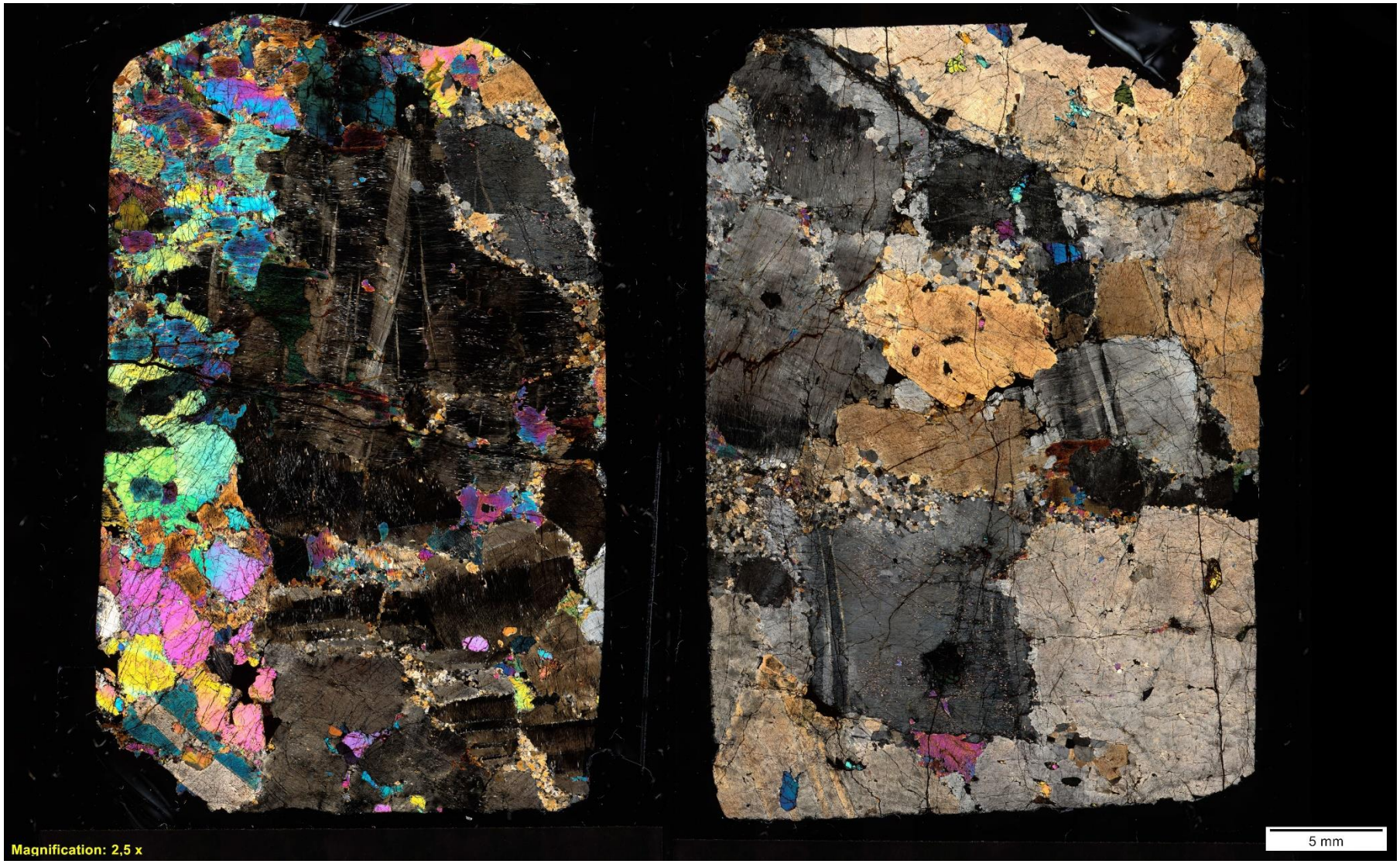

Figure 8.5: *Scan of thin sections AM19-008-2 (left) and AM19-008-3 (right) in XPL.*

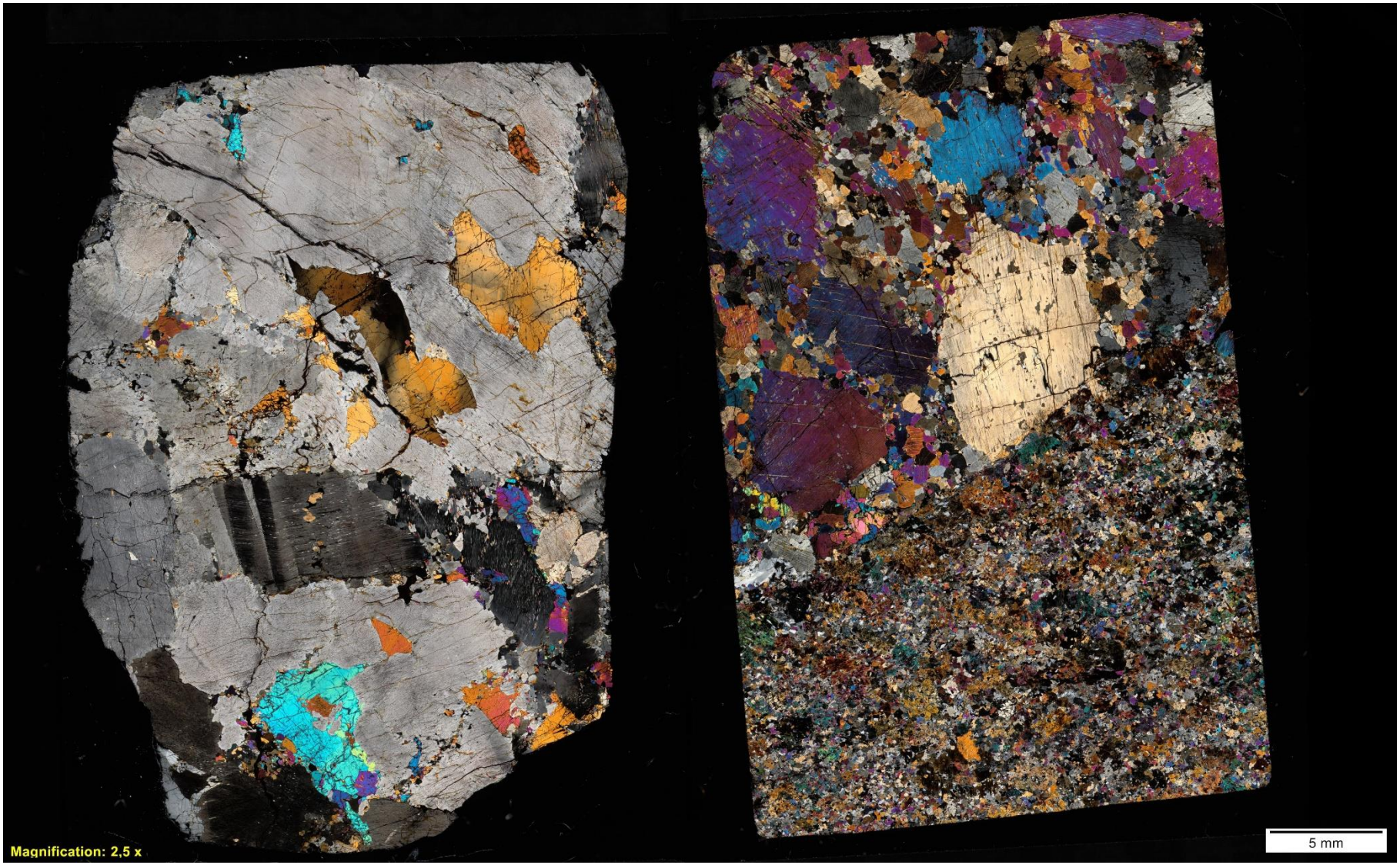

Figure 8.6: *Scan of thin sections AM19-008-4 (left) and AM19-008-5A (right) in XPL.*

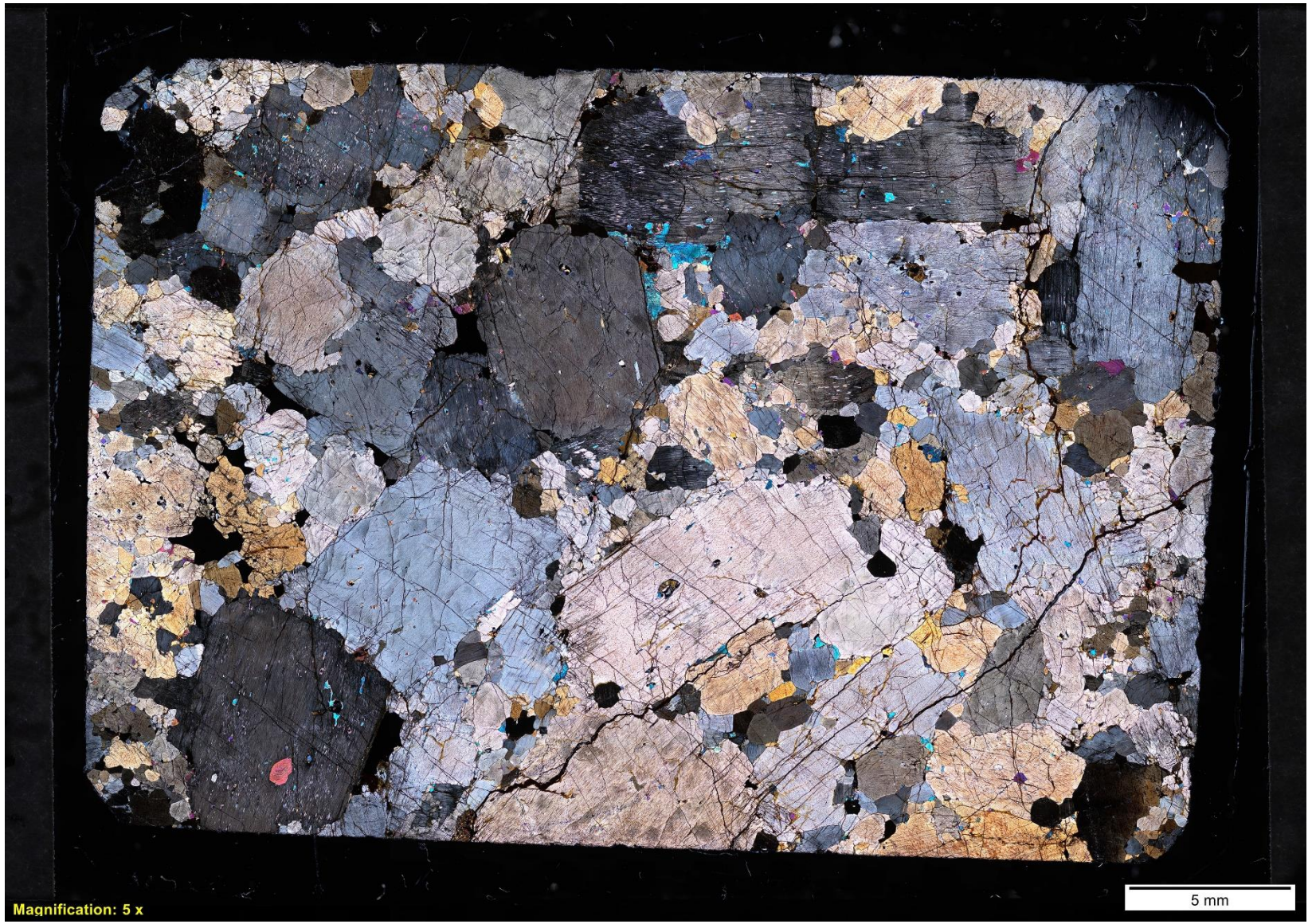

Figure 8.7: *Scan of thin section AM19-010 in XPL.*

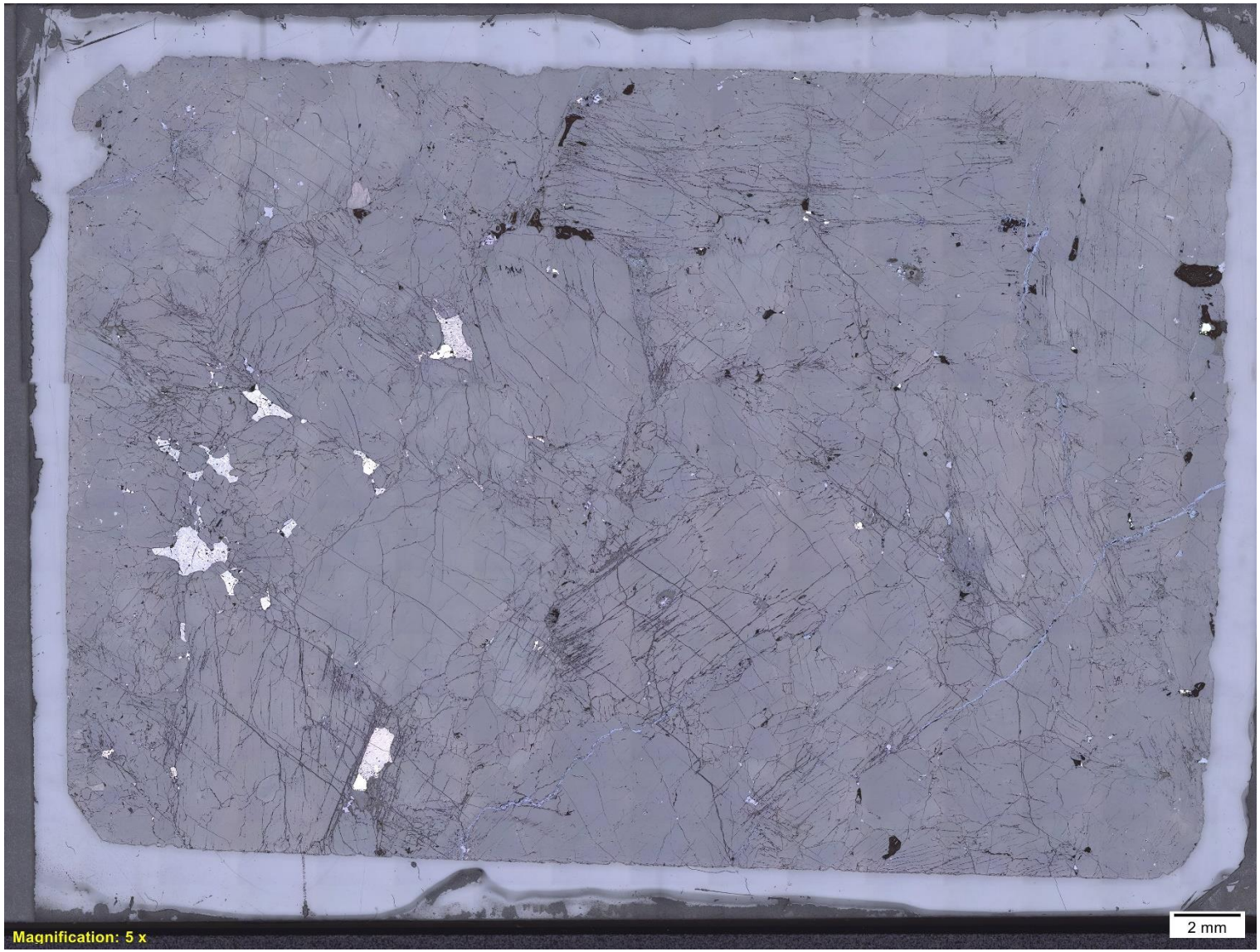

Figure 8.8: *Scan of thin section AM19-010 in reflected light, highlighting sulfides.*

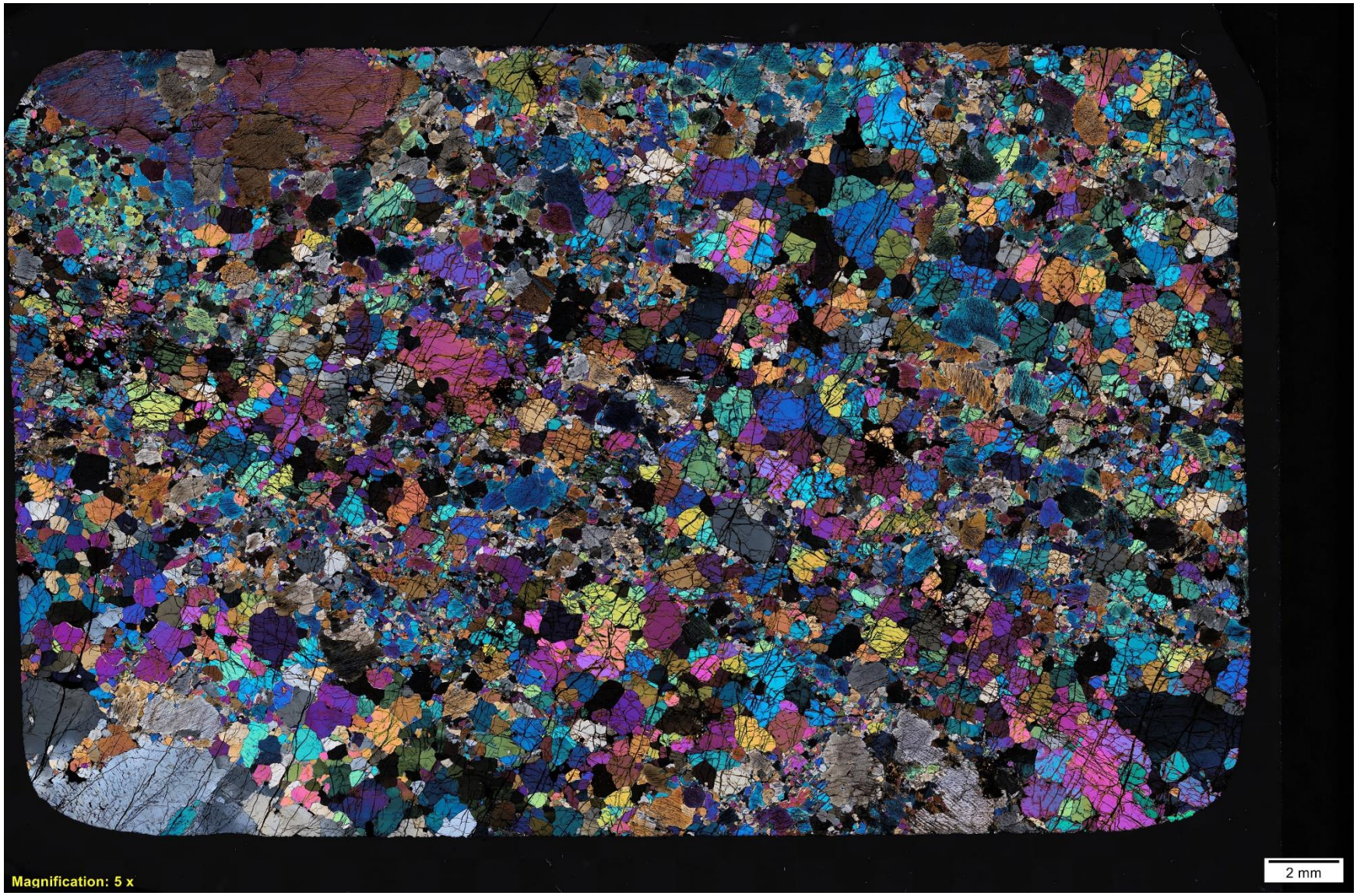

Figure 8.9: *Scan of thin section AM19-XX in XPL.*

Appendix B Whole-Rock Analysis

Table 8.1: *Major elements whole-rock analysis for all samples.*

SAMPLE	Pass2mm	Pass75um	Au	Pt	Pd	SiO2	Al2O3	Fe2O3	CaO	MgO	Na2O	K2O	Cr2O3	TiO2	MnO	P2O5	SrO	BaO	LOI	Total
DESCRIPTION	%	%	ppm	ppm	ppm	%	%	%	%	%	%	%	%	%	%	%	%	%	%	%
AM19-002-1			0.001	<0.005	0.003	41.1	0.67	16.35	3.48	38.2	0.11	<0.01	0.171	0.15	0.2	0.01	<0.01	<0.01	1.33	101.77
AM19-002-2			0.001	0.022	0.035	37	0.43	15.75	1.72	34.6	0.06	<0.01	0.11	0.1	0.18	0.01	<0.01	<0.01	11.1	101.06
AM19-002-3			0.001	0.01	0.009	37.3	0.61	15.3	2.34	32.8	0.07	<0.01	0.16	0.13	0.18	0.01	<0.01	<0.01	10.95	99.85
AM19-002-4			0.002	0.019	0.009	38.5	0.32	17.4	1.29	40.5	0.06	0.01	0.107	0.08	0.21	0.01	<0.01	<0.01	0.38	98.87
AM19-002-5			0.001	0.01	0.005	40.7	0.57	16.8	3.11	38.6	0.09	<0.01	0.146	0.12	0.2	0.01	<0.01	<0.01	0.48	100.83
AM19-002-6			0.001	0.013	0.006	40.6	0.61	16.85	3.3	38.2	0.1	<0.01	0.16	0.13	0.2	0.01	<0.01	<0.01	0.56	100.72
AM19-002-7			0.002	0.01	0.008	42.3	0.96	15.5	5.21	36.3	0.15	<0.01	0.265	0.21	0.19	0.01	<0.01	<0.01	-0.07	101.03
AM19-002-8	86.2	97.6	0.002	0.005	0.007	40.9	0.53	16.95	2.75	39.6	0.1	0.01	0.141	0.12	0.2	0.01	<0.01	<0.01	-0.35	100.96
AM19-002-9			0.003	0.02	0.025	40.6	0.56	16.95	2.88	39.2	0.1	<0.01	0.149	0.13	0.2	0.02	<0.01	<0.01	-0.2	100.59
AM19-005-1A	79.1	96.4	<0.001	0.026	0.04	37.4	0.53	15	2.74	32.3	0.05	<0.01	0.141	0.12	0.18	0.01	<0.01	<0.01	10.8	99.27
AM19-005-1B			0.003	0.03	0.053	36.7	0.43	15.15	1.89	33.1	0.03	0.01	0.124	0.1	0.18	0.01	<0.01	<0.01	11	98.72
AM19-006-1-1	79.8	97.2	0.004	0.008	0.005	51.3	3.66	15.3	2.72	25.5	0.22	0.05	0.212	0.72	0.23	0.03	<0.01	<0.01	-0.14	99.8
AM19-006-1-2			0.004	0.008	0.006	50.7	3.97	14.35	4.16	24	0.28	0.06	0.233	0.8	0.22	0.02	<0.01	<0.01	-0.03	98.76
AM19-006-1-3			0.005	0.008	0.006	49.8	2.62	16.35	1.65	28.1	0.09	0.02	0.173	0.5	0.24	0.02	<0.01	<0.01	-0.24	99.32
AM19-007-X			0.006	<0.005	0.004	43.4	3.25	16.25	8.9	27.5	0.36	<0.01	0.17	0.56	0.19	0.02	<0.01	<0.01	0.47	101.07
AM19-007-02			0.001	<0.005	<0.001	46.7	4.46	12.15	14.65	19.65	0.48	0.01	0.283	1.1	0.18	0.01	<0.01	<0.01	0.51	100.18
AM19-008-1			<0.001	0.005	0.003	40.2	0.54	20.3	2.14	36.6	0.06	<0.01	0.106	0.15	0.23	0.01	<0.01	<0.01	-0.87	99.47
AM19-008-2-1			0.004	0.009	0.01	46.8	4.07	14	9.31	22.1	0.38	0.05	0.305	1.12	0.21	0.02	<0.01	<0.01	0.01	98.38
AM19-008-2-2			0.005	0.008	0.006	46.7	4.36	16.1	7.25	23.7	0.46	0.05	0.227	1.18	0.21	0.03	<0.01	<0.01	-0.04	100.23
AM19-008-2-3			0.006	0.012	0.01	48	4.04	14.35	9.06	21.9	0.39	0.04	0.288	1.13	0.21	0.02	<0.01	<0.01	0.08	99.51
AM19-008-3			0.007	0.012	0.011	50.7	3.12	15.55	3.27	25.4	0.16	0.03	0.235	0.66	0.23	0.01	<0.01	<0.01	0.16	99.53
AM19-008-4			0.002	0.008	0.007	50.2	2.98	16.4	2.24	27.2	0.13	0.03	0.199	0.6	0.23	0.01	<0.01	<0.01	-0.07	100.15
AM19-XX			0.001	<0.005	<0.001	49.1	4.54	9.36	17.75	16.75	0.5	0.01	0.565	1.24	0.17	0.01	<0.01	<0.01	0.09	100.09
AM19-XX1			<0.001	<0.005	0.002	41.9	0.99	14.65	4.53	37.3	0.14	<0.01	0.135	0.27	0.18	0.02	<0.01	<0.01	1.36	101.48

Table 8.2: *Minor elements whole-rock analysis for all samples.*

SAMPLE	Ba	Ce	Cr	Cs	Dy	Er	Eu	Ga	Gd	Hf	Ho	La	Lu	Nb	Nd	Pr	Rb	Sm	Sn	Sr	Ta	Tb	Th	Tm	U	V	W	Y	Yb	Zr
DESCRIPTION	ppm	ppm	ppm	ppm	ppm	ppm	ppm	ppm	ppm	ppm	ppm	ppm	ppm	ppm	ppm	ppm	ppm	ppm	ppm	ppm	ppm	ppm	ppm	ppm	ppm	ppm	ppm	ppm	ppm	ppm
AM19-002-1	1.5	0.9	1280	0.02	0.37	0.2	0.12	1.7	0.49	0.3	0.07	0.4	0.02	0.2	1.2	0.19	0.2	0.27	2	8.5	0.1	0.08	<0.05	0.01	<0.05	22	<1	2.1	0.14	3
AM19-002-2	1.9	0.6	840	0.01	0.29	0.09	0.07	1	0.24	0.3	0.03	0.3	0.02	<0.2	0.7	0.11	0.2	0.24	1	4.8	0.1	0.03	<0.05	0.02	<0.05	6	<1	1.1	0.12	2
AM19-002-3	3.2	1	1270	0.02	0.3	0.24	0.09	1.3	0.37	0.3	0.06	0.4	0.03	5.4	1.1	0.15	0.2	0.27	1	6.4	0.5	0.06	<0.05	0.01	<0.05	22	<1	1.7	0.2	5
AM19-002-4	2.2	0.5	820	<0.01	0.15	0.11	0.05	1.1	0.17	0.6	0.05	0.3	0.02	1.2	0.6	0.1	0.2	0.14	1	3.7	0.3	0.04	<0.05	<0.01	<0.05	14	2	0.9	0.11	24
AM19-002-5	2.5	0.9	1150	<0.01	0.34	0.16	0.1	1.5	0.33	0.3	0.04	0.4	0.03	0.4	0.8	0.15	<0.2	0.37	1	7.9	0.2	0.06	<0.05	0.01	<0.05	33	<1	1.6	0.15	3
AM19-002-6	2.5	1	1210	0.03	0.35	0.23	0.11	1.7	0.4	0.3	0.07	0.4	0.02	0.3	0.9	0.16	<0.2	0.35	1	7.8	0.2	0.06	<0.05	0.02	<0.05	13	<1	1.7	0.2	3
AM19-002-7	1.5	1.4	2260	<0.01	0.58	0.3	0.19	2.4	0.56	0.2	0.11	0.5	0.05	0.3	1.6	0.26	0.2	0.61	1	11.9	0.1	0.1	<0.05	0.03	<0.05	105	1	2.8	0.28	5
AM19-002-8	1.8	0.9	1090	<0.01	0.18	0.17	0.06	1.5	0.3	0.3	0.04	0.5	0.02	0.3	1	0.16	0.3	0.28	2	6.4	0.2	0.05	<0.05	0.01	<0.05	16	1	1.5	0.11	3
AM19-002-9	1.7	0.9	1120	0.01	0.38	0.27	0.08	1.4	0.36	0.2	0.06	0.4	0.02	<0.2	1	0.16	0.3	0.29	2	6.8	0.1	0.05	<0.05	<0.01	<0.05	11	<1	1.6	0.15	3
AM19-005-1A	1.6	0.7	1020	0.02	0.36	0.22	0.07	1.5	0.43	0.2	0.03	0.3	0.02	<0.2	0.9	0.14	0.2	0.34	1	8	0.1	0.05	<0.05	0.02	<0.05	11	<1	1.5	0.15	3
AM19-005-1B	2.1	0.7	930	<0.01	0.23	0.12	0.05	1.2	0.22	0.3	0.02	0.3	0.01	0.3	0.6	0.1	0.2	0.1	1	4.8	0.1	0.04	<0.05	0.01	<0.05	5	1	1.3	0.17	9
AM19-006-1-1	15.4	3.3	1710	0.04	0.9	0.65	0.2	8.4	0.65	0.6	0.18	1.5	0.08	2.2	2.2	0.48	1.4	0.63	2	40	0.3	0.13	0.13	0.08	<0.05	172	1	4.6	0.56	18
AM19-006-1-2	15.7	3.9	1900	0.02	1.13	0.72	0.33	8.1	0.99	0.8	0.22	1.7	0.09	2.2	3	0.6	0.9	0.87	1	47.1	0.1	0.17	0.15	0.1	0.05	200	1	5.5	0.54	21
AM19-006-1-3	6	1.5	1340	<0.01	0.57	0.46	0.14	7	0.37	0.4	0.1	0.7	0.07	0.8	1.1	0.23	0.9	0.3	1	8.5	0.2	0.1	0.13	0.05	<0.05	119	1	3	0.37	10
AM19-007-X	5.2	3.3	1320	0.01	1.4	0.87	0.42	6.4	1.52	0.7	0.27	1.2	0.07	0.4	3.8	0.54	0.4	1.26	2	53.1	0.1	0.22	<0.05	0.07	<0.05	135	1	6.6	0.52	14
AM19-007-02	3.6	6.5	2200	0.03	2.42	1.26	0.86	7.7	3.07	1.3	0.51	1.8	0.14	0.5	7	1.21	<0.2	2.6	2	55.8	<0.1	0.52	<0.05	0.16	<0.05	247	1	12	0.95	32
AM19-008-2-1	11.2	5.7	2290	0.05	2.07	1.37	0.65	8.1	2.27	1.1	0.4	2	0.15	2.5	5.5	0.96	1	2.08	1	44.6	0.2	0.36	0.18	0.15	0.07	225	3	9.5	1.04	33
AM19-008-2-2	13.9	6.6	1790	0.02	1.89	1.13	0.72	8.1	2.15	1.2	0.35	2.4	0.12	3.6	5.6	1.03	1	1.64	1	85.6	0.2	0.31	0.17	0.11	<0.05	204	<1	8.6	0.82	34
AM19-008-2-3	7.5	5.5	2160	0.04	2.02	1.18	0.63	8	2.27	1.1	0.38	2	0.11	2.2	5.3	0.9	0.8	1.76	1	41.7	0.1	0.38	0.15	0.1	0.06	234	1	9.1	0.71	30
AM19-008-1	1.1	0.8	820	0.03	0.38	0.31	0.14	1.3	0.31	0.2	0.05	0.4	0.03	<0.2	0.9	0.16	<0.2	0.34	1	5.9	0.1	0.06	<0.05	0.03	<0.05	46	1	1.6	0.17	4
AM19-008-3	6.1	2	1740	0.04	0.91	0.62	0.19	6.8	0.69	0.5	0.14	0.9	0.09	1.2	1.8	0.33	0.7	0.56	1	11.2	0.1	0.16	0.08	0.09	<0.05	162	1	4.4	0.63	15
AM19-008-4	7.6	2	1450	0.02	0.56	0.4	0.13	8	0.42	0.5	0.13	0.9	0.07	1.1	1.4	0.3	0.7	0.36	1	13.8	0.2	0.1	0.1	0.08	<0.05	119	1	3.7	0.55	13
AM19-XX	4.3	7.5	4560	0.01	3.07	1.74	1.06	11.4	3.23	1.3	0.72	2.1	0.19	0.7	9.8	1.53	0.5	2.79	2	48.4	0.2	0.51	0.08	0.23	<0.05	301	<1	15.9	1.28	35

AM19-XX1	1.5	2	960	0.01	0.58	0.31	0.21	2.4	0.51	0.4	0.11	0.7	0.05	0.3	2	0.31	0.2	0.6	1	12.6	0.1	0.1	<0.05	0.03	<0.05	35	<1	3	0.23	8

Appendix C Normative Calculations From Whole-Rock Analysis

Table 8.3: *Normalisation calculation values of samples AM19-006-1, AM19-006-2 and AM19-006-3.*

Sample	Results		Sample	Results		Sample	Results	
AM19-006-1-1	Quartz	0	**AM19-006-1-2**	Quartz	0	**AM19-006-1-3**	Quartz	0
	Plagioclase	10.8573268		Plagioclase	12.0558249		Plagioclase	7.58643763
	(Albite)	1.88720718		(Albite)	2.42794741		(Albite)	0.7758997
	(Anorthite)	8.9701196		(Anorthite)	9.62787745		(Anorthite)	6.81053793
	Orthoclase	0.30587842		Orthoclase	0.36987991		Orthoclase	0.12289708
	Nepheline	0		Nepheline	0		Nepheline	0
	Leucite	0		Leucite	0		Leucite	0
	Kalsilite	0		Kalsilite	0		Kalsilite	0
	Corundum	0		Corundum	0		Corundum	0
	Diopside	3.61937279		Diopside	9.11950202		Diopside	1.11908058
	Enstatite	75.6013189		Hypersthene	69.3568402		Hypersthene	72.1638722
	Wollastonite	0		Wollastonite	0		Wollastonite	0
	Olivine	5.08231018		Olivine	4.51042086		Olivine	14.7977298
	Larnite	0		Larnite	0		Larnite	0
	Aegirine	0		Aegirine	0		Aegirine	0
	K2SiO3	0		K2SiO3	0		K2SiO3	0
	Na2SiO3	0		Na2SiO3	0		Na2SiO3	0
	Rutile	0		Rutile	0		Rutile	0
	Ilmenite	1.38626797		Ilmenite	1.55700147		Ilmenite	0.96749977
	Magnetite	2.69868604		Magnetite	2.55856926		Magnetite	2.89831019
	Hematite	0		Hematite	0		Hematite	0
	Apatite	0.07203483		Apatite	0.048544		Apatite	0.04826335
	Zircon	0.00366689		Zircon	0.00432443		Zircon	0.00204735
	Perovskite	0		Perovskite	0		Perovskite	0
	Chromite	0.37313719		Chromite	0.41909297		Chromite	0.29386198
	Titanite	0		Titanite	0		Titanite	0
	Pyrite	0		Pyrite	0		Pyrite	0
	Halite	0		Halite	0		Halite	0

Fluorite	0	Fluorite	0	Fluorite	0
Anhydrite	0	Anhydrite	0	Anhydrite	0
Na2SO4	0	Na2SO4	0	Na2SO4	0
Calcite	0	Calcite	0	Calcite	0
Na2CO3	0	Na2CO3	0	Na2CO3	0
Total	100	Total	100	Total	100
Fe3+/(Total Fe) in rock	11.9999574	Fe3+/(Total Fe) in rock	11.9999574	Fe3+/(Total Fe) in rock	11.9999574
Mg/(Mg+Total Fe) in rock	76.7538222	Mg/(Mg+Total Fe) in rock	76.8158248	Mg/(Mg+Total Fe) in rock	77.2973589
Mg/(Mg+Fe2+) in rock	78.956334	Mg/(Mg+Fe2+) in rock	79.0140682	Mg/(Mg+Fe2+) in rock	79.462152
Mg/(Mg+Fe2+) in silicates	80.8647067	Mg/(Mg+Fe2+) in silicates	81.1152556	Mg/(Mg+Fe2+) in silicates	80.9803731
Ca/(Ca+Na) in rock	87.2320969	Ca/(Ca+Na) in rock	89.1422958	Ca/(Ca+Na) in rock	91.0160742
Plagioclase An content	81.7518172	Plagioclase An content	78.8921739	Plagioclase An content	89.2162681
Differentiation Index	11.1632052	Differentiation Index	12.4257048	Differentiation Index	7.70933471
Aluminum Saturation Index	0.69191365	Aluminum Saturation Index	0.49370265	Aluminum Saturation Index	0.83925111
Alkalinity Index	8.79716304	Alkalinity Index	7.55365459	Alkalinity Index	15.4383295
Calculated density, g/cc	3.32019584	Calculated density, g/cc	3.3048203	Calculated density, g/cc	3.35461249
Calculated liquid density, g/cc	2.79656975	Calculated liquid density, g/cc	2.79043001	Calculated liquid density, g/cc	2.8245526
Calculated viscosity, dry, Pas	0.13023338	Calculated viscosity, dry, Pas	0.13682587	Calculated viscosity, dry, Pas	0.09857754
Calculated viscosity, wet, Pas	0.123007	Calculated viscosity, wet, Pas	0.12949542	Calculated viscosity, wet, Pas	0.0933736
Estimated liquidus temp., °C	1176.70536	Estimated liquidus temp., °C	1177.64794	Estimated liquidus temp., °C	1199.9357
Estimated H2O content, wt. %	0.5450744	Estimated H2O content, wt. %	0.54212202	Estimated H2O content, wt. %	0.44131546
Normalised analysis		***Normalised analysis***		***Normalised analysis***	
SiO2	52.0073455	SiO2	51.9559225	SiO2	50.7400052
TiO2	0.72992766	TiO2	0.81981732	TiO2	0.5094378
Al2O3	3.71046558	Al2O3	4.06834344	Al2O3	2.66945409
Fe2O3	1.86131552	Fe2O3	1.76465678	Fe2O3	1.99903394
FeO	12.2821523	FeO	11.644336	FeO	13.1909067
MnO	0.23317133	MnO	0.22544976	MnO	0.24453015
MgO	25.8516045	MgO	24.5945195	MgO	28.6304046

CaO	2.75750448	CaO	4.26305005	CaO	1.68114475
Na2O	0.22303345	Na2O	0.28693606	Na2O	0.0916988
K2O	0.05068942	K2O	0.0614863	K2O	0.02037751
P2O5	0.03041365	P2O5	0.02049543	P2O5	0.02037751
CO2	0	CO2	0	CO2	0
SO3	0	SO3	0	SO3	0
S	0	S	0	S	0
F	0	F	0	F	0
Cl	0	Cl	0	Cl	0
Sr	0.00479559	Sr	0.00570799	Sr	0.00102418
Ba	0.00174303	Ba	0.00179624	Ba	0.00068251
Ni	0	Ni	0	Ni	0
Cr	0.25337302	Cr	0.28457558	Cr	0.19954594
Zr	0.00246497	Zr	0.00290696	Zr	0.0013763
Total	100	Total	100	Total	100

Table 8.4: *Normalisation calculation values samples AM19-008-2-1, AM19-008-2-2 and AM19-008-2-3.*

Sample	Results		Sample	Results		Sample	Results	
AM19-008-2-1	Quartz	0	**AM19-008-2-2**	Quartz	0	**AM19-008-2-3**	Quartz	0
	Plagioclase	12.8278143		Plagioclase	13.7249685		Plagioclase	12.6812993
	(Albite)	3.30901233		(Albite)	3.93576901		(Albite)	3.36049551
	(Anorthite)	9.51880199		(Anorthite)	9.78919949		(Anorthite)	9.3208038
	Orthoclase	0.30875176		Orthoclase	0.30447224		Orthoclase	0.24380985
	Nepheline	0		Nepheline	0		Nepheline	0
	Leucite	0		Leucite	0		Leucite	0
	Kalsilite	0		Kalsilite	0		Kalsilite	0
	Corundum	0		Corundum	0		Corundum	0
	Diopside	30.3204795		Diopside	21.1700231		Diopside	29.0933823
	Hypersthene	29.4492995		Hypersthene	32.2205557		Hypersthene	35.0989154
	Wollastonite	0		Wollastonite	0		Wollastonite	0
	Olivine	21.8350765		Olivine	27.0131332		Olivine	17.6268893
	Larnite	0		Larnite	0		Larnite	0
	Aegirine	0		Aegirine	0		Aegirine	0
	K2SiO3	0		K2SiO3	0		K2SiO3	0
	Na2SiO3	0		Na2SiO3	0		Na2SiO3	0
	Rutile	0		Rutile	0		Rutile	0
	Ilmenite	2.18902441		Ilmenite	2.26606086		Ilmenite	2.18542018
	Magnetite	2.50672595		Magnetite	2.83244626		Magnetite	2.54246302
	Hematite	0		Hematite	0		Hematite	0
	Apatite	0.04874939		Apatite	0.07184845		Apatite	0.04823842
	Zircon	0.00682428		Zircon	0.00690842		Zircon	0.00613887
	Perovskite	0		Perovskite	0		Perovskite	0
	Chromite	0.50725438		Chromite	0.3895833		Chromite	0.47344332
	Titanite	0		Titanite	0		Titanite	0
	Pyrite	0		Pyrite	0		Pyrite	0
	Halite	0		Halite	0		Halite	0

Fluorite	0	Fluorite	0	Fluorite	0
Anhydrite	0	Anhydrite	0	Anhydrite	0
Na2SO4	0	Na2SO4	0	Na2SO4	0
Calcite	0	Calcite	0	Calcite	0
Na2CO3	0	Na2CO3	0	Na2CO3	0
Total	100	Total	100	Total	100
Fe3+/(Total Fe) in rock	11.9999574	Fe3+/(Total Fe) in rock	11.9999574	Fe3+/(Total Fe) in rock	11.9999574
Mg/(Mg+Total Fe) in rock	75.7708485	Mg/(Mg+Total Fe) in rock	74.465256	Mg/(Mg+Total Fe) in rock	75.1452408
Mg/(Mg+Fe2+) in rock	78.0398476	Mg/(Mg+Fe2+) in rock	76.8191153	Mg/(Mg+Fe2+) in rock	77.4553949
Mg/(Mg+Fe2+) in silicates	80.7735575	Mg/(Mg+Fe2+) in silicates	79.4801147	Mg/(Mg+Fe2+) in silicates	80.2041963
Ca/(Ca+Na) in rock	93.1218005	Ca/(Ca+Na) in rock	89.7007545	Ca/(Ca+Na) in rock	92.7731629
Plagioclase An content	73.0555117	Plagioclase An content	70.0985466	Plagioclase An content	72.3318377
Differentiation Index	13.1365661	Differentiation Index	14.0294407	Differentiation Index	12.9251092
Aluminum Saturation Index	0.23179677	Aluminum Saturation Index	0.31320121	Aluminum Saturation Index	0.23612514
Alkalinity Index	5.99182583	Alkalinity Index	5.37696412	Alkalinity Index	5.89879776
Calculated density, g/cc	3.30701113	Calculated density, g/cc	3.32107344	Calculated density, g/cc	3.30891566
Calculated liquid density, g/cc	2.82776341	Calculated liquid density, g/cc	2.84575002	Calculated liquid density, g/cc	2.82261452
Calculated viscosity, dry, Pas	0.09483016	Calculated viscosity, dry, Pas	0.07774037	Calculated viscosity, dry, Pas	0.10513822
Calculated viscosity, wet, Pas	0.09141061	Calculated viscosity, wet, Pas	0.07500392	Calculated viscosity, wet, Pas	0.10111959
Estimated liquidus temp., °C	1247.18465	Estimated liquidus temp., °C	1264.45468	Estimated liquidus temp., °C	1234.03603
Estimated H2O content, wt. %	0.28431263	Estimated H2O content, wt. %	0.23780969	Estimated H2O content, wt. %	0.32297746
Normalized analysis		***Normalized analysis***		***Normalized analysis***	
SiO2	48.1623212	SiO2	47.2201485	SiO2	48.8796491
TiO2	1.15260256	TiO2	1.19314294	TiO2	1.15070841
Al2O3	4.18847537	Al2O3	4.40856204	Al2O3	4.11403714
Fe2O3	1.72890384	Fe2O3	1.95351878	Fe2O3	1.75355741
FeO	11.4084152	FeO	12.8905685	FeO	11.5710953
MnO	0.21611298	MnO	0.212339	MnO	0.21384846
MgO	22.7433184	MgO	23.9639726	MgO	22.3013399

CaO	9.58100878	CaO	7.3307511	CaO	9.22603377
Na2O	0.39106158	Na2O	0.46512352	Na2O	0.39714715
K2O	0.05145547	K2O	0.0505569	K2O	0.04073304
P2O5	0.02058219	P2O5	0.03033414	P2O5	0.02036652
CO2	0	CO2	0	CO2	0
SO3	0	SO3	0	SO3	0
S	0	S	0	S	0
F	0	F	0	F	0
Cl	0	Cl	0	Cl	0
Sr	0.0054279	Sr	0.01023574	Sr	0.00502178
Ba	0.00128682	Ba	0.00156914	Ba	0.00085268
Ni	0	Ni	0	Ni	0
Cr	0.34444031	Cr	0.26453335	Cr	0.32148264
Zr	0.00458741	Zr	0.00464389	Zr	0.00412668
Total	100	Total	100	Total	100

Table 8.5: *Normalisation calculation values of samples AM19-008-1, AM19-008-3 and AM19-008-4.*

Sample	Results		Sample	Results		Sample	Results	
AM19-008-1	Quartz	0	AM19-008-3	Quartz	0	AM19-008-4	Quartz	0
	Plagioclase	1.70637123		Plagioclase	9.24197729		Plagioclase	8.66207346
	(Albite)	0.51504261		(Albite)	1.38121788		(Albite)	1.11346229
	(Anorthite)	1.19132862		(Anorthite)	7.86075941		(Anorthite)	7.54861116
	Orthoclase	0.0604031		Orthoclase	0.18339243		Orthoclase	0.1825735
	Nepheline	0		Nepheline	0		Nepheline	0
	Leucite	0		Leucite	0		Leucite	0
	Kalsilite	0		Kalsilite	0		Kalsilite	0
	Corundum	0		Corundum	0		Corundum	0
	Diopside	7.60761963		Diopside	6.9056336		Diopside	2.91198727
	Hypersthene	9.70999165		Hypersthene	72.5673029		Hypersthene	70.9768603
	Wollastonite	0		Wollastonite	0		Wollastonite	0
	Olivine	76.8396734		Olivine	6.65338465		Olivine	12.882226
	Larnite	0		Larnite	0		Larnite	0
	Aegirine	0		Aegirine	0		Aegirine	0
	K2SiO3	0		K2SiO3	0		K2SiO3	0
	Na2SiO3	0		Na2SiO3	0		Na2SiO3	0
	Rutile	0		Rutile	0		Rutile	0
	Ilmenite	0.28900208		Ilmenite	1.27880386		Ilmenite	1.15345646
	Magnetite	3.58304269		Magnetite	2.76017511		Magnetite	2.88828498
	Hematite	0		Hematite	0		Hematite	0
	Apatite	0.02402793		Apatite	0.02416387		Apatite	0.02397488
	Zircon	0.00081542		Zircon	0.00307512		Zircon	0.00264426
	Perovskite	0		Perovskite	0		Perovskite	0
	Chromite	0.17905287		Chromite	0.38209116		Chromite	0.31591896
	Titanite	0		Titanite	0		Titanite	0
	Pyrite	0		Pyrite	0		Pyrite	0
	Halite	0		Halite	0		Halite	0

Fluorite	0	Fluorite	0	Fluorite	0
Anhydrite	0	Anhydrite	0	Anhydrite	0
Na2SO4	0	Na2SO4	0	Na2SO4	0
Calcite	0	Calcite	0	Calcite	0
Na2CO3	0	Na2CO3	0	Na2CO3	0
Total	100	Total	100	Total	100
Fe3+/(Total Fe) in rock	11.9999574	Fe3+/(Total Fe) in rock	11.9999574	Fe3+/(Total Fe) in rock	11.9999574
Mg/(Mg+Total Fe) in rock	78.1266836	Mg/(Mg+Total Fe) in rock	76.3925958	Mg/(Mg+Total Fe) in rock	76.6664594
Mg/(Mg+Fe2+) in rock	80.2326204	Mg/(Mg+Fe2+) in rock	78.6197991	Mg/(Mg+Fe2+) in rock	78.8749703
Mg/(Mg+Fe2+) in silicates	81.2867831	Mg/(Mg+Fe2+) in silicates	80.4644484	Mg/(Mg+Fe2+) in silicates	80.568547
Ca/(Ca+Na) in rock	95.171271	Ca/(Ca+Na) in rock	91.8657874	Ca/(Ca+Na) in rock	90.4958459
Plagioclase An content	68.5550006	Plagioclase An content	84.2869989	Plagioclase An content	86.467926
Differentiation Index	1.76677434	Differentiation Index	9.42536972	Differentiation Index	8.84464696
Aluminum Saturation Index	0.13579878	Aluminum Saturation Index	0.50183761	Aluminum Saturation Index	0.69381497
Alkalinity Index	4.93014737	Alkalinity Index	10.5516396	Alkalinity Index	12.097311
Calculated density, g/cc	3.44785035	Calculated density, g/cc	3.33548519	Calculated density, g/cc	3.34743283
Calculated liquid density, g/cc	2.97169488	Calculated liquid density, g/cc	2.80628067	Calculated liquid density, g/cc	2.82117738
Calculated viscosity, dry, Pas	-0.0357995	Calculated viscosity, dry, Pas	0.12388403	Calculated viscosity, dry, Pas	0.10482486
Calculated viscosity, wet, Pas	-0.03650318	Calculated viscosity, wet, Pas	0.11718764	Calculated viscosity, wet, Pas	0.09944953
Estimated liquidus temp., °C	1382.45531	Estimated liquidus temp., °C	1181.87147	Estimated liquidus temp., °C	1198.56633
Estimated H2O content, wt. %	0.10425586	Estimated H2O content, wt. %	0.52127829	Estimated H2O content, wt. %	0.44748232
Normalised analysis		***Normalised analysis***		***Normalised analysis***	
SiO2	40.7825802	SiO2	51.7255063	SiO2	50.8147118
TiO2	0.15217381	TiO2	0.67334979	TiO2	0.60734715
Al2O3	0.5478257	Al2O3	3.18310808	Al2O3	3.01649086
Fe2O3	2.47130262	Fe2O3	1.90374349	Fe2O3	1.99209866
FeO	16.307238	FeO	12.5621192	FeO	13.1451433
MnO	0.23333317	MnO	0.2346522	MnO	0.23281641
MgO	37.1304088	MgO	25.9137645	MgO	27.5330709

CaO	2.17101297	CaO	3.33614213	CaO	2.26742937
Na2O	0.06086952	Na2O	0.16323631	Na2O	0.13159188
K2O	0.01014492	K2O	0.03060681	K2O	0.03036736
P2O5	0.01014492	P2O5	0.01020227	P2O5	0.01012245
CO2	0	CO2	0	CO2	0
SO3	0	SO3	0	SO3	0
S	0	S	0	S	0
F	0	F	0	F	0
Cl	0	Cl	0	Cl	0
Sr	0.00070784	Sr	0.00135129	Sr	0.00165196
Ba	0.00012459	Ba	0.00069481	Ba	0.00085889
Ni	0	Ni	0	Ni	0
Cr	0.12158484	Cr	0.25945555	Cr	0.21452143
Zr	0.00054815	Zr	0.00206719	Zr	0.00177755
Total	100	Total	100	Total	100

Table 8.6: *Normalisation calculation values of samples AM19-XX, AM19-005-1A and AM19-005-1B.*

Sample	Results		Sample	Results		Sample	Results	
AM19-XX	Quartz	0	**AM19-005-1A**	Quartz	0	**AM19-005-1B**	Quartz	0
	Plagioclase	14.4475125		Plagioclase	1.85261373		Plagioclase	1.46116407
	(Albite)	4.26143673		(Albite)	0.48535271		(Albite)	0.29379241
	(Anorthite)	10.1860758		(Anorthite)	1.36726102		(Anorthite)	1.16737165
	Orthoclase	0.06127909		Orthoclase	0.06853785		Orthoclase	0.0693798
	Nepheline	0		Nepheline	0		Nepheline	0
	Leucite	0		Leucite	0		Leucite	0
	Kalsilite	0		Kalsilite	0		Kalsilite	0
	Corundum	0		Corundum	0		Corundum	0
	Diopside	62.485058		Diopside	11.2763219		Diopside	7.65441383
	Hypersthene	6.01045926		Hypersthene	15.5187074		Hypersthene	16.2546583
	Wollastonite	0		Wollastonite	0		Wollastonite	0
	Olivine	11.963768		Olivine	67.7487076		Olivine	71.0287244
	Larnite	0		Larnite	0		Larnite	0
	Aegirine	0		Aegirine	0		Aegirine	0
	K2SiO3	0		K2SiO3	0		K2SiO3	0
	Na2SiO3	0		Na2SiO3	0		Na2SiO3	0
	Rutile	0		Rutile	0		Rutile	0
	Ilmenite	2.37205917		Ilmenite	0.26144871		Ilmenite	0.21980477
	Magnetite	1.64030996		Magnetite	2.99393764		Magnetite	3.0506753
	Hematite	0		Hematite	0		Hematite	0
	Apatite	0.0238567		Apatite	0.02717139		Apatite	0.02741219
	Zircon	0.00708406		Zircon	0.00069157		Zircon	0.0020931
	Perovskite	0		Perovskite	0		Perovskite	0
	Chromite	0.98861322		Chromite	0.2518623		Chromite	0.23167427
	Titanite	0		Titanite	0		Titanite	0
	Pyrite	0		Pyrite	0		Pyrite	0
	Halite	0		Halite	0		Halite	0

Fluorite	0	Fluorite	0	Fluorite	0
Anhydrite	0	Anhydrite	0	Anhydrite	0
Na2SO4	0	Na2SO4	0	Na2SO4	0
Calcite	0	Calcite	0	Calcite	0
Na2CO3	0	Na2CO3	0	Na2CO3	0
Total	100	Total	100	Total	100
Fe3+/(Total Fe) in rock	11.9999574	Fe3+/(Total Fe) in rock	11.9999574	Fe3+/(Total Fe) in rock	11.9999574
Mg/(Mg+Total Fe) in rock	77.9986861	Mg/(Mg+Total Fe) in rock	81.0099045	Mg/(Mg+Total Fe) in rock	81.2322077
Mg/(Mg+Fe2+) in rock	80.1138095	Mg/(Mg+Fe2+) in rock	82.8990099	Mg/(Mg+Fe2+) in rock	83.1038112
Mg/(Mg+Fe2+) in silicates	84.092172	Mg/(Mg+Fe2+) in silicates	83.8721903	Mg/(Mg+Fe2+) in silicates	84.0386447
Ca/(Ca+Na) in rock	95.1497004	Ca/(Ca+Na) in rock	96.8033199	Ca/(Ca+Na) in rock	97.2077779
Plagioclase An content	69.2585965	Plagioclase An content	72.6415268	Plagioclase An content	78.9257927
Differentiation Index	14.5087916	Differentiation Index	1.92115159	Differentiation Index	1.53054387
Aluminum Saturation Index	0.13723564	Aluminum Saturation Index	0.10493145	Aluminum Saturation Index	0.12382728
Alkalinity Index	5.44774162	Alkalinity Index	5.69407406	Alkalinity Index	7.14555327
Calculated density, g/cc	3.25080771	Calculated density, g/cc	3.40438895	Calculated density, g/cc	3.41080939
Calculated liquid density, g/cc	2.78454767	Calculated liquid density, g/cc	2.92561372	Calculated liquid density, g/cc	2.9337354
Calculated viscosity, dry, Pas	0.14105102	Calculated viscosity, dry, Pas	-0.01472938	Calculated viscosity, dry, Pas	-0.02173704
Calculated viscosity, wet, Pas	0.13588498	Calculated viscosity, wet, Pas	-0.01562209	Calculated viscosity, wet, Pas	-0.02256322
Estimated liquidus temp., °C	1223.49004	Estimated liquidus temp., °C	1343.54084	Estimated liquidus temp., °C	1351.41978
Estimated H2O content, wt. %	0.36889897	Estimated H2O content, wt. %	0.11996149	Estimated H2O content, wt. %	0.11499589
Normalized analysis		***Normalized analysis***		***Normalized analysis***	
SiO2	49.4549896	SiO2	42.9055735	SiO2	42.475735
TiO2	1.24896511	TiO2	0.13766494	TiO2	0.1157377
Al2O3	4.57282388	Al2O3	0.60802016	Al2O3	0.4976721
Fe2O3	1.13132066	Fe2O3	2.06497413	Fe2O3	2.10411134
FeO	7.46517851	FeO	13.6260223	FeO	13.8842747
MnO	0.17122909	MnO	0.20649741	MnO	0.20832786
MgO	16.8711013	MgO	37.0548135	MgO	38.3091779

CaO	17.8783313	CaO	3.1433495	CaO	2.18744248
Na2O	0.50361497	Na2O	0.05736039	Na2O	0.03472131
K2O	0.0100723	K2O	0.01147208	K2O	0.01157377
P2O5	0.0100723	P2O5	0.01147208	P2O5	0.01157377
CO2	0	CO2	0	CO2	0
SO3	0	SO3	0	SO3	0
S	0	S	0	S	0
F	0	F	0	F	0
Cl	0	Cl	0	Cl	0
Sr	0.00576513	Sr	0.00108534	Sr	0.00065698
Ba	0.00048354	Ba	0.00020493	Ba	0.00027135
Ni	0	Ni	0	Ni	0
Cr	0.67129034	Cr	0.17102485	Cr	0.15731666
Zr	0.00476199	Zr	0.0004649	Zr	0.00140705
Total	100	Total	100	Total	100

Table 8.7: *Normalisation calculation values of samples AM19-XX1, AM19-002-1 and AM19-002-2.*

Sample	Results		Sample	Results		Sample	Results	
AM19-XX1	Quartz	0	**AM19-002-1**	Quartz	0	**AM19-002-2**	Quartz	0
	Plagioclase	3.26575418		Plagioclase	2.25722902		Plagioclase	1.55956918
	(Albite)	1.19861753		(Albite)	0.93990495		(Albite)	0.57304081
	(Anorthite)	2.06713665		(Anorthite)	1.31732407		(Anorthite)	0.98652837
	Orthoclase	0.06040889		Orthoclase	0.0602892		Orthoclase	0.067571
	Nepheline	0		Nepheline	0		Nepheline	0
	Leucite	0		Leucite	0		Leucite	0
	Kalsilite	0		Kalsilite	0		Kalsilite	0
	Corundum	0		Corundum	0		Corundum	0
	Diopside	16.3653203		Diopside	12.7686954		Diopside	6.8271462
	Hypersthene	4.57187618		Hypersthene	4.23558454		Hypersthene	12.3167022
	Wollastonite	0		Wollastonite	0		Wollastonite	0
	Olivine	72.4041172		Olivine	77.2152032		Olivine	75.6903927
	Larnite	0		Larnite	0		Larnite	0
	Aegirine	0		Aegirine	0		Aegirine	0
	K2SiO3	0		K2SiO3	0		K2SiO3	0
	Na2SiO3	0		Na2SiO3	0		Na2SiO3	0
	Rutile	0		Rutile	0		Rutile	0
	Ilmenite	0.51884083		Ilmenite	0.2876738		Ilmenite	0.21436412
	Magnetite	2.57901724		Magnetite	2.87258601		Magnetite	3.09299267
	Hematite	0		Hematite	0		Hematite	0
	Apatite	0.02396497		Apatite	0.02391749		Apatite	0.02673367
	Zircon	0.00162656		Zircon	0.00060875		Zircon	0.00045362
	Perovskite	0		Perovskite	0		Perovskite	0
	Chromite	0.20907367		Chromite	0.27821257		Chromite	0.20407468
	Titanite	0		Titanite	0		Titanite	0
	Pyrite	0		Pyrite	0		Pyrite	0
	Halite	0		Halite	0		Halite	0

Fluorite	0	Fluorite	0	Fluorite	0
Anhydrite	0	Anhydrite	0	Anhydrite	0
Na2SO4	0	Na2SO4	0	Na2SO4	0
Calcite	0	Calcite	0	Calcite	0
Na2CO3	0	Na2CO3	0	Na2CO3	0
Total	100	Total	100	Total	100
Fe3+/(Total Fe) in rock	11.9999574	Fe3+/(Total Fe) in rock	11.9999574	Fe3+/(Total Fe) in rock	11.9999574
Mg/(Mg+Total Fe) in rock	83.4545334	Mg/(Mg+Total Fe) in rock	82.2334468	Mg/(Mg+Total Fe) in rock	81.3156187
Mg/(Mg+Fe2+) in rock	85.1450448	Mg/(Mg+Fe2+) in rock	84.0248386	Mg/(Mg+Fe2+) in rock	83.1806263
Mg/(Mg+Fe2+) in silicates	86.1575837	Mg/(Mg+Fe2+) in silicates	84.9721242	Mg/(Mg+Fe2+) in silicates	84.1061683
Ca/(Ca+Na) in rock	94.7035418	Ca/(Ca+Na) in rock	94.5894003	Ca/(Ca+Na) in rock	94.0621761
Plagioclase An content	61.9120563	Plagioclase An content	56.9154057	Plagioclase An content	61.8705355
Differentiation Index	3.32616308	Differentiation Index	2.31751822	Differentiation Index	1.62714018
Aluminum Saturation Index	0.11711152	Aluminum Saturation Index	0.10315531	Aluminum Saturation Index	0.13383778
Alkalinity Index	4.10553376	Alkalinity Index	3.49349455	Alkalinity Index	3.92585809
Calculated density, g/cc	3.36905307	Calculated density, g/cc	3.3954321	Calculated density, g/cc	3.41310875
Calculated liquid density, g/cc	2.91177469	Calculated liquid density, g/cc	2.93475791	Calculated liquid density, g/cc	2.94281878
Calculated viscosity, dry, Pas	-0.01882713	Calculated viscosity, dry, Pas	-0.03010324	Calculated viscosity, dry, Pas	-0.02987032
Calculated viscosity, wet, Pas	-0.0196555	Calculated viscosity, wet, Pas	-0.03084204	Calculated viscosity, wet, Pas	-0.03062191
Estimated liquidus temp., °C	1352.89217	Estimated liquidus temp., °C	1369.23622	Estimated liquidus temp., °C	1364.48494
Estimated H2O content, wt. %	0.11412688	Estimated H2O content, wt. %	0.1074066	Estimated H2O content, wt. %	0.10889072
Normalised analysis		***Normalised analysis***		***Normalised analysis***	
SiO2	42.395408	SiO2	41.5037524	SiO2	41.7629604
TiO2	0.27319237	TiO2	0.15147355	TiO2	0.11287287
Al2O3	1.00170534	Al2O3	0.67658185	Al2O3	0.48535332
Fe2O3	1.77878585	Fe2O3	1.98127402	Fe2O3	2.13329717

FeO	11.7375687	FeO	13.0737153	FeO	14.0768615
MnO	0.18212824	MnO	0.20196473	MnO	0.20317116
MgO	37.7410195	MgO	38.5752637	MgO	39.0540116
CaO	4.58356082	CaO	3.51418633	CaO	1.9414133
Na2O	0.1416553	Na2O	0.1110806	Na2O	0.06772372
K2O	0.01011824	K2O	0.01009824	K2O	0.01128729
P2O5	0.01011824	P2O5	0.01009824	P2O5	0.01128729
CO2	0	CO2	0	CO2	0
SO3	0	SO3	0	SO3	0
S	0	S	0	S	0
F	0	F	0	F	0
Cl	0	Cl	0	Cl	0
Sr	0.00150768	Sr	0.00101508	Sr	0.00064072
Ba	0.00016945	Ba	0.00016911	Ba	0.00023943
Ni	0	Ni	0	Ni	0
Cr	0.14196882	Cr	0.18891761	Cr	0.13857528
Zr	0.00109342	Zr	0.00040922	Zr	0.00030494
Total	100	Total	100	Total	100

Table 8.8: *Normalisation calculation values of samples AM19-002-3, AM19-002-4 and AM19-002-5.*

Sample	Results		Sample	Results		Sample	Results	
AM19-002-3	Quartz	0	AM19-002-4	Quartz	0	AM19-002-5	Quartz	0
	Plagioclase	2.183279		Plagioclase	1.11530281		Plagioclase	1.90372965
	(Albite)	0.67623276		(Albite)	0.5235509		(Albite)	0.77001342
	(Anorthite)	1.50704624		(Anorthite)	0.59175191		(Anorthite)	1.13371623
	Orthoclase	0.06894932		Orthoclase	0.06186072		Orthoclase	0.06077745
	Nepheline	0		Nepheline	0		Nepheline	0
	Leucite	0		Leucite	0		Leucite	0
	Kalsilite	0		Kalsilite	0		Kalsilite	0
	Corundum	0		Corundum	0		Corundum	0
	Diopside	9.30066433		Diopside	4.72705777		Diopside	11.4604273
	Hypersthene	15.277268		Hypersthene	1.46116672		Hypersthene	3.81420516
	Wollastonite	0		Wollastonite	0		Wollastonite	0
	Olivine	69.5085258		Olivine	89.1446083		Olivine	79.3000949
	Larnite	0		Larnite	0		Larnite	0
	Aegirine	0		Aegirine	0		Aegirine	0
	K2SiO3	0		K2SiO3	0		K2SiO3	0
	Na2SiO3	0		Na2SiO3	0		Na2SiO3	0
	Rutile	0		Rutile	0		Rutile	0
	Ilmenite	0.28187679		Ilmenite	0.15668068		Ilmenite	0.23043838
	Magnetite	3.03916046		Magnetite	3.12191403		Magnetite	2.9554873
	Hematite	0		Hematite	0		Hematite	0
	Apatite	0.02704099		Apatite	0.02442486		Apatite	0.0239486
	Zircon	0.00114709		Zircon	0.00497333		Zircon	0.00060954
	Perovskite	0		Perovskite	0		Perovskite	0
	Chromite	0.31208825		Chromite	0.18201075		Chromite	0.25028173
	Titanite	0		Titanite	0		Titanite	0
	Pyrite	0		Pyrite	0		Pyrite	0
	Halite	0		Halite	0		Halite	0

Fluorite	0	Fluorite	0	Fluorite	0
Anhydrite	0	Anhydrite	0	Anhydrite	0
Na2SO4	0	Na2SO4	0	Na2SO4	0
Calcite	0	Calcite	0	Calcite	0
Na2CO3	0	Na2CO3	0	Na2CO3	0
Total	100	Total	100	Total	100
Fe3+/(Total Fe) in rock	11.9999574	Fe3+/(Total Fe) in rock	11.9999574	Fe3+/(Total Fe) in rock	11.9999574
Mg/(Mg+Total Fe) in rock	80.9414854	Mg/(Mg+Total Fe) in rock	82.1782143	Mg/(Mg+Total Fe) in rock	81.9876388
Mg/(Mg+Fe2+) in rock	82.835955	Mg/(Mg+Fe2+) in rock	83.9740898	Mg/(Mg+Fe2+) in rock	83.7989323
Mg/(Mg+Fe2+) in silicates	83.8436832	Mg/(Mg+Fe2+) in silicates	84.8178997	Mg/(Mg+Fe2+) in silicates	84.719063
Ca/(Ca+Na) in rock	94.8645823	Ca/(Ca+Na) in rock	92.2365612	Ca/(Ca+Na) in rock	95.0237327
Plagioclase An content	67.7474808	Plagioclase An content	51.5813424	Plagioclase An content	58.1192309
Differentiation Index	2.25222833	Differentiation Index	1.17716352	Differentiation Index	1.9645071
Aluminum Saturation Index	0.1400189	Aluminum Saturation Index	0.13163112	Aluminum Saturation Index	0.09845513
Alkalinity Index	4.84199368	Alkalinity Index	2.92156881	Alkalinity Index	3.58754322
Calculated density, g/cc	3.40593309	Calculated density, g/cc	3.42020837	Calculated density, g/cc	3.403231
Calculated liquid density, g/cc	2.92973688 -	Calculated liquid density, g/cc	2.96817342 -	Calculated liquid density, g/cc	2.94277977 -
Calculated viscosity, dry, Pas	0.01844525 -	Calculated viscosity, dry, Pas	0.05285881 -	Calculated viscosity, dry, Pas	0.03451628 -
Calculated viscosity, wet, Pas	0.01929662	Calculated viscosity, wet, Pas	0.05348572	Calculated viscosity, wet, Pas	0.03522678
Estimated liquidus temp., °C	1349.40791	Estimated liquidus temp., °C	1402.242	Estimated liquidus temp., °C	1375.66038
Estimated H2O content, wt. %	0.11640456	Estimated H2O content, wt. %	0.10307314	Estimated H2O content, wt. %	0.1056252
Normalised analysis		***Normalised analysis***		***Normalised analysis***	
SiO2	42.5854934	SiO2	39.7031095	SiO2	41.1532796
TiO2	0.14842129	TiO2	0.08249997	TiO2	0.12133645
Al2O3	0.69643836	Al2O3	0.32999987	Al2O3	0.57634814
Fe2O3	2.0961653	Fe2O3	2.15324916	Fe2O3	2.03845238
FeO	13.8318416	FeO	14.2085175	FeO	13.4510148
MnO	0.2055064	MnO	0.21656242	MnO	0.20222742
MgO	37.4478333	MgO	41.7656087	MgO	39.0298917

CaO	2.67158323	CaO	1.33031198	CaO	3.14463635
Na2O	0.07991916	Na2O	0.06187498	Na2O	0.09100234
K2O	0.01141702	K2O	0.0103125	K2O	0.01011137
P2O5	0.01141702	P2O5	0.0103125	P2O5	0.01011137
CO2	0	CO2	0	CO2	0
SO3	0	SO3	0	SO3	0
S	0	S	0	S	0
F	0	F	0	F	0
Cl	0	Cl	0	Cl	0
Sr	0.00086411	Sr	0.00045123	Sr	0.00094465
Ba	0.00040789	Ba	0.00025329	Ba	0.00028222
Ni	0	Ni	0	Ni	0
Cr	0.21192076	Cr	0.1235932	Cr	0.16995143
Zr	0.00077111	Zr	0.00334324	Zr	0.00040975
Total	100	Total	100	Total	100

Table 8.9: *Normalisation calculation values of samples AM19-002-6, AM19-002-7 and AM19-002-8.*

Sample	Results		Sample	Results		Sample	Results	
AM19-002-6	Quartz	0	AM19-002-7	Quartz	0	AM19-002-8	Quartz	0
	Plagioclase	2.05832776		Plagioclase	3.19165121		Plagioclase	1.81646258
	(Albite)	0.8572663		(Albite)	1.27169105		(Albite)	0.84753345
	(Anorthite)	1.20106146		(Anorthite)	1.91996016		(Anorthite)	0.96892913
	Orthoclase	0.06089792		Orthoclase	0.05981893		Orthoclase	0.05992234
	Nepheline	0		Nepheline	0		Nepheline	0
	Leucite	0		Leucite	0		Leucite	0
	Kalsilite	0		Kalsilite	0		Kalsilite	0
	Corundum	0		Corundum	0		Corundum	0
	Diopside	12.193961		Diopside	19.0173782		Diopside	10.0486365
	Hypersthene	3.17675369		Hypersthene	3.68886655		Hypersthene	3.57954221
	Wollastonite	0		Wollastonite	0		Wollastonite	0
	Olivine	79.0012956		Olivine	70.4285537		Olivine	81.0539755
	Larnite	0		Larnite	0		Larnite	0
	Aegirine	0		Aegirine	0		Aegirine	0
	K2SiO3	0		K2SiO3	0		K2SiO3	0
	Na2SiO3	0		Na2SiO3	0		Na2SiO3	0
	Rutile	0		Rutile	0		Rutile	0
	Ilmenite	0.2501364		Ilmenite	0.39960181		Ilmenite	0.2282737
	Magnetite	2.97015893		Magnetite	2.70200462		Magnetite	2.95386459
	Hematite	0		Hematite	0		Hematite	0
	Apatite	0.02399607		Apatite	0.02373093		Apatite	0.02372363
	Zircon	0.00061075		Zircon	0.00100667		Zircon	0.00060382
	Perovskite	0		Perovskite	0		Perovskite	0
	Chromite	0.26386188		Chromite	0.48738743		Chromite	0.23499514
	Titanite	0		Titanite	0		Titanite	0
	Pyrite	0		Pyrite	0		Pyrite	0
	Halite	0		Halite	0		Halite	0

Fluorite	0	Fluorite	0	Fluorite	0
Anhydrite	0	Anhydrite	0	Anhydrite	0
Na2SO4	0	Na2SO4	0	Na2SO4	0
Calcite	0	Calcite	0	Calcite	0
Na2CO3	0	Na2CO3	0	Na2CO3	0
Total	100	Total	100	Total	100
Fe3+/(Total Fe) in rock	11.9999574	Fe3+/(Total Fe) in rock	11.9999574	Fe3+/(Total Fe) in rock	11.9999574
Mg/(Mg+Total Fe) in rock	81.7890707	Mg/(Mg+Total Fe) in rock	82.2680476	Mg/(Mg+Total Fe) in rock	82.2327699
Mg/(Mg+Fe2+) in rock	83.6163418	Mg/(Mg+Fe2+) in rock	84.056627	Mg/(Mg+Fe2+) in rock	84.0242166
Mg/(Mg+Fe2+) in silicates	84.55877	Mg/(Mg+Fe2+) in silicates	85.1509845	Mg/(Mg+Fe2+) in silicates	84.9297556
Ca/(Ca+Na) in rock	94.8013558	Ca/(Ca+Na) in rock	95.0479418	Ca/(Ca+Na) in rock	93.8258216
Plagioclase An content	56.9064159	Plagioclase An content	58.7291186	Plagioclase An content	51.8662012
Differentiation Index	2.11922568	Differentiation Index	3.25147015	Differentiation Index	1.87638492
Aluminum Saturation Index	0.09916537	Aluminum Saturation Index	0.09890503	Aluminum Saturation Index	0.10288559
Alkalinity Index	3.47907278	Alkalinity Index	3.72686836	Alkalinity Index	3.02280094
Calculated density, g/cc	3.4034448	Calculated density, g/cc	3.37957274	Calculated density, g/cc	3.40344357
Calculated liquid density, g/cc	2.94296684 -	Calculated liquid density, g/cc	2.91539636 -	Calculated liquid density, g/cc	2.9451116 -
Calculated viscosity, dry, Pas	0.03399868 -	Calculated viscosity, dry, Pas	0.01625269 -	Calculated viscosity, dry, Pas	0.03751801 -
Calculated viscosity, wet, Pas	0.03471152	Calculated viscosity, wet, Pas	0.01710001	Calculated viscosity, wet, Pas	0.03821153
Estimated liquidus temp., °C	1376.02221	Estimated liquidus temp., °C	1353.13415	Estimated liquidus temp., °C	1379.0738
Estimated H2O content, wt. %	0.10555799	Estimated H2O content, wt. %	0.1147947	Estimated H2O content, wt. %	0.10488592
Normalised analysis		***Normalised analysis***		***Normalised analysis***	
SiO2	41.1335402	SiO2	42.3822068	SiO2	40.9670597
TiO2	0.13170838	TiO2	0.21040812	TiO2	0.12019675
Al2O3	0.61801624	Al2O3	0.96186569	Al2O3	0.53086899
Fe2O3	2.04857188	Fe2O3	1.86361477	Fe2O3	2.03733495
FeO	13.5177897	FeO	12.2973242	FeO	13.4436413
MnO	0.20262828	MnO	0.19036925	MnO	0.20032792
MgO	38.7020009	MgO	36.3705463	MgO	39.6649282

CaO	3.34336657	CaO	5.22012524	CaO	2.7545089
Na2O	0.10131414	Na2O	0.15029151	Na2O	0.10016396
K2O	0.01013141	K2O	0.01001943	K2O	0.0100164
P2O5	0.01013141	P2O5	0.01001943	P2O5	0.0100164
CO2	0	CO2	0	CO2	0
SO3	0	SO3	0	SO3	0
S	0	S	0	S	0
F	0	F	0	F	0
Cl	0	Cl	0	Cl	0
Sr	0.00093454	Sr	0.00141002	Sr	0.0007581
Ba	0.00028278	Ba	0.00016779	Ba	0.00020129
Ni	0	Ni	0	Ni	0
Cr	0.17917291	Cr	0.33095471	Cr	0.15957135
Zr	0.00041057	Zr	0.00067671	Zr	0.00040591
Total	100	Total	100	Total	100

Table 8.10: *Normalisation calculation values of samples AM19-002-9, AM19-007-X and AM19-007-02.*

Sample	Results		Sample	Results		Sample	Results	
AM19-002-9	Quartz	0	**AM19-007-X**	Quartz	0	**AM19-007-02**	Quartz	0
	Plagioclase	1.90851952		Plagioclase	10.3493592		Plagioclase	14.2382155
	(Albite)	0.85201886		(Albite)	3.07048252		(Albite)	4.11713609
	(Anorthite)	1.05650066		(Anorthite)	7.2788767		(Anorthite)	10.1210795
	Orthoclase	0.06019865		Orthoclase	0.06169169		Orthoclase	0.06138329
	Nepheline	0		Nepheline	0		Nepheline	0
	Leucite	0		Leucite	0		Leucite	0
	Kalsilite	0		Kalsilite	0		Kalsilite	0
	Corundum	0		Corundum	0		Corundum	0
	Diopside	10.5546929		Diopside	29.6909235		Diopside	50.7686503
	Hypersthene	2.841826		Hypersthene	3.12722019		Hypersthene	4.53609932
	Wollastonite	0		Wollastonite	0		Wollastonite	0
	Olivine	81.1494633		Olivine	52.5119498		Olivine	25.6245493
	Larnite	0		Larnite	0		Larnite	0
	Aegirine	0		Aegirine	0		Aegirine	0
	K2SiO3	0		K2SiO3	0		K2SiO3	0
	Na2SiO3	0		Na2SiO3	0		Na2SiO3	0
	Rutile	0		Rutile	0		Rutile	0
	Ilmenite	0.24860528		Ilmenite	1.07203743		Ilmenite	2.11770013
	Magnetite	2.96949734		Magnetite	2.84984688		Magnetite	2.14286245
	Hematite	0		Hematite	0		Hematite	0
	Apatite	0.02384919		Apatite	0.04774836		Apatite	0.02400924
	Zircon	0.00060701		Zircon	0.0028357		Zircon	0.00651827
	Perovskite	0		Perovskite	0		Perovskite	0
	Chromite	0.24274079		Chromite	0.28638719		Chromite	0.48001211
	Titanite	0		Titanite	0		Titanite	0
	Pyrite	0		Pyrite	0		Pyrite	0
	Halite	0		Halite	0		Halite	0

Fluorite	0	Fluorite	0	Fluorite	0
Anhydrite	0	Anhydrite	0	Anhydrite	0
Na2SO4	0	Na2SO4	0	Na2SO4	0
Calcite	0	Calcite	0	Calcite	0
Na2CO3	0	Na2CO3	0	Na2CO3	0
Total	100	Total	100	Total	100
Fe3+/(Total Fe) in rock	11.9999574	Fe3+/(Total Fe) in rock	11.9999574	Fe3+/(Total Fe) in rock	11.9999574
Mg/(Mg+Total Fe) in rock	82.0839531	Mg/(Mg+Total Fe) in rock	77.0251161	Mg/(Mg+Total Fe) in rock	76.2128581
Mg/(Mg+Fe2+) in rock	83.8874648	Mg/(Mg+Fe2+) in rock	79.2088863	Mg/(Mg+Fe2+) in rock	78.4522355
Mg/(Mg+Fe2+) in silicates	84.8107409	Mg/(Mg+Fe2+) in silicates	80.8812246	Mg/(Mg+Fe2+) in silicates	81.3960438
Ca/(Ca+Na) in rock	94.0880408	Ca/(Ca+Na) in rock	93.1794101	Ca/(Ca+Na) in rock	94.402713
Plagioclase An content	53.8903802	Plagioclase An content	69.0821654	Plagioclase An content	69.8525049
Differentiation Index	1.96871817	Differentiation Index	10.4110509	Differentiation Index	14.2995988
Aluminum Saturation Index	0.10394019	Aluminum Saturation Index	0.19418242	Aluminum Saturation Index	0.16269897
Alkalinity Index	3.19390288	Alkalinity Index	5.38918825	Alkalinity Index	5.57172022
Calculated density, g/cc	3.40427909	Calculated density, g/cc	3.3446513	Calculated density, g/cc	3.27924416
Calculated liquid density, g/cc	2.94629554	Calculated liquid density, g/cc	2.88937189	Calculated liquid density, g/cc	2.82185913
Calculated viscosity, dry, Pas	-0.03783201	Calculated viscosity, dry, Pas	0.02312144	Calculated viscosity, dry, Pas	0.09657953
Calculated viscosity, wet, Pas	-0.03852334	Calculated viscosity, wet, Pas	0.02189103	Calculated viscosity, wet, Pas	0.09363126
Estimated liquidus temp., °C	1380.63686	Estimated liquidus temp., °C	1328.13546	Estimated liquidus temp., °C	1262.28953
Estimated H2O content, wt. %	0.10460645	Estimated H2O content, wt. %	0.13280899	Estimated H2O content, wt. %	0.24419036
Normalised analysis		***Normalised analysis***		***Normalised analysis***	
SiO2	40.8817862	SiO2	43.7460194	SiO2	47.338269
TiO2	0.13090227	TiO2	0.56446477	TiO2	1.11503417
Al2O3	0.56388671	Al2O3	3.27591159	Al2O3	4.52095674
Fe2O3	2.04811707	Fe2O3	1.96554695	Fe2O3	1.47792711
FeO	13.5147886	FeO	12.9699381	FeO	9.75230998
MnO	0.20138811	MnO	0.19151483	MnO	0.18246014
MgO	39.4720695	MgO	27.7192519	MgO	19.918565

CaO	2.89998878	CaO	8.97095789	CaO	14.8502279
Na2O	0.10069405	Na2O	0.36287021	Na2O	0.48656037
K2O	0.01006941	K2O	0.01007973	K2O	0.01013667
P2O5	0.01006941	P2O5	0.02015946	P2O5	0.01013667
CO2	0	CO2	0	CO2	0
SO3	0	SO3	0	SO3	0
S	0	S	0	S	0
F	0	F	0	F	0
Cl	0	Cl	0	Cl	0
Sr	0.00080974	Sr	0.00632963	Sr	0.00668905
Ba	0.00019111	Ba	0.00058518	Ba	0.00040741
Ni	0	Ni	0	Ni	0
Cr	0.16483096	Cr	0.19446421	Cr	0.32593808
Zr	0.00040805	Zr	0.0019062	Zr	0.00438165
Total	100	Total	100	Total	100

Table 8.11: *Normative calculation data for rock IUGS classification identification (Figure 4.24). Yellow = pyroxenite pegmatite and ol-websterite, orange = lherzolite, blue = dunite, green = wehrlite.*

Sample	Ol	Cpx	Opx	ID
AM19-006-1-1	5.08231018	3.61937279	75.6013189	opx
AM19-006-1-2	4.51042086	9.11950202	69.3568402	opx
AM19-006-1-3	14.7977298	1.11908058	72.1638722	opx
AM19-008-2-1	21.8350765	30.3204795	29.4492995	(ol-webst)
AM19-008-2-2	27.0131332	21.1700231	32.2205557	(ol-webst)
AM19-008-2-3	17.6268893	29.0933823	35.0989154	(ol-webst)
AM19-008-1	76.8396734	7.60761963	9.70999165	Lherz
AM19-008-3	6.65338465	6.9056336	72.5673029	opx
AM19-008-4	12.882226	2.91198727	70.9768603	opx
AM19-XX	11.963768	62.485058	6.01045926	(ol-webst)
AM19-005-1A	67.7487076	11.2763219	15.5187074	Lherz
AM19-005-1B	71.0287244	7.65441383	16.2546583	Lherz
AM19-XX1	72.4041172	16.3653203	4.57187618	Wehr
AM19-002-1	77.2152032	12.7686954	4.23558454	Wehr
AM19-002-2	75.6903927	6.8271462	12.3167022	Lherz
AM19-002-3	69.5085258	9.30066433	15.277268	Lherz
AM19-002-4	89.1446083	4.72705777	1.46116672	Dunite
AM19-002-5	79.3000949	11.4604273	3.81420516	Wehr
AM19-002-6	79.0012956	12.193961	3.17675369	Wehr
AM19-002-7	70.4285537	19.0173782	3.68886655	Wehr
AM19-002-8	81.0539755	10.0486365	3.57954221	Wehr
AM19-002-9	81.1494633	10.5546929	2.841826	Wehr
AM19-007-X	52.5119498	29.6909235	3.12722019	Wehr
AM19-007-02	25.6245493	50.7686503	4.53609932	(ol-webst)

Appendix D SEM Analysis Graphs and Tables

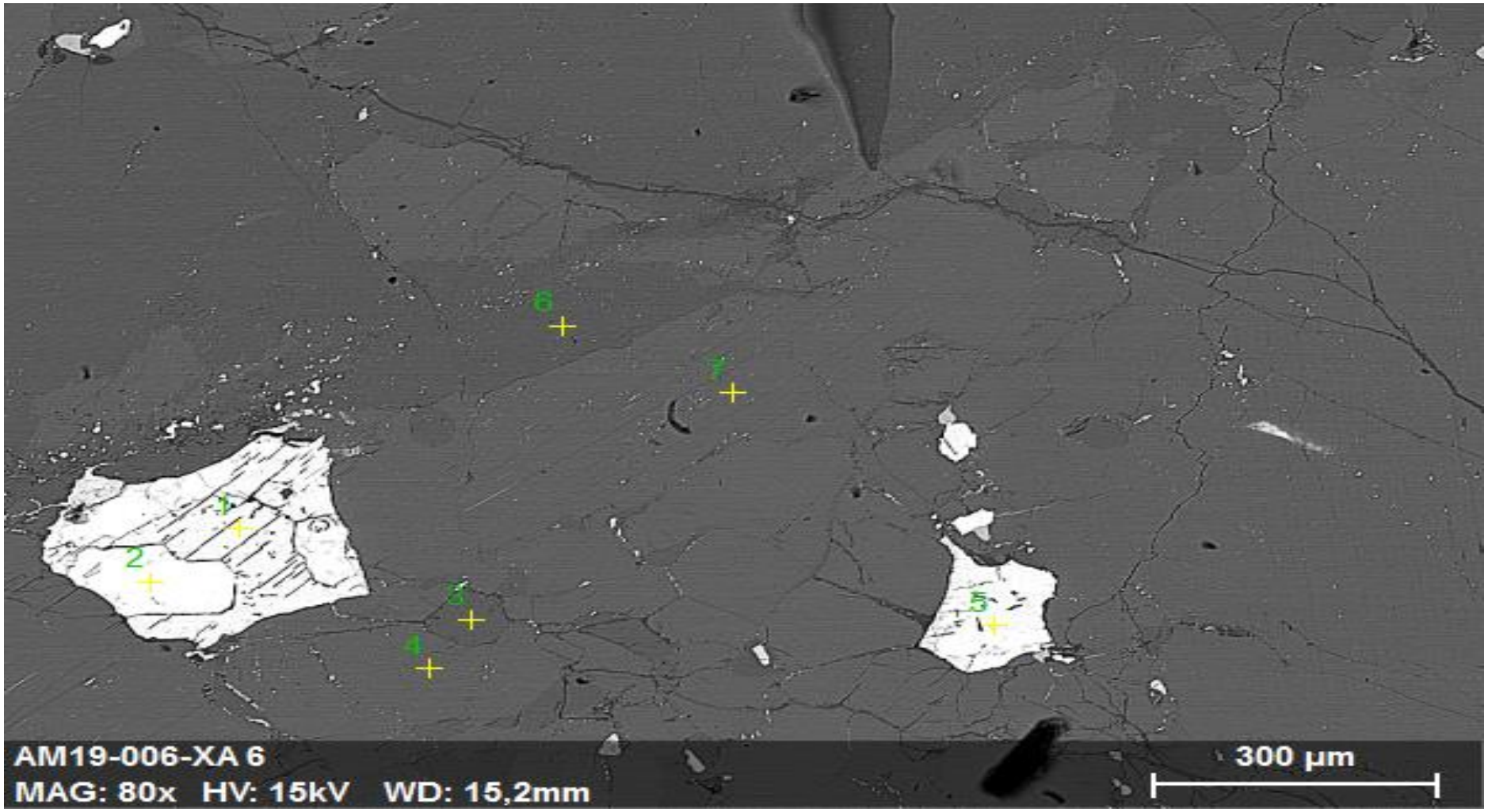

Figure 8.10: *EDS image from thin section AM19-006-XA depicting an example of host-rock to sulfide analysis.*

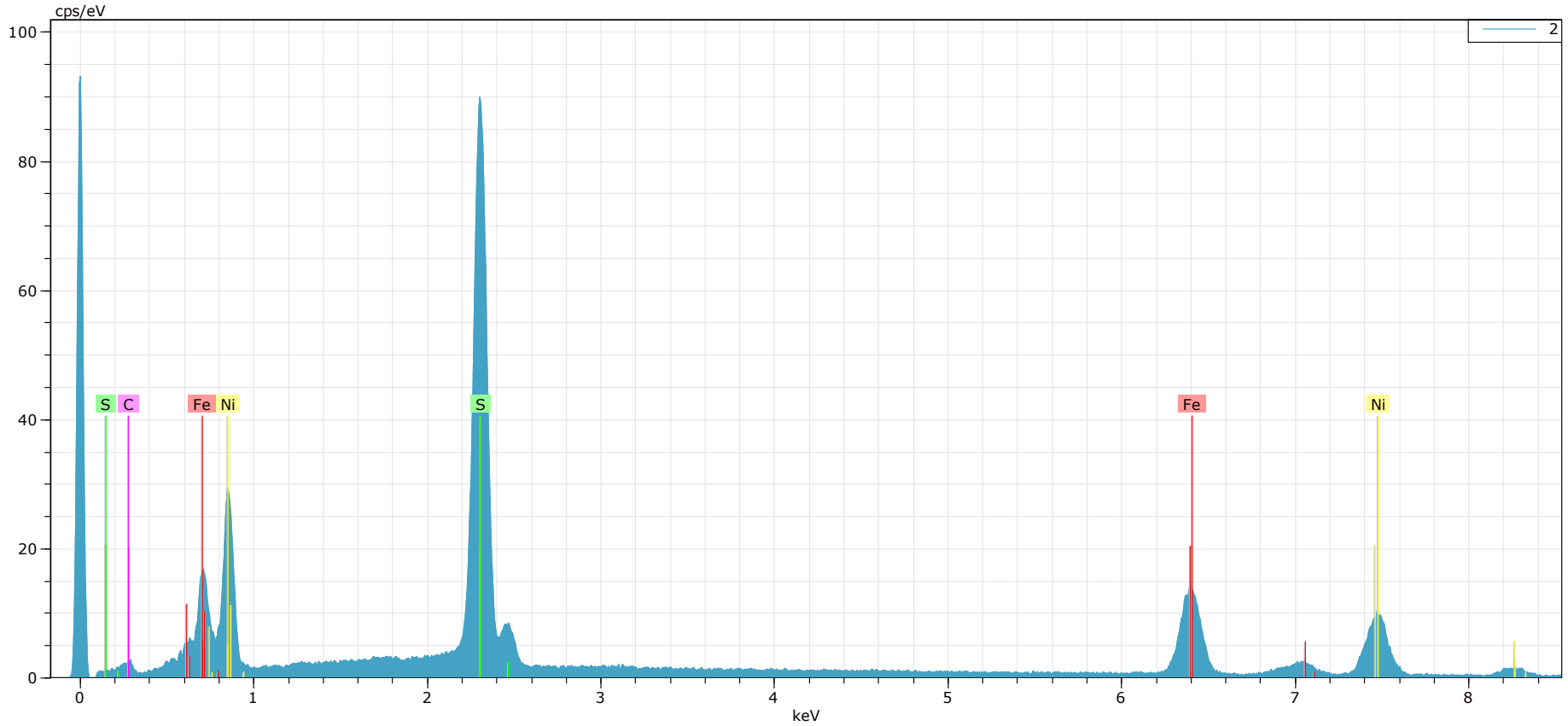

Figure 8.10a: *Graph displaying results from Fig. 6.10, analysis point 2 (point number marked green in all EDS images).*

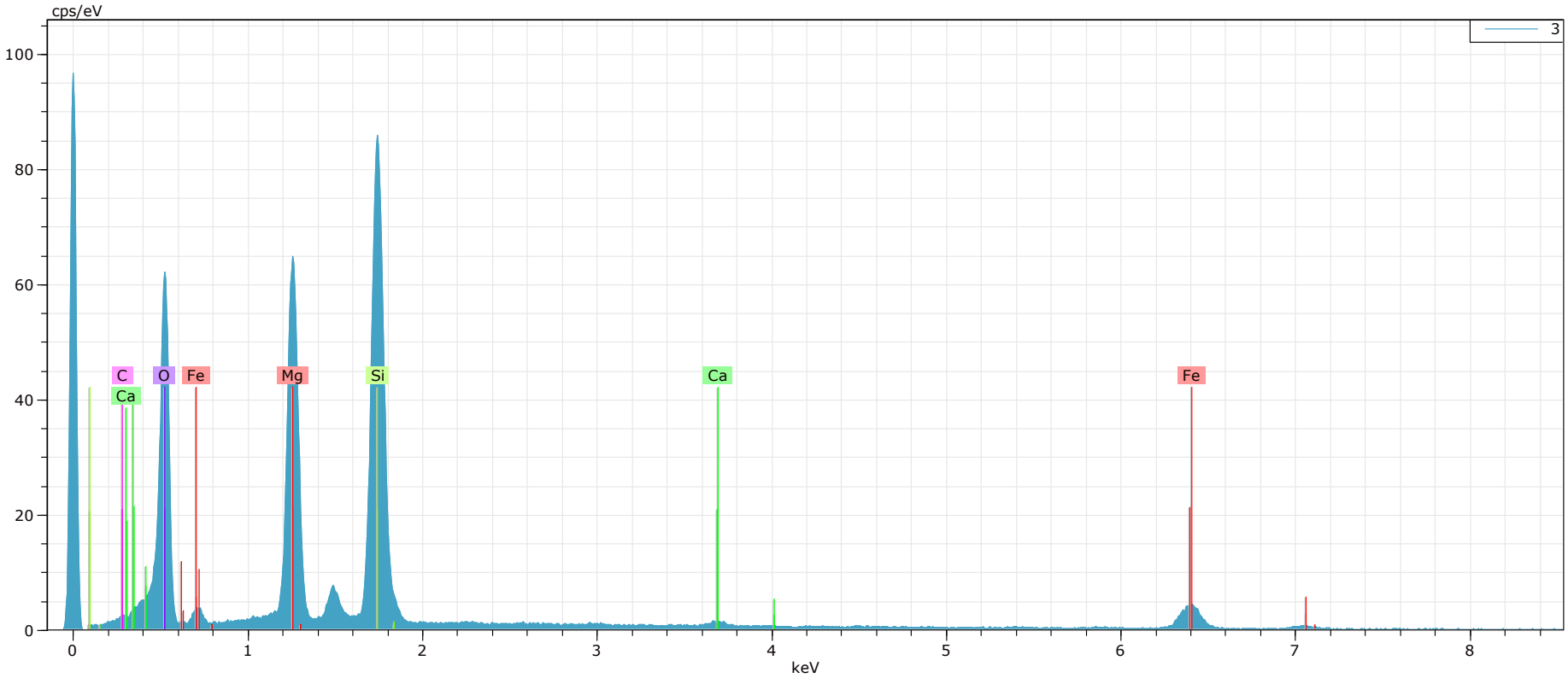

Figure 8.10b: *Graph displaying results from Fig. 6.10, analysis point 3.*

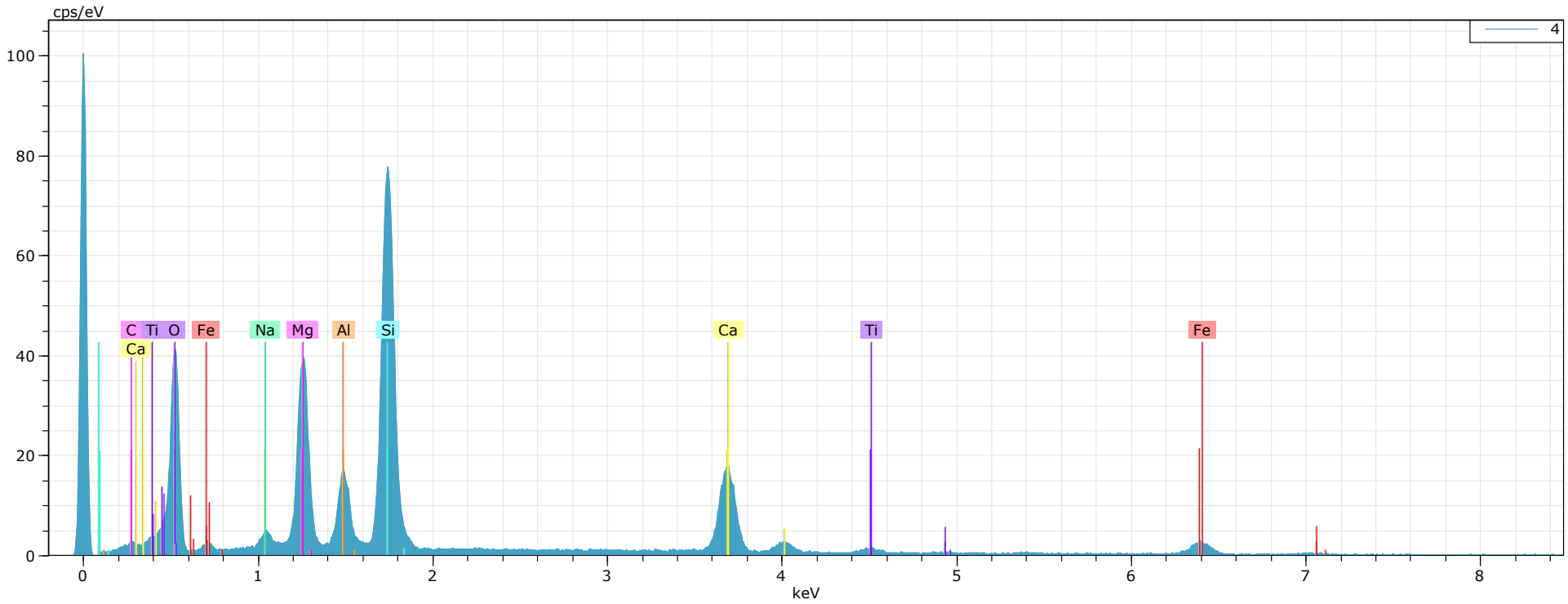

Figure 8.10c: *Graph displaying results from Fig. 6.10, analysis point 4.*

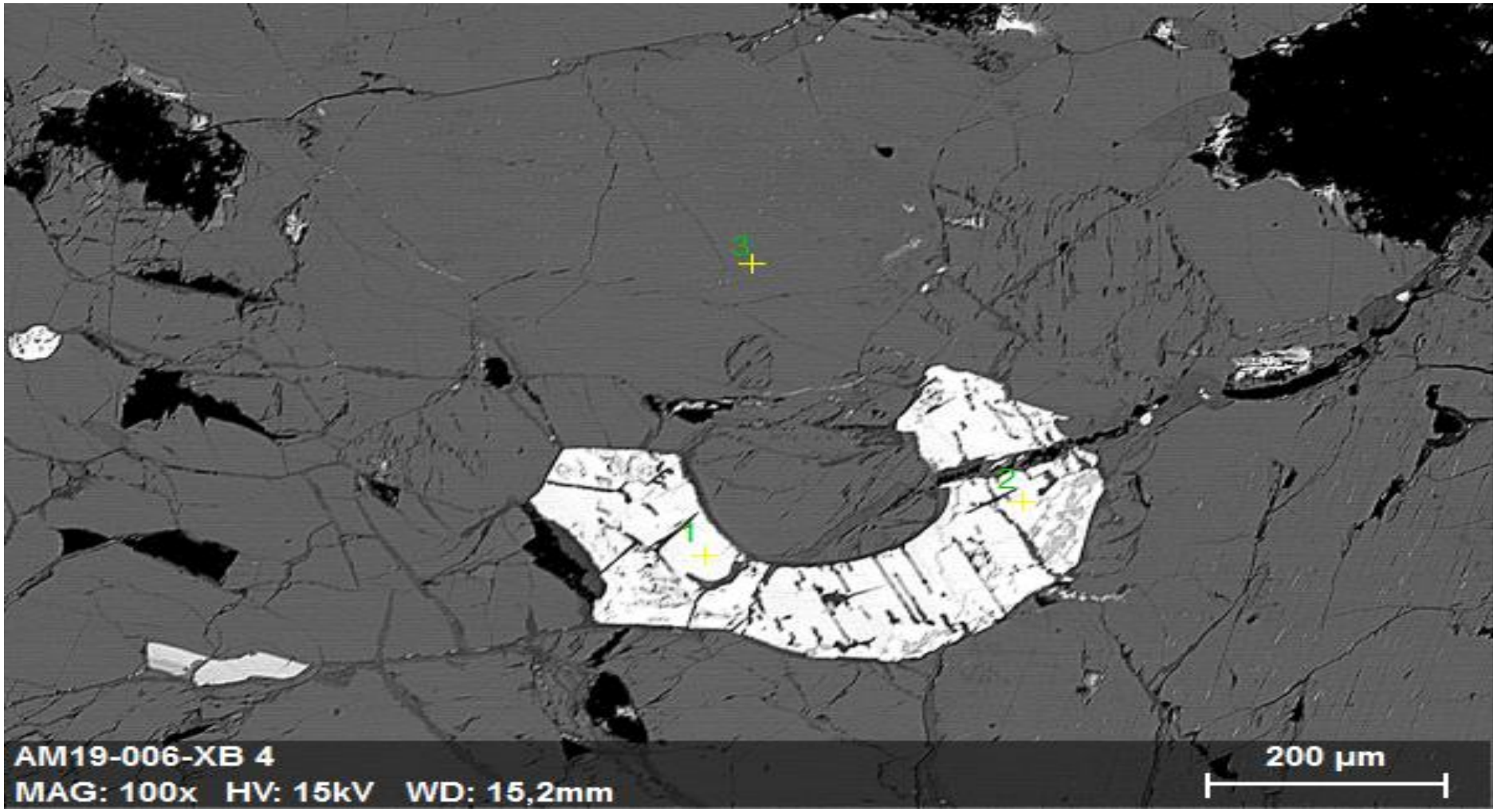

Figure 8.11: *EDS image from thin section AM19-006-XA depicting an example of host-rock to sulfide analysis.*

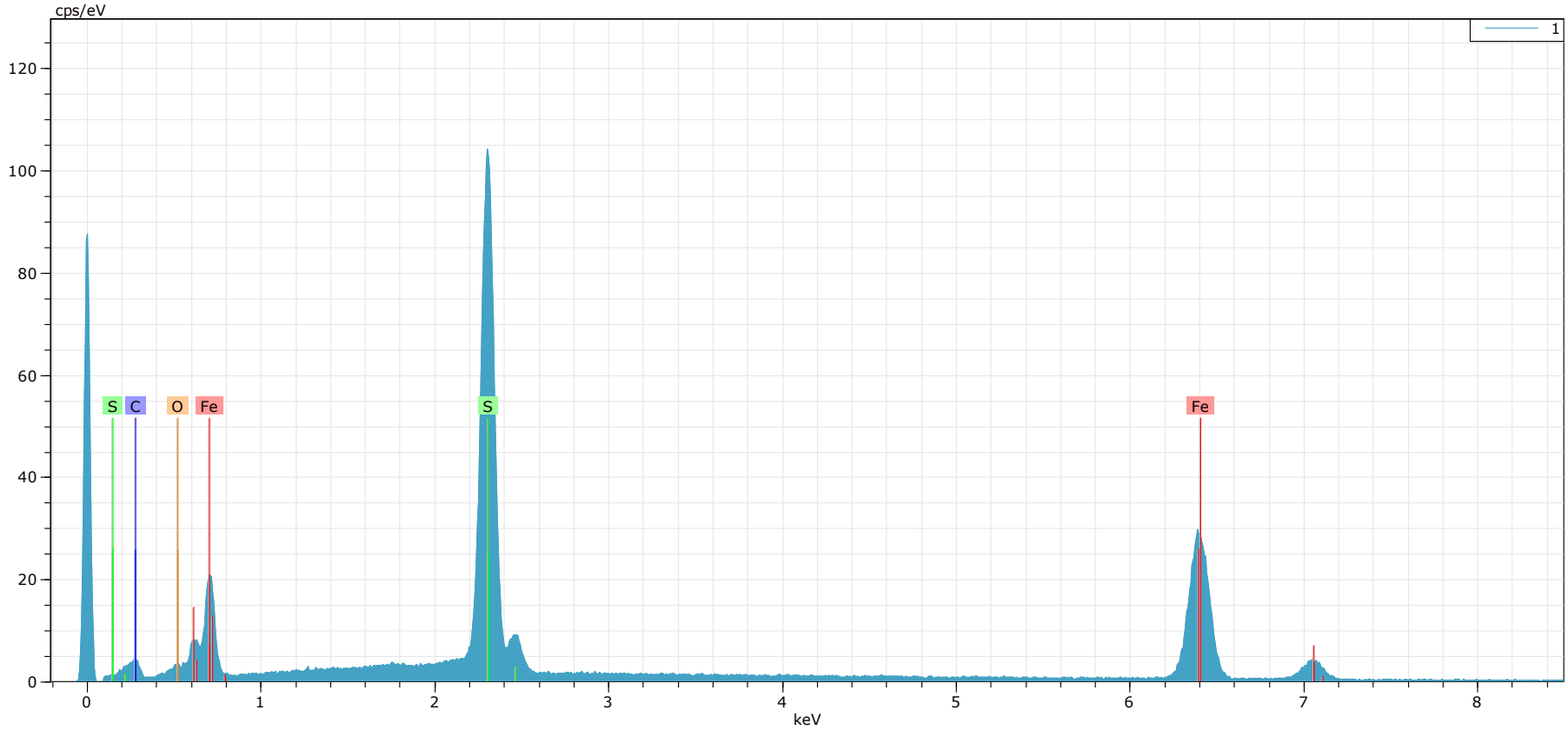

Figure 8.11a: *Graph displaying results from Fig. 6.11, analysis point 1.*

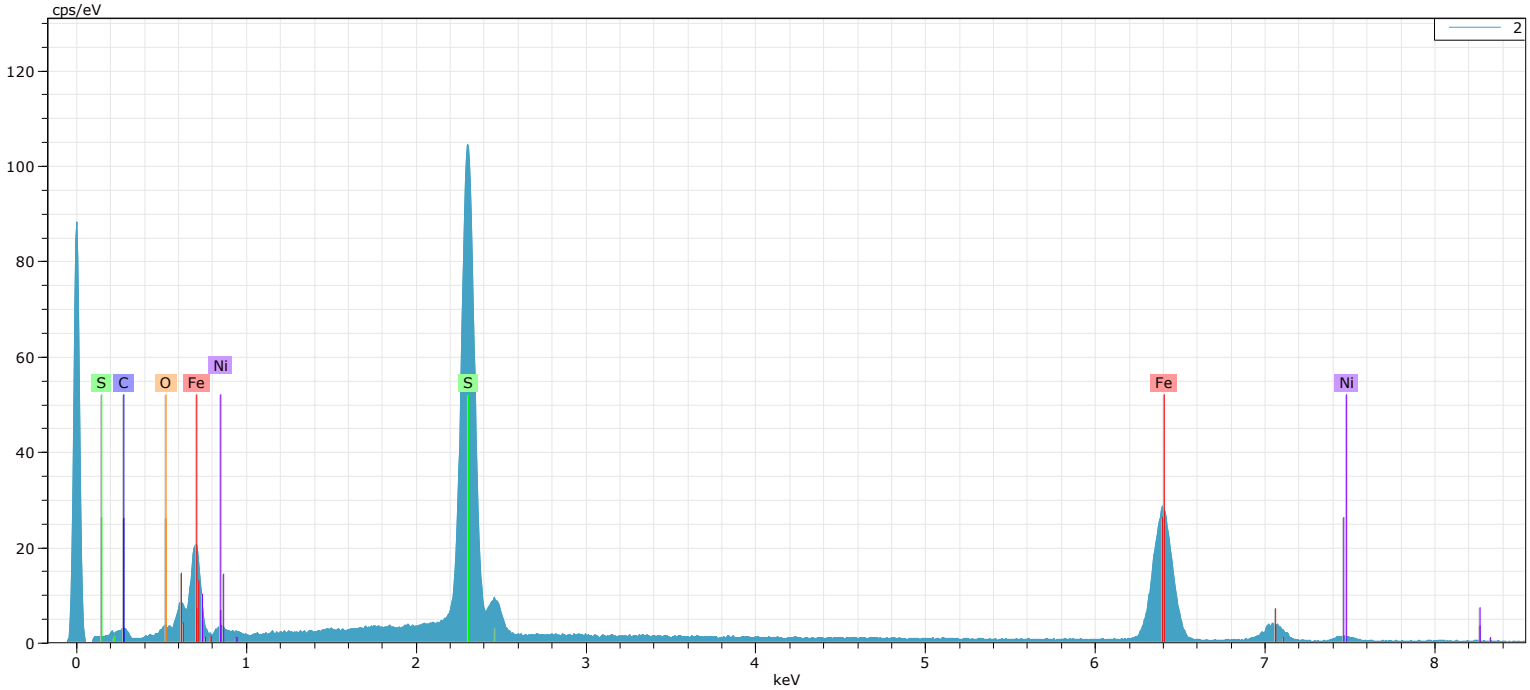

Figure 8.11b: *Graph displaying results from Fig. 6.11, analysis point 2.*

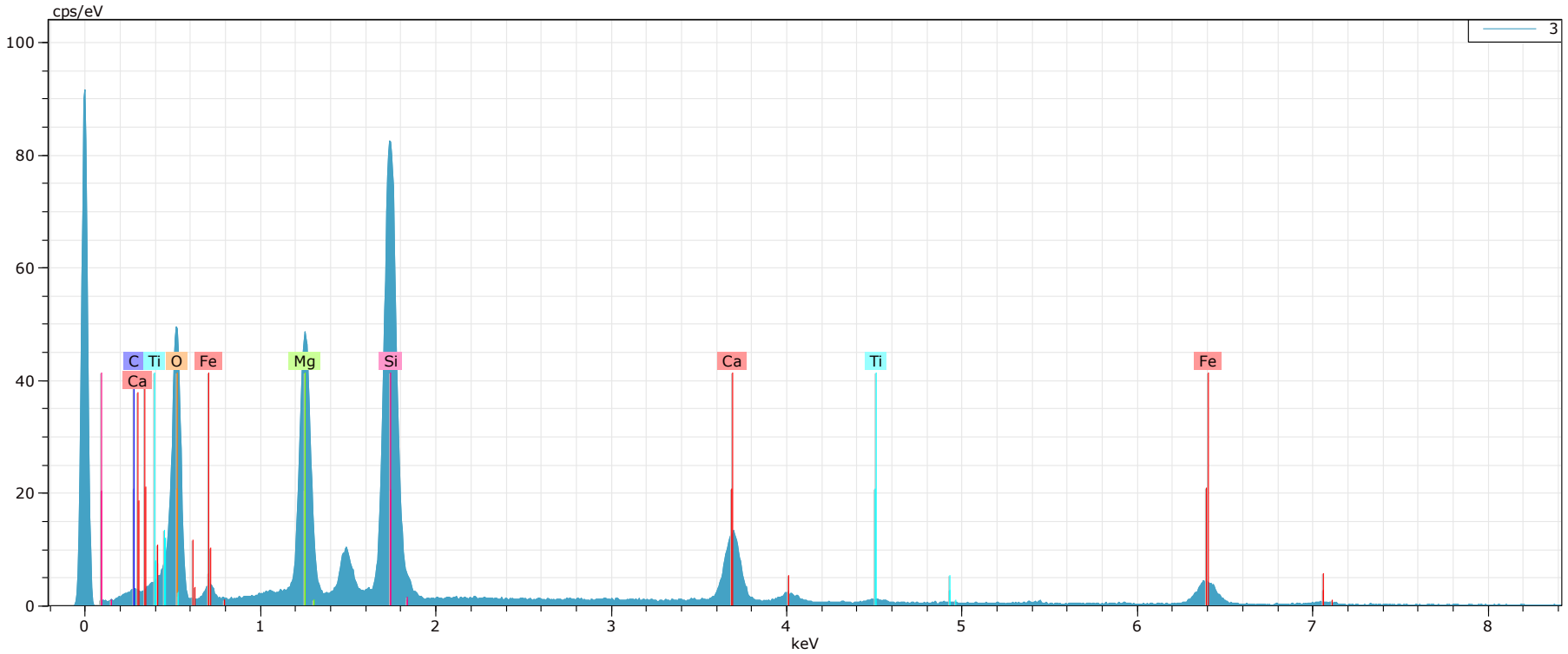

Figure 8.11c: *Graph displaying results from Fig. 6.11, analysis point 3.*

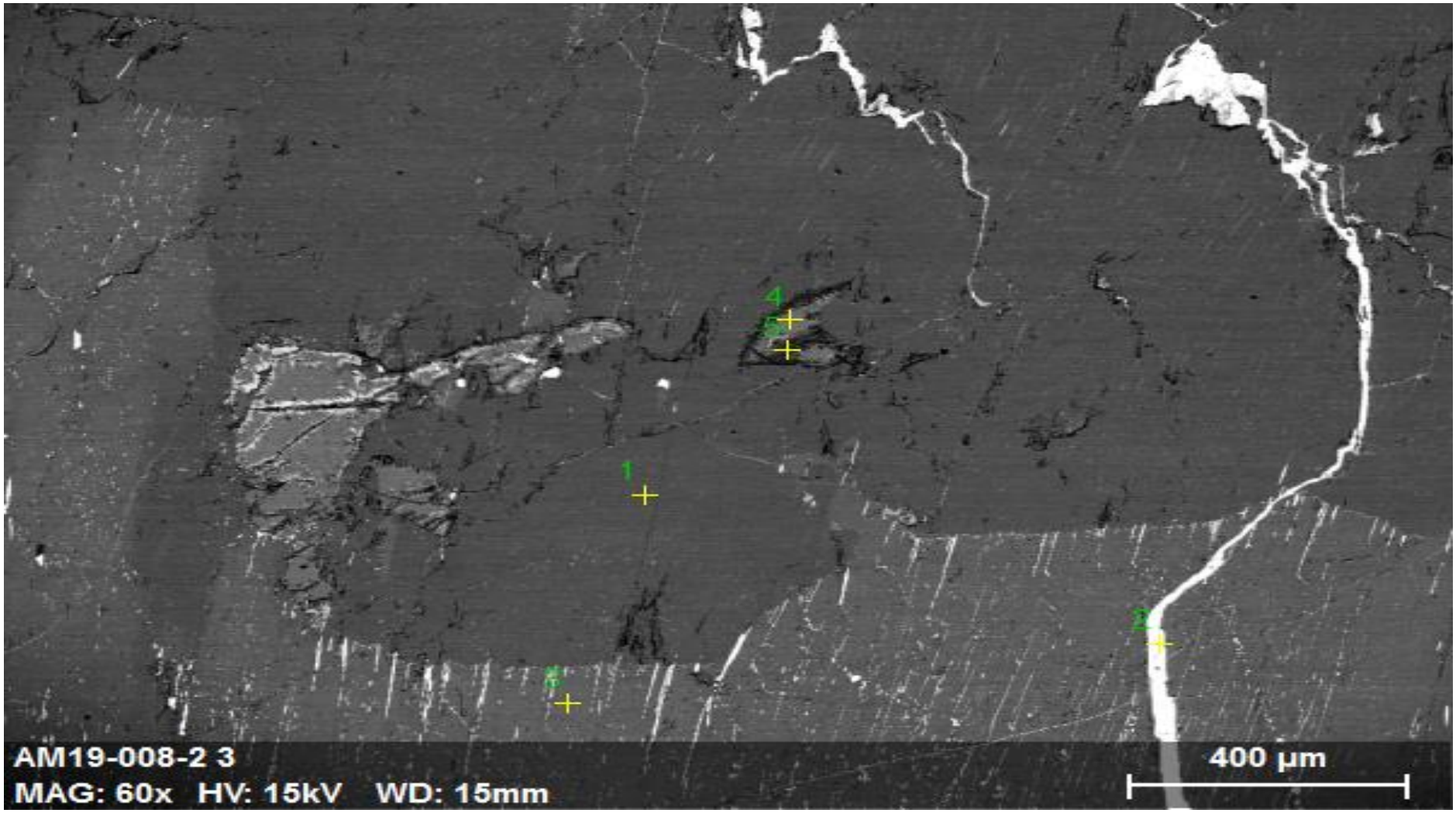

Figure 8.12: *EDS image and graph from SEM, where point 3 matches amphibole composition.*

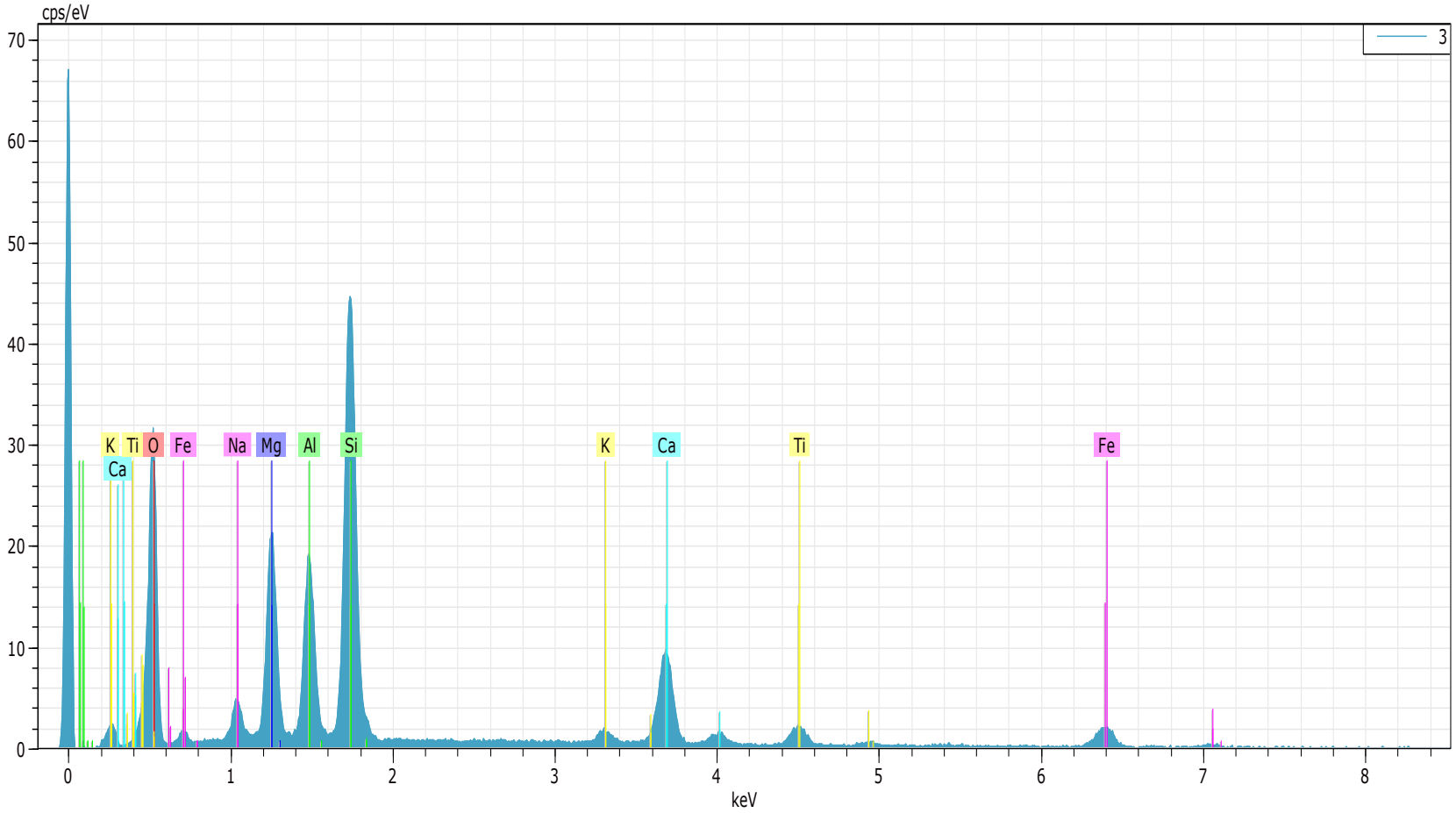

Figure 8.12a: *Graph displaying results from Fig. 6.12, analysis point 3.*

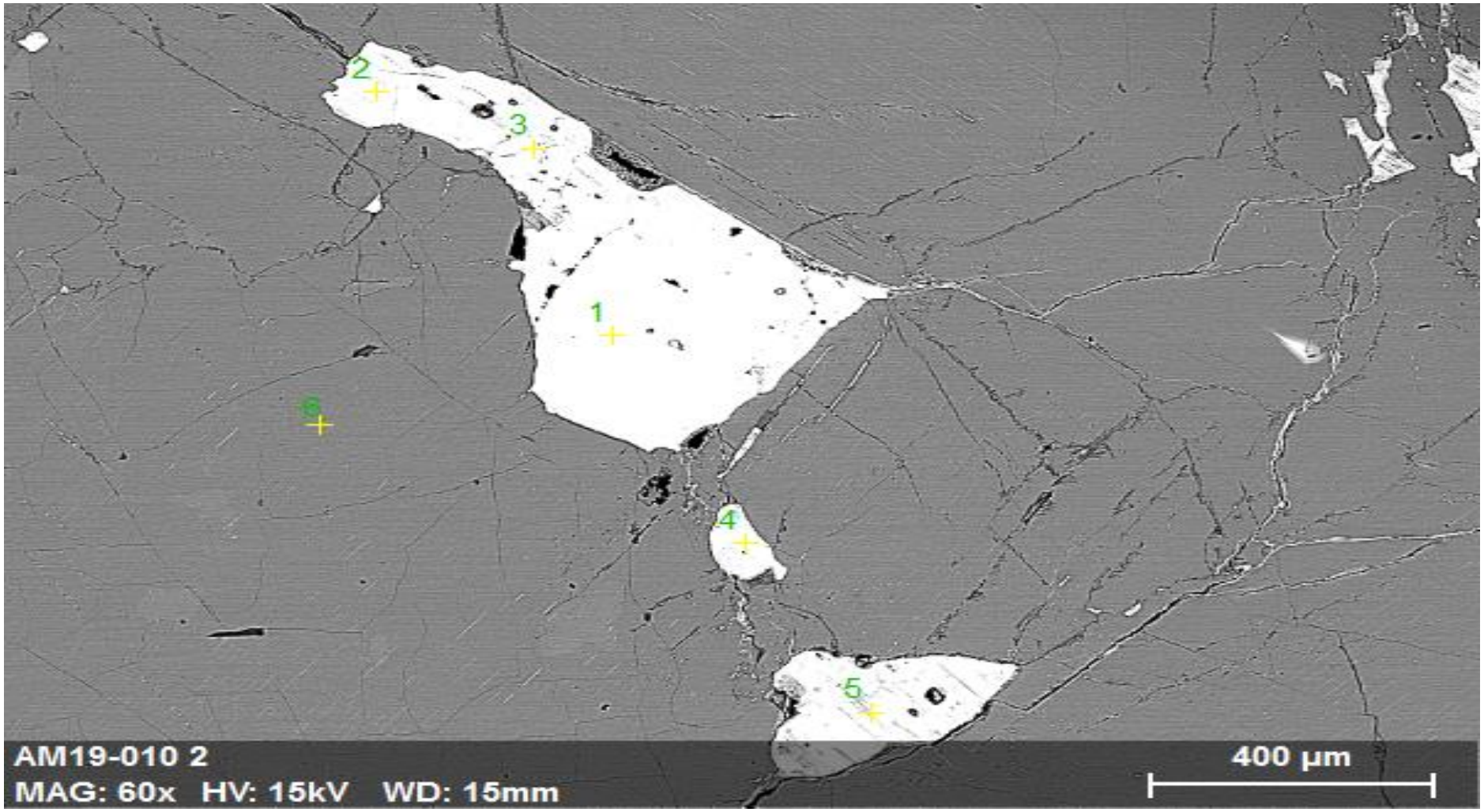

Figure 8.13: *EDS image of sample AM19-010 verifying mineralogy Cbn and Po.*

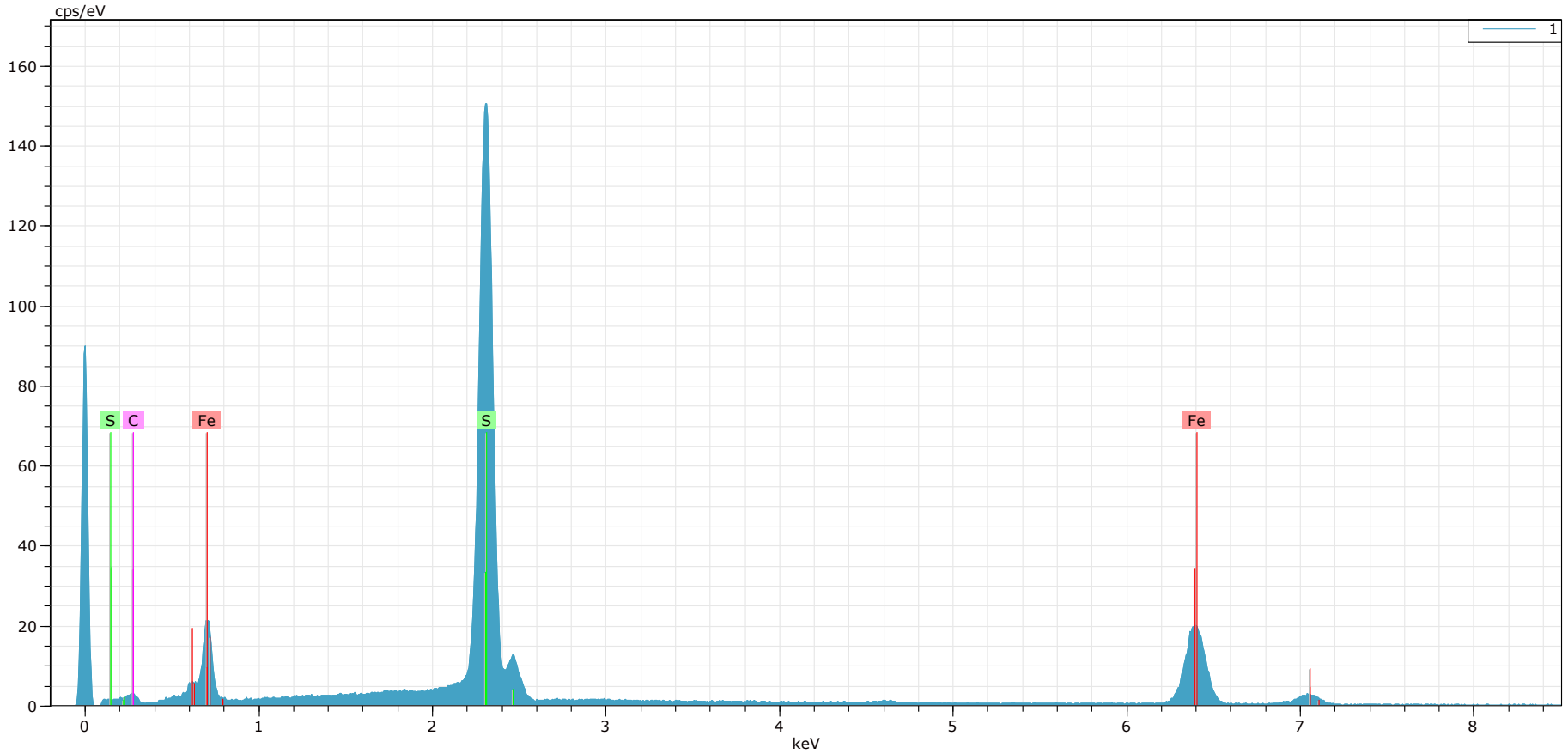

Figure 8.13a: *Graph displaying results from Fig. 6.13, analysis point 1.*

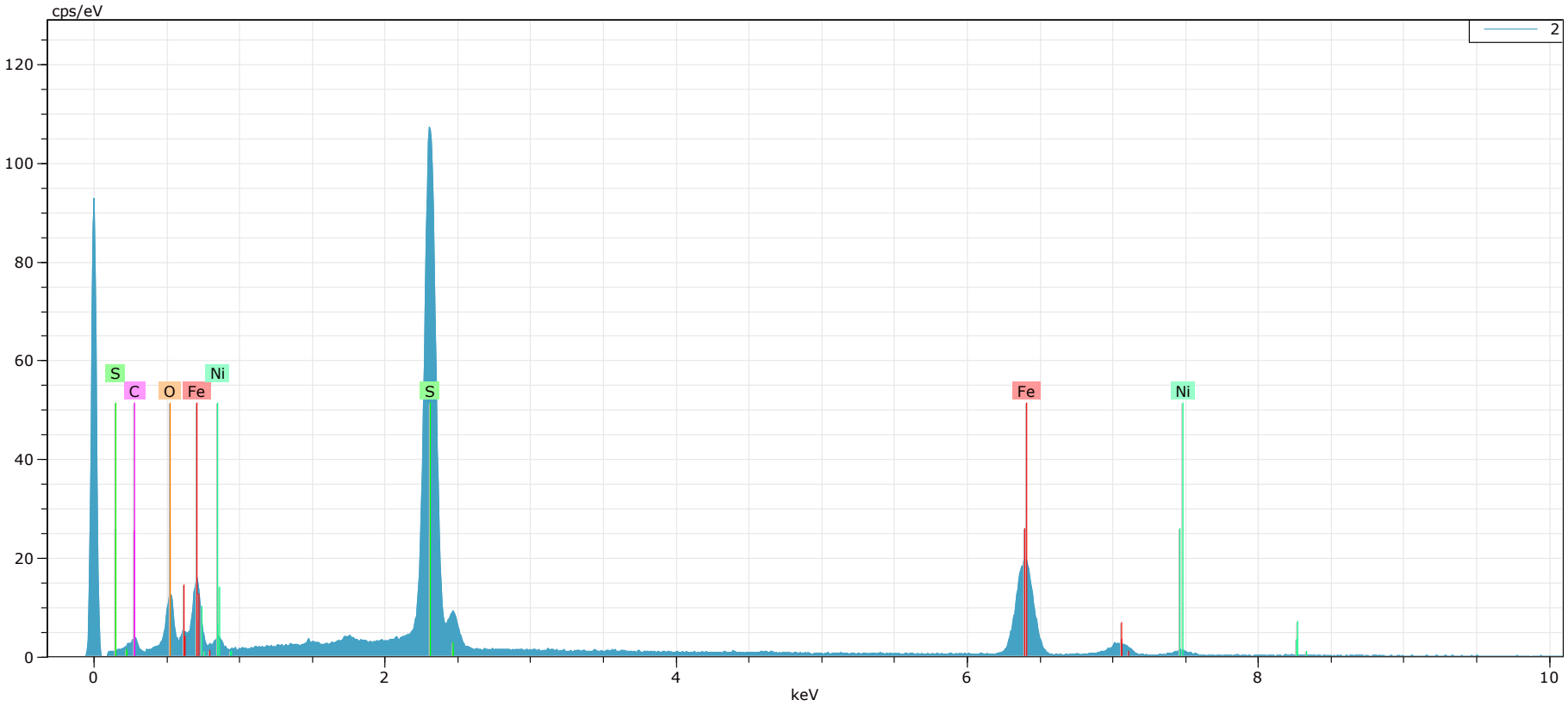

Figure 8.13b: *Graph displaying results from Fig. 6.13, analysis point 2.*

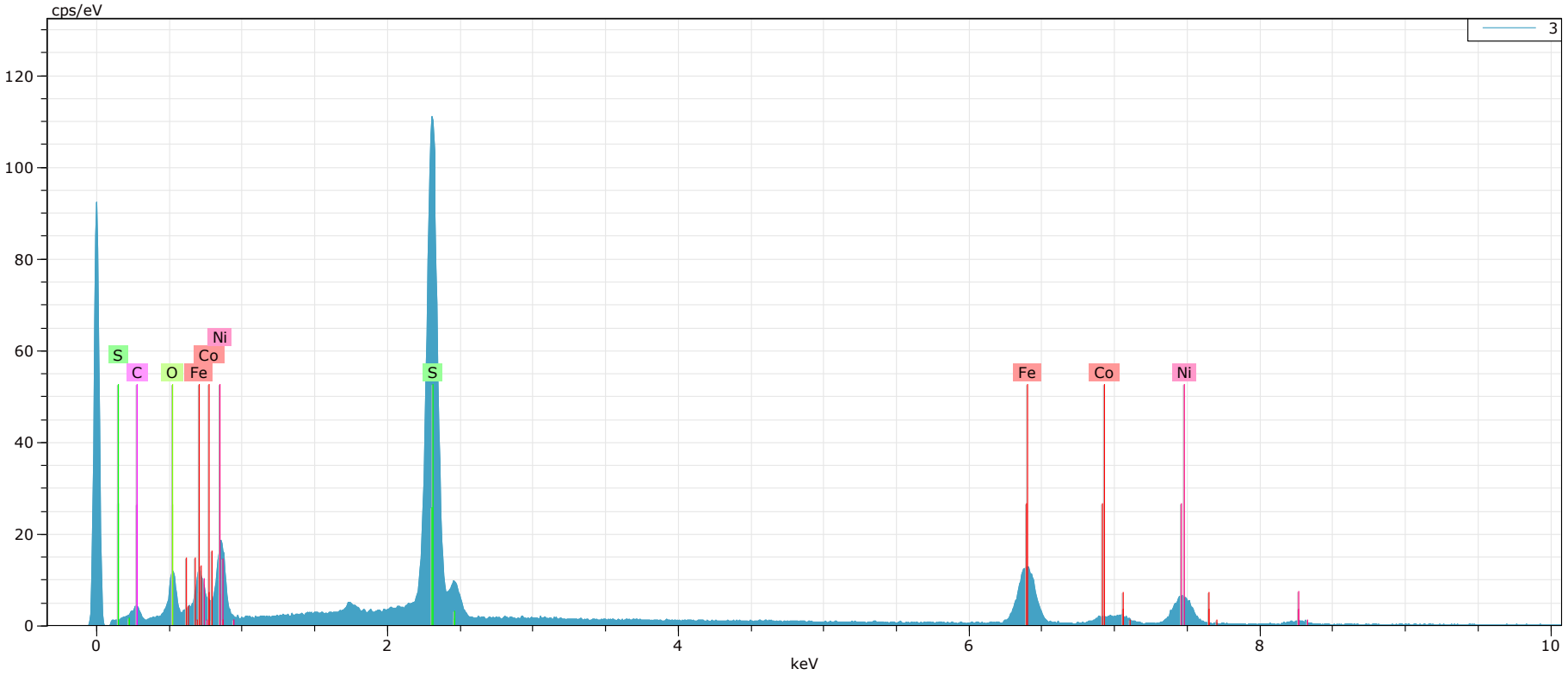

Figure 8.13c: *Graph displaying results from Fig. 6.13, analysis point 2.*

Appendix E EPMA Analysis Tables

Table 8.12: *EPMA data point results from XA_Diop1-15 with accompanying image (next page). LOD = Limit Of Detection.*

Original data point name	Renamed data point	Na2O(Mass%)	MgO(Mass%)	Al2O3(Mass%)	CaO(Mass%)	K2O(Mass%)	Cr2O3(Mass%)	FeO(Mass%)	MnO(Mass%)	NiO(Mass%)	TiO2(Mass%)	SiO2(Mass%)	Total:
XA_Opx1_5 Line 001+P4:Q42	XA_Diop1	0.5129	14.58	5.14	23.31	LOD	0.3794	4.23	0.1071	LOD	1.2802	49.32	98.8596
XA_Opx1_5 Line 002	XA_Diop2	0.5947	12.71	5.71	21.77	0.0089	0.3729	4.05	0.0871	0.0034	1.1739	45.21	91.6909
XA_Opx1_5 Line 003	XA_Diop3	0.5019	15.07	5.61	21.81	LOD	0.4769	4.95	0.1383	0.0093	1.5234	47.78	97.8698
XA_Opx1_5 Line 004	XA_Diop4	0.5454	14.16	5.83	23.07	LOD	0.4018	4.66	0.0981	LOD	1.5766	48.22	98.5619
XA_Opx1_5 Line 005	XA_Diop5	0.4927	15.35	5.65	21.09	0.0047	0.4309	5.98	0.1347	0.0271	1.6169	48.18	98.957
XA_Opx1_5 Line 006	XA_Diop6	0.5659	14.46	5.46	22.44	0.0071	0.4154	5.43	0.1058	0.0228	1.6113	48.01	98.5283
XA_Opx1_5 Line 007	XA_Diop7	0.5816	14.32	5.33	22.86	0.01	0.3859	5.43	0.1258	0.033	1.5739	48.51	99.1602
XA_Opx1_5 Line 008	XA_Diop8	0.536	14.77	5.23	21.7	0.0061	0.3791	5.97	0.1593	0.022	1.4763	48.37	98.6188
XA_Opx1_5 Line 009	XA_Diop9	0.5195	15.14	5.13	21.77	0.005	0.3759	5.73	0.1615	0.0347	1.5439	48.3	98.7105
XA_Opx1_5 Line 010	XA_Diop10	0.4407	18.06	4.62	16.5	LOD	0.2653	8.5	0.1998	0.0355	1.1993	49.52	99.3406
XA_Opx1_5 Line 011	XA_Diop11	0.5032	15.77	4.99	19.94	LOD	0.4121	6.49	0.2102	0.0491	1.4221	48.65	98.4367
XA_Opx1_5 Line 012	XA_Diop12	0.5458	14.55	5.15	22.87	LOD	0.437	5.42	0.1504	0.0245	1.4582	48.61	99.2159
XA_Opx1_5 Line 013	XA_Diop13	0.5489	14.41	5.17	22.75	LOD	0.3681	5.3	0.1548	0.044	1.4769	48.94	99.1627
XA_Opx1_5 Line 014	XA_Diop14	0.4333	15.8	4.94	21.78	0.0044	0.4051	5.52	0.1602	0.0178	1.2891	48.67	99.0199
XA_Opx1_5 Line 015	XA_Diop15	0.0202	29.9	2.22	0.3534	0.0167	0.167	13.16	0.297	0.0042	0.1776	53.33	99.6461

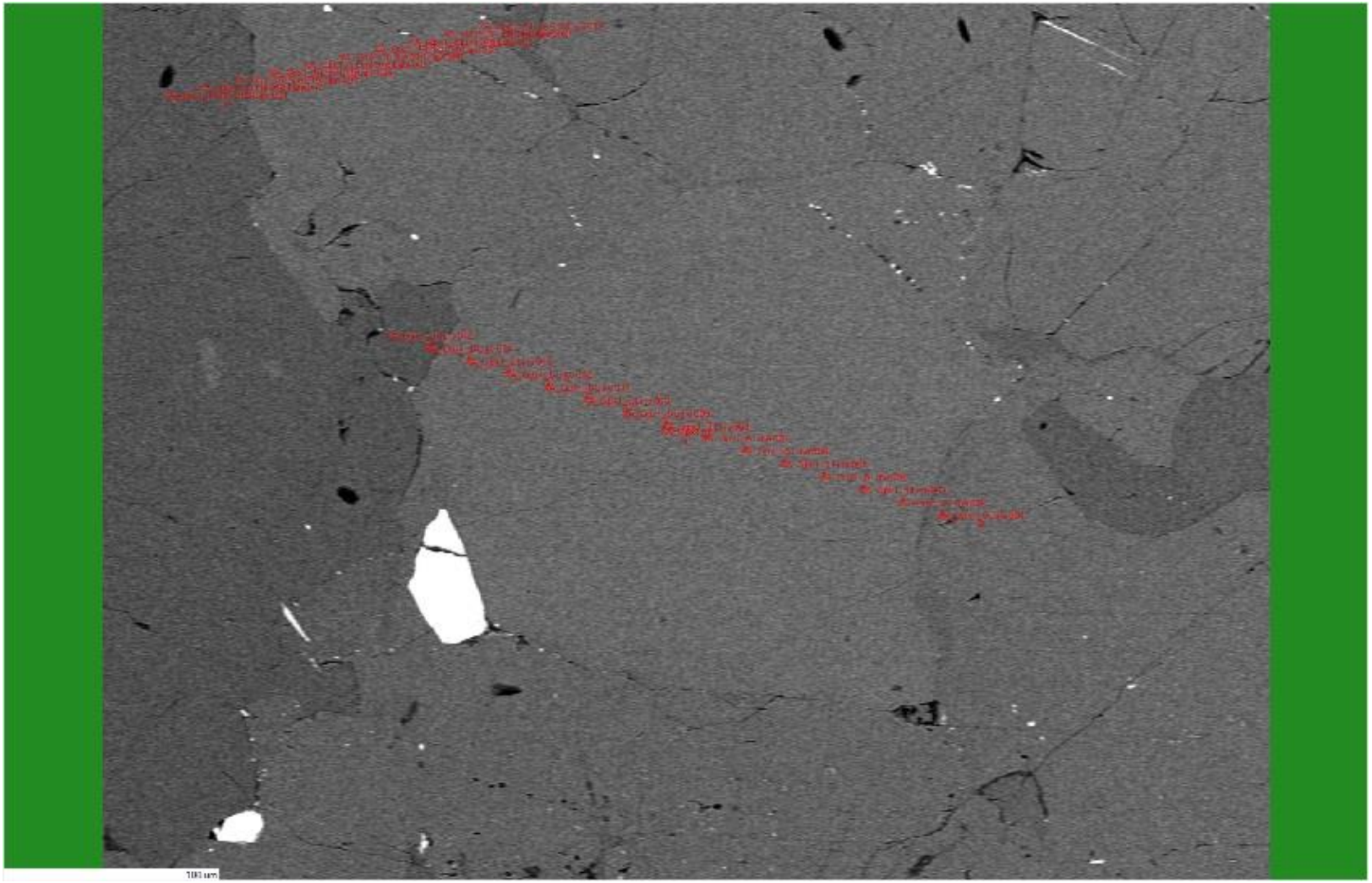

Table 8.13: *EPMA data point results from profile XA1_Diop1-10 with accompanying image (next page).*

Original data point name	Renamed data point	Na2O(Mass%)	MgO(Mass%)	Al2O3(Mass%)	CaO(Mass%)	K2O(Mass%)	Cr2O3(Mass%)	FeO(Mass%)	MnO(Mass%)	NiO(Mass%)	TiO2(Mass%)	SiO2(Mass%)	Total:
XA_Opx1_5 Line 016 Line 001	XA1_Diop1	LOD	29.52	3.1	0.2804	LOD	0.1703	12.76	0.2847	0.0491	0.1916	53.01	99.3661
XA_Opx1_5 Line 016 Line 002	XA1_Diop2	0.4322	14.8	5.06	23.25	LOD	0.4109	4.84	0.1091	0.0211	1.3159	48.89	99.1292
XA_Opx1_5 Line 016 Line 003	XA1_Diop3	0.3185	15.69	8.7	20.17	0.013	1.1679	6.76	0.1032	0.0506	0.8779	44.5	98.3511
XA_Opx1_5 Line 016 Line 004	XA1_Diop4	0.4503	14.69	4.96	23.1	LOD	0.38	4.8	0.1181	0.0127	1.2878	48.66	98.4589
XA_Opx1_5 Line 016 Line 005	XA1_Diop5	0.6016	14.68	5.67	22.43	LOD	0.4452	4.87	0.1158	LOD	1.5391	48.29	98.6417
XA_Opx1_5 Line 016 Line 006	XA1_Diop6	0.6759	14.3	5.88	22.66	0.0154	0.4226	4.66	0.0925	LOD	1.6246	48.48	98.811
XA_Opx1_5 Line 016 Line 007	XA1_Diop7	0.5479	15.4	5.67	21.19	0.0095	0.3792	5.22	0.1135	0.0228	1.5086	48.26	98.3215
XA_Opx1_5 Line 016 Line 008	XA1_Diop8	0.4977	15.43	5.46	22.02	LOD	0.378	4.91	0.1025	LOD	1.5482	48.47	98.8164
XA_Opx1_5 Line 016 Line 009	XA1_Diop9	0.4656	14.71	4.99	23.06	LOD	0.3783	4.83	0.1181	0.0178	1.2934	48.81	98.6732
XA_Opx1_5 Line 016 Line 010	XA1_Diop10	0.0058	29.79	2.12	0.7036	LOD	0.0992	13.03	0.2836	0.0042	0.1021	53.02	99.1585

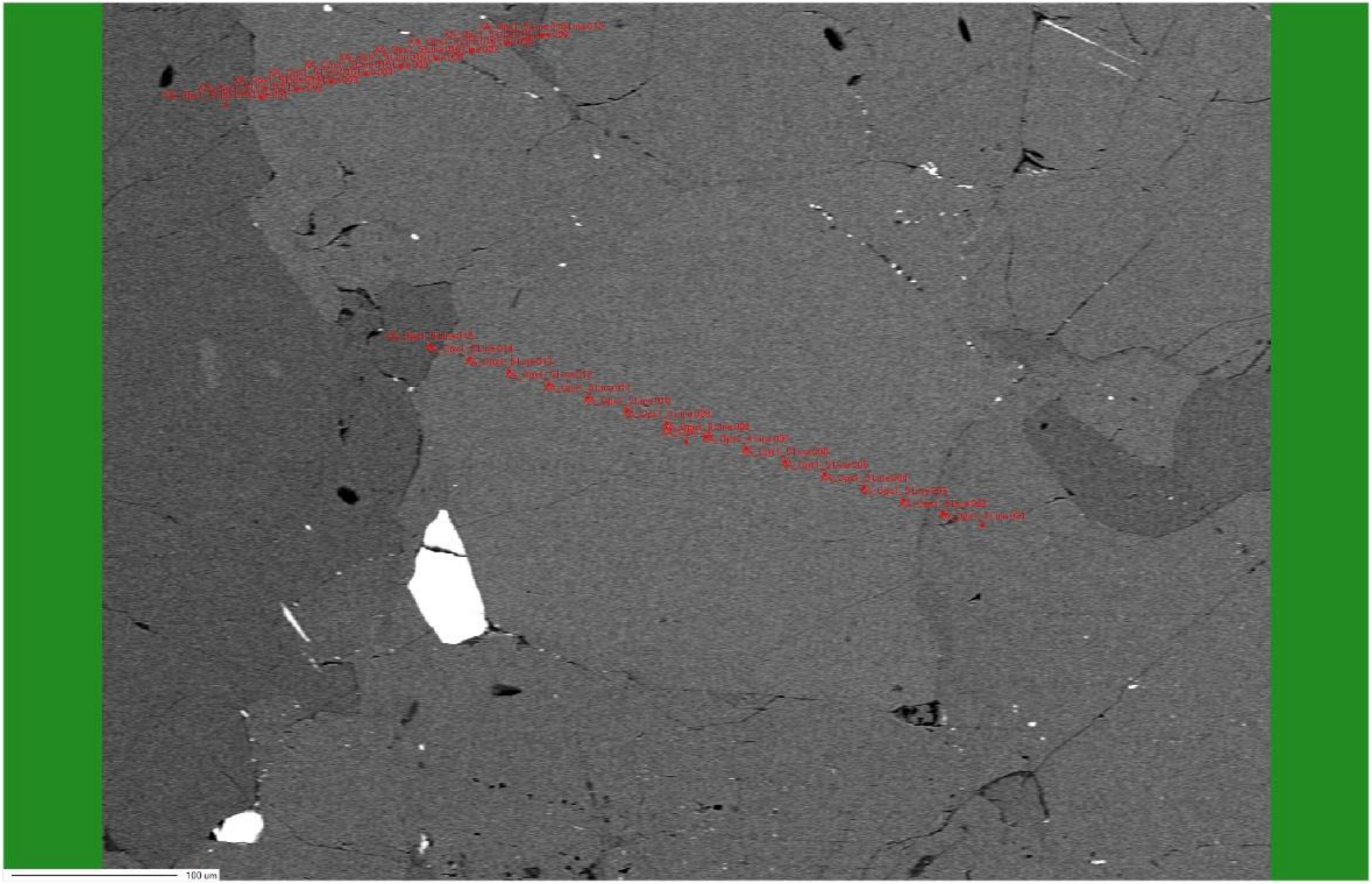
100 um

Table 8.14: *EPMA data points from profile XA2_Diop1-9 with accompanying image (next page).*

Original data point name	Renamed data point	Na2O(Mass%)	MgO(Mass%)	Al2O3(Mass%)	CaO(Mass%)	K2O(Mass%)	Cr2O3(Mass%)	FeO(Mass%)	MnO(Mass%)	NiO(Mass%)	TiO2(Mass%)	SiO2(Mass%)	Total:
XA_Opx1_5 Line 016 Line 011 Line 001	XA2_Diop1	0.463	15.23	4.6	21.73	LOD	0.4727	5.12	0.1492	0.0161	1.1549	49.44	98.3759
XA_Opx1_5 Line 016 Line 011 Line 002	XA2_Diop2	0.469	16.4	4.48	19.78	LOD	0.3961	6.25	0.1702	LOD	1.0877	49.91	98.943
XA_Opx1_5 Line 016 Line 011 Line 003	XA2_Diop3	0.5918	14.46	4.8	22.98	0.0026	0.5138	4.92	0.1302	0.0245	1.2757	48.46	98.1586
XA_Opx1_5 Line 016 Line 011 Line 004	XA2_Diop4	0.399	17.8	4.24	17.76	LOD	0.3509	6.92	0.1444	0.0127	1.0121	50.04	98.6791
XA_Opx1_5 Line 016 Line 011 Line 005	XA2_Diop5	0.5175	15.09	4.51	22.08	LOD	0.4579	5.01	0.167	0.0102	1.1864	48.99	98.019
XA_Opx1_5 Line 016 Line 011 Line 006	XA2_Diop6	0.5467	14.83	4.53	22.75	0.0056	0.4546	4.95	0.1246	0.038	1.1881	49.31	98.7276
XA_Opx1_5 Line 016 Line 011 Line 007	XA2_Diop7	0.273	21.27	3.57	11.99	LOD	0.2391	9.7	0.2412	0.0558	0.6	51.52	99.4591
XA_Opx1_5 Line 016 Line 011 Line 008	XA2_Diop8	0.5446	14.57	4.7	22.73	LOD	0.5079	5.06	0.1567	0.038	1.2688	48.64	98.216
XA_Opx1_5 Line 016 Line 011 Line 009	XA2_Diop9	0.4919	14.47	4.79	23.28	LOD	0.4186	4.62	0.1201	0.0354	1.372	48.68	98.278

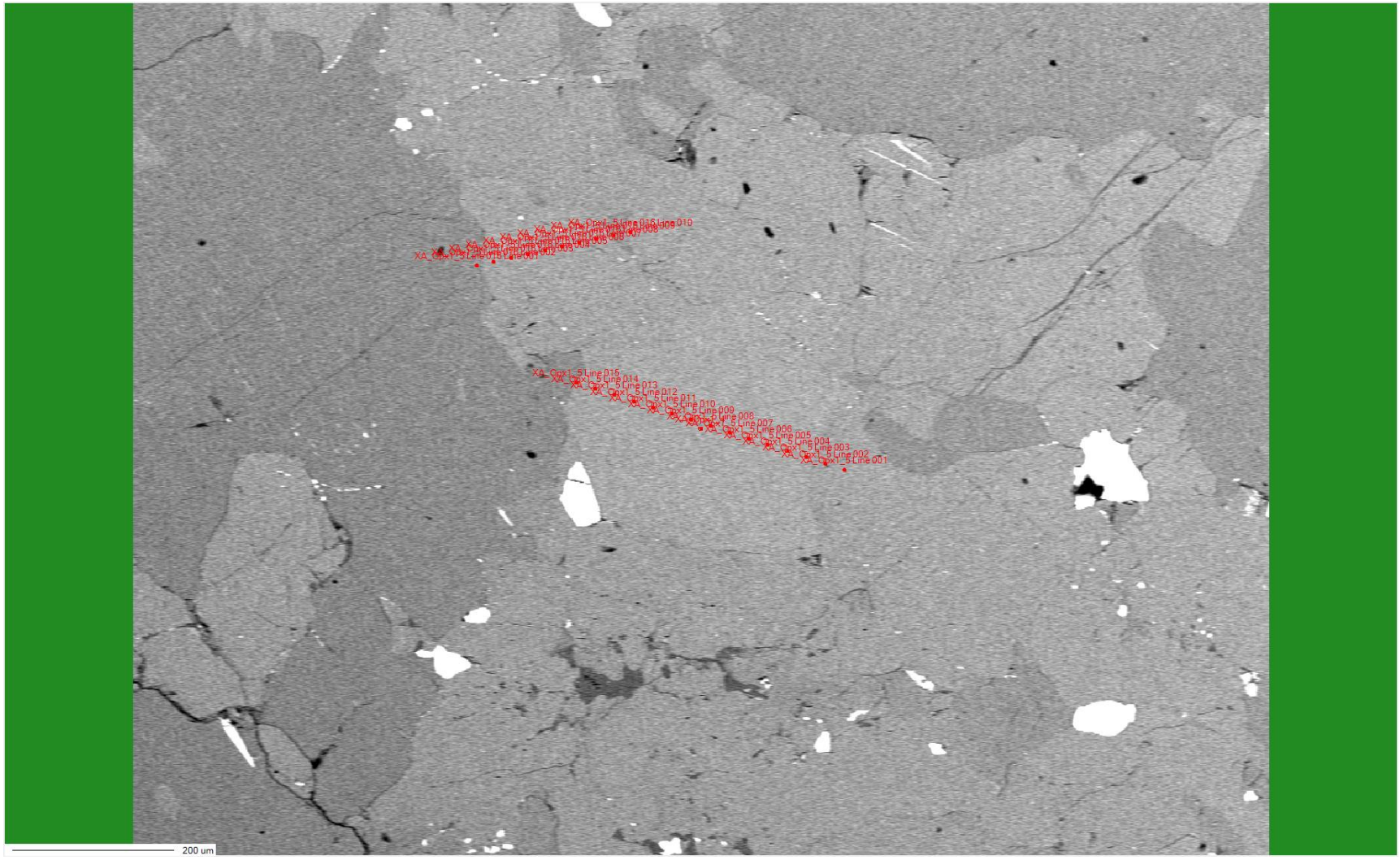
200 um

Table 8.15: *EPMA data points from profile XA3_Diop1-21 with accompanying image (next page).*

Original data point name	Renamed data point	Na2O(Mass%)	MgO(Mass%)	Al2O3(Mass%)	CaO(Mass%)	K2O(Mass%)	Cr2O3(Mass%)	FeO(Mass%)	MnO(Mass%)	NiO(Mass%)	TiO2(Mass%)	SiO2(Mass%)	Total:
XA_Opx1_5 Line 016 Line 011 Line 010_co	XA3_Diop1	0.5071	14.23	5.29	23.12	LOD	0.438	4.78	0.1278	0.0143	1.5149	48.66	98.6821
XA_Opx1_5 Line 016 Line 011 Line 010_co	XA3_Diop2	0.612	14.74	4.59	22.22	LOD	0.6026	4.99	0.0967	LOD	1.2617	49.52	98.633
XA_Opx1_5 Line 016 Line 011 Line 010_co	XA3_Diop3	0.6008	14.63	4.64	22.32	0.0108	0.6608	5.02	0.1099	0.0244	1.2752	48.71	98.0019
XA_Opx1_5 Line 016 Line 011 Line 010_co	XA3_Diop4	0.6039	14.9	4.72	21.79	0.0018	0.621	5.5	0.1299	0.0253	1.2961	49.13	98.718
XA_Opx1_5 Line 016 Line 011 Line 010_co	XA3_Diop5	0.6321	14.65	4.76	22.41	LOD	0.5272	4.85	0.1566	0.0447	1.32	48.67	98.0206
XA_Opx1_5 Line 016 Line 011 Line 010_co	XA3_Diop6	0.4088	17.72	3.9	14.43	LOD	1.3984	12.51	0.1911	0.0798	0.8056	47.37	98.8137
XA_Opx1_5 Line 016 Line 011 Line 010_co	XA3_Diop7	0.6154	14.6	4.64	22.49	0.0017	0.5845	5.08	0.1533	0.0329	1.2796	49.27	98.7474
XA_Opx1_5 Line 016 Line 011 Line 010_co	XA3_Diop8	0.4227	17.83	4.39	17.27	0.0009	0.3819	7.28	0.2027	0.0388	1.0692	50.07	98.9562
XA_Opx1_5 Line 016 Line 011 Line 010_co	XA3_Diop9	0.6218	14.42	4.8	22.41	0.0008	0.4991	4.99	0.1221	0.016	1.3181	49.02	98.2179
XA_Opx1_5 Line 016 Line 011 Line 010_co	XA3_Diop10	0.5852	14.4	4.9	22.59	LOD	0.4751	4.82	0.1377	0.0152	1.4301	49.13	98.4833
XA_Opx1_5 Line 016 Line 011 Line 010_co	XA3_Diop11	0.4856	16.45	4.53	19.74	LOD	0.448	6.24	0.1795	0.0042	1.2896	49.4	98.7669
XA_Opx1_5 Line 016 Line 011 Line 010_co	XA3_Diop12	0.0153	29.96	2.68	0.5155	0.0005	0.1665	12.83	0.2277	0.0827	0.2033	52.68	99.3615
XA_Opx1_5 Line 016 Line 011 Line 010_co	XA3_Diop13	0.0502	29.26	2.65	1.46	0.0005	0.192	12.69	0.2553	0.0346	0.1434	53.11	99.846
XA_Opx1_5 Line 016 Line 011 Line 010_co	XA3_Diop14	LOD	29.34	2.89	0.6025	0.0056	0.1931	13.16	0.208	0.0566	0.236	53.15	99.8418
XA_Opx1_5 Line 016 Line 011 Line 010_co	XA3_Diop15	LOD	29.05	2.99	0.687	LOD	0.1666	12.97	0.2641	0.0617	0.1987	53.2	99.5881
XA_Opx1_5 Line 016 Line 011 Line 010_co	XA3_Diop16	LOD	29.12	3.27	0.6169	0.0013	0.1539	13.05	0.2102	0.0499	0.1924	52.57	99.2346
XA_Opx1_5 Line 016 Line 011 Line 010_co	XA3_Diop17	0.0488	29.14	3.2	0.3849	LOD	0.1555	13.07	0.2608	0.0845	0.3057	52.59	99.2402
XA_Opx1_5 Line 016 Line 011 Line 010_co	XA3_Diop18	0.0054	29.38	3.09	0.3275	0.0063	0.1553	13.36	0.263	0.0042	0.1753	52.69	99.457
XA_Opx1_5 Line 016 Line 011 Line 010_co	XA3_Diop19	0.0472	28.48	2.61	2.11	0.0029	0.2176	12.14	0.2434	0.0186	0.1989	52.3	98.3686
XA_Opx1_5 Line 016 Line 011 Line 010_co	XA3_Diop20	0.0364	29.5	2.67	0.5048	LOD	0.1476	13.24	0.2619	0.011	0.2294	52.81	99.4111
XA_Opx1_5 Line 016 Line 011 Line 010_co	XA3_Diop21	LOD	29.29	2.59	0.7573	LOD	0.181	12.61	0.2775	0.0397	0.1899	52.73	98.6654

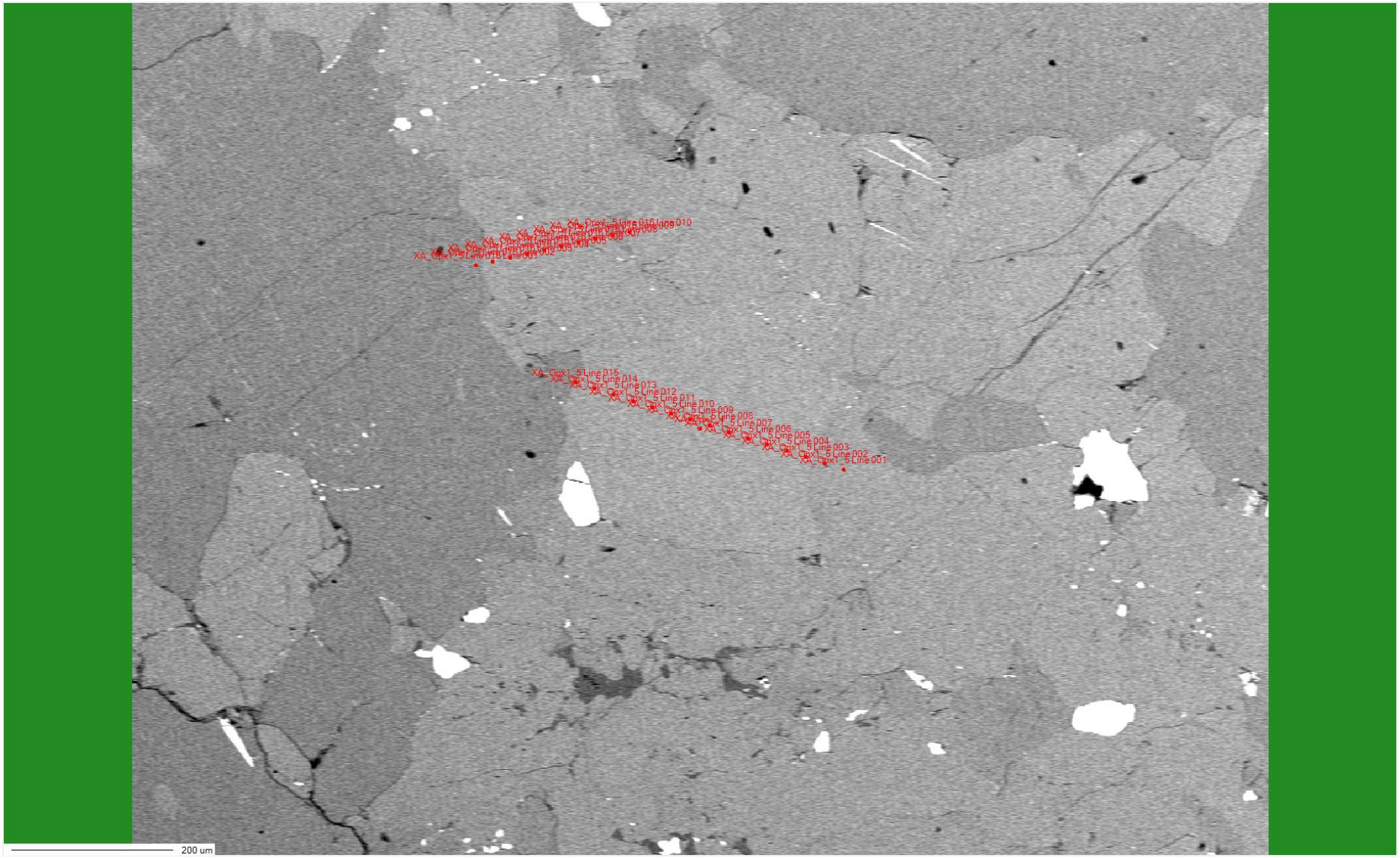
200 um

Table 8.16: *EPMA data point results from profile XA1_Ol1-10 with accompanying images (next page).*

Original data point name	Renamed data point	Na2O(Mass%)	MgO(Mass%)	Al2O3(Mass%)	CaO(Mass%)	K2O(Mass%)	Cr2O3(Mass%)	FeO(Mass%)	MnO(Mass%)	NiO(Mass%)	TiO2(Mass%)	SiO2(Mass%)	Total:
XA_Ol2_line1 Line 001	XA1_Ol1	0.0309	25.68	0.3299	1.2057	LOD	0.24	29.33	0.2533	0.1284	0.0314	34.34	91.5696
XA_Ol2_line1 Line 002	XA1_Ol2	LOD	41.4	LOD	LOD	LOD	0.0198	19.94	0.2765	0.1402	0.0116	38.45	100.2381
XA_Ol2_line1 Line 003	XA1_Ol3	LOD	41.7	LOD	LOD	LOD	0.0229	19.74	0.2342	0.1511	0.0067	38.51	100.3649
XA_Ol2_line1 Line 004	XA1_Ol4	LOD	40.9	0.0022	0.0151	LOD	LOD	19.99	0.2657	0.1579	0.015	37.33	98.6759
XA_Ol2_line1 Line 005	XA1_Ol5	0.0084	41.54	LOD	0.0055	LOD	0.0061	20.19	0.2514	0.1779	0.0068	38.59	100.7761
XA_Ol2_line1 Line 006	XA1_Ol6	0.0112	41.67	0.0006	LOD	LOD	0.0061	20.09	0.2918	0.141	LOD	38.56	100.7707
XA_Ol2_line1 Line 007	XA1_Ol7	0.0538	41.61	LOD	0.0078	LOD	0.0243	20.45	0.25	0.1525	LOD	37.9	100.4484
XA_Ol2_line1 Line 008	XA1_Ol8	LOD	41.62	LOD	LOD	LOD	0.0076	20.16	0.2186	0.182	0.0063	38.12	100.3145
XA_Ol2_line1 Line 009	XA1_Ol9	0.0412	41.35	LOD	LOD	0.0004	LOD	20.15	0.2174	0.1459	0.0117	38.21	100.1266
XA_Ol2_line1 Line 010	XA1_Ol10	0.0007	41.45	LOD	0.0104	LOD	0.0182	20.01	0.2834	0.1926	LOD	38.13	100.0953

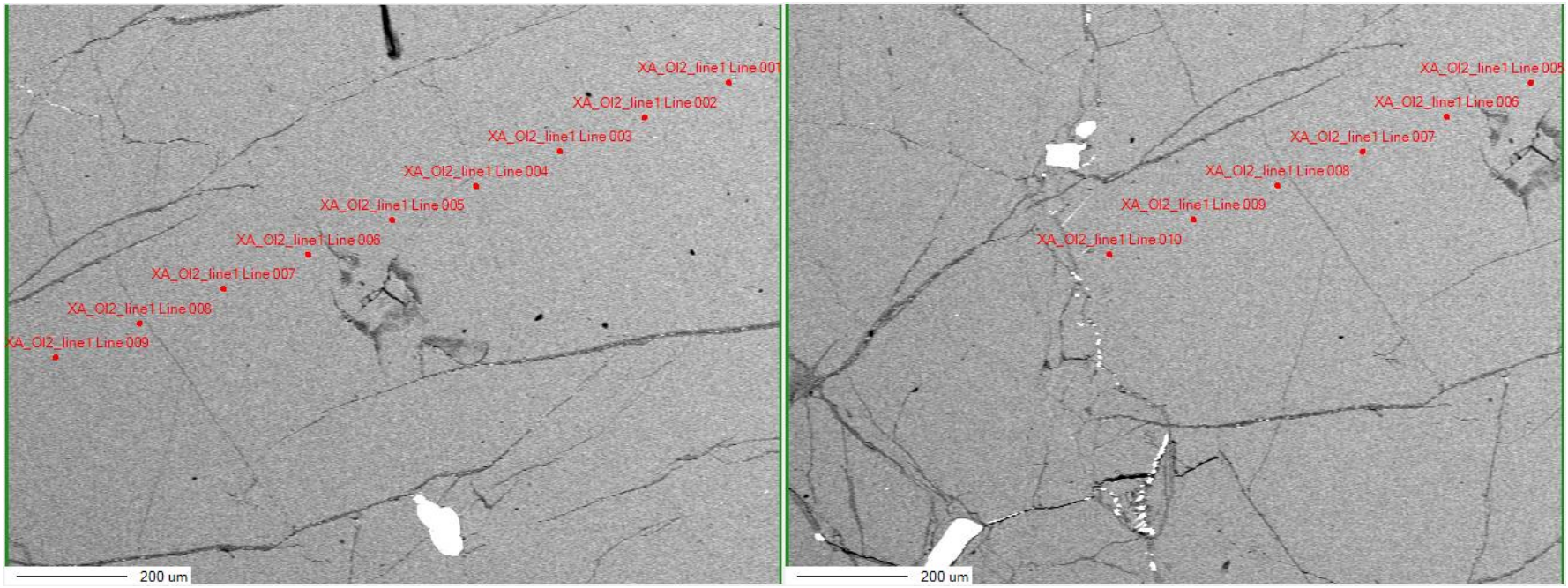
XA_OI2_line1 Line 001
XA_OI2_line1 Line 002
XA_OI2_line1 Line 003
XA_OI2_line1 Line 004
XA_OI2_line1 Line 005
XA_OI2_line1 Line 006
XA_OI2_line1 Line 007
XA_OI2_line1 Line 008
XA_OI2_line1 Line 009
200 um
XA_OI2_line1 Line 005
XA_OI2_line1 Line 006
XA_OI2_line1 Line 007
XA_OI2_line1 Line 008
XA_OI2_line1 Line 009
XA_OI2_line1 Line 010
200 um

Table 8.17: *EPMA data points from profile XA2_Ol1-10 (no accompanying image).*

Original data point name	Renamed data point	Na2O(Mass%)	MgO(Mass%)	Al2O3(Mass%)	CaO(Mass%)	K2O(Mass%)	Cr2O3(Mass%)	FeO(Mass%)	MnO(Mass%)	NiO(Mass%)	TiO2(Mass%)	SiO2(Mass%)	Total:
XA_Ol2_line2 Line 011 Line 001	XA2_Ol1	0.016	41.44	LOD	LOD	0.0132	0.0046	20.48	0.3207	0.1274	0.0157	38.2	100.6176
XA_Ol2_line2 Line 011 Line 002	XA2_Ol2	0.0113	41.49	LOD	LOD	0.011	LOD	19.92	0.2534	0.1023	0.0154	38.11	99.9134
XA_Ol2_line2 Line 011 Line 003	XA2_Ol3	0.0182	41.43	LOD	LOD	LOD	0.0122	20.18	0.2469	0.1006	LOD	38.52	100.5079
XA_Ol2_line2 Line 011 Line 004	XA2_Ol4	LOD	41.18	LOD	LOD	0.0004	LOD	20.14	0.2726	0.1289	0.008	38.23	99.9599
XA_Ol2_line2 Line 011 Line 005	XA2_Ol5	LOD	41.61	LOD	LOD	LOD	0.0152	20.28	0.2794	0.1157	0.0096	38.45	100.7599
XA_Ol2_line2 Line 011 Line 006	XA2_Ol6	LOD	41.64	LOD	LOD	LOD	0.0091	20.07	0.2814	0.1189	0.0064	38.29	100.4158
XA_Ol2_line2 Line 011 Line 007	XA2_Ol7	0.0364	41.53	LOD	LOD	LOD	0.0258	20.19	0.2487	0.1265	0.0053	38.35	100.5127
XA_Ol2_line2 Line 011 Line 008	XA2_Ol8	LOD	41.64	LOD	LOD	LOD	0.0091	20.09	0.2586	0.129	0.0123	38.58	100.719
XA_Ol2_line2 Line 011 Line 009	XA2_Ol9	LOD	41.57	LOD	LOD	LOD	LOD	20.01	0.2056	0.1845	0.0091	38.07	100.0492
XA_Ol2_line2 Line 011 Line 010	XA2_Ol10	0.0119	41.74	LOD	LOD	LOD	0.0061	19.79	0.2738	0.1332	0.0292	37.85	99.8342

Table 8.18: *EPMA data points from profile XA1_Aeg1-30 with accompanying images (next 2 pages).*

Original data point name	Renamed data point	Na2O(Mass%)	MgO(Mass%)	Al2O3(Mass%)	CaO(Mass%)	K2O(Mass%)	Cr2O3(Mass%)	FeO(Mass%)	MnO(Mass%)	NiO(Mass%)	TiO2(Mass%)	SiO2(Mass%)	Total:
XA_Cpxoropx_line Line 001	XA1_Aeg1	0.0104	29.24	3.14	0.7077	0.0101	0.2119	13	0.2584	0.0676	0.2734	52.3	99.2195
XA_Cpxoropx_line Line 002	XA1_Aeg2	0	29.32	3.16	0.619	LOD	0.209	12.72	0.2178	0.0718	0.1999	52.4	98.9175
XA_Cpxoropx_line Line 003	XA1_Aeg3	0.0629	28.13	3.23	2.66	LOD	0.1925	12.18	0.273	0.0203	0.3282	52.61	99.6869
XA_Cpxoropx_line Line 004	XA1_Aeg4	0.0175	29.71	2.69	0.2623	LOD	0.2025	13.03	0.2343	0.0447	0.156	53.12	99.4673
XA_Cpxoropx_line Line 005	XA1_Aeg5	LOD	29.74	3.16	0.3016	LOD	0.1443	13.18	0.2551	0.0219	0.2447	52.34	99.3876
XA_Cpxoropx_line Line 006	XA1_Aeg6	LOD	29.67	2.98	0.3747	0.0026	0.2057	12.91	0.2981	0.0397	0.2471	52.46	99.1879
XA_Cpxoropx_line Line 007	XA1_Aeg7	0.0262	29.57	3.06	0.513	LOD	0.1445	12.98	0.2993	0.0194	0.2294	53.24	100.0818
XA_Cpxoropx_line Line 008	XA1_Aeg8	LOD	27.16	3.07	0.7695	LOD	0.0737	11.67	0.2462	0.0667	0.1913	45.07	88.3174
XA_Cpxoropx_line Line 009	XA1_Aeg9	0.0977	26.88	3.56	4.52	LOD	0.1425	11.51	0.2445	0.0304	0.537	51.84	99.3621
XA_Cpxoropx_line Line 010	XA1_Aeg10	0.0108	29.48	3.17	0.4391	0.0063	0.11	12.86	0.3058	0.0498	0.2312	52.55	99.213
XA_Cpxoropx_line Line 011	XA1_Aeg11	LOD	29.18	3.14	0.3062	LOD	0.1428	13.04	0.2463	0.0296	0.2417	52.83	99.1566
XA_Cpxoropx_line Line 012	XA1_Aeg12	LOD	29.16	3.62	0.5838	LOD	0.1317	13.29	0.2451	0.0582	0.2971	51.84	99.2259
XA_Cpxoropx_line Line 013	XA1_Aeg13	LOD	29.84	2.23	0.2182	LOD	0.0847	13.16	0.2507	0.0177	0.0861	53.27	99.1574
XA_Cpxoropx_line Line 014	XA1_Aeg14	0.0277	29.41	3.21	0.3152	LOD	0.1833	13.19	0.246	0.0169	0.2042	52.44	99.2433
XA_Cpxoropx_line Line 015	XA1_Aeg15	0.0376	29.59	3.01	0.6639	LOD	0.1898	12.99	0.2614	0.0616	0.1977	53.01	100.012
XA_Cpxoropx_line Line 016	XA1_Aeg16	0.0121	29.67	2.93	0.3538	0.0144	0.1508	12.61	0.2286	0.0819	0.2226	53.32	99.5942
XA_Cpxoropx_line Line 017	XA1_Aeg17	0.0106	29.69	3.18	0.3324	LOD	0.2163	13.05	0.3064	0.0338	0.1866	52.91	99.9161
XA_Cpxoropx_line Line 018	XA1_Aeg18	0.6446	14.37	5.35	22.78	LOD	0.349	4.82	0.1298	LOD	1.6356	48.78	98.859
XA_Cpxoropx_line Line 019	XA1_Aeg19	0.5873	14.74	5.06	22.8	LOD	0.4259	4.59	0.1409	0.0606	1.4718	48.84	98.7165
XA_Cpxoropx_line Line 020	XA1_Aeg20	3.68	10.53	15.61	10.73	0.0783	0.2138	6.64	0.1147	0.0563	1.5525	38.27	87.4756
XA_Cpxoropx_line Line 021	XA1_Aeg21	LOD	29.84	2.86	0.1956	LOD	0.1675	13.52	0.2923	0.0346	0.1469	52.84	99.8969
XA_Cpxoropx_line Line 022	XA1_Aeg22	LOD	29.86	2.76	0.3295	LOD	0.1755	13.17	0.2636	0.0489	0.2035	52.92	99.731
XA_Cpxoropx_line Line 023	XA1_Aeg23	0.0331	29.04	3.25	1.73	LOD	0.1921	12.32	0.2682	0.0548	0.2546	52.76	99.9028
XA_Cpxoropx_line Line 024	XA1_Aeg24	0.1044	25.78	3.69	6.85	LOD	0.191	10.32	0.2479	0.0396	0.5752	51.72	99.5181
XA_Cpxoropx_line Line 025	XA1_Aeg25	0.0384	42.18	0.0063	0.006	LOD	LOD	20.36	0.2826	0.1618	0.0159	38.04	101.091
XA_Cpxoropx_line Line 026	XA1_Aeg26	1.83	16.44	7.75	18.45	0.084	0.281	5.75	0.0388	0.048	1.5232	46.85	99.045
XA_Cpxoropx_line Line 027	XA1_Aeg27	0.0221	29.09	3.19	1.1412	LOD	0.2094	12.44	0.2311	0.0422	0.1855	52.85	99.4015
XA_Cpxoropx_line Line 028	XA1_Aeg28	0.0569	28.98	3.15	1.61	0.0017	0.1402	12.47	0.2807	0.0347	0.2251	52.94	99.8893
XA_Cpxoropx_line Line 029	XA1_Aeg29	0.0162	29.43	2.77	0.7724	0.0029	0.1385	12.56	0.3313	0.0245	0.2188	52.91	99.1746
XA_Cpxoropx_line Line 030	XA1_Aeg30	LOD	29.42	3.12	0.3875	0.0063	0.1036	12.99	0.3168	0.0363	0.2526	52.58	99.2131

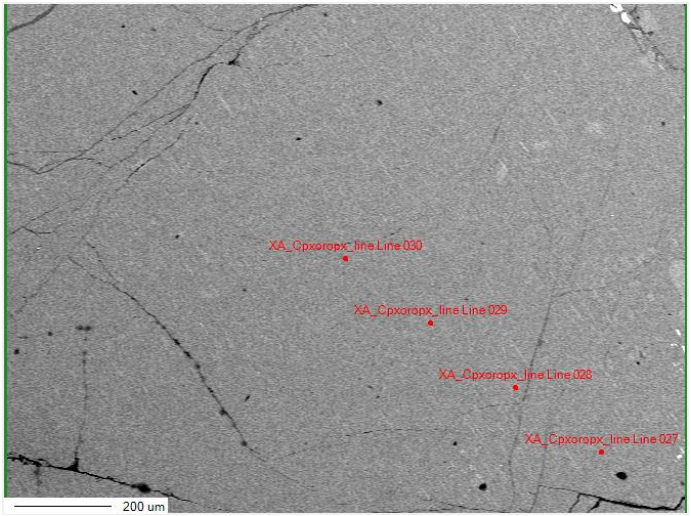
XA_Cpxoropx_line Line 030
XA_Cpxoropx_line Line 029
XA_Cpxoropx_line Line 028
XA_Cpxoropx_line Line 027
200 um

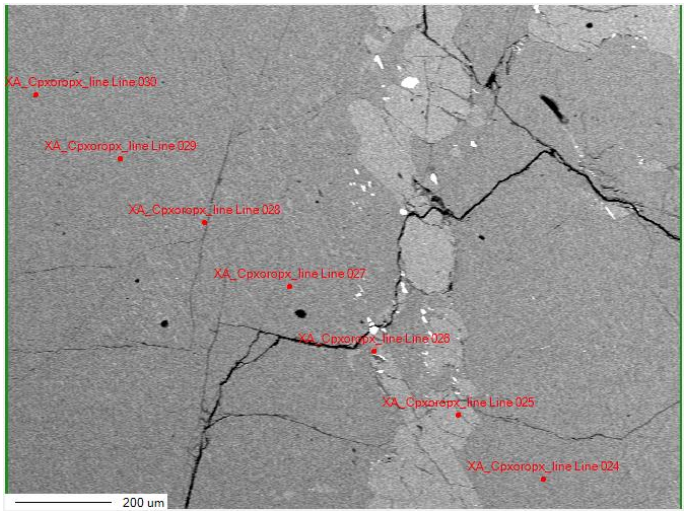
XA_Cpxoropx_line Line 030
XA_Cpxoropx_line Line 029
XA_Cpxoropx_line Line 028
XA_Cpxoropx_line Line 027
XA_Cpxoropx_line Line 026
XA_Cpxoropx_line Line 025
XA_Cpxoropx_line Line 024
200 um

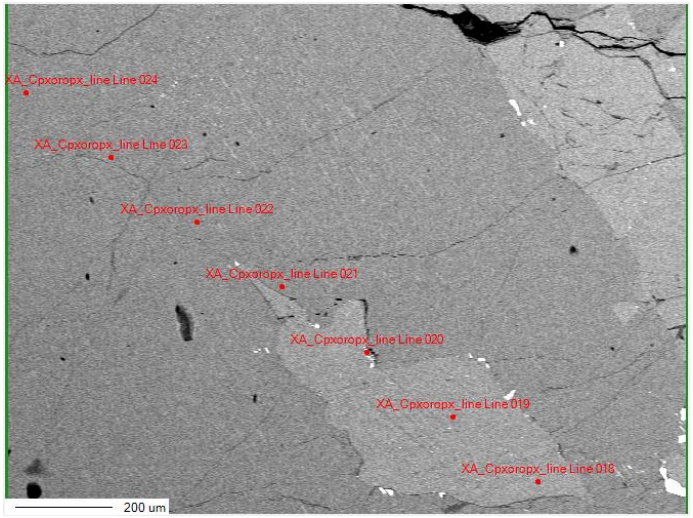
XA_Cpxoropx_line Line 024
XA_Cpxoropx_line Line 023
XA_Cpxoropx_line Line 022
XA_Cpxoropx_line Line 021
XA_Cpxoropx_line Line 020
XA_Cpxoropx_line Line 019
XA_Cpxoropx_line Line 018
200 um

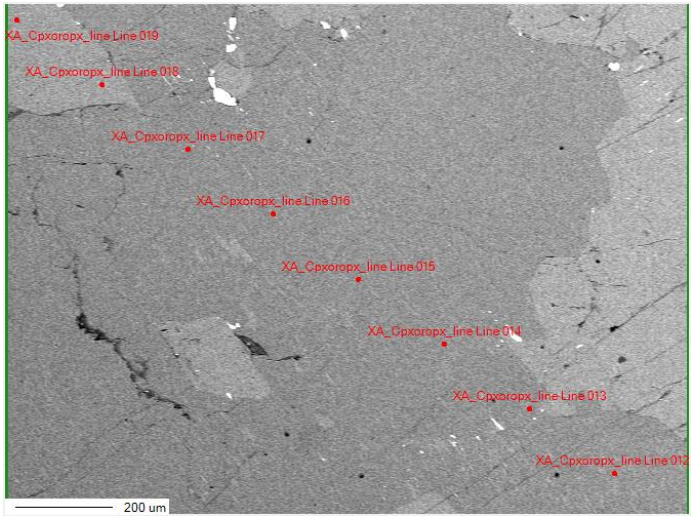
XA_Cpxoropx_line Line 019
XA_Cpxoropx_line Line 018
XA_Cpxoropx_line Line 017
XA_Cpxoropx_line Line 016
XA_Cpxoropx_line Line 015
XA_Cpxoropx_line Line 014
XA_Cpxoropx_line Line 013
XA_Cpxoropx_line Line 012
200 um

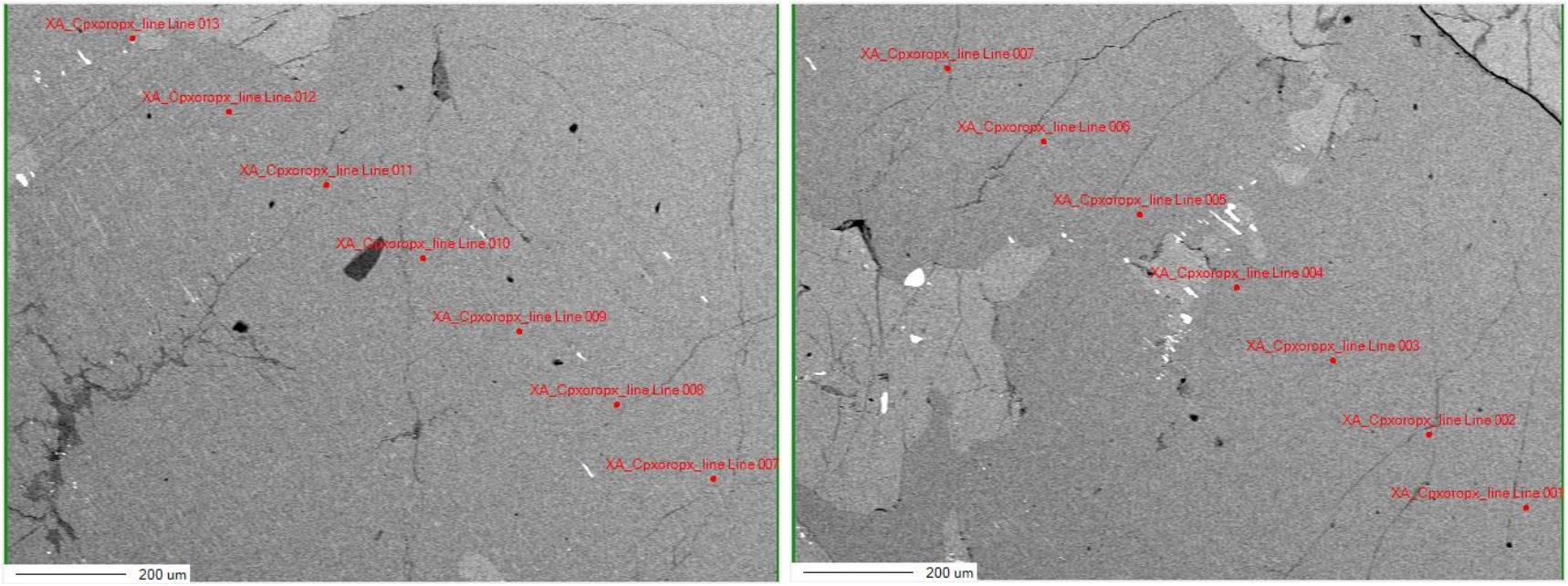
XA_Cpxoropx_line Line 013
XA_Cpxoropx_line Line 012
XA_Cpxoropx_line Line 011
XA_Cpxoropx_line Line 010
XA_Cpxoropx_line Line 009
XA_Cpxoropx_line Line 008
XA_Cpxoropx_line Line 007
200 um
XA_Cpxoropx_line Line 007
XA_Cpxoropx_line Line 006
XA_Cpxoropx_line Line 005
XA_Cpxoropx_line Line 004
XA_Cpxoropx_line Line 003
XA_Cpxoropx_line Line 002
XA_Cpxoropx_line Line 001
200 um

Table 8.19: *EPMA data point results from profile XA4_Diop1-20 with accompanying image (next page).*

Original data point name	Renamed data point	Na2O(Mass%)	MgO(Mass%)	Al2O3(Mass%)	CaO(Mass%)	K2O(Mass%)	Cr2O3(Mass%)	FeO(Mass%)	MnO(Mass%)	NiO(Mass%)	TiO2(Mass%)	SiO2(Mass%)	Total:
XA_opx_line3 Line 001	XA4_Diop1	0.4839	16.31	4.82	19.63	0.0049	0.301	5.84	0.1402	0.0353	1.2627	49.87	98.698
XA_opx_line3 Line 002	XA4_Diop2	0.447	18.41	4.77	15.41	LOD	0.341	7.36	0.1796	0.0168	0.9982	50.59	98.5226
XA_opx_line3 Line 003	XA4_Diop3	0.5712	14.46	5.27	22.74	0.0001	0.448	4.73	0.1126	0.0285	1.3766	49.75	99.487
XA_opx_line3 Line 004	XA4_Diop4	0.0387	26.64	3.22	1.69	LOD	0.2487	14.58	0.2925	0.0117	0.1777	53.1	99.9993
XA_opx_line3 Line 005	XA4_Diop5	0.4074	16.89	5.03	19	LOD	0.3933	6.71	0.1388	0.0193	1.168	49.32	99.0768
XA_opx_line3 Line 006	XA4_Diop6	0.592	14.32	5.53	22.14	0.0015	0.52	5.27	0.1291	0.036	1.3503	48.84	98.7289
XA_opx_line3 Line 007	XA4_Diop7	0.4665	16.61	5.14	17.7	0.0031	0.4368	6.6	0.1531	LOD	1.2165	50.31	98.636
XA_opx_line3 Line 008	XA4_Diop8	0.5142	14.87	5.31	21.94	0.0065	0.5709	5.47	0.1443	LOD	1.2824	48.88	98.9883
XA_opx_line3 Line 009	XA4_Diop9	0.5092	14.78	5.37	21.78	0.0031	0.445	5.34	0.1598	0.0243	1.4194	49.58	99.4108
XA_opx_line3 Line 010	XA4_Diop10	0.0295	22.12	0.5163	25.21	LOD	0.0161	5.24	0.3332	0.0158	0.0251	14.72	68.226
XA_opx_line3 Line 011	XA4_Diop11	0.0318	19.62	0.3405	25.35	0.0046	LOD	5.56	0.2976	0.0083	0.0211	4.2	55.4339
XA_opx_line3 Line 012	XA4_Diop12	0.5573	14.4	4.85	22.62	0.0064	0.4162	5.23	0.1422	LOD	1.2978	49.69	99.2099
XA_opx_line3 Line 013	XA4_Diop13	0.5676	14.25	5.23	22.54	0.0135	0.4541	5.22	0.1287	0.0042	1.3849	49.07	98.863
XA_opx_line3 Line 014	XA4_Diop14	0.7293	14.35	4.63	22.94	0.0572	0.4583	5.17	0.1631	0.0251	1.2899	49.59	99.4029
XA_opx_line3 Line 015	XA4_Diop15	0.478	16.6	4.65	18.59	LOD	0.3496	6.58	0.2212	0.0419	1.1665	50.47	99.1472
XA_opx_line3 Line 016	XA4_Diop16	0.3899	17.66	4.68	17.39	LOD	0.4168	7.91	0.2295	0.0251	1.2397	49.75	99.691
XA_opx_line3 Line 017	XA4_Diop17	0.4067	18.07	4.3	16.25	LOD	0.3664	8.54	0.1921	0.0234	1.0829	51.05	100.2815
XA_opx_line3 Line 018	XA4_Diop18	0.5107	14.88	5.13	22.39	0.0067	0.4666	5.31	0.1732	0.0234	1.402	49.1	99.3926
XA_opx_line3 Line 019	XA4_Diop19	0.5277	14.81	4.98	22.24	LOD	0.5225	5.43	0.1851	0.0033	1.32	49.99	100.0086
XA_opx_line3 Line 020	XA4_Diop20	0.2803	21.23	3.8	10.29	LOD	0.3146	10.13	0.1701	0.021	0.6573	51.93	98.8233

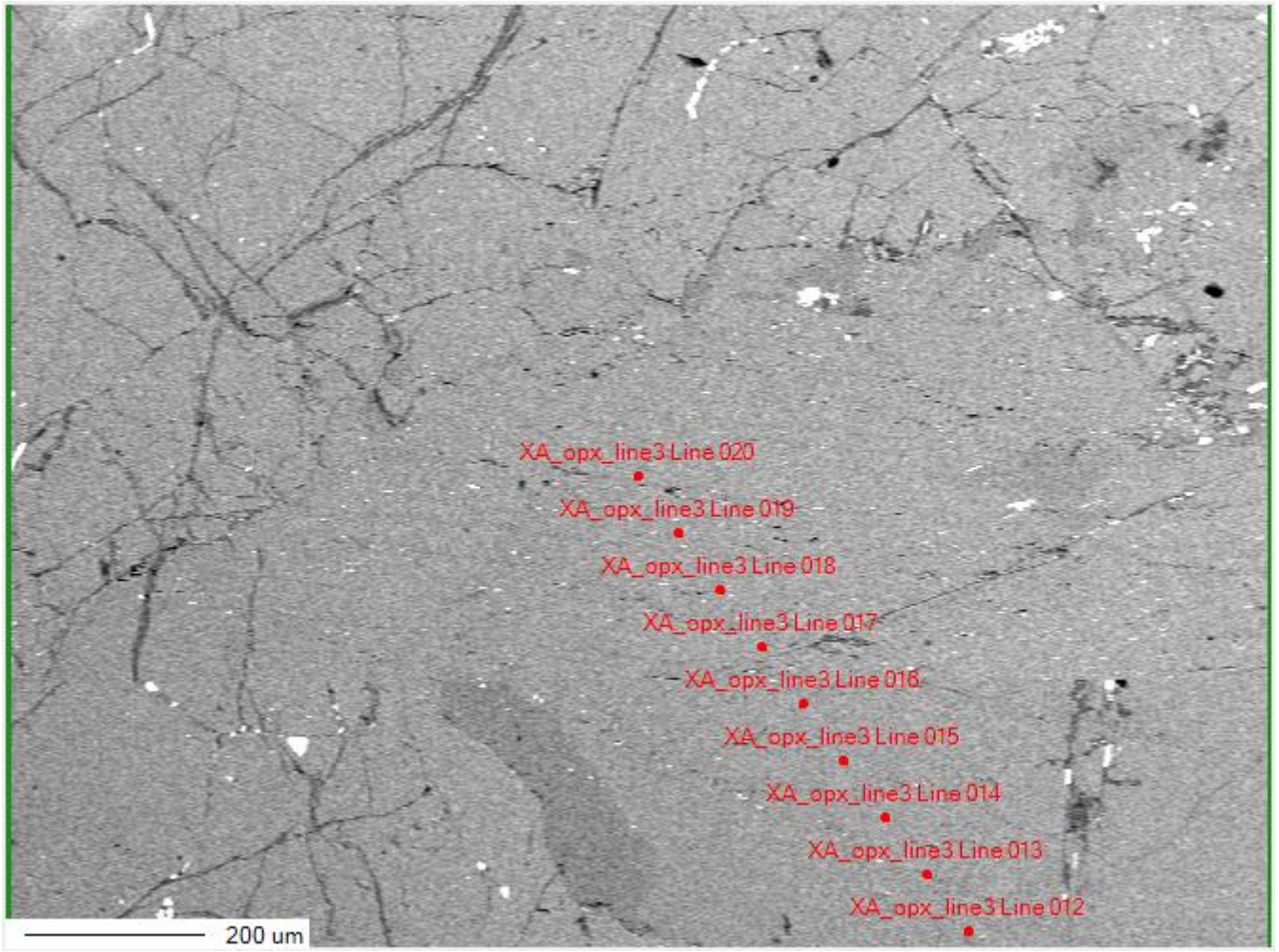
XA_opx_line3 Line 020
XA_opx_line3 Line 019
XA_opx_line3 Line 018
XA_opx_line3 Line 017
XA_opx_line3 Line 016
XA_opx_line3 Line 015
XA_opx_line3 Line 014
XA_opx_line3 Line 013
XA_opx_line3 Line 012
200 um

Table 8.20: *EPMA data point results from profile XA5_Diop1-20 with accompanying images (next page).*

Original data point name	Renamed data point	Na2O(Mass%)	MgO(Mass%)	Al2O3(Mass%)	CaO(Mass%)	K2O(Mass%)	Cr2O3(Mass%)	FeO(Mass%)	MnO(Mass%)	NiO(Mass%)	TiO2(Mass%)	SiO2(Mass%)	Total:
XA_possiblycpx_line3 Line 001	XA5_Diop1	0.5188	14.98	4.89	22.45	LOD	0.4213	4.97	0.1786	0.0075	1.2441	49.54	99.2003
XA_possiblycpx_line3 Line 002	XA5_Diop2	0.5178	15.55	5.02	21.35	0.0008	0.3596	5.39	0.1589	0.0201	1.3686	49.83	99.5658
XA_possiblycpx_line3 Line 003	XA5_Diop3	0.5114	14.9	5.19	21.93	0.0019	0.4195	5.31	0.1633	0.0578	1.3544	49.2	99.0383
XA_possiblycpx_line3 Line 004	XA5_Diop4	0.5313	14.73	4.66	23.11	LOD	0.3879	4.55	0.1225	0.0469	1.09	49.85	99.0786
XA_possiblycpx_line3 Line 005	XA5_Diop5	0.5136	15.01	5.12	21.3	LOD	0.569	6.48	0.1419	0.0268	1.4866	48.71	99.3579
XA_possiblycpx_line3 Line 006	XA5_Diop6	0.5562	14.79	5.28	22.11	0.0064	0.3914	5.21	0.1475	0.036	1.379	49.6	99.5065
XA_possiblycpx_line3 Line 007	XA5_Diop7	0.6219	14.34	5.38	22.76	LOD	0.4061	5.06	0.1861	0.0151	1.3997	48.69	98.8589
XA_possiblycpx_line3 Line 008	XA5_Diop8	0.323	19.16	4.59	14.65	0.0076	0.2781	8.68	0.1779	0.0335	1.0038	50.6	99.5039
XA_possiblycpx_line3 Line 009	XA5_Diop9	0.5743	14.5	5.28	22.29	0.0001	0.3738	5.12	0.1641	0.0209	1.2452	49.61	99.1784
XA_possiblycpx_line3 Line 010	XA5_Diop10	0.5382	14.67	5.19	22.25	LOD	0.3058	5.13	0.0903	0.0142	1.2663	49.33	98.7848
XA_possiblycpx_line3 Line 011	XA5_Diop11	0.4736	15.54	5.15	20.33	0.0106	0.4548	5.98	0.1441	LOD	1.2205	49.58	98.8836
XA_possiblycpx_line3 Line 012	XA5_Diop12	0.5425	14.49	5.13	22.47	LOD	0.435	5.59	0.1212	0.0268	1.2294	49.22	99.2549
XA_possiblycpx_line3 Line 013	XA5_Diop13	0.4543	16.5	4.8	18.99	LOD	0.3302	6.32	0.1496	0.0092	1.0675	49.48	98.1008
XA_possiblycpx_line3 Line 014	XA5_Diop14	0.562	14.66	5.11	22.38	0.0135	0.3849	5.25	0.1564	0.0251	1.2617	49.22	99.0236
XA_possiblycpx_line3 Line 015	XA5_Diop15	0.4257	16.7	4.53	18.88	LOD	0.3687	6.83	0.1551	LOD	1.1047	50.78	99.7742
XA_possiblycpx_line3 Line 016	XA5_Diop16	0.5238	14.6	4.77	23.08	0.005	0.3633	4.85	0.1081	0.0075	1.1866	49.91	99.4043
XA_possiblycpx_line3 Line 017	XA5_Diop17	0.4527	15.3	5.03	20.88	LOD	0.4097	6	0.1298	0.0376	1.2984	49.26	98.7982
XA_possiblycpx_line3 Line 018	XA5_Diop18	0.4902	15.58	5.15	21.31	0.0019	0.3962	5.21	0.1432	0.0075	1.3583	49.13	98.7773
XA_possiblycpx_line3 Line 019	XA5_Diop19	0.4531	16.03	5.01	19.41	0.0118	0.3625	6.17	0.1727	0.051	1.2563	48.89	97.8174
XA_possiblycpx_line3 Line 020	XA5_Diop20	0.52	14.65	4.83	22.88	LOD	0.3875	4.88	0.1566	LOD	1.2088	49.78	99.2929

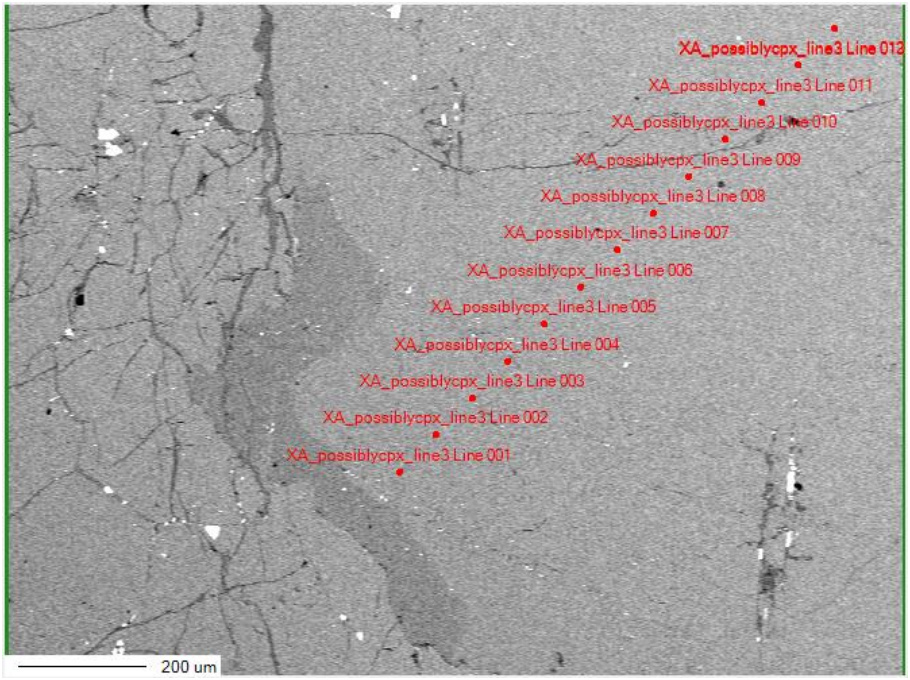
XA_possiblycpx_line3 Line 012
XA_possiblycpx_line3 Line 011
XA_possiblycpx_line3 Line 010
XA_possiblycpx_line3 Line 009
XA_possiblycpx_line3 Line 008
XA_possiblycpx_line3 Line 007
XA_possiblycpx_line3 Line 006
XA_possiblycpx_line3 Line 005
XA_possiblycpx_line3 Line 004
XA_possiblycpx_line3 Line 003
XA_possiblycpx_line3 Line 002
XA_possiblycpx_line3 Line 001
200 um

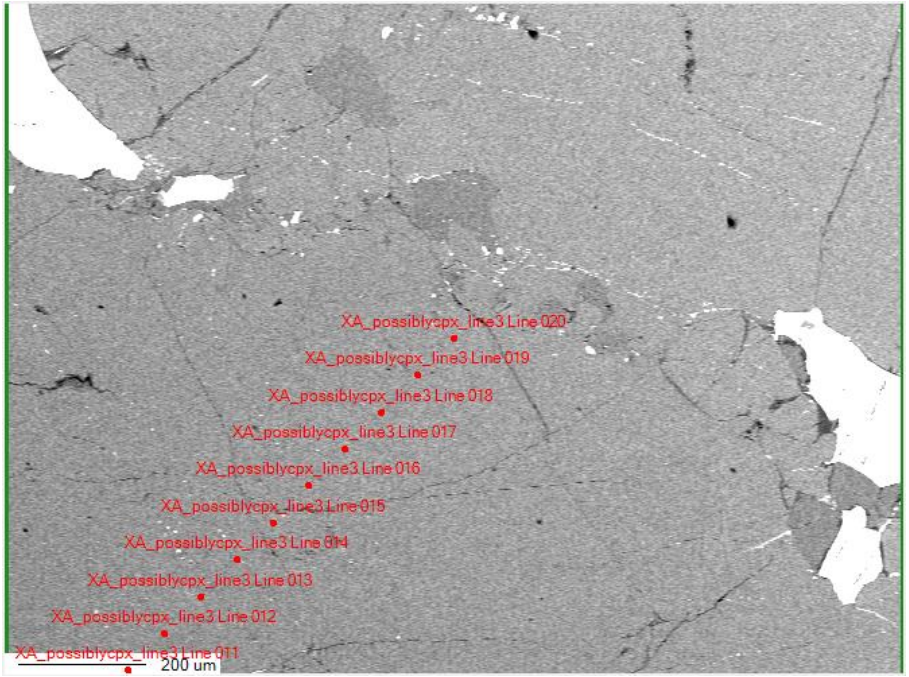
XA_possiblycpx_line3 Line 020
XA_possiblycpx_line3 Line 019
XA_possiblycpx_line3 Line 018
XA_possiblycpx_line3 Line 017
XA_possiblycpx_line3 Line 016
XA_possiblycpx_line3 Line 015
XA_possiblycpx_line3 Line 014
XA_possiblycpx_line3 Line 013
XA_possiblycpx_line3 Line 012
XA_possiblycpx_line3 Line 011
200 um

Table 8.21: *EPMA data point results from profile XA1_Enst1-20 with accompanying image (next page).*

Original data point name	Renamed data point	Na2O(Mass%)	MgO(Mass%)	Al2O3(Mass%)	CaO(Mass%)	K2O(Mass%)	Cr2O3(Mass%)	FeO(Mass%)	MnO(Mass%)	NiO(Mass%)	TiO2(Mass%)	SiO2(Mass%)	Total:
XA_opx_line4 Line 001	XA1_Enst1	0.0453	27.71	3.1	2.36	0.0151	0.2397	12.17	0.2088	0.021	0.2444	53.36	99.4743
XA_opx_line4 Line 002	XA1_Enst2	0.0757	27.13	3.14	3.21	0.0017	0.1948	12.09	0.2256	0.0403	0.2576	53.42	99.7857
XA_opx_line4 Line 003	XA1_Enst3	0.0179	29.04	3.01	0.6966	LOD	0.1886	13.33	0.2349	0.0596	0.2409	52.99	99.8085
XA_opx_line4 Line 004	XA1_Enst4	LOD	27.78	2.07	0.5268	LOD	0.1767	15.19	0.3209	0.0652	3.64	50.87	100.6396
XA_opx_line4 Line 005	XA1_Enst5	0.1299	25.37	2.94	4.81	0.0013	0.1781	10.55	0.1894	0.0486	0.9796	47.06	92.2569
XA_opx_line4 Line 006	XA1_Enst6	0.0115	29.08	2.86	0.6708	LOD	0.1654	13.2	0.2709	0.0436	0.4876	52.99	99.7798
XA_opx_line4 Line 007	XA1_Enst7	0.0343	29.01	3.09	0.6288	0.0088	0.1934	13.07	0.2787	0.0403	0.2712	52.87	99.4955
XA_opx_line4 Line 008	XA1_Enst8	0.1319	24.95	3.74	6.55	LOD	0.2392	10.22	0.2161	0.0244	0.5618	52.52	99.1534
XA_opx_line4 Line 009	XA1_Enst9	0.0668	28.32	2.65	2.58	LOD	0.1664	12	0.219	0.0638	0.1991	53.92	100.1851
XA_opx_line4 Line 010	XA1_Enst10	0.0099	29.08	2.66	1.47	LOD	0.1629	12.34	0.2768	0.0361	0.1655	53.95	100.1512
XA_opx_line4 Line 011	XA1_Enst11	0.0051	29.36	2.99	0.3638	LOD	0.1937	12.79	0.2712	0.0159	0.1631	53.78	99.9328
XA_opx_line4 Line 012	XA1_Enst12	0.0545	28.11	3.04	2.36	0.0029	0.146	11.94	0.2157	0.0437	0.2603	53.83	100.0031
XA_opx_line4 Line 013	XA1_Enst13	0.0429	28.65	3.41	1.51	LOD	0.1692	12.31	0.2309	0.0621	0.2706	53.56	100.2157
XA_opx_line4 Line 014	XA1_Enst14	0.0735	27.98	2.84	3.27	0.0101	0.1448	11.5	0.241	0.0437	0.166	53.94	100.2091
XA_opx_line4 Line 015	XA1_Enst15	0.0263	28.62	3.31	1.86	LOD	0.1925	12.49	0.2308	0.0159	0.2138	52.44	99.3993
XA_opx_line4 Line 016	XA1_Enst16	0.1235	22.42	1.6485	5.88	0.006	0.1993	15.35	0.2656	0.0739	8.56	45.46	99.9868
XA_opx_line4 Line 017	XA1_Enst17	0.0087	27.67	2.1	0.5268	LOD	0.1922	15.37	0.2599	0.0709	4.7	50.14	101.0385
XA_opx_line4 Line 018	XA1_Enst18	0.0461	28.11	3.25	2.42	LOD	0.1992	11.98	0.2384	0.057	0.2328	53.58	100.1135
XA_opx_line4 Line 019	XA1_Enst19	0.0524	29.03	3.01	1.55	LOD	0.1787	11.97	0.2395	0.0302	0.1806	53.79	100.0314
XA_opx_line4 Line 020	XA1_Enst20	0.0524	27.86	3.39	3.03	LOD	0.1977	11.86	0.269	0.078	0.249	53.09	100.0761

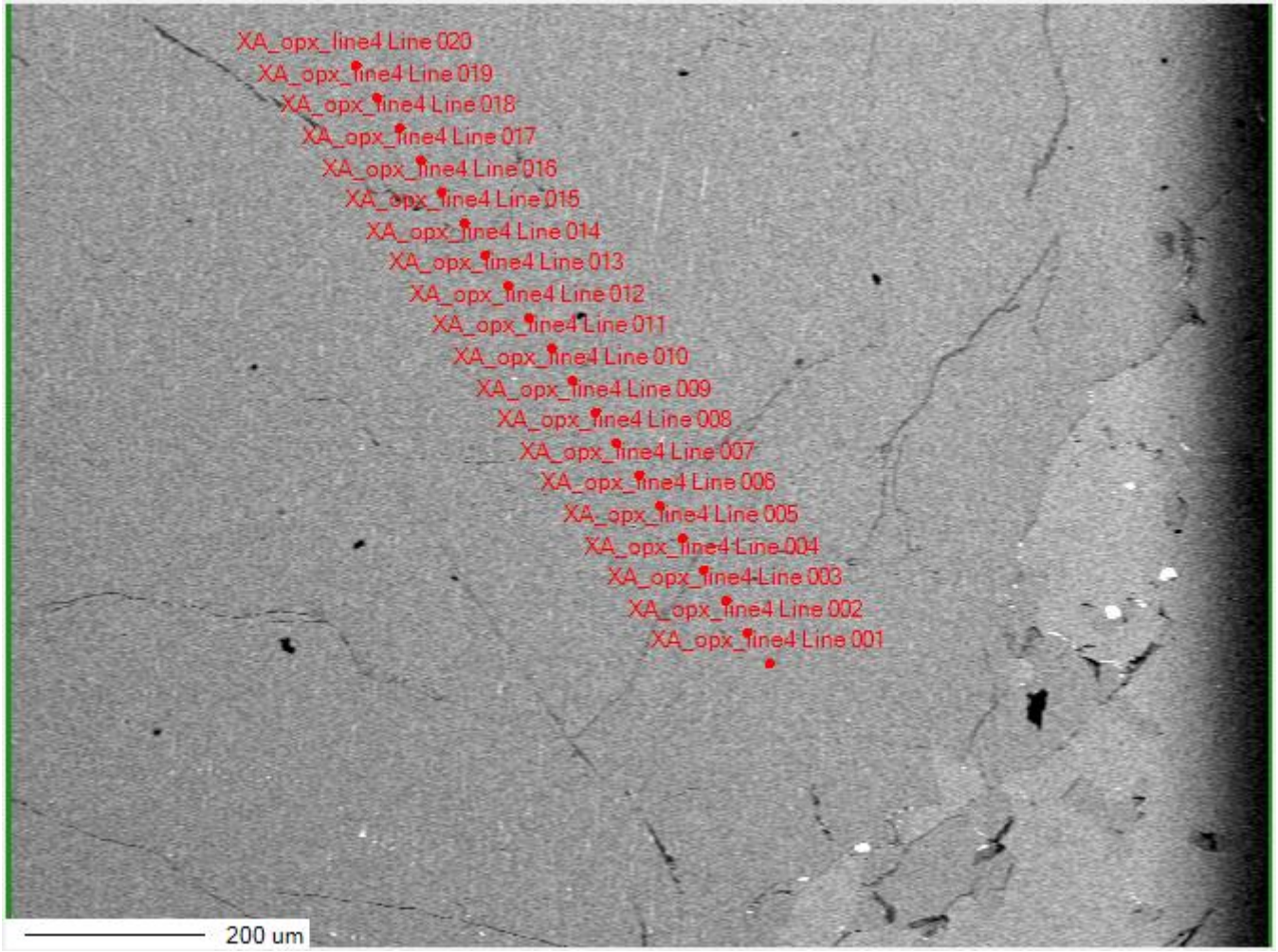
XA_opx_line4 Line 020
XA_opx_line4 Line 019
XA_opx_line4 Line 018
XA_opx_line4 Line 017
XA_opx_line4 Line 016
XA_opx_line4 Line 015
XA_opx_line4 Line 014
XA_opx_line4 Line 013
XA_opx_line4 Line 012
XA_opx_line4 Line 011
XA_opx_line4 Line 010
XA_opx_line4 Line 009
XA_opx_line4 Line 008
XA_opx_line4 Line 007
XA_opx_line4 Line 006
XA_opx_line4 Line 005
XA_opx_line4 Line 004
XA_opx_line4 Line 003
XA_opx_line4 Line 002
XA_opx_line4 Line 001
200 um

Table 8.22: *EPMA data point results from profile XA2_Enst1-20 (no accompanying image).*

Original data point name	Renamed data point	Na2O(Mass%)	MgO(Mass%)	Al2O3(Mass%)	CaO(Mass%)	K2O(Mass%)	Cr2O3(Mass%)	FeO(Mass%)	MnO(Mass%)	NiO(Mass%)	TiO2(Mass%)	SiO2(Mass%)	Total:
XA_opx_line5 Line 001	XA2_Enst1	0.0303	28.77	2.76	1.0908	LOD	0.1672	12.6	0.2732	0.0487	0.2369	53.39	99.3671
XA_opx_line5 Line 002	XA2_Enst2	LOD	29.36	2.84	0.6007	LOD	0.1591	12.72	0.2117	0.0754	0.2516	53.27	99.4885
XA_opx_line5 Line 003	XA2_Enst3	0.0267	28.78	2.65	0.7464	0.0012	0.1807	12.9	0.2706	0.036	0.1335	53.65	99.3751
XA_opx_line5 Line 004	XA2_Enst4	0.0215	29.04	3.01	0.6121	LOD	0.1775	12.99	0.2378	0.0519	0.2138	53.15	99.5046
XA_opx_line5 Line 005	XA2_Enst5	LOD	28.94	2.98	0.5041	0.0015	0.1794	12.62	0.226	0.0251	0.1698	53.62	99.2659
XA_opx_line5 Line 006	XA2_Enst6	LOD	29.87	1.97	0.552	0.006	0.173	12.68	0.2933	0.0528	0.1637	54.17	99.9308
XA_opx_line5 Line 007	XA2_Enst7	0.0319	28.47	2.86	1.86	LOD	0.1389	12.3	0.206	0.0502	0.2565	53.34	99.5135
XA_opx_line5 Line 008	XA2_Enst8	0.047	29.08	2.95	0.4837	LOD	0.1277	12.64	0.2835	0.0352	0.183	53.2	99.0301
XA_opx_line5 Line 009	XA2_Enst9	0.4151	14.93	4.64	23.15	0.0181	0.2267	4.4	0.11	0.0334	1.465	49.62	99.0083
XA_opx_line5 Line 010	XA2_Enst10	0.0716	27.85	2.38	3.03	0.0033	0.136	12.03	0.23	0.0686	0.1154	53.52	99.4349
XA_opx_line5 Line 011	XA2_Enst11	0.1262	27.24	2.88	4.08	0.0119	0.1883	11	0.1963	0.0384	0.2603	53.51	99.5314
XA_opx_line5 Line 012	XA2_Enst12	0.0716	28.46	2.62	1.73	0.0091	0.1969	11.97	0.2409	0.0226	0.2595	53.79	99.3706
XA_opx_line5 Line 013	XA2_Enst13	0.043	28.27	2.71	2.02	0.0175	0.194	12	0.2534	0.0235	0.1826	52.98	98.694
XA_opx_line5 Line 014	XA2_Enst14	0.0363	27.99	3.18	2.77	0.0085	0.2271	12.08	0.2545	LOD	0.2185	53.27	100.0349
XA_opx_line5 Line 015	XA2_Enst15	0.0185	26.15	4.01	8.74	0.0018	0.2307	10.8	0.1951	0.0509	0.0598	36.78	87.0368
XA_opx_line5 Line 016	XA2_Enst16	0.0146	29.05	2.85	0.5197	0.0066	0.1542	13.05	0.2171	0.0343	0.1579	53.18	99.2344
XA_opx_line5 Line 017	XA2_Enst17	0.0293	28.75	2.68	1.2287	0.004	0.1984	12.68	0.2742	0.0118	0.243	53.47	99.5694
XA_opx_line5 Line 018	XA2_Enst18	0.0382	26.41	1.98	2.79	0.0093	0.2292	13.97	0.2819	0.0425	4.16	50.51	100.4211
XA_opx_line5 Line 019	XA2_Enst19	0.0246	29.37	2.39	0.8298	0.0095	0.1872	12.9	0.2577	0.0838	0.1823	53.7	99.9349
XA_opx_line5 Line 020	XA2_Enst20	0.0387	28.35	2.72	2.11	LOD	0.1675	12.07	0.2611	0.0352	0.227	54.02	99.9995

Table 8.23: *EPMA data point results from profile XA3_Enst1-20 with accompanying images (next page).*

Original data point name	Renamed data point	Na2O(Mass%)	MgO(Mass%)	Al2O3(Mass%)	CaO(Mass%)	K2O(Mass%)	Cr2O3(Mass%)	FeO(Mass%)	MnO(Mass%)	NiO(Mass%)	TiO2(Mass%)	SiO2(Mass%)	Total:
XA_opx_line6 Line 001	XA3_Enst1	0.0169	29.33	2.7	0.3867	0.0125	0.1775	13.23	0.2835	0.0084	0.9053	53.13	100.1808
XA_opx_line6 Line 002	XA3_Enst2	0.0266	29.25	2.93	0.9321	0.0022	0.1185	12.6	0.2672	0.0284	0.1327	54.36	100.6477
XA_opx_line6 Line 003	XA3_Enst3	0.0443	28.57	3.1	1.3424	0.0085	0.1701	12.5	0.2541	0.0251	0.2367	53.92	100.1712
XA_opx_line6 Line 004	XA3_Enst4	1.6	25.11	2.53	1.55	0.038	0.1241	9.74	0.2131	0.0285	0.1827	48.82	89.9364
XA_opx_line6 Line 005	XA3_Enst5	0.0768	28.39	3.15	2.47	0.0227	0.236	11.99	0.2355	0.0318	0.2114	53.13	99.9442
XA_opx_line6 Line 006	XA3_Enst6	0.0183	28.64	3.23	1.44	0.0086	0.2292	12.54	0.2571	0.0318	0.2111	53.91	100.5161
XA_opx_line6 Line 007	XA3_Enst7	0.0394	27.72	2.92	3.26	0.0081	0.174	11.6	0.2358	0.0519	0.2451	53.38	99.6343
XA_opx_line6 Line 008	XA3_Enst8	0.0513	25.9	2.32	3.27	0.006	0.1862	14.61	0.233	0.0033	4.69	49.25	100.5198
XA_opx_line6 Line 009	XA3_Enst9	0.0471	27.86	3.05	3.13	LOD	0.2129	11.74	0.1962	0.0686	0.286	52.7	99.2908
XA_opx_line6 Line 010	XA3_Enst10	0.0275	28.71	3.05	0.6754	0.0115	0.2565	13.01	0.2612	0.0777	0.2712	53.29	99.641
XA_opx_line6 Line 011	XA3_Enst11	0.0363	29.23	2.81	0.6601	0.0211	0.1946	13.11	0.2474	0.0142	0.5656	53.58	100.4693
XA_opx_line6 Line 012	XA3_Enst12	0.068	28.15	2.79	3.11	0.0002	0.2116	11.81	0.238	0.0419	0.2067	53.96	100.5864
XA_opx_line6 Line 013	XA3_Enst13	0.0592	28.34	3.01	1.82	0.0094	0.1967	12.44	0.2563	0.0603	0.2316	53.4	99.8235
XA_opx_line6 Line 014	XA3_Enst14	0.0382	28.82	3.04	1.51	0.0042	0.2106	12.35	0.2996	0.0552	0.1792	53.72	100.227
XA_opx_line6 Line 015	XA3_Enst15	0.0338	28.62	2.16	0.8553	0.016	0.1396	13.98	0.2367	0.0525	2.82	51.15	100.0639
XA_opx_line6 Line 016	XA3_Enst16	0.0414	29.17	2.9	0.7006	LOD	0.2166	12.76	0.2856	0.0645	0.2578	54.11	100.5065
XA_opx_line6 Line 017	XA3_Enst17	0.0514	29.13	2.87	1.1177	0.0217	0.2026	12.43	0.2604	0.0552	0.3108	53.23	99.6798
XA_opx_line6 Line 018	XA3_Enst18	0.1254	25.48	3.38	7.22	LOD	0.3048	10.04	0.2666	0.0786	0.4689	52.69	100.0543
XA_opx_line6 Line 019	XA3_Enst19	0.0198	28.71	2.38	1.9	0.0038	0.2572	12.82	0.3233	0.0551	0.9031	53.54	100.9123
XA_opx_line6 Line 020	XA3_Enst20	0.027	28.88	2.96	1.1495	0.0211	0.173	12.39	0.2005	0.0259	0.1486	53.54	99.5156

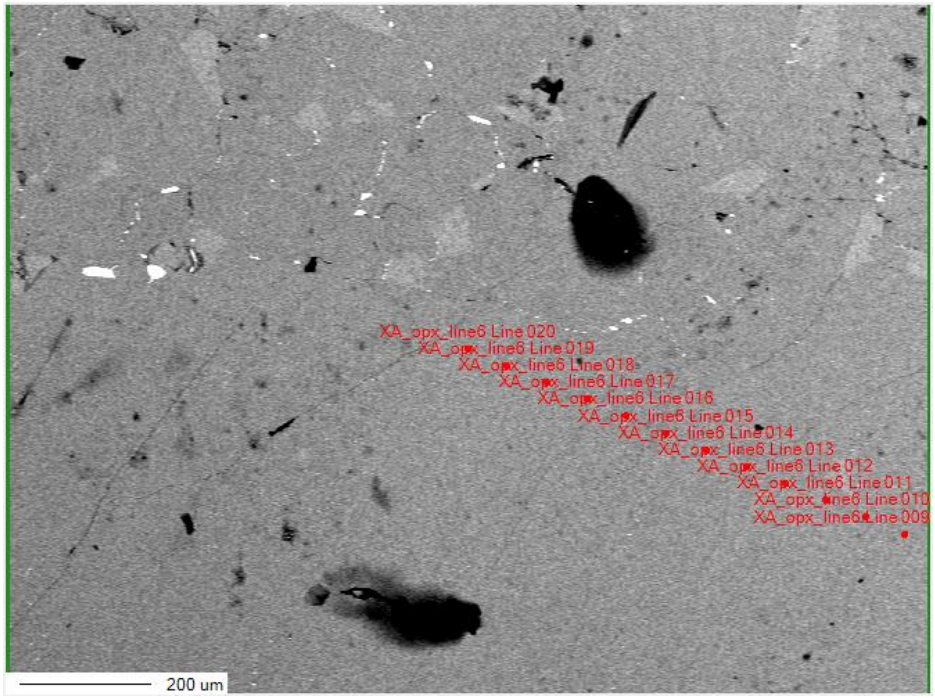
XA_opx_line6 Line 020
XA_opx_line6 Line 019
XA_opx_line6 Line 018
XA_opx_line6 Line 017
XA_opx_line6 Line 016
XA_opx_line6 Line 015
XA_opx_line6 Line 014
XA_opx_line6 Line 013
XA_opx_line6 Line 012
XA_opx_line6 Line 011
XA_opx_line6 Line 010
XA_opx_line6 Line 009
200 um

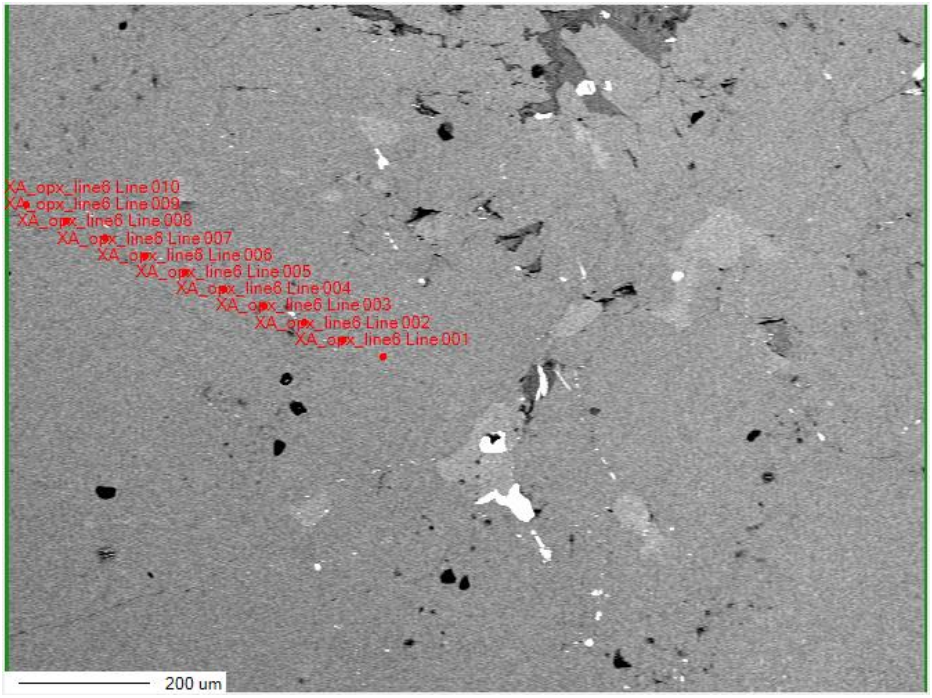
XA_opx_line6 Line 010
XA_opx_line6 Line 009
XA_opx_line6 Line 008
XA_opx_line6 Line 007
XA_opx_line6 Line 006
XA_opx_line6 Line 005
XA_opx_line6 Line 004
XA_opx_line6 Line 003
XA_opx_line6 Line 002
XA_opx_line6 Line 001
200 um

Table 8.24: *EPMA data points from profile XA3_Ol1-20 with accompanying images (next page).*

Original data point name	Renamed data point	Na2O(Mass%)	MgO(Mass%)	Al2O3(Mass%)	CaO(Mass%)	K2O(Mass%)	Cr2O3(Mass%)	FeO(Mass%)	MnO(Mass%)	NiO(Mass%)	TiO2(Mass%)	SiO2(Mass%)	Total:
XA_Ol_line5 Line 001	XA3_Ol1	0.0079	41.32	LOD	LOD	0.0081	0.0361	20.11	0.2818	0.1525	0.0215	38.46	100.3979
XA_Ol_line5 Line 002	XA3_Ol2	0.0055	41.36	LOD	LOD	0.0055	LOD	20.26	0.2947	0.16	0.0153	39.01	101.111
XA_Ol_line5 Line 003	XA3_Ol3	LOD	41.25	LOD	LOD	0.0067	LOD	19.65	0.2411	0.1841	0.0046	39.04	100.3765
XA_Ol_line5 Line 004	XA3_Ol4	LOD	41.35	LOD	LOD	LOD	LOD	20	0.28	0.1104	0.0172	39.01	100.7676
XA_Ol_line5 Line 005	XA3_Ol5	0.0208	41.48	LOD	LOD	LOD	LOD	20.27	0.2506	0.1277	0.0113	38.74	100.9004
XA_Ol_line5 Line 006	XA3_Ol6	0.0396	41.31	LOD	LOD	LOD	0.009	20.4	0.2688	0.141	LOD	39.19	101.3584
XA_Ol_line5 Line 007	XA3_Ol7	LOD	41.29	LOD	0.0018	LOD	0.0165	20.21	0.2829	0.1335	0.0051	38.87	100.8098
XA_Ol_line5 Line 008	XA3_Ol8	0.0158	41.14	LOD	0.0028	LOD	0.003	20.22	0.2525	0.1359	LOD	39.03	100.8
XA_Ol_line5 Line 009	XA3_Ol9	0.011	41.79	LOD	LOD	LOD	LOD	19.88	0.2376	0.1608	0.0128	39.53	101.6222
XA_Ol_line5 Line 010	XA3_Ol10	LOD	41.29	LOD	LOD	LOD	0.0045	19.96	0.2859	0.1367	0.0125	39.16	100.8496
XA_Ol_line5 Line 011	XA3_Ol11	0.0587	29.91	14.02	LOD	LOD	3.45	24.15	0.2509	0.1286	0.0189	23.76	95.7471
XA_Ol_line5 Line 012	XA3_Ol12	LOD	41.41	LOD	0.0008	LOD	0.006	19.95	0.2698	0.1284	0.0264	39.11	100.9014
XA_Ol_line5 Line 013	XA3_Ol13	LOD	41.56	LOD	LOD	LOD	LOD	20.02	0.3031	0.1384	LOD	38.82	100.8415
XA_Ol_line5 Line 014	XA3_Ol14	0.0137	31.12	0.6225	0.1245	LOD	0.0341	12.83	0.2607	0.1027	0.0384	51.24	96.3866
XA_Ol_line5 Line 015	XA3_Ol15	LOD	41.52	LOD	LOD	LOD	0.0256	19.93	0.2461	0.1524	0.0086	38.67	100.5527
XA_Ol_line5 Line 016	XA3_Ol16	0.0282	41.21	LOD	LOD	LOD	LOD	19.94	0.287	0.1218	0.0219	39.26	100.8689
XA_Ol_line5 Line 017	XA3_Ol17	LOD	41.48	LOD	LOD	0.0074	LOD	20.19	0.289	0.1442	0.0216	39	101.1322
XA_Ol_line5 Line 018	XA3_Ol18	0.0139	41.39	0.0037	LOD	LOD	0.012	20.01	0.244	0.1458	0.0177	38.89	100.7271
XA_Ol_line5 Line 019	XA3_Ol19	0.0359	40.96	LOD	LOD	LOD	0.0015	19.83	0.2397	0.1691	LOD	39.04	100.2762
XA_Ol_line5 Line 020	XA3_Ol20	0.0097	41.3	LOD	LOD	LOD	0.009	19.78	0.2795	0.1947	LOD	38.77	100.3429

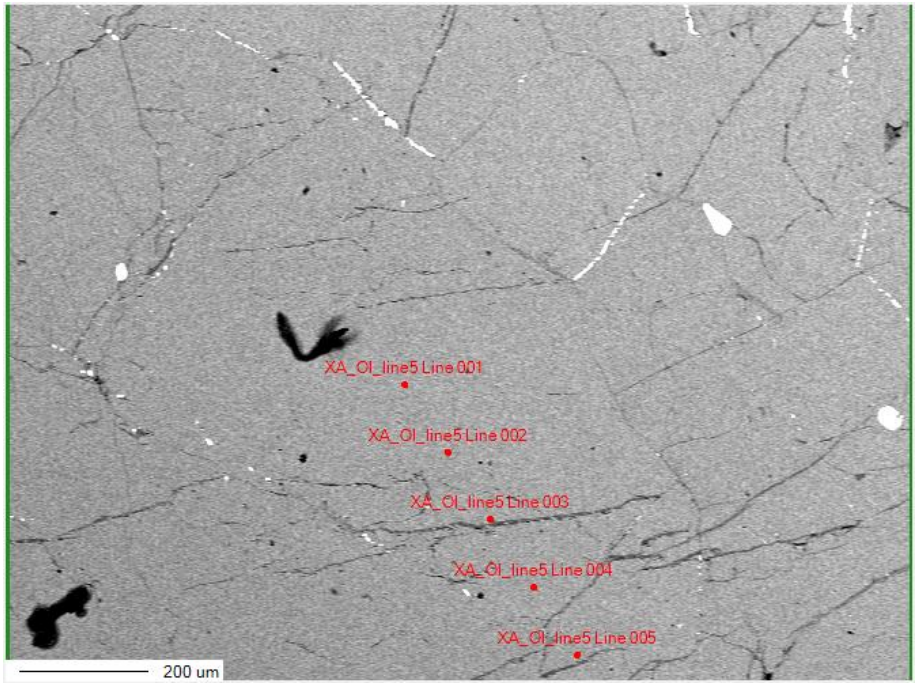
XA_OI_line5 Line 001
XA_OI_line5 Line 002
XA_OI_line5 Line 003
XA_OI_line5 Line 004
XA_OI_line5 Line 005
200 um

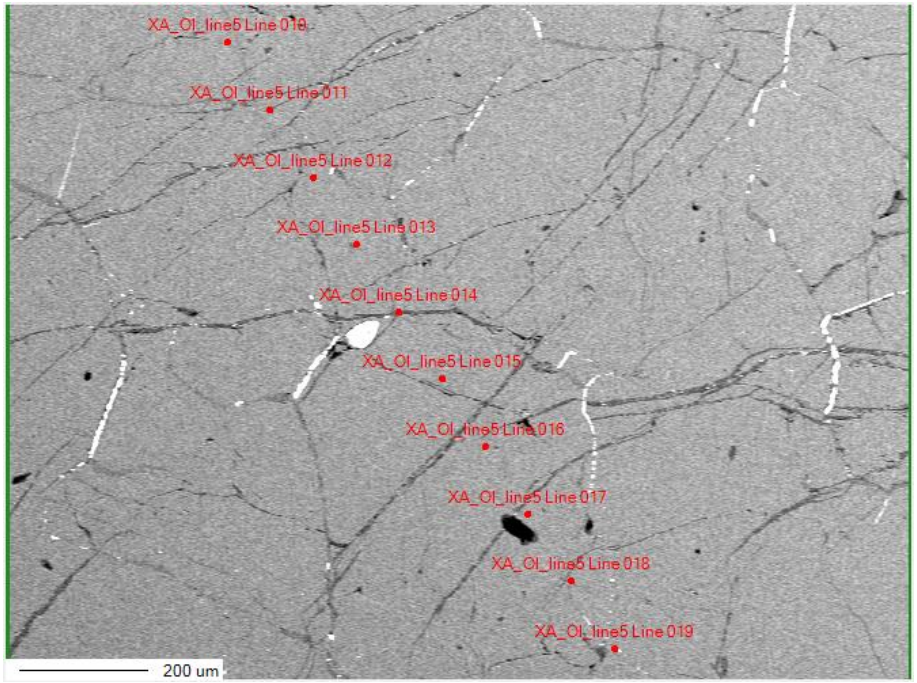
XA_OI_line5 Line 010
XA_OI_line5 Line 011
XA_OI_line5 Line 012
XA_OI_line5 Line 013
XA_OI_line5 Line 014
XA_OI_line5 Line 015
XA_OI_line5 Line 016
XA_OI_line5 Line 017
XA_OI_line5 Line 018
XA_OI_line5 Line 019
200 um

Table 8.25: *EPMA data point results from profile XB_Diop1-30 with accompanying images (next 2 pages).*

Original data point name	Renamed data point	Na2O(Mass%)	MgO(Mass%)	Al2O3(Mass%)	CaO(Mass%)	K2O(Mass%)	Cr2O3(Mass%)	FeO(Mass%)	MnO(Mass%)	NiO(Mass%)	TiO2(Mass%)	SiO2(Mass%)	Total:
XB_cpxline1 Line 001	XB1_Diop1	0.0496	29.11	3.18	0.3043	LOD	0.2313	13.29	0.2688	0.0527	0.1776	53.68	100.3443
XB_cpxline1 Line 002	XB1_Diop2	0.0085	29.6	2.73	0.3324	LOD	0.1725	13.16	0.3037	0.0736	0.1272	54.32	100.8279
XB_cpxline1 Line 003	XB1_Diop3	LOD	29.24	2.97	0.3946	LOD	0.1694	13.1	0.2363	0.0468	0.131	53.94	100.2281
XB_cpxline1 Line 004	XB1_Diop4	0.5639	14.71	4.92	23.35	LOD	0.3218	4.52	0.1396	0.0167	1.3894	50.29	100.2214
XB_cpxline1 Line 005	XB1_Diop5	0.5425	14.39	5.04	22.72	0.0034	0.3675	5.15	0.1733	LOD	1.4266	49.83	99.6433
XB_cpxline1 Line 006	XB1_Diop6	0.4637	15.57	4.27	20.63	LOD	0.4443	6.88	0.126	0.0258	1.0697	50.06	99.5395
XB_cpxline1 Line 007	XB1_Diop7	0.5679	14.41	5.27	22.67	LOD	0.4514	5.3	0.1471	0.0242	1.5691	49.7	100.1097
XB_cpxline1 Line 008	XB1_Diop8	0.5676	14.59	4.78	22.58	0.0063	0.3933	5.41	0.1548	0.0108	1.4322	50.3	100.225
XB_cpxline1 Line 009	XB1_Diop9	0.5954	14.24	5.12	22.96	LOD	0.456	5.2	0.1744	0.0225	1.5033	50.01	100.2816
XB_cpxline1 Line 010	XB1_Diop10	0.5958	14.29	5.31	22.59	LOD	0.4999	5.22	0.1569	0.0467	1.5306	49.8	100.0399
XB_cpxline1 Line 011	XB1_Diop11	0.5628	14.68	4.93	22.76	LOD	0.5305	5.36	0.1251	0.015	1.4193	50.33	100.7127
XB_cpxline1 Line 012	XB1_Diop12	0.551	14.44	5	22.75	0.0043	0.4754	5.51	0.1405	0.0242	1.5591	49.97	100.4245
XB_cpxline1 Line 013	XB1_Diop13	0.4935	15.29	4.77	21.48	LOD	0.5002	6.02	0.1481	0.03	1.4095	49.73	99.8713
XB_cpxline1 Line 014	XB1_Diop14	0.5482	14.38	5.19	22.87	LOD	0.405	4.82	0.1569	0.0258	1.4868	49.8	99.6827
XB_cpxline1 Line 015	XB1_Diop15	0.0419	27.36	3.15	2.84	0.0001	0.1929	12.95	0.2456	0.0333	0.2968	53.83	100.9406
XB_cpxline1 Line 016	XB1_Diop16	0.0582	27.12	3.38	2.46	LOD	0.2358	13.45	0.3017	0.05	0.2896	52.73	100.0753
XB_cpxline1 Line 017	XB1_Diop17	0.5661	14.16	5.35	22.78	0.0099	0.4258	4.93	0.1525	0.0391	1.485	50.19	100.0884
XB_cpxline1 Line 018	XB1_Diop18	0.0061	20.43	1.7346	0.7658	LOD	0.1661	25.75	0.402	LOD	18.15	35.59	102.9946
XB_cpxline1 Line 019	XB1_Diop19	0.5884	14.04	5.13	22.95	LOD	0.4071	5.3	0.1205	0.0133	1.4898	49.39	99.4291
XB_cpxline1 Line 020	XB1_Diop20	0.5618	14.04	4.95	22.91	LOD	0.4377	5.34	0.1391	0.0058	1.4239	50.02	99.8283
XB_cpxline1 Line 021	XB1_Diop21	0.5965	13.88	5.77	23.2	LOD	0.4507	5.24	0.1084	0.0191	1.73	49.3	100.2947
XB_cpxline1 Line 022	XB1_Diop22	0.0248	26.51	3.41	0.304	LOD	0.2815	16.25	0.3426	0.0648	0.1612	52.21	99.5589
XB_cpxline1 Line 023	XB1_Diop23	0.5768	13.82	5.34	23.07	0.0048	0.4057	5.19	0.126	LOD	1.5308	49.71	99.7741
XB_cpxline1 Line 024	XB1_Diop24	0.5303	15.14	5.28	20.31	LOD	0.3909	6.89	0.1806	0.0042	1.5383	49.66	99.9243
XB_cpxline1 Line 025	XB1_Diop25	0.6025	13.78	5.63	23.06	LOD	0.4585	5.34	0.1544	0.0224	1.6632	49.34	100.051
XB_cpxline1 Line 026	XB1_Diop26	0.0193	26.67	3.27	0.2767	LOD	0.2498	16.11	0.3777	0.0333	0.1807	52.41	99.5975
XB_cpxline1 Line 027	XB1_Diop27	0.5836	14.36	4.65	22.85	0.0113	0.4367	5.23	0.0954	LOD	1.2867	49.52	99.0237
XB_cpxline1 Line 028	XB1_Diop28	0.6252	13.81	5.32	22.81	0.0016	0.5083	5.4	0.149	0.0258	1.513	49.89	100.0529
XB_cpxline1 Line 029	XB1_Diop29	0.6376	13.76	5.65	22.79	LOD	0.4758	5.25	0.1521	0.0266	1.68	49.12	99.5421
XB_cpxline1 Line 030	XB1_Diop30	0.6067	14	4.87	22.97	LOD	0.5145	5.22	0.1598	0.0108	1.3441	49.71	99.4059

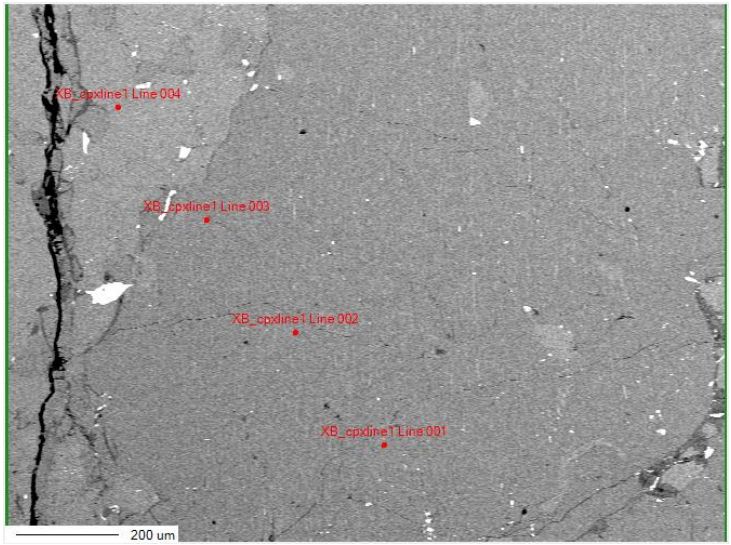
XB_cpxline1 Line 004
XB_cpxline1 Line 003
XB_cpxline1 Line 002
XB_cpxline1 Line 001
200 um

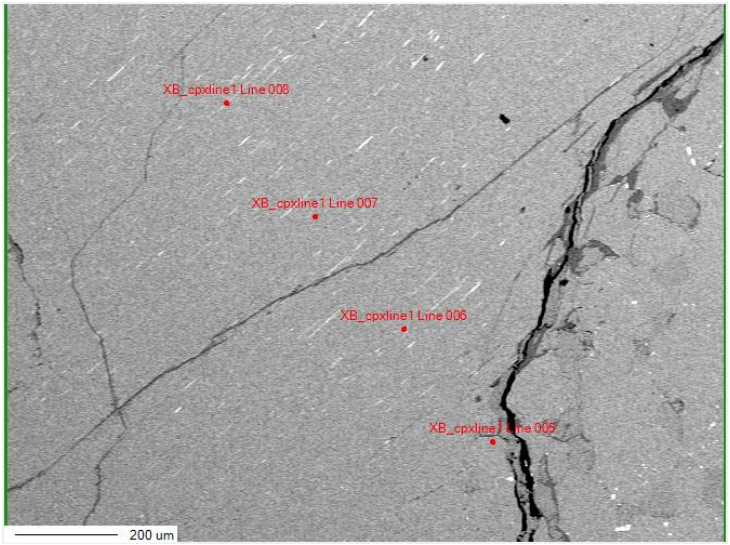
XB_cpxline1 Line 008
XB_cpxline1 Line 007
XB_cpxline1 Line 006
XB_cpxline1 Line 005
200 um

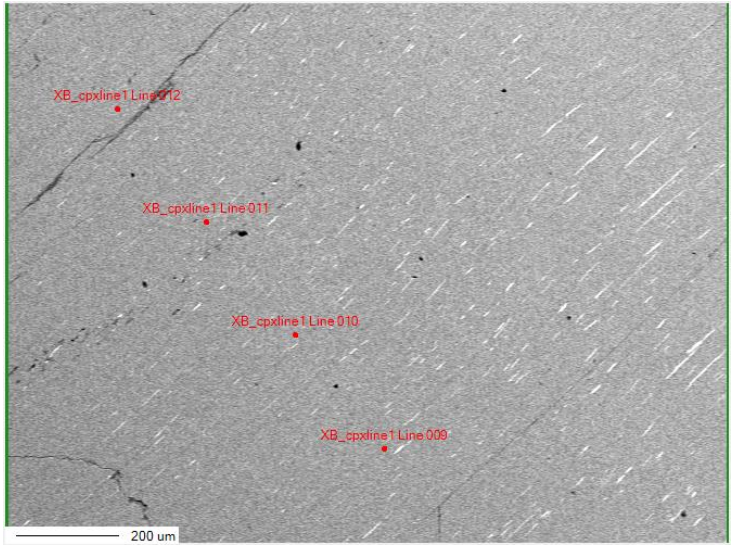
XB_cpxline1 Line 012
XB_cpxline1 Line 011
XB_cpxline1 Line 010
XB_cpxline1 Line 009
200 um

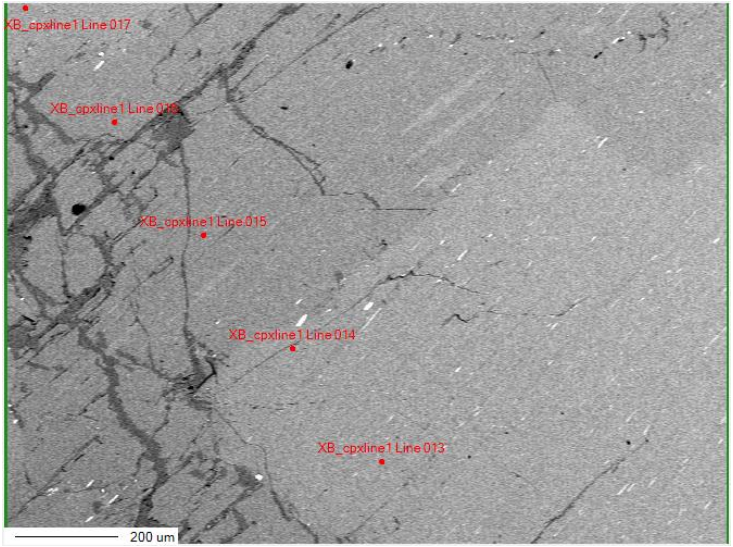
XB_cpxline1 Line 017
XB_cpxline1 Line 016
XB_cpxline1 Line 015
XB_cpxline1 Line 014
XB_cpxline1 Line 013
200 um

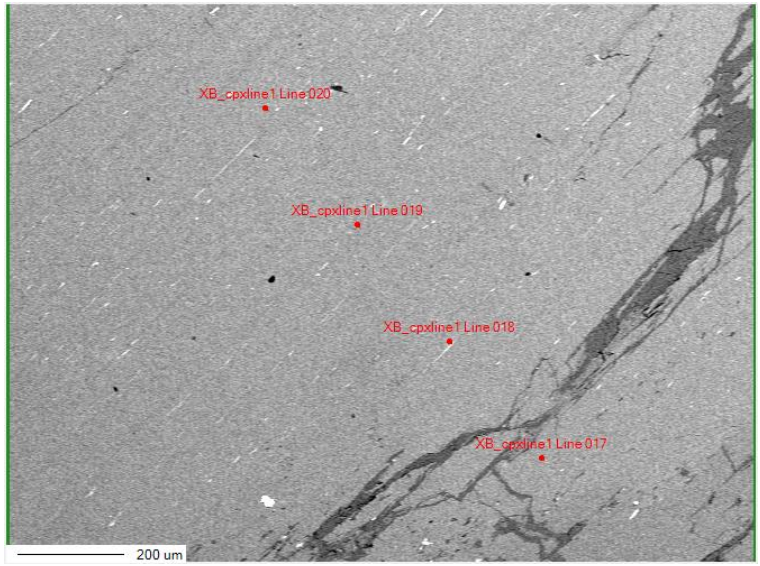
XB_cpxline1 Line 020
XB_cpxline1 Line 019
XB_cpxline1 Line 018
XB_cpxline1 Line 017
200 um

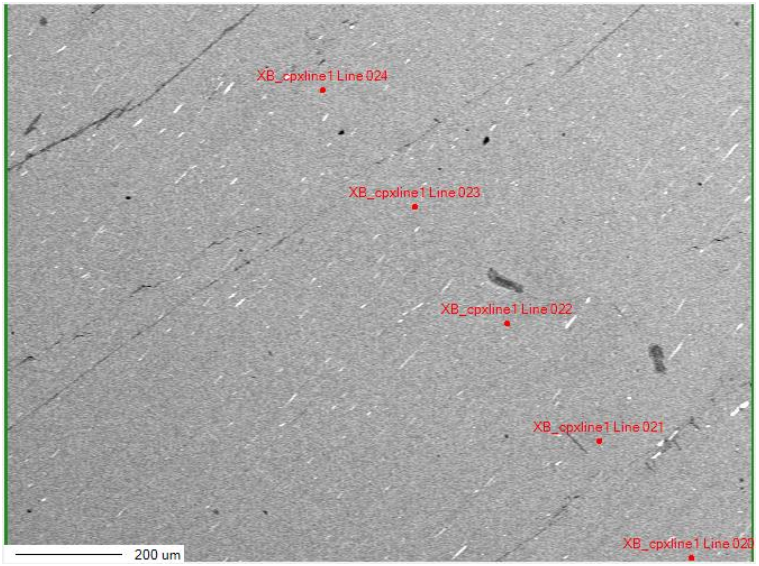
XB_cpxline1 Line 024
XB_cpxline1 Line 023
XB_cpxline1 Line 022
XB_cpxline1 Line 021
XB_cpxline1 Line 020
200 um

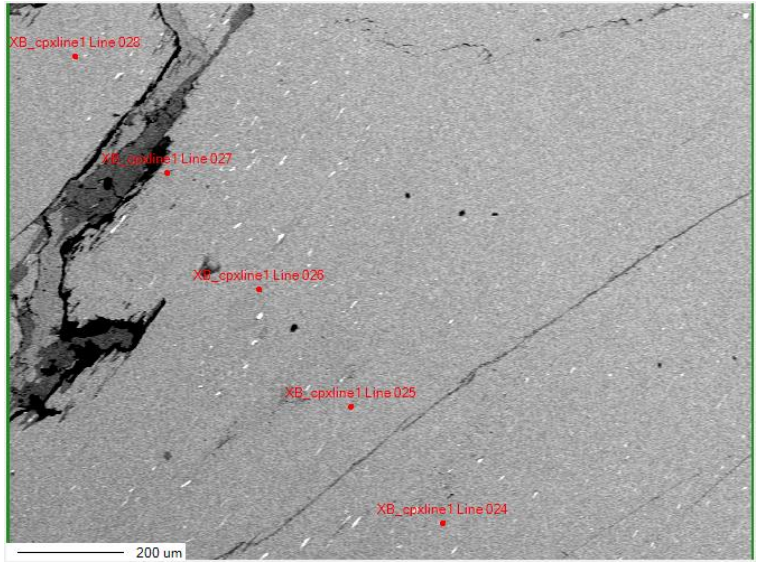
XB_cpxline1 Line 028
XB_cpxline1 Line 027
XB_cpxline1 Line 026
XB_cpxline1 Line 025
XB_cpxline1 Line 024
200 um

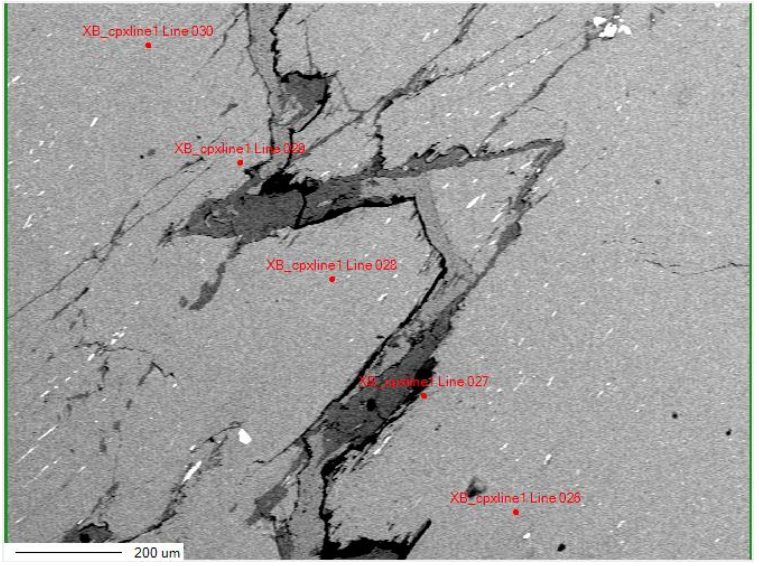
XB_cpxline1 Line 030
XB_cpxline1 Line 029
XB_cpxline1 Line 028
XB_cpxline1 Line 027
XB_cpxline1 Line 026
200 um

Table 8.26: *EPMA data point results from profile XB1_Enst1-20 with accompanying images (next page).*

Original data point name	Renamed data point	Na2O(Mass%)	MgO(Mass%)	Al2O3(Mass%)	CaO(Mass%)	K2O(Mass%)	Cr2O3(Mass%)	FeO(Mass%)	MnO(Mass%)	NiO(Mass%)	TiO2(Mass%)	SiO2(Mass%)	Total:
XB_acrossopx_line1 Line 001	XB1_Enst1	0.0058	29.4	3.14	0.3163	0.0079	0.2268	12.66	0.2479	0.0409	0.1724	53.8	100.018
XB_acrossopx_line1 Line 002	XB1_Enst2	0.0282	29.34	2.49	0.9693	0.0004	0.1862	13.03	0.2301	0.0441	1.1584	53.45	100.9267
XB_acrossopx_line1 Line 003	XB1_Enst3	0.0782	27.41	2.67	4.02	LOD	0.2257	11.13	0.1819	0.0484	0.2073	54.02	99.9915
XB_acrossopx_line1 Line 004	XB1_Enst4	LOD	29.39	2.84	0.5147	0.0246	0.1814	12.71	0.2843	0.0091	0.1374	53.98	100.0715
XB_acrossopx_line1 Line 005	XB1_Enst5	0.0519	28.87	3.07	1.2588	0.0071	0.1878	12.73	0.2474	0.0441	0.2551	54.32	101.0422
XB_acrossopx_line1 Line 006	XB1_Enst6	0.0504	28.39	3	1.69	LOD	0.1478	12.18	0.2791	0.0083	0.2019	54.12	100.0675
XB_acrossopx_line1 Line 007	XB1_Enst7	0.0422	28.76	3.24	1.74	LOD	0.1959	12.53	0.2466	0.0342	0.3062	53.53	100.6251
XB_acrossopx_line1 Line 008	XB1_Enst8	0.1758	25.54	3.55	6.1	0.0085	0.2641	10.35	0.1796	0.0633	0.5021	52.71	99.4434
XB_acrossopx_line1 Line 009	XB1_Enst9	0.0329	29.53	2.82	0.6149	0.0174	0.1799	13.01	0.2508	0.0442	0.1465	54.17	100.8166
XB_acrossopx_line1 Line 010	XB1_Enst10	0.5292	14.5	5.13	23.04	0.009	0.2865	5.01	0.0997	LOD	1.517	49.91	100.0314
XB_acrossopx_line1 Line 011	XB1_Enst11	0.0582	29.56	3.36	0.5187	LOD	0.231	13.06	0.293	0.0416	0.3046	53.41	100.8371
XB_acrossopx_line1 Line 012	XB1_Enst12	0.1039	25.82	3.88	6.15	0.0009	0.2841	10.43	0.2512	0.0175	0.4954	51.94	99.373
XB_acrossopx_line1 Line 013	XB1_Enst13	LOD	41.92	LOD	0	0.0019	0.0105	19.65	0.2318	0.2333	0.0153	38.97	101.0328
XB_acrossopx_line1 Line 014	XB1_Enst14	0.0898	29.54	3.32	0.5424	0.0126	0.203	12.66	0.2537	0.0258	0.2083	53.56	100.4156
XB_acrossopx_line1 Line 015	XB1_Enst15	0.0851	28.08	3.32	2.96	LOD	0.2415	11.74	0.2616	0.0308	0.3054	53.74	100.7644
XB_acrossopx_line1 Line 016	XB1_Enst16	0.0719	27.12	2.89	3.45	0.0019	0.224	12.33	0.2192	0.0341	0.2766	52.31	98.9277
XB_acrossopx_line1 Line 017	XB1_Enst17	LOD	29.89	3.3	0.2321	LOD	0.1784	12.61	0.2366	0.0175	0.1316	54.07	100.6662
XB_acrossopx_line1 Line 018	XB1_Enst18	LOD	LOD	LOD	0	LOD	0.0281	82.83	0.0142	LOD	LOD	0.0211	82.8934
XB_acrossopx_line1 Line 019	XB1_Enst19	0.0671	28.14	3.48	2.76	LOD	0.2229	11.84	0.2248	0.0366	0.328	53.25	100.3494
XB_acrossopx_line1 Line 020	XB1_Enst20	0.0457	28.19	3.43	2.67	0.0027	0.195	12.02	0.2206	0.0517	0.3784	53.7	100.9041

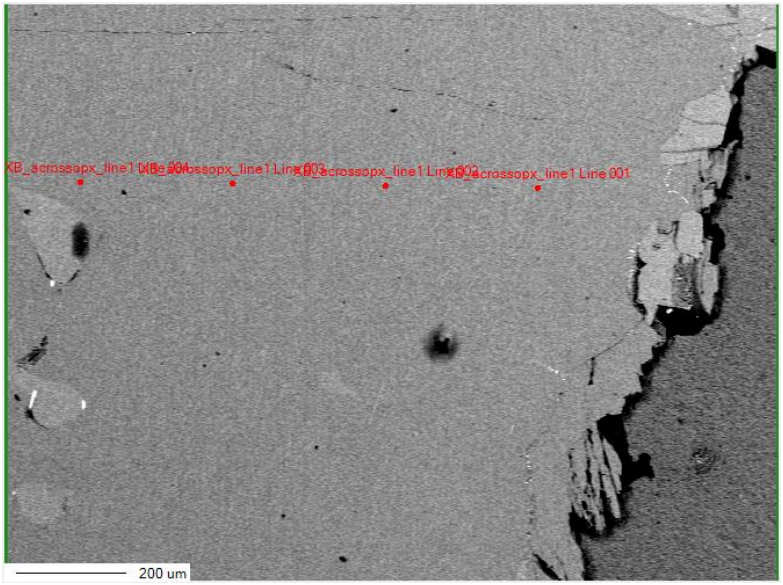
XB_acrossopx_line1 Line 001
200 um

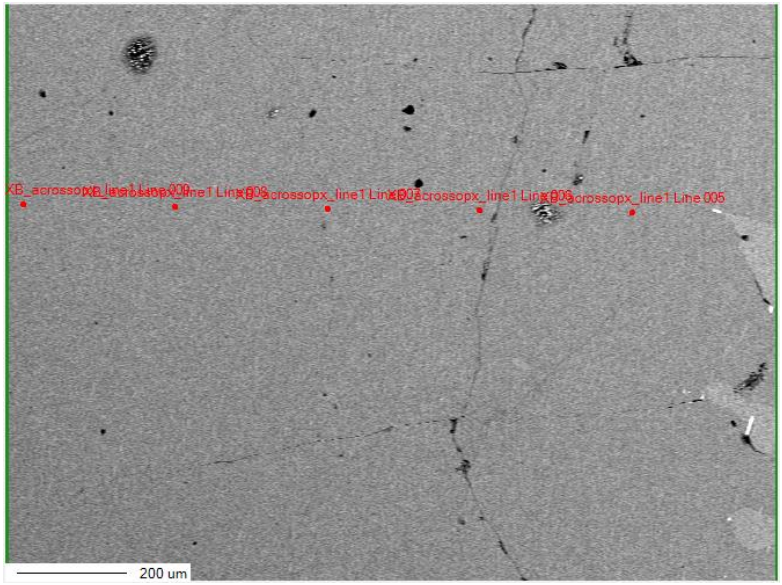
XB_acrossopx_line1 Line 005
200 um

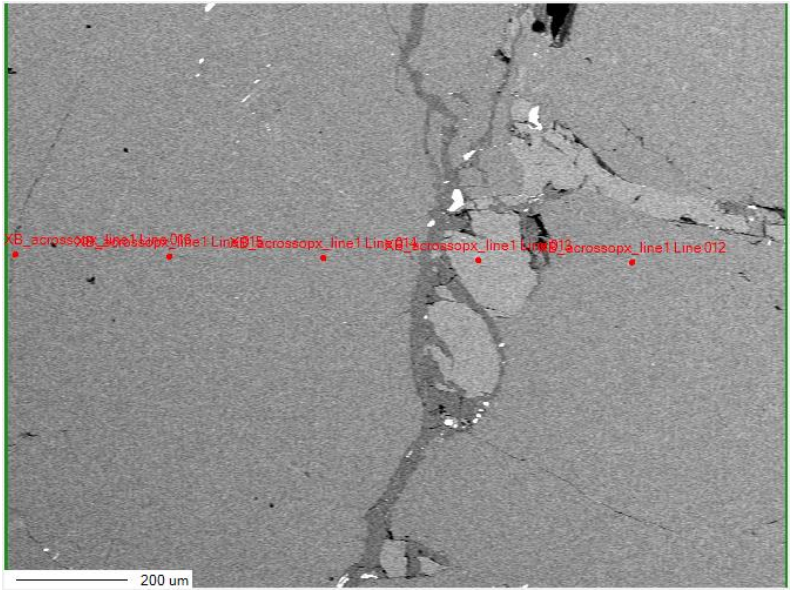
XB_acrossopx_line1 Line 012
200 um

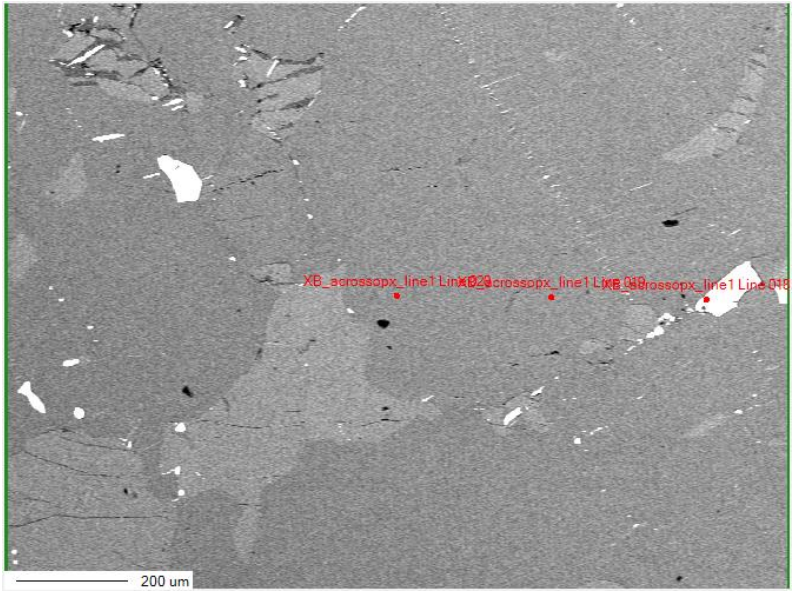
200 um

Table 8.27: *EPMA data point results from profile XB2_Enst1-20 with accompanying images (next two pages).*

Original data point name	Renamed data point	Na2O(Mass%)	MgO(Mass%)	Al2O3(Mass%)	CaO(Mass%)	K2O(Mass%)	Cr2O3(Mass%)	FeO(Mass%)	MnO(Mass%)	NiO(Mass%)	TiO2(Mass%)	SiO2(Mass%)	Total:
XB_opxcross_line2 Line 001	XB2_Enst1	0.0775	18.34	1.185	1.64	LOD	0.0445	4.84	0.1282	0.0318	0.0883	38.79	65.1653
XB_opxcross_line2 Line 002	XB2_Enst2	0.027	22.37	1.5653	0.5724	0.0083	0.1465	9.56	0.2122	0.0509	0.0846	46.3	80.8972
XB_opxcross_line2 Line 003	XB2_Enst3	0.0644	20.95	1.0569	1.68	0.0018	0.1446	10.63	0.2105	0.0249	1.5682	45.88	82.2113
XB_opxcross_line2 Line 004	XB2_Enst4	0.0656	23.72	1.6508	0.4418	0.0091	0.1104	10.29	0.2216	0.0384	0.107	48.06	84.7147
XB_opxcross_line2 Line 005	XB2_Enst5	0.1112	24.33	1.92	0.5542	0.0074	0.1349	11.08	0.2073	0.015	0.1325	48.83	87.3225
XB_opxcross_line2 Line 006	XB2_Enst6	0.0686	24.05	2.18	1.3668	LOD	0.1915	10.5	0.2042	0.0683	0.1746	49.46	88.264
XB_opxcross_line2 Line 007	XB2_Enst7	0.1019	24.75	1.97	1.2888	LOD	0.2495	11.3	0.2123	0.0441	0.1955	49.86	89.9721
XB_opxcross_line2 Line 008	XB2_Enst8	0.0327	25.64	2.19	0.4731	0.0042	0.1345	11.76	0.249	0.0524	0.1975	50.28	91.0134
XB_opxcross_line2 Line 009	XB2_Enst9	0.0331	26.25	2.17	0.7583	LOD	0.1346	11.9	0.2122	0.0349	0.1488	50.81	92.4519
XB_opxcross_line2 Line 010	XB2_Enst10	0.0504	26.22	2.47	1.1583	0.0015	0.1841	12.12	0.2079	0.0307	0.1628	51.17	93.7757
XB_opxcross_line2 Line 011	XB2_Enst11	0.0366	26.79	2.52	0.4451	LOD	0.1481	12.51	0.2595	0.0382	0.207	51.68	94.6345
XB_opxcross_line2 Line 012	XB2_Enst12	0.0335	27.42	2.59	0.615	0.0052	0.1989	12.61	0.2722	0.0771	0.1538	52.44	96.4157
XB_opxcross_line2 Line 013	XB2_Enst13	0.4374	15.32	3.35	17.82	0.0192	0.2291	6.79	0.1392	0.0421	3.54	47.2	94.887
XB_opxcross_line2 Line 014	XB2_Enst14	0.0183	28.32	2.82	0.3266	LOD	0.148	13.07	0.2421	0.0622	0.2057	52.56	97.7729
XB_opxcross_line2 Line 015	XB2_Enst15	0.0133	28.54	2.52	0.6479	LOD	0.1481	13.02	0.2594	0.078	0.2631	53.05	98.5398
XB_opxcross_line2 Line 016	XB2_Enst16	0.0621	27.58	2.72	2.57	0.0069	0.1661	11.87	0.2317	0.0266	0.2218	53.31	98.7652
XB_opxcross_line2 Line 017	XB2_Enst17	0.0177	29.63	2.42	0.3406	0.0009	0.1526	13.21	0.2819	0.024	0.182	53.79	100.0497
XB_opxcross_line2 Line 018	XB2_Enst18	0.0203	29.28	2.76	0.7483	0.0253	0.1914	12.91	0.2485	0.0398	0.3175	53.94	100.4811
XB_opxcross_line2 Line 019	XB2_Enst19	0.0297	28.38	3.11	2.04	0.0054	0.2393	13.21	0.2601	0.0165	1.1492	52.55	100.9902
XB_opxcross_line2 Line 020	XB2_Enst20	0.0368	29.34	2.77	0.5542	LOD	0.1713	12.76	0.2581	0.0381	0.2919	54.57	100.7904

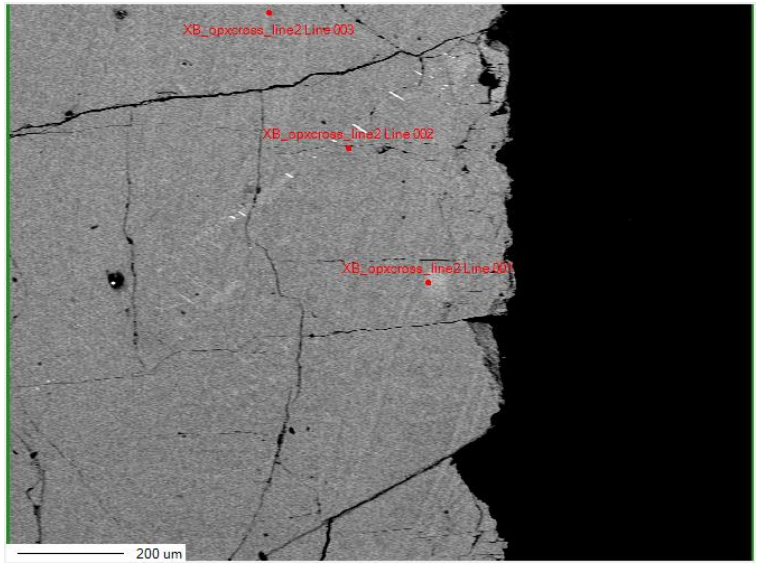
XB_opxcross_line2 Line 003
XB_opxcross_line2 Line 002
XB_opxcross_line2 Line 001
200 um

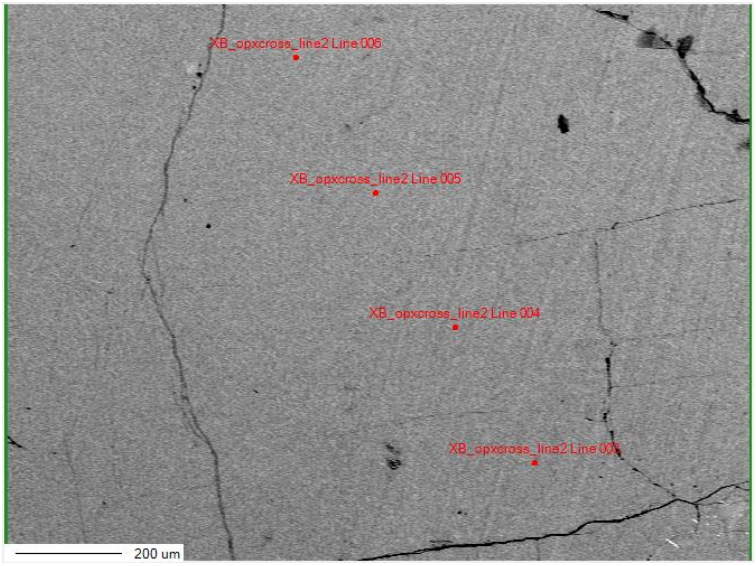
XB_opxcross_line2 Line 006
XB_opxcross_line2 Line 005
XB_opxcross_line2 Line 004
XB_opxcross_line2 Line 003
200 um

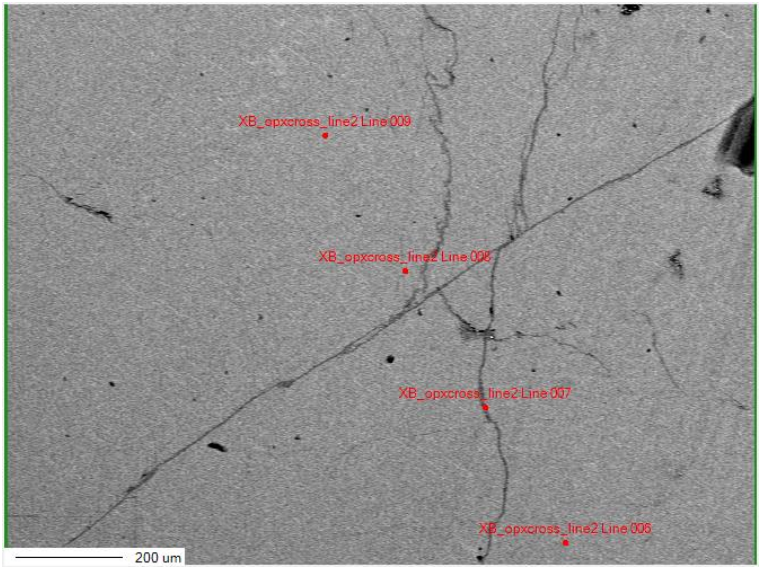
XB_opxcross_line2 Line 009
XB_opxcross_line2 Line 008
XB_opxcross_line2 Line 007
XB_opxcross_line2 Line 006
200 um

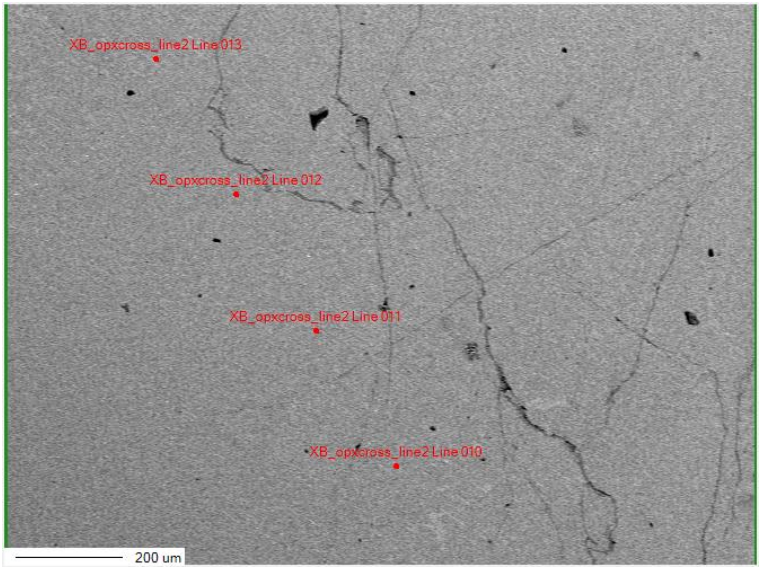
XB_opxcross_line2 Line 013
XB_opxcross_line2 Line 012
XB_opxcross_line2 Line 011
XB_opxcross_line2 Line 010
200 um

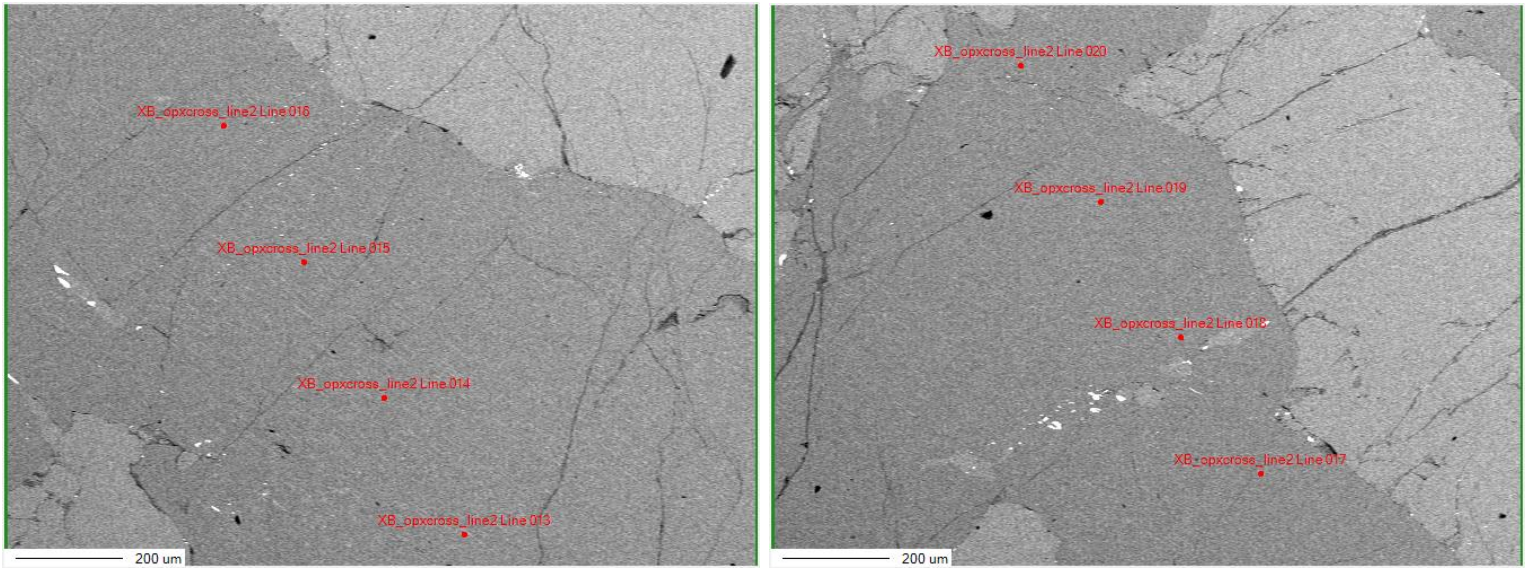
XB_opxcross_line2 Line 016
XB_opxcross_line2 Line 015
XB_opxcross_line2 Line 014
XB_opxcross_line2 Line 013
200 um
XB_opxcross_line2 Line 020
XB_opxcross_line2 Line 019
XB_opxcross_line2 Line 018
XB_opxcross_line2 Line 017
200 um

Table 8.28: *EPMA data point results from profile XB2_Diop1-20 with accompanying images (next page).*

Original data point name	Renamed data point	Na2O(Mass%)	MgO(Mass%)	Al2O3(Mass%)	CaO(Mass%)	K2O(Mass%)	Cr2O3(Mass%)	FeO(Mass%)	MnO(Mass%)	NiO(Mass%)	TiO2(Mass%)	SiO2(Mass%)	Total:
XB_cpxcross_line2 Line 001	XB2_Diop1	0.5262	16.86	4.6	18.87	0.0038	0.3973	6.85	0.1695	0.033	1.2825	50.76	100.3523
XB_cpxcross_line2 Line 002	XB2_Diop2	0.5756	14.94	4.94	21.66	0.0081	0.4895	5.3	0.122	0.019	1.4641	50.4	99.9183
XB_cpxcross_line2 Line 003	XB2_Diop3	0.2844	27.23	3.24	8.7	0.0066	0.2396	8.81	0.2445	0.0199	0.6044	50.29	99.6694
XB_cpxcross_line2 Line 004	XB2_Diop4	0.6381	14.21	4.92	22.64	LOD	0.4231	5.08	0.1287	0.0066	1.3789	49.96	99.3854
XB_cpxcross_line2 Line 005	XB2_Diop5	0.6304	14.54	4.98	22.6	LOD	0.3942	5.11	0.144	0.0157	1.4777	49.54	99.432
XB_cpxcross_line2 Line 006	XB2_Diop6	0.546	14.48	4.94	22.77	LOD	0.4471	5.12	0.1112	0.0348	1.4708	49.92	99.8399
XB_cpxcross_line2 Line 007	XB2_Diop7	0.5025	14.54	4.64	23.21	0.0094	0.3705	4.95	0.1374	0.0307	1.3947	50.39	100.1752
XB_cpxcross_line2 Line 008	XB2_Diop8	0.604	14.92	4.95	22.27	LOD	0.3797	5.14	0.1112	0.0414	1.4464	49.4	99.2627
XB_cpxcross_line2 Line 009	XB2_Diop9	0.5563	14.37	4.77	22.82	LOD	0.4728	5.08	0.121	0.0298	1.3689	50.33	99.9188
XB_cpxcross_line2 Line 010	XB2_Diop10	0.5516	14.48	4.75	23.03	0.0006	0.4666	5.28	0.1332	0.0141	1.3315	49.99	100.0276
XB_cpxcross_line2 Line 011	XB2_Diop11	0.5643	14.38	5.11	23.36	LOD	0.4207	4.78	0.1627	0.01	1.5182	49.92	100.2259
XB_cpxcross_line2 Line 012	XB2_Diop12	0.6736	14.93	4.61	23.15	LOD	0.3904	4.67	0.1224	0.0208	1.2491	50.33	100.1463
XB_cpxcross_line2 Line 013	XB2_Diop13	0.4963	14.6	4.79	23.24	0.0088	0.43	5.08	0.1266	LOD	1.4245	50.21	100.4062
XB_cpxcross_line2 Line 014	XB2_Diop14	0.5133	14.77	5.04	21.97	LOD	0.4373	5.5	0.1276	LOD	1.4865	49.82	99.6647
XB_cpxcross_line2 Line 015	XB2_Diop15	0.559	14.87	4.66	22.31	0.0035	0.3684	5.49	0.1778	0.0274	1.267	49.81	99.5431
XB_cpxcross_line2 Line 016	XB2_Diop16	0.5235	14.81	4.46	23.24	LOD	0.4501	4.52	0.0984	0.0058	1.1916	51.04	100.3394
XB_cpxcross_line2 Line 017	XB2_Diop17	0.5557	14.77	4.87	21.68	0.0036	0.4061	6.07	0.1417	0.0265	1.3218	49.75	99.5954
XB_cpxcross_line2 Line 018	XB2_Diop18	0.5278	14.63	4.9	23.09	LOD	0.4833	4.76	0.1453	0.0531	1.3027	50.34	100.2322
XB_cpxcross_line2 Line 019	XB2_Diop19	0.5575	14.53	5.34	22.64	0.0057	0.5759	5.01	0.1517	0.0091	1.4673	49.47	99.7572
XB_cpxcross_line2 Line 020	XB2_Diop20	0.0082	29.67	2.76	0.2299	LOD	0.1593	12.58	0.2489	0.0033	0.1091	54.44	100.2087

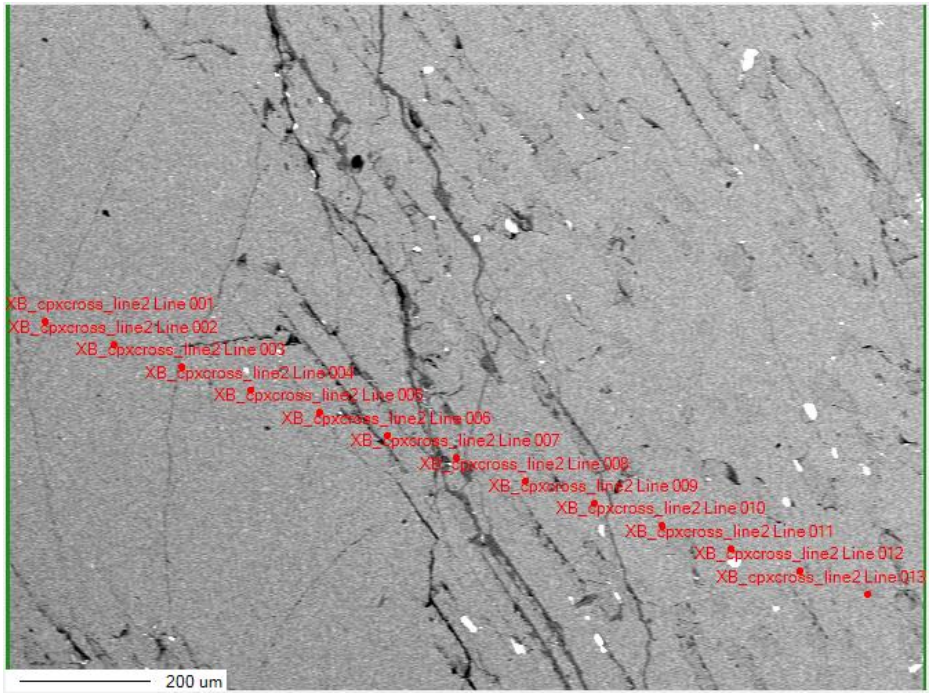
XB_cpxcross_line2 Line 001
XB_cpxcross_line2 Line 002
XB_cpxcross_line2 Line 003
XB_cpxcross_line2 Line 004
XB_cpxcross_line2 Line 005
XB_cpxcross_line2 Line 006
XB_cpxcross_line2 Line 007
XB_cpxcross_line2 Line 008
XB_cpxcross_line2 Line 009
XB_cpxcross_line2 Line 010
XB_cpxcross_line2 Line 011
XB_cpxcross_line2 Line 012
XB_cpxcross_line2 Line 013
200 um

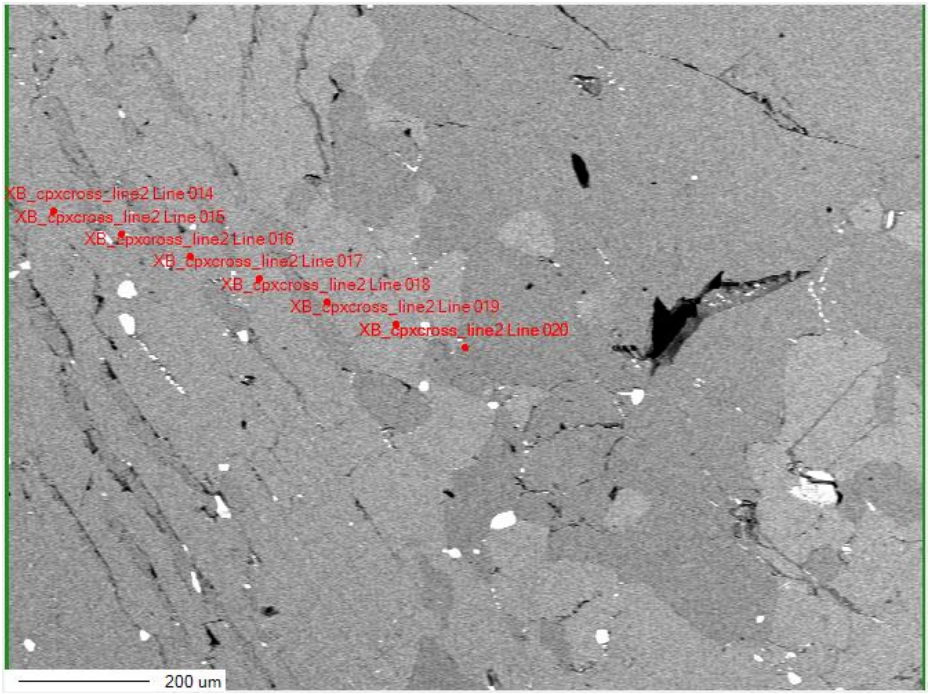
XB_cpxcross_line2 Line 014
XB_cpxcross_line2 Line 015
XB_cpxcross_line2 Line 016
XB_cpxcross_line2 Line 017
XB_cpxcross_line2 Line 018
XB_cpxcross_line2 Line 019
XB_cpxcross_line2 Line 020
200 um

Table 8.29: *EPMA data point results from profile XB3_Enst1-4 with image (below).*

Original data point name	Renamed data point	Na2O(Mass%)	MgO(Mass%)	Al2O3(Mass%)	CaO(Mass%)	K2O(Mass%)	Cr2O3(Mass%)	FeO(Mass%)	MnO(Mass%)	NiO(Mass%)	TiO2(Mass%)	SiO2(Mass%)	Total:
XB_opxcross_line3 Line 001	XB3_Enst1	0.1281	25.99	2.42	6.87	0.0072	0.1931	10.14	0.2043	0.0341	0.6073	53.88	100.4741
XB_opxcross_line3 Line 002	XB3_Enst2	LOD	28.96	3.03	0.9389	LOD	0.1963	12.77	0.2509	0.0133	0.1582	53.54	99.8576
XB_opxcross_line3 Line 003	XB3_Enst3	0.085	29.01	2.72	0.2927	0.0023	0.1919	12.5	0.274	0.0399	0.3554	53.49	98.9612
XB_opxcross_line3 Line 004	XB3_Enst4	LOD	29.63	1.6955	0.4067	LOD	0.1486	12.72	0.2849	0.0549	0.0662	55.33	100.3368

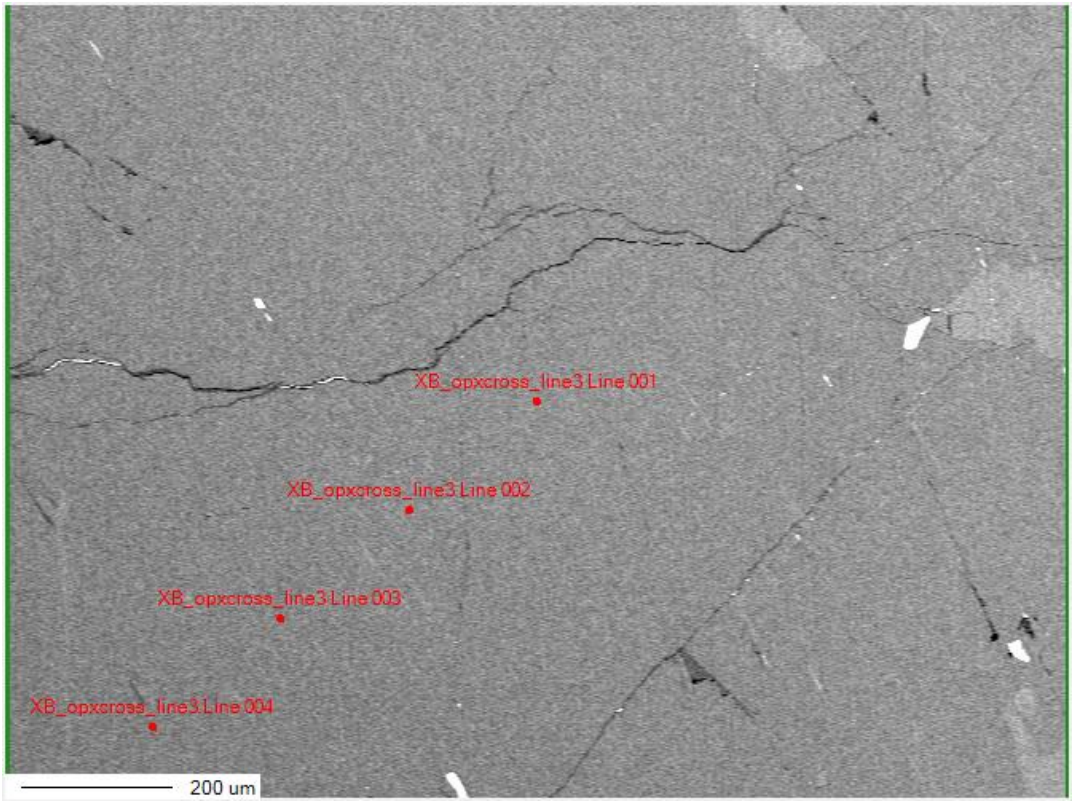

Table 8.30: *EPMA data points (complete table for all samples, including all calibration points). LOD = Limit Of Detection.*

Point	Comment	Na2O(Mass%)	MgO(Mass%)	Al2O3(Mass%)	CaO(Mass%)	K2O(Mass %)	Cr2O3(Mass%)	FeO(Mass%)	MnO(Mass%)	NiO(Mass%)	TiO2(Mass%)	SiO2(Mass%)	Total(Mass%)
1	std_ol1	0.0829	52.7	LOD	LOD	0.0085	LOD	6.88	0.088	0.4208	0.0096	41.48	101.6698
2	std_di1	0.0128	18.38	0.0571	25.71	0.0006	0.0033	0.058	0.0462	0.0102	0.0674	54.83	99.1756
3	std_ab1	11.34	LOD	19.43	0.2787	0.15	LOD	LOD	LOD	LOD	0.0205	68.24	99.4592
4	std_grt	0.0138	4.36	20.09	0.3509	LOD	LOD	36.97	0.2149	LOD	0.0082	37.15	99.1578
5	XA_Ol1_1	0.0252	40.98	0.0165	LOD	LOD	0.0367	19.82	0.2384	0.1399	LOD	38.68	99.9367
6	XA_Ol1_2	0.024	41.49	LOD	LOD	LOD	LOD	20.01	0.2536	0.1129	0.0252	38.9	100.8157
7	XA_Ol1_3	0.4058	41.46	LOD	LOD	LOD	0.0077	19.82	0.2635	0.1686	0.0177	38.12	100.2633
8	XA_Opx1_1	0.0216	29.27	2.58	0.6659	LOD	0.1262	13.07	0.2387	0.0365	0.2249	53.41	99.6438
9	XA_Opx1_2	0.1567	29.19	2.73	0.7988	0.087	0.1501	12.78	0.2819	0.0637	0.2281	53.11	99.5763
10	XA_Opx1_3	0.2717	29.26	2.97	0.7293	LOD	0.1437	12.97	0.2145	0.0212	0.227	53.01	99.8174
11	XA_Opx1_4	0.4974	15.48	5.05	20.93	0.0016	0.4104	6.28	0.1387	0.0165	1.4397	48.88	99.1243
12	XA_Opx1_5 Line 001	0.5129	14.58	5.14	23.31	LOD	0.3794	4.23	0.1071	LOD	1.2802	49.32	98.8596
13	XA_Opx1_5 Line 002	0.5947	12.71	5.71	21.77	0.0089	0.3729	4.05	0.0871	0.0034	1.1739	45.21	91.6909
14	XA_Opx1_5 Line 003	0.5019	15.07	5.61	21.81	LOD	0.4769	4.95	0.1383	0.0093	1.5234	47.78	97.8698
15	XA_Opx1_5 Line 004	0.5454	14.16	5.83	23.07	LOD	0.4018	4.66	0.0981	LOD	1.5766	48.22	98.5619
16	XA_Opx1_5 Line 005	0.4927	15.35	5.65	21.09	0.0047	0.4309	5.98	0.1347	0.0271	1.6169	48.18	98.957
17	XA_Opx1_5 Line 006	0.5659	14.46	5.46	22.44	0.0071	0.4154	5.43	0.1058	0.0228	1.6113	48.01	98.5283
18	XA_Opx1_5 Line 007	0.5816	14.32	5.33	22.86	0.01	0.3859	5.43	0.1258	0.033	1.5739	48.51	99.1602
19	XA_Opx1_5 Line 008	0.536	14.77	5.23	21.7	0.0061	0.3791	5.97	0.1593	0.022	1.4763	48.37	98.6188
20	XA_Opx1_5 Line 009	0.5195	15.14	5.13	21.77	0.005	0.3759	5.73	0.1615	0.0347	1.5439	48.3	98.7105
21	XA_Opx1_5 Line 010	0.4407	18.06	4.62	16.5	LOD	0.2653	8.5	0.1998	0.0355	1.1993	49.52	99.3406
22	XA_Opx1_5 Line 011	0.5032	15.77	4.99	19.94	LOD	0.4121	6.49	0.2102	0.0491	1.4221	48.65	98.4367
23	XA_Opx1_5 Line 012	0.5458	14.55	5.15	22.87	LOD	0.437	5.42	0.1504	0.0245	1.4582	48.61	99.2159
24	XA_Opx1_5 Line 013	0.5489	14.41	5.17	22.75	LOD	0.3681	5.3	0.1548	0.044	1.4769	48.94	99.1627
25	XA_Opx1_5 Line 014	0.4333	15.8	4.94	21.78	0.0044	0.4051	5.52	0.1602	0.0178	1.2891	48.67	99.0199
26	XA_Opx1_5 Line 015	0.0202	29.9	2.22	0.3534	0.0167	0.167	13.16	0.297	0.0042	0.1776	53.33	99.6461
27	XA_Opx1_5 Line 016 Line 001	LOD	29.52	3.1	0.2804	LOD	0.1703	12.76	0.2847	0.0491	0.1916	53.01	99.3661
28	XA_Opx1_5 Line 016 Line 002	0.4322	14.8	5.06	23.25	LOD	0.4109	4.84	0.1091	0.0211	1.3159	48.89	99.1292
29	XA_Opx1_5 Line 016 Line 003	0.3185	15.69	8.7	20.17	0.013	1.1679	6.76	0.1032	0.0506	0.8779	44.5	98.3511

30	XA_Opx1_5 Line 016 Line 004	0.4503	14.69	4.96	23.1	LOD	0.38	4.8	0.1181	0.0127	1.2878	48.66	98.4589
31	XA_Opx1_5 Line 016 Line 005	0.6016	14.68	5.67	22.43	LOD	0.4452	4.87	0.1158	LOD	1.5391	48.29	98.6417
32	XA_Opx1_5 Line 016 Line 006	0.6759	14.3	5.88	22.66	0.0154	0.4226	4.66	0.0925	LOD	1.6246	48.48	98.811
33	XA_Opx1_5 Line 016 Line 007	0.5479	15.4	5.67	21.19	0.0095	0.3792	5.22	0.1135	0.0228	1.5086	48.26	98.3215
34	XA_Opx1_5 Line 016 Line 008	0.4977	15.43	5.46	22.02	LOD	0.378	4.91	0.1025	LOD	1.5482	48.47	98.8164
35	XA_Opx1_5 Line 016 Line 009	0.4656	14.71	4.99	23.06	LOD	0.3783	4.83	0.1181	0.0178	1.2934	48.81	98.6732
36	XA_Opx1_5 Line 016 Line 010	0.0058	29.79	2.12	0.7036	LOD	0.0992	13.03	0.2836	0.0042	0.1021	53.02	99.1585
37	XA_Opx1_5 Line 016 Line 011 Line 001	0.463	15.23	4.6	21.73	LOD	0.4727	5.12	0.1492	0.0161	1.1549	49.44	98.3759
38	XA_Opx1_5 Line 016 Line 011 Line 002	0.469	16.4	4.48	19.78	LOD	0.3961	6.25	0.1702	LOD	1.0877	49.91	98.943
39	XA_Opx1_5 Line 016 Line 011 Line 003	0.5918	14.46	4.8	22.98	0.0026	0.5138	4.92	0.1302	0.0245	1.2757	48.46	98.1586
40	XA_Opx1_5 Line 016 Line 011 Line 004	0.399	17.8	4.24	17.76	LOD	0.3509	6.92	0.1444	0.0127	1.0121	50.04	98.6791
41	XA_Opx1_5 Line 016 Line 011 Line 005	0.5175	15.09	4.51	22.08	LOD	0.4579	5.01	0.167	0.0102	1.1864	48.99	98.019
42	XA_Opx1_5 Line 016 Line 011 Line 006	0.5467	14.83	4.53	22.75	0.0056	0.4546	4.95	0.1246	0.038	1.1881	49.31	98.7276
43	XA_Opx1_5 Line 016 Line 011 Line 007	0.273	21.27	3.57	11.99	LOD	0.2391	9.7	0.2412	0.0558	0.6	51.52	99.4591
44	XA_Opx1_5 Line 016 Line 011 Line 008	0.5446	14.57	4.7	22.73	LOD	0.5079	5.06	0.1567	0.038	1.2688	48.64	98.216
45	XA_Opx1_5 Line 016 Line 011 Line 009	0.4919	14.47	4.79	23.28	LOD	0.4186	4.62	0.1201	0.0354	1.372	48.68	98.278
46	XA_Opx1_5 Line 016 Line 011 Line 010_co	0.5071	14.23	5.29	23.12	LOD	0.438	4.78	0.1278	0.0143	1.5149	48.66	98.6821
47	XA_Opx1_5 Line 016 Line 011 Line 010_co	0.612	14.74	4.59	22.22	LOD	0.6026	4.99	0.0967	LOD	1.2617	49.52	98.633
48	XA_Opx1_5 Line 016 Line 011 Line 010_co	0.6008	14.63	4.64	22.32	0.0108	0.6608	5.02	0.1099	0.0244	1.2752	48.71	98.0019
49	XA_Opx1_5 Line 016 Line 011 Line 010_co	0.6039	14.9	4.72	21.79	0.0018	0.621	5.5	0.1299	0.0253	1.2961	49.13	98.718
50	XA_Opx1_5 Line 016 Line 011 Line 010_co	0.6321	14.65	4.76	22.41	LOD	0.5272	4.85	0.1566	0.0447	1.32	48.67	98.0206
51	XA_Opx1_5 Line 016 Line 011 Line 010_co	0.4088	17.72	3.9	14.43	LOD	1.3984	12.51	0.1911	0.0798	0.8056	47.37	98.8137
52	XA_Opx1_5 Line 016 Line 011 Line 010_co	0.6154	14.6	4.64	22.49	0.0017	0.5845	5.08	0.1533	0.0329	1.2796	49.27	98.7474
53	XA_Opx1_5 Line 016 Line 011 Line 010_co	0.4227	17.83	4.39	17.27	0.0009	0.3819	7.28	0.2027	0.0388	1.0692	50.07	98.9562
54	XA_Opx1_5 Line 016 Line 011 Line 010_co	0.6218	14.42	4.8	22.41	0.0008	0.4991	4.99	0.1221	0.016	1.3181	49.02	98.2179
55	XA_Opx1_5 Line 016 Line 011 Line 010_co	0.5852	14.4	4.9	22.59	LOD	0.4751	4.82	0.1377	0.0152	1.4301	49.13	98.4833
56	XA_Opx1_5 Line 016 Line 011 Line 010_co	0.4856	16.45	4.53	19.74	LOD	0.448	6.24	0.1795	0.0042	1.2896	49.4	98.7669
57	XA_Opx1_5 Line 016 Line 011 Line 010_co	0.0153	29.96	2.68	0.5155	0.0005	0.1665	12.83	0.2277	0.0827	0.2033	52.68	99.3615
58	XA_Opx1_5 Line 016 Line 011 Line 010_co	0.0502	29.26	2.65	1.46	0.0005	0.192	12.69	0.2553	0.0346	0.1434	53.11	99.846
59	XA_Opx1_5 Line 016 Line 011 Line 010_co	LOD	29.34	2.89	0.6025	0.0056	0.1931	13.16	0.208	0.0566	0.236	53.15	99.8418
60	XA_Opx1_5 Line 016 Line 011 Line 010_co	LOD	29.05	2.99	0.687	LOD	0.1666	12.97	0.2641	0.0617	0.1987	53.2	99.5881

61	XA_Opx1_5 Line 016 Line 011 Line 010_co	LOD	29.12	3.27	0.6169	0.0013	0.1539	13.05	0.2102	0.0499	0.1924	52.57	99.2346
62	XA_Opx1_5 Line 016 Line 011 Line 010_co	0.0488	29.14	3.2	0.3849	LOD	0.1555	13.07	0.2608	0.0845	0.3057	52.59	99.2402
63	XA_Opx1_5 Line 016 Line 011 Line 010_co	0.0054	29.38	3.09	0.3275	0.0063	0.1553	13.36	0.263	0.0042	0.1753	52.69	99.457
64	XA_Opx1_5 Line 016 Line 011 Line 010_co	0.0472	28.48	2.61	2.11	0.0029	0.2176	12.14	0.2434	0.0186	0.1989	52.3	98.3686
65	XA_Opx1_5 Line 016 Line 011 Line 010_co	0.0364	29.5	2.67	0.5048	LOD	0.1476	13.24	0.2619	0.011	0.2294	52.81	99.4111
66	XA_Opx1_5 Line 016 Line 011 Line 010_co	LOD	29.29	2.59	0.7573	LOD	0.181	12.61	0.2775	0.0397	0.1899	52.73	98.6654
67	XA_Ol2_line1 Line 001	0.0309	25.68	0.3299	1.2057	LOD	0.24	29.33	0.2533	0.1284	0.0314	34.34	91.5696
68	XA_Ol2_line1 Line 002	LOD	41.4	LOD	LOD	LOD	0.0198	19.94	0.2765	0.1402	0.0116	38.45	100.2381
69	XA_Ol2_line1 Line 003	LOD	41.7	LOD	LOD	LOD	0.0229	19.74	0.2342	0.1511	0.0067	38.51	100.3649
70	XA_Ol2_line1 Line 004	LOD	40.9	0.0022	0.0151	LOD	LOD	19.99	0.2657	0.1579	0.015	37.33	98.6759
71	XA_Ol2_line1 Line 005	0.0084	41.54	LOD	0.0055	LOD	0.0061	20.19	0.2514	0.1779	0.0068	38.59	100.7761
72	XA_Ol2_line1 Line 006	0.0112	41.67	0.0006	LOD	LOD	0.0061	20.09	0.2918	0.141	LOD	38.56	100.7707
73	XA_Ol2_line1 Line 007	0.0538	41.61	LOD	0.0078	LOD	0.0243	20.45	0.25	0.1525	LOD	37.9	100.4484
74	XA_Ol2_line1 Line 008	LOD	41.62	LOD	LOD	LOD	0.0076	20.16	0.2186	0.182	0.0063	38.12	100.3145
75	XA_Ol2_line1 Line 009	0.0412	41.35	LOD	LOD	0.0004	LOD	20.15	0.2174	0.1459	0.0117	38.21	100.1266
76	XA_Ol2_line1 Line 010	0.0007	41.45	LOD	0.0104	LOD	0.0182	20.01	0.2834	0.1926	LOD	38.13	100.0953
77	XA_Ol2_line2 Line 011 Line 001	0.016	41.44	LOD	LOD	0.0132	0.0046	20.48	0.3207	0.1274	0.0157	38.2	100.6176
78	XA_Ol2_line2 Line 011 Line 002	0.0113	41.49	LOD	LOD	0.011	LOD	19.92	0.2534	0.1023	0.0154	38.11	99.9134
79	XA_Ol2_line2 Line 011 Line 003	0.0182	41.43	LOD	LOD	LOD	0.0122	20.18	0.2469	0.1006	LOD	38.52	100.5079
80	XA_Ol2_line2 Line 011 Line 004	LOD	41.18	LOD	LOD	0.0004	LOD	20.14	0.2726	0.1289	0.008	38.23	99.9599
81	XA_Ol2_line2 Line 011 Line 005	LOD	41.61	LOD	LOD	LOD	0.0152	20.28	0.2794	0.1157	0.0096	38.45	100.7599
82	XA_Ol2_line2 Line 011 Line 006	LOD	41.64	LOD	LOD	LOD	0.0091	20.07	0.2814	0.1189	0.0064	38.29	100.4158
83	XA_Ol2_line2 Line 011 Line 007	0.0364	41.53	LOD	LOD	LOD	0.0258	20.19	0.2487	0.1265	0.0053	38.35	100.5127
84	XA_Ol2_line2 Line 011 Line 008	LOD	41.64	LOD	LOD	LOD	0.0091	20.09	0.2586	0.129	0.0123	38.58	100.719
85	XA_Ol2_line2 Line 011 Line 009	LOD	41.57	LOD	LOD	LOD	LOD	20.01	0.2056	0.1845	0.0091	38.07	100.0492
86	XA_Ol2_line2 Line 011 Line 010	0.0119	41.74	LOD	LOD	LOD	0.0061	19.79	0.2738	0.1332	0.0292	37.85	99.8342
87	XA_Cpxoropx_line Line 001	0.0104	29.24	3.14	0.7077	0.0101	0.2119	13	0.2584	0.0676	0.2734	52.3	99.2195
88	XA_Cpxoropx_line Line 002	LOD	29.32	3.16	0.619	LOD	0.209	12.72	0.2178	0.0718	0.1999	52.4	98.9175
89	XA_Cpxoropx_line Line 003	0.0629	28.13	3.23	2.66	LOD	0.1925	12.18	0.273	0.0203	0.3282	52.61	99.6869
90	XA_Cpxoropx_line Line 004	0.0175	29.71	2.69	0.2623	LOD	0.2025	13.03	0.2343	0.0447	0.156	53.12	99.4673
91	XA_Cpxoropx_line Line 005	LOD	29.74	3.16	0.3016	LOD	0.1443	13.18	0.2551	0.0219	0.2447	52.34	99.3876

92	XA_Cpxoropx_line Line 006	LOD	29.67	2.98	0.3747	0.0026	0.2057	12.91	0.2981	0.0397	0.2471	52.46	99.1879
93	XA_Cpxoropx_line Line 007	0.0262	29.57	3.06	0.513	LOD	0.1445	12.98	0.2993	0.0194	0.2294	53.24	100.0818
94	XA_Cpxoropx_line Line 008	LOD	27.16	3.07	0.7695	LOD	0.0737	11.67	0.2462	0.0667	0.1913	45.07	88.3174
95	XA_Cpxoropx_line Line 009	0.0977	26.88	3.56	4.52	LOD	0.1425	11.51	0.2445	0.0304	0.537	51.84	99.3621
96	XA_Cpxoropx_line Line 010	0.0108	29.48	3.17	0.4391	0.0063	0.11	12.86	0.3058	0.0498	0.2312	52.55	99.213
97	XA_Cpxoropx_line Line 011	LOD	29.18	3.14	0.3062	LOD	0.1428	13.04	0.2463	0.0296	0.2417	52.83	99.1566
98	XA_Cpxoropx_line Line 012	LOD	29.16	3.62	0.5838	LOD	0.1317	13.29	0.2451	0.0582	0.2971	51.84	99.2259
99	XA_Cpxoropx_line Line 013	LOD	29.84	2.23	0.2182	LOD	0.0847	13.16	0.2507	0.0177	0.0861	53.27	99.1574
100	XA_Cpxoropx_line Line 014	0.0277	29.41	3.21	0.3152	LOD	0.1833	13.19	0.246	0.0169	0.2042	52.44	99.2433
101	XA_Cpxoropx_line Line 015	0.0376	29.59	3.01	0.6639	LOD	0.1898	12.99	0.2614	0.0616	0.1977	53.01	100.012
102	XA_Cpxoropx_line Line 016	0.0121	29.67	2.93	0.3538	0.0144	0.1508	12.61	0.2286	0.0819	0.2226	53.32	99.5942
103	XA_Cpxoropx_line Line 017	0.0106	29.69	3.18	0.3324	LOD	0.2163	13.05	0.3064	0.0338	0.1866	52.91	99.9161
104	XA_Cpxoropx_line Line 018	0.6446	14.37	5.35	22.78	LOD	0.349	4.82	0.1298	LOD	1.6356	48.78	98.859
105	XA_Cpxoropx_line Line 019	0.5873	14.74	5.06	22.8	LOD	0.4259	4.59	0.1409	0.0606	1.4718	48.84	98.7165
106	XA_Cpxoropx_line Line 020	3.68	10.53	15.61	10.73	0.0783	0.2138	6.64	0.1147	0.0563	1.5525	38.27	87.4756
107	XA_Cpxoropx_line Line 021	LOD	29.84	2.86	0.1956	LOD	0.1675	13.52	0.2923	0.0346	0.1469	52.84	99.8969
108	XA_Cpxoropx_line Line 022	LOD	29.86	2.76	0.3295	LOD	0.1755	13.17	0.2636	0.0489	0.2035	52.92	99.731
109	XA_Cpxoropx_line Line 023	0.0331	29.04	3.25	1.73	LOD	0.1921	12.32	0.2682	0.0548	0.2546	52.76	99.9028
110	XA_Cpxoropx_line Line 024	0.1044	25.78	3.69	6.85	LOD	0.191	10.32	0.2479	0.0396	0.5752	51.72	99.5181
111	XA_Cpxoropx_line Line 025	0.0384	42.18	0.0063	0.006	LOD	LOD	20.36	0.2826	0.1618	0.0159	38.04	101.091
112	XA_Cpxoropx_line Line 026	1.83	16.44	7.75	18.45	0.084	0.281	5.75	0.0388	0.048	1.5232	46.85	99.045
113	XA_Cpxoropx_line Line 027	0.0221	29.09	3.19	1.1412	LOD	0.2094	12.44	0.2311	0.0422	0.1855	52.85	99.4015
114	XA_Cpxoropx_line Line 028	0.0569	28.98	3.15	1.61	0.0017	0.1402	12.47	0.2807	0.0347	0.2251	52.94	99.8893
115	XA_Cpxoropx_line Line 029	0.0162	29.43	2.77	0.7724	0.0029	0.1385	12.56	0.3313	0.0245	0.2188	52.91	99.1746
116	XA_Cpxoropx_line Line 030	LOD	29.42	3.12	0.3875	0.0063	0.1036	12.99	0.3168	0.0363	0.2526	52.58	99.2131
117	XA_Cpxoropx_line Line 031_boundarycross	0.5583	14.53	5.15	22.57	0.0007	0.4957	4.96	0.162	0.0295	1.3826	49.34	99.1788
118	XA_Cpxoropx_line Line 031_boundarycross	0.4867	16.81	4.72	18.7	LOD	0.2969	6.41	0.1474	0.0405	1.1454	49.4	98.1569
119	XA_Cpxoropx_line Line 031_boundarycross	0.5799	14.24	5.4	23.1	0.0021	0.4698	4.73	0.0943	0.0387	1.4514	48.52	98.6262
120	XA_Cpxoropx_line Line 031_boundarycross	0.5749	14.28	5.21	22.9	0.0085	0.4489	4.69	0.1099	0.0076	1.3495	49.27	98.8493
121	XA_Cpxoropx_line Line 031_boundarycross	0.4514	16.86	4.69	18.94	LOD	0.3763	6.52	0.1707	0.0346	1.1399	49.74	98.9229
122	XA_Cpxoropx_line Line 031_boundarycross	0.4917	14.56	4.6	23.06	LOD	0.4536	4.88	0.1432	0.0413	1.1226	49.49	98.8424

123	XA_Cpxoropx_line Line 031_boundarycross	0.4769	16.39	4.54	19.51	0.0072	0.4195	6.77	0.1527	LOD	1.1538	49.49	98.9101
124	XA_Cpxoropx_line Line 031_boundarycross	0.5403	15.28	4.88	22.18	LOD	0.4043	4.97	0.1387	0.0615	1.2935	49.65	99.3983
125	XA_Cpxoropx_line Line 031_boundarycross	0.5278	14.81	5.04	21.17	0.01	0.524	6.29	0.2059	0.0235	1.4276	48.79	98.8188
126	XA_Cpxoropx_line Line 031_boundarycross	0.5372	15.65	4.93	20.46	LOD	0.4082	5.25	0.1219	LOD	1.2307	49.18	97.768
127	XA_Cpxoropx_line Line 031_boundarycross	0.452	16.73	5.62	18.69	LOD	0.5426	7.27	0.1911	0.0328	1.0398	49.36	99.9283
128	XA_Cpxoropx_line Line 031_boundarycross	0.053	26.3	3.2	2.1	LOD	0.3145	15.15	0.3118	0.0445	0.7607	51.3	99.5345
129	XA_Cpxoropx_line Line 031_boundarycross	0.149	24.25	3.82	6.07	LOD	0.2515	13.21	0.3134	0.0513	0.4689	51.2	99.7841
130	XA_Cpxoropx_line Line 031_boundarycross	0.5277	15.67	4.7	20.81	0.01	0.4236	5.99	0.1627	0.0025	1.1984	49.46	98.9549
131	XA_Cpxoropx_line Line 031_boundarycross	0.1371	23.98	3.48	7.34	LOD	0.2278	12.24	0.2583	0.0421	0.4416	53.03	101.1769
132	XA_Cpxoropx_line Line 031_boundarycross	0.4932	16.37	4.7	19.78	0.0053	0.729	6.36	0.1604	0.0093	1.2549	49.76	99.6221
133	XA_Cpxoropx_line Line 031_boundarycross	0.5056	14.71	4.78	22.89	0.0072	0.4812	4.48	0.132	0.0539	1.2955	49.82	99.1554
134	XA_Cpxoropx_line Line 031_boundarycross	0.5043	14.5	4.61	23.09	0.0043	0.3955	5.14	0.1617	0.0337	1.1386	48.8	98.3781
135	XA_Cpxoropx_line Line 031_boundarycross	0.4202	16.99	4.05	18.12	0.0055	0.2937	5.71	0.0687	0.0067	0.8269	47.88	94.3717
136	XA_Cpxoropx_line Line 031_boundarycross	0.008	29.93	2.72	0.3814	0.0057	0.1336	15.33	0.3228	0.0084	0.1825	52.77	101.7924
137	XA_Cpxoropx_line Line 031_boundarycross	0.4	15.34	3.11	23.53	0.0088	0.202	4.82	0.1396	0.0092	0.5314	50.92	99.011
138	XA_Cpxoropx_line Line 031_boundarycross	0.4622	14.62	4.49	23.08	LOD	0.4609	4.71	0.1307	0.021	1.0582	50.12	99.153
139	XA_Cpxoropx_line Line 031_boundarycross	0.4832	16.28	4.51	19.99	0.0051	0.4664	6.27	0.1768	0.0109	1.1479	50.2	99.5403
140	XA_Cpxoropx_line Line 031_boundarycross	0.2727	20.04	3.77	14.65	0.0054	0.3229	9.53	0.2156	0.0293	0.8548	50.3	99.9907
141	XA_Cpxoropx_line Line 031_boundarycross	0.5823	14.52	4.99	22.82	0.0094	0.4654	4.92	0.134	0.0143	1.2549	49.54	99.2503
142	XA_Cpxoropx_line Line 031_boundarycross	0.3798	18.06	4.54	15.82	0.0088	0.3503	8.01	0.2105	0.0059	1.0439	50.24	98.6692
143	XA_Cpxoropx_line Line 031_boundarycross	0.5405	14.51	5.41	22.11	0.0067	0.4645	5.72	0.1428	0.0008	1.3161	48.4	98.6214
144	XA_Cpxoropx_line Line 031_boundarycross	0.5557	15.23	5.44	20.62	LOD	0.4667	6	0.1526	0.0319	1.2134	49.11	98.8203
145	XA_Cpxoropx_line Line 031_boundarycross	0.4928	15.24	5.16	20.67	0.0004	0.4458	5.98	0.1382	0.0177	1.2829	49.26	98.6878
146	XA_Cpxoropx_line Line 031_boundarycross	0.4531	16.75	5.05	17.42	0.0051	0.4198	7.52	0.1387	0.0184	1.0997	49.4	98.2748
147	XA_opx_line3 Line 001	0.4839	16.31	4.82	19.63	0.0049	0.301	5.84	0.1402	0.0353	1.2627	49.87	98.698
148	XA_opx_line3 Line 002	0.447	18.41	4.77	15.41	LOD	0.341	7.36	0.1796	0.0168	0.9982	50.59	98.5226
149	XA_opx_line3 Line 003	0.5712	14.46	5.27	22.74	0.0001	0.448	4.73	0.1126	0.0285	1.3766	49.75	99.487
150	XA_opx_line3 Line 004	0.0387	26.64	3.22	1.69	LOD	0.2487	14.58	0.2925	0.0117	0.1777	53.1	99.9993
151	XA_opx_line3 Line 005	0.4074	16.89	5.03	19	LOD	0.3933	6.71	0.1388	0.0193	1.168	49.32	99.0768
152	XA_opx_line3 Line 006	0.592	14.32	5.53	22.14	0.0015	0.52	5.27	0.1291	0.036	1.3503	48.84	98.7289
153	XA_opx_line3 Line 007	0.4665	16.61	5.14	17.7	0.0031	0.4368	6.6	0.1531	0	1.2165	50.31	98.636

154	XA_opx_line3 Line 008	0.5142	14.87	5.31	21.94	0.0065	0.5709	5.47	0.1443	LOD	1.2824	48.88	98.9883
155	XA_opx_line3 Line 009	0.5092	14.78	5.37	21.78	0.0031	0.445	5.34	0.1598	0.0243	1.4194	49.58	99.4108
156	XA_opx_line3 Line 010	0.0295	22.12	0.5163	25.21	LOD	0.0161	5.24	0.3332	0.0158	0.0251	14.72	68.226
157	XA_opx_line3 Line 011	0.0318	19.62	0.3405	25.35	0.0046	LOD	5.56	0.2976	0.0083	0.0211	4.2	55.4339
158	XA_opx_line3 Line 012	0.5573	14.4	4.85	22.62	0.0064	0.4162	5.23	0.1422	LOD	1.2978	49.69	99.2099
159	XA_opx_line3 Line 013	0.5676	14.25	5.23	22.54	0.0135	0.4541	5.22	0.1287	0.0042	1.3849	49.07	98.863
160	XA_opx_line3 Line 014	0.7293	14.35	4.63	22.94	0.0572	0.4583	5.17	0.1631	0.0251	1.2899	49.59	99.4029
161	XA_opx_line3 Line 015	0.478	16.6	4.65	18.59	LOD	0.3496	6.58	0.2212	0.0419	1.1665	50.47	99.1472
162	XA_opx_line3 Line 016	0.3899	17.66	4.68	17.39	LOD	0.4168	7.91	0.2295	0.0251	1.2397	49.75	99.691
163	XA_opx_line3 Line 017	0.4067	18.07	4.3	16.25	LOD	0.3664	8.54	0.1921	0.0234	1.0829	51.05	100.2815
164	XA_opx_line3 Line 018	0.5107	14.88	5.13	22.39	0.0067	0.4666	5.31	0.1732	0.0234	1.402	49.1	99.3926
165	XA_opx_line3 Line 019	0.5277	14.81	4.98	22.24	LOD	0.5225	5.43	0.1851	0.0033	1.32	49.99	100.0086
166	XA_opx_line3 Line 020	0.2803	21.23	3.8	10.29	LOD	0.3146	10.13	0.1701	0.021	0.6573	51.93	98.8233
167	XA_possiblycpx_line3 Line 001	0.5188	14.98	4.89	22.45	LOD	0.4213	4.97	0.1786	0.0075	1.2441	49.54	99.2003
168	XA_possiblycpx_line3 Line 002	0.5178	15.55	5.02	21.35	0.0008	0.3596	5.39	0.1589	0.0201	1.3686	49.83	99.5658
169	XA_possiblycpx_line3 Line 003	0.5114	14.9	5.19	21.93	0.0019	0.4195	5.31	0.1633	0.0578	1.3544	49.2	99.0383
170	XA_possiblycpx_line3 Line 004	0.5313	14.73	4.66	23.11	LOD	0.3879	4.55	0.1225	0.0469	1.09	49.85	99.0786
171	XA_possiblycpx_line3 Line 005	0.5136	15.01	5.12	21.3	LOD	0.569	6.48	0.1419	0.0268	1.4866	48.71	99.3579
172	XA_possiblycpx_line3 Line 006	0.5562	14.79	5.28	22.11	0.0064	0.3914	5.21	0.1475	0.036	1.379	49.6	99.5065
173	XA_possiblycpx_line3 Line 007	0.6219	14.34	5.38	22.76	LOD	0.4061	5.06	0.1861	0.0151	1.3997	48.69	98.8589
174	XA_possiblycpx_line3 Line 008	0.323	19.16	4.59	14.65	0.0076	0.2781	8.68	0.1779	0.0335	1.0038	50.6	99.5039
175	XA_possiblycpx_line3 Line 009	0.5743	14.5	5.28	22.29	0.0001	0.3738	5.12	0.1641	0.0209	1.2452	49.61	99.1784
176	XA_possiblycpx_line3 Line 010	0.5382	14.67	5.19	22.25	LOD	0.3058	5.13	0.0903	0.0142	1.2663	49.33	98.7848
177	XA_possiblycpx_line3 Line 011	0.4736	15.54	5.15	20.33	0.0106	0.4548	5.98	0.1441	LOD	1.2205	49.58	98.8836
178	XA_possiblycpx_line3 Line 012	0.5425	14.49	5.13	22.47	LOD	0.435	5.59	0.1212	0.0268	1.2294	49.22	99.2549
179	XA_possiblycpx_line3 Line 013	0.4543	16.5	4.8	18.99	LOD	0.3302	6.32	0.1496	0.0092	1.0675	49.48	98.1008
180	XA_possiblycpx_line3 Line 014	0.562	14.66	5.11	22.38	0.0135	0.3849	5.25	0.1564	0.0251	1.2617	49.22	99.0236
181	XA_possiblycpx_line3 Line 015	0.4257	16.7	4.53	18.88	LOD	0.3687	6.83	0.1551	LOD	1.1047	50.78	99.7742
182	XA_possiblycpx_line3 Line 016	0.5238	14.6	4.77	23.08	0.005	0.3633	4.85	0.1081	0.0075	1.1866	49.91	99.4043
183	XA_possiblycpx_line3 Line 017	0.4527	15.3	5.03	20.88	LOD	0.4097	6	0.1298	0.0376	1.2984	49.26	98.7982
184	XA_possiblycpx_line3 Line 018	0.4902	15.58	5.15	21.31	0.0019	0.3962	5.21	0.1432	0.0075	1.3583	49.13	98.7773

185	XA_possiblycpx_line3 Line 019	0.4531	16.03	5.01	19.41	0.0118	0.3625	6.17	0.1727	0.051	1.2563	48.89	97.8174
186	XA_possiblycpx_line3 Line 020	0.52	14.65	4.83	22.88	LOD	0.3875	4.88	0.1566	LOD	1.2088	49.78	99.2929
187	XA_opx_line4 Line 001	0.0453	27.71	3.1	2.36	0.0151	0.2397	12.17	0.2088	0.021	0.2444	53.36	99.4743
188	XA_opx_line4 Line 002	0.0757	27.13	3.14	3.21	0.0017	0.1948	12.09	0.2256	0.0403	0.2576	53.42	99.7857
189	XA_opx_line4 Line 003	0.0179	29.04	3.01	0.6966	LOD	0.1886	13.33	0.2349	0.0596	0.2409	52.99	99.8085
190	XA_opx_line4 Line 004	LOD	27.78	2.07	0.5268	LOD	0.1767	15.19	0.3209	0.0652	3.64	50.87	100.6396
191	XA_opx_line4 Line 005	0.1299	25.37	2.94	4.81	0.0013	0.1781	10.55	0.1894	0.0486	0.9796	47.06	92.2569
192	XA_opx_line4 Line 006	0.0115	29.08	2.86	0.6708	LOD	0.1654	13.2	0.2709	0.0436	0.4876	52.99	99.7798
193	XA_opx_line4 Line 007	0.0343	29.01	3.09	0.6288	0.0088	0.1934	13.07	0.2787	0.0403	0.2712	52.87	99.4955
194	XA_opx_line4 Line 008	0.1319	24.95	3.74	6.55	LOD	0.2392	10.22	0.2161	0.0244	0.5618	52.52	99.1534
195	XA_opx_line4 Line 009	0.0668	28.32	2.65	2.58	LOD	0.1664	12	0.219	0.0638	0.1991	53.92	100.1851
196	XA_opx_line4 Line 010	0.0099	29.08	2.66	1.47	LOD	0.1629	12.34	0.2768	0.0361	0.1655	53.95	100.1512
197	XA_opx_line4 Line 011	0.0051	29.36	2.99	0.3638	LOD	0.1937	12.79	0.2712	0.0159	0.1631	53.78	99.9328
198	XA_opx_line4 Line 012	0.0545	28.11	3.04	2.36	0.0029	0.146	11.94	0.2157	0.0437	0.2603	53.83	100.0031
199	XA_opx_line4 Line 013	0.0429	28.65	3.41	1.51	LOD	0.1692	12.31	0.2309	0.0621	0.2706	53.56	100.2157
200	XA_opx_line4 Line 014	0.0735	27.98	2.84	3.27	0.0101	0.1448	11.5	0.241	0.0437	0.166	53.94	100.2091
201	XA_opx_line4 Line 015	0.0263	28.62	3.31	1.86	LOD	0.1925	12.49	0.2308	0.0159	0.2138	52.44	99.3993
202	XA_opx_line4 Line 016	0.1235	22.42	1.6485	5.88	0.006	0.1993	15.35	0.2656	0.0739	8.56	45.46	99.9868
203	XA_opx_line4 Line 017	0.0087	27.67	2.1	0.5268	LOD	0.1922	15.37	0.2599	0.0709	4.7	50.14	101.0385
204	XA_opx_line4 Line 018	0.0461	28.11	3.25	2.42	LOD	0.1992	11.98	0.2384	0.057	0.2328	53.58	100.1135
205	XA_opx_line4 Line 019	0.0524	29.03	3.01	1.55	LOD	0.1787	11.97	0.2395	0.0302	0.1806	53.79	100.0314
206	XA_opx_line4 Line 020	0.0524	27.86	3.39	3.03	LOD	0.1977	11.86	0.269	0.078	0.249	53.09	100.0761
207	XA_opx_line5 Line 001	0.0303	28.77	2.76	1.0908	LOD	0.1672	12.6	0.2732	0.0487	0.2369	53.39	99.3671
208	XA_opx_line5 Line 002	LOD	29.36	2.84	0.6007	LOD	0.1591	12.72	0.2117	0.0754	0.2516	53.27	99.4885
209	XA_opx_line5 Line 003	0.0267	28.78	2.65	0.7464	0.0012	0.1807	12.9	0.2706	0.036	0.1335	53.65	99.3751
210	XA_opx_line5 Line 004	0.0215	29.04	3.01	0.6121	LOD	0.1775	12.99	0.2378	0.0519	0.2138	53.15	99.5046
211	XA_opx_line5 Line 005	LOD	28.94	2.98	0.5041	0.0015	0.1794	12.62	0.226	0.0251	0.1698	53.62	99.2659
212	XA_opx_line5 Line 006	LOD	29.87	1.97	0.552	0.006	0.173	12.68	0.2933	0.0528	0.1637	54.17	99.9308
213	XA_opx_line5 Line 007	0.0319	28.47	2.86	1.86	LOD	0.1389	12.3	0.206	0.0502	0.2565	53.34	99.5135
214	XA_opx_line5 Line 008	0.047	29.08	2.95	0.4837	LOD	0.1277	12.64	0.2835	0.0352	0.183	53.2	99.0301
215	XA_opx_line5 Line 009	0.4151	14.93	4.64	23.15	0.0181	0.2267	4.4	0.11	0.0334	1.465	49.62	99.0083

216	XA_opx_line5 Line 010	0.0716	27.85	2.38	3.03	0.0033	0.136	12.03	0.23	0.0686	0.1154	53.52	99.4349
217	XA_opx_line5 Line 011	0.1262	27.24	2.88	4.08	0.0119	0.1883	11	0.1963	0.0384	0.2603	53.51	99.5314
218	XA_opx_line5 Line 012	0.0716	28.46	2.62	1.73	0.0091	0.1969	11.97	0.2409	0.0226	0.2595	53.79	99.3706
219	XA_opx_line5 Line 013	0.043	28.27	2.71	2.02	0.0175	0.194	12	0.2534	0.0235	0.1826	52.98	98.694
220	XA_opx_line5 Line 014	0.0363	27.99	3.18	2.77	0.0085	0.2271	12.08	0.2545	LOD	0.2185	53.27	100.0349
221	XA_opx_line5 Line 015	0.0185	26.15	4.01	8.74	0.0018	0.2307	10.8	0.1951	0.0509	0.0598	36.78	87.0368
222	XA_opx_line5 Line 016	0.0146	29.05	2.85	0.5197	0.0066	0.1542	13.05	0.2171	0.0343	0.1579	53.18	99.2344
223	XA_opx_line5 Line 017	0.0293	28.75	2.68	1.2287	0.004	0.1984	12.68	0.2742	0.0118	0.243	53.47	99.5694
224	XA_opx_line5 Line 018	0.0382	26.41	1.98	2.79	0.0093	0.2292	13.97	0.2819	0.0425	4.16	50.51	100.4211
225	XA_opx_line5 Line 019	0.0246	29.37	2.39	0.8298	0.0095	0.1872	12.9	0.2577	0.0838	0.1823	53.7	99.9349
226	XA_opx_line5 Line 020	0.0387	28.35	2.72	2.11	LOD	0.1675	12.07	0.2611	0.0352	0.227	54.02	99.9995
227	XA_opx_line6 Line 001	0.0169	29.33	2.7	0.3867	0.0125	0.1775	13.23	0.2835	0.0084	0.9053	53.13	100.1808
228	XA_opx_line6 Line 002	0.0266	29.25	2.93	0.9321	0.0022	0.1185	12.6	0.2672	0.0284	0.1327	54.36	100.6477
229	XA_opx_line6 Line 003	0.0443	28.57	3.1	1.3424	0.0085	0.1701	12.5	0.2541	0.0251	0.2367	53.92	100.1712
230	XA_opx_line6 Line 004	1.6	25.11	2.53	1.55	0.038	0.1241	9.74	0.2131	0.0285	0.1827	48.82	89.9364
231	XA_opx_line6 Line 005	0.0768	28.39	3.15	2.47	0.0227	0.236	11.99	0.2355	0.0318	0.2114	53.13	99.9442
232	XA_opx_line6 Line 006	0.0183	28.64	3.23	1.44	0.0086	0.2292	12.54	0.2571	0.0318	0.2111	53.91	100.5161
233	XA_opx_line6 Line 007	0.0394	27.72	2.92	3.26	0.0081	0.174	11.6	0.2358	0.0519	0.2451	53.38	99.6343
234	XA_opx_line6 Line 008	0.0513	25.9	2.32	3.27	0.006	0.1862	14.61	0.233	0.0033	4.69	49.25	100.5198
235	XA_opx_line6 Line 009	0.0471	27.86	3.05	3.13	LOD	0.2129	11.74	0.1962	0.0686	0.286	52.7	99.2908
236	XA_opx_line6 Line 010	0.0275	28.71	3.05	0.6754	0.0115	0.2565	13.01	0.2612	0.0777	0.2712	53.29	99.641
237	XA_opx_line6 Line 011	0.0363	29.23	2.81	0.6601	0.0211	0.1946	13.11	0.2474	0.0142	0.5656	53.58	100.4693
238	XA_opx_line6 Line 012	0.068	28.15	2.79	3.11	0.0002	0.2116	11.81	0.238	0.0419	0.2067	53.96	100.5864
239	XA_opx_line6 Line 013	0.0592	28.34	3.01	1.82	0.0094	0.1967	12.44	0.2563	0.0603	0.2316	53.4	99.8235
240	XA_opx_line6 Line 014	0.0382	28.82	3.04	1.51	0.0042	0.2106	12.35	0.2996	0.0552	0.1792	53.72	100.227
241	XA_opx_line6 Line 015	0.0338	28.62	2.16	0.8553	0.016	0.1396	13.98	0.2367	0.0525	2.82	51.15	100.0639
242	XA_opx_line6 Line 016	0.0414	29.17	2.9	0.7006	LOD	0.2166	12.76	0.2856	0.0645	0.2578	54.11	100.5065
243	XA_opx_line6 Line 017	0.0514	29.13	2.87	1.1177	0.0217	0.2026	12.43	0.2604	0.0552	0.3108	53.23	99.6798
244	XA_opx_line6 Line 018	0.1254	25.48	3.38	7.22	LOD	0.3048	10.04	0.2666	0.0786	0.4689	52.69	100.0543
245	XA_opx_line6 Line 019	0.0198	28.71	2.38	1.9	0.0038	0.2572	12.82	0.3233	0.0551	0.9031	53.54	100.9123
246	XA_opx_line6 Line 020	0.027	28.88	2.96	1.1495	0.0211	0.173	12.39	0.2005	0.0259	0.1486	53.54	99.5156

247	XA_Ol_line5 Line 001	0.0079	41.32	LOD	LOD	0.0081	0.0361	20.11	0.2818	0.1525	0.0215	38.46	100.3979
248	XA_Ol_line5 Line 002	0.0055	41.36	LOD	LOD	0.0055	LOD	20.26	0.2947	0.16	0.0153	39.01	101.111
249	XA_Ol_line5 Line 003	LOD	41.25	LOD	LOD	0.0067	LOD	19.65	0.2411	0.1841	0.0046	39.04	100.3765
250	XA_Ol_line5 Line 004	LOD	41.35	LOD	LOD	LOD	LOD	20	0.28	0.1104	0.0172	39.01	100.7676
251	XA_Ol_line5 Line 005	0.0208	41.48	LOD	LOD	LOD	LOD	20.27	0.2506	0.1277	0.0113	38.74	100.9004
252	XA_Ol_line5 Line 006	0.0396	41.31	LOD	LOD	LOD	0.009	20.4	0.2688	0.141	LOD	39.19	101.3584
253	XA_Ol_line5 Line 007	LOD	41.29	LOD	0.0018	LOD	0.0165	20.21	0.2829	0.1335	0.0051	38.87	100.8098
254	XA_Ol_line5 Line 008	0.0158	41.14	LOD	0.0028	LOD	0.003	20.22	0.2525	0.1359	LOD	39.03	100.8
255	XA_Ol_line5 Line 009	0.011	41.79	LOD	LOD	LOD	LOD	19.88	0.2376	0.1608	0.0128	39.53	101.6222
256	XA_Ol_line5 Line 010	LOD	41.29	LOD	LOD	LOD	0.0045	19.96	0.2859	0.1367	0.0125	39.16	100.8496
257	XA_Ol_line5 Line 011	0.0587	29.91	14.02	LOD	LOD	3.45	24.15	0.2509	0.1286	0.0189	23.76	95.7471
258	XA_Ol_line5 Line 012	LOD	41.41	LOD	0.0008	LOD	0.006	19.95	0.2698	0.1284	0.0264	39.11	100.9014
259	XA_Ol_line5 Line 013	LOD	41.56	LOD	LOD	LOD	LOD	20.02	0.3031	0.1384	LOD	38.82	100.8415
260	XA_Ol_line5 Line 014	0.0137	31.12	0.6225	0.1245	LOD	0.0341	12.83	0.2607	0.1027	0.0384	51.24	96.3866
261	XA_Ol_line5 Line 015	LOD	41.52	LOD	LOD	LOD	0.0256	19.93	0.2461	0.1524	0.0086	38.67	100.5527
262	XA_Ol_line5 Line 016	0.0282	41.21	LOD	LOD	LOD	LOD	19.94	0.287	0.1218	0.0219	39.26	100.8689
263	XA_Ol_line5 Line 017	LOD	41.48	LOD	LOD	0.0074	LOD	20.19	0.289	0.1442	0.0216	39	101.1322
264	XA_Ol_line5 Line 018	0.0139	41.39	0.0037	LOD	LOD	0.012	20.01	0.244	0.1458	0.0177	38.89	100.7271
265	XA_Ol_line5 Line 019	0.0359	40.96	LOD	LOD	LOD	0.0015	19.83	0.2397	0.1691	LOD	39.04	100.2762
266	XA_Ol_line5 Line 020	0.0097	41.3	LOD	LOD	LOD	0.009	19.78	0.2795	0.1947	LOD	38.77	100.3429
267	std_ol1	0.011	52.66	LOD	LOD	0.0054	LOD	6.7	0.0964	0.4676	LOD	41.54	101.4804
268	std_di1	LOD	18.5	0.0484	25.63	LOD	LOD	0.0346	0.0332	LOD	0.0932	54.99	99.3294
269	std_ab1	11.36	LOD	19.62	0.2359	0.164	LOD	0.0049	0.0144	LOD	0.0065	68.97	100.3757
270	std_grt	0.0255	4.4	20.5	0.3606	LOD	0.0056	36.51	0.224	LOD	LOD	37.52	99.5457
271	XA_Ol_line5 Line 020	0.0192	41.26	LOD	LOD	LOD	0.0045	20.15	0.2509	0.1577	0.0069	39.17	101.0192
272	XB_cpxline1 Line 001	0.0496	29.11	3.18	0.3043	LOD	0.2313	13.29	0.2688	0.0527	0.1776	53.68	100.3443
273	XB_cpxline1 Line 002	0.0085	29.6	2.73	0.3324	LOD	0.1725	13.16	0.3037	0.0736	0.1272	54.32	100.8279
274	XB_cpxline1 Line 003	LOD	29.24	2.97	0.3946	LOD	0.1694	13.1	0.2363	0.0468	0.131	53.94	100.2281
275	XB_cpxline1 Line 004	0.5639	14.71	4.92	23.35	LOD	0.3218	4.52	0.1396	0.0167	1.3894	50.29	100.2214
276	XB_cpxline1 Line 005	0.5425	14.39	5.04	22.72	0.0034	0.3675	5.15	0.1733	LOD	1.4266	49.83	99.6433
277	XB_cpxline1 Line 006	0.4637	15.57	4.27	20.63	LOD	0.4443	6.88	0.126	0.0258	1.0697	50.06	99.5395

278	XB_cpxline1 Line 007	0.5679	14.41	5.27	22.67	LOD	0.4514	5.3	0.1471	0.0242	1.5691	49.7	100.1097
279	XB_cpxline1 Line 008	0.5676	14.59	4.78	22.58	0.0063	0.3933	5.41	0.1548	0.0108	1.4322	50.3	100.225
280	XB_cpxline1 Line 009	0.5954	14.24	5.12	22.96	LOD	0.456	5.2	0.1744	0.0225	1.5033	50.01	100.2816
281	XB_cpxline1 Line 010	0.5958	14.29	5.31	22.59	LOD	0.4999	5.22	0.1569	0.0467	1.5306	49.8	100.0399
282	XB_cpxline1 Line 011	0.5628	14.68	4.93	22.76	LOD	0.5305	5.36	0.1251	0.015	1.4193	50.33	100.7127
283	XB_cpxline1 Line 012	0.551	14.44	5	22.75	0.0043	0.4754	5.51	0.1405	0.0242	1.5591	49.97	100.4245
284	XB_cpxline1 Line 013	0.4935	15.29	4.77	21.48	LOD	0.5002	6.02	0.1481	0.03	1.4095	49.73	99.8713
285	XB_cpxline1 Line 014	0.5482	14.38	5.19	22.87	LOD	0.405	4.82	0.1569	0.0258	1.4868	49.8	99.6827
286	XB_cpxline1 Line 015	0.0419	27.36	3.15	2.84	0.0001	0.1929	12.95	0.2456	0.0333	0.2968	53.83	100.9406
287	XB_cpxline1 Line 016	0.0582	27.12	3.38	2.46	LOD	0.2358	13.45	0.3017	0.05	0.2896	52.73	100.0753
288	XB_cpxline1 Line 017	0.5661	14.16	5.35	22.78	0.0099	0.4258	4.93	0.1525	0.0391	1.485	50.19	100.0884
289	XB_cpxline1 Line 018	0.0061	20.43	1.7346	0.7658	LOD	0.1661	25.75	0.402	LOD	18.15	35.59	102.9946
290	XB_cpxline1 Line 019	0.5884	14.04	5.13	22.95	LOD	0.4071	5.3	0.1205	0.0133	1.4898	49.39	99.4291
291	XB_cpxline1 Line 020	0.5618	14.04	4.95	22.91	LOD	0.4377	5.34	0.1391	0.0058	1.4239	50.02	99.8283
292	XB_cpxline1 Line 021	0.5965	13.88	5.77	23.2	LOD	0.4507	5.24	0.1084	0.0191	1.73	49.3	100.2947
293	XB_cpxline1 Line 022	0.0248	26.51	3.41	0.304	LOD	0.2815	16.25	0.3426	0.0648	0.1612	52.21	99.5589
294	XB_cpxline1 Line 023	0.5768	13.82	5.34	23.07	0.0048	0.4057	5.19	0.126	LOD	1.5308	49.71	99.7741
295	XB_cpxline1 Line 024	0.5303	15.14	5.28	20.31	LOD	0.3909	6.89	0.1806	0.0042	1.5383	49.66	99.9243
296	XB_cpxline1 Line 025	0.6025	13.78	5.63	23.06	LOD	0.4585	5.34	0.1544	0.0224	1.6632	49.34	100.051
297	XB_cpxline1 Line 026	0.0193	26.67	3.27	0.2767	LOD	0.2498	16.11	0.3777	0.0333	0.1807	52.41	99.5975
298	XB_cpxline1 Line 027	0.5836	14.36	4.65	22.85	0.0113	0.4367	5.23	0.0954	LOD	1.2867	49.52	99.0237
299	XB_cpxline1 Line 028	0.6252	13.81	5.32	22.81	0.0016	0.5083	5.4	0.149	0.0258	1.513	49.89	100.0529
300	XB_cpxline1 Line 029	0.6376	13.76	5.65	22.79	LOD	0.4758	5.25	0.1521	0.0266	1.68	49.12	99.5421
301	XB_cpxline1 Line 030	0.6067	14	4.87	22.97	LOD	0.5145	5.22	0.1598	0.0108	1.3441	49.71	99.4059
302	std_ol1	0.0143	52.76	LOD	LOD	LOD	0.0111	6.83	0.092	0.3753	0.0005	41.72	101.8032
303	std_di1	0.0366	18.55	0.0481	25.81	LOD	LOD	0.0477	0.0675	LOD	0.1135	55.73	100.4034
304	std_ab1	11.3	LOD	19.6	0.2532	0.143	0.0098	LOD	0.011	LOD	0.0146	68.57	99.9016
305	std_grt	0.0618	4.28	20.48	0.3399	LOD	LOD	36.47	0.2486	LOD	0.0063	37.13	99.0166
306	XB_opx_cpx_ol_cross_1 Line 001	0.0182	28	3.06	1.0178	LOD	0.2255	14.2	0.2777	0.0133	0.1645	52.96	99.937
307	XB_opx_cpx_ol_cross_1 Line 002	0.0119	28.42	2.69	0.2013	0.0027	0.1556	14.7	0.2981	0.0408	0.1218	53.71	100.3522
308	XB_opx_cpx_ol_cross_1 Line 003	LOD	29.16	2.03	0.231	0.0131	0.1083	13.98	0.3477	0.0376	0.1252	55.07	101.1029

309	XB_opx_cpx_ol_cross_1 Line 004	LOD	28.5	3.1	0.2708	LOD	0.2935	14.12	0.2853	0.0467	0.1677	53.87	100.654
310	XB_opx_cpx_ol_cross_1 Line 005	LOD	28.28	3.43	0.2135	0.0033	0.2605	14.44	0.3087	0.04	0.3665	53.54	100.8825
311	XB_opx_cpx_ol_cross_1 Line 006	0.5527	14.8	4.61	23.15	0.0039	0.5097	4.33	0.1195	0.0308	1.3239	50.72	100.1505
312	XB_opx_cpx_ol_cross_1 Line 007	0.6375	14.45	4.84	22.83	0.01	0.5022	5.27	0.1435	0.0117	1.3457	50.37	100.4106
313	XB_opx_cpx_ol_cross_1 Line 008	0.5475	15.13	4.64	22.31	LOD	0.4751	5.13	0.148	0.0058	1.177	50.71	100.2734
314	XB_opx_cpx_ol_cross_1 Line 009	0.2152	22.51	3.65	8.85	LOD	0.4294	11.93	0.2751	0.0266	0.4735	52.66	101.0198
315	XB_opx_cpx_ol_cross_1 Line 010	0.6218	14.03	5.19	22.8	LOD	0.5532	5.14	0.1609	0.0274	1.3641	49.88	99.7674
316	XB_opx_cpx_ol_cross_1 Line 011	0.63	14.11	5.35	22.95	0.0034	0.4231	5.4	0.1106	LOD	1.5138	49.52	100.0109
317	XB_opx_cpx_ol_cross_1 Line 012	1.2937	14.53	8.3	18.49	LOD	0.423	6.39	0.1138	0.015	1.3675	47.47	98.393
318	XB_opx_cpx_ol_cross_1 Line 013	0.5215	14.64	4.96	22.42	LOD	0.4603	5.57	0.1403	LOD	1.4257	49.54	99.6778
319	XB_opx_cpx_ol_cross_1 Line 014	0.5813	14.37	4.72	22.88	LOD	0.5013	5.15	0.1404	0.0283	1.3542	50.76	100.4855
320	XB_opx_cpx_ol_cross_1 Line 015	0.6236	14.23	5.15	22.78	LOD	0.3979	5.26	0.1732	0.0541	1.5241	49.75	99.9429
321	XB_opx_cpx_ol_cross_1 Line 016	0.6074	14.41	5.03	23.12	0.0129	0.4514	5.08	0.1239	0.0241	1.4739	50	100.3336
322	XB_opx_cpx_ol_cross_1 Line 017	0.0409	26.57	3.24	1.2909	LOD	0.3308	15.2	0.2956	0.0616	0.1065	53.02	100.1563
323	XB_opx_cpx_ol_cross_1 Line 018	0.6025	14.48	4.86	22.93	0.0104	0.5892	5.18	0.0898	0.0083	1.323	49.7	99.7732
324	XB_opx_cpx_ol_cross_1 Line 019	0.4954	15.39	4.48	21.47	LOD	0.528	5.84	0.1236	LOD	1.2117	50.33	99.8687
325	XB_opx_cpx_ol_cross_1 Line 020	0.4692	16.2	4.37	19.85	0.0003	0.449	6.34	0.1992	0.0017	1.0282	51.11	100.0176
326	XB_opx_cpx_ol_cross_1 Line 021	0.5915	14.41	4.76	22.39	LOD	0.661	5.43	0.1752	LOD	1.3409	49.66	99.4186
327	XB_opx_cpx_ol_cross_1 Line 022	0.5128	15.67	4.22	21.34	LOD	0.5709	5.79	0.1601	LOD	1.1074	50.7	100.0712
328	XB_opx_cpx_ol_cross_1 Line 023	0.4776	15.57	4.61	21.5	LOD	0.5272	5.62	0.149	0.0433	1.2592	50.45	100.2063
329	XB_opx_cpx_ol_cross_1 Line 024	0.5795	14.35	4.95	22.43	LOD	0.497	5.48	0.1183	0.015	1.3947	49.84	99.6545
330	XB_opx_cpx_ol_cross_1 Line 025	0.3732	19.27	4.31	14.85	0.0123	0.4212	8.53	0.1866	0.0557	1.042	50.61	99.661
331	XB_opx_cpx_ol_cross_1 Line 026	0.538	14.76	4.57	22.25	LOD	0.5168	5.16	0.1337	0.0092	1.2421	50.18	99.3598
332	XB_opx_cpx_ol_cross_1 Line 027	0.6519	14.25	4.96	22.94	LOD	0.5552	5.28	0.126	0.0416	1.3482	50.12	100.2729
333	XB_opx_cpx_ol_cross_1 Line 028	0.5543	14.9	4.75	22.11	0.0032	0.553	5.57	0.127	0.0383	1.2645	50.3	100.1703
334	XB_opx_cpx_ol_cross_1 Line 029	0.6115	14.25	5.08	22.66	0.0002	0.5385	5.65	0.1259	0.0399	1.3762	49.47	99.8022
335	XB_opx_cpx_ol_cross_1 Line 030	0.5871	14.78	4.71	22.33	0.0125	0.6399	5.18	0.1653	0.0208	1.2552	49.7	99.3808
336	std_ol1	LOD	52.81	LOD	0.0087	LOD	0.0143	6.68	0.0898	0.4638	LOD	41.55	101.6166
337	std_di1	0.0117	18.67	0.0453	25.93	LOD	0.0033	0.0403	0.0232	0.0552	0.0524	55.5	100.3314
338	std_ab1	11.42	0.0037	19.72	0.2261	0.1523	LOD	0.0136	0.0011	LOD	0.0038	69.24	100.7806
339	std_grt	0.0264	4.37	20.69	0.3433	LOD	0.0155	36.56	0.2269	0.0057	0.039	37.25	99.5268

340	XB_opx_cpx_ol_cross_1 Line 030	0.6066	14.62	4.8	22.61	0.0054	0.6241	5.08	0.1215	0.0415	1.2833	50.04	99.8324
341	XB_opx_cpx_ol_cross_1 Line 031 Line 001	0.0107	28.83	2.19	0.836	LOD	0.2041	14.38	0.261	0.069	3.34	51.49	101.6108
342	XB_opx_cpx_ol_cross_1 Line 031 Line 002	0.0137	29.23	1.8211	0.1421	0.0092	0.1167	11.45	0.2534	0.0167	0.0829	51.02	94.1558
343	XB_opx_cpx_ol_cross_1 Line 031 Line 003	0.0361	30.09	2.43	0.3026	0.0113	0.1119	12.29	0.2369	0.0459	0.1388	54.39	100.0835
344	XB_opx_cpx_ol_cross_1 Line 031 Line 004	0.0808	29.65	1.8097	0.6367	0.0033	0.0854	12.35	0.2443	0.0517	0.3873	53.77	99.0692
345	XB_opx_cpx_ol_cross_1 Line 031 Line 005	0.0206	29.44	2.64	1.0883	LOD	0.2333	12.31	0.2217	0.0392	0.2654	54.15	100.4085
346	XB_opx_cpx_ol_cross_1 Line 031 Line 006	0.0177	29.33	3.09	0.778	LOD	0.1848	12.73	0.2758	0.0834	0.3971	53.9	100.7868
347	XB_opx_cpx_ol_cross_1 Line 031 Line 007	0.0708	28.13	2.07	3.74	LOD	0.1863	10.99	0.2752	0.05	0.1438	55.19	100.8461
348	XB_opx_cpx_ol_cross_1 Line 031 Line 008	0.039	29.37	2.63	1.1667	0.0088	0.1431	12.21	0.2889	0.0316	0.1299	54.53	100.548
349	XB_opx_cpx_ol_cross_1 Line 031 Line 009	0.0434	28.64	3.28	1.94	0.0043	0.2554	12.07	0.2141	0.0701	0.1895	53.37	100.0768
350	XB_opx_cpx_ol_cross_1 Line 031 Line 010	0.2566	17.39	2.2	22.63	0.0158	0.1614	4.02	0.0943	LOD	0.4437	53.31	100.5218
351	XB_opx_cpx_ol_cross_1 Line 031 Line 011	0.4751	14.9	5.07	23.61	LOD	0.3742	4.08	0.0756	LOD	1.4005	50.57	100.5554
352	XB_opx_cpx_ol_cross_1 Line 031 Line 012	0.0629	28.03	3.49	2.47	0.0082	0.2895	11.86	0.2528	0.0533	0.3345	53.84	100.6912
353	XB_opx_cpx_ol_cross_1 Line 031 Line 013	LOD	29.42	3.32	0.395	0.0007	0.158	12.8	0.259	0.0533	0.3507	53.97	100.7267
354	XB_opx_cpx_ol_cross_1 Line 031 Line 014	0.002	29.52	2.68	0.6103	LOD	0.1906	12.62	0.2711	0.0399	0.1834	54.26	100.3773
355	XB_opx_cpx_ol_cross_1 Line 031 Line 015	0.0516	29.32	2.83	0.5605	LOD	0.1796	12.84	0.2612	0.0624	0.1192	54	100.2245
356	XB_opx_cpx_ol_cross_1 Line 031 Line 016	0.0187	29.5	2.79	0.2828	0.011	0.1546	13.1	0.272	0.0042	0.0524	53.35	99.5357
357	XB_opx_cpx_ol_cross_1 Line 031 Line 017	LOD	29.13	2.91	0.892	0.001	0.1987	12.55	0.2594	0.0333	0.155	54.08	100.2094
358	XB_opx_cpx_ol_cross_1 Line 031 Line 018	0.0289	29.85	3.2	0.2946	0.0081	0.2356	12.72	0.2398	0.0625	0.1918	53.93	100.7613
359	XB_opx_cpx_ol_cross_1 Line 031 Line 019	0.0098	30.01	2.52	0.2524	LOD	0.1969	12.7	0.28	0.0225	0.125	54.67	100.7866
360	XB_opx_cpx_ol_cross_1 Line 031 Line 020	0.0319	29.55	3.16	0.3918	LOD	0.2389	12.59	0.2398	0.0608	0.176	54.5	100.9392
361	std_ol1	0.0318	52.56	LOD	LOD	0.0056	0.0444	6.86	0.0951	0.4473	0.0089	41.86	101.9131
362	std_di1	0.0168	18.72	0.0564	25.61	LOD	0.0049	0.0549	0.0739	LOD	0.0599	55.97	100.5668
363	std_ab1	11.42	LOD	19.69	0.2299	0.1534	LOD	0.0044	0.0265	LOD	LOD	68.66	100.1842
364	std_grt	0.0244	4.37	20.58	0.3553	LOD	0.0028	36.52	0.1931	LOD	0.0191	37.44	99.5047
365	XB_opx_cpx_ol_cross_1 Line 031 Line 020	0.0189	29.69	3.07	0.4702	LOD	0.2376	12.67	0.2444	0.065	0.1845	54.23	100.8806
366	XB_opx_cpx_ol_cross_1 Line 031 Line 021	0.0233	29.66	2.74	0.2783	LOD	0.1923	12.79	0.268	0.0533	0.1787	54.91	101.0939
367	XB_opx_cpx_ol_cross_1 Line 031 Line 021	0.0467	28.47	1.6748	1.53	0.0685	0.1361	13.1	0.2265	0.0333	0.0114	50.74	96.0373
368	XB_opx_cpx_ol_cross_1 Line 031 Line 021	0.1061	19.59	1.625	4	0.006	0.1018	10.04	0.201	0.005	0.0972	31.31	67.0821
369	XB_opx_cpx_ol_cross_1 Line 031 Line 021	0.0078	29.14	3.02	0.4444	LOD	0.1715	13.36	0.2696	0.0582	0.1145	54.01	100.596
370	XB_opx_cpx_ol_cross_1 Line 031 Line 021	0.0169	28.81	2.84	0.8884	LOD	0.1874	13.01	0.2614	0.0441	0.0985	54.32	100.4767

371	XB_opx_cpx_ol_cross_1 Line 031 Line 021	0.0261	29.49	2.31	0.8524	LOD	0.1448	12.03	0.2606	0.0558	1.461	54.61	101.2407
372	XB_opx_cpx_ol_cross_1 Line 031 Line 021	0.0354	29.44	3.16	0.9476	LOD	0.27	12.34	0.257	0.0624	0.1821	53.87	100.5645
373	XB_opx_cpx_ol_cross_1 Line 031 Line 021	LOD	25.99	1.3095	0.8874	0.0027	0.0341	10.29	0.2007	0.0616	0.1289	44.16	83.0649
374	XB_opx_cpx_ol_cross_1 Line 031 Line 021	0.0346	27.83	2.23	1.3047	LOD	0.2111	14.67	0.2621	0.0621	4.51	49.96	101.0746
375	XB_opx_cpx_ol_cross_1 Line 031 Line 021	LOD	28.56	1.4218	0.1604	0.0006	0.0476	14.72	0.2779	0.0158	0.0765	55.32	100.6006
376	XB_opx_cpx_ol_cross_1 Line 031 Line 021	LOD	28.88	2.7	0.3672	0.005	0.2028	13.04	0.2202	0.0216	0.2221	53.7	99.3589
377	XB_opx_cpx_ol_cross_1 Line 031 Line 021	LOD	23.44	1.2329	0.1801	LOD	LOD	10.7	0.2006	0.0808	0.0952	41.07	76.9996
378	XB_opx_cpx_ol_cross_1 Line 031 Line 021	LOD	29.59	2.48	0.3542	0.0076	0.2	12.67	0.2572	0.0225	0.2001	54.13	99.9116
379	XB_opx_cpx_ol_cross_1 Line 031 Line 021	0.0291	28.87	3.19	0.7195	LOD	0.237	12.95	0.257	0.0258	0.1649	53.48	99.9233
380	XB_opx_cpx_ol_cross_1 Line 031 Line 021	0.0143	29.12	2.44	0.2822	LOD	0.2345	14.09	0.2738	0.0598	1.2345	53.23	100.9791
381	XB_opx_cpx_ol_cross_1 Line 031 Line 021	0.4611	17.42	4.61	17.63	0.0007	0.2887	7.21	0.179	0.015	1.1646	50.59	99.5691
382	XB_opx_cpx_ol_cross_1 Line 031 Line 021	0.2438	22.15	3.43	10.06	LOD	0.4018	11.11	0.2411	0.0448	0.6973	52.01	100.3888
383	XB_opx_cpx_ol_cross_1 Line 031 Line 021	0.682	14.73	4.85	22.43	0.0006	0.4448	4.99	0.1574	0.0407	1.4109	50.09	99.8264
384	XB_opx_cpx_ol_cross_1 Line 031 Line 021	0.6367	14.77	4.85	22.99	0.0032	0.5341	4.81	0.1127	0.015	1.4236	50.08	100.2253
385	XB_opx_cpx_ol_cross_1 Line 031 Line 021	0.019	24.61	2.1	0.2465	0.0053	0.0894	11.37	0.2643	0.0591	0.1755	40.85	79.7891
386	XB_opx_cpx_ol_cross_1 Line 031 Line 021	LOD	29.16	2.84	0.2707	LOD	0.2026	13.27	0.3014	0.0292	0.1789	53.64	99.8928
387	XB_opx_cpx_ol_cross_1 Line 031 Line 021	0.0171	28.46	2.31	0.2846	LOD	0.1487	13.04	0.2877	0.0167	0.2413	53.83	98.6361
388	XB_opx_cpx_ol_cross_1 Line 031 Line 021	0.0373	28.81	3.06	1.71	0.0005	0.2194	12.44	0.2271	0.0108	0.1904	54.53	101.2355
389	XB_opx_cpx_ol_cross_1 Line 031 Line 021	0.0208	25.29	2.7	0.2915	0.007	0.194	12.72	0.2545	0.0549	0.1932	45.93	87.6559
390	XB_opx_cpx_ol_cross_1 Line 031 Line 021	0.055	29.3	3.02	0.6587	0.0041	0.1629	12.89	0.2443	0.0659	0.2041	53.65	100.255
391	XB_opx_cpx_ol_cross_1 Line 031 Line 021	0.2605	29.32	3.06	0.5126	0.0176	0.1846	12.68	0.2387	0.0383	0.184	53.92	100.4163
392	XB_opx_cpx_ol_cross_1 Line 031 Line 021	0.0252	28.81	2.96	1.47	LOD	0.2179	12.14	0.2261	0.0492	0.2464	53.59	99.7348
393	XB_opx_cpx_ol_cross_1 Line 031 Line 021	0.0206	29.24	2.51	0.1993	LOD	0.2336	11.95	0.2679	0.0242	0.2059	45.04	89.6915
394	XB_opx_cpx_ol_cross_1 Line 031 Line 021	0.0063	29.3	3.07	0.4839	0.0041	0.1425	12.91	0.3145	0.0341	0.1869	53.3	99.7523
395	XB_opx_cpx_ol_cross_1 Line 031 Line 021	0.548	15.64	4.81	22.35	0.004	0.3644	4.44	0.1074	0.0375	1.2869	50.34	99.9282
396	std_ol1	LOD	52.51	LOD	0.001	LOD	0.008	6.77	0.1117	0.3992	0.0215	41.62	101.4414
397	std_di1	0.0448	18.89	0.0595	25.64	LOD	LOD	0.0507	0.0586	0.01	0.108	54.96	99.8216
398	std_ab1	11.28	LOD	19.74	0.306	0.2847	LOD	0.0148	0.0077	0.0017	0.0099	68.78	100.4248
399	std_grt	0.0182	4.32	20.44	0.3422	LOD	0.0379	36.15	0.1892	0.0228	0.0196	37.71	99.2499
400	XB_opx_cpx_ol_cross_1 Line 031 Line 021	0.5901	15.53	4.75	21.9	LOD	0.33	4.62	0.0843	0.0183	1.2624	49.91	98.9951
401	XB_opx_cpx_ol_cross_1 Line 031 Line 021	0.0348	28.88	3.14	1.41	LOD	0.258	12.34	0.2356	0.045	0.239	53.93	100.5124

402	XB_opx_cpx_ol_cross_1 Line 031 Line 021	0.0244	29.17	3.11	0.3214	0.0084	0.2108	12.91	0.228	0.0534	0.2188	53.85	100.1052
403	XB_opx_cpx_ol_cross_1 Line 031 Line 021	0.0405	28.91	2.33	0.2763	0.0131	0.1691	12.88	0.2551	0.0534	0.7574	53.87	99.5549
404	XB_opx_cpx_ol_cross_1 Line 031 Line 021	0.0325	28.28	2.75	1.41	0.0055	0.2126	12.81	0.2234	0.0324	1.0529	53.25	100.0593
405	XB_opx_cpx_ol_cross_1 Line 031 Line 021	0.0417	28.62	2.97	1.6	0.0081	0.1785	12.64	0.2658	0.03	0.1693	53.54	100.0634
406	XB_opx_cpx_ol_cross_1 Line 031 Line 021	0.0485	28.42	3.06	1.79	0.0144	0.1585	12.48	0.2485	0.0375	0.1737	53.96	100.3911
407	XB_opx_cpx_ol_cross_1 Line 031 Line 021	0.0701	29.58	2.77	0.3615	0.027	0.1706	12.93	0.2574	0.0642	0.1767	54.03	100.4375
408	XB_opx_cpx_ol_cross_1 Line 031 Line 021	0.0241	29.59	2.61	0.4893	0.0065	0.1739	12.9	0.2468	0.0834	0.1546	54.55	100.8286
409	XB_opx_cpx_ol_cross_1 Line 031 Line 021	0.0314	29.69	2.8	0.3103	0.0634	0.2219	12.76	0.2889	0.0525	0.1881	53.83	100.2365
410	XB_opx_cpx_ol_cross_1 Line 031 Line 021	0.4441	14.56	5.25	23.6	LOD	0.2984	4.42	0.08	0.0308	1.6455	49.29	99.6188
411	XB_opx_cpx_ol_cross_1 Line 031 Line 021	0.0449	28.65	2.93	1.52	0.0079	0.1865	12.48	0.2607	0.0517	0.1737	53.75	100.0554
412	XB_opx_cpx_ol_cross_1 Line 031 Line 021	0.0479	28.99	2.93	0.7551	0.005	0.2034	12.69	0.2617	0.0634	0.2602	54	100.2067
413	XB_opx_cpx_ol_cross_1 Line 031 Line 021	0.1632	29.41	2.32	0.2788	LOD	0.1779	13.76	0.2254	0.0449	1.97	52.45	100.8002
414	XB_opx_cpx_ol_cross_1 Line 031 Line 021	0.0133	29	3.25	0.2708	LOD	0.2064	12.65	0.2107	0.0433	0.1756	53.73	99.5501
415	XB_opx_cpx_ol_cross_1 Line 031 Line 021	0.0253	29.32	2.71	0.1409	LOD	0.2073	13.41	0.2788	0.0492	0.2221	54.08	100.4436
416	XB_opx_cpx_ol_cross_1 Line 031 Line 021	LOD	29.77	2.69	0.2416	0.0073	0.1025	12.79	0.2425	0.0509	0.1502	54.19	100.235
417	XB_opx_cpx_ol_cross_1 Line 031 Line 021	0.0149	29.65	2.77	0.3017	0.0062	0.1474	12.82	0.2031	0.0584	0.1313	53.82	99.923
418	XB_opx_cpx_ol_cross_1 Line 031 Line 021	0.1056	26.55	3.12	5.37	0.019	0.1522	10.76	0.2177	0.0458	0.8531	52.46	99.6534
419	XB_opx_cpx_ol_cross_1 Line 031 Line 021	0.0167	29.38	2.65	1.0248	0.0203	0.0932	12.85	0.2848	0.0651	0.1958	53.8	100.3807
420	XB_opx_cpx_ol_cross_1 Line 031 Line 021	0.0233	29.66	2.58	0.4167	0.0003	0.1892	12.81	0.2465	0.0575	0.1051	53.86	99.9486
421	XB_acrossopx_line1 Line 001	0.0058	29.4	3.14	0.3163	0.0079	0.2268	12.66	0.2479	0.0409	0.1724	53.8	100.018
422	XB_acrossopx_line1 Line 002	0.0282	29.34	2.49	0.9693	0.0004	0.1862	13.03	0.2301	0.0441	1.1584	53.45	100.9267
423	XB_acrossopx_line1 Line 003	0.0782	27.41	2.67	4.02	LOD	0.2257	11.13	0.1819	0.0484	0.2073	54.02	99.9915
424	XB_acrossopx_line1 Line 004	LOD	29.39	2.84	0.5147	0.0246	0.1814	12.71	0.2843	0.0091	0.1374	53.98	100.0715
425	XB_acrossopx_line1 Line 005	0.0519	28.87	3.07	1.2588	0.0071	0.1878	12.73	0.2474	0.0441	0.2551	54.32	101.0422
426	XB_acrossopx_line1 Line 006	0.0504	28.39	3	1.69	LOD	0.1478	12.18	0.2791	0.0083	0.2019	54.12	100.0675
427	XB_acrossopx_line1 Line 007	0.0422	28.76	3.24	1.74	LOD	0.1959	12.53	0.2466	0.0342	0.3062	53.53	100.6251
428	XB_acrossopx_line1 Line 008	0.1758	25.54	3.55	6.1	0.0085	0.2641	10.35	0.1796	0.0633	0.5021	52.71	99.4434
429	XB_acrossopx_line1 Line 009	0.0329	29.53	2.82	0.6149	0.0174	0.1799	13.01	0.2508	0.0442	0.1465	54.17	100.8166
430	XB_acrossopx_line1 Line 010	0.5292	14.5	5.13	23.04	0.009	0.2865	5.01	0.0997	LOD	1.517	49.91	100.0314
431	XB_acrossopx_line1 Line 011	0.0582	29.56	3.36	0.5187	LOD	0.231	13.06	0.293	0.0416	0.3046	53.41	100.8371
432	XB_acrossopx_line1 Line 012	0.1039	25.82	3.88	6.15	0.0009	0.2841	10.43	0.2512	0.0175	0.4954	51.94	99.373

433	XB_acrossopx_line1 Line 013	LOD	41.92	LOD	LOD	0.0019	0.0105	19.65	0.2318	0.2333	0.0153	38.97	101.0328
434	XB_acrossopx_line1 Line 014	0.0898	29.54	3.32	0.5424	0.0126	0.203	12.66	0.2537	0.0258	0.2083	53.56	100.4156
435	XB_acrossopx_line1 Line 015	0.0851	28.08	3.32	2.96	LOD	0.2415	11.74	0.2616	0.0308	0.3054	53.74	100.7644
436	XB_acrossopx_line1 Line 016	0.0719	27.12	2.89	3.45	0.0019	0.224	12.33	0.2192	0.0341	0.2766	52.31	98.9277
437	XB_acrossopx_line1 Line 017	LOD	29.89	3.3	0.2321	LOD	0.1784	12.61	0.2366	0.0175	0.1316	54.07	100.6662
438	XB_acrossopx_line1 Line 018	LOD	LOD	LOD	LOD	LOD	0.0281	82.83	0.0142	LOD	LOD	0.0211	82.8934
439	XB_acrossopx_line1 Line 019	0.0671	28.14	3.48	2.76	LOD	0.2229	11.84	0.2248	0.0366	0.328	53.25	100.3494
440	XB_acrossopx_line1 Line 020	0.0457	28.19	3.43	2.67	0.0027	0.195	12.02	0.2206	0.0517	0.3784	53.7	100.9041
441	std_ol1	0.0682	52.68	0.0006	LOD	0.0064	0.0032	6.66	0.0929	0.4064	LOD	41.84	101.7577
442	std_di1	0.0094	18.55	0.0385	25.73	LOD	LOD	0.0583	0.074	LOD	0.0816	55.73	100.2718
443	std_ab1	11.33	LOD	19.83	0.3802	0.1895	LOD	0.0101	LOD	LOD	0.0136	69.04	100.7934
444	std_grt	0.0548	4.31	20.41	0.3771	0.0008	0.0239	36.49	0.2111	LOD	LOD	37.62	99.4977
445	XB_opxcross_line2 Line 001	0.0775	18.34	1.185	1.64	LOD	0.0445	4.84	0.1282	0.0318	0.0883	38.79	65.1653
446	XB_opxcross_line2 Line 002	0.027	22.37	1.5653	0.5724	0.0083	0.1465	9.56	0.2122	0.0509	0.0846	46.3	80.8972
447	XB_opxcross_line2 Line 003	0.0644	20.95	1.0569	1.68	0.0018	0.1446	10.63	0.2105	0.0249	1.5682	45.88	82.2113
448	XB_opxcross_line2 Line 004	0.0656	23.72	1.6508	0.4418	0.0091	0.1104	10.29	0.2216	0.0384	0.107	48.06	84.7147
449	XB_opxcross_line2 Line 005	0.1112	24.33	1.92	0.5542	0.0074	0.1349	11.08	0.2073	0.015	0.1325	48.83	87.3225
450	XB_opxcross_line2 Line 006	0.0686	24.05	2.18	1.3668	LOD	0.1915	10.5	0.2042	0.0683	0.1746	49.46	88.264
451	XB_opxcross_line2 Line 007	0.1019	24.75	1.97	1.2888	LOD	0.2495	11.3	0.2123	0.0441	0.1955	49.86	89.9721
452	XB_opxcross_line2 Line 008	0.0327	25.64	2.19	0.4731	0.0042	0.1345	11.76	0.249	0.0524	0.1975	50.28	91.0134
453	XB_opxcross_line2 Line 009	0.0331	26.25	2.17	0.7583	LOD	0.1346	11.9	0.2122	0.0349	0.1488	50.81	92.4519
454	XB_opxcross_line2 Line 010	0.0504	26.22	2.47	1.1583	0.0015	0.1841	12.12	0.2079	0.0307	0.1628	51.17	93.7757
455	XB_opxcross_line2 Line 011	0.0366	26.79	2.52	0.4451	LOD	0.1481	12.51	0.2595	0.0382	0.207	51.68	94.6345
456	XB_opxcross_line2 Line 012	0.0335	27.42	2.59	0.615	0.0052	0.1989	12.61	0.2722	0.0771	0.1538	52.44	96.4157
457	XB_opxcross_line2 Line 013	0.4374	15.32	3.35	17.82	0.0192	0.2291	6.79	0.1392	0.0421	3.54	47.2	94.887
458	XB_opxcross_line2 Line 014	0.0183	28.32	2.82	0.3266	LOD	0.148	13.07	0.2421	0.0622	0.2057	52.56	97.7729
459	XB_opxcross_line2 Line 015	0.0133	28.54	2.52	0.6479	LOD	0.1481	13.02	0.2594	0.078	0.2631	53.05	98.5398
460	XB_opxcross_line2 Line 016	0.0621	27.58	2.72	2.57	0.0069	0.1661	11.87	0.2317	0.0266	0.2218	53.31	98.7652
461	XB_opxcross_line2 Line 017	0.0177	29.63	2.42	0.3406	0.0009	0.1526	13.21	0.2819	0.024	0.182	53.79	100.0497
462	XB_opxcross_line2 Line 018	0.0203	29.28	2.76	0.7483	0.0253	0.1914	12.91	0.2485	0.0398	0.3175	53.94	100.4811
463	XB_opxcross_line2 Line 019	0.0297	28.38	3.11	2.04	0.0054	0.2393	13.21	0.2601	0.0165	1.1492	52.55	100.9902

464	XB_opxcross_line2 Line 020	0.0368	29.34	2.77	0.5542	LOD	0.1713	12.76	0.2581	0.0381	0.2919	54.57	100.7904
465	XB_cpxcross_line2 Line 001	0.5262	16.86	4.6	18.87	0.0038	0.3973	6.85	0.1695	0.033	1.2825	50.76	100.3523
466	XB_cpxcross_line2 Line 002	0.5756	14.94	4.94	21.66	0.0081	0.4895	5.3	0.122	0.019	1.4641	50.4	99.9183
467	XB_cpxcross_line2 Line 003	0.2844	27.23	3.24	8.7	0.0066	0.2396	8.81	0.2445	0.0199	0.6044	50.29	99.6694
468	XB_cpxcross_line2 Line 004	0.6381	14.21	4.92	22.64	LOD	0.4231	5.08	0.1287	0.0066	1.3789	49.96	99.3854
469	XB_cpxcross_line2 Line 005	0.6304	14.54	4.98	22.6	LOD	0.3942	5.11	0.144	0.0157	1.4777	49.54	99.432
470	XB_cpxcross_line2 Line 006	0.546	14.48	4.94	22.77	LOD	0.4471	5.12	0.1112	0.0348	1.4708	49.92	99.8399
471	XB_cpxcross_line2 Line 007	0.5025	14.54	4.64	23.21	0.0094	0.3705	4.95	0.1374	0.0307	1.3947	50.39	100.1752
472	XB_cpxcross_line2 Line 008	0.604	14.92	4.95	22.27	LOD	0.3797	5.14	0.1112	0.0414	1.4464	49.4	99.2627
473	XB_cpxcross_line2 Line 009	0.5563	14.37	4.77	22.82	LOD	0.4728	5.08	0.121	0.0298	1.3689	50.33	99.9188
474	XB_cpxcross_line2 Line 010	0.5516	14.48	4.75	23.03	0.0006	0.4666	5.28	0.1332	0.0141	1.3315	49.99	100.0276
475	XB_cpxcross_line2 Line 011	0.5643	14.38	5.11	23.36	LOD	0.4207	4.78	0.1627	0.01	1.5182	49.92	100.2259
476	XB_cpxcross_line2 Line 012	0.6736	14.93	4.61	23.15	LOD	0.3904	4.67	0.1224	0.0208	1.2491	50.33	100.1463
477	XB_cpxcross_line2 Line 013	0.4963	14.6	4.79	23.24	0.0088	0.43	5.08	0.1266	LOD	1.4245	50.21	100.4062
478	XB_cpxcross_line2 Line 014	0.5133	14.77	5.04	21.97	LOD	0.4373	5.5	0.1276	LOD	1.4865	49.82	99.6647
479	XB_cpxcross_line2 Line 015	0.559	14.87	4.66	22.31	0.0035	0.3684	5.49	0.1778	0.0274	1.267	49.81	99.5431
480	XB_cpxcross_line2 Line 016	0.5235	14.81	4.46	23.24	LOD	0.4501	4.52	0.0984	0.0058	1.1916	51.04	100.3394
481	XB_cpxcross_line2 Line 017	0.5557	14.77	4.87	21.68	0.0036	0.4061	6.07	0.1417	0.0265	1.3218	49.75	99.5954
482	XB_cpxcross_line2 Line 018	0.5278	14.63	4.9	23.09	LOD	0.4833	4.76	0.1453	0.0531	1.3027	50.34	100.2322
483	XB_cpxcross_line2 Line 019	0.5575	14.53	5.34	22.64	0.0057	0.5759	5.01	0.1517	0.0091	1.4673	49.47	99.7572
484	XB_cpxcross_line2 Line 020	0.0082	29.67	2.76	0.2299	LOD	0.1593	12.58	0.2489	0.0033	0.1091	54.44	100.2087
485	std_ol1	0.0056	52.83	LOD	LOD	LOD	LOD	6.78	0.1255	0.4039	0.0079	41.62	101.7729
486	std_di1	0.0171	18.58	0.0394	25.7	0.0001	0.013	0.0194	0.0683	0.0191	0.0642	55.59	100.1106
487	std_ab1	11.41	LOD	19.87	0.3793	0.2032	LOD	0.0096	0.0088	0.0293	LOD	68.77	100.6802
488	std_grt	0.0462	4.41	20.66	0.3411	LOD	LOD	36.31	0.2198	LOD	0.0052	37.25	99.2423
489	XB_cpxcross_line2 Line 020	0.0053	29.7	2.73	0.2411	LOD	0.1794	12.84	0.2804	0.0707	0.1276	54.3	100.4745
490	XB_opxcross_line3 Line 001	0.1281	25.99	2.42	6.87	0.0072	0.1931	10.14	0.2043	0.0341	0.6073	53.88	100.4741
491	XB_opxcross_line3 Line 002	LOD	28.96	3.03	0.9389	LOD	0.1963	12.77	0.2509	0.0133	0.1582	53.54	99.8576
492	XB_opxcross_line3 Line 003	0.085	29.01	2.72	0.2927	0.0023	0.1919	12.5	0.274	0.0399	0.3554	53.49	98.9612
493	XB_opxcross_line3 Line 004	LOD	29.63	1.6955	0.4067	LOD	0.1486	12.72	0.2849	0.0549	0.0662	55.33	100.3368
494	XB_opxcross_line3 Line 005	0.3408	0.0024	LOD	1.53	0.0015	LOD	7.78	0.0088	LOD	LOD	LOD	9.6635

Appendix F XRD Analysis

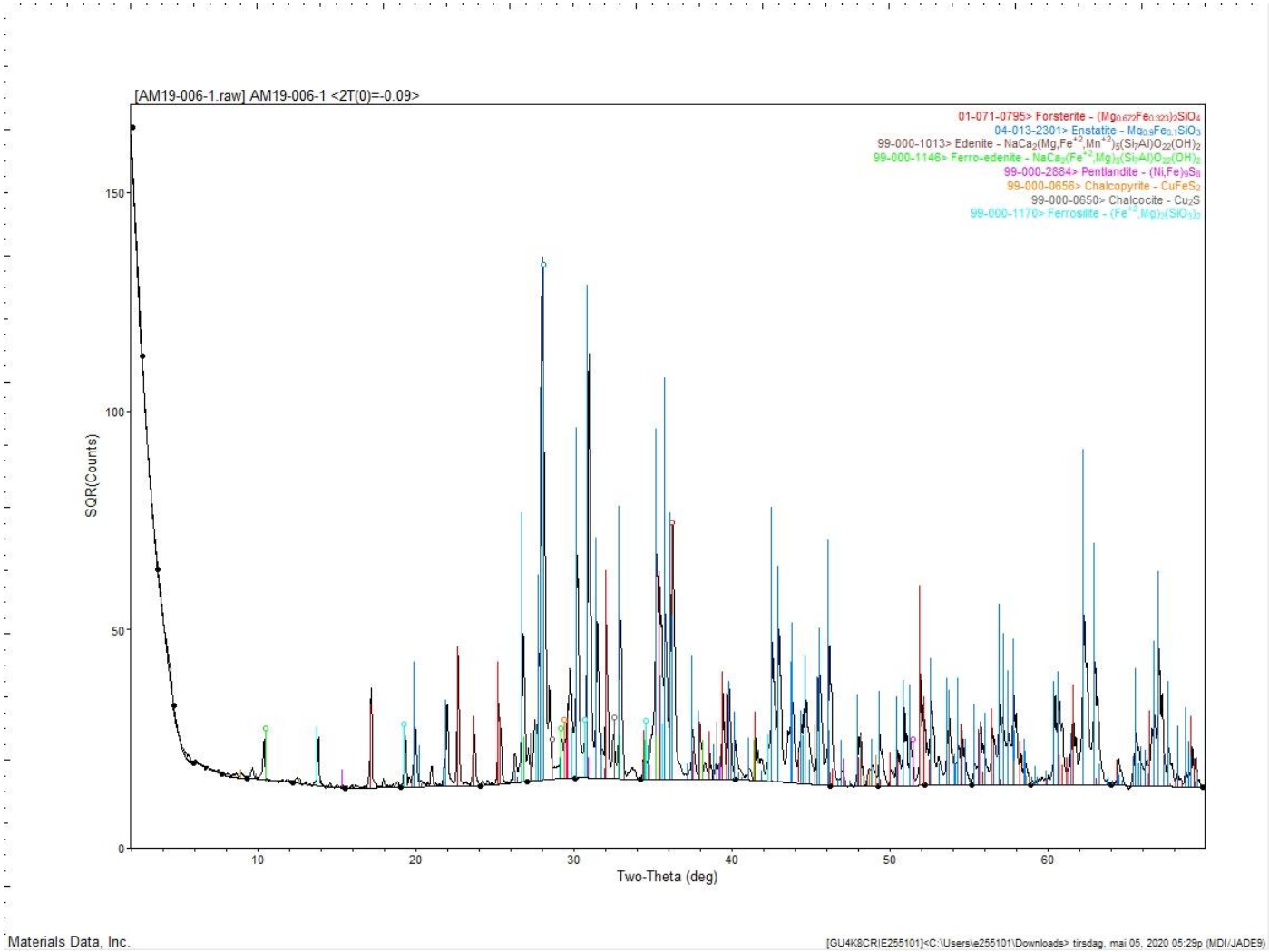

Figure 8.14: *XRD results from sample AM19-006-1.*

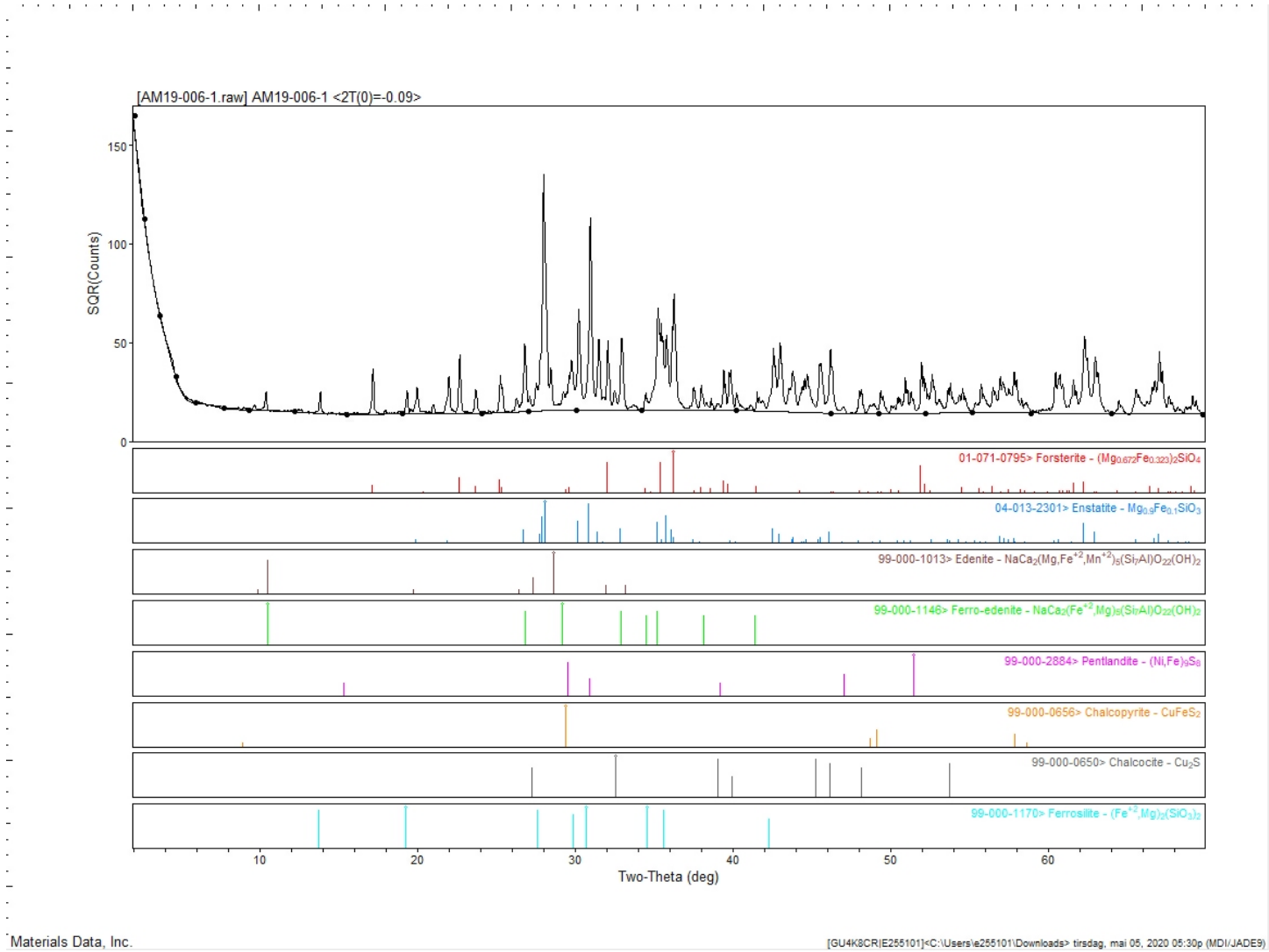

Figure 8.14a: *XRD results from sample AM19-006-1 (part-image view).*

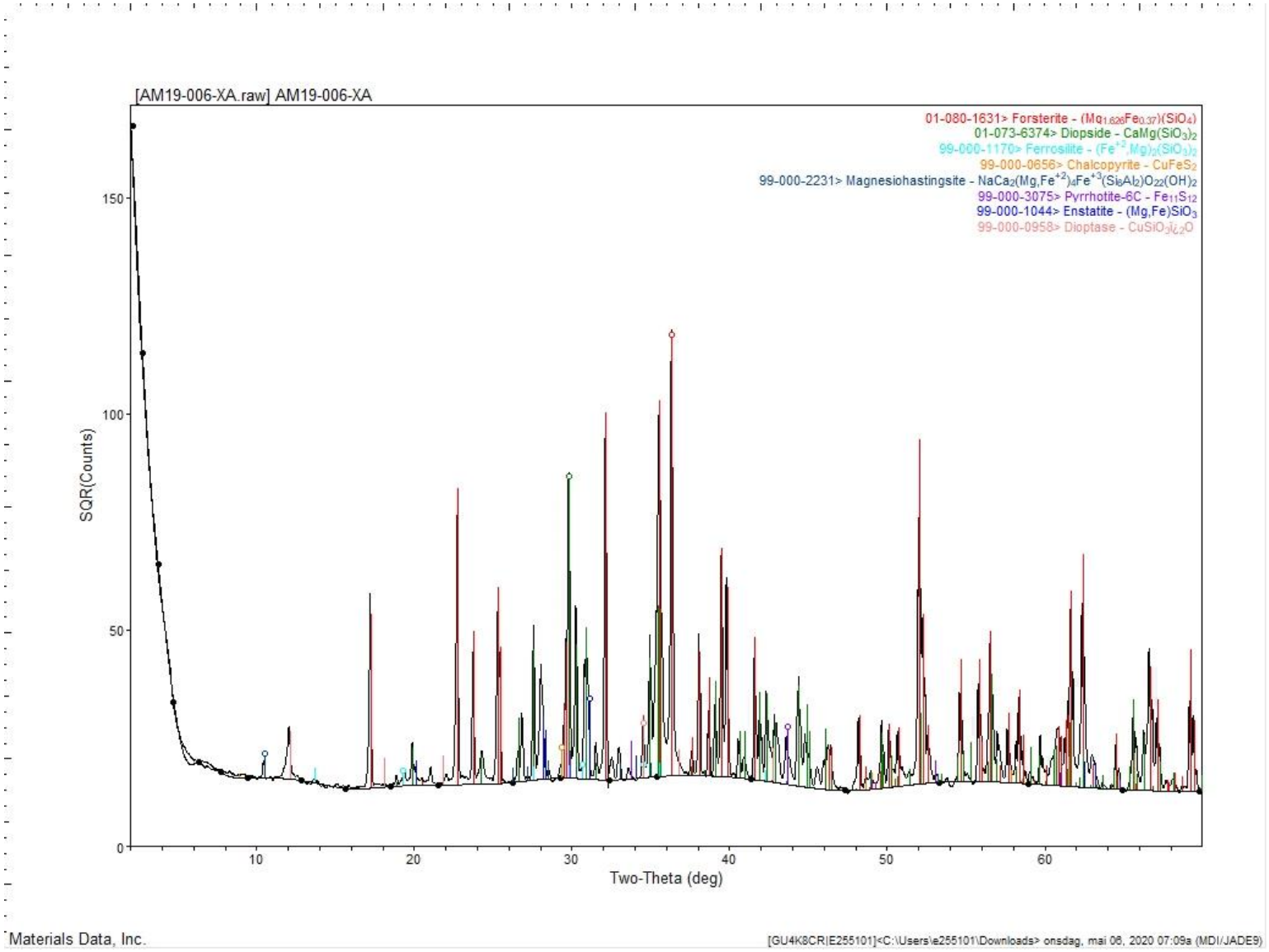

Figure 8.15: *XRD results from sample AM19-006-XA.*

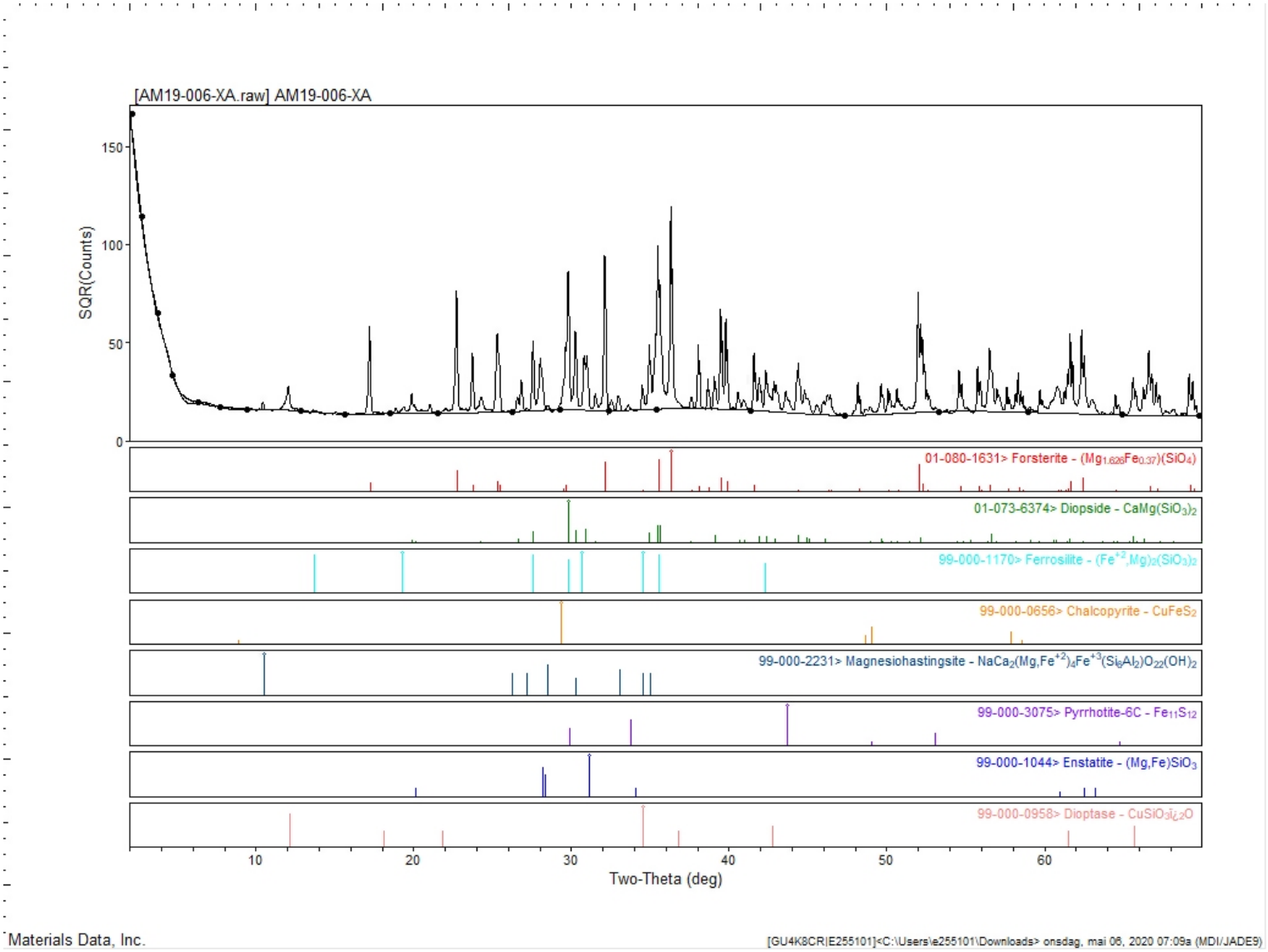

Figure 8.15a: *XRD results from sample AM19-006-XA (part-image view).*

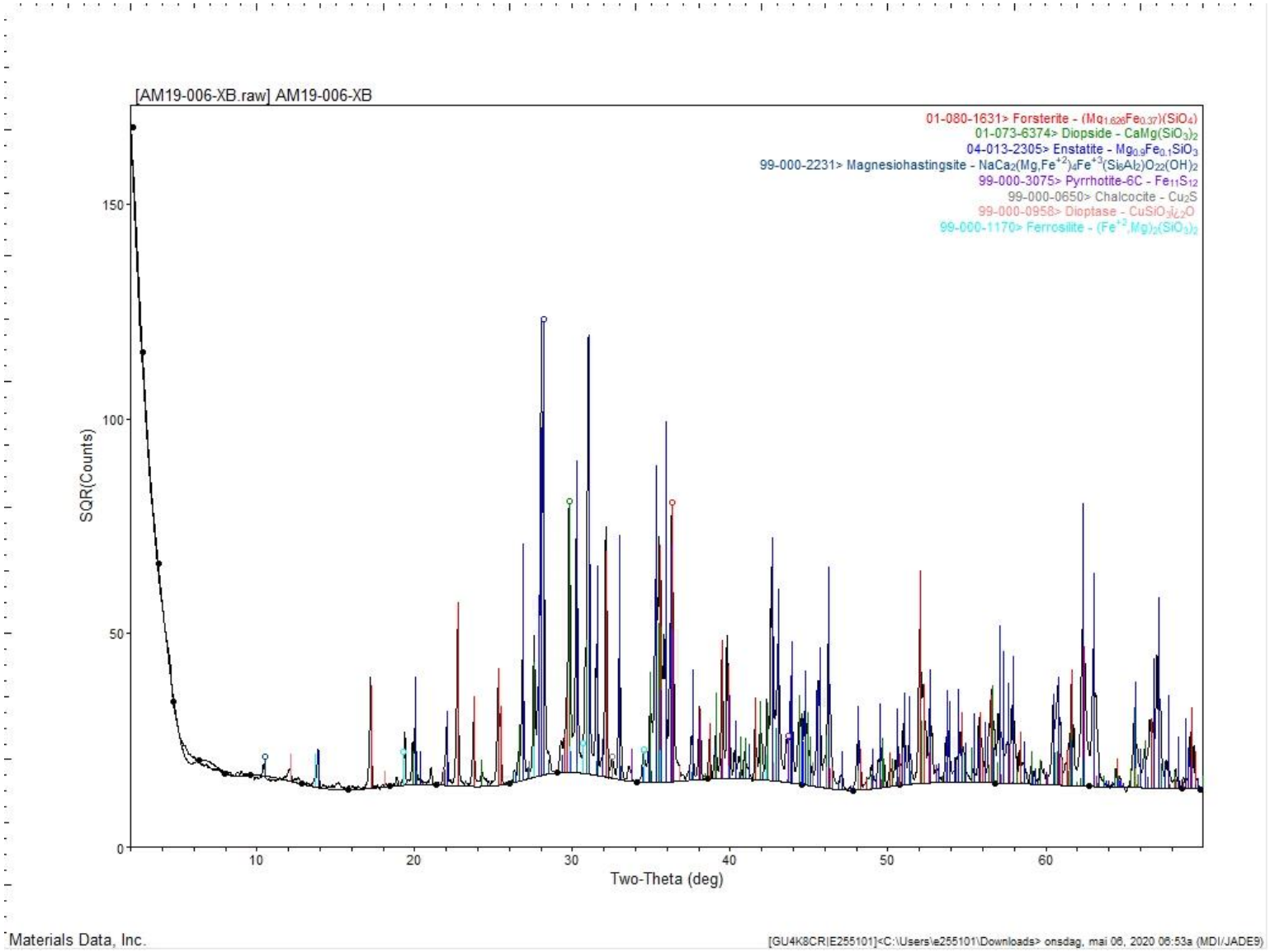

Figure 8.16: *XRD results from sample AM19-006-XB.*

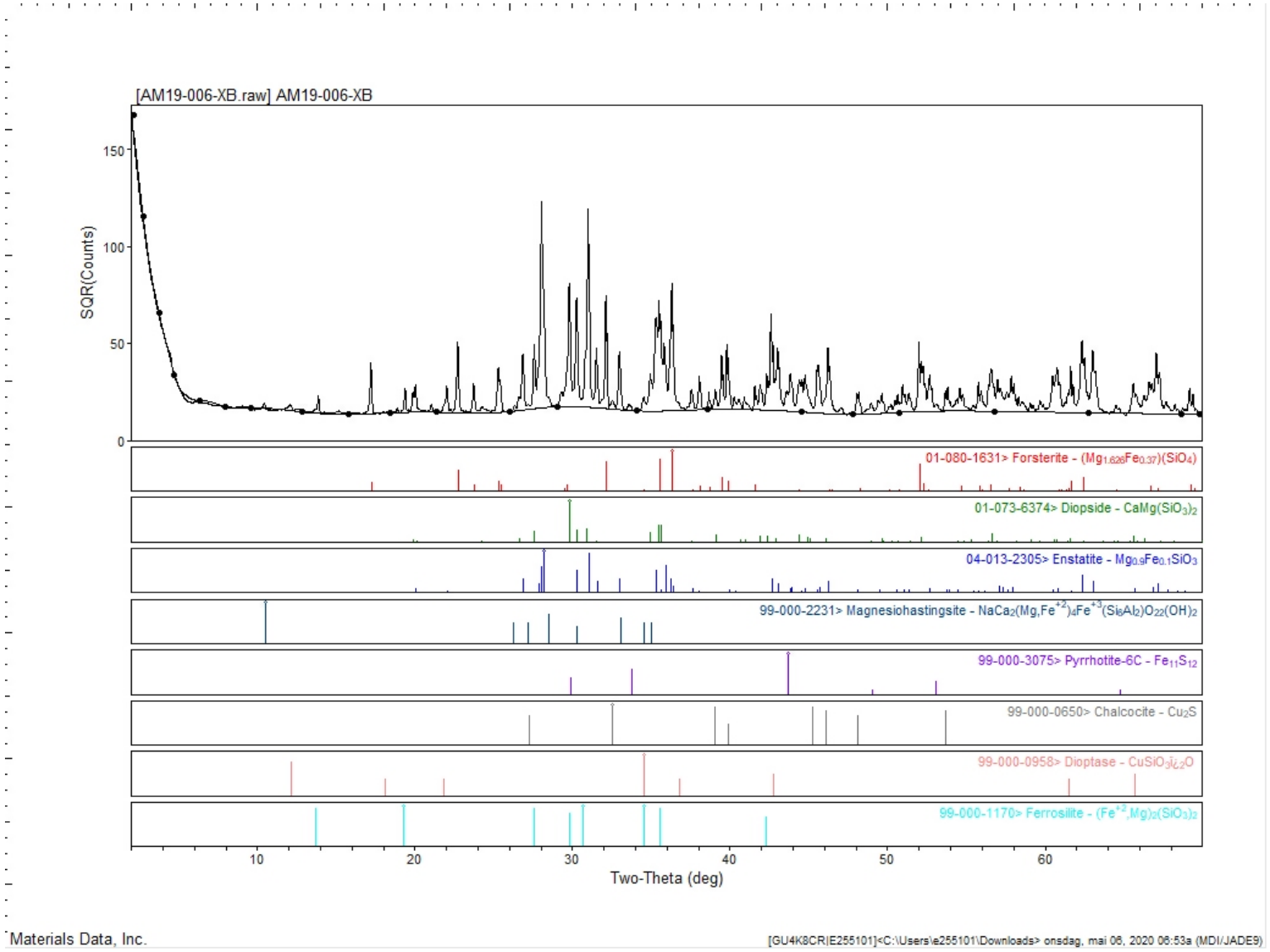

Figure 8.16a: *XRD results from sample AM19-006-XB (part-image view).*

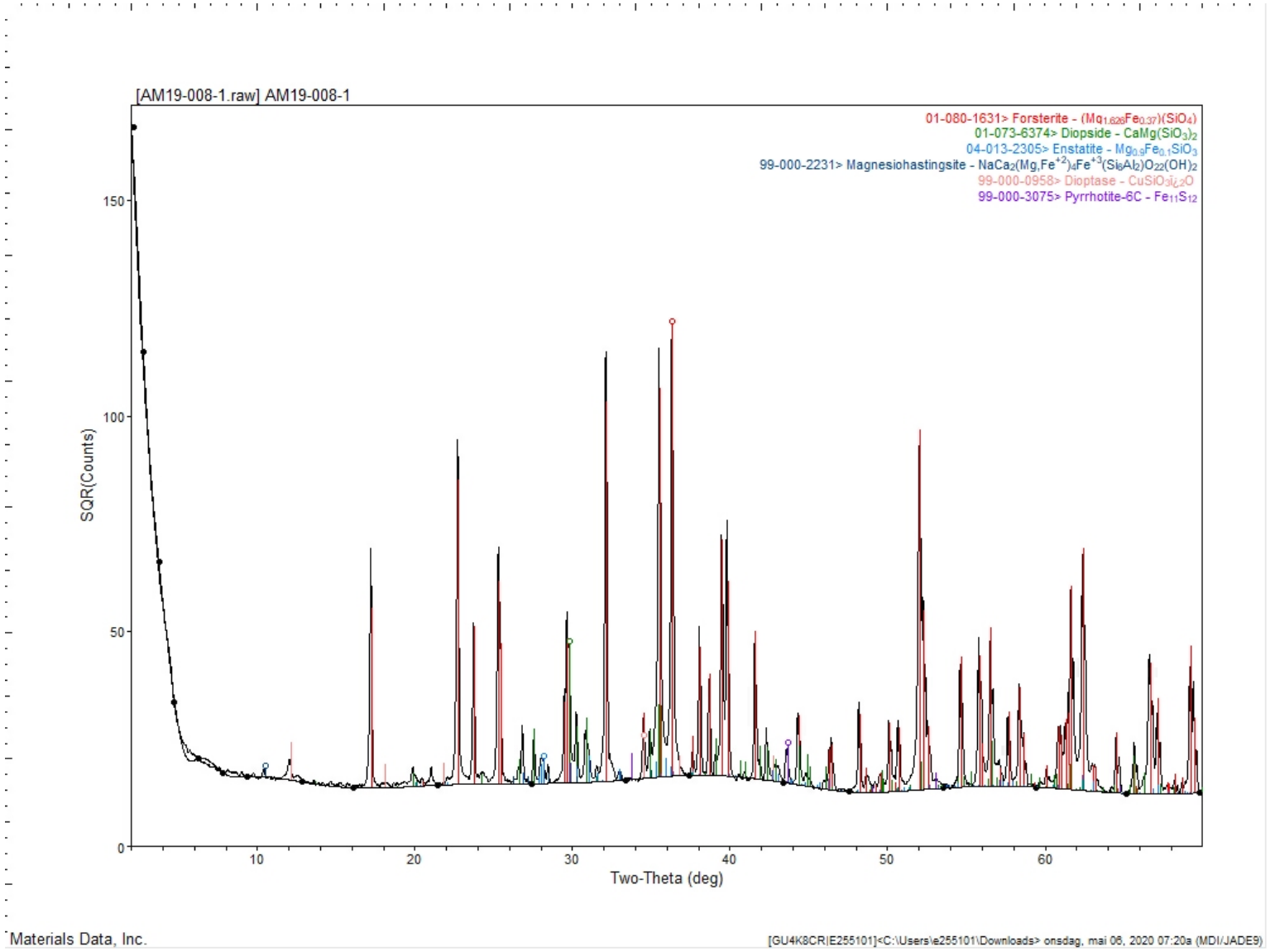

Figure 8.17: *XRD results from sample AM19-008-1.*

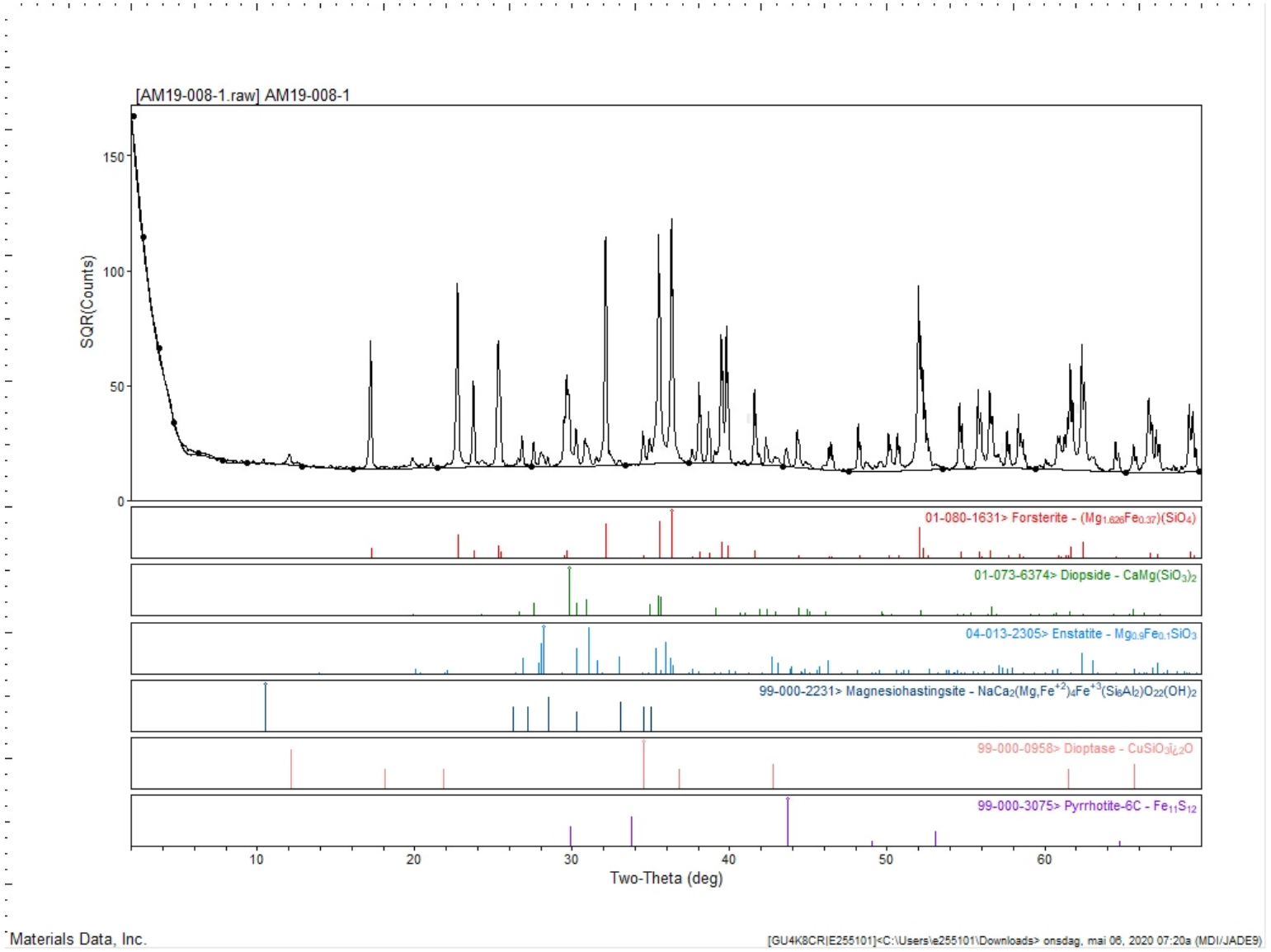

Figure 8.17a: *XRD results from sample AM19-008-1 (part-image view).*

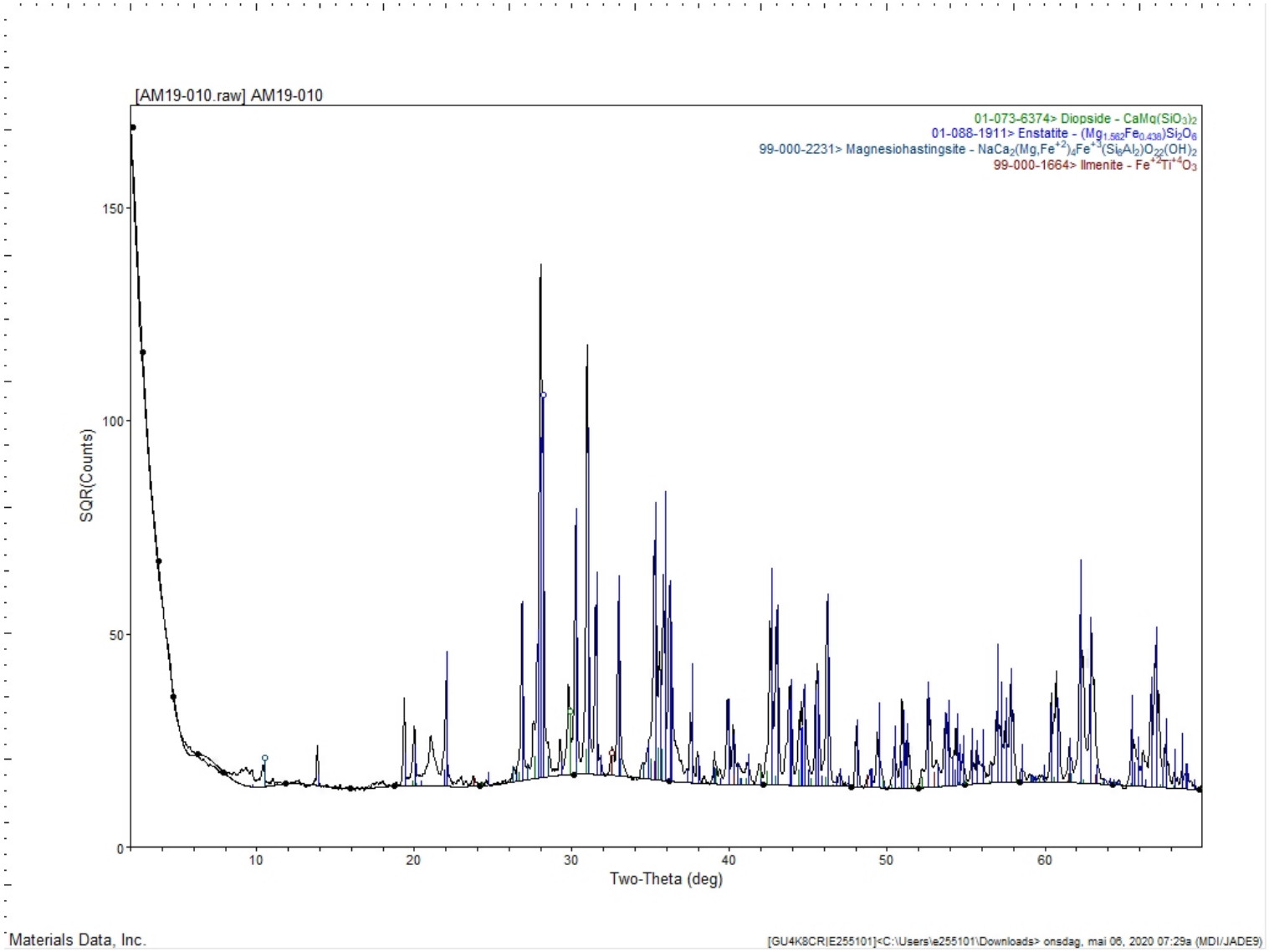

Figure 8.18: *XRD results from sample AM19-010.*

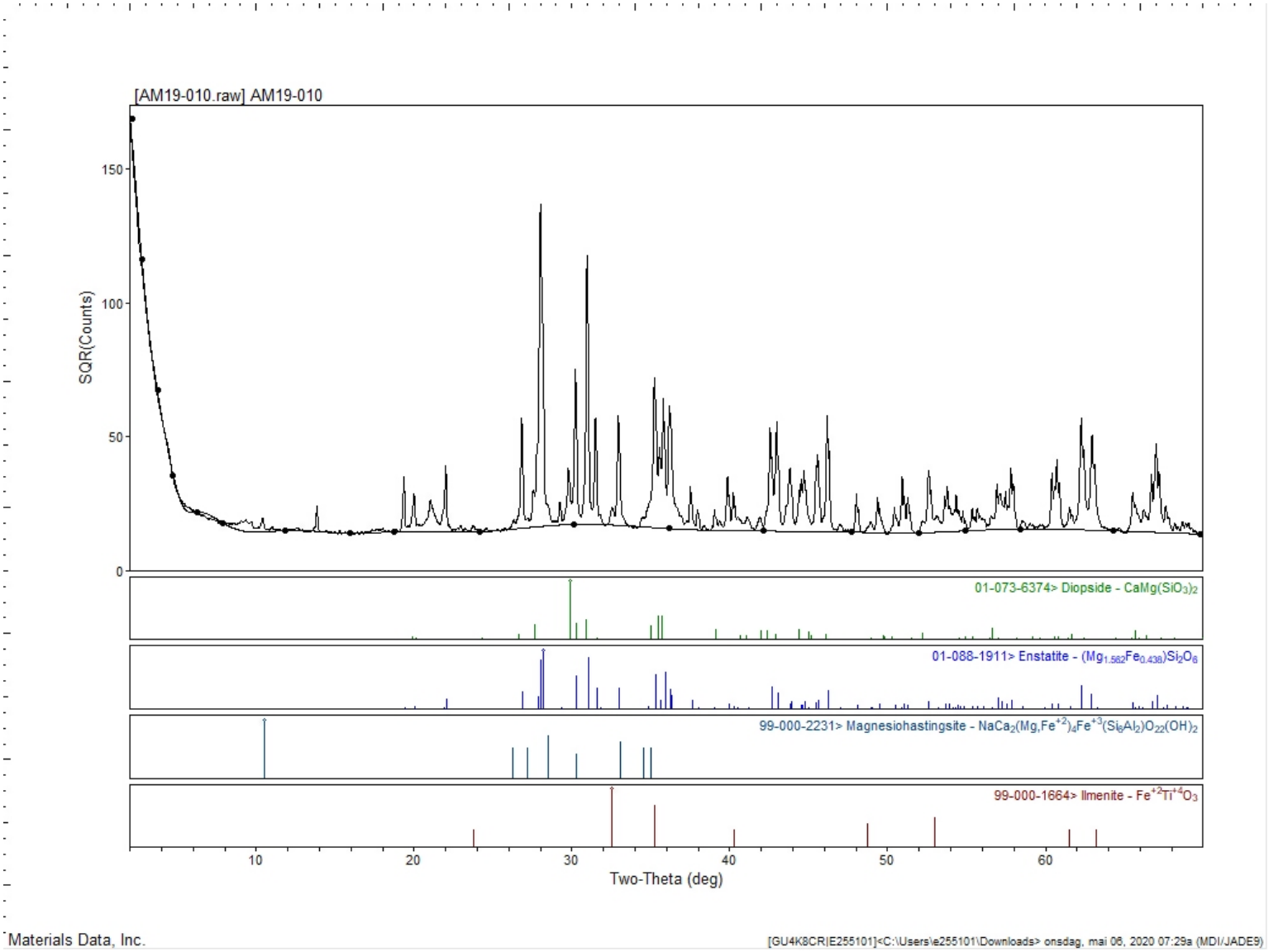

Figure 8.18a: *XRD results from sample AM19-010 (part-image view).*

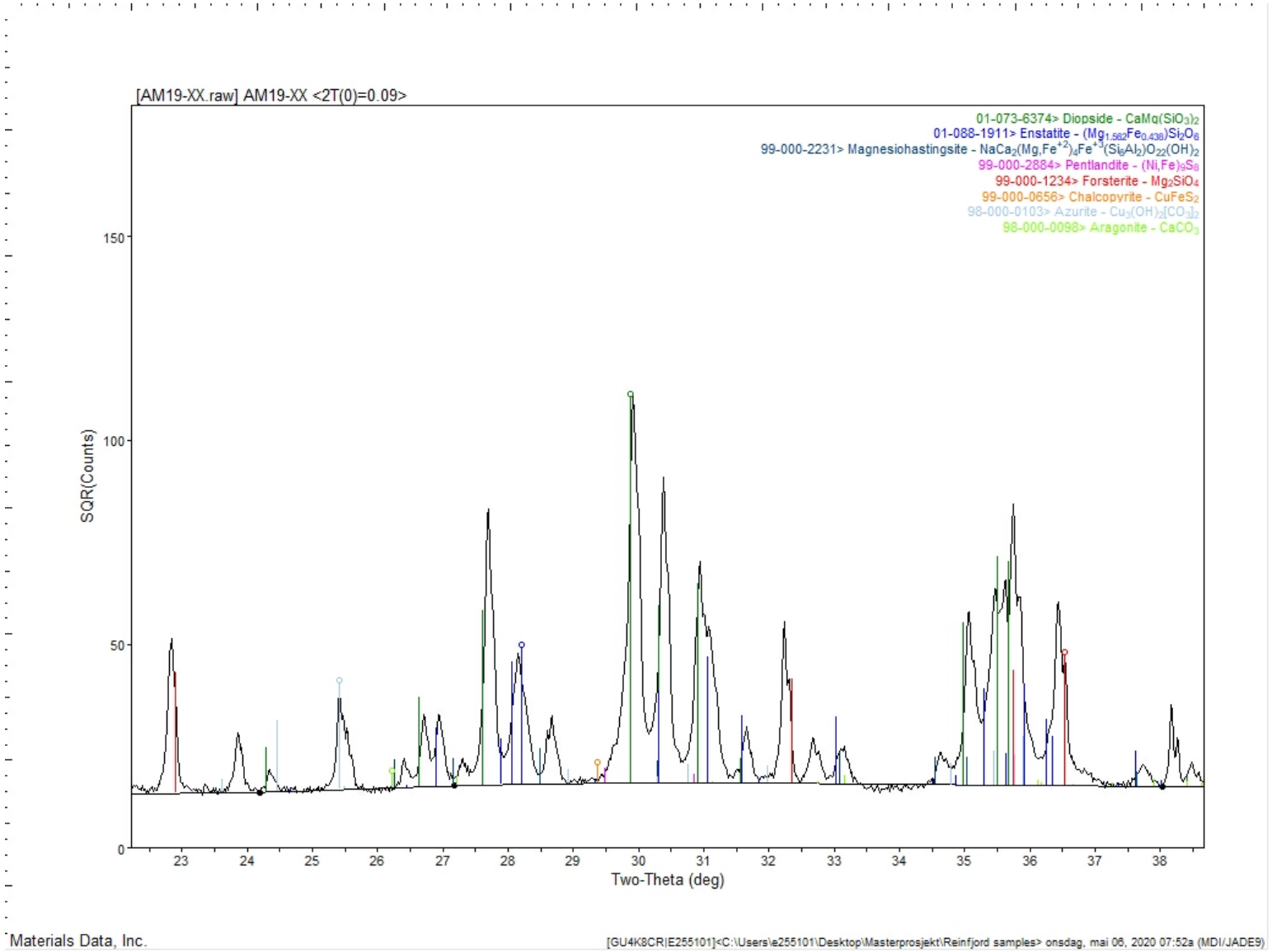

Figure 8.19: *XRD results from sample AM19-XX.*

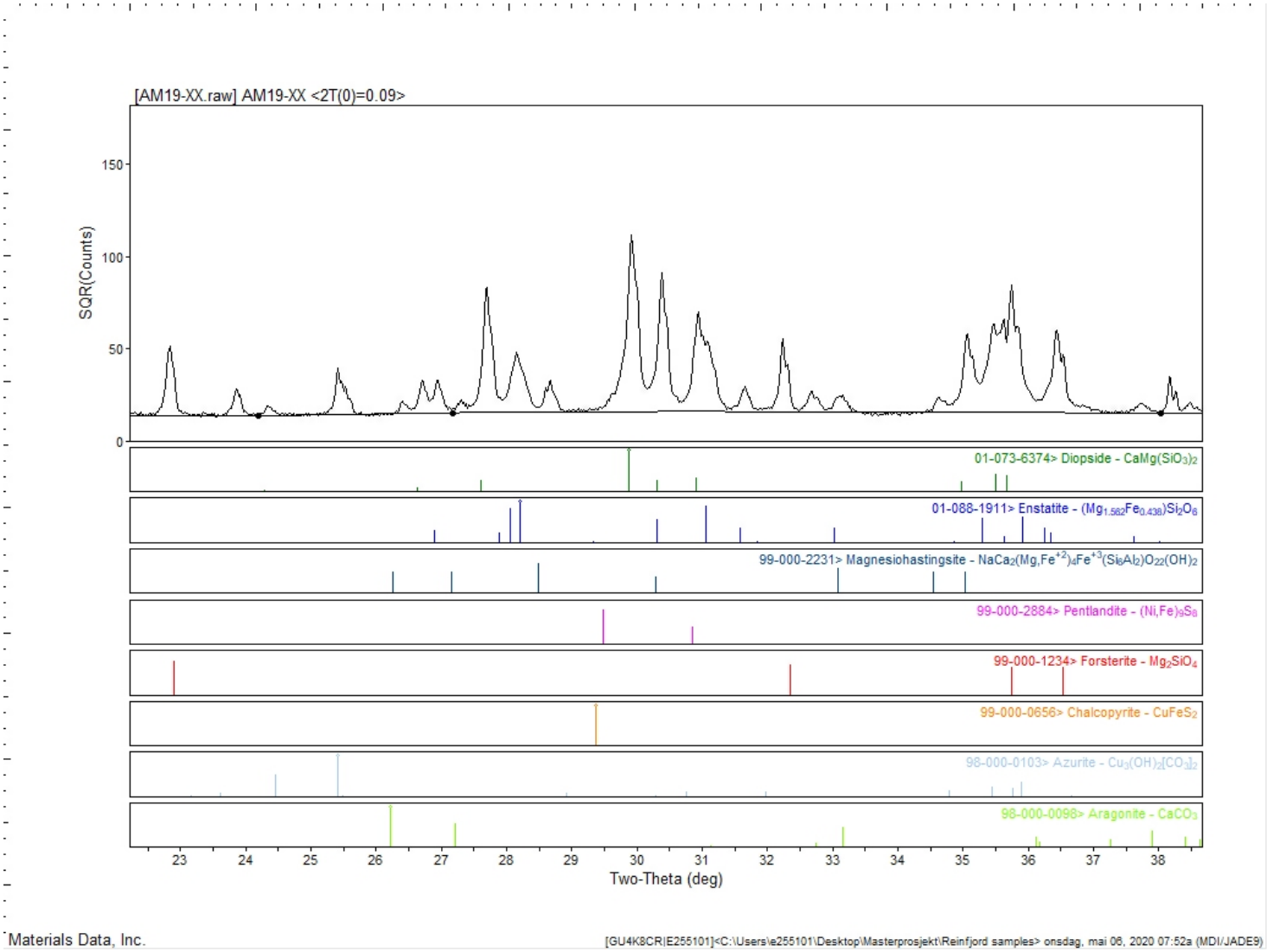

Figure 8.19a: *XRD results from sample AM19-XX (part-image view).*

Appendix G

Geochemical Comparison: Drillhole RF-1 to Pyroxenite Pegmatite

Table 8.31: *Geochemical analysis of major elements comparing drillhole RF-1 to pyroxenite pegmatite samples from this study. Highlighted in yellow is primary and notable differences of interest.*

SAMPLE	Depth from	Depth to	Au__ppb master	Pd_ppb master	Pt_ppb master	Pt/Pd	Au/(Pt+Pd)	SiO2175X	Al2O3175X	Fe2O3175X	CaO175X	MgO175X	Na2O175X	K2O175X	TiO2175X	MnO175X	P2O5175X
RF-1	107.75	109.45	22	297	271	0.91	0.04	43.2	1.8	17.4	1.29	32.4	0.086	0.009	0.361	0.217	0.014
RF-1	110.2	110.6	47	117	69	0.59	0.25	47.9	2.89	15.4	1.83	28	0.174	0.024	0.56	0.217	0.014
SAMPLE DESCRIPTION	Pass2mm %	Pass75um %	Au ppb	Pt ppb	Pd ppb	Pt/Pd	Au/(Pt+Pd)	SiO2 %	Al2O3 %	Fe2O3 %	CaO %	MgO %	Na2O %	K2O %	TiO2 %	MnO %	P2O5 %
AM19-006-1-1	79.8	97.2	4	8	5	1.6	0.30769231	51.3	3.66	15.3	2.72	25.5	0.22	0.05	0.72	0.23	0.03
AM19-006-1-2			4	8	6	1.33333333	0.28571429	50.7	3.97	14.35	4.16	24	0.28	0.06	0.8	0.22	0.02
AM19-006-1-3			5	8	6	1.33333333	0.35714286	49.8	2.62	16.35	1.65	28.1	0.09	0.02	0.5	0.24	0.02
AM19-008-2-1			4	9	11	0.81818182	0.2	46.8	4.07	14	9.31	22.1	0.38	0.05	1.12	0.21	0.02
AM19-008-2-2			5	8	6	1.33333333	0.35714286	46.7	4.36	16.1	7.25	23.7	0.46	0.05	1.18	0.21	0.03
AM19-008-2-3			6	12	10	1.2	0.27272727	48	4.04	14.35	9.06	21.9	0.39	0.04	1.13	0.21	0.02
AM19-008-3			7	12	11	1.09090909	0.30434783	50.7	3.12	15.55	3.27	25.4	0.16	0.03	0.66	0.23	0.01
AM19-008-4			2	8	7	1.14285714	0.13333333	50.2	2.98	16.4	2.24	27.2	0.13	0.03	0.6	0.23	0.01
AM19-XX			1	5	1	5	0.16666667	49.1	4.54	9.36	17.75	16.75	0.5	0.01	1.24	0.17	0.01
AM19-007-02			1	5	1	5	0.16666667	46.7	4.46	12.15	14.65	19.65	0.48	0.01	1.1	0.18	0.01

Table 8.32: *Geochemical analysis of minor elements comparing drillhole RF-1 to pyroxenite pegmatite samples from this study. Highlighted in red is primary and notable differences of interest.*

SAMPLE	Depth from	Depth to	Ba175X	Ce175X	Cr, ppm	Ga175X	La175X	Nb175X	Rb175X	Sn175X	Sr175X	Th175X	U175X	V175X	Y175X	Zr175X
RF-1	107.75	109.45	<0.003	<0.003	1268	<0.002	<0.003	<0.0007	0.0018	0.0022	<0.001	<0.001	<0.001	0.0082	<0.0007	<0.001
RF-1	110.2	110.6	<0.003	<0.003	1798	<0.002	<0.003	<0.0007	0.0014	0.0023	0.0017	<0.001	<0.001	0.0118	<0.0007	0.0016
SAMPLE DESCRIPTION			**Ba ppm**	**Ce ppm**	**Cr ppm**	**Ga ppm**	**La ppm**	**Nb ppm**	**Rb ppm**	**Sn ppm**	**Sr ppm**	**Th ppm**	**U ppm**	**V ppm**	**Y ppm**	**Zr ppm**
AM19-006-1-1	n/a	n/a	**15.4**	**3.3**	1710	**8.4**	**1.5**	**2.2**	1.4	2	**40**	0.13	<0.05	**172**	4.6	18
AM19-006-1-2	n/a	n/a	**15.7**	**3.9**	1900	**8.1**	**1.7**	**2.2**	0.9	1	**47.1**	0.15	0.05	**200**	5.5	21
AM19-006-1-3	n/a	n/a	**6**	**1.5**	1340	**7**	**0.7**	**0.8**	0.9	1	**8.5**	0.13	<0.05	**119**	3	10
AM19-008-2-1	n/a	n/a	**11.2**	**5.7**	2290	**8.1**	**2**	**2.5**	1	1	**44.6**	0.18	0.07	**225**	9.5	33
AM19-008-2-2	n/a	n/a	**13.9**	**6.6**	1790	**8.1**	**2.4**	**3.6**	1	1	**85.6**	0.17	<0.05	**204**	8.6	34
AM19-008-2-3	n/a	n/a	**7.5**	**5.5**	2160	**8**	**2**	**2.2**	0.8	1	**41.7**	0.15	0.06	**234**	9.1	30
AM19-008-3	n/a	n/a	**6.1**	**2**	1740	**6.8**	**0.9**	**1.2**	0.7	1	**11.2**	0.08	<0.05	**162**	4.4	15
AM19-008-4	n/a	n/a	**7.6**	**2**	1450	**8**	**0.9**	**1.1**	0.7	1	**13.8**	0.1	<0.05	**119**	3.7	13
AM19-XX	n/a	n/a	**4.3**	**7.5**	4560	**11.4**	**2.1**	**0.7**	0.5	2	**48.4**	0.08	<0.05	**301**	15.9	35
AM19-007-02	n/a	n/a	**3.6**	**6.5**	2200	**7.7**	**1.8**	**0.5**	<0.2	2	**55.8**	<0.05	<0.05	**247**	12	32